Environmental Engineering

Liangtong Zhan · Yunmin Chen
Abdelmalek Bouazza *Editors*

Proceedings of the 8th International Congress on Environmental Geotechnics Volume 3

Towards a Sustainable Geoenvironment

Springer

Environmental Science and Engineering

Environmental Engineering

Series editors

Ulrich Förstner, Hamburg, Germany
Wim H. Rulkens, Wageningen, The Netherlands
Wim Salomons, Haren, The Netherlands

More information about this series at http://www.springer.com/series/3172

Liangtong Zhan · Yunmin Chen
Abdelmalek Bouazza
Editors

Proceedings of the 8th International Congress on Environmental Geotechnics Volume 3

Towards a Sustainable Geoenvironment

Springer

Editors
Liangtong Zhan
MOE Key Laboratory of Soft Soils and Geoenvironmental Engineering, College of Civil Engineering and Architecture
Zhejiang University
Hangzhou, China

Yunmin Chen
MOE Key Laboratory of Soft Soils and Geoenvironmental Engineering, College of Civil Engineering and Architecture
Zhejiang University
Hangzhou, China

Abdelmalek Bouazza
Department of Civil Engineering
Monash University
Clayton, VIC, Australia

ISSN 1863-5520 ISSN 1863-5539 (electronic)
Environmental Science and Engineering
ISSN 1431-2492
Environmental Engineering
ISBN 978-981-13-2226-6 ISBN 978-981-13-2227-3 (eBook)
https://doi.org/10.1007/978-981-13-2227-3

Library of Congress Control Number: 2018957622

© Springer Nature Singapore Pte Ltd. 2019, corrected publication 2019
This work is subject to copyright. All rights are reserved by the Publisher, whether the whole or part of the material is concerned, specifically the rights of translation, reprinting, reuse of illustrations, recitation, broadcasting, reproduction on microfilms or in any other physical way, and transmission or information storage and retrieval, electronic adaptation, computer software, or by similar or dissimilar methodology now known or hereafter developed.
The use of general descriptive names, registered names, trademarks, service marks, etc. in this publication does not imply, even in the absence of a specific statement, that such names are exempt from the relevant protective laws and regulations and therefore free for general use.
The publisher, the authors and the editors are safe to assume that the advice and information in this book are believed to be true and accurate at the date of publication. Neither the publisher nor the authors or the editors give a warranty, express or implied, with respect to the material contained herein or for any errors or omissions that may have been made. The publisher remains neutral with regard to jurisdictional claims in published maps and institutional affiliations.

This Springer imprint is published by the registered company Springer Nature Singapore Pte Ltd.
The registered company address is: 152 Beach Road, #21-01/04 Gateway East, Singapore 189721, Singapore

Preface

Issues associated with environmental geotechnics continue to be a major preoccupation for governments, public and private organizations and the general community around the world. With the support from the International Society for Soil Mechanics and Geotechnical Engineering (ISSMGE) and the Technical Committee of Environmental Geotechnics (TC215), the Environmental Geotechnics Congress Series has been held regularly since 1994 (Canada 1994; Japan 1996; Portugal 1998; Brazil 2002; UK 2006; India 2010; Australia 2014) and established itself as a highly influential forum for exchange and discussion on the subject. Following the success of 7ICEG in Melbourne, 2014, the 8th International Congress on Environmental Geotechnics (8ICEG) held on 28 October–1 November 2018 in Hangzhou, China, continues tackling challenging issues in the broad range of environmental geotechnics.

The congress theme is "Towards a Sustainable Geoenvironment". "Sustainable Development is to meet the needs of the present without compromising the ability of future generations to meet their own needs". Geoenvironment is a specific compartment of the environment and comprises portions of geosphere, hydrosphere and biosphere. Under this theme, the congress will cover a broad range of topics and will provide an excellent opportunity for academics, engineers, scientists, government officials, regulators and planners to present, discuss and exchange the latest advancements and developments in the research and application of environmental geotechnics.

Out of 340 abstracts received, 8ICEG chose 255 full manuscripts and 6 extended abstracts submitted from 28 countries and regions in 5 continents for publication in this conference proceedings, which provides a platform for scholars and practitioners to share and exchange their experiences with their peers, especially with those from developing countries with impending geoenvironmental issues. There are several features of the proceedings:

- Eleven comprehensive manuscripts, together with 6 extended abstracts, were contributed from the Plenary Lecturers from 11 countries, which includes 8 academicians, 4 editors of major journals and 6 chairpersons of international

renowned organizations. Their contributions provided in-depth insights into the chosen topics.

- Emerging topics, such as sustainability, bio-geoengineering and geoenvironmental aspects in energy geotechnics have strong appearance, which suggests developments towards a better living geoenvironment is the focus for future developments.
- Manuscripts from "Belt and Road Countries" emerged and showed strong presence in 8ICEG, including 24 manuscripts from 10 countries. Environmental problems in those countries take high priority for the governments.

Financial supports from the National Natural Science Foundation of China (41842018) and the Chinese Program of Introducing Talents of Discipline to University (the 111 Project, B18047) are acknowledged. The time and efforts of the associate editors and the reviewers for the proceedings are greatly appreciated.

We hope you enjoy 8ICEG in the beautiful city of Hangzhou!

Sincerely yours,

Liangtong Zhan
Yunmin Chen
Abdelmalek Bouazza
Editors of the Proceedings of 8ICEG

The original version of the book was revised: The book was inadvertently published without incorporating the author corrections. The correction to the book is available at https://doi.org/10.1007/978-981-13-2227-3_70

Organization

List of Associate Editors

Bate Bate	Zhejiang U., China
Jiannan Chen	Southwest Jiaotong U., China
Yonggui Chen	Tongji U., China
Chungfai Chiu	Hohai U., China
Yanjun Du	Southeast U., China
Jia He	Hohai U., China
Qi Li	Inst. of Rock and Soil Mechanics, CAS, China
Yuchao Li	Zhejiang U., China
Jiangfeng Liu	China U. of Mining and Tech., China
Zhibin Liu	Southeast U., China
Hefu Pu	Huazhong U. of Sci. and Tech., China
Chaosheng Tang	Nanjing U., China
Dongxing Wang	Wuhan U., China
Fei Wang	Southeast U., China
Haijian Xie	Zhejiang U., China
Hui Xu	Zhejiang Sci-Tech. U., China
Sifa Xu	Zhejiang U. of Tech., China
Wenjie Xu	Zhejiang U., China
Xiaobing Xu	Zhejiang U. of Tech., China
Yongfu Xu	Shanghai Jiaotong U., China
Chuang Yu	Wenzhou U., China
Shuai Zhang	Zhejiang U., China
Wenjie Zhang	Shanghai U., China
Zhenying Zhang	Zhejiang Sci-Tech U., China
Zhihong Zhang	Beijing U. of Tech., China
Lingling Zeng	Fuzhou U., China
Weilie Zou	Wuhan U., China

List of Committees

International Advisory Committee

Craig H. Benson, USA
Malek Bouazza, Australia
Zuyu Chen, China
Raffaello Cossu, Italy
Pierre Delage, France
Roger Frank, France
Delwyn G. Fredlund, Canada
Russell Jones, UK
Edward Kavazanjian, USA
Yuanming Lai, China
Mario Manassero, Italy
Charles W. W. Ng, Hong Kong SAR
William Powrie, UK
R. Kerry Rowe, Canada
Daichao Sheng, Australia
Devendra N. Singh, India
Kenichi Soga, USA
Hywel R. Thomas, UK
Ikuo Towhata, Japan
Ju Wang, China
Weimin Ye, China
Jianmin Zhang, China
Jorge G. Zornberg, USA

Technical Committee

Chair: Yunmin Chen, China
Co-chair: Malek Bouazza, Australia; Liangtong Zhan, China
Secretary: Bate Bate, China; Shuai Zhang, China

Ishtiaque Anwar, Singapore
D. N. Arnepalli, India
Kazem Badv, Iran
Xiaohong Bai, China
Loretta Batali, Romania
Maria Eugenia Boscov, Brazil
Herminia Cano, Spain
Roger Clark, UK
Dimitrios Coumoulos, Greece
John Cowland, Hong Kong SAR
Yujun Cui, France
Manoj Datta, India
Gemmina Di Emidio, Belgium
Andrea Dominijanni, Italy
Abbas El-Zein, Australia
Evelina Fratalocchi, Italy
Eugene Gallagher, UK
Antonio Gens, Spain
Jean-Pierre Gourc, France
Pinjing He, China
Georg Heerten, Germany
Liming Hu, China
Stephan Jefferis, UK
Han-Yong Jeon, South Korea
Takeshi Katsumi, Japan
Edward Kavazanjian, USA
Eugeniusz Koda, Poland
Hideo Komine, Japan
Lingwei Kong, China
Craig Lake, Canada
William Likos, USA
Zhiping Lin, Taiwan
Xianchang Ling, China
Songyu Liu, China
Lurdes Lopes, Portugal
Mario Manassero, Italy
Nicola Moraci, Italy
Catherine Mulligan, Canada
V. G. Ofrikhter, Russia
Ernest Olinic, Romania
Ali Pak, Iran
Marina Pantazidou, Greece
Fernando Pardo, Spain
G. V. Ramana, India

Krishna Reddy, USA
Sergio Anibal Reyes, Argentina
António Roque, Portugal
R. Kerry Rowe, Canada
Aykut Senol, Turkey
Charles Shackelford, USA
Jianyong Shi, China
Luis Sopeña, Spain
Douglas I Stewart, UK
Antônio Thomé, Brazil
Marc Van Den Broeck, Belgium
Qiang Xue, China
Albert Yeung, Hong Kong SAR
Yeliz Yukselen, Turkey
Dimitrios Zekkos, USA
Honglei Zhou, China
Wei Zhu, China

Organizing Committee

Chair: Liangtong Zhan, Zhejiang U., China
Secretary: Bate Bate, Zhejiang U., China; Wenjie Xu, Zhejiang U., China

Andrea Dominijanni (Secretary of TC215)	ISSMGE, Italy
Elizabeth Peggs (Secretary of IGS)	USA
Johnny Cheuk (Secretary of HKGES)	Hong Kong, China
Marco Ritzkowski (Managing Director of IWWG)	Italy
Jiannan Chen	Southwest Jiaotong U., China
Chaosheng Tang	Nanjing U., China
Yonggui Chen	Tongji U., China
Suqin Tang	Hangzhou Environ. Group Co., Ltd., China
Abraham C. F. Chiu	Hohai U., China
Xiaowu Tang	Zhejiang U., China
Yanjun Du	Southeast U., China
Haijian Xie	Zhejiang U., China
Shijing Feng	Tongji U., China
Yongfu Xu	Shanghai Jiaotong U., China
Ankit Garg	Shantou U., China
Sifa Xu	Zhejiang U. of Tech., China
Han Ke	Zhejiang U., China
Chuang Yu	Wenzhou U., China
Qi Li	Inst. of Rock and Soil Mechanics, CAS, China
Lingling Zeng	Fuzhou U., China
Yuchao Li	Zhejiang U., China
Jianhong Zhang	Tsinghua U., China
Jiangfeng Liu	China U. of Mining and Tech., China
Wenjie Zhang	Shanghai U., China
Yang Liu	Hunan U. of Sci. and Tech., China
Zhenying Zhang	Zhejiang Sci-Tech U., China

Yuemiao Liu	Beijing Research Inst. Uranium Geology, China
Zhihong Zhang	Beijing U. of Tech., China
Fan Lv	Tongji U., China
Weilie Zou	Wuhan U., China
Hefu Pu	Huazhong U. of Sci. and Tech., China

Organized by

Ministry of Education Key Laboratory of Soft Soils and Geoenvironmental Engineering, Zhejiang University

The Chinese Institution of Soil Mechanics and Geotechnical Engineering (CISMGE)

The Hong Kong Geotechnical Society (HKGES)

Under the Auspices of

TC215 Environmental Geotechnics, ISSMGE

Supported by

International Geosynthetics Society (IGS)

International Waste Working Group (IWWG)

Commission on Radioactive Waste Disposal of International Society for Rock Mechanics (ISRM)

Commission on Waste Disposal of the International Association of Engineering Geology and the Environment (IAEG)

List of Plenary Lectures

Speakers	Affiliation	Topic
Distinguished Lecture		
Kerry Rowe	Queens University, Canada	Environmental Geotechnics: Past, Present and Future
Kerry Rowe Lecture		
Mario Manassero	Politecnico di Torino, Italy	On the Fabric and State Parameters of Active Clays for Contaminant Control
Keynote Lectures		
Craig Benson	University of Virginia, USA	Sustainability in Reuse of Solid Wastes
Ningwu Chang	California EPA, USA	Brownfield Redevelopment at Contaminated Landfill Site
Yunmin Chen	Zhejiang University, China	Waste Mechanics and Sustainable Landfilling Technology: Comparison between HFWC and LFWC MSWs
Hywel Thomas	Cardiff University, UK	Deep Ground and Energy: Carbon Sequestration and Coal Gasification
Invited Lectures		
Malek Bouazza	Monash University, Australia	Failures in Containment Systems: Lessons Learned
Michael A. Celia	Hamburg University, Germany	Modeling Geological Storage of Carbon Dioxide with a Focus on Leakage Risk Assessment
Pierre Delage	Ecole des ponts Paris Tech, France	Micro-macro Effects in Bentonite Engineered Barriers for Radioactive Waste Disposal
Nathalie Touze Foltz	Irstea, France	Performance Issues of Barrier Systems for Landfills
Stephan Jeffries	Environmental Geotechnics Limited, UK	Low Permeability Vertical Barriers: The State of the Art and the Research Needs for the Future

Takeshi Katsumi	Kyoto University, Japan	Towards Sustainable Soil Management Reuse of Excavated Soils with Natural Contamination
Ed Kavazanjian	Arizona State University, USA	Biogeotechnical Engineering Applications for Environmental Protection and Restoration
Olaf Kolditz	Dresden University of Technology, Germany	Workflows in Environmental Geotechnics: Status-Quo and Perspectives
William Powrie	University of Southampton, UK	Climate and Vegetation Impacts on Infrastructure Cuttings and Embankments
Krishna Reddy	University of Illinois at Chicago, USA	Risk, Sustainability and Resiliency Considerations in Polluted Site Remediation
Devendra Narain Singh	Indian Institute of Technology, India	Centrifuge Modeling of Contaminant Transport in Geomaterials
Rainer Stegmann	Hamburg University, Germany	Development of Waste Management in The Last 30 Years
Antonio Thome	University of Passo Fundo, Brazil	Remediation Technologies Applied in Polluted Soils: New Perspectives in This Field
Fuming Wang	Zhengzhou University, China	Jet Grouting for Leakage Prevention
General Report		
Charles Shackelford	Colorado State University, USA	Pollutant Transport
William Powrie	University of Southamptom, UK	Waste Mechanics

Contents

Biogeotechnical Engineering

Geoenvironmental Risk Assessment, Management and Sustainability

Geoenvironmental Aspect in Energy Geotechnology

(Edited by Wenjie Xu, Qi Li, and Yonggui Chen)

A Preliminary Simulation of CO_2-EOR and Storage in One Heavy Oil Carbonate Oilfield Offshore Guangdong, China

Pengchun Li[1,2(✉)], Jiemin Lu[3], Di Zhou[1], and Xi Liang[4]

[1] CAS Key Laboratory of Ocean and Marginal Sea Geology, South China Sea Institute of Oceanology, Guangzhou 510301, China
lypengchun@scsio.ac.cn
[2] State Key Laboratory of Oil and Gas Reservoir Geology and Exploitation, Chengdu University of Technology, Chengdu 610051, China
[3] Bureau of Economic Geology, The University of Texas at Austin, Austin, TX 78713, USA
[4] UK-China (Guangdong) CCUS Centre, Guangzhou 510663, China

Abstract. This paper presents the first study on CO_2-EOR potential of the LH11-1 oilfield offshore Guangdong Province, China. LH11-1 field is a reef heavy oilfield (16–23° API), and overall development efficiency is not ideal. In this study, the CO_2 flooding potential in LH11-1 field was evaluated through a compositional simulation using the Petrel and CMG-GEM tools. A detailed fluid characterization was performed to accurately represent the reservoir fluid. 1D slim tube and core flood simulations were interpreted to understand the physical mechanisms of oil recovery. A reservoir geological (structure, facies and fluids) model was constructed in Petrel system and the model was calibrated using manual and assisted history matching methods. The natural depletion and continuous CO_2 injection scenarios were simulated by GEM. Results indicate that the minimum miscibility pressure (MMP) of crude oil in Liuhua field is approximately 20 MPa. Therefore, the mechanism of oil recovery by CO_2 EOR in Liuhua field should be suitable for immiscible CO_2 flooding. The continuous CO_2 injection would recover an incremental 7% of OOIP in Liuhua field, and the CO_2 storage efficiency is relatively high with more than 95.5% of injection CO_2 has been stored in the reservoir which indicate an important significance for CO_2-EOR and storage potential in offshore carbonate oilfield.

Keywords: CO_2-EOR · CO_2 storage · Heavy oil · Compositional simulation Offshore carbonate reservoir

1 Introduction

CO_2 Enhanced Oil Recovery (CO_2-EOR), as an effective technology to improve crude oil recovery, has gain a new role in CO_2 geological sequestration [1]. CO_2-EOR has been field tested for oil recovery with varying degrees of success [2, 3]. Application of CO_2 injection in heavy oil reservoirs has received less attention compared to light oil reservoirs. There are two reported reasons for this; it is believed that in heavy oil

© Springer Nature Singapore Pte Ltd. 2019
L. Zhan et al. (Eds.): ICEG 2018, ESE, pp. 3–16, 2019.
https://doi.org/10.1007/978-981-13-2227-3_1

reservoirs, CO_2 lacks acceptable sweep efficiency due to the large viscosity contrast between CO_2 and oil as well as unlikely development of a miscible front in heavy oil reservoirs [4].

The Liuhua 11-1 field is the largest carbonate oilfield with a very strong bottom-water drive and with 20° API gravity crude oil in northern South China Sea [5]. Since the field produced, the oil production of Liuhua field declined very quickly with highest water cut and lowest recovery rate [6]. At present, the oilfield is still produced through horizontal wells and natural depletion operations, and does not take into account enhanced oil recovery technology because of limitation of gas source supply and complex reservoir and marine conditions [7]. The suitability and potential of CO_2-EOR and sequestration of Liuhua field is of great significance for Guangdong coastal CO_2 emission reduction [8–11]. In this paper, the suitability of CO_2-EOR is investigated to address enhanced oil recovery in Liuhua field. The mechanism and potential of CO_2-EOR and storage in Liuhua field were simulated and analyzed.

2 Background

2.1 Geography and Geology

The Liuhua 11-1 field, located in the South China Sea, is 210 km southeast of Hong Kong in a water depth of approximately 300 m (Fig. 1a) [12, 13]. The Liuhua 11-1 Field is situated in the topmost, geographically more restricted and youngest part of the carbonate platform formed on top of the subsiding Dongsha horst block in the Pearl River Mouth basin. The Pearl River Mouth basin, offshore Guangdong, is a typical passive margin basin and occupies the southwestern part of the rifted Atlantic-type continental shelf of China [14]. The Dongsha Massif is one of these basement highs and Liuhua Field is located on the western plunge of the Dongsha Massif [15]. The Zhujiang Formation comprises early Miocene platform carbonates that were deposited on top of the Dongsha and Shenhu horst blocks (Fig. 1). These horst blocks were subaerially exposed highs during the Oligocene. During the Early Miocene the Dongsha massif gradually submerged and was covered by a carbonate platform (Zhujiang Formation) favored by the overall warm climate and eustatic optimum of this period. The horst blocks are flanked by sag basins, characterized mainly by hemi-pelagic argillaceous deposits [16]. Presently, the Zhujiang carbonates are buried below 1250 m of mainly siliciclastic sedimentary rocks and lie in water depths of approximately 300 m [17, 18].

2.2 Petroleum Geology

Structure. The Liuhua Field is a NW-SE trending, elongate reefal buildup bounded to the north and south by Late Tertiary normal faults (Fig. 2). The field is primarily a stratigraphic trap formed as an isolated Lower Miocene reefal buildup developed over a subtle basement high (Fig. 3). The structure is 13 km long and 4 km wide with a closure area of 59.2 km^2 and a vertical closure high of 87.0 m. It has an oil column height of 75 m and original OWC at 1247 m. It is composed of two high points,

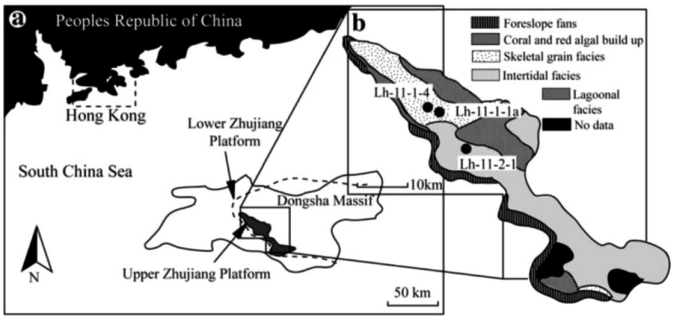

Fig. 1. (a) Geographic and geologic setting of Liuhua-11-1 oilfield; (b) Regional distribution of depositional facies [17, 18]

including the west peak near A1 well and the east peak north of 3 well. Principal part of the structure is relatively flat; two wings were cut by main faults. The boundary faults, parallel to the axis of structure, have maximum vertical displacement of 70 m and the flat extension of 2–8 km, and extend longitudinally from basement upward to the bottom of the quaternary formation [6, 7]. Some small normal faults, parallel to the axis and having vertical displacement of 5–20 m, do not have significant impact on fluid flow. A number of circular karstic sinkholes, identified from 3-D seismic survey, are present along the southern boundary fault [13].

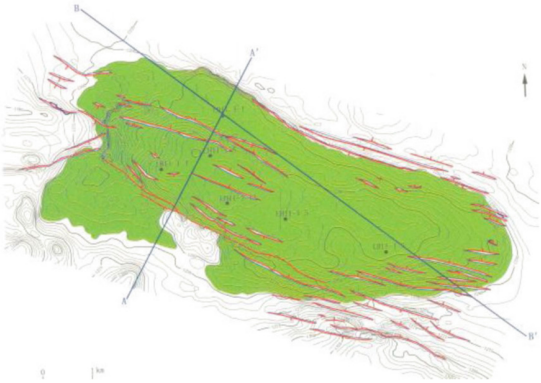

Fig. 2. Map showing top-Zhujiang carbonate structure and location of discovery and appraisal wells in the Liuhua11-1 oilfield [7]

Reservoir Property. The reservoir in the Liuhua 11-1 Field consists of Middle Miocene stones with a packstone matrix and foram-algal grainstones and packstones of the Zhujiang Formation, which composed alternating porous and tight zones corresponding to discrete lithological packages [14]. The oil-bearing reservoir is a 75 m thick, multi-layered reef limestone unit. It comprises six diagenetically defined units labeled A-F (Fig. 3) from top to bottom with areas A, C and E being tight [12, 19].

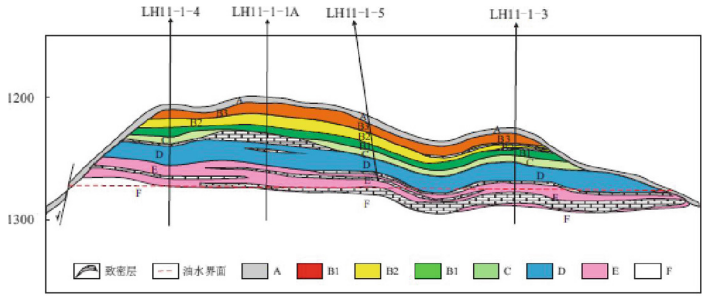

Fig. 3. Geological section map of Liuhua 11-1 Field [19]

The Liuhua 11-1 oilfield produces biodegraded crude with formation density of 0.899–0.930 g/cm^3 and viscosity 46.5–162.1 mPa · s, and API gravity of 16–22 degree and low solution gas [5, 6, 12]. The initial formation pressure in Liuhua 11-1 oilfield is 12.66 MPa, the saturation pressure is 2.19 MPa, the formation pressure coefficient is 1.05, and the formation temperature is 52.2 °C, which show a normal temperature and pressure system. For crude oil, the proven geological reserve is 1.66×10^8 m^3 (1.55×10^8 t), the technically recoverable reserve is 0.26×10^8 m^3 (0.24×10^8 t), and the economically recoverable reserve is 2547.20×10^4 m^3 (2379.08×10^4 t) [6, 7]. The reservoir is highly stratified and is underlain by a large, permeable aquifer. Water influx from the aquifer is expected to provide the energy for oil recovery and to dictate the recovery performance of the reservoir [20].

Production History. Liuhua oilfield was discovered in 1987 and started oil production in 1996. The production is being developed with twenty-five long-radius horizontal wells drilled from a floating production system tied to a modular sub-sea structure. As shown in Fig. 4, the water cut of the oilfield increased rapidly at the beginning of development, and the production decreased quickly too. The cumulative oil production was 1018.5×10^4m^3 by the end of 2001, and the water cut was up to 93.8%. When water cut is more than 90%, the rate of production decline and the increase of water cut have been slowed down. Although measures such as adjustment and drilling are adopted, the oil recovery rate is still very low. On May 13, 2006, the oil field was shut down because of effecting of strong typhoon named "Pearl". It was successfully reproduced on June 27, 2007. The cumulative oil production of the field was 1519.3×10^4 m^3 by the end of December 2007.

3 Methodology

3.1 Data Sources

The oilfield geology and development data used in this study are all from database built by South China Sea Institute of Oceanology (SCSIO), Chinese Academy of Sciences through collecting the public data such as published papers, books, reports, atlas, and so on. Due to data limitation, the production information of Liuhua11-1 oilfield is only

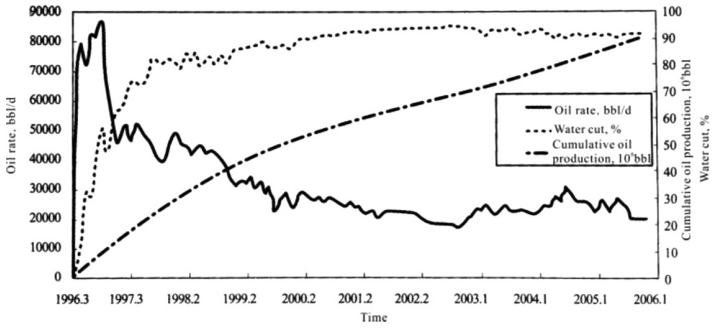

Fig. 4. Production history curves of Liuhua11-1 oilfield [6]

by the end of 2005. The modeling and simulation information used in this paper are mainly collected from four books as follows: Development of Oil and Gas fields of China [6], Petroleum geology of China [21], Atlas of oil and gas basins, China Sea [22], and Development practices of typical oilfield offshore Chia [23].

3.2 Methods

The 3D geological model of the Liuhua11-1 reef reservoir was built on the Petrel platform, and then compositional simulation was run using the GEM reservoir simulator of the Computer Measurement (Group CMG) [24]. Firstly, a detailed fluid characterization model was built to represent the reservoir fluid in order to study the fluid properties and its effect on the potential of EOR. Next, an analogous 3-D reservoir model was built using the structure & isopach maps, and logging and well core data available from 5 wells to simulate an approximate history match of the field production. The model was also used to evaluate mitigation techniques, which could be helpful for evaluation of CO_2-EOR and storage potential. A summary of the methodology is:

(1) Detailed fluid characterization to capture the fluid properties;
(2) Slim tube simulation to estimate the minimum miscibility pressure;
(3) Building an approximate 3D model of the reservoir using data from logging, cores, and structure and isopach maps;
(4) Perform an approximate history match using the field production data to attain reasonably oil distribution, close breakthrough time and productivity behavior;
(5) Evaluate CO_2-EOR and storage potential techniques.

4 Model Description

4.1 Fluid Model

Equation of State (EOS) Development. In order to forecast and monitor the CO_2 gas displacement process proposed for the Liuhua11-1 reefal reservoir, a description of the

reservoir fluids was necessary which captures the wide changes in compositions and physical properties expected in CO_2 flooding process. Because the detailed oil composition of laboratory data was poor, we simulated the composition of the crude oil using WINPROP's 'Recombination' option based on information of the oil chromatogram, gas/oil ratio, dissolved gas content, oil density, and viscosity (Table 1). This resulted in a crude oil with 8 light components ($C_{1–3}$, $C_{11–15}$, $C_{16–17}$, C_{18}, $C_{19–20}$, $C_{21–25}$, $C_{26–35}$ and C_{31}^{+}) listed in Table 2. We then matched them with laboratory oil properties using WINPROP through regression parameters Omega A and Omega B to obtain the composition as shown in Fig. 5. Finally, an EOS was developed based on the Peng-Robinson formulation. The EOS parameters were adjusted by regression of the 1998 data and the 1980 data. The resulted EOS then was input into CMG-GEM for the simulation.

Table 1. Parameters of fluid property in Liuhua11-1 oilfield [6]

Property	Formation value	Mean value
Initially formation pressure (MPa)	12.66	
Reservoir temperature (°C)	52.22	
Saturation pressure (MPa)	0.63–5.78	2.19
Specific gravity	Oil: 0.92	0.92
	Gas: 0.597–1.55	1.0735
Oil density (g/cm^3)	0.899–0.903	0.901
Oil viscosity (mPa · S)	46.5–162.1	104.3
Oil compressibility coefficient	6.28–7.8	7
Gas-oil ratio (m^3/m^3)	1.6–13.4	7.5

Slim Tube Simulation. In order to determine the MMP and displacement mechanisms of the CO_2 flooding into the Liuhua 11-1 carbonate oil reservoir, a set of 1D compositional model mimicking slim tubes were used at a range of constant reservoir temperature and pressure, because presently there are no laboratory slim tube experiments from crude oil sample. The main parameters used in numerical simulation are shown in Table 3. The results show that when the injection pressure reaches ~20 MPa (Fig. 6), the oil recovery factor stopped fast increase. This indicates that the minimum miscible pressure is 20 MPa, which is much higher than the original formation pressure (12.66 MPa) in Liuhua11-1 reservoir. Therefore, the CO_2 flooding will be in immiscible state under the Liuhua11-1 reservoir condition.

4.2 Reservoir Model

A structural model for the Liuhua 11-1 oilfield was built in Petrel platform. The reservoir top of structure values and each sub-interval thickness as determined by log analysis was imported into the reservoir simulation mapping package on the Petrel platform to develop the structural description. The model is 15,300 m long and 6850 m wide, has thickness of 66.4 m, and covers the entire area of reefal reservoir at depths

Table 2. Composition of the 8-component systems for oil in Liuhua11-1 oilfield model

Components	C_{1-3}	C_{11-15}	C_{16-17}	C_{18}	C_{19-20}	C_{21-25}	C_{26-35}	C_{31}^{+}
Normalized composition	0.047	0.132	0.141	0.088	0.099	0.258	0.121	0.114

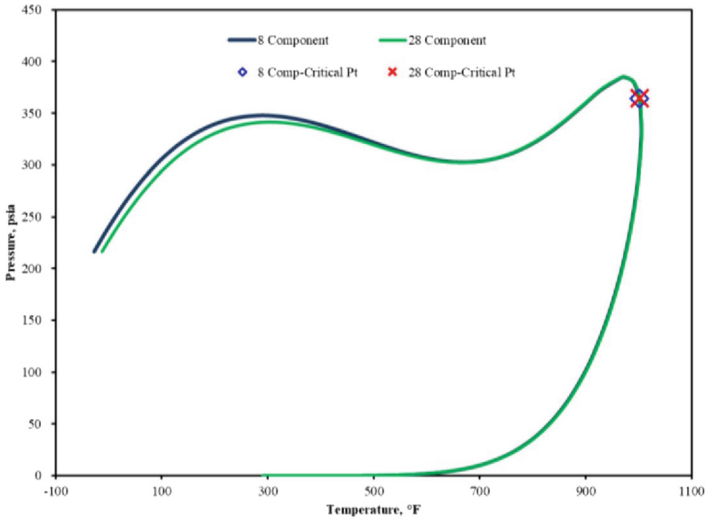

Fig. 5. Phase diagrams with the 28 component and 8 pseudo-component systems

Table 3. Main parameters used in 1-D miscible flooding model

Parameters	Value
The size of the slim tube (m)	40 * 0.02
The node number	200
The size of grid elements along x(m) y, z (m)	0.2 0.02
Initial oil saturation	0.8
Initial water saturation	0.2
Initial gas saturation	0.0
Porosity	0.25
Permeability at x direction (mD)	651
Initial temperature (°C)	52.2
Initial pressure (MPa)	12.660
CO_2 injection rate of injection well (cc/hr)	3
Wellbore flow pressure (MPa)	12.65
Rock compressibility (1/kPa)	2e−5
Reference pressure (kPa)	2000

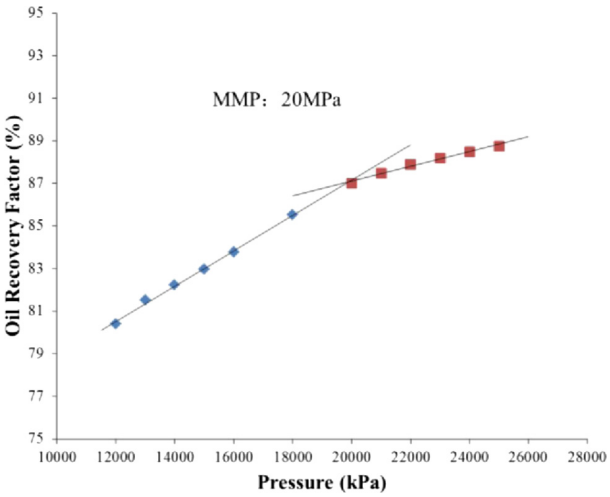

Fig. 6. Oil recovery versus injection pressures at 1.2 PV of CO_2 injections for oil showing MMP estimated at 20 MPa.

from 1162.5 m to 1247 m. The model consists of 306 × 137 × 40 (total of 1,676,880) grid cells, and each cell is approximately 50 × 50 × 1.66 m. The porosity and permeability were interpreted from the 5 well logs including 1A, 3, 4, 5 and 6 wells. The porosity and permeability were calculated for each layer in each well from log analysis and core plug measured as described in Story et al. (2000) and contoured to control their vertical variations in the property model. Finally, interpolation with a Gaussian Random Simulation process was used to construct a 3D porosity model (Fig. 7a) and permeability model (Fig. 7b). The average porosity and permeability in the 3D property model are 25.27% and 621 mD, respectively. The resulted models had relatively uniform characteristics as observed from logs and field data (Table 4), which indicates that the 3D property model is reliable and can be used in further compositional simulations.

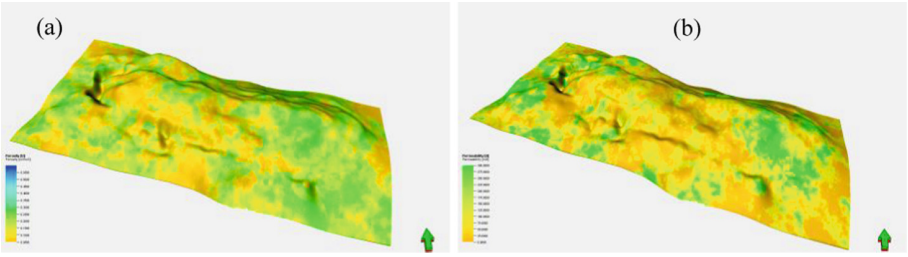

Fig. 7. 3D property models of porosity (a) and permeability (b) for the Liuhua11-1 reservoirs.

Table 4. Comparison of the parameters between the Liuhua11-1 model and the field data

		Field	Model
Porosity, %	Range	0.9–38.8%	4.43–47.28%
	Mean	21.3%	25.27%
Permeability, mD	Range	0.01–9,329	5.28–2,181
	Mean	651	621

Note: Field data were derived from Liu (2011).

The model was then scaled up and imported into CMG-GEM calculator for further reservoir simulations. The scale-up model contains 136,800 grid blocks with NX = 76, NY = 45 and NZ = 40. The relative permeability curves were derived from core sample test data [5]. The capillary pressure (P_c) curve was referenced from typical carbonate rock data [25, 26]. Well positions were chosen to be representative of the actual positions of the wells as shown in Fig. 2 [6, 7]. The model was initialized at conditions at the beginning of production from the Field.

4.3 History Match

Simulation runs to "history match" the reservoir's pre-CO_2 flood oil and water production during primary depletion, were run using scale-up reservoir and fluid model described above in GEM simulator. For this paper, both oil reserves and production history of the reservoir were matched. The reservoir pressures, oil rates, and water cut were the major parameters to be matched. Because of the variability of the historical data caused by pump operating conditions, temporary shut-ins and gauge accuracy, we focused on matching the monthly average performance of oil rate and cumulative oil production instead of the transient variations of data. During matching process, reservoir parameters known to have large uncertainties and questionable data quality were adjusted. The primary parameters that were adjusted included the relative permeability and capillary pressure (Fig. 8b). After several simulation runs and after several adjustments were made to the relative permeability curves (Fig. 8) and well productivity indices, we obtained a good history match with the cumulative oil production and oil rate data (Fig. 9). After the history matching, the reservoir mode is assumed to be an approximation of the field in terms of the pressure and residual oil saturation.

5 Results

5.1 Oil Recovery

After the history matching process, the model is set for simulation of natural depletion production and continuous CO_2 flooding scenarios. The variation curves of simulation results of CO_2 flooding and also natural depletion scenarios were shown in Figs. 10 and 11. In contrast, the oil production rate of CO_2 flooding declined slowly with long time of high rate, relatively (Fig. 10a), and the cumulative oil production have an

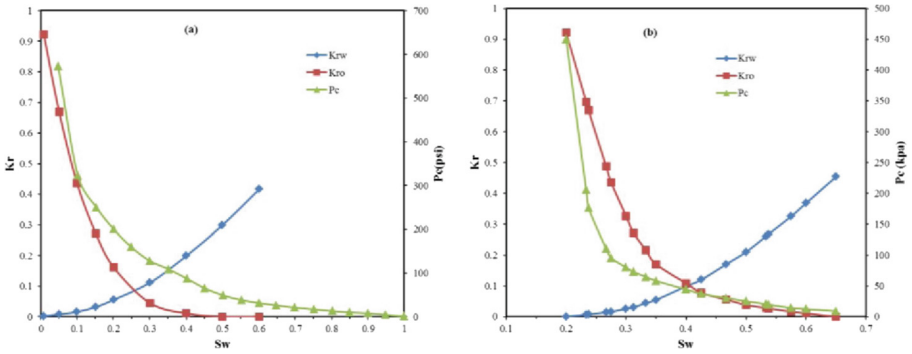

Fig. 8. Relative permeability (Kr) curves for water and oil phases based on measurement of core samples [5] and capillary pressure (Pc) curve according to typical carbonate rock [25, 26] (a) and the adjusted results after history match (b). Krw is the relative permeability of water, Kro is the oil permeability relative to water, Pc is the oil-water capillary pressure.

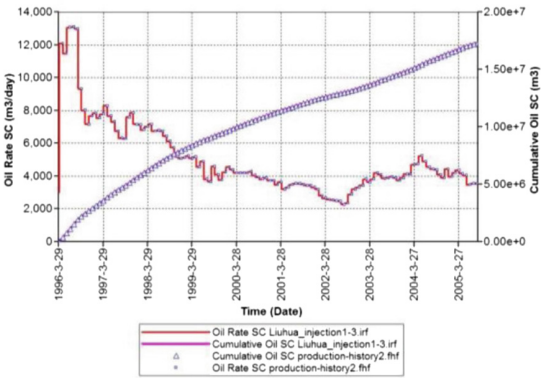

Fig. 9. Field history match of primary oil production in the reservoir model. History production data refer from Liu (2011).

obvious enhancement (Fig. 10b). The ultimate cumulative oil production at end of 20 simulation years is up to $28.8 \times 10^6 m^3$, which shows a significant increase than the natural depletion result of $19.8 \times 10^6 m^3$.

The water cut trend of the CO_2 flooding shows a low values than natural depletion scenario as shown in Fig. 11a, which indicates that continuous CO_2 injection operation is benefit for declining the water cut. The ultimate oil recovery of continuous injection of CO_2 at the end of 20 simulation years is 21.1%, which is much higher than 14.5% of primary recovery factor of natural depletion production (Fig. 11b). Therefore, continuous injection of CO_2 recovers approximately an incremental 7% of OOIP which shows an obvious enhancement of oil recovery.

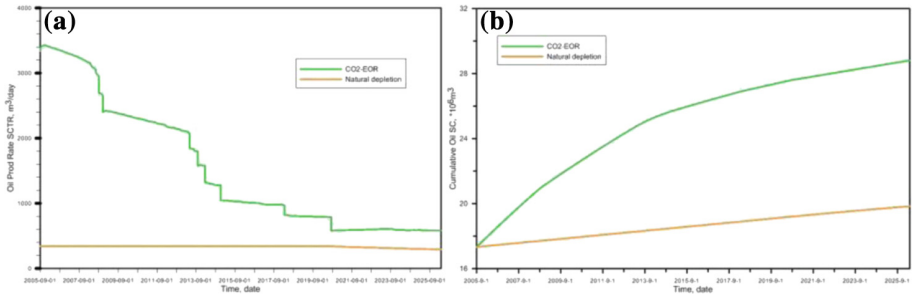

Fig. 10. Result curves of oil production rate (a) and cumulative oil production (b) compared to natural depletion operations.

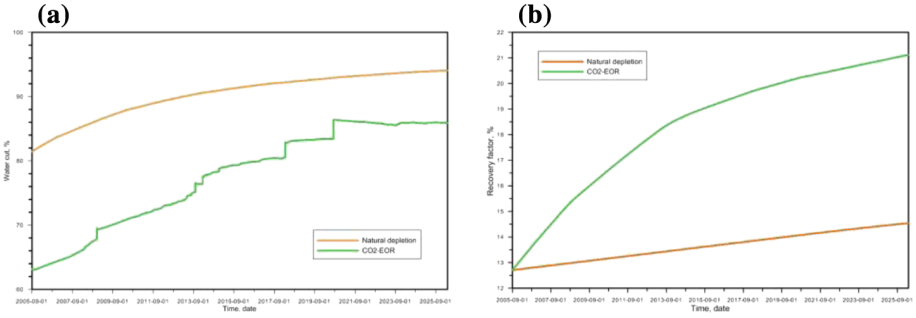

Fig. 11. Result curves of water cut (a) and recovery factor (b) compared to natural depletion operations.

5.2 CO_2 Stored

The curves of cumulative CO_2 injection and production results were shown in Fig. 12. Results indicate that the volume of CO_2 produced is very small, and the most CO_2 of the injection were stored in oil reservoirs. The mass of CO_2 of ultimately stored in reservoir is calculated through mass of produced taken from injected. The results show that the volume of CO_2 stored increased with the continuous CO_2 injection, the ultimate CO_2 stored in reservoir at the end of 20 simulation years is up to 1 544 Mt, and more than 95.5% of injection CO_2 have been stored in the reservoir, which is very beneficial to long time and large scale CO_2 geological storage for CCUS project operations.

6 Conclusions

(1) By using 1D slime tube simulation model, the minimum miscibility pressure for CO_2 and reservoir oil of Liuhua field was determined as value of 20 MPa.
(2) The mechanism of oil recovery by CO_2 EOR in Liuhua field should be suitable for immiscible CO_2 flooding with characterization of shallow buried depth, high viscosity and heavy gravity of oil and high minimum miscibility pressure.

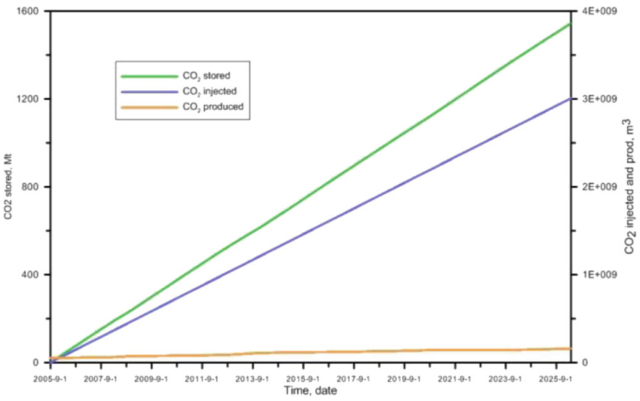

Fig. 12. Result curves of cumulative CO_2 injected, produced and stored

(3) Continuous CO_2 injection would recover the oil from recovery factor of 14.5% of primary natural depletion production to 21.1%, which shows an obvious enhancement potential for oil production.
(4) CO_2 storage efficiency in Liuhua field is relatively high with more than 95.5% of injection CO_2 have been stored in the reservoir which indicate an important significance for CO_2 storage potential in offshore carbonate oilfield.

Acknowledgments. We gratefully acknowledge the funding supported by open fund (PLC20180801) of State Key Laboratory of Oil and Gas Reservoir Geology and Exploitation (Chengdu University of Technology), the National Natural Science Foundation of China (No. 41372256) and the Key Logic project of Department of Energy, USA (No. K6000-797). We are grateful to Susan Hovorka, Seyyed Hosseini, Núñez-López Vanessa, Reza Ganjdanesh and other stuff in the Bureau of Economic Geology, The University of Texas in Austin for their support and help in all the technical applications of reservoir modelling and simulation.

References

1. IPCC (2005) In: Metz B, Davidson O, Coninck HC, Loos M, Meyer LA (eds) Special Report on Carbon Dioxide Capture and Storage. Cambridge University Press, Cambridge/New York
2. Azzolina NA, Nakles DV, Gorecki CD, Peck WD, Ayash SC, Melzer LS, Chatterjee S (2015) CO_2 storage associated with CO_2 enhanced oil recovery: a statistical analysis of historical operations. Int J Greenhouse Gas Control 37:384–397
3. Ettehadtavakkol A, Lake LW, Bryant SL (2014) CO_2-EOR and storage design optimization. Int J Greenhouse Gas Control 25:79–92
4. Cuthiell D, Kissel G, Jackson C, Frauenfeld T, Fisher D, Rispler K (2006) Viscous fingering effects in solvent displacement of heavy oil. J Can Pet Technol 45:29–39
5. Story C, Peng P, Sullivan C, Dong LJ (2000) An Integrated Geoscience and Reservoir Simulation Study of The Liuhua 11-1 Field: South China Sea, Offshore Technology Conference, OTC11958, pp 1–11

6. Liu B (2011) Development of Oil and Gas fields of China. Volume of oil and gas fields in eastern South China Sea. Edited by editorial committee of "Development of Oil and Gas fields of China", Petroleum Industry Press, Beijing
7. Zhu W, Mi L (2010) Atlas of Oil and Gas Basins. China Sea Petroleum Industry Press, Beijing
8. Li P, Zhou D, Zhang C, Zhang Y, Peng J (2013) Potential of sub-seafloor CO_2 geological storage in Northern South China sea and its importance for CCS development in South China. Energy Procedia 37:5191–5200
9. Li X, Zhou D, Li P, Wu Y, Liang X, Wei N, Haszeldine S, Senior B, Shu Y, Li J, Chen Y (2015) CO_2 offshore Storage in China: Research Review and Plan for Demonstration Project, UK-China (Guangdong) CCUS Centre, pp 46
10. Zhou D, Li P, Liang X, Liu M, Wang L (2018) A long-term strategic plan of offshore CO_2 transport and storage in northern South China Sea for a low-carbon development in Guangdong province, China. Int J Greenhouse Gas Control 70:76–87
11. Zhou D, Zhao D, Liu Q, Li X-C, Li J, Gibbons J, Liang X (2013) The GDCCSR project promoting regional CCS-readiness in the Guangdong Province, South China. Energy Procedia 37:7622–7632
12. Heubeck C, Story K, Peng P, Sullivan C, Duff S (2004) An integrated reservoir study of the Liuhua 11-1 field using a high-resolution three-dimensional seismic data set. Seismic Imaging Carbonate Reserv Syst: AAPG Memoir 81:149–168
13. Story C, Peng P, Lin JD (2000) Liuhua 11-1 field, South China sea: a shallow carbonate reservoir developed using ultrahigh-resolution 3-D seismic, inversion, and attribute-based reservoir modeling. Lead Edge 19:834–844
14. Zampetti V, Sattler U, Braaksma H (2005) Well log and seismic character of Liuhua 11-1 Field, South China Sea; relationship between diagenesis and seismic reflections. Sed Geol 175:217–236
15. Turner NL, Zhong HP (1996) The lower Miocene Liuhua carbonate reservoir, Pearl River Mouth Basin, offshore People's Republic of China. In: Circum-Pacific Energy and Mineral Resources Conference Transactions, Circum-Pacific Council for Energy and Mineral Resources, pp 657–666
16. Moldovanyi EP, Wall FM, Yan ZJ (1995) Regional exposure events and platform evolution of Zhuijang Formation carbonates, Pearl river Mouth Basin: evidence for primary and diagenetic seismic facies. In: Budd DA, Saller AH, Harris PM (eds.) Unconformities and Porosity in Carbonate Strata, pp 125–140. American Association of Petroleum Geologists Memoir
17. Sattler U, Immenhauser A, Schlager W, Zampetti V (2009) Drowning history of a Miocene carbonate platform (Zhujiang Formation, South China Sea). Sed Geol 219:318–331
18. Sattler U, Zampetti V, Schlager W, Immenhauser A (2004) Late leaching under deep burial conditions: a case study from the Miocene Zhujiang Carbonate Reservoir, South China Sea. Mar Pet Geol 21:977–992
19. Liu M, Feng Q, Xiao W, Wu Q, Dan Z (2015) Fast coning of bottom water in bioherm oilfield of LH11–1. J Southwest Pet Univ (Sci Technol Ed) 37:49–56
20. Peng CP, Bateman CF, Kaffenes JM, Yanosil JL, Liu H (1994) Extended production tests in the Liuhua 11-1 reservoir. SPE Reserv Eng 169–174
21. Zhai G, Wang S (1990) Petroleum geology of China, Vol. 16, Oil and gas bearing areas on the continental shelf and ints neighbouring regions, in, Petroleum Industry Press, Beijing
22. Zhu W, Mi L, Zhang H (2010) Atlas of Oil and Gas Basins, China Sea. Petroleum Industry Press, Beijing
23. Zhou S (2009) Development Practices of Typical Oilfield Offshore China. Petroleum Industry Press, Beijing

24. CMG (2010)GEM User's Guide. Computer Modeling Group Ltd. (CMG), Calgary
25. Hulea IN, Nicholls CA (2012) Carbonate rock characterization and modeling: capillary pressure and permeability in multimodal rocks—a look beyond sample specific heterogeneity. AAPG Bull 96:1627–1642
26. Hulea IN (2013) Capillary pressure and permeability prediction in carbonate rocks - new methods for fractures detection and accurate matrix properties prediction. In: SPE Middle East Oil and Gas Show and Conference, Society of Petroleum Engineers, Manama, Bahrain, pp 1–7

Dynamic Optical Fiber Monitoring of Water-Saturated Sandstone During Supercritical CO_2 Injection at Different Sequestration Pressures

Chengkai Fan[1,2], Qi Li[1,2(✉)], Xiaying Li[1,2], Zhiyong Niu[1,2], and Liang Xu[1,2]

[1] State Key Laboratory of Geomechanics and Geotechnical Engineering, Institute of Rock and Soil Mechanics, Chinese Academy of Sciences, Wuhan 430071, China
qli@whrsm.ac.cn
[2] University of Chinese Academy of Sciences, Beijing 100049, China

Abstract. In this paper, two intact cylindrical sandstones were bonded with the fiber Bragg grating sensors for laboratory experimental studying the injection and migration process of carbon dioxide (CO_2) under varying temperature and sequestration pressures. A series of core flooding experiments were conducted under undrained conditions with different confining and pore pressures without changing the effective confining pressure. As a result, the strain responses of CO_2 in three different states after injecting into specimen rose with the increase in the pore pressure. And the dynamic strain responses of supercritical CO_2 ($scCO_2$) was slightly higher than that of liquid CO_2 due to the character of sCO_2 and the effect of temperature. The initial time differences of axial strain measurement along the three gratings on a single fiber can precisely indicate the migration fronts of $scCO_2$ plume. The difference in strain response time of the three gratings is in a descending order of liquid CO_2, $scCO_2$, and gaseous CO_2.

Keywords: Fiber Bragg Grating (FBG) · Geologic CO_2 storage
Core flooding · Sandstone · Supercritical CO_2

1 Introduction

Excessive emissions of CO_2 will increase the degree of instability in earth's climate [1, 2]. Supercritical CO_2 ($scCO_2$) injected into underground deep reservoir is considered to be an efficient and safe method of reducing the emission. In particular, the injecting of $scCO_2$ into deep saline aquifers utilizing diffusion and dissolution mechanisms to achieve the purpose of sequestering CO_2 is currently the focus of research [3]. Not only that, the process of flow and migration of $scCO_2$ in porous media [4], the dissolution and trapping mechanism [3] and the mechanics principle of pore structure [5] are the first choice to explore for researchers. Currently, the storage mechanism of $scCO_2$ is mainly studied through experiments and numerical simulations. For numerical simulations, the mechanical and chemical mechanisms can be explored on a micro or a macro scale. In terms of experimentation, there are various methods such as magnetic resonance, X-ray CT images, ultrasonic, and microseismic techniques to observe the

© Springer Nature Singapore Pte Ltd. 2019
L. Zhan et al. (Eds.): ICEG 2018, ESE, pp. 17–24, 2019.
https://doi.org/10.1007/978-981-13-2227-3_2

migration and transport characteristics of CO_2 at an experimental scale [4, 6, 7]. However, there have been relatively few qualitative and quantitative studies on the frontier of $scCO_2$ migration and the strain responses during the process of the $scCO_2$ displacement.

In order to precisely monitor the mechanical response and migration front information of $scCO_2$ under the different temperature and pressure conditions, an advanced optical fiber sensing technique was utilized in this experiment. In this study, comparing the displacement process and dynamic strain responses of CO_2 in three different states, the migration characteristics of $scCO_2$ under different pressure conditions were investigated.

2 Rock Preparation

The specimens utilized in the experiment were exploited from the Penglaizhen Formation in the late of Jurassic Period of Sichuan Basin in China (Fig. 1(a)). Two sandstone samples with a diameter of 50 mm and a height of 125 mm were cored from a block of outcrop rock and the stratification planes were not obvious. The pore volume and absolute permeability measured in the laboratory were respectively about 230 cm^3 (approximately equal to a porosity of 21%) and 490 mD (liquid permeability). The sandstones were mainly comprised of brittle minerals such as quartz accounting for 50.5%, feldspar 26.2%, calcite 16.5% and a small amount of clay minerals. Two FBG sensors were paste on the surface of the specimen axially in a parallel manner and each fiber was carved with three consecutive gratings (Fig. 1(b) and (d)). Then, the entire sample was smeared and wrapped with silica gel, curing for at least 8 h (Fig. 1(c)).

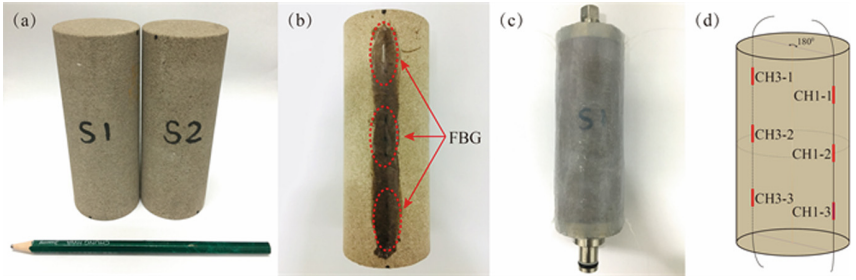

Fig. 1. The specimens used in the experimental study. (a) Two sandstones collected from the Penglaizhen Group; (b) Two FBG sensors bonded on the sandstone surface in axial direction; (c) Sandstone coated with silica gel; (d) Pasting style of the FBG on specimen.

3 Experimental Setup and Monitoring Technique

3.1 Experimental Apparatus

The FBG sensing system assembled for $scCO_2$ displacement tests using vertical experimental apparatus is shown in Fig. 2. The experimental system consisted of an

injection subsystem, a core chamber, a temperature control system, a back pressure valve and the data acquisition equipment. The sandstone specimen with the pasted FBG sensors was then installed in core holder. Water/CO_2 was compressed and injected into the sandstone through the pump A at varying pressures or at a stable flow rate. Prior to that, constant confining pressure was applied with water through pump B which served as a hydraulic fluid system for the core chamber. The temperature-control system was composed of a preheating system and a thermostat, where the maximum heating temperature values were all up to 150 °C. The compressed CO_2 was reserved in the preheating vessel briefly before reaching the target value (45 °C) and then was injected into the specimen under a thermostatic environment monitored by thermostat for simulating the supercritical sequestration state. A back pressure valve was used to control the velocity of outlet fluids at a constant pressure. The dynamic migration information of the fluids was collected by the FBG sensing system in real time, the variation of pressure upstream and downstream was synchronously recorded by the pressure gauges.

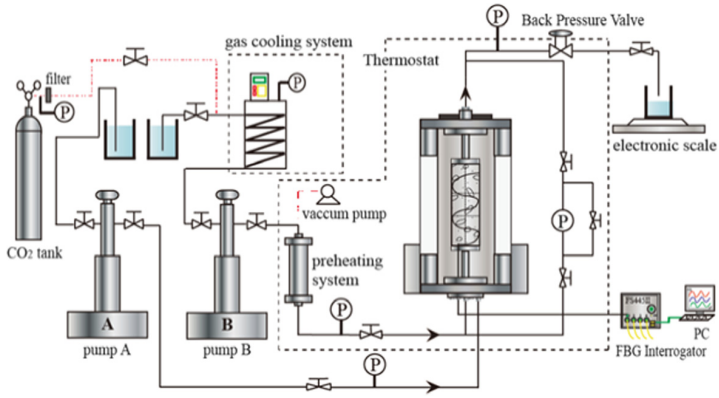

Fig. 2. The Schematic diagram of experimental system.

3.2 Monitoring Method

The FBG sensors were engraved with three gratings for monitoring the strain responses at three positions along the axial direction of the specimen. The principle of FBG sensor system is such that when a broadband spectrum light propagates through the grating only a specific Bragg wavelength can be reflected back to be received by a demodulator. And the Bragg wavelength of light shift is consequentially a response to variations in strain and temperature. Thus, the FBG sensor can accurately measure the small strain changes caused by the variation of the environmental stress state when the ambient temperature remains unchanged or fluctuates a little. In our experiments, the FBG wavelength interrogator with version FS445 II was used to collect and analyze the light signals such as Bragg wavelength shifts and to be demodulated by a computer software.

The FBG interrogator is equipped with four optical fiber acceptors (4 channels). In our tests, the fiber pigtail ports of the two axial FBG sensors was connected to channel CH1 and Channel CH3 respectively, and a FBG sensor for temperature compensation was linked to channel CH4. The information on these three FBG sensors is listed in Table 1.

Table 1. The concrete parameters of three FBG sensors on each specimen

Specimen	Channel	Code name	λ_{B0} (nm)	Λ (mm)	L (mm)	Pasting style and function
S1, S2	CH1	CH1-1	1550.5	40	10	Axial direction along the specimen for monitoring strain responses
		CH1-2	1553.5			
		CH1-3	1556.5			
	CH3	CH3-1	1550.5			
		CH3-2	1553.5			
		CH3-3	1556.5			
	CH4	CH4-1	1550.5	-	-	For temperature compensation

λ_{B0}: Initial Bragg wavelength of a grating. Λ: Grating period or the interval of two adjacent grating centers. L: The length of a grating.

3.3 Experimental Procedure

The temperature was controlled by an air-conditioner with the temperature setting of 20 °C during the entire experiment. The complete preparatory work of the general test procedure is outlined below:

i. Under the room temperature at 20 °C, the deionized water for delivering confining pressure (P_c) was injected into core chamber by pump A at a constant pressure of 2 MPa. Then the specimen was saturated with deionized water injected by pump B at a pore pressure (P_p) of 0.5 MPa for 24 h. After complete saturation, P_c was adjusted to 10 MPa. At the same time, the high-purity CO_2 was compressed in pump B at a gas pressure of 2 MPa. After obtaining an equilibrium state, the valve was slowly opened to inject the CO_2 into the specimen for 5 h under the condition of undrained displacement. After the displacement, water and CO_2 were drained from the downstream export. The specimen was washed two or three times and then was saturated again.
ii. After that, at the constant effective confining pressure of 8 MPa, P_c was increased to 16 MPa. Accordingly, CO_2 was compressed with a P_p of 8 MPa and was then injected into specimen for displacing 5 h.
iii. In order to simulate the migration process of $scCO_2$ into the underground thermal layer, the preheating and the core holder heating system were simultaneously heated to 45 °C for 8 h to ensure stable temperature environment exceeding the critical temperature, the step ii was repeated after washing and saturating the sandstone.

4 Results and Discussion

4.1 The Dynamic Stress Perturbation of CO_2 in Different States

The detailed state parameters of CO_2 under this experimental conditions are listed in Table 2. The variation of the relative strains were measured during the injection. The CH1 channel measurement results in specimen S1 are mainly discussed in this paper. The dynamic injection and migration information of CO_2 with different states in the specimen are shown in Fig. 3. The strain responses of the specimen after injecting CO_2 at different P_p at an effective P_c of 8 MPa at temperature 20 °C are shown in Fig. 3(a)–(b). Additionally, Fig. 3(c) shows the migration process of CO_2 at a P_p of 8 MPa after heating the system to 45 °C.

Table 2. The state parameters of CO_2 under different experimental conditions

Temperature (°C)	Pressure (MPa)	State	[a]Density of CO_2 ρ (g/cm^3)	[b]Kinematic viscosity coefficient $\eta \times 10^{-7}$ (m^2/s)	[c]Dynamic viscosity coefficient $\mu \times 10^{-5}$(Pa · s)	[d]Compressibility factor Z
20	2	Gaseous	0.0408	3.67	1.50	0.8857
	8	Liquid	0.7734	0.979	7.57	0.1745
45	8	Supercritical	0.241	0.873	2.11	0.5522

a, b, c, d from http://www.ap1700.com/.

At the initial stage of the injection, the relative microstrains of the specimen surface abruptly reached to the strain peak and then were gradually stabilized during the 5-h displacement process. Since the gas pressure was greater than the P_p of the water (0.5 MPa) that was used to saturate the sandstone, a small amount of CO_2 flashily rushed to the top of the specimen under the undrained hydrostatic pressure condition. Thus, the strain values of the three gratings belonging to the same optical fiber accordingly mutated. For instance, in Fig. 3(a), the three gratings CH1-1, CH1-2, and CH1-3 were influenced by the disturbance of the rock surface stress field caused by the change of P_p and the relative microstrain values measured by the three gratings were different. That was because the measuring accuracy of the grating was not only related to the structure of the grating itself, but was also influenced by the pasting effect, the properties of viscose and its thickness. In Fig. 3(a)–(c), the relative microstrains measured by the gratings increased as the gas pressure increased from 2 to 8 MPa under the effective confining pressure of 8 MPa. The volume of CO_2 injected into the specimen was kept constant (approximately 1 mL in each trial). When the P_c was increased, the pore volume within the specimen relatively decreased. As a result, the injection of the same volume of CO_2 with the rising of the gas (liquid CO_2 or $scCO_2$) pressure lead to relative discharge of more pore water. Thus, the pore water pressure relatively dropped inside the specimen, the effective stress and the internal and external stress field disturbances of the specimen increased more synchronously. Comparing liquid CO_2 and $scCO_2$ injection disturbances, we can see that the strain responses

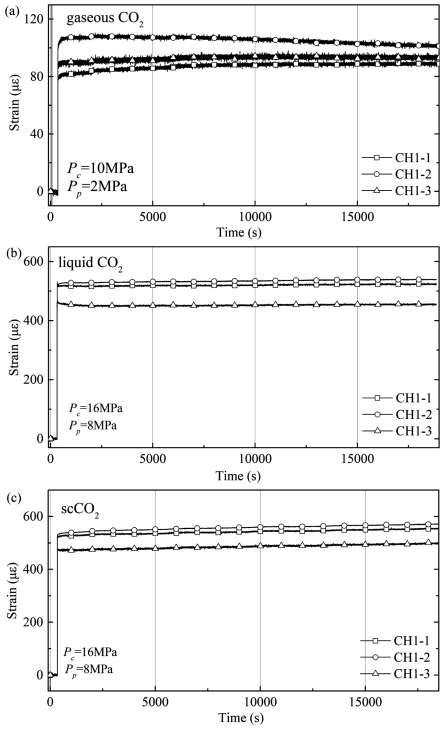

Fig. 3. The relative strain responses induced by CO_2 injection perturbation in sandstone under the same effective confining pressure of 8 MPa. The temperature setting was 20 °C in 3(a)–(b) and 45 °C in 3(c).

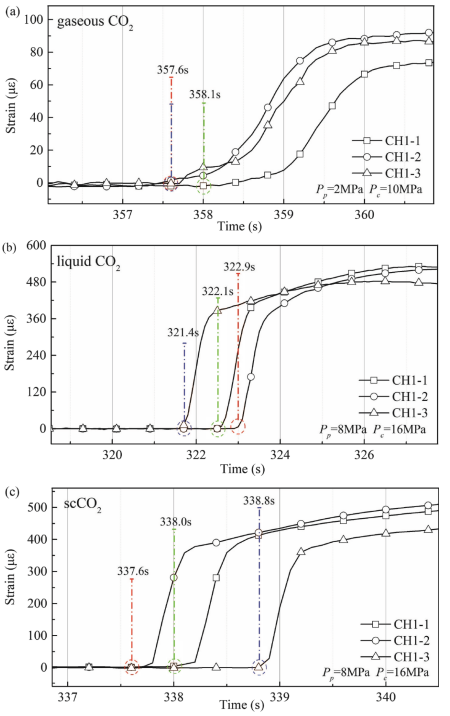

Fig. 4. The migration front information of CO_2 in different states monitored by FBG sensor of the CH1 interface.

caused by the injection of $scCO_2$ was greater than that of liquid CO_2 under the same effective P_c. As can be seen in Fig. 3(b) and (c), the average microstrain measured by three gratings of the CH1 was 505.58 με and 542.58 με for liquid CO_2 and $scCO_2$ respectively. It can be explained that the difference of strain responses may be related to the state of CO_2 because the $scCO_2$ has a lower viscosity and a faster dissipating speed than water. While injecting CO_2, the drainage speed and disturbance responses of $scCO_2$ were more obvious due to its own characteristics. Additionally, increased temperature condition at 45 °C caused thermal expansion of CO_2 resulting in relative increase of pore pressure and accordingly higher strain disturbance.

4.2 The Observation and Comparison of the Migration Front of CO_2

The migration front and pressure conduction information of different states of CO_2 measured by FBG at grating CH1 interface are shown in Fig. 4. Corresponding to the pressure setting conditions in Fig. 3, the measurement analysis results in Fig. 4(a)–(c) are in one-to-one relationship with the initial pressure mutation stages in Fig. 3(a)–(c).

Since the three grating on a single fiber were pasted along the axial direction of the specimen, theoretically, time differences in the strain perturbations measured by the three grating may exist. Thus, it is possible to observe the migration front of gaseous CO_2 or even $scCO_2$ based on such a time difference. Analyses of the measurement results of CH1 showed that the three gratings actually have a measuring time difference, that is, the sequential positions of CO_2 migration in different states. For the gaseous CO_2, the time differences among the strain mutation points of the three gratings was small. For liquid CO_2, the time differences among the three strain jump points was apparent and the maximum time difference was up to 1.5 s. It was conjectured that since the kinematic viscosity of the gaseous CO_2 was much smaller than that of the liquid state but its dissipation rate was faster. As a result, the strain mutations of the three gratings were almost simultaneous. Interestingly, for $scCO_2$, due to its unique physical properties such as the viscosity value being between that of the gas and the liquid state, its mobility was stronger than that of the liquid CO_2. Hence, the measurement results showed that the time difference values of the three gratings were also between the other two states, with a maximum value of 1.2 s.

5 Conclusions

The following conclusions can be derived from the experiments.

i. The strain responses of three different states of CO_2 after injecting into specimen increases with increasing pore pressure. Under the same stress conditions, the disturbance caused by $scCO_2$ is slightly higher than that of liquid CO_2 due to the character of $scCO_2$ and the effect of temperature.
ii. The migration front of CO_2 can be precisely captured by the FBG sensing system. The time differences of strain response of the three gratings on the same fiber can reflect the permeation and transport information of CO_2 in three different states. Among them, the differences in strain response time of three gratings are liquid CO_2, $scCO_2$, and gaseous CO_2 in a descending order.

Acknowledgement. This work was supported by the funding of the National Natural Science Foundation of China (Grant No. 41274111).

References

1. Bachu S, Adams JJ (2003) Sequestration of CO_2 in geological media in response to climate change: capacity of deep saline aquifers to sequester CO_2 in solution. Energy Convers Manag 44:3151–3175
2. Lei X, Xue Z (2009) Ultrasonic velocity and attenuation during CO_2 injection into water-saturated porous sandstone: measurements using difference seismic tomography. Phys Earth Planet Inter 176:224–234
3. Chang C, Zhou Q, Guo J, Yu Q (2014) Supercritical CO_2 dissolution and mass transfer in low-permeability sandstone: effect of concentration difference in water-flood experiments. Int J Greenhouse Gas Control 28:328–342

4. Sun Y, Li Q, Fan C (2017) Laboratory core flooding experiments in reservoir sandstone under different sequestration pressures using multichannel fiber Bragg grating sensor arrays. Int J Greenhouse Gas Control 60:186–198
5. Agartan E, Trevisan L, Cihan A, Birkholzer J, Zhou Q, Illangasekare TH (2015) Experimental study on effects of geologic heterogeneity in enhancing dissolution trapping of supercritical CO_2. Water Resour Res 51:1635–1648
6. Sun Y, Li Q, Fan C, Yang D, Li X, Sun A (2017) Fiber-optic monitoring of evaporation-induced axial strain of sandstone under ambient laboratory conditions. Environ Earth Sci 76 (10):379
7. Li Q, Sun Y, Fan C, Li X, Xu L (2017) Experimental setup and application of high-precision fiber Bragg grating sensors for laboratory core flooding monitoring. JpGU-AGU Joint Meeting 2017, Makuhari Messe, Chiba, Japan

Heat Transfer in Gas Hydrate Bearing Sandstones

Zhiqiang Liu[1,2], Linlin Wang[1,2(✉)], and Guangqing Zhang[1,2]

[1] State Key Laboratory of Petroleum Resources and Prospecting, China University of Petroleum, Beijing, China
linlin.wang@cup.edu.cn
[2] College of Petroleum Engineering, China University of Petroleum, Beijing, China

Abstract. Gas hydrate is encountered in reservoir rock at low temperature and high pressure circumstances. Exploitation gas hydrate commonly invokes to heating or reducing pressure, leading the solid phase transited into liquid phase. With phase transition, the heat is transferred not only in the form of specific heat but also in the form of latent heat. Moreover, the melting point is not constant but depends on the pore size for the phase transition in porous solid. Considering these characteristics, a governing equation of heat transfer with phase transition is established using the equivalent heat capacity method. The equivalent heat capacity is assessed by the pore size distribution curve. Heating tests are conducted and simulated using the model established. The process of heat transfer and its dependences on temperature are discussed.

Keywords: Gas hydrate · Phase transition · Porous solid · Heat transfer
Pore size distribution

1 Introduction

Gas hydrate is solid clathrate compound in which gas molecules are lodged within ice crystals [1–4]. Hydrates, stable under the condition of high pressure and low temperature, generally exist in the deep oceans and permafrost layers [5–7]. The amount of carbon bound in gas hydrates is conservatively estimated to total twice the amount of carbon found in all known fossil fuels on earth [8]. It is recognized as the most potential energy source for replacing traditional fossil fuels and has attracted wide attention due to its widespread on earth.

The exploitation of gas hydrate in deep oceans is not only influenced by temperature and pressure, but the geological structure and submarine engineering make it more complicated. Therefore, the exploitation of gas hydrates on land may be a better way in a certain extent. As gas hydrates become instability once the balance being destroyed, there are three possible methods of hydrate dissociation for gas production (depressurization, thermal stimulation, and use of inhibitors) [9–14]. Comparing with the exploitation of hydrates in deep oceans, it has no limitation in platform on the land. Due to the great convenience in transportation, it also has an advantage in commercial exploitation. But it should be noted that the influence in the permafrost layers cannot be

© Springer Nature Singapore Pte Ltd. 2019
L. Zhan et al. (Eds.): ICEG 2018, ESE, pp. 25–32, 2019.
https://doi.org/10.1007/978-981-13-2227-3_3

ignored. Ice in the permafrost maintains the stability of the skeleton under the condition of perennial low temperature. Changes in temperature and pressure during exploitation can cause phase transition, reducing the strength of soil skeleton, which will influence the wellbore stability.

In this paper, the temperature evolution in the exploitation of gas hydrates in the permafrost layers is studied. A governing equation of heat transfer with phase transition at low temperature is established through combing both the specific heat and latent heat terms into a single "equivalent heat capacity" term. Based on the Gibbs-Thomson equation [18, 19], the relation between ice content and temperature is assessed by the pore size distribution curve from mercury intrusion porosimetry (MIP) data. We simulate the temperature disturbance with the model established in the exploitation, providing the basis of the theory for further studying in wellbore stability.

2 Theoretical Modeling

According to Poisson's law [20], considering the heat conduction as the only form of energy exchange in rocks, the governing equation of heat transfer is

$$\rho c \frac{dT}{dt} = \nabla(\lambda \nabla T) \tag{1}$$

where T is temperature, t is time, ρ is the density of rock (kg/m^3), c is specific heat (J/kg · K), and λ is thermal conductivity (W/m · K). ∇ is gradient operator. With temperature change, phase transition occurs in the pores, heat is transited both in form of specific heat, that only temperature change with time, and latent heat, that only phase change with time. Therefore, the governing equation of heat conduction with phase transition is:

$$\rho c \frac{dT}{dt} - L\rho_i \frac{d\theta_i}{dt} = \nabla(\lambda \nabla T) \tag{2}$$

where L is the latent heat of fusion per unit mass of water (3.33×10^5 J/kg), and θ_i is the volumetric fraction of ice, ρ_i is the density of ice. Assuming the freezing/thawing process is instantaneous, we get $d\theta_i/dt = (d\theta_i/dT)(dT/dt)$. Accordingly, Eq. (2) can be rewritten as

$$\left(\rho c - L\rho_i \frac{d\theta_i}{dT}\right) \frac{dT}{dt} = \nabla(\lambda \nabla T) \tag{3}$$

where ρc-$L\rho_i d\theta_i/dT$ is termed equivalent volumetric heat capacity and the term $d\theta_i/dT$ should be determined once solve it. When freezing in the pores, the melting temperature is not constant but depends on the pore size (i.e., the curvature of the pore). The phase transition in porous solids is governed by the Gibbs-Thomson equation

$$r_i = \frac{2\bar{V}_i \gamma_{iw} \cos \alpha}{(S_w - S_i)(T_m - T)} \tag{4}$$

where r_i is the smallest pore access radius of the pore volume currently invaded by ice crystals, S is molar entropy of material (J/mol · K), $\bar{V}_i$ represents the molar volume of ice (m^3/mol), γ_{iw} is the water-ice interface stress (0.04 J/m^2), and α is the contact angle of water-ice interface ($\alpha = 0$ in thawing process). Gibbs-Thomson equation reveals that it exists a critical radius of pores for a given temperature: ice crystal forms in the pores bigger than that but cannot for the pores smaller than that (Fig. 1). This is also the principle of measuring the pore size distribution through the relation between ice content and temperature.

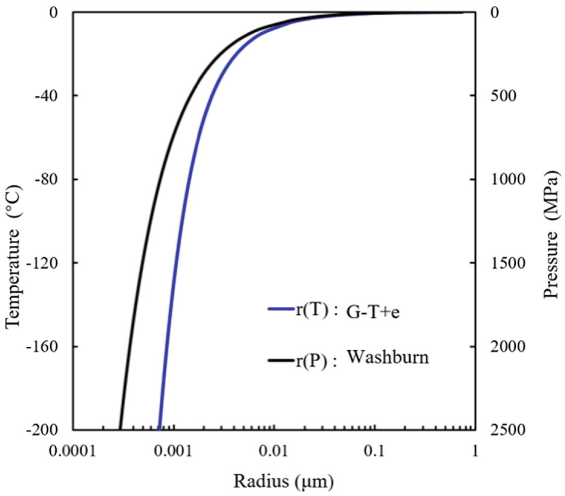

Fig. 1. Relation among the smallest pore access radius with temperature. r(T): Gibbs-Thomson equation considering the pre-melting film (G-T+e); r(P): Relation among the pore radius with Hg pressure in mercury intrusion porosimetry (MIP).

However, because of disjoining pressure, it exists a pre-melting liquid film between pore wall and pore ice, which never freezes (e is 1 nm here). Therefore, the real pore size occurring freezing should consider the thickness of this pre-melting film and is then expressed by

$$r = r_i + e \tag{5}$$

The relation between ice content and temperature can be obtained using Eqs. (4) and (5) if the pore size distribution is known. The pore size distribution is commonly obtained by MIP which determined by the Washburn equation:

$$r = \frac{2\sigma_{Hg}\cos\alpha_{Hg}}{p} \tag{6}$$

where p is the mercury pressure (MPa), σ_{Hg} is the interfacial tension for Hg (0.48 mN/m), α_{Hg} is the contact angle of liquid column and wall surface ($\cos\alpha_{Hg}$ = 0.765 for Hg).

Combining Eqs. (4)–(6), we can get the relation between the melting point and intrusion pressure for the pores with a given radius:

$$p = \frac{2\sigma_{Hg}\cos\alpha_{Hg}}{\frac{2\bar{V}_i\gamma_{iw}\cos\alpha}{(S_w - S_i)(T_m - T)} + e} \tag{7}$$

The evolution of ice content with temperature can be assessed from the data of MIP through replacing p with T using Eq. (7). Nevertheless, it should be noted that equations above relating ice content with temperature is based on the assumption that freezing/melting occurs independently in each pore. However, freezing depends on pore connection, that is, freezing in pore also depends on its entrance pore. Considering a large pore with a smaller entrance pore, with decreasing temperature, the large pore would not freeze firstly but at the same temperature when the smaller entrance pore freezes. Conversely, due to existing the pre-melting liquid film, melting process involves no surface energy cost and thus occurs independently in each pore. Therefore, the above-established model merely holds for the melting process that is not affected by the pore connectivity.

3 Simulation

The fluid in the wellbore will cause temperature disturbance in the permafrost layers during exploitation. Considering this problem, the simulated model is established (shown in Fig. 2). The diameter of wellbore is 200 mm, and the permafrost layer is homogeneous with radius of more than 10 m. Being in contact with the atmosphere, the wellbore boundary is convective boundary, and the outer boundary is free boundary. Assuming the initial temperature of permafrost layers is −4 °C, and the temperature of well fluid is 5 °C.

The pore size distribution curve is obtained from the experimental data of rock A (shown in Fig. 3a, the peak is about 10 μm). In order to investigate the influence of pore size distribution during heat transfer process, the pore size distribution of rock B is obtained by shifting the curve of rock A (the peak is about 50 μm). The relation between ice and temperature of A and B is obtained through the Eqs. (8) and (9) (shown in Fig. 3b). The change rate of ice content with temperature for A and B both large near 0 °C, while the ice content of B is larger than A due to the difference of porosity. Then, the heat transfer process is simulated.

The temperature distribution evolves over time (from 1 h to 30d), the temperature distribution of the sample is obtained in the direction of radial (R-axis in this work,

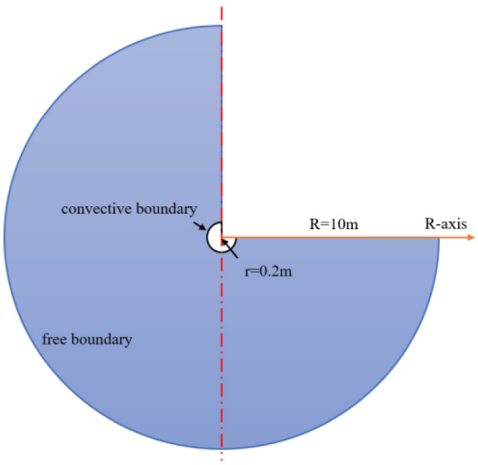

Fig. 2. Geometric model

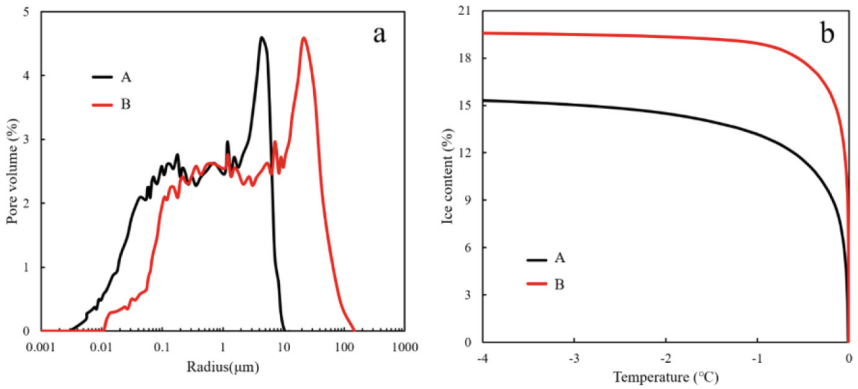

Fig. 3. a.The pore distribution curve of sample A and B; b. Ice content vs temperature in pores.

shown in Fig. 4). At different moments, the temperature is gradually decreasing along the R-axis. The temperature gradient is larger, the temperature is propagated faster.

The temperature curve of A and B at the same point in the wellbore is shown in Fig. 5. The temperature gradually increases with time, both temperature evolution curves feature a plateau regime, that is, temperature remains quasi-constant with time when the temperature reaches zero. The temperature of B is rising faster than A. Assuming temperature remains quasi-constant with time when the rate of temperature change over time is less than 0.01 ($dT/dt < 0.01$), the length of temperature plateau of B is larger than A.

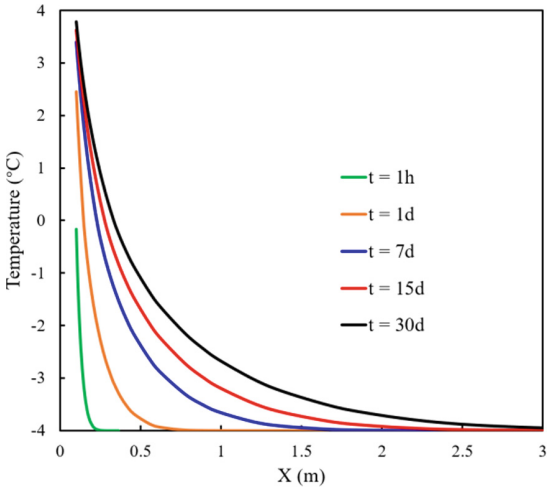

Fig. 4. Temperature distribution of permafrost at different moments

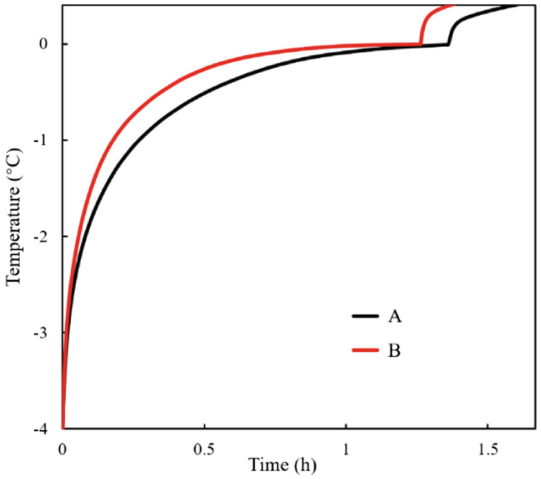

Fig. 5. Temperature vs time for sample A and B

4 Discussion

From the simulation, it can be demonstrated that the appearance of temperature plateau is related to a sharp rise in the equivalent heat capacity (due to a dramatic increase in the latent heat term) at the corresponding temperature regime. The dramatic increase in the latent term is related to a rapid accumulation of ice content, implying a significant phase transition (Fig. 3). It also can be seen from Eq. (3) that the latent heat increases suddenly when ice content rapid changes over temperature with other parameters remain constant, equaling to increase the equivalent volumetric heat capacity. Under

similar pore size distribution, the initial heating rate of B is larger than A due to the difference of porosity. Besides, in smaller temperature range, the length of temperature plateau of B is larger than A as the change of ice content of B is larger.

As discussed previously, temperature plateau studied is determined by the relation between ice content and temperature. In this paper, the relation between ice content and temperature is assessed by the pore size distribution curve which obtained from MIP data, that is, the pore size distribution can be obtained by measuring the temperature evolution curve of material saturated water at low temperature.

5 Conclusion

This paper studies heat transfer in gas hydrate sediment during exploitation. The main conclusions are as follows:

(1) A governing equation is established describing the heat transfer in rocks at low temperature, which both specific heat and latent heat terms are combined into equivalent heat capacity. The evolution of ice content with temperature using the pore size distribution from MIP data.
(2) The temperature of samples remains quasi-constant for some moment. This is mainly related to intense phase transition that absorbs a great quantity of latent heat. Moreover, our investigations demonstrate that the position and length of this temperature plateau can be predicted by the pore size distribution data.

References

1. Ripmeester JA, Tse JS, Ratcliffe CI et al (1987) A new clathrate hydrate structure. Nature 325(6100):135–136
2. Dendy Sloan E Jr (1998) Gas hydrates: review of physical/chemical properties. Energy Fuels 12(2):191–196
3. Kvenvolden KA (1993) Gas hydrate-geological perspective and global change. Rev Geophys 31(2):173–187
4. Koh CA (2002) Towards a fundamental understanding of natural gas hydrates. Chem Soc Rev 31(3):157–167
5. Sloan ED Jr, Koh C (2007) Clathrate Hydrates of Natural Gases. CRC Press, Boca Raton
6. Macdonald IR, Guinasso NLJ, Sassen R et al (1994) Gas hydrate that breaches the sea floor on the continental slope of the Gulf of Mexico. Geology 22(8):699–702
7. Milkov AV (2004) Global estimates of hydrate-bound gas in marine sediments: how much is really out there. Earth-Sci Rev 66(3):183–197
8. Lee SY, Holder GD (2001) Methane hydrates potential as a future energy source. Fuel Process Technol 71(1–3):181–186
9. Makogon IUF (1981) Hydrates of Natural Gas. PennWell Books, Tulsa
10. Makogon IUF (1997) Hydrates of Hydrocarbons. PennWell Books, Tulsa
11. Moridis GJ, Reagan MT (2007) Strategies for gas production from oceanic class 3 hydrate accumulations. Lawrence Berkeley National Laboratory

12. Moridis GJ, Reagan MT (2007) Gas production from class 2 hydrate accumulations in the permafrost. In: SPE Annual Technical Conference and Exhibition. Society of Petroleum Engineers
13. Marcelle-De Silva J, Dawe R (2011) Towards commercial gas production from hydrate deposits. Energies 4(2):215–238
14. Stevens JC, Howard JJ, Baldwin BA, et al (2008) Experimental hydrate formation and gas production scenarios based on CO2 sequestration. In: Proceedings of the 6th International Conference on Gas Hydrates, pp 6–10
15. Freij-Ayoub R, Tan C, Clennell B, Tohidi B, Yang J (2007) A wellbore stability model for hydrate bearing sediments. J Petrol Sci Eng 57(1):209–220
16. Tan C, Freij-Ayoub R, Clennell M, et al (2005) Managing wellbore instability risk in gas hydrate-bearing sediments. In: SPE
17. Long X, Tjok KM, Wright CS, et al (2014) Assessing well integrity using numerical simulation of wellbore stability during production in gas hydrate bearing sediments. In: Offshore Technology Conference
18. Coussy O (2011) Mechanics and Physics of Porous Solids. Wiley, Hoboken
19. Sun Z, Scherer GW (2010) Pore size and shape in mortar by thermoporometry. Cem Concr Res 40(5):740–751
20. Bergman TL, Incropera FP (2011) Fundamentals of Heat and Mass Transfer. Wiley, Hoboken

Hydraulic Characterisation of Clay Rock Under Consideration of Coupled THM Properties

Hua Shao[1(✉)], Jürgen Hesser[1], Olaf Kolditz[2], and Wenqing Wang[2]

[1] Federal Institute for Geosciences and Natural Resources, Stilleweg 2, 30655 Hanover, Germany
shao@bgr.de
[2] Helmholtz-Centre for Environmental Research (UFZ), Permoserstraße 15, 04318 Leipzig, Germany

Abstract. Clay rock is being investigated in many countries as a potential host rock for nuclear waste repositories. Due to the state of over-consolidation and water saturation, characterisation of undisturbed rock with regard to its hydraulic and mechanical properties is a big challenge. Increased complexity is caused by temperature change in the repository of high-level waste. In situ measurement of single component, e.g. rock permeability, was conducted in the Mont Terri Rock Laboratory (CH) and the French Underground Research Laboratory Bure. Several so-called heater experiments are being carried out at different scale. The measured data including temperature, humidity, pore pressure, and deformation in various boreholes shows strong coupling effects. For interpretation of the experimental data, a numerical 3D code OpenGeoSys (OGS) was developed taking into account the strongly coupled thermal, hydraulic and mechanical processes. Because of the significant dependency of the thermal conductivity on the water saturation, the determination of the saturation state, which is again controlled by hydraulic permeability, is therefore important. The evaluated permeability from packer tests can be validated using numerical modelling. The state-dependency on the pressure, saturation and temperature is discussed.

Keywords: Disposal of nuclear waste · Underground laboratories
Hydraulic measurement · Coupled THM modelling · OpenGeoSys

1 Introduction

For the disposal of radioactive waste, the permeability of the rock plays an essential role with respect to the barrier effect of the host rock. The knowledge of the permeability and their spatial distribution around the disposal facilities in the potential rocks are essential for the safety analysis of a repository.

As an alternative activity to the research work in rock salt and crystalline rock, the Federal Institute for Geosciences and Natural Resources (BGR) has participated in the international research projects in the Mont Terri Rock Laboratory in Switzerland since 1996 and in the French Underground Research Laboratory Bure since 2004. Both sites are located in a ductile clay formation, which is highly consolidated and water

© Springer Nature Singapore Pte Ltd. 2019
L. Zhan et al. (Eds.): ICEG 2018, ESE, pp. 33–40, 2019.
https://doi.org/10.1007/978-981-13-2227-3_4

saturated. The focus of the research programs is to characterisation of thermal, hydraulic and mechanical properties of the claystone.

Due to the significant interaction between thermal, hydraulic and mechanical processes (THM), the result of a single measurement is often ambiguous. Therefore, a synthetic analysis of hydraulic properties taking account of the results from different measurement methods is therefore inevitable.

In order to meet this high demand, not only the hydraulic *in situ* measurements but also THM-coupled model approaches are used for the evaluation and interpretation of the measured data.

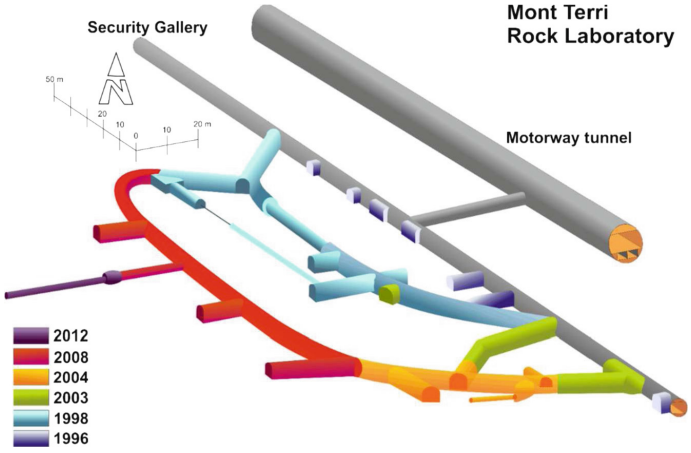

Fig. 1. Locations for hydraulic packer tests (red-marked), HM coupled Mine-by tests (blue), and THM coupled heater experiments (green) (Thury and Bossart 1999; www.mont-terri.ch)

2 Underground Laboratories in Clay Rock

The Mont Terri Rock Laboratory is located in the north-west of Switzerland and is located in the folded Opalinus Clay with an overburden of about 200 m in thickness. The laboratory was constructed from the Security Gallery of a motorway tunnel from Switzerland to France and was extended continuously. The recent extension 2018 is under construction. The Opalinus Clay is a heavily stratified Mesozoic claystone. The layering with an angle of inclination of approximately 45° determines the rock properties and is the cause of the anisotropies with respect to thermal conductivity, hydraulic permeability and mechanical deformability.

The Bure Underground Laboratory is located approximately 500 m below the surface of the terrain in the Callovo-Oxfordian claystone of the Paris basin. The sediment layers are quasi-horizontal with an angle of inclination of 1.5 °C to the southwest. At both locations, the clay stones are water saturated in the undisturbed state. The pore water pressure in Mont Terri is 20 bar and in Bure about 45–50 bar, which are correspond to the hydrostatic pressure.

3 Hydraulic Packer Test and Uncertainties

To determine the intrinsic permeability of a rock, hydraulic or pneumatic packer test in a pre-drilled borehole is still a mostly used *in situ* method. This method is not a non-destructive one, because the drilling disturbs the initial rock state and may change the rock properties in the near of a borehole (so-called BDZ: borehole damaged/disturbed zone) (Schuster et al. 2017). If the borehole is not perpendicular to the bedding plane, breakouts (damage) occur and significantly change the hydraulic and mechanical properties.

Successful measurement has been done to characterise hydraulic properties in the near-field (EDZ: excavation damaged zone). In various locations (Fig. 1), numerous boreholes were drilled in different directions parallel and perpendicular to the bedding plane for the hydraulic testing. A typical distribution of the permeability along the borehole around the tunnel is exhibited in Fig. 2. Up to a distance of 2.5 m to the tunnel wall without shotcrete supporting, a significant increase in permeability was measured. This increase was caused on the one hand by stress redistribution. The consequences are micro-cracks and damage around the opening. On the other hand, the ventilation leads to a reduction of moisture in the mountains via the micro- and macro-cracks. The reduction of the water saturation is associated with a shrinkage of the clay rock, so that the permeability increases further.

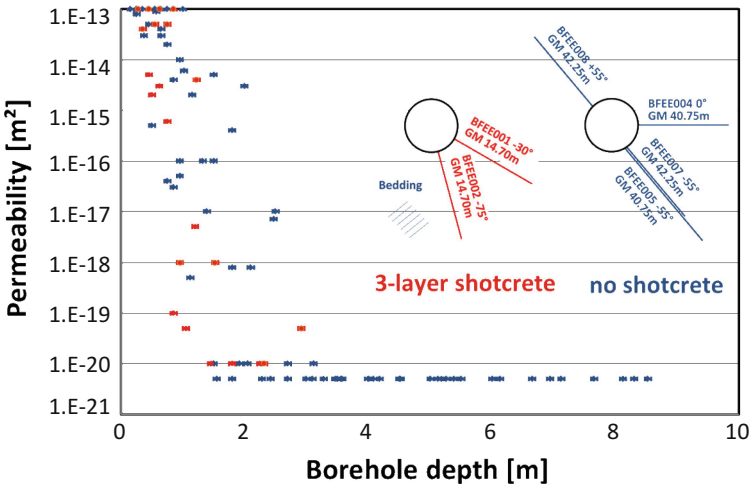

Fig. 2. Permeability distribution around the FE-tunnel (Fig. 2.1) (Shao et al. 2016)

For the extreme low permeable media, a pulse injection and a subsequent (long-term) recovery phase is an effective way. Due to possible swelling deformation by water in the (partially) saturated clay rock, which changes the material structure, noble gas (e.g. nitrogen) was used as injection medium. The intrinsic permeability can then be evaluated using a numerical two-phase flow model from the measured permeability

to gas. In this two-phase flow system, the gas entry pressure and the relationship between the relative gas permeability and the saturation are two important factors, which are determined beforehand in the laboratory.

Therefore, the injection pressure is a crucial factor. If the pressure is too low, the gas will not overcome the entry threshold and flow into the formation, in case of injection pressure of two and four bars (Fig. 3). However, if the pressure is too high, a dilatancy-controlled flow may occur. The latter may also change the pore structure and corresponding permeability. Based on the observation of the injection pressure dependent flow in the saturated clay material, we have to ask what the intrinsic permeability of clay rock is and how this value can be determined in a correct manner. The usually measured permeability value up to date is the hydraulic permeability of the saturated clay. Hence, a permeability in the 'undisturbed' rock can only be estimated, but not be determined to be lower than 10^{-20} m^2.

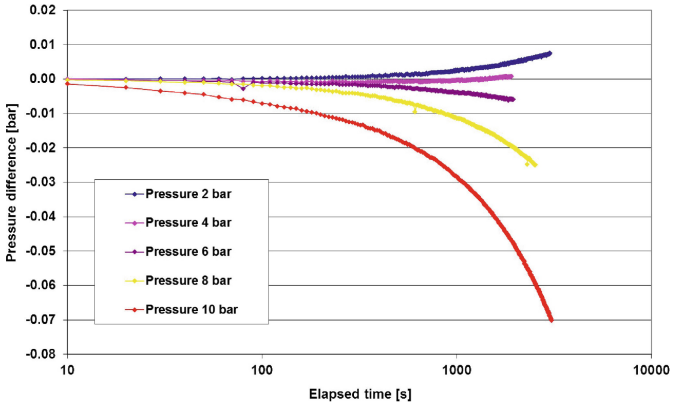

Fig. 3. Evolution of normalized pressure difference under different injection pressure, indicating the influence of the pore pressure, entry threshold, and dilatancy pathway of the surrounding rock

The measurement of permeability in clay rock is therefore with a significant uncertainty. This uncertainty is even bigger, if the temperature effect by heat input in a heat-generating waste repository is considered. The permeability may change due to thermal expansion and desaturation after a long-term heat load. This is the reason why we measure not only the permeability in boreholes. We have to consider also the permeability change under the operation (desaturation phase) and repository conditions (heating phase).

4 Excavation and Heater Experiments

Numerous large-scale tests including excavation and heater experiments have been conducted in the underground laboratories Mont Terri (Fig. 1), e.g. the Mine-by test (Vietor 2009), HG-A (Xu et al. 2013), FE (Müller et al. 2017), HE-E (Gaus et al. 2014)

and Bure (GCS, TED, ACL) to obtain a better understanding of coupled HM and THM processes.

A mine-by experiment is an effective method to monitor pore pressure change and deformation as well as stress change during an underground excavation. From the measured data, the interaction between hydraulic and mechanical properties can be analysed with the help of numerical approaches (Sect. 5). A mine-by experiment can qualitatively determine the extension of an excavation-damaged zone around the opening. The time-dependent deformation process is clearly a product of the change of pore pressure on the one hand and on the other hand the change of mechanical properties induced by the hydraulic desaturation around the opening (Fig. 4).

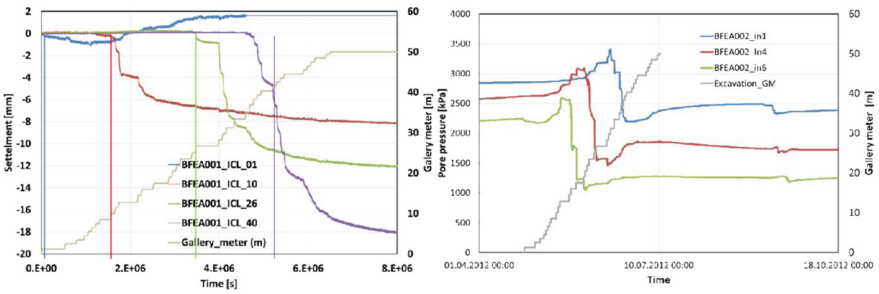

Fig. 4. Development of deformation and pore water pressure during a Mine-by experiment

A heater experiment in the underground laboratory simulates a real repository for disposal of heat generating waste. The data from such experiment reflect the long-term phenomenon during the post-closure phase. This valuable dataset serves to interpret the time-dependent rock state under a certain thermal-hydraulic-mechanical condition. As an example, we introduce only the result from the heater experiment FE (full-scale emplacement) conducted in the Mont Terri Rock Laboratory in the Sect. 5 with the aim of determination of rock permeability.

5 Coupled HM and THM Modelling

Numerical coupled HM and THM modelling were performed using the finite element code OGS (Kolditz et al. 2014) to interpret the measured data and to understand the experimental findings. The open source code OGS was originally designed for simulation of groundwater movement and pollutant transport and developed to a fully coupled thermal, hydraulic and mechanical model for porous media and fractured rock. The code is widely used in the groundwater management, geotechnical application, CO_2 storage, geothermal energy and energy storage.

For the modelling of the heater experiment, three conservation equations of energy, mass and momentum are implemented in a sequential calculation algorithm. Terzaghi's effective stress concept and the Richards' flow model for the unsaturated flow are used.

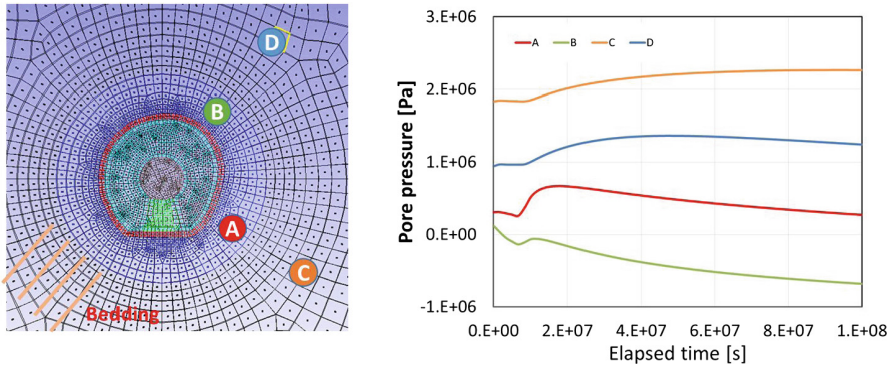

Fig. 5. Characteristic curves for pressure at different locations due to heating

Important in the numerical modelling is a possibly complete representation of the experimental set-up and test procedure. The modelling of excavation procedure of the FE-tunnel is therefore necessary and determines an initial state about the hydraulic and mechanical conditions, namely the distribution of saturation, pore pressure and stress state for the modelling of the subsequent heater test. A zone around the test tunnel is assumed as a regular EDZ with increased permeability (Fig. 3). Under the heating condition, four different types of pore pressure evolution can be characterised with identification of unsaturated state and hydraulic connection to the excavated gallery (Table 1). While the negative pressure (suction) at the point B indicates an unsaturated state, the continuous increase of the pore pressure at the point C is the result of a thermal expansion of the pore water in the low permeable zone. All 20 pore pressure sensors evaluated in this study can be characterised by these four categories.

Table 1. Characterisation of pore pressure development

Category	Description	Permeability zone	Connectivity
C1 (B)	Low pressure/negative (unsaturated)	High	High
C2 (A)	Pressure increase/decrease fast	High	Low
C3 (D)	Pressure increase/decrease slow	Low	Relative high
C4 (C)	Pressure increase slow and continuously	Low	Low

Local heterogeneity is not considered in this idealised model yet. The comparison between measured and modelled results (Fig. 6, left) shows in some observation points different behaviour of the pressure evolution. The low pressure at BFEB006 may suggest that the sensor is located in a strongly damaged zone with a higher permeability than 1E-18 m^2 as assumed in the model.

In the far-field (Fig. 5, right) all pressure sensors respond to the temperature change, however, the pressure increase begins earlier than the temperature rise. The pressure increase at the farthest sensor BFEA007 may indicate that the porosity decrease induced by thermal expansion of the solid phase. Much better results can be

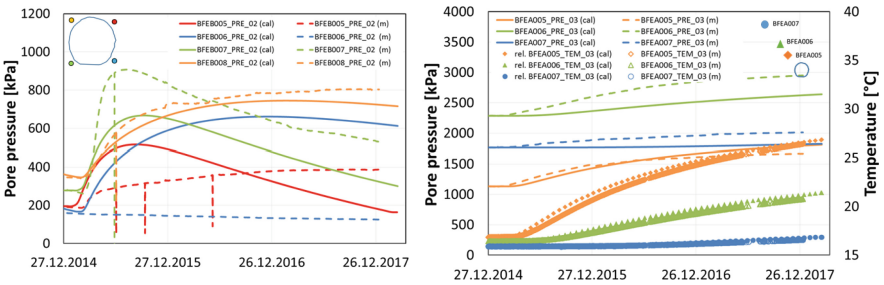

Fig. 6. Evolution of pore pressure in the near- and far-field around the FE tunnel

achieved when we consider the porosity and permeability change in the model. The permeability may be suggested to be lower than 1E-20/5E-21 m^2 used in the model calculation.

6 Conclusions

Rock permeability is a key parameter with respect to the barrier performance for a repository. Determination of intrinsic permeability in clay rock is crucial due to strong interaction between thermal, hydraulic and mechanical properties. To minimise the uncertainty of the measurement results from the *in situ* packer test, we introduce a synthetic analysis of all measured parameters from excavation tests and heater experiments using a coupled THM model.

The evaluated permeability in the undisturbed rock and near-field around the excavated gallery may be used as reference parameter, which can, however, be validated in the numerical THM model for simulation of the heater experiment. The homogeneous model can not fit all measured data in all sensors installed, but an estimation of the parameter change can be made according to the characteristics exhibited in the numerical solutions.

References

Gaus I, Garitte B, Senger R, Gens A, Vasconcelos R, Garcia-Sineriz JL, Trick T, Wiezo-rek K, Czaikowski O, Schuster K, Mayor JC, Velasco M, Kuhlmann U, Villar MV (2014) The HE-E Experiment: layout, Interpretation and THM modelling. Arbeitsbericht NAB 14-53

Kolditz O, Shao H, Wang W-Q, Bauer B (2014) Thermo-Hydro-Mechanical-Chemical Processes in Fractured Porous Media – Modelling and Benchmarking. Springer, Heidelberg

Müller HR, Garitte B, Vogt T, Köhler S, Sakaki T, Weber HP, Spillmann T, Hertrich M, Becker JK, Giroud N, Cloet V, Diomidis N, Vietor T (2017) Implementation of the full-scale (FE) experiment at the Mont Terri rock laboratory. Swiss J. Geosci.

Schuster K, Amann F, Yong S, Bossart P, Connolly P (2017) High-resolution mini-seismic methods applied in the Mont Terri rock laboratory (Switzerland), Swiss J. Geosci. https://doi.org/10.1007/s00015-016-0241-4

Shao H, Paul B, Wang XR, Hesser J, Becker J, Garitte B, Müller H (2016) The influence of different supports on the properties of the excavation damaged zone along the FE tunnel in the Mont Terri Underground Rock Laboratory, Geological Society London

Thury M, Bossart P (1999) Mont Terri Rock Laboratory – Results of the hydrogeological, geochemical and geotechnical experiments, Swiss National Hydrological and Geological Survey, Bern

Vietor T (2009) MB experiment: Database of report. Mont Terri Technical Note TN2009, Mont Terri Project, Saint Ursanne, Switzerland

Xu WJ, Shao H, Marschall P, Hesser J, Kolditz O (2013) Analysis of flow path around the sealing section HG-A experiment in the Mont Terri rock laboratory. Environ Earth Sci 70:3363. https://doi.org/10.1007/s12665-013-2403-2

Mixed Region Simulation on Subsurface Gas Storage of CO_2 and CH_4 in a Power-to-Gas System

Jianli Ma[1,2], Qi Li[1,2(✉)], Michael Kühn[3], and Xiaying Li[1,2]

[1] State Key Laboratory of Geomechanics and Geotechnical Engineering, Institute of Rock and Soil Mechanics, Chinese Academy of Sciences, Wuhan 430071, China
qli@whrsm.ac.cn
[2] University of Chinese Academy of Sciences, Beijing 100049, China
[3] GFZ German Research Centre for Geosciences, Fluid Systems Modelling, Potsdam, Germany

Abstract. Power-to-Gas (PtG) is a chemical energy storage technology that converts electrical energy into a high-energy density combustible gas. This technology alleviates the contradiction between power supply and demand due to the intermittent electricity production from environment-friendly renewable energy. Hydrogen (H_2), produced by electrolysis, can be used to produce synthetic methane (CH_4) by reacting with carbon dioxide (CO_2) that is captured from carbon emission sources. Subsurface gas storage is one of the most important processes in a PtG system. However, nearly a half of the total stored gas is used as cushion gas to maintain a suitable reservoir pressure, indicating large amounts of CH_4 might be wasted and trapped in geological formations. Based on a PtG system, CO_2 can be a promising choice as a cushion gas due to its high effective compressibility near its critical conditions. In this paper, a numerical model is established based on the theory of the fluid flow and molecular diffusion to study the role of CO_2 as a cushion gas in increasing the gas storage capacity. The accuracy of this model is verified by comparing with that of Curtis M. Oldenburg. However, because of the declining purity of recovered gas induced by the convection and diffusion of two kinds of gases in the same reservoir. The influences of reservoir thickness on the distribution of mixed region are discussed. The results show that thicker reservoir would be a better choice for the geological storage of CH_4 with CO_2 as a cushion gas.

Keywords: Power-to-Gas (PtG) system · Subsurface gas storage
CO_2 · CH_4 · Cushion gas

1 Introduction

One of the disadvantages of the renewable energy is inherently intermittent. In that way, large amounts of power will be wasted in the time of low power consumption. As a reliable and efficient technology, Power-to-Gas (PtG) might contribute to effectively utilize the renewable energy and transform to the power grid in scales of time, space

© Springer Nature Singapore Pte Ltd. 2019
L. Zhan et al. (Eds.): ICEG 2018, ESE, pp. 41–48, 2019.
https://doi.org/10.1007/978-981-13-2227-3_5

and intensity. PtG is a chemical energy storage technology that converts electrical energy into a high-energy density combustible gas. The Hydrogen (H_2), produced from the electrolyzed water, reacts with the captured Carbon Dioxide (CO_2) to produce synthetic methane (CH_4), thereby achieving carbon neutralization. The specific process is shown in Fig. 1.

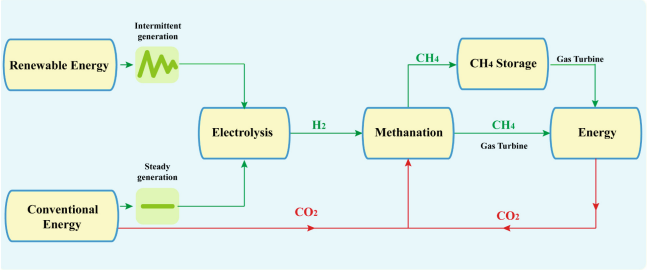

Fig. 1. Power-to-gas flow chart

In terms of CH_4 storage, there are numbers of ways to store such as the gas tank, gas pipeline and subsurface storage. Compared to other storage methods, subsurface gas storage can provide the mid and long-term or seasonal energy storage cycle due to its superior economy and large storage capacity [1]. However, nearly 40%–70% of total stored gas is used as cushion gas to maintain suitable reservoir pressure, which means large amounts of gases will be trapped in the geological formations and cannot be extracted [2]. Using native gas as the cushion gas may lead to a huge amount of energy waste. In addition, a great compressibility of cushion gas is necessary. Otherwise, the reservoir pressure will rise sharply during the injection of methane, and the stability of the reservoir will be threatened.

Based on the PtG system and the physical properties requirement of cushion gas, CO_2 is considered as a great choice because of the high compressibility near its critical conditions (31.06 °C and 7.38 MPa) [3, 4]. What's more, using CO_2 as cushion gas also makes a great contribution on carbon sequestration [5].

In this paper, the distribution and migration of mixed fluids in the process of dynamic injections are simulated based on the physical properties of CH_4 and CO_2. Influence of reservoir thickness on the distribution of the gases mixed region were analyzed as well. Simulation results can provide a theoretical and technical support for optimization of subsurface energy storage processes in a PtG system and engineering applications.

2 Modelling

2.1 Physical Properties of CH_4, CO_2 and Their Mixtures

It can be seen in Figs. 2 and 3 [6] that the density and dynamic viscosity of CH_4 ranges from nearly 20 to 220 kg/m^3, and 1.2×10^{-5} to 2.6×10^{-5} Pa · s with the change of

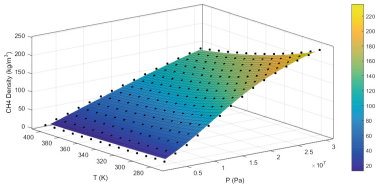

Fig. 2. CH_4 density changes with temperature and pressure

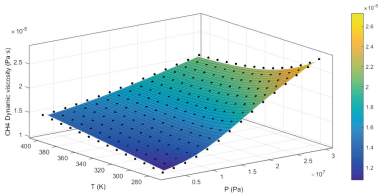

Fig. 3. CH_4 dynamic viscosity changes with temperature and pressure

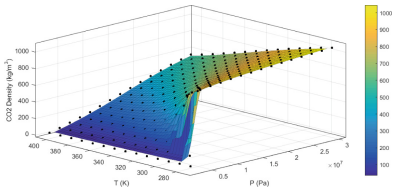

Fig. 4. CO_2 density changes with temperature and pressure

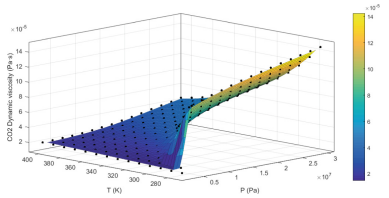

Fig. 5. CO_2 dynamic viscosity changes with temperature and pressure

temperature (273–403 K) and pressure(0–30 MPa), respectively. However, in Figs. 4 and 5 [7], when the temperature is 300–320 K and the pressure is 6 to 8 MPa, the density of CO_2 suddenly increases by approximately 6 times, which fully demonstrates extremely high compressibility of CO_2 near the supercritical state [7]. In the same conditions, the density of CH_4 only steadily increased by ~ 2 times. As for the dynamic viscosity of CO_2, which also has a similar behavior when it comes to critical conditions. Compared to CH_4, the viscosity of CO_2 is nearly 10 times than that of CH_4 at the critical conditions, and it is still increased with the increasing pressure [7]. Therefore, large differences in the density and dynamic viscosity may reduce the mixing degree of the two kinds of fluids to some extent.

Once the miscibility occurs between fluids, the mixed fluid will have different physical properties based on the degree of mixing. Assume that the temperature is 313 K in Fig. 6 [8, 9], when CO_2 mixed with a small amount of CH_4, the density and dynamic viscosity of the mixture are mostly changed, which demonstrates that the physical properties of the mixtures strongly correlate with the mixing degree. Therefore, the density and dynamic viscosity parameters of the mixtures cannot be obtained simply by the weighted average, but only be modeled in strict accordance with changes in its real physical properties.

2.2 Modelling Methods

The miscibility of the two fluids in the reservoir and its effect on the injection of CH_4 are studied. Simulation results presented below are carried out by using commercial finite element software COMSOL Multiphysics. By modifying the average density and viscosity module in COMSOL, the actual physical properties of the mixture of CH_4 and

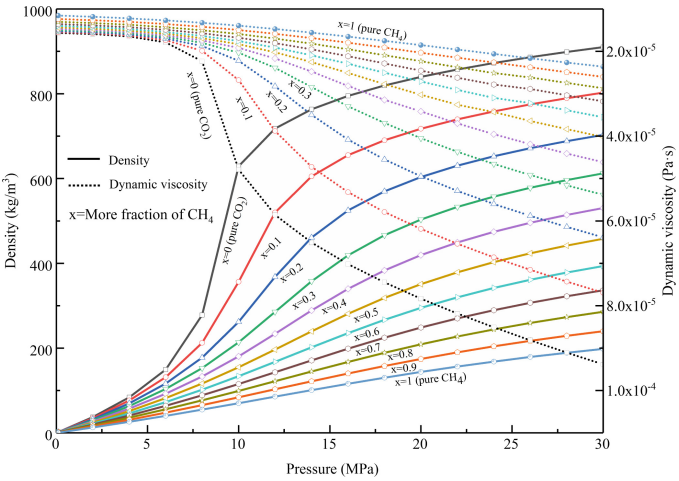

Fig. 6. Density and dynamic viscosity of two fluids mixtures (8, 9)

CO_2 are clearly described. Based on the principle of mass conservation, the continuity equation of fluid flow can be obtained.

$$\frac{\partial(\rho\phi)}{\partial t} + \nabla(\rho \boldsymbol{u}) = 0 \tag{1}$$

where ρ is density of the mixed fluid (kg/m^3); ϕ is effective porosity of the reservoir; $\boldsymbol{u}$ is Darcy velocity (m/s) of the fluid which can be obtained by Darcy's law.

$$\boldsymbol{u} = -\frac{k}{\mu}(\nabla p + \rho g) \tag{2}$$

where k is permeability of the reservoir (m^2); μ is viscosity of the mixed fluid (Pa · s); p is pore pressure (Pa); g is gravity acceleration (9.81 m/s^2).

According to Fick's law, the diffusion flux of a component fluid is proportional to its concentration.

$$\boldsymbol{J}_i = -D\nabla c_i \tag{3}$$

where $\boldsymbol{J}_i$ is diffusion flux of single component in multi-component gases (kg/(m^2 · s)); D is mass diffusion coefficient (m^2/s); c_i concentration of a single component in multi-component gases (kg/m^3). The diffusion equation can be obtained by combining this equation with Eq. (1).

$$\frac{\partial(\phi c_i)}{\partial t} + \nabla(c_i \boldsymbol{u}) = \nabla(D_c \nabla c_i) \tag{4}$$

where $c_i = S_i \rho_i$, and S_i is the mole fraction of a component gas. In addition, $S_{co_2} + S_{CH_4} = 1$.

3 Model Validation

This section is to show the accuracy of this model by comparing with the model of Curtis M. Oldenburg [10]. The model system is a two-dimensional reservoir with a thickness of 22 m and a length of 1000 m (Fig. 7). The model is axisymmetric, so only half of the domain is considered in the following sections. The domain is discretized into 4400 uniform grids (22 × 200 grids in Y and X directions, respectively). The injection/production well is set on the left side at Y = −3 m. All the boundaries are no flow, and initial pressure in the reservoir is 6 MPa. The initial mole fraction of CO_2 is 1 and CH_4 is 0.

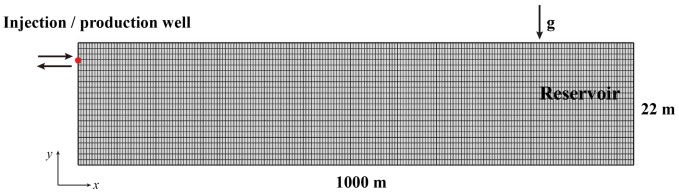

Fig. 7. Sketch of two-dimensional half-reservoir model

Table 1. Properties of the gas storage reservoir

Properties	Value	Units
Porosity	0.3	–
Residual liquid saturation	0.26	–
Permeability (isotropic)	1×10^{-12}	m^2
Molecular diffusion efficient	1×10^{-6}	$m^2 \cdot s^{-1}$
Temperature	313	K
CH_4 injection rate	0.018375	$kg \cdot s^{-1}$

The physical properties of the model reservoir are shown in Table 1. The reservoir temperature in this model is set to 313 K, which is constant with that of Curtis M. Oldenburg, and maintains unchanged.

Figure 8 shows the pressure evolutions calculated by COMSOL Multiphysics software and the Oldenburg's model, respectively. The slight difference of the two results comes from the difference in software development principles and the fluid mixture model description method. When CH_4 is used as the cushion gas in the reservoir, the difference is extremely small. Because no CO_2 but CH_4 in the reservoir means no miscibility problems. When CO_2 is used as the cushion gas, the situation is different. Any difference related to miscibility problems between Oldenburg's model and the model in this paper will affect the results. However, the difference of pressure evolution between them are very small and the trend is consistent.

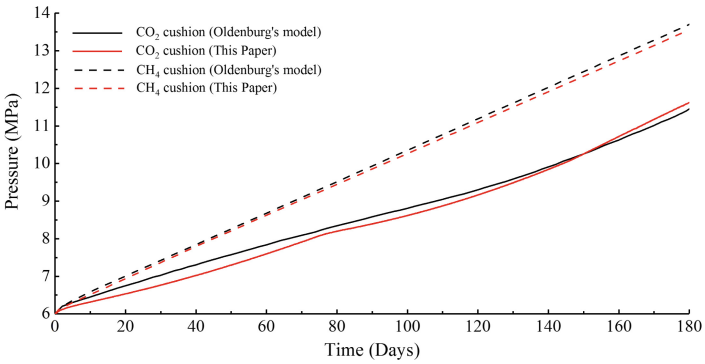

Fig. 8. Comparison of pressure evolutions

After 30, 90, and 180 days of injection, the distribution of mixing area is different. For the clear description of the miscibility, the mixing degree of the two fluids is quantified by

$$m = \frac{V_{mix}}{V}$$

where m is mixing degree, V_{mix} is the volume of the mixing area, and V is the volume of the reservoir. Based on numerical calculation and image processing, the mixing degree on days of 30, 90, and 180 of two models are shown in Table 2. With the increase of the injection time, the mixing degree increases significantly. By comparing the two models, the difference is less than 3% indicating the model of this paper is feasible and accurate.

Table 2. Comparison of mixing degree on days of 30, 90, and 180

Oldenburg's model		Model in this paper	
Time (days)	m	Time (days)	m
30	7.89%	30	6.69%
90	13.57%	90	14.21%
180	15.65%	180	18.47%

4 The Influence of Reservoir Thickness on Mixed Region

This section focuses on the influence of reservoir thickness on the distribution of mixed regions. The distribution of the mixed regions is calculated after 30, 90, and 180 days of CH_4 injection. The legend on the right side shows the mass fraction of CH_4 with values range from 0–1 (the same below). The distribution of the miscible interface between two fluids is clearly shown in Fig. 9 based on the contour of the mass fraction of CH_4. Due to the molecular diffusion and the disturbance of the injection pressure, the

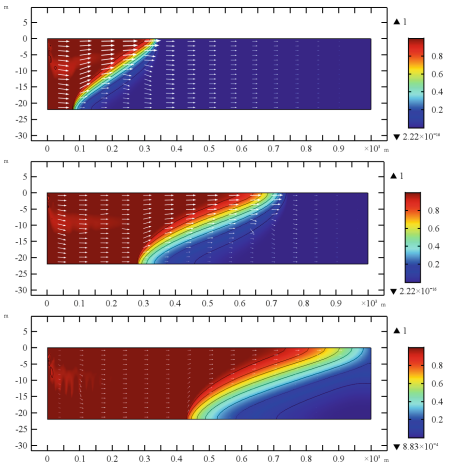

Fig. 9. Mixed region in a thickness of 22 m reservoir on days of 30, 90, and 180

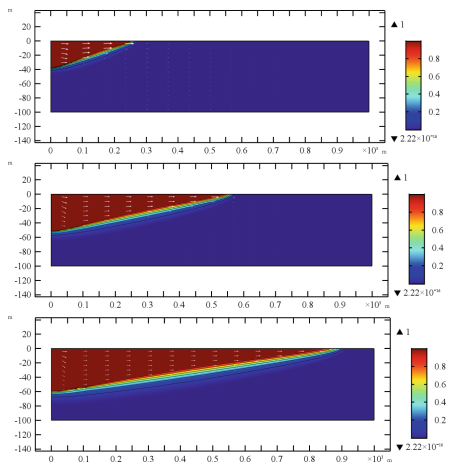

Fig. 10. Mixed region in a thickness of 100 m reservoir on days of 30, 90, and 180

mixing area gradually increases with the injection time, and as well as for the *m* value. The white arrows represent the velocity magnitude and direction of Darcy flow in the reservoir.

To further clarify the influence of reservoir thickness on the distribution of the mixed region, the thickness of the reservoir in the Fig. 9 was increased to 100 m. Calculations were made with the same conditions and are shown in Fig. 10. It is obviously found that with the increasing thickness, the fluid gradually shifts from the horizontal flow to the upper and lower stratified flow. Therefore, the miscible interface between those two kinds of fluids gradually decrease. Due to the difference of density, an increase in reservoir thickness leaves enough space for fluid stratification. However, the Darcy velocity in the reservoir has been significantly reduced even though the injection rate has no change, indicating that the reservoir still has sufficient energy storage capacity.

5 Conclusions

The process of subsurface CH_4 storage with CO_2 as the cushion gas in the reservoir is studied in this paper, and the conclusion is drawn as follows:

(i) The density and dynamic viscosity of the mixed fluid of CO_2 and CH_4 are related with mixing degree, therefore a simple average model is no longer applicable. In this paper, a two-dimensional axisymmetric finite element model was established based on the interpolation calculations of the NIST database.

(ii) The accuracy of this modelling process is verified by comparing with the model of Curtis M. Oldenburg.

(iii) During the CH_4 injection process, the thickness of the geological reservoir has a significant effect on the distribution of the two fluid mixing regions. It is found that the mixing degree will be reduced with the increasing reservoir thickness. A large reservoir thickness will transform the horizontal flow into the upper and lower stratified flows due to the large density difference between CO_2 and CH_4 in the reservoir.

References

1. Tek MR (1989) Underground Storage of Natural Gas: Gulf Pub. Co., Book Division, pp 15–21
2. Niu Chuankai TY (2014) Numerical simulation and analysis of migration law of gas mixture using carbon dioxide as cushion gas in underground gas storage reservoir. J Harbin Inst Technol (New Series) 21(3):121–128
3. Holloway S (2005) Underground sequestration of carbon dioxide—a viable greenhouse gas mitigation option. Energy 30(11–12):2318–2333
4. Kühn M, Nakaten N, Streibel M, Kempka T (2014) CO_2 geological storage and utilization for a carbon neutral "power-to-gas-to-power" cycle to even out fluctuations of renewable energy provision. Energy Procedia 63:8044–8049
5. Kühn M, Streibel M, Nakaten N, Kempka T (2014) Integrated underground gas storage of CO_2 and CH_4 to decarbonise the "power-to-gas-to-gas-to-power" technology. Energy Procedia 59(5):9–15
6. Setzmann U, Wagner W (1991) A new equation of state and tables of thermodynamic properties for methane covering the range from the melting line to 625 K at pressures up to 100 MPa. J Phys Chem Ref Data 20(6):1061–1155
7. Span R, Wagner W (1996) A new equation of state for carbon dioxide covering the fluid region from the triple-point temperature to 1100 K at pressures up to 800 MPa. J Phys Chem Ref Data 25(6):1509–1596
8. Kunz O, Wagner W (2012) The GERG-2008 wide-range equation of state for natural gases and other mixtures: an expansion of GERG-2004. J Chem Eng Data 57(11):3032–3091
9. US Department of Commerce N. NIST 14. NIST Mixture Property Database. World Wide Web-Internet and Web Information Systems
10. Oldenburg CM (2003) Carbon dioxide as cushion gas for natural gas storage. Energy Fuels 17(1):240–246

Carbon Sequestration in Malaysian Oil Palm Plantations – An Overview

Nik Norsyahariati Nik Daud[1(✉)], Anijiofor Sandra Chinenyenwa[1], Thomas Hywel Rhys[2], Lum Ken[2], and Hosking Lee[2]

[1] Department of Civil Engineering, Engineering Faculty, Universiti Putra Malaysia, 43400 Serdang, Selangor, Malaysia
niknor@upm.edu.my
[2] Geoenvironmental Research Center, Cardiff School of Engineering, Cardiff University, Queen's Building, the Parade, Newport Road, Cardiff CF24 34A, UK

Abstract. This paper examines the potential for soil carbon sequestration in the oil palm plantations of Malaysia. Due to the rising awareness of climate change and its negative influence on the environment, the contributions of both human and natural processes towards climate change are being widely studied. In Malaysia, peatlands are used as oil palm plantations and store large amounts of soil organic carbon, which if not maintained could have a serious and negative influence on the environment if allowed to escape to the atmosphere as carbon dioxide. The escape of major nutrients including carbon (as carbon dioxide) and nitrogen (as nitrous oxide) as a result of land use change has seriously degraded the peatlands and resulted in a net release of greenhouse gases. Measures to promote carbon sequestration in soil address the soil degradation by preserving and increasing the soil organic carbon pool. This paper addresses the important topics of peatland degradation and the associated carbon sequestration potential by considering: (i) the impact of peatland conversion on soil properties, (ii) relevant factors influencing the soil organic carbon, (iii) the application of biofertiliser and waste biomass to restore depleted soil organic carbon (SOC) pools, (iv) the economic valuation of soil carbon sequestration, and (v) the contribution policy and management practices.

Keywords: Carbon sequestration · Peatland · Oil palm plantation
Soil carbon · Biomass

1 Introduction

Oil palm is cultivated as a perennial crop across Southeast Asia. Although vital to the economy of Malaysia and a catalyst for rural development, the widespread drainage of tropical peatland to accommodate industrial oil palm plantations has promoted a significant loss of soil C [1]. Drainage of the peatland disrupts the soil C dynamics by increasing soil aeration, leading to increased soil respiration as microorganisms have more oxygen available for metabolic activity. Tropical peatland constitutes in the range of 30–45 Mha, about 10–12% of the global peatland [2, 3] and store an estimated 120 billion tonnes of carbon, or approximately 5% of the world's terrestrial carbon [4].

© Springer Nature Singapore Pte Ltd. 2019
L. Zhan et al. (Eds.): ICEG 2018, ESE, pp. 49–56, 2019.
https://doi.org/10.1007/978-981-13-2227-3_6

Therefore, the loss of carbon stored in peatlands through land use conversion to oil palm plantations is of potential significance to the global carbon cycle and climate change [5].

Malaysia is a leading country in oil palm production, which has resulted in increased oil palm plantations from 642,000 ha in 1975 to just over 4.3 Mha in 2007, with most expansion occurring in Peninsular Malaysia and Sabah. The country is particularly suited to oil palm planting since it lies within the humid tropic region ±10° North and South of the Equator, where growing conditions including ample sunshine and abundant rainfall are ideal.

In 2008, at least 510,000 ha of peatland in Malaysia supported oil palm plantations [6]. Malaysia has some of the most widespread tropical peatland in the world consisting of peat swamp forest, occurring in more than six of the 13 states and covering an area of about 2.13 Mha, approximately 6.46% of the total land area [4]. The peatlands are mostly found in the states of Selangor, Johor, Perak, Pahang, Sabah and Sarawak, with the largest area found in Sarawak at more than 1 Mha (Table 1). Approximately 50% of the total peatland area in Malaysia is designated as permanent reserves, while the remaining areas have been converted for other uses [4]. Malaysia has the second largest extent of peatlands in Southeast Asia after Indonesia, most of which are still intact and therefore contributing to sequestering carbon from the atmosphere and acting as a store for large amounts of carbon.

Table 1. State forest land distribution in Malaysia [4]

Area	Total peatland (Mha)	Peatland forest		Converted to other uses (Mha)
		Permanent reserves (Mha)	Other forests (Mha)	
Peninsular Malaysia	0.717	0.191	0.109	0.417
Sarawak	1.289	0.771	0.349	0.169
Sabah	0.124	0.124	0	0
Total	**2.131**	**1.086**	**0.458**	**0.586**

The current work addresses the peatland degradation associated with Malaysian oil palm plantations. As a means to restore and protect the depleted pool of soil C in cultivated peatland, the potential for soil C sequestration is examined by considering the use of waste biomass and linking to policy developments through improved land management practices.

2 Peatland Properties and Degradation

A major characteristic of peat swamp forests is that they are permanently water-logged leading to reduced decomposition of organic matter from plant litter, which then accumulates as peat. Peat can develop over both sand and clay, however water logging is vital for the maintenance of the soil organic carbon (SOC) and continued

accumulation of peat. Most peat swamp forest is made up of peat soil and waters that are acidic (pH of 3.5), with a high carbon/nitrogen ratio and low nutrient content, supporting plants and animals that do not occur in the other tropical forests of Asia [6].

The advantages of peatland include (i) socio-economics and direct uses (forestry, agriculture, infrastructure, community livelihood, wildlife capture, tourism/recreation, water supply etc.), (ii) conservational purposes (water retention, carbon sequestration, flood mitigation, maintenance of base flow in rivers, sediment, nutrient and toxicant removal) and (iii) other attributes including biological diversity, cultural/spiritual value, historical value, and aesthetic value [4, 6].

Peatlands are the most highly threatened of all forests and wetlands in Malaysia because, of the uses described, intensive agriculture has led to vast areas being cleared and burnt, principally for oil palm plantations and other agricultural products. Peatland fires are another major issue, associated with periodic droughts and closely-linked with forest clearance and drainage activities by the forestry and agricultural sectors. Detrimental impacts of peatland fires are the negative effects on the socio-economy of local communities dependent on peatland resources, environmental pollution, and the significant decrease or loss of important floral and faunal populations. This has contributed towards the challenge facing Malaysia to meet its national and international commitments toward climate change and biodiversity conservation, as well as achieving economic targets [6]. Presently, there are no specific policies and guidelines associated with sustainable peatland management in Malaysia, which further contributes to the unsustainable use and degradation of peatlands and their resources.

Peatland degradation leads to the loss of soil C and, in the long term, peatland around Malaysia could be permanently flooded, acidic, and unproductive [6]. In West Johor, where peatlands were drained for oil palm development over 30 years ago, settling as a result of oxidation and compaction occasioned regular flooding because the land dropped to sea and river levels [7]. Similarly, a large area of peatland in Malaysia has been drained for agricultural purposes, especially large scale oil palm plantations, which could lead to further reclamation and subsequent drainage and degradation of intact peatland areas. Furthermore, the production of 1 ton of palm oil on fully-drained peatland can result in 10–30 tonnes CO_2 emissions as a result of peat oxidation [8]. The main aim of reducing CO_2 emissions through biofuels may therefore actually cause substantially increased CO_2 emissions if plantations are established on peatland areas [9].

3 Soil Organic Carbon and Options for Restoration

SOC includes decomposed plant, animal, and microbial residues and is significant in biofuel production [10, 11] since intensive cultivation leads to SOC losses and hence a decreased soil productivity. Net losses of SOC lead to increased CO_2 emissions to the atmosphere from the soil, whereas net increases in SOC represent a removal of CO_2 and carbon sequestration. Land use changes significantly modify SOC dynamics, making sustainable development and crop management essential [12, 13].

Distributions of SOC are more spatially and temporally variable in oil palm plantations than for most other crops [14]. A study by Ref. [15] in Indonesia showed

that the drainage required for cultivating oil palm in peatlands leads to soil subsidence, potentially increasing future flood risks and, moreover, the costs of CO_2 emissions are not considered. Several studies have highlighted techniques of mitigating CO_2 emissions to the atmosphere, such as through the natural sequestration of CO_2 in soil via plants and the storage of CO_2 in deep geological reservoirs [16]. Peat swamp forests are one of the few ecosystems which are significant carbon stores and sinks in their natural state. Hence, conservation measures and the proper maintenance of peatland are essential means to reduce greenhouse gas emissions from these key ecosystems.

Restoring degraded soils and ecosystems is a way to increase soil C storage and sequestration, because most degraded soils have a depleted SOC pool. This can be achieved through judicious land use practices and management of agricultural and perennial land [17]. Converting degraded soils under agriculture and other land uses into forests and perennial land use enhances the SOC pool. However, the amount of soil carbon sequestration with afforestation depends on certain factors such as climate, soil type, species and nutrient management.

While much research has been done on how plants, free-living microbial decomposers, and soil minerals affect the soil C pool, it is recently coming to light that mycorrhizal fungi may play an important role in maintaining this pool as well. In some ecosystems, the biomass of mycorrhizal fungi can be comparable to the biomass of fine roots [18]. Based on the magnitude of mycorrhizal fungal inputs to the soil carbon pool, some have suggested that variation in the recalcitrance of mycorrhizal biomass may be important for predicting soil C storage, as it would affect the rate at which the contribution of mycorrhizal fungi to soil carbon is returned to the atmosphere [19].

It is possible that, in the short term, an arbuscular mycorrhizal fungal (AMF)-mediated increase in decomposition of labile plant litter may lead to a reduction of soil C. However, the C balance is offset by a long-term gain in recalcitrant compounds as presented by Ref. [20]. Contributions of AMF are likely to be further amplified through physically protecting soil organic matter from decomposition by means of soil aggregation [21] and via a general increase in plant productivity (from eCO_2), hence significantly higher deep soil litter input.

4 Application of Biofertiliser and Biomass to Restore Depleted SOC Pools

In Malaysia's oil palm plantation areas, more than 66.63 million tons of biomass residues were produced in 2010, including shells, palm kernels, empty fruit bunches (EFB), fronds, and trunks. These oil palm residues have the potential to be used as a renewable energy resource [22]. According to Ref. [23], the addition of organic material sources such as empty fruit bunches and palm fronds as the palm trees grow will be a rise in soil C. Biochar is a relatively stable carbon rich product that remains when plant biomass is pyrolyzed. The application of biochar to soil aims to improve soil fertility and raise agricultural productivity. However, the sequestration capacity and the carbon retained in biochar depend on the production temperature, type of biomass, soil and agro-climatic conditions [24]. Moreover, a combination of biochar with fertilizers is needed to see the effects on agricultural yield [25].

5 Economic Valuation of Soil Carbon Sequestration

Carbon sequestration in soils has emerged as a promising option contributing towards meeting the challenges of climate change and global warming [26, 27]. It is a passive sequestration option, compared to the active option of capturing CO_2 from point source emitters (power plants, industry) and storing in deep geological reservoirs.

A study conducted on soil C in different ages of oil palm plantation showed that the carbon sequestration followed a comparable trend, whereby soil C stocks change with time for all ages and only stabilise from 9 years old onwards [14, 28].

Ref. [29], who performed a study in Muaro Jambi, Indonesia, indicated that the total economic return from a production forest (1.3 million rupiah/hectare/year) is higher than the economic returns from a protected forest (968,604 rupiah/hectare/year). The analysis of these returns is based on the carbon sequestration value of the forests as a key component (an indirect use value), in terms of net carbon emissions resulting from land use changes valued at the social price of carbon. The carbon emissions from peat conversion accounts for positive emission from drainage, net of carbon sequestration provided by alternative land use, for example oil palm plantations.

However, the costs of SOC sequestration must also be considered in order to evaluate the economic viability of this technique. For example, methods of soil C sequestration such as precision farming involving the use of fertilizers, pesticides, and nutrient cycling through manuring have cost implications [30–33]. Therefore, these factors could be an impediment to developing a user-friendly system for effective monitoring of soil C sequestration rates.

6 Contribution to Policy and Management Practices

Challenges related to energy resources, global climate change, material use, and waste generation are high on political and policy agendas worldwide. Of relevance to the present study, the relationship between soil C content and soil organic matter (SOM) should be highlighted. The addition of organic material sources from oil palm bio-mass may result in the restoration of depleted soil C pools [23]. Soil erosion is a major factor depleting the SOC pool on sloping lands. The application of empty fruit bunch (EFB) as a mulching material commonly practiced in oil palm estates was the best current practice for sloping lands due to its high amount of organic matter and humic acids, which assist in retaining soil particles by improving soil aggregate stability and aggregation [34].

Ref. [35] indicated that depletion of the SOC pool on agricultural soils is exacerbated by and in turn also exacerbates soil degradation, which comprises physical degradation (i.e., reduction in aggregation, decline in soil structure, crusting, compaction, reduction in water infiltration capacity and water/air imbalance leading to anaerobisis) and erosion, chemical degradation (i.e., nutrient depletion, decline in pH and acidification, build-up of salts in the root zone, nutrient/elemental imbalance and disruption in elemental cycles), and biological degradation (i.e., reduction in activity and species diversity of soil fauna, decline in biomass C and depletion of SOC pool).

Recent work by Ref. [36] discusses how arbuscular mycorrhizal fungi (AMF) application might benefit oil palm cultivation through more sustainable management and the practical use of AMF for oil palm plantations. They suggest that application of AMF technology is one option that can benefit both agronomic plant health and ecosystems. Moreover, AMF have the potential to increase conventional agricultural productivity and are crucial for the sustainable functioning of agricultural ecosystems.

7 Conclusion

Oil palm agriculture linked to the draining of tropical peatlands has resulted in the loss of valuable benefits of these important ecosystems, including the loss of stored soil organic carbon as carbon dioxide. This paper suggests a good potential for combining the regeneration of degraded peatland in Malaysia with soil carbon sequestration. The main relevant properties of peatland have been discussed alongside proposed options for restoration, centered on the use of oil palm biomass residues and arbuscular mycorrhizal fungi as a biofertiliser. It is hoped that this work is the first step towards field trials that would target the increase in recalcitrant soil carbon using the biomass/biofertiliser approach. Such field trials are necessary to evaluate the potential of the approach and would ultimately aim to inform specific policies and guidelines associated with sustainable peatland management in Malaysia.

References

1. Melling L, Hatano R, Goh KJ (2004) Global warming potential from soils in tropical peatland of Sarawak Malaysia. Phyton 45:275–284
2. Rieley JO, Ahmad-Shah AA, Brady MA (1996) The extent and nature of tropical peat swamps. In: Maltby E (ed) Tropical Lowland Peatlands of South East Asia, Proceedings of a Workshop on Integrated Planning and Management of Tropical Lowland Peatlands, Cisarua, Indonesia
3. Rieley JO, Wüst RAJ, Jauhiainen J, Page SE, Wösten H, Hooijer A, Siegert F, Limin S, Vasander H, Stahlhut M (2008) Tropical peatlands: carbon stores, carbon gas emissions and contribution to climate change processes. In: Laine J (ed) Peatlands and Climate Change. International Peatland Society, Jyväskylä, pp 129–162
4. ASEAN 2010–2018. Sustainable management of Peatland Forests in South East Asia. ASEAN Peatland Forests Project. Global Environmental Centre
5. Sorensen KW (1993) Indonesian peat swamp forests and their role as a carbon sink. Chemosphere 27(6):1065–1082
6. Wetlands International (2010) A quick scan of peatland in Malaysia. Wetlands International-Malaysia: Petaling Jaya, Malaysia
7. Pahang Forestry Department (2005) Pekan Peat Swamp Forest, Pahang, Malaysia. The role of water in conserving peat swamp forests. Pahang Forestry Department: Kuantan, Malaysia
8. Hooijer A, Silvius M, Wösten H, Page S (2006) PEAT-CO_2, Assessment of CO_2 emissions from drained peatlands in SE Asia. Delft Hydraulics report Q3943: Delft, Netherlands
9. Silvius M (2007) Palm oil expansion could boost carbon: the growing use of palm oil for biofuels production is often in conflict with environmental concerns. Bioenergy Bus 1:14–15

10. Adler PR, Del Grosso SJ, Parton WJ (2007) Life-cycle assessment of net greenhouse gas flux for bioenergy cropping systems. Ecol Appl 17:675–691
11. Anderson-Teixeira KJ, Davis SC, Masters MD, Delucia EH (2009) Changes in soil organic carbon under biofuel crops. Global Change Biology Bioenergy 1:75–96
12. Lal R (1997) Residue management, conservation tillage and soil restoration for mitigating greenhouse effect by CO_2-enrichment. Soil Tillage Res 43:81–107
13. Six J, Feller C, Denef K (2002) Soil carbon matter, biota and aggregation in temperate and tropical soils—effects of no-tillage. Agronomy 22:755–775
14. Haron K, Brookes PC, Zakaria ZZ (1998) Microbial biomass and soil organic matter dynamics in oil palm (Elaeis guineensis Jacq.) plantations West Malaysia. Soil Biol Biochem 30:547–552
15. Sumarga E, Hein L, Hooijer A, Vernimmen R (2016) Hydrological and economic effects of oil palm cultivation in Indonesian peatlands. Ecol Soc 21(2):52
16. Huisingh D, Zhang Z, Moore JC, Qiao Q, Li Q (2015) Recent advances in carbon emissions reduction: policies, technologies, monitoring, assessment and modeling. J Clean Prod 103:1–12
17. Lal R (2001) Potential of soil carbon sequestration in forest ecosystem. In: Lal R (ed) Soil Carbon Sequestration and the Greenhouse Effect, vol 57, pp 137–154. Soil Science Society of America Special Publication, Madison (2001)
18. Wallander H, Goransson H, Rosengren U (2004) Production, standing biomass and natural abundance of 15N and 13C in ectomycorrhizal mycelia collected at different soil depths in two forest types. Oecologia 139:89–97
19. Langley JA, Hungate BA (2003) Mycorrhizal controls on belowground litter quality. Ecology 84:2302–2312
20. Verbruggen E, Veresoglou SD, Anderson IC, Caruso T, Hammer EC, Kohler J, Rillig MC (2013) Arbuscular mycorrhizal fungi – short-term liability but long-term benefits for soil carbon storage? New Phytol 197:366–368
21. Rillig MC (2004) Arbuscular mycorrhizae and terrestrial ecosystem processes. Ecol Lett 7:740–754
22. Chun SG, Kok TT, Keat TL, Subhash B (2009) Status, perspective and challenges in Malaysia. Biores Technol 101:4834–4841
23. Sommer R, Denich M, Vlek PLG (2000) Carbon storage and root penetration in deep soils under small farmer land-use systems in the Eastern Amazon region, Brazil. Plant and Soil, Dordrecht 219:231–241
24. Johannes L (2007) Bio-energy in the black. Ecol Environ 5(7):381–387
25. Zwieten LV, Kimber S, Morris S, Chan KY, Downie A, Rust J (2010) Effects of biochar from slow pyrolysis of papermill waste on agronomic performance and soil fertility. Plant Soil 327:235–246
26. Schmidt MWI, Torn MS, Abiven S, Dittmar T, Guggenberger G, Janssens IA, Kleber M, Kogel-Knabner I, Lehmann J, Manning DAC, Nannipieri P, Rasse DP, Weiner S, Trumbore SE (2011) Persistence of soil organic matter as an ecosystem property. Nature 478 (7367):49–56
27. Boot-Handford ME, Abanades JC, Anthony EJ, Blunt MJ, Brandani S, Mac Dowell N, Fernandez JR, Ferrari M-C, Gross R, Hallett JP, Haszeldine RS, Heptonstall P, Lyngfelt A, Makuch Z, Mangano E, Porter RTJ, Pourkashanian M, Rochelle GT, Shah N, Yao JG, Fennell PS (2014) Carbon capture and storage update. Energy Environ Sci 7(1):130–189
28. Roslee R, Rahim SA, Idris WMR (2016) Soil carbon sequestration in different ages of oil palm plantations. Am-Eurasian J Agric Environ Sci 16(5):1004–1007
29. Abt. Ecosystem (2014) Valuation Based Strategic Environmental Assessment: Muaro Jambi Case Study. http://www.abtassociates.com/AbtAssociates/files/83/83fdcb11-dece-4cc2-973a-76bde787c455.pdf

30. Jenkinson DS, Hart PBS, Rayner JH, Parry LC (1987) Modelling the turnover of organic matter in long-term experiments at Rothamstedt, UK. INTECOL Bull 15:1–8
31. Intergovernmental Panel on Climate Change, (IPCC) (1996) Climate Change 1995: Impact, Adaptations and Mitigation of Climate Change: Scientific Technical Analyses. Working Group 1. Cambridge Univ. Press, Cambridge, UK
32. Smith P, Powlson DS (2000) Considering manure and carbon sequestration. Science 287:428–429
33. Matson PA, Naylor R, Ortiz-Monasterio I (2000) Integration of environmental, agronomic and economic aspects of fertilizer management. Science 280:112–115
34. Lee YP, Christopher TBS, Gph KJ, Abolfatah M (2012) Effects of four soil conservation methods on soil aggregate stability. Malays J Soil Sci 16:43–56
35. Lal R (2004) Soil carbon sequestration to mitigate climate change: a review. Geoderma 123:1–22
36. Phosri C, Rodriguez A, Sanders IR, Jeffries P (2010) The role of mycorrhizas in more sustainable oil palm cultivation. Agr Ecosyst Environ 135:187–193

Thermal Volumetric Behaviour of Compacted GMZ Bentonite Saturated with Salt Solution

Yong-Gui Chen[1(✉)], Xin-xin Dong[1], Xu-dong Zhang[1,2], Wei-Min Ye[1], and Yu-Jun Cui[3]

[1] Department of Geotechnical Engineering, Tongji University, Shanghai 200092, People's Republic of China
dongxx022l@tongji.edu.cn
[2] Anhui Transport Consulting and Design Institute Co., Ltd, Hefei 230088, People's Republic of China
[3] Laboratory Navier/CERMES, Ecole des Ponts-ParisTech, 77455 Marne-la-Vallée, France

Abstract. Gaomiaozi (GMZ) bentonite has been confirmed as the buffer material in the Chinese disposal program of high-level waste. To investigate the thermal volumetric behaviour of compacted GMZ bentonite, several stress paths were performed on the specimens presaturated with NaCl solutions to obtain the scheduled OCR and verticle stress. Then multi-step heating-cooling tests were conducted. Test results show that thermal volume change strongly depends on the vertical pressure, OCR and concentration of the presaturation solution. For the specimens presaturation with deionized water, heating induces contraction below the transition temperature and followed by dilation at normal consolidation state, while only induces dilation at overconsolidation state. A larger vertical pressure leads to a larger transition temperature. For the specimens presaturated with NaCl solutions, heating basically induces dilation. The specimens with large vertical pressure accumulate a total contraction after a thermal cycle. For a given concentration and verticle pressure, the specimens cumulate a larger irreversible dilation at higher OCR. The influence of salt solution is non-monotonic. The dilute solution and high saline solution significantly promote the thermal expansion of saturated GMZ bentonite during heating.

Keywords: GMZ bentonite · Thermal volumetric behaviour · Salt solution Vertical pressure · OCR

1 Introduction

The conceptual design of high-level radioactive waste (HLW) repository normally contains an engineered barrier system (EBS), in which compacted bentonite blocks are assembled around the waste canister. Once placed, bentonite blocks are gradually hydrated with porewater inflow from the host rock, providing buffer functions such as sealing the gap, supporting the canister and retarding the nuclide migration (Sellin and Leupin 2013). The decay heat of HLW and water chemistry are the main concerns in a real repository. High decay heat generates a temperature gradient within the EBS, leading to a differential hydration swelling and thermal expansion of the buffer

© Springer Nature Singapore Pte Ltd. 2019
L. Zhan et al. (Eds.): ICEG 2018, ESE, pp. 57–64, 2019.
https://doi.org/10.1007/978-981-13-2227-3_7

material. The salinity of groundwater in the disposal area changes over time in the extremely long disposal time, affecting the thermal properties after the buffer reached its saturation. Temperature fluctuation may occur during the operation period on account of the increasing amount of disposal, decreasing in decay heat and variation in thermal conductivity. Thermal volume change and thermal stress lead to periodical changes of the stress state within the EBS. Consequently, degeneration of the buffer functions accumulates.

A few tests were performed to investigate the thermal volume change of saturated clay. Generally, the volume change during heating is closely related to the consolidation state. Under drained conditions, a highly overconsolidated soil exhibits dilation and followed by contraction during heating, whereas exhibits contraction at normally consolidated or lightly overconsolidated conditions (Towhata et al. 1993; Abuel-Naga et al. 2007; Ng et al. 2016). The transition temperatures from the dilation to contraction were observed decreasing with the OCR (Baldi et al. 1988; Towhata et al. 1993; Sultan et al. 2002). In addition, a larger irreversible contraction is accumulated after the thermal cycle at lower OCR (Baldi et al. 1991; Uchaipichat and Khalili 2009; Favero et al. 2016). Except for the OCR, suction condition and stress state play significate role. Some tests were performed to investigate the thermal behaviour of unsaturated claystone and compacted bentonite. Heating-cooling tests conducted by Romero et al. (2003) on Boom clay, Romero et al. (2005) on FEBEX bentonite and Tang et al. (2008) on MX80 bentonite revealed that heating induces a reversible expansion under low pressure and high suction but an irreversible contraction under high pressure and low suction, while cooling only induces reversible contraction. Similar results were obtained on the unsaturated compacted GMZ bentonite (Cui et al. 2011; Ye et al. 2013).

Thermal volume change of compacted clay mainly originates from two parts: (1) thermal expansion of porewater (including the adsorbed water and free water) and solid phase. (2) volume shrink due to the dehydration of adsorbed water at high temperature. Since thermal expansion of the adsorbed water in clay is insignificant as compared to the free water (Baldi et al. 1988), the net effect of these two contradictory roles may depend on the relative amount of free water. In compacted bentonite, absorbed water exists in the intra-aggregate pores, while free water exists in the inter-aggregate pores. At high suction (low water content), a small amount of water exists in the intra-aggregate and inter-aggregate pores. Hence, thermal expansion of the clay lamellae dominates the thermal behaviour. After the intra-aggregate pores reached saturation at low suction (high water content), dehydration of the adsorbed water during heating will partially offset or exceed the thermal expansion of free water and clay lamellae. In addition, a higher OCR implies a higher degree of consolidation of the soil. Less amount of free water remains in the condition of higher OCR. Consequently, compacted clay presents a larger dilation at higher OCR during heating. In other aspects, thermal expansion of the clay lamellae and thermal dehydration of the absorbed water are reversible in the cooling process, whereas thermal expansion of the free water induces plastic deformations. Therefore, compacted bentonite exhibits a reversible expansion at high suction but accumulates an irreversible contraction at high suction. This thermoplastic yielding during heating in drained condition has been well

described in the previous studies (Hueckel and Baldi 1990; Cui et al. 2000; Abuel-Naga et al. 2007; Ma et al. 2017).

Influences of the porewater chemistry on the thermal properties of compacted clay are rarely explored. The saline effects on the thermal behaviour are within the consideration in compacted bentonite. This study explores the saline effects on the thermal volumetric behaviour of compacted GMZ bentonite, the selected buffer material in the Chinese disposal programme of HLW. Deionized water and NaCl solutions were employed, and temperatures 20–80 °C was chosen. Various stress paths were conducted prior to the thermal cycle to obtain the designed OCR, verticle pressure and concentration of the presaturation solution. Deformation of the specimens during the thermal cycle is recorded. Effects of the OCR, vertical pressure and concentration on the thermal volume change are analyzed.

2 Material and Method

2.1 Material and Sample Preparation

The GMZ bentonite used in the present study was exploited from Gaomiaozi County, Inner Mongolia Autonomous Region, China. It is a sodium bentonite with a large specific surface area and high cation exchange capacity (Wen 2006). The salts NaCl used in the experiments are of analytical grade corresponding to a purity of 99%. The salt solutions were prepared using deionized water.

GMZ bentonite powder at an initial water content of 10.75% was used for sample preparation. A total mass of 37.2 g bentonite powders was put into the stainless steel ring and statically compacted at a constant loading rate of 0.4 kN/min to a designed maximum compaction pressure of 50 kN. The pressure was maintained for 1 h to minimize the rebound of the specimen. A total number of sixteen as-compacted cylindrical specimens with the target dry density of 1.70 g/cm^3 and a dimension of 10 mm in height and 50 mm in diameter were prepared for the tests.

2.2 Test Apparatus

An oedometer was developed for the vertical stress and temperature controlled test (Fig. 1). It is composed of a test cell, a loading system, a temperature control system, a peristaltic pump and a data gauge. The testing cell composes of a basement, a stainless steel sample ring, two porous stones, a stainless steel piston and a top cover with a central hole. All these parts are fixed with screws. Two outlets are designed in the basement. One connects to the solution bottle and the other to the peristaltic pump. The loading system was employed for the application of vertical stress. Oil bath system was employed for the temperature control. The data gauge was installed at the top of the piston for monitoring the deformation.

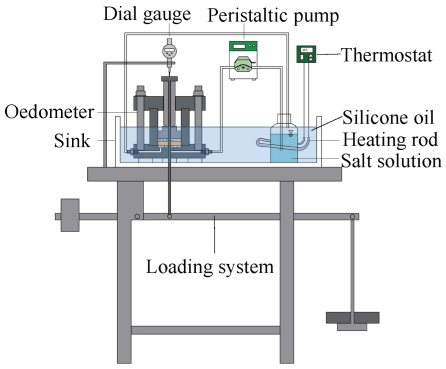

Fig. 1. Setup for the heating-cooling tests at constant pressure

2.3 Test Procedures

The test apparatus was firstly calibrated in consideration of thermal expansion. The strain of specimens was revised after the tests. Then, four different paths were performed to obtain the designed OCR, vertical pressure and concentration of salt solution. In all tests, the specimen was firstly saturated with a certain salt solution under vertical pressure of 0.1 MPa at 20 °C (SUL path). The specimens were considered as normal consolidated after the SUL path. Then different stress paths were conducted. In test 1, no additional stress path was performed (p = 0.1 Mpa, OCR = 1). In test 2, the specimen was loaded to 1.0 MPa (p = 1.0 Mpa, OCR = 1). In test 3, the specimen was firstly loaded to 1.0 MPa and subsequently unload to 0.5 MPa (p = 0.5 Mpa, OCR = 2). In test 4, the specimen was firstly loaded to 1.0 MPa and then unload to 0.1 MPa (p = 0.1 Mpa, OCR = 10). Finally, the multi-step heating-cooling cycle was conducted. In all tests, the next stage proceeded when the deformation remains constant within 24 h in the current stage.

3 Results and Analysis

3.1 Effect of Verticle Pressure and OCR on Thermal Volumetric Behaviour

The thermal strain during the heating-cooling cycles for specimens presaturated with the certain solution was presented in Fig. 2. It is observed that the thermal volume change strongly depends on the verticle pressure and OCR. For the specimen presaturated with deionized water, heating induces contraction and followed by dilation at the normal consolidation state (OCR = 1), while only induces dilation at overconsolidation state (OCR = 2, 10). This is consistent with previous studies on the non-expansive clay (Towhata et al. 1993; Abuel-Naga et al. 2007; Ng et al. 2016). It is also noted that, at normal consolidation state (OCR = 1), a larger vertical pressure leads to a larger transition temperature, i.e. 40 °C at p = 0.1 MPa and about 55 °C at p = 1.0 MPa. This positive correlation between the transition temperature and verticle pressure is also

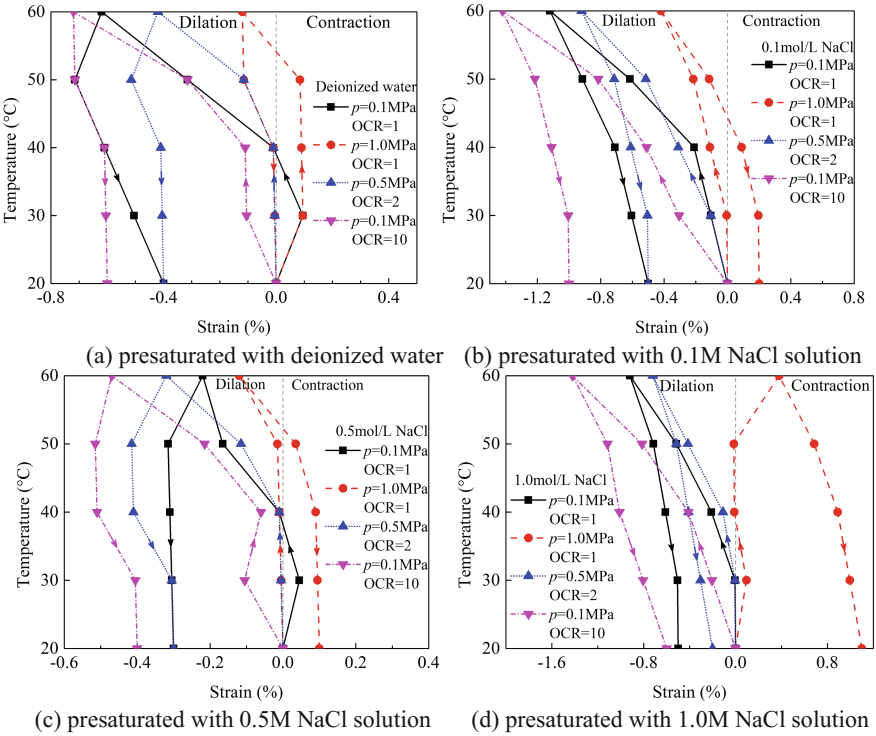

Fig. 2. Thermal volume change depending on the vertical pressure and OCR

verified for the unsaturated GMZ bentonite (Ye et al. 2013). In addition, for the specimen presaturated with NaCl solutions, heating basically only induces dilation. In all cases, cooling only induces contraction. Despite the concentration of the presaturation solutions, the specimens with large verticle pressure (p = 1.0 MPa) accumulate a total contraction after the heating-cooling cycle, while others (p = 0.1, 0.5 MPa) accumulate a total dilation. The specimen cumulates larger irreversible dilation at higher OCR.

3.2 Effect of Solution Concentration on Thermal Volumetric Behaviour

The thermal strain during the heating-cooling cycles for the specimens at certain verticle pressure and OCR were presented in Fig. 3. At OCR = 1, a transition temperature can be identified for the specimens presaturated with deionized water and 0.5 mol/L NaCl solution. Despite the concentration, heating induces dilation at overconsolidation state. The specimens presaturated with high saline solution (1.0 mol/L) cumulate large dilation under low vertical pressure (p = 0.1 MPa), while cumulate large contraction under large vertical pressure (p = 1.0 MPa). It is noted that the influence of solution concentration on the thermal strain is non-monotonic when

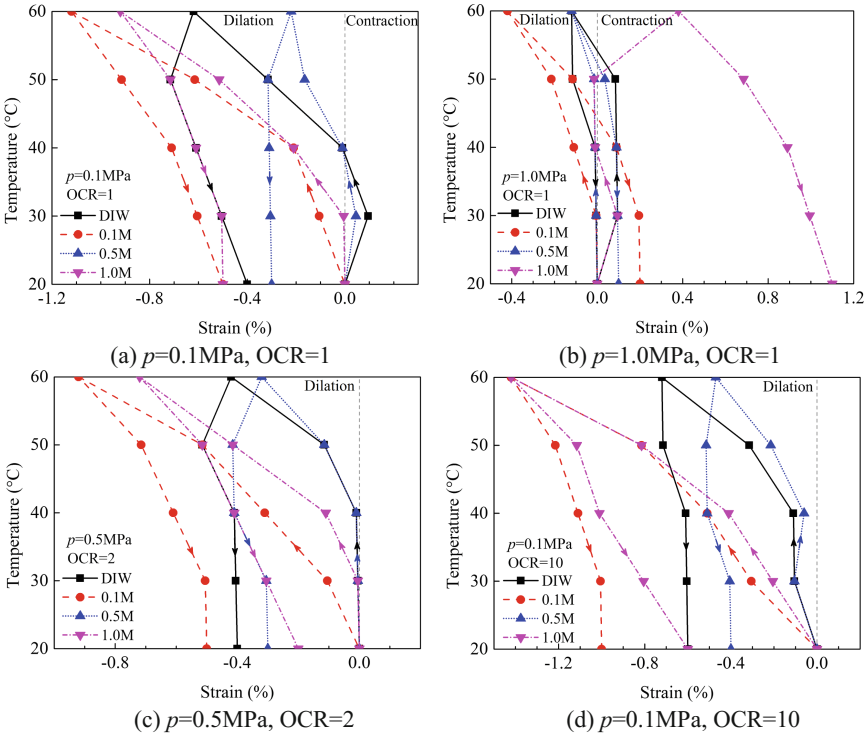

Fig. 3. Thermal volume change depending on the concentration of presaturation solution

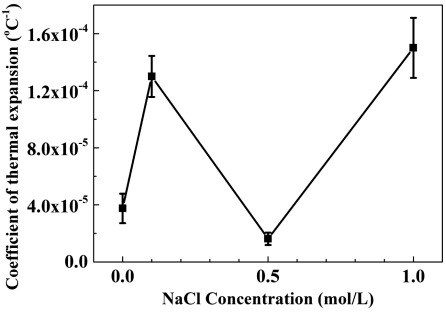

Fig. 4. Coefficient of thermal expansion depending on the concentration

compared with the vertical pressure and OCR. In all cases, dilute solution (0.1 mol/L) promotes the dilation during heating.

The coefficient of thermal expansion is calculated via the thermal strain. As is shown in Fig. 4, it is in a wide range of $(1.6 - 15) \times 10^{-5}$ °C^{-1}, which is lower than that in the unsaturated conditions (1×10^{-4} °C^{-1}) (Ye et al. 2013). The influence of saline solution on the coefficient of thermal expansion is remarkable but also non-monotonic. The dilute solution (0.1 mol/L) and high saline solution (1.0 mol/L)

significantly promote the thermal expansion. The possible reason is that saline solution yields different consolidation state after the SUL process. Barbour and Fredlund (1989) explained that porewater chemistry produces osmotic consolidation in clayey soil. By compressing the diffuse double layers, high saline solutions harden the soil, i.e. a higher degree of consolidation. However, the influence of dilute solution is beyond the explanation and need further exploration.

4 Conclusions

The following conclusions can be drawn from the test results:

(1) For the specimens presaturated with deionized water, heating induces contraction below the transition temperature and followed by dilation at normal consolidation state, while only induces dilation at overconsolidation state. A larger vertical pressure leads to a larger transition temperature. For the specimens presaturated with NaCl solution, heating basically induces dilation.

(2) Despite the concentration of the salt solution, the specimens with large vertical pressure accumulate a total contraction after the thermal cycle. For a given concentration and vertical pressure (p = 0.1 MPa), the specimen cumulates larger irreversible dilation at higher OCR.

(3) The specimens presaturated with high saline solution cumulate large dilation under low vertical pressure, while cumulate large contraction under large vertical pressure. The coefficient of thermal expansion after saturated with NaCl solutions is in a wide range of $(1.6 - 15) \times 10^{-5}$ °C^{-1}. The dilute solution and high saline solution significantly promote the thermal expansion.

Acknowledgements. The authors are grateful to the National Natural Science Foundation of China (41422207 & 41772279), China Atomic Energy Authority ([2011]1051) and Fundamental Research Funds for the Central Universities.

References

Abuel-Naga HM, Bouazza BA, Ramana GV (2007) Volume change behaviour of saturated clays under drained heating conditions: experimental results and constitutive modelling. Can Geotech J 44:942–956

Baldi G, Hueckel T, Peano A, Pellegrini R (1991) Developments in Modelling of Thermo-Hydro-Mechanical Behaviour of Boom Clay and Clay-Based Buffer Materials. Commission of European Communities, Luxembourg

Baldi G, Hueckel T, Pellegrini R (1988) Thermal volume changes of the mineral water-system in low-porosity clay soils. Can Geotech J 25:807–825

Barbour SL, Fredlund DG (1989) Mechanisms of osmotic flow and volume change in clay soils. Can Geotech J 26:551–562

Cui YJ, Sultan N, Delage P (2000) A thermomechanical model for saturated clays. Can Geotech J 37:607–620

Cui YJ, Tang AN, Qian LX, Ye WM, Chen B (2011) Thermal-mechanical behavior of compacted GMZ bentonite. Soils Found 51:1065–1074

Favero V, Ferrari A, Laloui L (2016) Thermo-mechanical volume change behaviour of Opalinus Clay. Int J Rock Mech Min Sci 90:15–25

Hueckel T, Baldi G (1990) Thermoplasticity of saturated clays - experimental constitutive study. J Geotech Eng-ASCE 116:1778–1796

Ma QJ, Ng CWW, Masin D, Zhou C (2017) An approach for modelling volume change of fine-grained soil subjected to thermal cycles. Can Geotech J 54:896–901

Ng C, Cheng Q, Zhou C, Alonso EE (2016) Volume changes of an unsaturated clay during heating and cooling. Geotechn Lett 6:192–198

Romero E, Gens A, Lloret A (2003) Suction effects on a compacted clay under non-isothermal conditions. Geotechnique 53:65–81

Romero E, Villar MV, Lloret A (2005) Thermo-hydro-mechanical behaviour of two heavily overconsolidated clays. Eng Geol 81:255–268

Sellin P, Leupin OX (2013) The use of clay as an engineered barrier in radioactive-waste management - a review. Clays Clay Miner 61:477–498

Sultan N, Delage P, Cui YJ (2002) Temperature effects on the volume change behaviour of Boom clay. Eng Geol 64:135–145

Tang AM, Cui YJ, Barnel N (2008) Thermo-mechanical behaviour of a compacted swelling clay. Geotechnique 58:45–54

Towhata I, Kuntiwattanakul P, Seko I, Ohishi K (1993) Volume change of clays induced by heating as observed in consolidation tests. Soils Found 33:170–183

Uchaipichat A, Khalili N (2009) Experimental investigation of thermohydro-mechanical behaviour of an unsaturated silt. Geotechnique 59:339–353

Wen ZJ (2006) Physical property of China's buffer material for high-level radioactive waste repositories. Chin J Rock Mechan Eng 25:794–800

Ye WM, Zhang YW, Chen YG, Chen B, Cui YJ (2013) Experimental investigation on the thermal volumetric behavior of highly compacted GMZ01 Bent. Appl Clay Sci 83–84:210–216

Studies on the Spatial Distribution of Radiogenic Elements in the Crystalline Basement Used for the Evaluation of Deep Geothermal Resources in the Southwestern Québec

Hejuan Liu(✉)

State Key Laboratory of Geomechanics and Geotechnical Engineering, Institute of Rock and Soil Mechanics, Chinese Academy of Sciences, Wuhan 430071, China
hjliu@whrsm.ac.cn

Abstract. Accurate assessment on the subsurface geothermal resources remains challengeable from the scientific point of view. The parameter uncertainties and incomplete knowledge of initial conditions for the subsurface environment make the prediction of subsurface temperature based on the thermal models present a strong uncertainty. Forward modeling of the temperature at depth may be highly dependent on the radiogenic heat production of the geological layers which are affected by the concentration of uranium, thorium and potassium, and density. It shows that the average concentration of uranium, thorium and potassium is 1.78 ppm, 6.01 ppm and 2.64%, with the standard deviation error of 3.57, 7.27 and 1.85 respectively for the selected region in southwestern Quebec. The sequential gaussian simulation (SGS) method was used to obtain the spatial distribution of the radiogenic elements in a selected region with the size of 35 km × 80 km. Using the density values for specific rocks, the distribution of the radiogenic heat production over the study area is also simulated. Results show that the difference between the minimum and the maximum radiogenic heat production value is 30% when considering the difference in density.

Keywords: Ordinary kriging · Sequential gaussian simulation
Radiogenic elements · Uncertainty · Geothermal energy

1 Introduction

The production of geothermal energy at depth has become a worldwide hot topic in recent years with the reduction in the drilling cost and the development of the reservoir stimulation technologies. However, the reliable assessment on the geothermal resources at depth is very challengeable because of the great uncertainties subsurface (Fuchs and Balling 2016). There are many methods for the spatial interpolation on variables (e.g. radiogenic elements concentration, thermal conductivity etc.) related with the geothermal energy assessment and they can be classified into three categories (Li and

© Springer Nature Singapore Pte Ltd. 2019
L. Zhan et al. (Eds.): ICEG 2018, ESE, pp. 65–72, 2019.
https://doi.org/10.1007/978-981-13-2227-3_8

Heap 2008): (1) non-geostatistical methods, (2) geostatistical methods and (3) combined methods. The stochastic simulation is a variogram based-model, general means for generating multiple realizations of a specific variable, rather than a map of local best estimates produced by kriging (Goovaerts 1997). Unlike kriging methods, the simulation approaches take into account both the spatial variation of raw data at sampled locations and the variation of estimates at unsampled locations (Delbari et al. 2009). Since 1990s, as a popular stochastic simulation method, the Sequential Gaussian Conditional Simulation method (SGCS) has been developed and often applied in the fields of hydrogeology, ecology, pedology, mining, petroleum etc. (Dubrule 1989; Caers 2005). It is used to model the continuous variables such as porosity, permeability, concentration of elements etc. SGCS is based on the Monte Carlo method and overcomes the smoothing effect induced by the kriging interpolation method. In comparison with the partial optimization of the estimator value in the kriging interpolation algorithm, the geostatistical stochastic simulation is able to assess the spatial distribution of desired variables and analyzing its uncertainty (Soltani et al. 2013), realizing the optimization of the estimator values in the whole region through multiple realizations based on the same input data (Zhao et al. 2010).

Parameters involved in the calculation of radiogenic heat production that may strongly affect the subsurface temperature distribution, include the concentration of uranium, thorium, potassium and density. However, because of the limited samples in the subsurface and the strong heterogeneity of the lithology in different geological formations, it is difficult to have a clear understanding on their spatial distribution over a large region. The assessment of the geothermal potential in the western St. Lawrence Lowlands located at the southwestern Quebec is highly dependent on the clear understanding on the characteristics of its basement. However, because of the limited samples and incomplete knowledge of the uncertainty associated with the distribution of radiogenic elements, it is meaningful to make a comparison by investigating the radiogenic characteristics of its neighbored outcropping regions (e.g., Portneuf-Mauricie domain, Parc des Laurentides domain, Morin Terrane etc.). The main objective of this study is to understand the spatial distribution of the radiogenic elements and the radiogenic heat production in the Grenville basement of the western St. Lawrence Lowlands using the geostatistics studies and the Sequential Gaussian Simulation (SGS) method.

2 Study Area

The Grenville Province (Fig. 1a) is composed of high-grade metamorphic terranes and thrust stacks along ductile shear zones, equivalent to the roots of a Himalayan-type collisional orogeny (Rivers 2015; Davidson 1984; Dufréchou et al. 2014). It was found that the north-south strike of the Grenville structure belt extends from Canada southward into the subsurface of the Appalachian basin (or foreland) (Shumaker and Wilson 1996), which belongs to part of the Appalachian orogeny that extends from Newfoundland to North Carolina. Grenvillian age rocks outcrop in southwestern Quebec in lithotectonic domains including Morin Terrane, Portneuf-Mauricie Domain and Parc des Laurentides Domain etc.

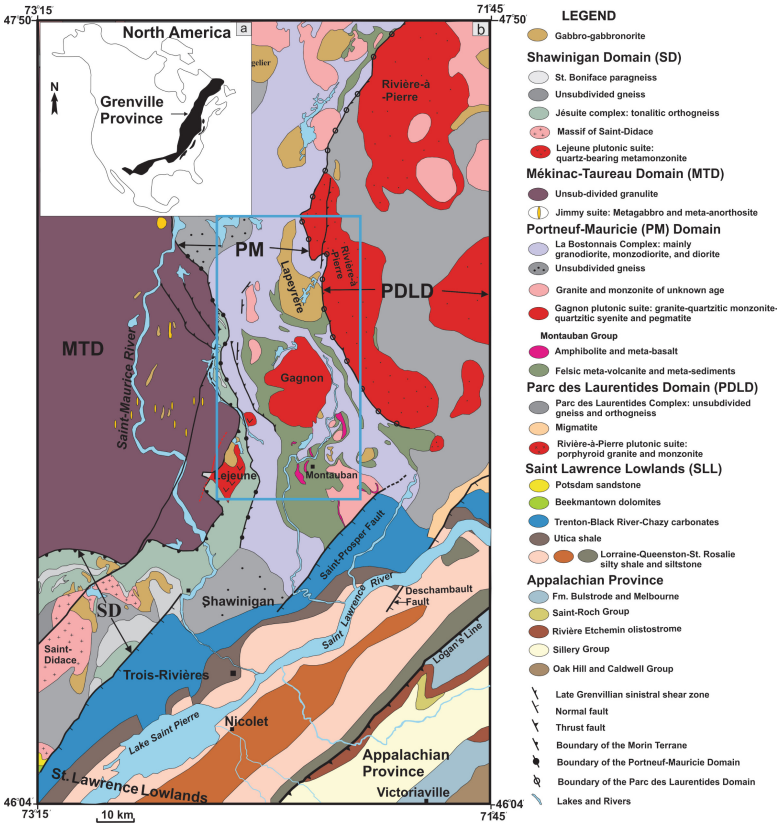

Fig. 1. Study area (surrounded by the blue rectangle) in the Grenville Province. **(a)** Location of the Grenville Province; **(b)** simplified geological map of the western St. Lawrence Lowlands and its neighbored geological regions composed of Grenville age rocks including Portneuf-Mauricie (PM) domain, Shawinigan domain (SD) that is part of the Morin Terrane (MT), Parc des Laurentides domain (PDLD) etc. (modified from Nadeau and Brouillette 1994, 1995; Sappin 2012).

The St. Lawrence Lowlands located at the southwestern Quebec is comprised of Cambrian to Ordovician sedimentary rocks and their crystalline basement is made up of rocks including granite, granitic gneiss, paragneiss, orthogneiss, gabbronorite, monzonite, and amphibolite etc. (Tremblay et al. 2003; Lavoie et al. 2009). Figure 1b shows the simplified geological map of the western part of the St. Lawrence Lowlands and its neighbored geological regions at Grenvillian age including the Portneuf-Mauricie (PM) domain, Morin Terrane (MT) and Parc des Laurentides domain (PDLD). The study area bounded by the blue rectangle covering intrusions of Gagnon, Lapeyrere and Montauban group is selected because of the rich data in the concentration of the radiogenic elements.

3 Methodology

3.1 Sampling

In the study area shown in Fig. 1b bounded by the blue rectangle, 170 samples were collected by using RS-230 spectrometer and compiled the available data from the Quebec Ministère des Ressources naturelles et de la Faune (SIGEOM). For the data collected from the SIGEOM database, most of the uranium concentration samples are based on NAA-neutron activation method, while the thorium concentration are mainly based on NAA and X-ray fluorescence, the potassium concentration are based on X-ray fluorescence and plasma emission spectrum. When a much larger region with the longitude in the range of W73°15' and W71°45' and the latitude in the range of N46° 04' and N47°50' shown in Fig. 1b is considered in the Grenville Province covering Morin Terrane, Portneuf-Mauricie domain, Parc des Laurentides domain, a total of 404 uranium data, 357 thorium data and 411 potassium data were collected.

3.2 Sequential Gaussian Simulation

In the SGS algorithm the mean and variance of the Gaussian distribution at any location along the simulation path is estimated by the kriging estimate and the kriging variance (Vidal and Archer 2015). Rather than choosing the mean as the estimate at each grid node like the kriging interpolation method, SGS uses a random deviate from the normal distribution. This random deviate is selected according to a uniform random number representing the probability level. The variable at each unknown grid node is simulated sequentially according to its normal conditional cumulative distribution function (ccdf). During the multiple realizations, it uses not only the original data but also all previous simulated values.

3.3 Calculation of Radiogenic Heat Production

When the concentration of the radiogenic elements including uranium, thorium and potassium is known, together with the values of density for the samples, the radiogenic heat production can be calculated using the following empirical function (Mareschal and Jaupart 2004; Rybach 1976):

$$A = \rho_r[9.52C_u + 2.56C_{Th} + 3.48C_k] \times 10^{-5} \quad (1)$$

where ρ_r is dry density of rock (kg/m^3), C_u is the uranium content (ppm), C_{Th} is the thorium content (ppm), and C_k is the potassium content (%).

4 Results and Discussion

4.1 Concentration of Radiogenic Elements at Sampled Sites

The average concentration of uranium, thorium and potassium is 1.78 ppm, 6.01 ppm and 2.64%, with the standard deviation error of 3.57, 7.27 and 1.85 respectively.

It presents that 90% of the total samples have the uranium concentration less than 3 ppm, 64% of the samples have the thorium concentration less than 5 ppm, and 56% of the samples have the potassium concentration less than 3%.

4.2 Spatial Distribution of Uranium, Thorium and Potassium Based on SGS

Based on SGS modeling method and the omni-directional variogram with the range of 3400 m shown in Fig. 2, spatial distribution of the uranium under 100 realizations is generated (see Fig. 3a) in the study area of 35 × 80 km^2, with the cell size of 175 m × 400 m performed using the geostatistics software - SGeMS (Remy et al. 2009). Using the same process above, the spatial distributions of the thorium and potassium are also simulated.

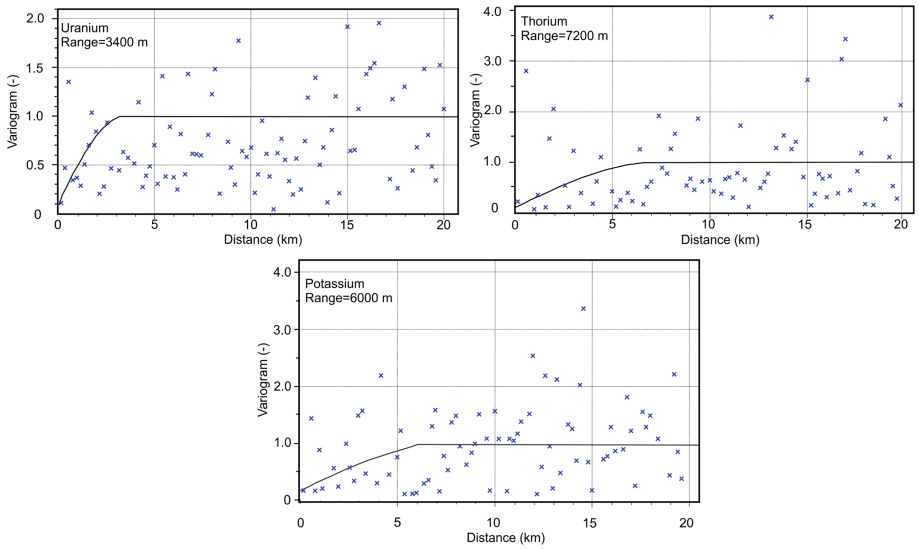

Fig. 2. The omni-directional variograms for the concentration of uranium, thorium and potassium in the study area

Except the uranium concentration, the distribution of the thorium (Fig. 3b) and potassium (Fig. 3c) using SGS simulation method are also shown by applying the omni-directional variograms with the range of 7200 m and 6000 m respectively (see in Fig. 2).

4.3 Spatial Distribution of the Radiogenic Heat Production Based on SGS

Based on the range of the density value (minimum, average and maximum) for the specific rock in the study area, using the empirical function Eq. 1, accordingly, three types of radiogenic heat production can be calculated and their spatial distribution can

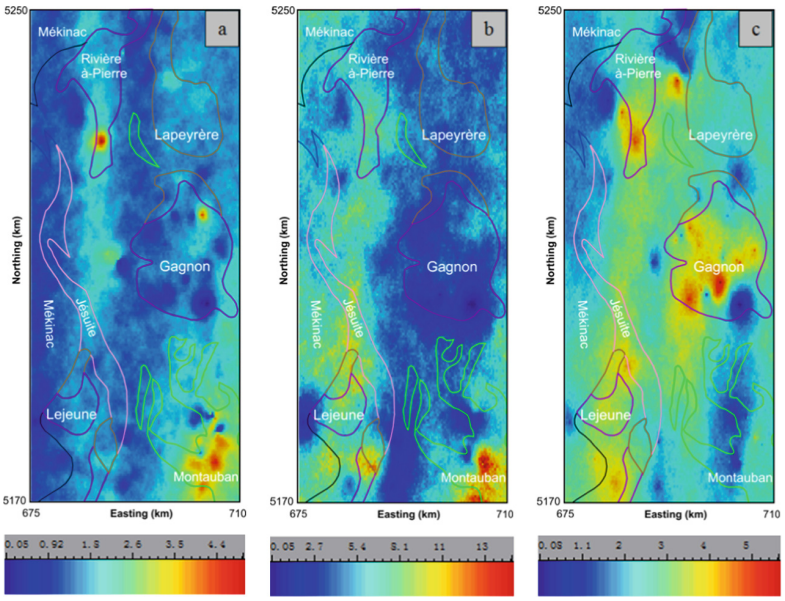

Fig. 3. The concentration of uranium(a), thorium(b) and potassium(c) by using conditional SGS simulation based on 100 realizations applying the omni-directional variograms shown in Fig. 2.

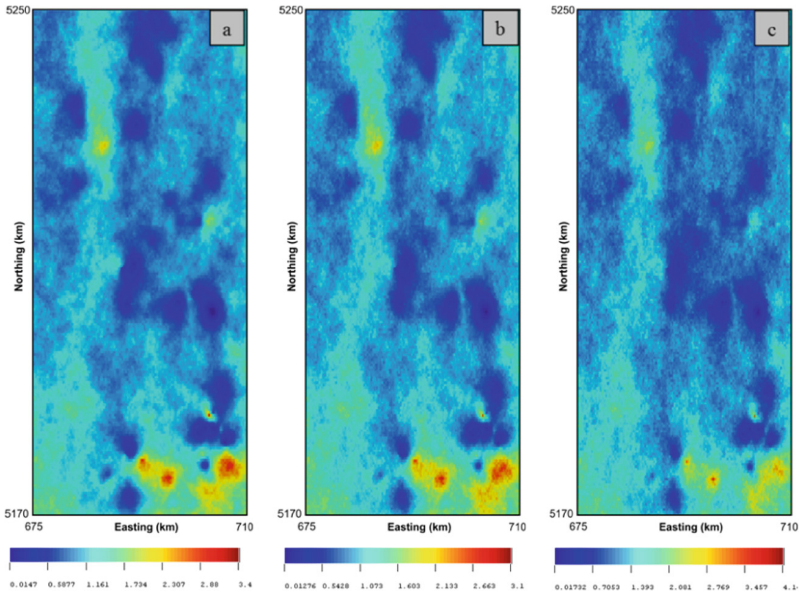

Fig. 4. Spatial distribution of the radiogenic heat production using the average (a), minimum (b) and maximum (c) density values for specific rocks at the sample points through applying the conditional SGS with 100 realizations

be simulated by applying the SGS method (Fig. 4). It shows that the difference between the minimum and maximum radiogenic heat production can reach to an extent of 30% compared Fig. 4a and c.

5 Conclusions

In the western St. Lawrence Lowlands, the radiogenic characteristics of its basement is less known. The information from the neighbored Grenville Province may provide a reference in understanding the heterogeneity of basement buried by the sedimentary rocks in the western St. Lawrence Lowlands. Some main conclusions are as follows: (1) radiogenic elements concentration for most samples in the research region is low; (2) The minimum and the maximum radiogenic heat production value is 30%. Results from this paper on the spatial distribution of the radiogenic heat production will be applied in the forward modeling of the subsurface temperature and the assessment on the geothermal resources in the western St. Lawrence Lowlands in the future.

Acknowledgements. The author acknowledge the support of the CAS Pioneer Hundred Talents Program in China. Besides, special thanks to Bernard Giroux and Erwan Gloaguen at INRS-ETE for their invaluable help in technical support of SGeMS software. Thanks to Aurelie Gicquel for providing some radiogenic elements data in the research region.

References

Caers J (2005) Petroleum geostatistics. SPE

Davidson A (1984) Identification of ductile shear zones in the south-western Grenville Province of the Canadian Shield. In: Kroner A, Greiling R (eds) Precambrian tectonics illustrated: Schweitzerbart'sche Verlagsbuchhandlung, Stuttgart, pp 263–279

Delbari M, Afrasiab P, Loiskandl W (2009) Using sequential Gaussian simulation to assess the field-scale spatial uncertainty of soil water content. CATENA 79:163–169

Dubrule O (1989) A review of stochastic models for petroleum reservoirs. In: Armstrong M (ed) Quantitative geology and geostatistics. Springer, Dordrecht, pp 493–506

Dufréchou G, Harris LB, Corriveau L (2014) Tectonic reactivation of transverse basement structures in the Grenville orogeny of SW Quebec, Canada: insights from gravity and aeromagnetic data. Precambr Res 241:61–84

Fuchs S, Balling N (2016) Improving the temperature predictions of subsurface thermal models by using high-quality input data. Part 1: uncertainty analysis of the thermal-conductivity parameterization. Geothermics 64:42–54

Goovaerts P (1997) Geostatistics for natural resources evaluation. Oxford University Press, New York

Lavoie D, Pinet N, Castonguay S, Dietrich J, Giles P, Fowler M, Thériault R, Laliberté JY, St P, Hinds S, Hicks L, Klassen H (2009) Hydrocarbon systems in the Paleozoic basins of eastern Canada-Presentations at the Calgary 2007 workshop. Geol. Surv. Canada Open File 5980:9–79

Li, J., Heap, A.D.: A review of spatial interpolation methods for environmental scientists. Geoscience Australia, p. 137. Record 2008/23 (2008)

Mareschal JC, Jaupart C (2004) Variations of surface heat flow and lithospheric thermal structure beneath the North American craton. Earth Planet Sci Lett 223:65–77

Nadeau L, Brouillette P (1994) Carte structurale de la région de La Tuque (SNRC 31P), Province de Grenville, Québec. Commission Géologique du Canada, dossier public 2938(1):250 000

Nadeau L, Brouillette P (1995) Carte structurale de la région de Shawinigan (SNRC 31I), Province de Grenville, Québec. Commission Géologique du Canada, dossier public 3012 (1):250 000

Remy N, Boucher A, Wu J (2009) Applied Geostatistics with SGeMS: A User's Guide. Cambridge University Press, Cambridge

Rivers T (2015) Tectonic setting and evolution of the Grenville orogeny: an assessment of progress over the last 40 years. Geosci Can 42:77–124

Rybach L (1976) Radioactive heat production in rocks and its relation to other petrophysical parameters. Pure appl Geophys 114:309–318

Sappin AA (2012) Pétrologie et métallogénie d'indices de Ni-Cu-éléments du Groupe du Platine du Domaine de Portneuf-Mauricie, Québec (Canada), Thèse de doctorat at Université Laval, p 70

Shumaker RC, Wilson TH (1996) Basement structure of the Appalachian foreland in West Virginia: its style and effect on sedimentation. In: Van der Pluijm BA, Catacosinos PA (eds), Basement and basins of Eastern North America, pp 139–155. Geol Soc Am

SIGEOM. http://sigeom.mines.gouv.qc.ca

Soltani F, Afzal P, Asghari O (2013) Sequential Gaussian simulation in the Sungun Cu porphyry deposit and comparing the stationary reproduction with ordinary kriging. Univ J Geosci 1(2):106–113

Tremblay A, Long B, Massé M (2003) Supracrustal faults of the St. Lawrence rift system, Québec: kinematics and geometry as revealed by field mapping and marine seismic reflection data. Tectonophysics 369:231–252

Vidal A, Archer R (2015) Geostatistical simulations of geothermal reservoirs: two-and multiple-point statistic models. In: Proceedings world geothermal congress 2015, Melbourne, Australia

Zhao YF, Sun ZY, Chen J (2010) Analysis and comparison in arithmetic for kriging interpolation and sequential gaussian conditional simulation. J Geo-Inf Sci 12(6):767–776

Accelerated Carbonation Technology of Reactive MgO-Stabilized Soil for Possible CO_2 Sequestration

Guanghua Cai[1(✉)], Songyu Liu[2], Guanghui Shao[1], Guangyin Du[2], and Liang Wang[2]

[1] School of Civil Engineering, Nanjing Forestry University, Nanjing 210037, China
ghcai@njfu.edu.cn
[2] Institute of Geotechnical Engineering, Southeast University, Nanjing 210096, China

Abstract. Nowadays, the cement industry is under pressure to reduce the carbon footprint and energy demands of cement-based construction materials. Carbonation technology is a process that the Ca-/Mg- alkaline materials can react with CO_2 to form stable carbonates, thus it is regarded as a potentially attractive technology of CO_2 sequestration, including mineral carbonation, cement/concrete carbonation, and carbonation of reactive MgO-stabilized material. This paper investigates the CO_2 uptake of reactive MgO-stabilized soils after accelerated carbonation under the high CO_2 concentration (99.9%). The CO_2 uptake is examined through the HNO_3 acidification test and thermal analysis technology. Key results revealed that the carbonation of reactive MgO-stabilized soils could consume large amounts of water and CO_2 to produce expansive carbonation products. The CO_2 uptake is observably affected by several factors such as MgO content, water content, carbonation time and CO_2 pressure. After the several hour's carbonation (about 3–6 h), the CO_2 uptake can basically achieves about 0.8–1.0 times matter quantity of reactive MgO.

Keywords: Accelerated carbonation · Reactive MgO · Greenhouse gas Sequestration · CO_2 uptake

1 Introduction

The control of greenhouse gas is arguably the most challenging environmental policy issue facing China and other countries (Li et al. 2013). Carbon dioxide (CO_2) is considered to be the major greenhouse gas contributing to global warming, and increased public awareness has led to greater concern over the impact of anthropogenic CO_2 emissions. Since the beginning of the industrial revolution, the average atmospheric concentration of CO_2 has increased from 280 ppm to 380 ppm, which results that the average global temperature has increased 0.6–1 °C in the same time period (Feely et al. 2004; Sabine et al. 2004). The rapid rise of CO_2 emissions is attributed to the use of fossil fuels and the calcination of cement industry, and continued uncontrolled CO_2 emissions may contribute to sea level increases and species extinction

© Springer Nature Singapore Pte Ltd. 2019
L. Zhan et al. (Eds.): ICEG 2018, ESE, pp. 73–80, 2019.
https://doi.org/10.1007/978-981-13-2227-3_9

(Keeling et al. 1995; Haselbach and Thomas 2014). In order to curtail CO_2 emissions into the atmosphere, several superior strategies have been suggested, which are reducing energy consumption, improving energy efficiency, switching to less carbon intense fuels, and using renewable energies (Hashim et al. 2005). These options, however, may not be enough to mitigate global warming in the future, so the technology of CO_2 capture, storage, and utilization provides a mid-term solution to mitigate environment impacts (Li et al. 2013). Therefore, most agree that in-situ or ex-situ carbon sequestration is one of the most promising approaches to reduce CO_2 emission in the immediate future (Olajire 2013). The possibility of fixing CO_2 as a stable solid carbonate minerals such as calcite, dolomite, magnesite or use it as a secondary product of commercial value is also attractive (Olajire 2010).

Moreover, the production of Portland cement involves severe environmental impacts, and its CO_2 emissions account for $\sim$5% to 8% of global anthropogenic emissions. Therefore, Portland cement is gradually replaced by alternative binders such as geopolymers, calcium carbide residues and reactive MgO in soil treatment processes (Andrzej and Karin 2013; Horpibulsuk et al. 2012; Jin et al. 2014; Sukmak et al. 2014). In recent studies, reactive MgO starts to draw people's attention due to the following reasons: (1) it can be used as an effective and sustainable alkali-activator of ground granulated blast-furnace slag in soil stabilization/solidification (Jin et al. 2014); (2) when reactive MgO is mixed alone as the binder in soils or concretes, it can absorb substantial quantities of CO_2 to produce hydrated magnesium carbonates (nesquehonite, dypingite, hydromagnesite, magnesite) in short term, generating higher strength, finer microstructure and lower permeability and facilitating the permanent storage of CO_2 (Cai et al. 2015a, b; Yi et al. 2013, 2016); and (3) reactive MgO is generally from the calcination of magnesite at a low temperature ($\sim$700–800 °C) or is "synthetically" produced from seawater and lake brines (Liska and Al-Tabbaa 2008). In addition, the formations of magnesium carbonates are influenced by various factors such as mix design, chemistry composition and particle size distribution of MgO, as well as CO_2 concentration, pressur and relative humidity (Liska et al. 2008; Unluer and Al-Tabbaa 2014; Vandeperre and Al-Tabbaa 2007; Yi et al. 2013, 2016). However, very limited studies have been conducted to investigate the influence of MgO activity index (c_A) and soil type on CO_2 sequestration.

2 Materials and Methods

2.1 Materials

The seven soils (labelled S1–S7) used in this study were sampled from seven construction sites (Xuzhou, Suqian, Nanjing, Hai'an, Nanjing, Wenzhou I, Wenzhou Π) from a depth of 2.0–3.0 m in eastern China. The Atterberg limits and classifications of soils were determined according to ASTM D4318 and ASTM D2487, respectively. The soil pH was measured by portable D-54 pH meter according to ASTM D4972. Two types of reactive MgO powders, light-burned MgO with higher activity index (denoted as H) and heavy-burned MgO with lower activity index (denoted as L) were used, they were purchased from Xingtai and Haicheng, respectively. The specific gravity was

Table 1. Physicochemical properties of materials.

Index	Value							MgO-H	MgO-L
	S1	S2	S3	S4	S5	S6	S7		
Water content, w_n(%)	26.1	25.0	29.2–31.0	39.0–42.4	33.6	48.8	47.3–50.0		
Specific gravity, G_s	2.68	2.71	2.72	2.72	2.72	2.73	2.71	1.65	2.25
Liquid limit, w_L (%)	34.1	33.8	40.0	51.9	48.6	61.6	65.2		
Plastic limit, w_P (%)	25.9	23.9	25.5	35.1	24.0	32.5	31.6		
Grain-size distribution (%)[a]									
< 0.002 mm	4.7	3.4	8.3	8.5	11.8	16.1	16.4	63.6	32
0.002–0.075 mm	45.3	66.6	85.0	86.5	69.2	73.0	82.6	36.4	68
0.075–2 mm	48.0	30.0	7.0	5.0	17.0	9.0	0.9	0	0
pH (water/soil = 1)[b]	8.02	8.07	7.85	7.59	8.33	8.07	8.14		

Note: [a]Measured by using a laser particle-size analyzer Mastersizer 2000;
[b]Measured as per ASTM D4972.

determined as per ASTM D854 (ASTM 2010b) and the grain size distribution was determined using a laser particle size analyzer Mastersizer 2000. To avoid the hydration of reactive MgO, water-free kerosene was used as the disperse medium. The basic physicochemical properties of the raw materials are shown in Table 1. Table 2 lists the chemical composition of the raw materials obtained by conducting the X-ray fluorescence spectrometry tests. To investigate the influence of activity index (c_A) on the strength properties of carbonated MgO-admixed soils, the mixed Type 1 and Type 2 MgO, denoted as H*i*L*j* representing *i*% Type 1 and *j*% Type 2 MgO (on dry soil weight basis) (*i*% + *j*% = 100%, and *i* is 0, 25, 50, 75, and 100 respectively), was mixed with the parent soil. Based on the Chinese Industry Standard (2006) (Eq. 1), the c_A of the MgO mixture was determined as 66.4, 69.7, 77.6, 82.3 and 85.9% for H0L100, H25L75, H50L50, H75L25, and H100L0, respectively. The CO_2 gas (concentration: 99.9%) used was supplied by Nanjing Third Bridge Industrial Gases Co, Ltd.

Table 2. Chemical composition (% weight) of the materials.

Oxides	MgO-H	MgO-L	S1	S2	S3	S4	S5	S6	S7
MgO	91.8	81.3	2.15	1.44	1.22	2.02	1.43	3.12	3.01
Al_2O_3	1.43	0.42	10.58	11.02	10.22	13.70	15.27	18.48	19.11
CaO	1.26	2.46	5.33	6.63	6.41	2.60	1.01	2.86	4.18
SiO_2	3.91	5.58	71.97	72.13	71.76	70.34	70.00	57.82	56.95
Fe_2O_3	0.30	0.22	4.45	3.94	3.57	5.60	6.51	9.78	9.52
Na_2O	–	–	1.5	0.3	3.1	–	1.43	–	0.90
K_2O	0.04	0.01	2.15	2.35	2.16	2.91	2.67	3.89	3.75
TiO_2	0.13	–	0.68	0.68	0.65	0.90	0.91	0.94	0.91
SO_3	0.40	0.1	0.16	0.21	0.27	1.26	–	0.90	0.53
P_2O_5	0.31	–	0.86	1.15	0.51	0.51	0.27	0.47	0.08
MnO_2	0.02	0.01	0.14	0.14	0.09	0.12	0.16	0.26	0.19
Others	0.38	9.87	0.02	0.03	0.04	0.05	0.04	1.48	0.87

$$c_A = \frac{40 \cdot (m_2 - m_1)}{18 \cdot m_1} \times 100\% \quad (1)$$

where m_1 and m_2 represent the dry mass of the samples before and after hydration (g), respectively; 18 and 40 are the molecular weights of H_2O and MgO (g/mol), respectively.

2.2 Specimen Preparation

To investigate the influence of MgO activity index, the mixing MgO contents were selected as 10, 15, 20, and 30% and the initial gravimetric water contents (w_0, on dry soil weight basis) were set as 20, 25 and 30%. Thus, the ratios of initial water content to MgO content (w_0/c) were 2.5, 2.0, 1.5, 1.0, and 0.8, respectively. To investigate the effect of soil type, the initial gravimetric water contents of the soils were set as $0.6w_L$, $0.7w_L$, $0.8w_L$ and $0.9w_L$, respectively. The specimen preparation and carbonation tests can also be found in Cai et al. (2015a, b). The air-dried sieved soils (<2.0 mm) were thoroughly mixed with reactive MgO by using a mechanical agitator for 5 min, and then the predetermined volume of distilled water was added into the dried mixture to be agitated for another 5 min until achieving a homogeneous state again.

Afterwards, the homogenized mixture was weighed and placed in a steel cylindrical mold (Φ50 mm × H100 mm) and then compacted with a hydraulic jack. Then, the specimens were immediately extruded from the molds and then measured for weight and dimension, respectively, and they were finally put in the fabricated carbonation apparatus (see Fig. 1) containing CO_2, and subjected to the accelerated carbonation under a gas pressure of 200 kPa for 12 h, which ensured the stable strength of specimens.

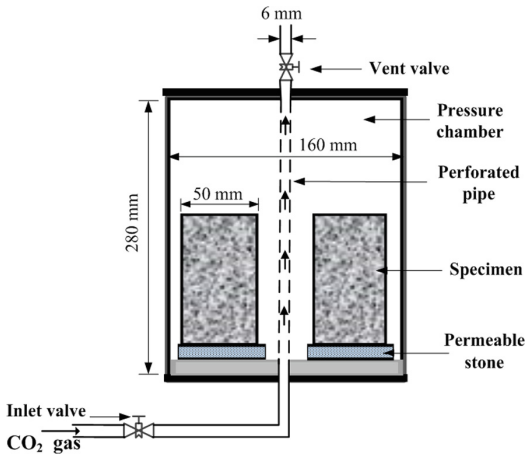

Fig. 1. The test setup used for carbonation of reactive MgO-treated soils.

2.3 Testing Methods

In this study, the acid digestion method involved the chemical decomposition of hydrated magnesium carbonates in the nitrate acid (HNO_3) solutions, which could be explained by the following reactions:

$$MgCO_3 + 2HNO_3 \rightarrow Mg(NO_3)_2 + CO_2 + H_2O \tag{2}$$

$$MgCO_3 \cdot 3H_2O + 2HNO_3 \rightarrow Mg(NO_3)_2 + CO_2 + 4H_2O \tag{3}$$

$$\begin{aligned} MgO + \ Mg(OH)_2 + 4MgCO_3 \cdot Mg(OH)_2 \cdot xH_2O + 14HNO_3 \\ \rightarrow 7Mg(NO_3)_2 + 4CO_2 + (9+x)H_2O \end{aligned} \tag{4}$$

where x is the number of crystal water contained in carbonates, such as hydromagnesite (x = 4) and dypingite (x = 5).

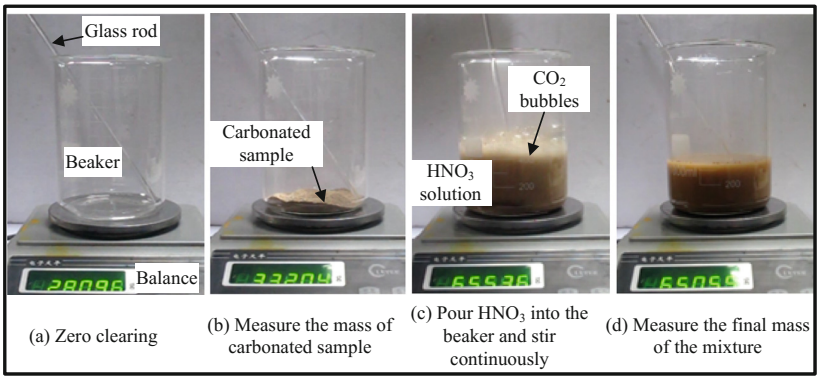

Fig. 2. Illustration photos of HNO_3 digestion method for measuring CO_2 content.

Figure 2 shows the testing process of acid digestion for measuring CO_2 content. The acid digestion, a reaction between powdery carbonated soils and 10% HNO_3, was performed in a beaker (1,000 mL). The beaker containing a glass rod for stirring was placed onto the electrical balance (accuracy: 0.01 g, range: 3,000 g) which was then zeroed out. About 50 g sieved carbonated soil (<2 mm) was put into the beaker and then measured (denoted as m_1, (g)). Subsequently, the pre-measured 10% HNO_3 (about 300 g, denoted as m_2 (g)) was added into the carbonated soil and stirred continuously by using the glass rod to eliminate the CO_2 gas. After the complete reaction (about 10 min), the mass of the mixture was measured again and denoted as m_3 (g). The CO_2 content could be calculated by using the following equation when the weight loss was given.

$$C_{CO_2} = \frac{m_1 + m_2 - m_3}{m_1/(1+w_f)} \times 100\% \tag{5}$$

where C_{CO2} is the content of CO_2 absorbed (%) and w_f is the gravimetric water content of tested carbonated soil (%).

3 Results and Analyses

Theoretically speaking, when the MgO admixed in the soil hydrates completely to form brucite and the brucite is also carbonated fully to generate hydrated magnesium carbonates including nesquehonite ($MgCO_3 \cdot 3H_2O$) and dypingite ($Mg_5(CO_3)_4(OH)_2$ $5H_2O$) or hydromagnesite ($Mg_5(CO_3)_4(OH)_2 \cdot 4H_2O$), MgO will consume 0.88 to 1.1 times CO_2 (on the weight basis) (Yi et al. 2016). Figure 3 presents the sequestrated CO_2 (represented as m_{CO2}/m_{MgO}) of carbonated MgO-stabilized soils. It can be observed from this figure that the sequestrated CO_2 generally decreases with increasing the w_0/c or reducing the MgO activity index. However, the m_{CO2}/m_{MgO} of the two samples is discovered to be more than 1.1, which is attributed to the factor that the acid digestion is an exothermic reaction and part of the HNO_3 solution evaporates (Yi et al. 2016). The results show that the MgO-stabilized soils with $w_0/c < 2.0$ could achieve a high carbonation degree (0.9 to 1.1) in a short time, while the stabilized soils with $w_0/c \geq 2.0$ could also achieve the carbonation degree of 0.66 to 0.83, indicating that the carbonation of reactive MgO-stabilized soils has a great potential in absorbing waste CO_2 and saving the cost of the ground improvement compared to the conventional PC stabilization.

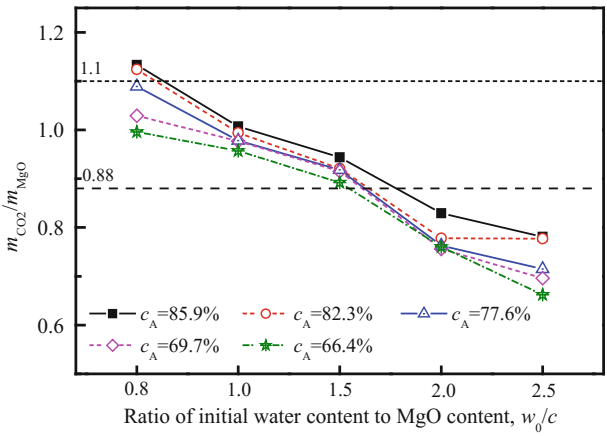

Fig. 3. CO_2 uptakes of carbonated soils with different MgO activity index.

Figure 4 illustrates the content of CO_2 absorbed in carbonated specimens. This was measured using the HNO_3 digestion method. It can be seen from this figure that the content of CO_2 within the specimens with higher liquid limit or initial water content is relatively lower. The above-mentioned results are explained by the following two reasons: (1) the reactive MgO-treated low-w_L silt (S2) with a loose large porosity is

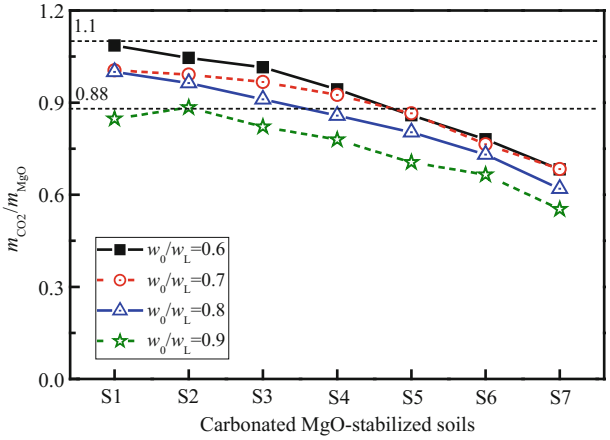

Fig. 4. CO_2 uptakes of carbonated MgO-stabilized soils with different soil.

prone to hydrate and absorb CO_2, while the reactive MgO-stabilized high-w_L clay (S7) has smaller porosity which makes it difficult for CO_2 to enter the soil; and (2) during the carbonating process, CO_2 pressure can break the inter-particle connection and form the main channel of gas infiltration, which reduces the CO_2 absorption of reactive MgO-stabilized soils. Generally, CO_2 is difficult to infiltrate into the high-w_L low-porosity clayey soils (e.g., S4, S5 and S7) which have the cation exchange between Mg^{2+} and the readily exchangeable cations, dominating the binder-soil interaction and resulting in a reduced thickness of double-diffusion layer as well as the formation of flocculation and agglomeration of clay particles (Mitchell and Soga 2005). However, it is easier for the low-w_L soils (e.g., S2 and S3) to absorb CO_2 to have carbonation reactions than high-w_L soils (e.g., S4, S5 and S7).

4 Conclusions

The carbonated MgO-stabilized soil achieved a high carbonation degree in several hours, with the maximum CO_2/MgO ratio in a range of 0.6–1.1, especially for low liquid-limit soils and high activity-index MgO. This study confirms that the MgO and its carbonation are promising as a more rapid and sustainable stabilization binder and CO_2 sequestration technology in terms of CO_2 emissions.

Acknowledgements. This work was financially supported by the High-level Talent Research Fund of Nanjing Forestry University (GXL2018028), the Science and Technology Project of Jiangsu Traffic Engineering Construction Bureau (2018T01), the National Natural Science Foundation of China (41330641, 51279032) and the National Key Research and Development Program of China (2016YFC0800201).

References

Haselbach L, Thomas A (2014) Carbon sequestration in concrete sidewalk samples. Constr Build Mater 54:47–52

Li L, Zhao N, Wei W, Sun Y (2013) A review of research progress on CO_2 capture, storage, and utilization in Chinese Academy of Sciences. Fuel 108:112–130

Olajire AA (2013) A review of mineral carbonation technology in sequestration of CO_2. J Petrol Sci Eng 109:364–392

Hashim H, Douglas P, Elkamel A, Croiset E (2005) Optimization model for energy planning with CO_2 emission considerations. Ind Eng Chem Res 44(4):879–890

Feely RA, Sabine CL, Lee K et al (2004) Impact of anthropogenic CO_2 on the $CaCO_3$ system in the oceans. Science 05:362–366

Keeling CD, Whorf TP, Wahlen M et al (1995) Inter-annual extremes in the rate of rise of atmospheric carbon dioxide since 1980. Nature 75:666–670

Olajire AA (2010) CO_2 capture and separation technologies for end-of-pipe applications—a review. Energy 35:2610–2628

Sabine CL, Feely RA, Gruber N et al (2004) The oceanic sink for anthropogenic CO_2. Science 305:367–371

Andrzej C, Karin HC (2013) Effects of reactive magnesia on microstructure and frost durability of portland cement-based binders. J Mater Civ Eng 25:1941–1950

Horpibulsuk S, Phetchuay C, Chinkulkijniwat A (2012) Soil stabilization by calcium carbide residue and fly ash. J Mater Civ Eng 24(2):184–193

Jin F, Gu K, Al-Tabbaa A (2014) Strength and drying shrinkage of reactive MgO modified alkali-activated slag paste. Constr Build Mater 51(1):395–404

Sukmak P, Silva DP, Horpibulsuk S et al (2014) Sulfate resistance of clay-portland cement and clay high-calcium fly ash geopolymer. J Mater Civ Eng 04014158:1–11

Yi Y, Liska M, Unluer C, Al-Tabbaa A (2013) Carbonating magnesia for soil stabilization. Can Geotech J 50(8):899–905

Yi Y, Lu KW, Liu SY et al (2016) Property changes of reactive magnesia-stabilized soil subjected to forced carbonation. Can Geotech J 53(2):314–325

Cai GH, Liu SY, Du YJ et al (2015a) Strength and deformation characteristics of carbonated reactive magnesia treated silt soil. J Central South Univ 22(5):1859–1868

Cai GH, Du YJ, Liu SY, Singh DN (2015b) Physical properties, electrical resistivity and strength characteristics of carbonated silty soil admixed with reactive magnesia. Can Geotech J 52(11):1699–1713

Liska M, Vandeperre LJ, Al-Tabbaa A (2008) Influence of carbonation on the properties of reactive magnesia cement-based pressed masonry units. Adv Cem Res 20(2):53–64

Vandeperre LJ, Al-Tabbaa A (2007) Accelerated carbonation of reactive MgO cements. Adv Cem Res 19(2):67–79

Unluer C, Al-Tabbaa A (2014) Enhancing the carbonation of MgO cement porous blocks through improved curing conditions. Cem Concr Res 59(5):55–65

Applicability of Sedimentary Rock in Hydraulic Barrier System Construction

S. Iso(✉), T. Motoshima, and H. Komine

Civil Engineering Department, Nuclear Facilities Division,
Taisei Corpration, 1-25-1 Nishisshinjuku, Shinjukuku, Tokyo 163-0606, Japan
endste00@pub.taisei.co.jp

Abstract. Controlled disposal sites generally rely on impermeable barrier layers to prevent groundwater contamination. Because bentonite has low hydraulic conductivity and high swelling pressures in the presence of water, soil-bentonite mixtures are commonly used with geomembrane to construct hydraulic barriers. If inexpensive materials could be used instead, the potential cost reduction is dramatic. Sedimentary rock is widely distributed in Japan, and it is common for such rock to be excavated from the disposal site itself. This study evaluated the water-shielding performance of bentonite mixtures made with friable Neocene mudstone and commercially available graded sand. The hydraulic conductivity of the friable Neocene mudstone mixture compared favourably with that of the purchased sand mixture, even at half of the standard bentonite mixing ratio (5%). The results also confirmed our hypothesis that the friability of the mudstone could be used practically to improve mixture performance. This study demonstrated the fundamental properties of an efficient construction method that utilised roller compaction to ensure an effective seal. Construction of hydraulic barrier layers using a method that takes advantage of the friability of in situ excavated sedimentary rock, without adjusting its grain size, has the potential to greatly lower construction costs.

Keywords: Sedimentary rock · Grain crushing · Waste disposal site
Characteristic of compaction · Hydraulic conductivity · Soil-bentonite mixture

1 Introduction

Controlled disposal site and intermediate storage facilities generally rely on impermeable barrier layers to prevent groundwater contamination and the inflow of seepage water. Because bentonite clay has low hydraulic conductivity and high swelling pressures in the presence of water, soil-bentonite mixtures are commonly used in conjunction with geomembrane to construct hydraulic barriers. The properties of such barriers must conform to strict requirements when used at controlled disposal facilities. For example, such barriers are usually required to have a thickness of 50 cm or more and a hydraulic conductivity of 10^{-8} m/s or less [1], therefore, a bentonite mixing ratio of about 5% to 15% is often used [2, 3].

The hydraulic conductivity and deformation properties of soil-bentonite mixtures are strongly controlled by the quality of the base materials. therefore, it is necessary to

© Springer Nature Singapore Pte Ltd. 2019
L. Zhan et al. (Eds.): ICEG 2018, ESE, pp. 81–88, 2019.
https://doi.org/10.1007/978-981-13-2227-3_10

select materials that mix well with bentonite and have appropriate compaction properties, thereby satisfying performance requirements such as acceptable water sealing ability. High-quality sand is generally used as the base material of the bentonite mixture. However, sedimentary rock is widely distributed in Japan, and because it is common for such rock to be excavated from a disposal site, it would be beneficial if it could be effectively used as the base material. If rock excavated in situ could be used for the construction of the barrier, the potential cost reduction is dramatic.

In this study, laboratory tests were conducted to investigate the influence of base material friability on the compaction properties and hydraulic conductivity of soil–bentonite mixtures. In addition, the applicability of such materials as base materials of the bentonite mixture was examined.

2 Fundamental Sample Properties

In this study, Na-type bentonite (Kunigel V1) was used. Fractured sedimentary rock (Pliocene mudstone, hereinafter referred to as mudstone) was selected as the base material for the soil–bentonite mixture, with weathered granite (hereinafter referred to as granite) and Inagi sand also used for comparison. The fundamental properties of the materials are summarised in Table 1. Two types of density test were carried out: (1) measurement of grain density following the procedures defined by Japanese Industrial Standard (JIS) A 1202 and (2) measurement of rock mass density following JIS A 1225 (paraffin method) [3]. For the granite, the grain densities obtained by both test methods were similar, indicating the presence of very few internal pores. On the other hand, for the mudstone, the presence of small internal pores was suggested by the density tests. A very low grain density, 1.391 g/cm^3, was obtained using JIS A 1225 (paraffin method), as compared with 2.553 g/cm^3 for JIS A 1202.

Table 1. Fundamental property

Contents		Granite	Mudstone	Inagi sand	Sodium bentonite
Physical properties	Moisture content (%)	1.11	31.88	3.95	8.0
	Soil particle density (g/cm^3)	2.644*1	2.553*1	2.638	2.79
		2.513*2	1.391*2		
	Slaking ratio (%) [4]	0.36	100	-	-
Chemical properties	Methylene blue capacity (mmol/100 g)	2.86	25.71	5.71	57.14

*1 JIS A 1202, *2 JIS 1225

In this study, to investigate the effect of grain size on the capability of the base material, the granite and mudstone were adjusted to the following grain sizes: (1) 5 to 20 mm (based on the Crushed Rock Standard 2005) and (2) a uniform coefficient Uc ≧ 10. The rocks were thus termed Granite (1), Granite (2), Mudstone (1) and Mudstone (2) according to grain size. The grain size distribution curves are shown in Fig. 1 respectively.

3 Compaction Properties and Crushing Capabilities of Soil-Bentonite Mixtures

3.1 Test Case

The bentonite mixtures were prepared such that the mixing ratios of the base material and bentonite were 95:5, 90:10 and 85:15 (dry mass percentages). Hereinafter, the mixing ratios of these bentonite mixtures are abbreviated as Bt = 5%, Bt = 10% and Bt = 15%, respectively.

3.2 Compaction Capabilities

In order to understand the compaction properties of the bentonite mixture, a soil compaction test was carried out in accordance to JIS A 12103. A mould with an inner diameter of 100 mm and a 2.5 kg rammer were used to compact the samples. A tamping method was adapted from the A-c method, and the compaction energy was set to 1 and 2 Ec in accordance to JIS A 1210. The bentonite mixtures were prepared the day before the test using a kneading mixer and then cured for 24 h after adjusting the water content.

Figure 2 shows the compaction curves of the bentonite mixtures. The zero air voids curve was determined from the average grain density of the granite and mudstone samples at Bt = 10%. The granite exhibited a compaction curve similar to that of the Inagi sand, with 80% saturation (Sr) and approximately 5% to 10% air-void content (va) at maximum dry density. In contrast, the mudstone did not show a distinctive change in the compaction curve. However, Mudstone (2) had an Sr = 90% and va = 0% to 5% at maximum dry density, indicating relatively satisfactory compaction properties.

3.3 Friability of Pliocene Mudstone

In order to investigate the friability of the base material in relation to compaction, grain size tests were conducted on the granite and mudstone before and after the compaction tests. The samples tested before compaction were prepared by adjusting the water

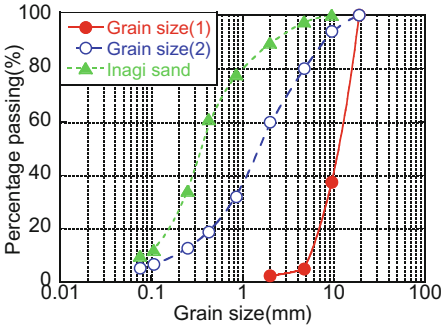

Fig. 1. Grain size distribution

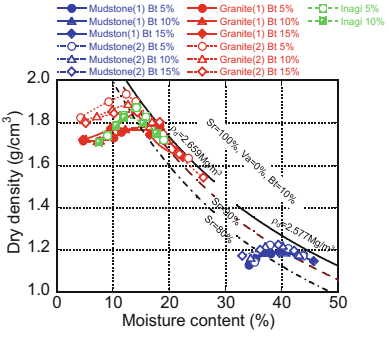

Fig. 2. Compaction curve (1Ec)

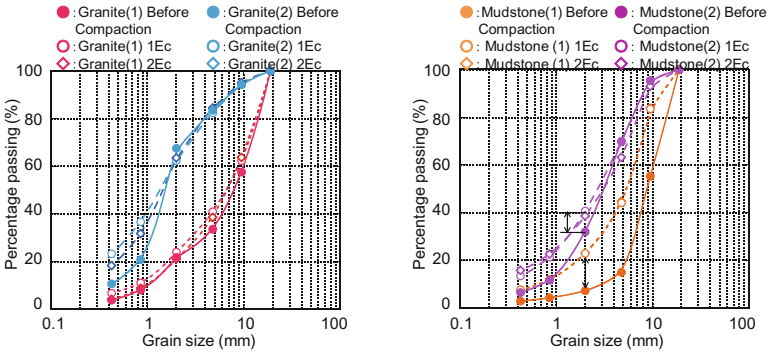

(a) Granite (b) Mudstone

Fig. 3. Compaction of grain size distribution before and after

content ratio using a mixer, followed by drying, whereas the samples tested after compaction were dried and then loosened after the test. Figures 3(a) and (b) show the grain size distribution curves before and after compaction of the granite and mudstone, respectively. As shown in Fig. 3(a), although some grain crushing occurred before and after compaction regardless of the initial grain size distribution, the grain size distribution did change significantly. On the other hand, as shown in Fig. 3(b), the mass percentage passing a grain size of 2 mm or less increased by 16% for Mudstone (1) and by 8% for Mudstone (2). Accordingly, the uniformity coefficients Uc increased from 2.6 to 9.3 and 4.9 to 10.6, respectively. In this test regime, as a lower uniformity coefficient indicates greater friability [5], Mudstones (1) and (2) showed the same grain size distribution after compaction due to crushing. This result might also explain why the dry density given in Fig. 5 in the next section was not controlled by compaction energy.

3.4 Influence of Base Material Crushing on Compaction

Figure 4 shows the relationship between maximum dry density and bentonite mixing ratio. The granite and Inagi sand showed decreases in the maximum dry density as the mixing ratio of bentonite increased, because they had single grain size distribution that difficult to compaction. The mudstone showed less influence on maximum dry density by the differences in grain size and bentonite mixing ratio. The maximum dry density of the mudstone was almost constant at around 1.2 g/cm^3. Granite (1) showed a similar tendency, remaining nearly unchanged at around 1.8 g/cm^3. These changes in maximum dry density during compaction were considered to be caused by changes in the grain size distribution of the base material due to compaction and the swelling of bentonite. In the mudstone and granite (1), even if the mixing ratio of bentonite was increased, the compaction energy would contribute to grain crushing, resulting in a better grain size distribution owing to improvement of the compaction properties. As a result, the decrease in maximum dry density would be limited. Particularly in the mudstone, a filling effect due to grain crushing occurred, and this explains why the

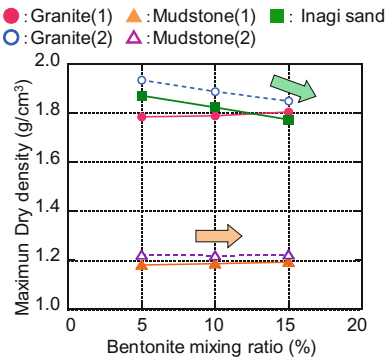

Fig. 4. Relationship between maximum dry density and bentonite mixing ratio

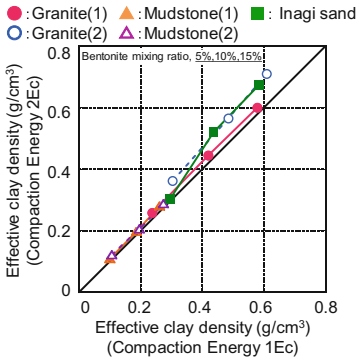

Fig. 5. Relationship of effective clay densities compacted by different loads

maximum dry density did not decrease as the mixing ratio of bentonite increased. In contrast, compaction of the Inagi sand and granite (2) became difficult at increased bentonite ratios [6]; thus, the maximum dry density decreased.

Figure 5 shows the effective clay density due to differences in compaction energy. The effective clay density was obtained by Eq. (1).

$$\rho_b = \frac{\rho_d(100 - R_s)}{100 - \rho_d \frac{R_s}{\rho_s}} \tag{1}$$

where ρ_b is the effective clay density (g/cm^3), ρ_d is the dry density (g/cm^3), R_s is the mixing ratio of the base material and ρ_s is the grain density of the base material. As shown in Fig. 4, the effective clay densities of the granite and Inagi sand were likely controlled by the magnitude of the compaction energy. However, regardless of the difference in grain size and bentonite mixing ratio, the mudstone was largely independent of compaction energy. The mudstone exhibited great grain friability, which contributed to crushing of the mudstone regardless of the compaction energy, resulting in improvement of the grain size distribution of the base material. This would explain why the grain size distribution of the soil–bentonite mixture as a whole was improved and the filling effect was increased (see Fig. 6). It is considered that the density of bentonite in the pores increased, thus resulting in a similar effective clay density regardless of the compaction energy. These compaction test results suggest a marked effect of grain crushing on the compaction properties of the mudstone.

4 Hydraulic Conductivity Characteristics

In order to investigate the hydraulic conductivity of the soil-bentonite mixture for different base materials, a falling head permeability test (JIS A 1218) was carried out. The permeability test was carried out using an acrylic column, as shown in Fig. 7. The specimen was compacted into a cylindrical acrylic cell with an inner diameter of 110 mm and a height of 100 mm. The target dry density of the specimen (Dc) was set

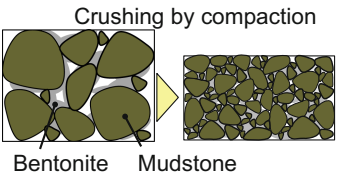

Fig. 6. Schematic view of grain crushed mechanism

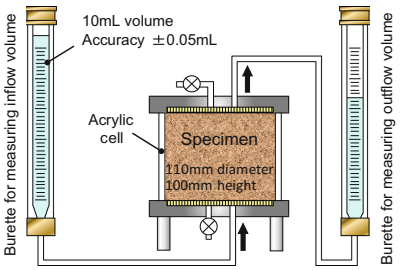

Fig. 7. Schematic view of permeability tester

at 95% based on the degree of compaction on the wet side, as provided by the soil compaction test. The specimens were saturated under back pressure conditions, and saturation of the specimen was assumed to have occurred once the inflow/outflow water volume and the change in unsteady hydraulic conductivity had stabilized.

Figure 8 summarizes the relationship between the hydraulic conductivity and the effective clay density. For each base material, the hydraulic conductivity tended to decrease with increasing effective clay density. When granite was used as the base material, $k = 10^{-10}$ m/s or less at Bt = 5% and 10^{-11} m/s at Bt = 10%. When mudstone was used as the base material, $k = 10^{-11}$ m/s at Bt = 5% and 10^{-12} m/s at Bt = 10%. Since the mudstone showed a lower hydraulic conductivity than did the granite and Inagi sand, the crushing effect due to compaction was believed to affect the development of the hydraulic conductivity. The soil–bentonite mixture with mudstone as the base material had a double structure, which was composed of microscopic gaps constituting the pores in the base material and macroscopic gaps between the grains of the base material. The latter was considered to affect the swelling deformation of the bentonite. It was assumed that the decrease in the permeability of the mudstone was more distinctive than that of either the granite or Inagi sand because of the synergistic effect of the increased specific surface area (due to grain crushing of the mudstone) and pore filling (associated with the swelling of montmorillonite contained in the mudstone). When the Bt = 15% or less, the influence of grain size and the swelling behaviour of the base material on the hydraulic conductivity of the soil–bentonite mixture was marked [6]. Therefore, both the bentonite mixing ratio and the grain size distribution and swelling characteristics of the base material should not be neglected.

5 Investigation of the Influence of Constituent Minerals

The results of the X-ray diffraction analysis of the mudstone used in this study are shown in Fig. 9. Quartz was the main constituent, with smectite and kaolin confirmed as the clay minerals. Furthermore, as shown in the results of the X-ray diffraction analysis of the sample treated with ethylene glycol, the peak shifted to a smaller angle, indicating the presence of smectite. The smectite content of the mudstone was 3.6 wt%. As shown in the results of previous studies, if the content of swellable clay minerals

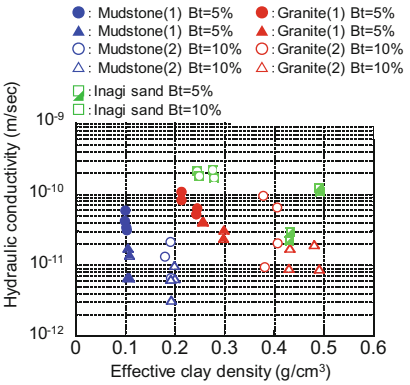

Fig. 8. Relationship between permeability and effective clay density

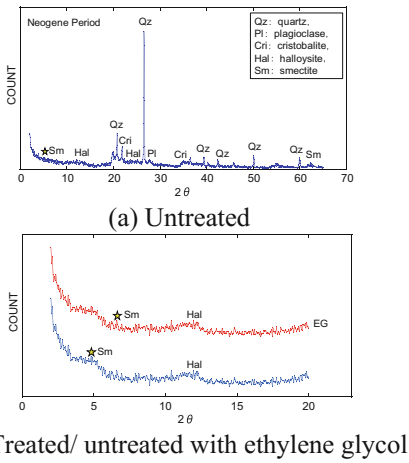

Fig. 9. X-ray diffractometer

such as smectite is 1.5 wt% or more, slaking occurs [7]. Therefore, the water sealing effect was presumably a result of the swelling of the base material itself. This hydraulic conductivity resulted in similar hydraulic conductivity obtained for the mudstone mixed at Bt = 5% and the Inagi sand mixed at Bt = 10%. In addition, the mudstone used in this study exhibited high friability. As the specific surface area was increased by grain crushing, the characteristics of the constituent swelling clay minerals were much more evident; therefore, sealing capability was developed in the fractured zone.

6 Conclusions

The findings of this study are summarised as follows.

(1) Improvement of the grain size distribution due to grain crushing during compaction was confirmed for the mudstone.
(2) The granite, mudstone and Inagi sand exhibited decreases in permeability with increasing effective clay density. The mudstone, in particular, exhibited a more significant decrease in permeability compared with the other two base materials. This was presumably due to an increase in specific surface area resulting from grain crushing and pore filling effects associated with the swelling behaviour of rock-forming minerals.
(3) The bentonite mixture consisting of mudstone with 5% bentonite exhibited low hydraulic conductivity. The mudstone in this study was estimated to contain 3.6wt % smectite. The content of smectite affects the low hydraulic conductivity because the base material swells by itself. However, when determining the bentonite mixing ratio, it is necessary to consider the manufacturing and construction methods used for the material, such as the mixing method and thickness of the soil–bentonite mixture, in order to ensure homogeneity of the soil–bentonite mixture.

The results of this study demonstrated the fundamental properties of friable sedimentary rock in relation to the development of an effective seal via the rolling compaction method. Therefore, the development of a construction technique that simply crushes excavated sedimentary rock appears possible. Utilisation of the friability characteristics of excavated sedimentary rock (without requiring grain size adjustment) when constructing a hydraulic barrier is expected to greatly lower construction costs.

References

1. Ordinance of the Prime Minister's Office and the Ministry of Welfare, Engineering Standards Pertaining to the Final Disposal Site for Municipal Solid Wastes and Final Disposal Site for Industrial Waste, Ordinance of the Ministry of the Environment No. 3
2. Komine H (2004) Simplified evaluation on hydraulic conductivities of sand-bentonite mixture backfill. Appl Clay Sci 26:13–19
3. Japanese Geotechnical Society Standards (2009) Laboratory Testing Standards of Geomaterials, vol 2
4. NEXCO (2006) Laboratory Testing of NEXCO, pp 20–22
5. Hareyuki Y, Ichirou K, Makoto F (1990) Compaction properties of crushed mudstone product by slaking
6. Ogata N, Komine H (1993) The relationship between permeability characteristics and aggregate and soil-bentonite mixtures, annual meeting of Japan Society of Civil Engineering, pp 1080–1081
7. Haruo H (2008) Clay Mineralogy-Basic of Clay Science. Asakura Publishing Corporation

Dissolved CO_2 Injection to Eliminate the Risk of CO_2 Leakage in Geologic Carbon Storage

Victor Vilarrasa[1,2(✉)], Maria Poo[1,2], Silvia De Simone[1,2,3], and Jesus Carrera[1,2]

[1] Institute of Environmental Assessment and Water Research, Spanish National Research Council (IDAEA-CSIC), Jordi Girona 18-26, 08034 Barcelona, Spain
victor.vilarrasa@idaea.csic.es

[2] Associated Unit: Hydrogeology Group (UPC-CSIC), Jordi Girona 1-3, 08034 Barcelona, Spain

[3] Department of Earth Science and Engineering, South Kensington Campus, Imperial College, London, UK

Abstract. Geologic carbon storage is usually viewed as injecting, or rather as storing, CO_2 in supercritical phase. This view is very demanding on the caprock, which must display: (1) high entry pressure to prevent an upward escape of CO_2 due to density effects; (2) low permeability to minimize the upwards displacement of the brine induced by the injected CO_2; and (3) high strength to ensure that the fluid pressure buildup does not lead to caprock failure. We analyze the possibility of injecting dissolved CO_2 and, possibly, other soluble gases for cases when the above requirements are not met. The approach consists of extracting saline water from one portion of the aquifer, reinjecting it in another portion of the aquifer and dissolving CO_2 downhole. Mixing at depth reduces the pressure required for brine and CO_2 injection at the surface. We find that dissolved CO_2 injection is feasible and eliminates the risk of CO_2 leakage because brine with dissolved CO_2 is denser than brine without dissolved CO_2 and thus, it sinks towards the bottom of the saline aquifer.

Keywords: CO_2 storage · Dissolved CO_2 · Leakage · Caprock Buoyancy

1 Introduction

Geologic carbon storage is usually considered as injecting CO_2 in free phase under supercritical or liquid (cold) conditions, which will eventually become supercritical under pressure and temperature reservoir conditions (Vilarrasa et al. 2013). This injection scheme leads to a CO_2-rich phase which floats on resident brine. Thus, CO_2 remains in the upper portion of the saline formation, which may lead to leakage across the caprock. While the concept is robust and simple, its application is hindered by two sets of difficulties (Fig. 1):

(1) Large volumes of CO_2, in the order of millions of tons per year, will have to be injected for industrial scale geologic carbon storage projects. Such injections will displace the resident brine, possibly polluting shallow drinking water aquifers

© Springer Nature Singapore Pte Ltd. 2019
L. Zhan et al. (Eds.): ICEG 2018, ESE, pp. 89–96, 2019.
https://doi.org/10.1007/978-981-13-2227-3_11

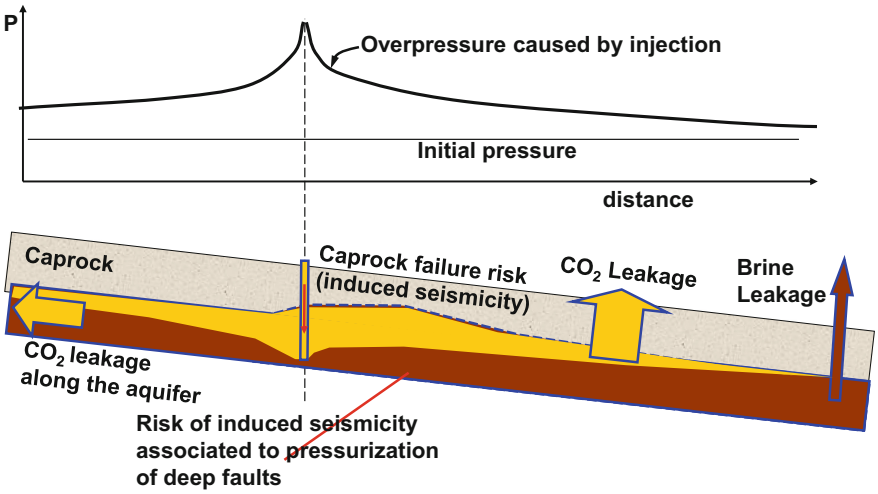

Fig. 1. Schematic representation of supercritical CO_2 storage and some of the difficulties it must overcome. Note that overpressure (above) can be large and extend over a large area, thus risking caprock sealing capacity and the occurrence of felt induced seismicity

(Birkholzer and Zhou 2009; Birkholzer et al. 2012). Additionally, a large pressure buildup will be generated, which may reactivate fractures or faults, potentially inducing felt earthquakes (Zoback and Gorelick 2012; Vilarrasa and Carrera, 2015),

(2) Supercritical CO_2 is lighter than the resident brine, so it may leak upwards along sloping aquifers, across the caprock, through faults or wells (Lindeberg 1997; Pruess 2008; Nordbotten et al. 2009; Humez et al. 2011).

These difficulties have motivated approaches for fluid pressure control. The main idea behind these approaches consists in pumping native brine from the storage formation where CO_2 will be injected. The pumped brine can be disposed of (e.g., in sites close to the sea), or desalinated (e.g., in water scarce regions) and the residual brine reinjected into a saline formation (Court et al. 2011; Bergmo et al. 2011). This concept includes approaches such as the "Active CO_2 Reservoir Management" (Buscheck et al. 2011, 2012) or the "Passive injection" strategy (Dempsey et al. 2014). These approaches increase CO_2 storage capacity and reduce the induced pressure buildup and associated risks. Nonetheless, the risk of leakage persists with these two storage strategies because the injected CO_2 is still buoyant and thus, stays at the top of the storage formation.

To overcome this issue, CO_2 can be injected dissolved into the brine. Dissolved CO_2 injection can be regarded as a special case of pressure control. By injecting CO_2 dissolved in the pumped brine, the risk of buoyant escape of CO_2 is eliminated. This is because the density of CO_2-rich brine is higher than that of resident brine and thus, the injected CO_2-rich brine will tend to sink towards the bottom of the storage formation (Fig. 2).

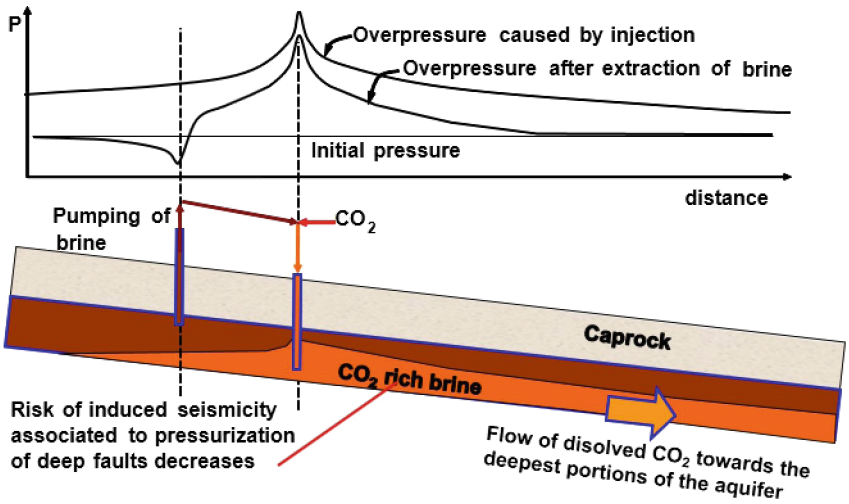

Fig. 2. Schematic representation of the dissolved CO_2 concept. Brine is pumped from the storage formation and reinjected after dissolving CO_2 in it. Note that both maximum pressure buildup and the area affected by overpressure are significantly reduced. Note also that the concept can be extended to other flue gases (Carrera et al. 2011)

It may be argued that CO_2 will dissolve naturally in the aquifer without the need of engineered actions. However, dissolving the whole CO_2 plume may require centuries. Actually, dissolution rates are slow for relatively low permeability media and only becomes quite fast in porous media with a high vertical permeability once convection develops under the CO_2 plume (Riaz et al. 2006; Hidalgo and Carrera, 2009; Pau et al. 2010; MacMinn et al. 2012; Elenius and Johannsen 2012). Even though CO_2 dissolution can be accelerated by fluctuating the injection rate (Bolster et al. 2009) and/or by alternating CO_2 and brine injection either in the well or at some distance (Leonenko and Keith, 2008; Hassanzadeh et al. 2008; Zhang and Agarwal 2012), some of the injected CO_2 will continue in free-phase.

The goal of this paper is to present the dynamics of a dipole system in which brine is pumped from one well and brine with dissolved CO_2 is injected in the other well. We aim to assess the feasibility of dissolved CO_2 injection as an effective storage strategy. We also investigate the effects of this storage approach on the rock geomechanical stability.

2 Dynamics of the Dipole System

The dynamics of a dipole system of dissolved CO_2 injection and brine pumping is non-trivial. The injected CO_2-rich brine is denser than the resident brine and, as a result, it tends to sink. However, this sinking tendency of CO_2-rich brine is counterbalanced by the high pressure at the injection well and by the drag generated by the pumping well. Consequently, part of the injected CO_2 may be pumped and returned to the surface,

which reduces the efficiency of the system. The critical pumping rate, Q_c [$L^3\ T^{-1}$], can be defined as the maximum flow rate that can be pumped with negligible CO_2 concentration (0.1% of saturation) (Pool et al. 2013).

To understand the system dynamics and thus, being able to optimize its design, we consider a homogeneous sloping aquifer of constant thickness b [L] and slope m [–] (Fig. 3). The dipole system consists of an injection-pumping well pair. A fully penetrating pumping well pumps brine from the storage formation at a constant flow rate, Q_p [$L^3\ T^{-1}$]. The pumped brine, CO_2 and, possibly other gases, are injected separately at the injection well, which is located at a distance d [L] downslope, and mixed downhole. The resulting CO_2-saturated brine is denser than the native brine, leading to a safe storage in which the CO_2-saturated brine will sink to the bottom of the storage formation.

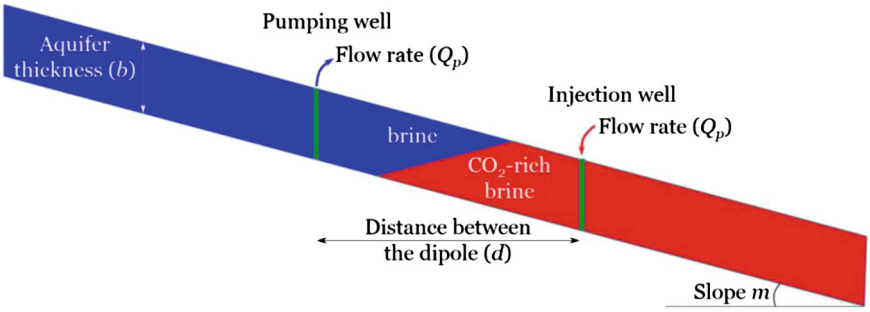

Fig. 3. Model set-up for the analysis of dissolved CO_2 injection in a dipole system in which brine is pumped and reinjected with CO_2 in the same saline formation through vertical wells in a sloping homogeneous aquifer

To illustrate the dynamics of the system, we show the case of a confined saline aquifer, with 20% slope, at a depth ranging from 1000 to 1800 m. The aquifer is assumed homogeneous and isotropic. The extent of the model is 4000 × 1000 × 50 m^3 and the distance between the fully penetrating injection-pumping well pair is 500 m. Water viscosity, μ [$M\ L^{-1}\ T^{-1}$], is assumed to be constant and equal to 0.4 mPa·s. The buoyancy factor is taken as $\varepsilon = 0.027$ ($\varepsilon = (\rho_s - \rho_b)/\rho_b$, where ρ_s [$M\ L^{-3}$] is the density of CO_2 saturated brine and ρ_b [$M\ L^{-3}$] is the density of resident brine).

Simulation results show that the movement of the injected CO_2-saturated brine plume is governed by two factors: (1) viscous forces induced by the pumping-injecting wells which produce a dipole flow field, and (2) buoyancy forces caused by the difference between the density of the injected CO_2-saturated brine and that of the resident brine. Buoyancy, f_b [$M\ L^{-2}\ T^{-2}$], is quantified by (Pool et al. 2013)

$$f_b = V' \Delta \rho m g \tag{1}$$

where V' [L^3 L^{-3}] is the dimensionless injected volume, which is given by $V' = Q_p t/(\pi d^2 b)$, t [T] is time, g is gravity [L T^{-2}] and $\Delta\rho = \rho_s - \rho_b$ Viscous forces, f_v [M L^{-2} T^{-2}], are given by (Pool et al. 2013)

$$f_v = \frac{Q_p \mu}{2\pi d b k} \tag{2}$$

where k [L^2] is the intrinsic permeability. While buoyancy forces grow with the plume size because they depend on the injected volume V', viscous forces remain constant over time. This difference explains the time dependent role of density. During the initial stage (Fig. 4a), viscous forces mainly control flow and transport and thus, CO_2-saturated brine migrates radially from the injection well and towards the pumping well. Similar effects would be obtained assuming constant density. Once the CO_2-saturated brine plume reaches the pumping well, CO_2 concentration in the pumping well rises gradually until an equilibrium between upslope forces caused by the pumping well and downslope forces driven by buoyancy effects is attained (Fig. 4b). At this instant of time (t_d [T]), the CO_2 mass fraction at the pumping well reaches its maximum. Afterwards, density-driven flow leads to a growth of the plume downslope along the bottom of the aquifer because buoyancy forces increase and start to dominate over viscous forces. As a result, the extent and weight of the plume rise, pulling the plume downslope. This pull retreats the CO_2-saturated brine plume towards the injection well, which leads to a decrease in the CO_2 mass fraction at the pumping well (Fig. 4c). Finally, steady state is reached (Fig. 4d). It should be highlighted that the first arrival decreases with the pumping rate, but the peak time remains constant, which is surprising and requires further analysis.

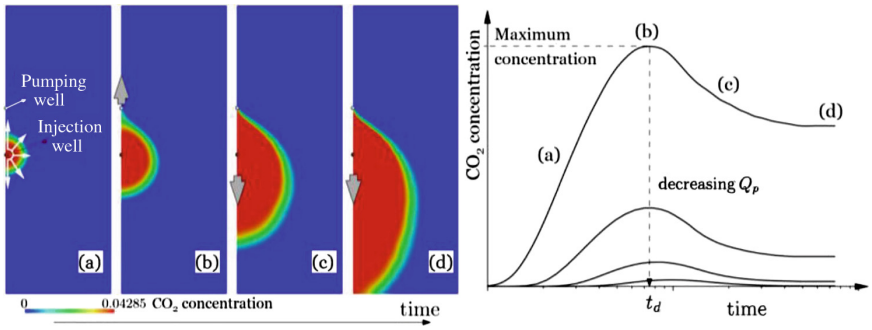

Fig. 4. The four stages (a-d) of dissolved CO_2 injection in a sloping aquifer: left, plan view of vertically averaged concentration; right, time evolution of CO_2 concentration at the pumping well (modified from Pool et al. 2013)

The first arrival time of the CO_2, which is controlled by the dipole nature of the flow field, can be computed by integrating the travel time along the flow line between the two wells, giving (Grove and Beetem 1971)

$$t_0 = \frac{\pi \phi b d^2}{3 Q_p} \tag{1.3}$$

where ϕ[L^3 L^{-3}] is porosity. This implies that the first arrival depends on the distance between the two wells, the aquifer thickness and the pumping rate. However, it is independent of the aquifer permeability. On the other hand, the time for which the CO_2 mass fraction at the pumping well peaks (t_d) is controlled by the balance between buoyancy and viscous forces. Since both are proportional to Q_p and inversely proportional to b, t_d becomes independent of both the flow rate and aquifer thickness. But t_d is affected by the aquifer slope and the aquifer permeability. On the one hand, an increase in the aquifer slope causes f_b to increase and thus, the time to balance viscous forces decreases. On the other hand, a decrease in permeability leads to an increase in f_v, which increases the time to reach equilibrium.

The response of the system is also affected by the well characteristics, i.e., vertical or horizontal, because pressure buildup evolution differs when injecting through horizontal and vertical wells. CO_2 injection induces a smaller overpressure when injecting through vertical than horizontal wells (Zhang and Agarwal 2012; Vilarrasa 2014). In contrast, it is the other way around for water injection (Zhang and Agarwal 2012). For CO_2 injection through a vertical well, pressure buildup peaks at the beginning of injection, but subsequently drops (Vilarrasa et al. 2016). However, pressure builds up continuously when injecting CO_2 through a horizontal well, which induces a higher pressure buildup in the long term (Zhang and Agarwal 2012). In contrast, water injection leads to higher pressure buildup when injecting through a vertical than a horizontal well. As a result, caprock and fault stability may be compromised. Even though caprock integrity is not a concern when injecting CO_2 dissolved in brine because it sinks, fault stability may be an issue because of potential felt induced seismicity (De Simone et al. 2017). Thus, horizontal wells are preferable for injection of CO_2-rich brine.

3 Conclusions

We have shown that dissolved CO_2 injection is feasible to store CO_2 in deep saline formations. This CO_2 storage concept displays a number of advantages over conventional supercritical CO_2 storage. First, it is easy to control and generates little overpressure, which reduces (virtually eliminates) induced seismicity risk. Second, since CO_2-rich brine is denser than native brine, CO_2 tends to sink towards the deepest portions of the storage formation, reducing (virtually eliminating) the risk of CO_2 leakage. Last but not least, for the same reason, there is no need for a caprock.

Acknowledgments. The authors acknowledge financial support from the "TRUST" project (European Community's Seventh Framework Programme FP7/2007-2013 under grant agreement n 309607) and from "FracRisk" project (European Community's Horizon 2020 Framework Programme H2020-EU.3.3.2.3 under grant agreement n 636811).

References

Bergmo P, Grimstad A, Lindeberg E (2011) Simultaneous CO_2 injection and water production to optimise aquifer storage capacity. Int J Greenhouse Gas Control 5(3):555–564

Birkholzer JT, Zhou Q (2009) Basin-scale hydrogeologic impacts of CO_2 storage: capacity and regulatory implications. Int J Greenhouse Gas Control 3:745–756

Birkholzer J, Cihan A, Zhou Q (2012) Impact-driven pressure management via targeted brine extraction– conceptual studies of CO_2 storage in saline formations. Int J Greenhouse Gas Control 7:168–180

Bolster D, Dentz M, Carrera J (2009) Effective two phase flow in heterogeneous media under temporal pressure fluctuations. Water Resour Res 45. https://doi.org/10.1029/2008WR007460

Buscheck TA, Sun Y, Hao Y, Wolery TJ, Bourcier W, Tompson AF et al (2011) Combining brine extraction, desalination, and residual-brine reinjection with CO_2 storage in saline formations: implications for pressure management, capacity, and risk mitigation. Energy Proced. 4:4283–4290

Buscheck A, Sun Y, Chen M, Hao Y, Wolery TJ, Bourcier W et al (2012) Active CO_2 reservoir management for carbon storage: analysis of operational strategies to relieve pressure buildup and improve injectivity. Int J Greenhouse Gas Control 6:230–245

Carrera J, Silva O, Ayora C (2011) Method and system for the storage of soluble gases in permeable geological formations. European patent application; N EP11382321.5

Court B, Celia MA, Nordbotten JN, Elliot TR (2011) Active and integrated management of water resources throughout CO_2 capture and sequestration operations. In: 10^{th} International conference on greenhouse gas control technologies GHGT-10, Energy Procedia, p 4:4221–4229

Dempsey D, Kelkar S, Pawar R (2014) Passive injection: a strategy for mitigating reservoir pressurization, induced seismicity and brine migration in geologic CO_2 storage. Int J Greenhouse Gas Control 28:96–113

De Simone S, Carrera J, Vilarrasa V (2017) Superposition approach to understand triggering mechanisms of post-injection induced seismicity. Geothermics 70:85–97

Elenius MT, Johannsen K (2012) On the time scales of nonlinear instability in miscible displacement porous media flow. Comput Geosci 16(4):901–911

Grove DB, Beetem WA (1971) Porosity and dispersion constant calculations for a fractured carbonate aquifer using 2 well tracer method. Water Resour Res 7(1):128–134

Hassanzadeh H, Pooladi-Darvish M, Keith D (2008) Accelerating CO_2 dissolution in saline aquifers for geological storage - mechanistic and sensitivity studies. Energy Fuels 23:3328–3336

Hidalgo J, Carrera J (2009) Effect of dispersion on the onset of convection during CO_2 sequestration. J Fluid Mech 640:443–454

Humez P, Audigane P, Lions J, Chiaberge C, Bellenfant G (2011) Modeling of CO_2 leakage up through an abandoned well from deep saline aquifer to shallow fresh groundwaters. Transp Porous Media 90:153–181

Leonenko Y, Keith D (2008) Reservoir engineering to accelerate the dissolution of CO_2 stored in aquifers. Environ Sci Technol 42:2742–2747

Lindeberg E (1997) Escape of CO_2 from aquifers. Energy Convers Manag 38:S235–S240

MacMinn C, Neufeld J, Hesse MA, Huppert H (2012) Spreading and convective dissolution of carbon dioxide in vertically confined horizontal aquifers. Water Resour Res 48. https://doi.org/10.1029/2012WR012286

Nordbotten J, Kavetski DC, Celia MA, Bachu S (2009) A semi-analytical model estimating leakage associated with CO2 storage in large-scale multi-layered geological systems with multiple leaky wells. Environ Sci Technol 43(3):743–749

Pau G, Bell J, Pruess K, Almgren A, Lijewski M, Zhang K (2010) High resolution simulation and characterization of density-driven flow in CO_2 storage in saline aquifers. Adv Water Resour 33(4):443–455

Pool M, Carrera J, Vilarrasa V, Silva O, Ayora C (2013) Dynamics and design of systems for geological storage of dissolved CO_2. Adv Water Resour 62:533–542

Pruess K (2008) Leakage of CO_2 from geologic storage: role of secondary accumulation at shallow depth. Int J Greenhouse Gas Control 2:37–46

Riaz A, Hesse MA, Tchelepi HA, Orr JF (2006) Onset of convection in a gravitationally unstable diffusive boundary layer in porous media. J Fluid Mech 548:87–111

Vilarrasa V, Silva O, Carrera J, Olivella S (2013) Liquid CO_2 injection for geological storage in deep saline aquifers. Int J Greenhouse Gas Control 14:84–96

Vilarrasa V (2014) Impact of CO_2 injection through horizontal and vertical wells on the caprock mechanical stability. Int J Rock Mech Min Sci 66:151–159

Vilarrasa V, Carrera J (2015) Geologic carbon storage is unlikely to trigger large earthquakes and reactivate faults through which CO_2 could leak. Proc National Acad Sci 112(19):5938–5943

Vilarrasa V, Carrera J, Olivella S (2016) Two-phase flow effects on the CO_2 injection pressure evolution and implications for the caprock geomechanical stability. In: E3S Web of conferences, vol 9. EDP Sciences, p 04007

Zhang Z, Agarwal R (2012) Numerical simulation and optimization of CO_2 sequestration in saline aquifers for vertical and horizontal well injection. Comput Geosci 16:891–899

Zoback MD, Gorelick SM (2012) Earthquake triggering and large-scale geologic storage of carbon dioxide. Proc National Acad Sci 109(26):10164–10168

Evaluating Influence of Cementation in Bentonite Buffer Material Based on the Swelling Properties of Bentonite Ore

D. Ito(✉), H. Komine, S. Morodome, T. Sekiguchi, and G. Miura

Department of Civil and Environmental Engineering, Waseda University, #203, Building 58, 3-4-1, Okubo, Shinjuku-Ku, Tokyo 169-8555, Japan
daichi_ito@akane.waseda.jp

Abstract. In geological disposal of high level radioactive waste, it is essential to start considering consolidation accompanying cementation, taking into consideration high earth pressure and solution of groundwater. For engineering application of natural analogue, the authors thought consolidated buffer material will have similar physical properties to bentonite ore. In this study, we aimed to quantitatively evaluate the influence of cementation on swelling properties. In order to achieve this aim, we focused on swelling pressure and swelling strain of bentonite, using two kinds of bentonite ore whose generation dates are different respectively. As a result, swelling pressure was decreased by approximately one order of magnitude due to the influence of cementation. In addition, the swelling strain of younger bentonite ore did not decline, but those of older bentonite ore declined about half of original whether consolidation was retained or not. Therefore, there is a possibility that the swelling deformation of buffer will decline as cementation gets stronger over the course of time.

Keywords: Bentonite · Swelling · Cementation · Radioactive waste
Long-term alteration

1 Background

After the accident of the Fukushima Daiichi Nuclear Power Station caused by the 2011 off the Pacific coast of Tohoku Earthquake, Japanese people's concern of radioactive waste disposal is rising. Consequently, the safety of geological disposal should be explained to get Japanese public's approval. For this purpose, it is necessary to establish a design specification of bentonite-based buffer material. In Japan, bentonite-based buffer is required for eleven functions, such as low water permeation and inhibition of transfer of radionuclide. Therefore, it is important to accurately find physical characteristics of bentonite.

Since sufficient decline in radioactivity of radioactive waste requires tens of thousands of years, it is necessary to reflect long-term alteration of bentonite in buffer material design. Taking into consideration high earth pressure due to depth of the underground facility and solution of salinity from sea water into groundwater, it is essential to start considering consolidation accompanying cementation. Figure 1 shows the concept of occurring cementation in the bentonite-based buffer material of

© Springer Nature Singapore Pte Ltd. 2019
L. Zhan et al. (Eds.): ICEG 2018, ESE, pp. 97–104, 2019.
https://doi.org/10.1007/978-981-13-2227-3_12

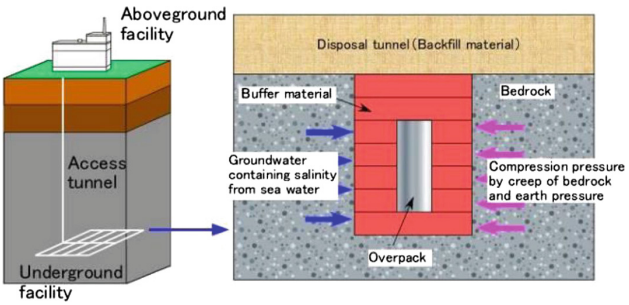

Fig. 1. The concept of occurring cementation in the bentonite-based buffer material of geological disposal

geological disposal. In this matter, there is a possibility to change the swelling properties of bentonite. It is difficult to reproduce long-term consolidation of buffer by only laboratory experiments. Some studies targeted natural bentonite placed deep underground for evaluating the long-term stability and alteration of smectite (cf. Pusch 1983). Therefore, for engineering application of natural analogue, the authors hypothesized consolidated buffer material will have similar physical properties to bentonite ore, which has been formed by sequential consolidation in natural ground. In this study, we aimed to quantitatively evaluate the influence of cementation on the swelling properties such as swelling pressure and swelling deformation of bentonite.

2 Swelling Properties of Bentonite Ore Samples

2.1 Sample Used in This Study and Method of Making Specimens

We used the ore samples of sodium bentonite mined from Japan and China. Japanese bentonite ore was mined from the Tsukinuno Clay Mine (Kunigel V1, Kunimine Industries), and Chinese ore was mined from the Liufangi Clay Mine (Jilin). Figure 2 shows the appearances of Japanese and Chinese bentonite ore. The generation age of Japanese ore is about 10 million years, and the Chinese ore is about 150 million years ago. Both bentonite ore were mined from depth of about 200–250 m. Table 1 also shows the fundamental properties of ore sample used in this study. The montmorillonite content was calculated from the MB adsorption amount test results assuming that the pure montmorillonite content was 140 mmol/100 g.

In this study, undisturbed specimens retaining the consolidation of ore and reconstituted specimens where consolidation were removed, were prepared by the following method. Undisturbed specimens were prepared using a trimming tool such as cutter ring to have a cylindrical shape. On the other hand, when making the reconstituted specimens, powdered sample obtained by pulverizing the ore was sieved through a 0.425 mm sieve, and a static load was applied to the powder sample until the dry density reached the same degree as that of the undisturbed specimen. Also, diameter of specimens which were used for measuring swelling pressure of Japanese

Fig. 2. The appearances of Japanese (left) and Chinese (right) bentonite ore

Table 1. Fundamental properties of bentonite ore samples

	Japanese ore (29–1)	Japanese ore (29–2)	Japanese ore (29–3)	Chinese ore
Particle density (Mg/m^3)	2.77	2.77	2.80	2.73
Liquid limit (%)	419.1	438.5	431.6	541.6
Plastic limit (%)	29.2	28.0	26.8	35.6
Plasticity index	389.9	410.5	404.8	506.0
Content of montmorillonite (%)	44.7	38.6	51.4	51.1
Swelling power (ml/2 g)	12	11	12	13

ore was 60 mm and diameter of the other specimens was 28 mm, and height of all specimens was 10 mm.

2.2 Experimental Method

In this study, swelling pressure and one-dimensional swelling deformation ratio were measured as physical properties related to the swelling property of bentonite.

Figure 3 shows the swelling pressure measurement apparatus. In this experiment, the swelling pressure is regarded as required pressure for suppressing swelling deformation of bentonite when water is supplied. The deformation toward the horizontal direction is constrained by SUS316L ring, and the deformation in the vertical direction is suppressed by tightening the clamp knob. For the swelling pressure measurement, a load cell with a maximum capacity of 50 kN and a minimum scale of 0.012 kN was used. The vertical pressure applied to the specimen was about 70 kPa. Since displacement in the vertical direction cannot be completely suppressed, a change in dry density due to swelling deformation occurs. Therefore, the displacement was measured with a displacement meter with a maximum capacity of 25 mm and a minimum scale of 0.002 mm, and the dry density was corrected using Eq. (1).

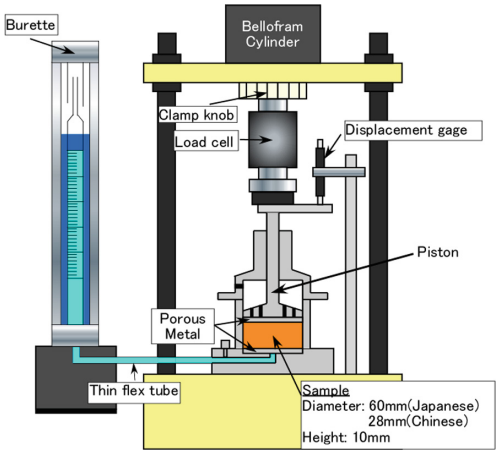

Fig. 3. The swelling pressure measurement apparatus

$$\rho_d = \frac{m}{A(H_0 + \Delta d)} \times 1000 \tag{1}$$

Where, d(Mg/m^3) is dry density correction value,
m(g) is dry mass of specimen,
A(mm^2) is sectional area of specimen,
H_0(mm) is initial specimen height,
Δd(mm) is the amount of swelling deformation.

Figure 4 shows the experimental apparatus for measuring the one-dimensional swelling strain. This experiment does not suppress the swelling in the vertical direction of the specimen and measures the amount of swelling deformation using a displacement gauge. The displacement gauge used for measuring deformation was same as the swelling pressure measurement apparatus. Lead balls were put in a polypropylene container so that the loading pressure would be 19.6 kPa. The one-dimensional swelling strain, which is the ratio of the swelling deformation amount to the initial height of the specimen, was used for the purpose of organizing the results, calculated by Eq. (2). In addition, we approximated the temporal change curve of the swelling strain with the hyperbolic curve expressed by the Eq. (3) and found the asymptotic line from the Eq. (4) to calculate the maximum swelling strain (Komine 1994). The experiment was terminated with the value of the swelling strain being 80% or more of the asymptotic section.

$$\varepsilon_s = \frac{\Delta S}{H_0} \times 100 \tag{2}$$

$$\varepsilon_s(t) = \frac{t}{a + bt}(\%) \tag{3}$$

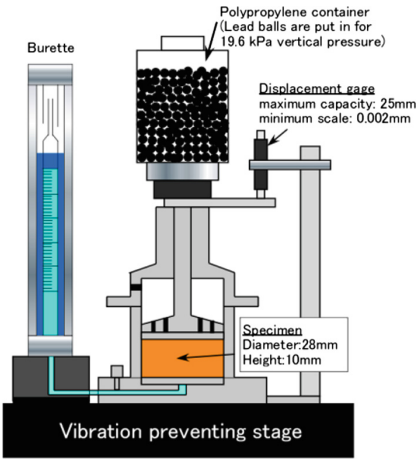

Fig. 4. Experimental apparatus for measuring the one-dimensional swelling strain

$$\varepsilon_{smax} = \lim_{t \to \infty} \varepsilon_s(t) = \frac{1}{b}(\%) \tag{4}$$

Where, $\varepsilon_s(\%)$ is the one-dimensional swelling strain,
ΔS(mm) is swelling deformation amount,
H_0(mm) is initial height of specimen,
t(min) is elapsed time,
a, b are the constants obtained by hyperbolic approximation,
$\varepsilon_{smax}(\%)$ is maximum swelling strain.

2.3 Experimental Results of Swelling Properties of Bentonite Ore

Figure 5 shows the time course of the swelling pressure (hereinafter referred to as Ps) in the undisturbed specimens and the reconstituted specimens in both Japanese and Chinese bentonite ore.

In Japanese ore, Ps of the reconstituted specimen rapidly increased after the start of the test until about 2000 min passed and eventually converged to a constant value. On the other hand, Ps did not rise sharply in the undisturbed specimens, and it tended to gradually rise from the beginning of the test. The maximum Ps in the experimental period was 440 kPa to 2100 kPa in the reconstituted specimens, while it remained at 75 to 150 kPa in the undisturbed specimens.

In Chinese ore, Ps of the undisturbed specimens increased immediately after the start of the test and the maximum Ps was 550 to 2450 kPa. On the other hand, the Ps of the reconstituted specimens continued to rise to about 5000 min, and thereafter it converged to a constant value. The maximum Ps of the reconstituted specimens was 5770 to 6220 kPa. From the above, it is said that the Ps of the undisturbed specimen in both Japanese and Chinese ore remained only about 1/3 to 1/10 of the reconstituted specimen. It is suggested that the swelling pressure of the bentonite buffer material may decrease due to consolidation.

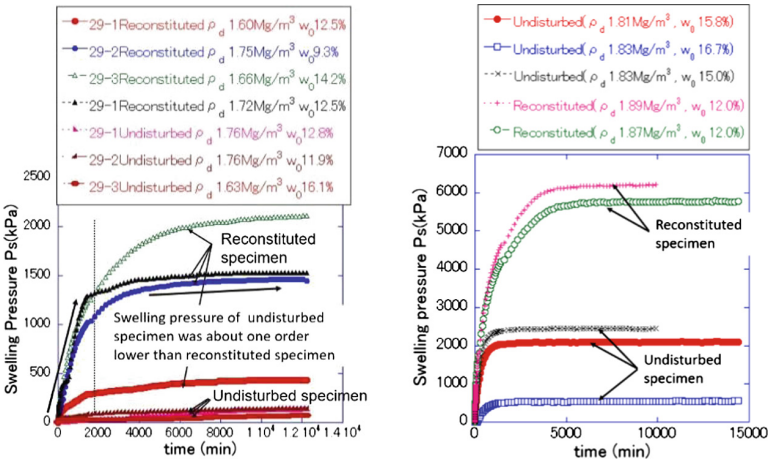

Fig. 5. The time course of the swelling pressure in Japanese (left) and Chinese (right) bentonite ore

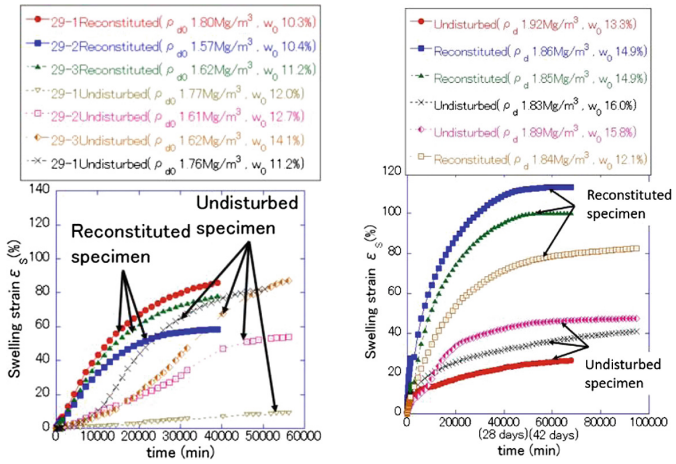

Fig. 6. Temporal change curve of one-dimensional swelling strain of Japanese (left) and Chinese (right) bentonite ore

Figure 6 shows the temporal change curve of the one-dimensional swelling strain (hereinafter referred to as ε_s) of both Japanese and Chinese bentonite ore.

In Japanese ore, ε_s of the reconstituted specimens increased immediately after the start of the test, and it converged to a constant value from about 30,000 min (21 days). ε_s of the undisturbed specimens rose sharply until about 10,000 min (7 days) elapsed. The maximum ε_s was 60 to 98% in reconstituted specimens and 10 to 110% in undisturbed specimens, which was almost the same range. From this, it can be said that

no significant decrease will occur despite the fact that there is a delay due to the consolidation caused by the glue effect in the Japanese ore originating from about 10 million years ago in the onset of the swelling deformation behavior.

In Chinese ore, the ε_s of the reconstituted specimens sharply increased after start, and it took a convergence to a constant value after about 40000 min (28 days) elapsed. On the other hand, in the undisturbed specimens, the increasing gradient of the ε_s after the start of the experiment was smaller than that of the reconstituted specimens, and the ε_s was about one third of that of the reconstituted specimens even after about 60,000 min (42 days). The maximum ε_s was 82 to 122% in the reconstituted specimens and 32 to 47% in the undisturbed test specimen. From the above, due to consolidation strengthening, it can be said that although the swelling deformability decreases, it is maintained to some extent in the Chinese ore originating from about 150 million years ago.

As a cause of the difference in swelling deformation behaviors between Japanese ore and Chinese ore, differences in strength of consolidation due to differences in generation age can be considered. In Japanese ore, although the consolidation power exceeds the swelling of montmorillonite immediately after the start of the experiment, it disappears gradually with the progress of swelling of montmorillonite, and swelling deformation is finally same as the reconstituted specimen. On the other hand, in Chinese ore, it is presumed that swelling deformability declines because the strength of consolidation is stronger than that of the Japanese ore. Therefore, consolidation continues to suppress swelling of montmorillonite due to water absorption. Further, based on the evaluation about microstructure of soil particles using SEM-EDX and mercury porosimeter analyses, we would like to pursue the mechanisms of decrease in swelling properties of the ore due to consolidation.

3 Conclusions

Swelling pressure of undisturbed specimens made of both Japanese and Chinese ores was about one order lower than that of reconstituted specimens by the effect of cementation. It is suggested that swelling pressure of bentonite-based buffer material decreases when being consolidated. The swelling deformation of Japanese ores did not differ much between undisturbed specimens and reconstituted specimens, but those of Chinese ores were different whether consolidation was retained or not. This is because Chinese ores are approximately ten times older than Japanese ores, so soil particles or minerals in Chinese ores are strongly attached to each other. Therefore, there is a possibility that the swelling deformation of buffer will decline as cementation gets stronger over the course of time.

Acknowledgement. This research was conducted with support from 'Waseda University Grants for Special Research Project (Grant B, 2017)'. Also, we got the bentonite ore samples by the support from Dr. M. Ito (Kunimine Industries) and Kunimain Co., Ltd.

References

Ogata N et al (1999) Enterprise technology for high level radioactive waste geological disposal,-volume 4. Des Manufact Proced Eng Barrier- J Nucl Fuel Cycle Environ 5(2):103–121

Pusch R (1983) Stability of deep-sited smectite minerals in crystalline rock – chem1ical aspects-SKBF-KBS TR83-16, p 1

Japan Bentonite Association (1977a) Japan Bentonite association standard, JBAS-107-91

Japan Bentonite Association (1977b) Japan Bentonite association standard, JBAS-104-77

Komine H, Ogata N (1994) Experimental study on swelling characteristics of compacted bentonite. Can Geotech J 31(4):478–490

Evaluation on Hydraulic Conductivity of Heavy Bentonite-Based Slurry for Using on Decommissioning of the Fukushima Daiichi Nuclear Power Station

E. Yoshikawa(✉), H. Komine, and S. Goto

Department of Civil and Environmental Engineering, Waseda University, #203, Building 58, 3-4-1, Okubo, Shinjyuku-ku, Tokyo 169-8555, Japan
e-ma@suou.waseda.jp

Abstract. The 2011 off the Pacific coast of Tohoku earthquake affected Japan, wreaking severe damage to the Nuclear Power Station in Fukushima. Heavy Bentonite-Based Slurry has been examined the use as filling-type water sealing materials in damaged nuclear reactors. This research was conducted to investigate and define the water stopping capabilities of Heavy Bentonite-Based Slurry for controlling the nuclear accidents. In this study, the falling head permeability tests were conducted to quantify it. The results show that the hydraulic conductivity decreased from k = 10^{-8} m/s to k = 10^{-10} m/s with sedimentation of specimens.

Keywords: Hydraulic conductivity · Falling head permeability test
Slurry · Bentonite · Barite

1 Introduction

The 2011 off the Pacific coast of Tohoku earthquake caused a severe accident at Fukushima Daiichi Nuclear Power Station (1F) in Japan. Since the accident, it has been a serious problem that cooling water has been contaminated by radioactive substances and leaked out from some cracks in the damaged nuclear building. In order to prevent diffusion of radioactive substances, it has been necessary to construct a liquid confinement under severe radiation.

Many requirements are placed on the material used to progress decommission 1F promptly and reliably. Historically, in oil well drilling, one of the principal functions performed by the drilling fluid is to form a low permeability filter cake which seals cracks and other openings. In water base muds the solids consist of clays added to provide the necessary viscous and filtration properties, heavy minerals, usually barite, added to increase the slurry's density. Both of high density and high-water content are required the materials to shield gamma ray and neutron beam. Therefore, drilling fluid has a possibility of using as water stopping material with radiation shielding capabilities.

© Springer Nature Singapore Pte Ltd. 2019
L. Zhan et al. (Eds.): ICEG 2018, ESE, pp. 105–112, 2019.
https://doi.org/10.1007/978-981-13-2227-3_13

Heavy Bentonite-Based Slurry, the filling type soil materials, has been developed based on drilling fluid. Its maximum specific gravity is of 2.5 even under more than 50% volumetric water content. Heavy Bentonite-Based Slurry, which consist of sodium-type bentonite suspension added barite powder. Figure 1 shows an image of the damaged nuclear reactor in 1F and the filling material. Some ef- fections of Heavy Bentonite-Based Slurry for filling in the damaged nuclear reactor are shown in Table 1. It is already clear that it has a greater gamma ray shielding capability and almost identical neutron beam shielding capability to those of tap water (Yoshikawa et al. 2017a, b). In this study, the water stopping capabilities of the Heavy Bentonite-Based Slurry was quantitatively evaluated by conducting a falling head permeability test.

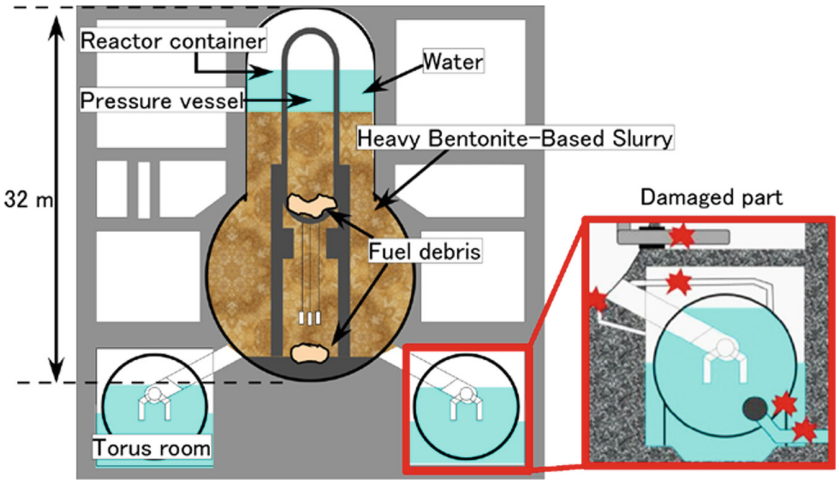

Fig. 1. Image of the nuclear reactor in Fukushima Daiichi NPS and the heavy bentonite-based slurry.

Table 1. Some effections of Heavy Bentonite-Based Slurry for filling in the damaged nuclear reactor.

Characteristics	Use and advantages
Fluidity	Filling construction Medium for removal of debris
Viscosity	Prevention of water leakage
Containment of clay	Adsorption of radioactive materials
High density	Gamma ray shielding
High water content	Neutron beam shielding Prevention of scattering of dust

2 Water Stopping Capabilities of Heavy Bentonite-Based Slurry

2.1 Materials and Experimental Methods

Three types of the slurries were used in this study that the bentonite slurry with specific gravity of 1.1 and two kinds of Heavy Bentonite-Based Slurry, of which specific gravity 1.8 and 2.5. Table 2 shows the composition of these slurries. Heavy Bentonite-Based Slurry is muddy water that consist of sodium-type bentonite for preventing soil particles sedimentation and weighted material, barite powder. Following to Japanese Industrial Standards A 1218: 2009 "Permeability test of soil", falling head permeability test using rigid mold was executed in this study. Since slurries were changed the volume easily by seepage power, transparent acrylic mold was used to measure specimen length L changing with water passage. The initial specimen length, Lo, was10 cm. The quantities of inflow water and outflow water were measured using the apparatus in Fig. 2, and the hydraulic conductivity was calculated using the Eqs. (1.1) and (1.2).

Where kT (m/s) is hydraulic conductivity at T °C,

$$k_T = 2.303 \frac{(a_{in} \times a_{out})L}{(a_{in} + a_{out})A(t_2 - t_1)} \log_{10} \frac{h_1}{h_2} \times \frac{1}{100} \tag{1.1}$$

$$k_{15} = k_T \times \frac{\eta_T}{\eta_{15}} \tag{1.2}$$

L (cm) is the height of the specimen,

ain (cm^2) is the cross sectional area of the burette on the inflow side, $aout$ (cm^2) is the cross sectional area of the burette on the outflow side,

A (cm^2) is cross sectional area of the specimen,

$t2$-ti (s) is measurement time,

hi (cm) is water level difference at time ti,

$h2$ (cm) is water level difference at time $t2$,

$ki5$ is the hydraulic conductivity at 15 °C temperature,

Table 2. Mixing ratio of slurries (to supply 1 m^3).

Name of specimen	Specific gravity p_t/p_w	Tap water (kg)	Barite (kg)	Sodium-bentonite (kg)	Sodium Pyrophosphate (kg)
Bentonite slurry	1.1	980	0	118	2.0
Heavy Bentonite-Based Slurry (1.8)	1.8	719	1007	71.9	1.4
Heavy Bentonite-Based Slurry (2.5)	2.5	493	1972	34.5	0.99

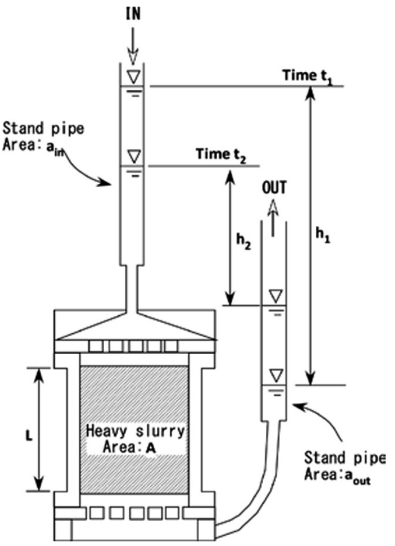

Fig. 2. Device of falling head permeability test.

Vt/*vu* is correction coefficient for calculating permeability coefficient at 15 °C temperature.

2.2 Result Offalling Head Permeability Test

Figure 3 shows decrease in hydraulic conductivity depend on elapsed time. The hydraulic conductivity was defined the value caused by slurry sedimentation in this study. Sedimentation rates of slurries, (Lo − L)/LoX 100, depend on total quantity of water flow (Fig. 4). Immediately after the start of the test, the hydraulic conductivities of the slurries were in the order of 10^{-8} m/s. As shown in Fig. 3, bentonite slurry without addition of barites was more affected by water supply to the inflow-side than

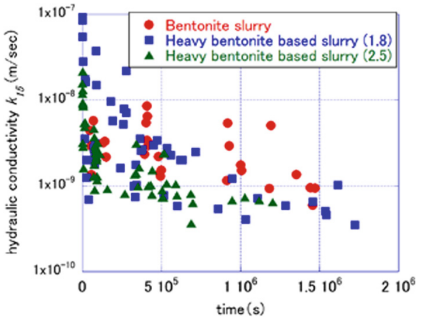

Fig. 3. Time dependant of hydraulic conductivity.

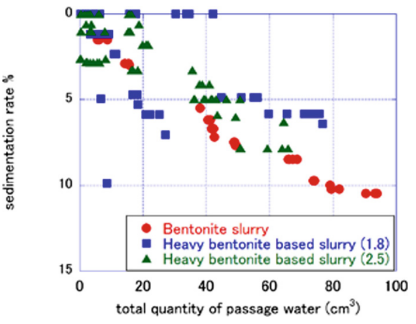

Fig. 4. Relationship between total quantity of passage water and sedimentation rate.

Heavy Bentonite-Based Slurries. It is thought that it took time to reach the steady state because the microstructure of the bentonite part was disturbed due to a sudden change in the dynamic water gradient due to the feed water. On the other hand, the hydraulic conductivity of Heavy Bentonite-Based Slurries gradually dropped into the order of 10^{-10} m/s with elapsed time. Therefore, it was shown that Heavy Bentonite-Based Slurries, that the slurry added barite powder, have more steady water sealing capabilities than pure bentonite slurry. It is conceivable to reduce the pore size with development of filter cake as a main factor of the decreasing in the hydraulic conductivity on time.

As shown in Fig. 4, the specimen length under the test had been decreased with the passage of water. The void ratio e was used as an alternative indicator for the intergranular distance, which related with development of filter cake, in the specimen. Figure 5, 6 and 7 show the relationship between the void ratio and the hydraulic conductivity. As shown in Fig. 5, the hydraulic conductivity of bentonite slurry had almost no influence due to decrease of void ratio. The concentrated bentonite suspension forming gel structure depend on attractive force of van der waals or electric bonds. In bentonite suspension, even if forming internal structure, it is not caused by friction of bentonite particles because they cannot contact each other directly due to diffusion double layer around themselves. Therefore, the gel structure may be weak and each bentonite particles can move easily by some power like seepage force. It is

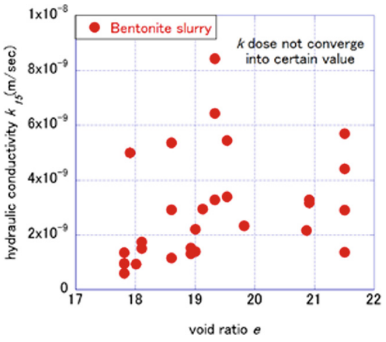

Fig. 5. Relationship between void ratio and hydraulic conductivity (1.1).

considered that the scattering of the hydraulic conductivity of bentonite slurry in Fig. 5 shows destruction of gel structure due to shear stress caused by temporary discontinuity of pressure gradient when supplying water.

From Figs. 6 and 7, Heavy Bentonite-Based Slurries decreased hydraulic conductivity with void ratio reduction due to sedimentation. It is considered that they were under unsteady state when rapid decrease of hydraulic conductivity occurred without change of void ratio. The barite particles seem to promote the decrease of the hydraulic conductivity in the slurry by concentrating bentonite suspension in the interstitial between the barite particles by sedimentation. Figure 8 shows the specimen of Heavy Bentonite-Based Slurry (2.5) after the permeability test. It self-stood because the

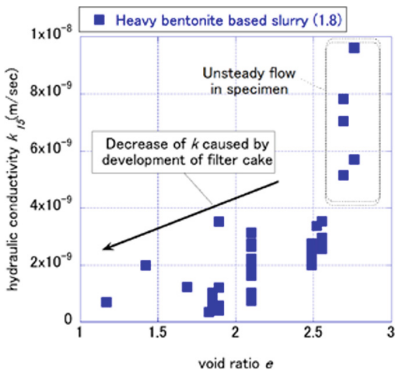

Fig. 6. Relationship between void ratio and hydraulic conductivity (1.8).

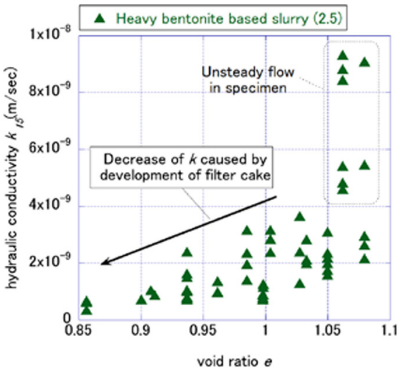

Fig. 7. Relationship between void ratio and hydraulic conductivity (2.5).

Fig. 8. Self-standing of consolidated part (left: with mold, right: without mold)

specimen formed internal structure due to friction among barite particles without separate to each solid material. It is considered that in Heavy Bentonite-Based Slurries, concentrated bentonite part in the frame structure formed by barite may enhance the water sealing capability of the materials. Figure 9 shows an image of mechanism in decrease of hydraulic conductivity on Heavy Bentonite-Based Slurry.

It has some advantages to add barite powder into the slurry as water sealing materials, because Heavy Bentonite-Based Slurries were not caused increasing of hydraulic conductivity by change of water pressure. When it is filled inside the damaged nuclear building in Fukushima Daiichi NPS, sedimentation and development of filter cake are promoted by water pressure of up to 40 m or its own weight, therefore it is expected that the hydraulic conductivity shows lower value.

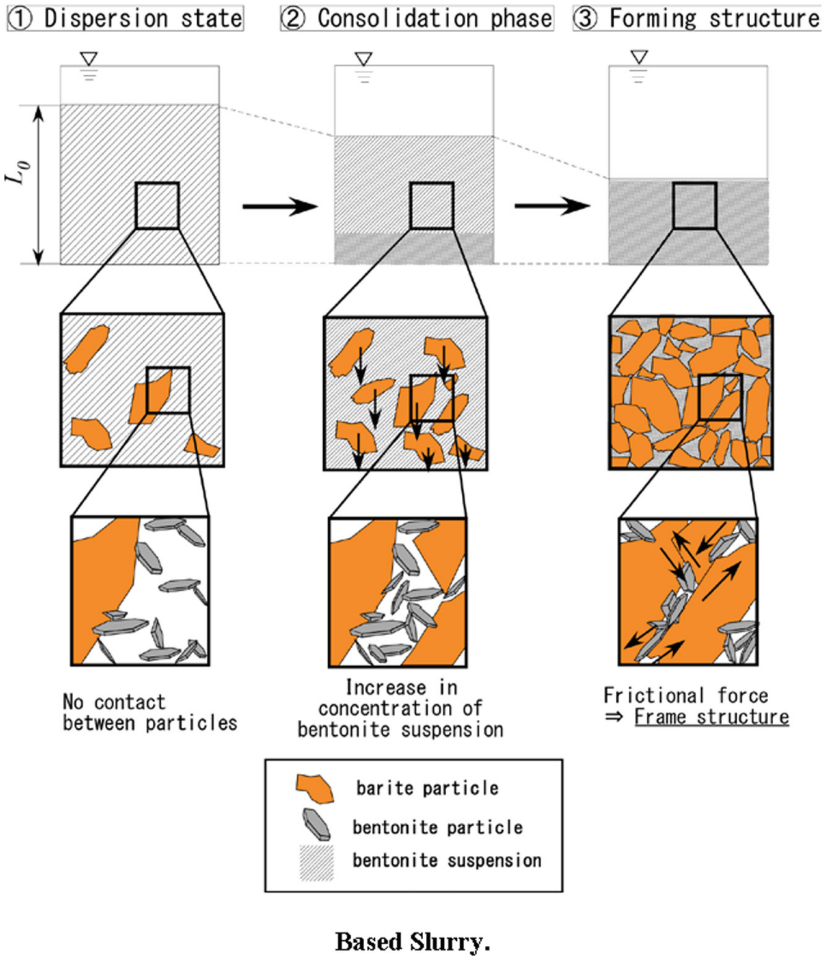

Fig. 9. Mechanism of decrease of hydraulic conductivity on Heavy Bentonite based Slurry.

3 Conclusions

In the permeability test under unrestrained and atmospheric conditions, the hydraulic conductivity of the Heavy Bentonite Based Slurries specific gravity of 1.8 and the specific gravity of 2.5 became 10^{-10} m/s by water passage for 24 h or more. There is a gradual decrease in hydraulic conductivity of Heavy Bentonite-Based Slurries due to a decrease in the void ratio by seepage force. On the other hand, in the bentonite slurry not containing barite powder, decrease in hydraulic conductivity with time cannot be confirmed. According to the test results, with respect to water sealing of bentonite slurry, addition of barite powder may have contributed to promotion of decrease of hydraulic conductivity.

Acknowledgement. This research was conducted with support from 'Human Resource Development and Research Program for Decommissioning of Fukushima Daiichi Nuclear Power Station' by the Japan Ministry of Education, Culture, Sports, Science and Technology.

References

Nuclear Emergency Response Headquarters (2015) Mid-to-Long Term Roadmap (RM) on de commissioning of Fukushima Daiichi Nuclear Power Station

Darley HCH, Grey GR (1988) Composition and Properties of Drilling and Completion Fluids, 5th edn. Gulf Professional Publishing, pp 38–41

Yoshikawa E, Komine H, Goto S et al (2017a) The quantitive evaluation for radiation shielding capabilities of soil materials. J Jpn Soc Civ Eng Ser C (Geosph Eng) 73(4):342–354

Yoshikawa E, Komine H, Goto S et al (2017) The evaluation for radiation shielding ability of the soil materials and application to design for construction. In: 19th ICSMGE, 3479–3482

Goto S et al (2017) Needs for the decommissioning geotechnical engineering for the Fuku shima Daiichi Nuclear power plant. In: 19th ICSMGE, pp 3119–3122

Nishigaki M, Komatsu M, Mikake S et al (2015) Evaluation on application of bentonite slurry grout for excavation disturbed zone in order to recover low permeable rock masses. J Jpn Soc Civ Eng Ser C (Geosph Eng) 806:55–66

Non-isothermal Gas Flow During Carbon Sequestration in Coalbeds

Min Chen(✉), Lee J. Hosking, and Hywel R. Thomas

Geoenvironmental Research Centre,
Cardiff School of Engineering, Cardiff University, Queen's Buildings,
The Parade, Newport Road, Cardiff CF24 3AA, UK
chenm24@cardiff.ac.uk

Abstract. This paper presents a numerical investigation of non-isothermal effects during high pressure carbon dioxide injection in deep coalbeds. Whilst coalbeds provide storage security owing to the large carbon dioxide adsorption capacity of coal, high pressure gas injection may disturb the temperature of the coalbed and influence flow behaviour. A numerical model of coupled heat transfer and gas flow incorporating the Joule-Thomson cooling effect is presented in this paper to study the temperature change induced by carbon dioxide injection. The numerical model is firstly compared with existing results in the literature for verification, and then applied to simulate changes in temperature and pressure of a coalbed during gas flow. Results of predicted temperature and pressure under different injection temperatures show that a zone of cooling occurs when gas injection under the same and low temperature than that of coalbeds, leading to a further drop of pressure in this zone. Although injection under higher temperature can suppress cooling effect, the time for pressure to reach steady state increases.

Keywords: Temperature change · Deep coalbeds · High pressure gas
Joule-Thomson cooling · Heat transfer

1 Introduction

Carbon dioxide (CO_2) sequestration in deep coal seams is a promising option for mitigating anthropogenic CO_2 emissions due to the high sorption capacity of coal | and the opportunity for enhanced coalbed methane recovery (Qu et al. 2017). The flow behaviour in coal seams has been studied extensively (e.g. Wang et al. 2007; Pini et al. 2011). Although the flow is generally non-isothermal, especially for gas flow, most studies assume that the temperature distribution is isothermal, or the temperature change is relatively small and can be neglected (e.g. Fathi and Akkutlu 2014). When gas flows from high pressure to low pressure, the average distance between molecules increases and the potential energy of the gas grows because of intermolecular attraction. Since the expansion process is adiabatic and the total energy remains constant, the increase in potential energy implies a decrease in the kinetic energy and temperature. This phenomenon is known as Joule-Thomas cooling (JTC) (Han et al. 2010; Singh et al. 2011).

© Springer Nature Singapore Pte Ltd. 2019
L. Zhan et al. (Eds.): ICEG 2018, ESE, pp. 113–120, 2019.
https://doi.org/10.1007/978-981-13-2227-3_14

Laboratory experiments and numerical simulations of the JTC effect during CO_2 injection have been performed in recent years (Duru and Horne 2010). For instance, a series of numerical simulations of CO_2 injection into a natural gas reservoir using TOUGH2/EOS7C have been performed by Oldenburg (2007), and the simulation results show that the temperature drop can be over 20 °C under a high injection rate into low permeability reservoirs. However, studies on the thermal response of deep coal seams to CO_2 injection are more limited. Most of studies have focused on the effect of temperature on adsorption and on evolution of the coal permeability (e.g. Krooss et al. 2002; Busch et al. 2004). CO_2 sequestration in coal seams is different from that in conventional reservoirs since adsorption-induced swelling has a significant effect on coal permeability. Nevertheless, the permeability in previous studies of thermal evolution during CO_2 injection remains constant.

This paper presents a numerical investigation of heat and gas transport in deep coal seams during the injection of CO_2. Coal compressibility, adsorption-induced strain and thermal strain are incorporated simultaneously. The numerical model is tested by comparing with an analytical solution. The theoretical developments are implemented into the computer code COMPASS, and applied to predict the temperature variation.

2 Governing Equations for Non-isothermal Gas Transport

The coal seam is assumed to be homogenous and isotropic and the effect of water is negligible (Liu et al. 2015). To analyse the thermal response of the coal reservoir simply, a single component gas is selected. The governing equations for gas and heat transport are presented in this section.

3 Gas Transport

When a sorbing porous medium is considered, the solid-gas interaction should be considered. The transport equation for a single component gas is described as

$$\frac{\partial\left[n\rho_g + (1-n)\rho_{ga}\rho_c V_{sg}\right]}{\partial t} = -\nabla\cdot\left(\rho_g \mathrm{v}\right) + Q_s \tag{1.1}$$

where ρ_g is the density of free phase gas; n is coal porosity; ρ_{ga} is the gas density at standard conditions; ρ_c is the coal density; V_{sg} is the content of adsorbed gas. For the coal-gas interactions, a Langmuir isotherm is used to describe the gas adsorption volume (Wu et al. 2010), the effect of temperature on gas adsorption is not considered, $V_{sg} = \frac{V_L P}{P_L + P}$, P is the gas pressure; V_{L} and P_{L} are Langmuir constants.

Application of the real gas law allows the pore gas pressure and gas density to be expressed in terms of the gas concentration, giving:

$$P = ZRTC \tag{1.2}$$

$$\rho_g = MC \tag{1.3}$$

where C is the gas concentration; M is the molar mass of the gas; Z is the gas compressibility factor, which is calculated using the classical Peng-Robinson equation of state (Peng and Robinson 1976); R is the universal constant, and T is the absolute gas temperature. Q_s is the gas source or sink.

The transport of gas obeys Darcy's law, and the effects of gravity are relatively small and can be neglected, giving:

$$v = -\frac{k}{\mu}\nabla \cdot P \tag{1.4}$$

where k is the permeability of the coal and μ is the viscosity of the gas.

If the effect of temperature on coal deformation is taken into account, and the adsorption-induced strain is approximately linearly proportional to the amount of adsorbed gas, the porosity model for coalbeds derived by Palmer and Mansoori (1996) under uniaxial conditions is modified as:

$$n = n_0 + \frac{1}{N}(P - P_0) + \left(\frac{K}{N} - 1\right)\alpha\Delta T + \left(\frac{K}{N} - 1\right)\varepsilon_L\left(\frac{P}{P_L + P} - \frac{P_0}{P_L + P_0}\right) \tag{1.5}$$

where N is constrained axial modulus, $N = E(1 - v)/[(1 + v)(1 - 2v)]$; n_0 is the initial porosity, K is the bulk modulus; E is Young's modulus and v is the Poisson's ratio; α is the thermal expansivity coefficient; ε_L is the Langmuir volumetric strain coefficient of the gas; P_0 is the initial pressure of gas, ΔT is the change of temperature. The typical relation between permeability and porosity gives is cubic law (Pan and Connell 2012):

$$k = k_0\left(\frac{n}{n_0}\right)^3 \tag{1.6}$$

where k_0 is the initial permeability of coalbeds.

3.1 Heat Transport

Conductive and convective heat fluxes are considered along with the Joule-Thomson effect, whereby the temperature change during gas expansion is added to the governing equation for heat transfer. Following an assumption of local thermal equilibrium between the fluid and solid skeleton, the energy balance equation for the solid and fluid parts becomes (Ziabakhsh-Ganji and Kooi 2014):

$$\begin{aligned}(\rho c)_{eff}\frac{\partial T}{\partial t} - n\left(\rho_g c_g \mu_{JT} + 1\right)\frac{\partial P}{\partial t} \\ = -\rho_g c_P \mathrm{v}(\nabla \mathrm{T} - \mu_{JT}\nabla P) + \nabla \cdot \left(\lambda_{eff}\nabla T + Q_T\right)\end{aligned} \tag{1.7}$$

For CO_2 sequestration in coal seams, the effective heat capacity, $(\rho c_P)eff$, and the effective thermal conductivity, λ_{eff} are expressed as:

$$(\rho c_P)_{eff} = (1-n)\rho_c c_s + n\rho_g c_g \tag{1.8}$$

$$\lambda_{eff} = (1-n)\lambda_s + n\lambda_g \tag{1.9}$$

where c_s and c_g are the specific heat capacity of solid phase and gas phase, respectively; λ_s and λ_g are thermal conductivity of solid and gas phase; Q_T is heat source/sink term, μ_{JT} is the Joule-Thomas coefficient, which is used to examine how T changes with P.

4 Model Verification

The theoretical formula has been implemented in an existing coupled thermal, hydraulic, chemical and mechanical (THCM) model, COMPASS, which adopts a Galerkin finite element approach and a finite difference scheme to solve the multi-physical problems within a coupled THCM system (Thomas et al. 2012). To verify the numerical model, the results obtained from numerical model are compared with those from the analytical solution for Joule-Thomson cooling effect derived by Mathias et al. (2010). A simple one dimensional radial geometry is selected to represent coal seams. The required parameters for numerical simulation are chosen from the study Mathias et al. (2010). Figure 1 shows the temperature distribution over the first 100 m radial distance from well at 90 days and 1 year. There is a good agreement between the temperature profiles obtained from the numerical simulation and analytical solution, indicating that the heat transport mechanism has been correctly implemented in the numerical model.

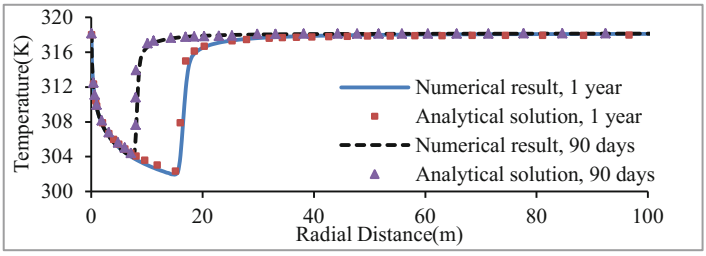

Fig. 1. Comparison between numerical results (line) and analytical solution (symbols)

5 Results

To analyse the thermal response of a deep coal seam to CO_2 injection, a 1-D radial domain with radius of 1000 m is chosen to represent an idealised coal formation. Material parameters are listed in Table 1. The CO_2 is injected into the coal seam at a pressure of 10 MPa and temperatures of 298 K, 318 K and 338 K, respectively, from

Table 1. Material parameters for the simulation case

Parameters	Value	Reference
Young's modulus of coal, E(MPa)	3950	Qu et al. (2012)
Poisson's ratio, v	0.339	Qu et al. (2012)
Initial porosity, n_0	0.05	Qu et al. (2014)
Dynamic viscosity, μ(Pa·s)	1.48e−5	Qu et al. (2012)
Density of CO_2 at standard condition, ρ_{ga}(kg/m^3)	1.98	Wu et al. (2010)
Coal density, ρ_c(kg/m^3)	1500	Qu et al. (2012)
Molar mass of CO_2, M(kg/mol)	0.044	–
Langmuir volume constant, V_L(m^3/kg)	0.043	Qu et al. (2012)
Langmuir pressure constant, P_L(MPa)	3.96	Qu et al. (2012)
Langmuir strain constant	0.03	(Qu et al. 2014)
Initial permeability, k_0(m^2)	1.0e−15	Zhu et al. (2011)
Specific heat capacity of coal, c_s(J/(kg·K))	1250	Qu et al. (2017)
Specific heat capacity of coal, c_g(J/(kg·K))	847	Qu et al. (2017)
Thermal conductivity of coal, λ_s(J/(m·s·K))	0.33	Qu et al. (2017)
Thermal conductivity of coal, λ_g(J/(m·s·K))	0.0246	Qu et al. (2017)
Initial temperature, T_0(K)	318	Given
Joule-Thomson coefficient, μ_{JT}(K/MPa)	2.0	Han et al. (2010)
Thermal expansion coefficient of coal, a(K^{-1})	9e−5	Qu et al. (2012)
Universal constant of gas, R(J/(K·mol))	8.3145	–

the middle of domain. The initial temperature is 45 °C. For simplicity, the Joule-Thomas coefficient is considered to be a constant. Figure 2 displays the predicted temperature and pressure responses after 10 days, 30 days, and 90 days of continuous injection.

It can be seen that JTC effect is highly dependent on the temperature discrepancy between the injected gas and coal reservoir. When the temperature of the gas is the same as that of the coal seam, a maximum cooling effect of approximately 8 K is observed in the vicinity of the wellbore after 10 days of injection, as shown in Fig. 2c. The minimum temperature increases and its radial location advances as injection continues, which shows that the cooling region can be heated again. The temperature difference between wellbore and the zone around it induces heat conduction. The change in temperature has an influence on gas pressure in the radial direction. Figure 2d shows that the decrease in temperature induces a further reduction of pressure in the zone of cooling. Similar to isothermal injection, when CO_2 is injected at a temperature lower than that of the reservoir, the zone near the wellbore is cooled, whereas the location of minimum temperature advances slowly and the zone of cooling is smaller than that under injection with the same temperature. It is worth noting that the pressure in the vicinity of the wellbore shows a considerable fluctuation in the cooled region compared with the other two scenarios, as shown in Fig. 2f. The further decrease in pressure is enhanced in the region of cooling. By contrast, a high injection temperature can suppress the JTC effect, although the time taken to reach the steady state increases, as shown in Figs. 2a and b.

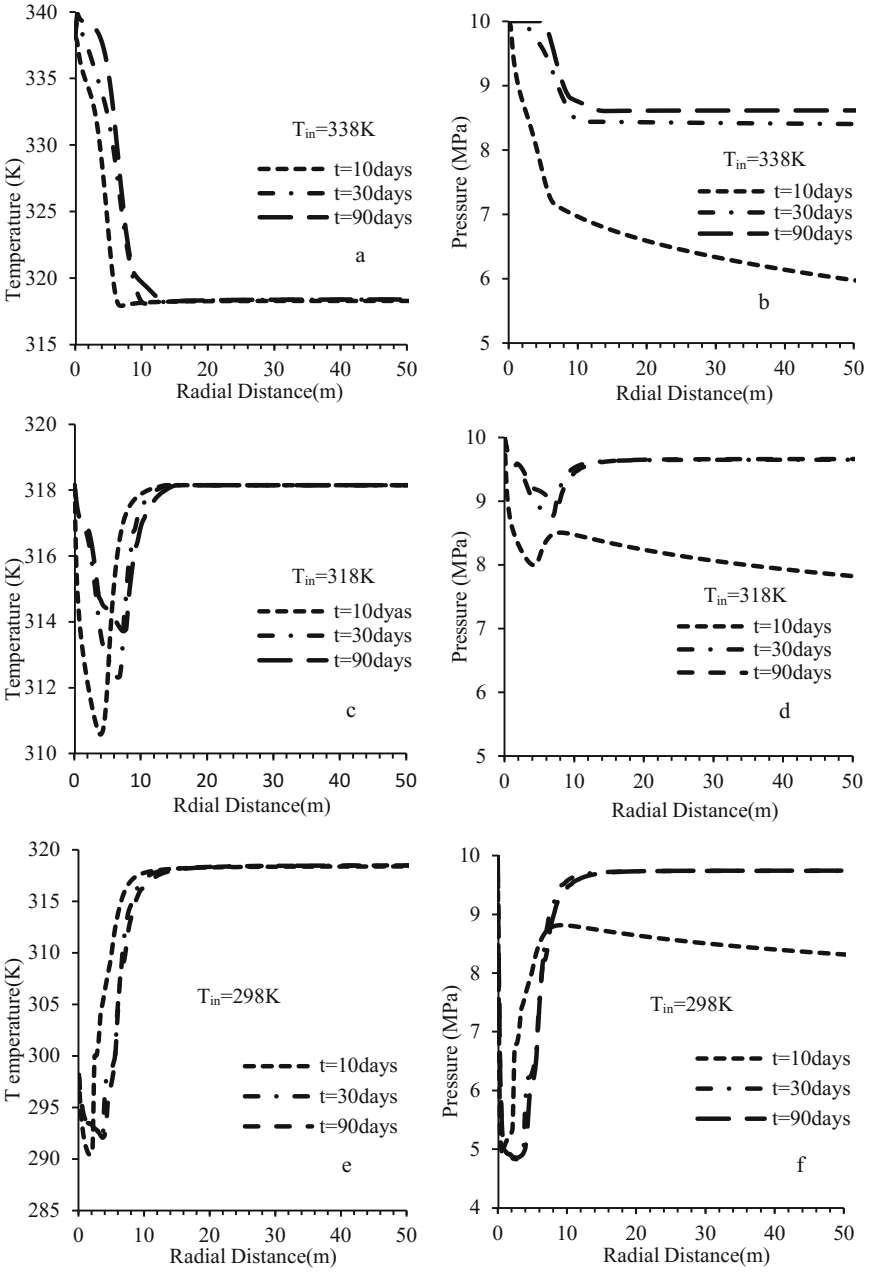

Fig. 2. Results of predicted temperature, pressure profiles over the first 40 m radial distance from well for the three different injection temperatures

6 Conclusions

To understand how the high pressure gas disturbs temperature of coal seams during CO_2 injection, a coupled gas flow and heat transport model incorporating effect of Joule-Thomson cooling (JTC) is presented in this study. The developed model is tested against an analytical benchmark and shows a good agreement. Three cases of carbon injection were simulated, each with a different injection temperature. The results show that temperature change of coal seams during CO_2 injection is affected by the injected temperature difference between the injected gas and the coal reservoir. Injection under the same and low temperature makes coal seam to displays a zone of cooling, leading to a further drop of pressure in this zone. There is no zone of cooling during injection under the higher temperature than reservoirs, whereas the time to reach steady state increases.

References

Busch A et al (2004) Methane and carbon dioxide adsorption-diffusion experiments on coal: upscaling and modeling. Int J Coal Geol 60(2):151–168

Duru OO, Horne RN (2010) Modeling reservoir temperature transients and reservoir-parameter estimation constrained to the model. SPE Reservoir Eval Eng 13(06):873–883

Fathi E, Akkutlu IY (2014) Multi-component gas transport and adsorption effects during CO_2 injection and enhanced shale gas recovery. Int J Coal Geol 123:52–61

Han WS et al (2010) Evaluation of potential nonisothermal processes and heat transport during CO_2 sequestration. J Geophys Res: Solid Earth 115(B7)

Krooss BV et al (2002) High-pressure methane and carbon dioxide adsorption on dry and moisture-equilibrated Pennsylvanian coals. Int J Coal Geol 51(2):6992

Liu Q et al (2015) A mathematical model of coupled gas flow and coal deformation with gas diffusion and klinkenberg effects. Rock Mech Rock Eng 48(3):1163–1180

Mathias SA et al (2010) Analytical solution for Joule-Thomson cooling during CO_2 geosequestration in depleted oil and gas reservoirs. Int J Greenhouse Gas Control 4(5):6–810

Oldenburg CM (2007) Joule-Thomson cooling due to CO_2 injection into natural gas reservoirs. Energy Convers Manag 48(6):1808–1815

Palmer I, Mansoori J (eds) (1996) How permeability depends on stress and pore pressure in coalbeds: a new model. In: SPE annual technical conference and exhibition. Society of Petroleum Engineers

Pan Z, Connell LD (2012) Modelling permeability for coal reservoirs: a review of analytical models and testing data. Int J Coal Geol 92:1–44

Peng D-Y, Robinson DB (1976) A new two-constant equation of state. Indus Eng Chem Fundam 15(1):59–64

Pini R et al (2011) A model for enhanced coal bed methane recovery aimed at carbon dioxide storage. Adsorption 17(5):889–900

Qu H et al (2012) Complex evolution of coal permeability during CO_2 injection under variable temperatures. Int J Greenhouse Gas Control 9:281–293

Qu H et al (2014) Impact of matrix swelling area propagation on the evolution of coal permeability under coupled multiple processes. J Nat Gas Sci Eng 18:451–466

Qu H et al (2017) Simulation of coal permeability under non-isothermal CO_2 injection. Int J Oil Gas Coal Technol 15(2):190–215

Singh A et al (2011) Numerical simulation of non-isothermal compositional gas flow: application to carbon dioxide injection into gas reservoirs. Energy 36(5):3446–3458

Thomas HR et al (2012) Diffusive reactive transport of multicomponent chemicals under coupled thermal, hydraulic, chemical and mechanical conditions. Geotech Geol Eng 30(4):841–857

Wang F et al (2007) Mass transfer in coal seams for CO_2 sequestration. AIChE J 53(4):1028–1049

Wu Y et al (2010) Dual poroelastic response of a coal seam to CO_2 injection. Int J Greenhouse Gas Control 4(4):668–678

Zhu W et al (2011) A model of coal-gas interaction under variable temperatures. Int J Coal Geol 86(2):213–221

Ziabakhsh-Ganji Z, Kooi H (2014) Sensitivity of Joule-Thomson cooling to impure CO_2 injection in depleted gas reservoirs. Appl Energy 113:434–451

Numerical Simulation of Subsurface Uranium (U) Leaching and Migration Under Geologic Carbon Storage Conditions

Liwei Zhang(✉), Xiuxiu Miao, Yan Wang, Hongwu Lei, and Xiaochun Li

State Key Laboratory of Geomechanics and Geotechnical Engineering, Institute of Rock and Soil Mechanics, Chinese Academy of Sciences, 430071 Wuhan, China
lwzhang@whrsm.ac.cn

Abstract. Geologic carbon storage (GCS) is the process to store large amount of carbon dioxide (CO_2) captured from stationary CO_2 emission sources in deep subsurface for permanent storage. GCS is widely recognized as a promising strategy to reduce emissions of greenhouse gas (GHG). However, the potential for mobilization of radioactive uranium (U) from U-bearing minerals in deep subsurface due to CO_2 injection remains a concern. In this study, A TOUGHREACT model was developed to investigate the potential of U-bearing mineral (UO_2) dissolution in a hypothetical deep CO_2 storage reservoir. An average reservoir temperature of 67.5 °C, an average reservoir pressure of 18.7 MPa and a CO_2 injection rate of 0.1 MMT/year (3.17 kg/s) were used in this study. Numerical simulation results show that HCO_3^- concentration increased as a result of CO_2 dissolution after injection of CO_2, which led to release of $[UO_2(CO_3)_3]^{4-}$. However, released $[UO_2(CO_3)_3]^{4-}$ did not migrate toward the shallow aquifer through leakage pathways specified in the model, while CO_2 could migrate upward through the leakage pathways. In summary, the area of uranium contamination is restrained in deep subsurface and notable migration of uranium to shallow aquifer caused by CO_2 injection does not occur.

Keywords: Geologic carbon storage · Uranium · Groundwater Contamination · TOUGHREACT

1 Introduction

Carbon capture and geological storage (CCGS) is the separation and capture of carbon dioxide (CO_2) from the emissions of industrial processes prior to release into the atmosphere and (long-term/permanent) storage of captured CO_2 in deep underground geologic formations (US-DOE-NETL 2015). It is considered a critical strategy to reverse the trend of increasing anthropogenic CO_2 emissions to the atmosphere (Altman et al. 2014). To increase storage capacity, CO_2 is injected underground as a supercritical fluid at depths of or greater than 800 m (Iglauer 2011). Possible repositories include depleted oil and gas reservoirs, saline aquifers, and unmineable coal beds (Benson and Cole 2008). The effectiveness of geological storage depends on a

© Springer Nature Singapore Pte Ltd. 2019
L. Zhan et al. (Eds.): ICEG 2018, ESE, pp. 121–128, 2019.
https://doi.org/10.1007/978-981-13-2227-3_15

combination of physical and geochemical trapping mechanisms: (1) physical trapping to block upward migration of CO_2 by the caprock; (2) physical trapping to retain CO_2 in the pore spaces of the formation by capillary forces; (3) geochemical trapping to dissolve CO_2 in the in-situ water, and then to react with rock minerals to form solid carbonate minerals, or to be preferentially adsorbed onto coal or organic-rich shales (IPCC 2005). With proper site selection and management of CO_2 storage projects, long-term storage can be achieved, and risks to humans and the environment are low; however, there are still concerns regarding potential hazards to groundwater caused by CO_2 or formation fluid leakage, brine displacement and pressure build-up (Bergman and Winter 1995; Holloway and Savage 1993; Lemieux 2011).

CO_2-induced contaminants mobilization is probably one of the greatest concerns associated with migration of CO_2 from deep geologic storage to near surface environments (Harvey et al. 2013). Most studies attribute the CO_2-induced mobilization of contaminants to the activity of H^+ and HCO_3^- (Harvey et al. 2012). When CO_2 dissolves in water it exists in chemical equilibrium with carbonic acid (H_2CO_3). Depending on solution pH, H_2CO_3 may exist in the form of bicarbonate ion (HCO_3^-), or carbonate ion (CO_3^{2-}):

$$H_2O + CO_2 \rightleftharpoons H_2CO_3 \rightleftharpoons HCO_3^- + H^+ \rightleftharpoons CO_3^{2-} + 2H^+ \tag{1.1}$$

A number of works covered mobilization of contaminants due to CO_2 migration from deep geologic storage to near-surface environments. Mason et al. (1997) found that in the presence of HCO_3^-, 75–90% uranium could be desorbed from contaminated soils. Yang et al. (2011) found that exchangeable concentrations of a wide range of metals (including copper, lead, chromium, arsenic and uranium) in an agricultural soil increased by up to 500% during a 3-day incubation period with CO_2 (25°C and 25 bars). A pilot-scale experiment on impure CO_2 aquifer storage containing N_2 and O_2 in the upper Yaojia Formation, China was conducted, and field monitoring results suggested that co-injection of oxygen enhanced dissolution of certain minerals in the aquifer formation and provided soluble ions such as uranium and SO_4^{2-} (Wei et al. 2015). While the possible deleterious effects in near-surface environments are widely investigated, few seem to have looked into contaminant mobilization in deep CO_2 storage reservoir which may cause contaminant migration from deep reservoir to shallow aquifer through fluid leakage. Zhang et al. (2017) simulated a deep-reservoir scenario to investigate the potential of As mobilization and shallow aquifer contamination caused by As mobilization. In this study, a leakage pathway close to CO_2 injection well connecting the reservoir with a shallow aquifer was constructed to investigate the potential of As migration along this leakage pathway.

Abandoned or uneconomic coal seams are potentially large storage reservoirs, and the preferential adsorption of CO_2 offer the opportunity for enhanced methane production. China is estimated to have 22.5×10^{12} m^3 coalbed methane reserve between 1000 m to 2000 m depth, accounting for 61.2% of all methane inventory in the country (Liu et al. 2009; Shen et al. 2014). Uranium is a known radioactive trace element in coal.

The average uranium concentration for common coals in China is 2.43 μg/g, and the concentration in some uranium-rich coals varies from a few hundreds to a few thousands of μg/g (Dai et al. 2012; Dai et al. 2015). CO_2 injection into coal formations may cause uraninite (UO_2, the most important uranium-bearing mineral) to dissolve, and released uranium may migrate toward shallow groundwater through leakage pathways like abandoned wells and faults. Two mechanisms of uranium mobilization induced by CO_2 injection are specified below:

(1) H^+-induced dissolution of UO_2 (Casas et al. 1998)

$$UO_2(s) + 4H^+ \rightleftharpoons U^{4+} + 2H_2O \tag{1.2}$$

(2) bicarbonate-induced oxidative dissolution of UO_2 (modified from Eliwa (2017) and Dunn et al. (2010))

$$UO_2(s) + 3HCO_3^- + 1/2O_2 \rightleftharpoons H_2O + UO_2(CO_3)_3^{4-} + H^+ \tag{1.3}$$

Unlike previous models that address CO_2 leakage–induced contaminant mobilization in shallow groundwater, this study aims to investigate the potential threat of uranium dissolution in deep CO_2 storage reservoir and migration of uranium from deep CO_2 storage reservoir towards shallow groundwater.

2 Methodology

A hypothetical 1900 m deep CO_2 storage reservoir with an average temperature of 67.5 °C, an average pressure of 18.7 MPa and a CO_2 injection rate of 0.1 MMT/year (3.17 kg/s) were simulated in TOUGHREACT to model the CO_2-induced uraninite dissolution and uranium transport processes. The aforementioned reservoir condition is hypothetical, however, it is common to find similar assumptions from published works. For instance, Gasperikova and Hoversten (2008) created a brine formation model with a 20 m thick reservoir at a depth of 1900 m and a temperature of 70 °C. Yang et al. (2017) investigated the CO_2-water-rock interactions on porosity and permeability for Shenhua's CCS demonstration project at an injection rate of 0.1 MMT/year, with depth ranging from 1576 m to 2232 m, temperature ranging from 55 to 67 °C, and pressure ranging from 16 to 21 MPa. Zhang et al. (2017) configured a deep CO_2 reservoir at a depth of 1830 m, an average temperature of 50 °C and an average reservoir pressure of 18.7 MPa to study As migration. A worst-case scenario consisting of a 140 m thick UO_2 layer (2 vol.% UO_2 and 98 vol.% quartz) in the reservoir formation right above the bottom of the injection well (−1970 m) is envisaged in this study. This scenario has two vertical leakage pathways: Pathway 1 (microannulus at the CO_2 injection well) and Pathway 2 (a leaky abandoned well). Important parameters of mineral dissolution are summarized in Table 1.

Table 1. Important mineral dissolution modeling parameters of quartz and UO_2

Mineral name	Mineral dissolution reactions	A_m (m^2/g)	Molar volume (cm^3/mol)	K_{eq} at 25 °C	k_m at 25 °C, (mol/(m^2s))	$\prod a_i^n$	E_a (kJ/mol)
Quartz (SiO_2)	SiO_2 (s) $\rightleftharpoons$ SiO_2 (aq)	0.10	22.69	$10^{-3.74}$	$10^{-13.99}$	1.0	91.3
Uraninite (UO_2)	UO_2 (s) + $4H^+ \rightleftharpoons$ U^{4+} + $2H_2O$	0.10	31.25	$10^{-4.84}$	$10^{-10.56}$	$[H^+]^{0.37}$	62.8
	UO_2 (s) + $3HCO_3^-$+1/2O_2 $\rightleftharpoons$ H_2O + $UO_2(CO_3)_3^{4-}$ + H^+			$10^{16.72}$	$10^{-7.46}$	$[H^+]^{0.37} \times [O_2(aq)]^{0.31}$	62.8

3 Results and Discussion

3.1 Migration of Injected CO_2

Figure 1 depicts CO_2 saturation profiles from the initiation of injection to several decades after active injection. Within active injection period (Fig. 1a–b), due to localized pressure increase, CO_2 plume expands around the injection well. Faster migration of CO_2 along the three defined pathways of leakage is noted. Injected CO_2 is able to migrate upward along the injection well and the abandoned well with time. By the end of active CO_2 injection (t = 30 years), maximum CO_2 saturation reaches 0.179 (Fig. 1b). The shape of CO_2 plume shrinks and the concentration decreased over years, as indicated in Fig. 1b–d. Seventy years after the termination of active injection (Fig. 1d), maximum CO_2 saturation drops to approximately 0.1, and the CO_2 saturation is relative even within the plume. Since UO_2 consumption of CO_2 is small, leakage and transport must be the main cause.

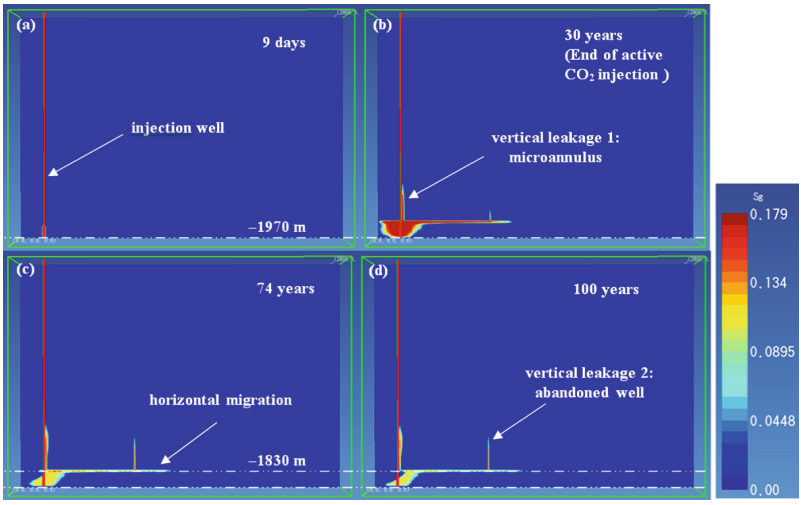

Fig. 1. Profiles of CO_2 saturation plume at: (a) t = 9 days; (b) t = 30 years; (c) t = 74 years; and (d) t = 100 years.

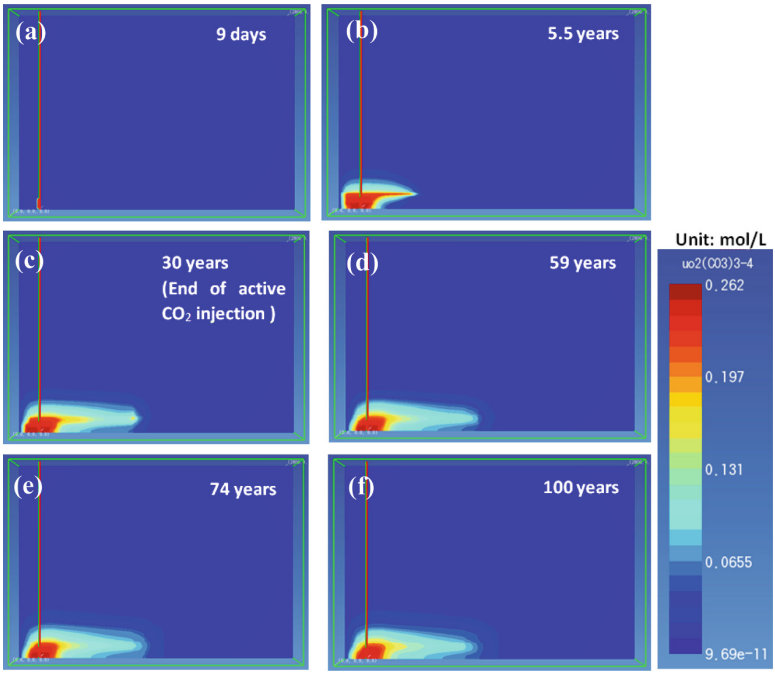

Fig. 2. Profiles of $UO_2(CO_3)_3^{4-}$ concentration at: (a) t = 9 days; (b) t = 5.5 years; (c) t = 30 years; (d) t = 59 years; (e) t = 74 years; and (f) t = 100 years.

3.2 Uranium Dissolution Induced by CO_2 Injection

Figure 2 shows the profiles of $UO_2(CO_3)_3^{4-}$ concentration over a hundred years. The $UO_2(CO_3)_3^{4-}$ plume expands fast for the thirty years of active CO_2 injection (Fig. 2a–c), yet almost remains the same for the next seven decades after active CO_2 injection (Fig. 2c–f). Because both CO_2 and UO_2 are abundant close to the injection well, more $UO_2(CO_3)_3^{4-}$ is dissolved close to the injection well, compared with regions far away from the injection well. Therefore, $UO_2(CO_3)_3^{4-}$ concentrates close to the injection well and gets diluted in regions far away from the injection well. It is also observed in Fig. 2b–f that $UO_2(CO_3)_3^{4-}$ dissolved from the reservoir rock is able to migrate into the caprock above the CO_2 storage reservoir. However, the high-permeability microannulus between the injection well and surrounding rock does not cause fast upward migration of $UO_2(CO_3)_3^{4-}$ along the CO_2 injection well, nor does the leaky pathway defined in the abandoned well allow preferential transport of $UO_2(CO_3)_3^{4-}$.

Figure 3 presents the profiles of U^{4+} concentration. Comparison between Figs. 3 and 2 shows that U^{4+} plume is larger than that of $UO_2(CO_3)_3^{4-}$, however, the concentration of U^{4+} is several orders of magnitude lower than that of $UO_2(CO_3)_3^{4-}$. Possible causes involved here are: (1) smaller molecular weight of U^{4+} that leads to faster diffusion than $UO_2(CO_3)_3^{4-}$; and (2) slower reaction between uraninite and H^+ that limits U^{4+} generation. Therefore, it is concluded that HCO_3^--induced UO_2 dissolution is the dominant U mobilization mechanism. Similar to $UO_2(CO_3)_3^{4-}$, U^{4+} is

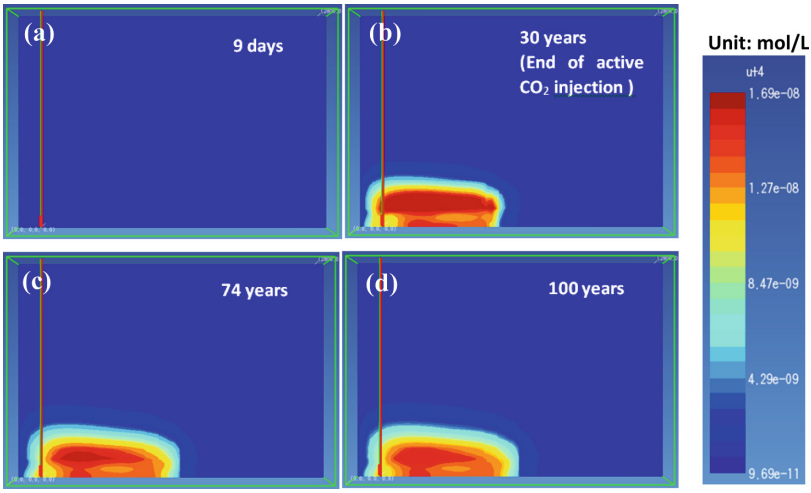

Fig. 3. Profiles of U^{4+} concentration at: (a) t = 9 days; (b) t = 30 years; (c) t = 74 years; and (d) t = 100 years.

contained within the reservoir and caprock area. The microannulus or the leaky abandoned well does not raise concern for U^{4+} migration to shallow aquifer.

4 Conclusions and Implications

A TOUGHREACT model was developed to simulate the dissolution and transport of U in a hypothetical deep carbon storage reservoir with three leakage pathways to investigate the potential of CO_2-induced U mobilization toward shallow aquifer. Two types of uranium mobilization mechanisms: H^+-induced mobilization and bicarbonate-induced mobilization are considered. This model is workable in assessing U mobilization risk in the application of CO_2 enhanced methane recovery from deep coalbed. Simulation results based on a worst-case scenario where a high U content layer (2 vol. % UO_2) connects to an injection well with developed microannulus and a leaky abandoned well show that:

(1) Injected CO_2 will release U from uraninite in the reservoir rock by the activity of HCO_3^- and H^+. HCO_3^--induced dissolution of UO_2 is the dominant dissolution mechanism. (2) CO_2 migrates fast along vertical leakage pathways, and intrusion of CO_2 into shallow groundwater is possible. (3) Even though U-bearing ions ($UO_2(CO_3)_3^{4-}$ and U^{4+}) are able to enter the caprock, these ions do not migrate upward along vertical leakage pathways.

In conclusion, uranium contamination is restrained in deep subsurface, and does not pose threat to shallow groundwater. It should be noted that the proposed model only considered transport and reaction processes. Comprehensive investigation on other factors that influence U mobilization needs to be conducted in the future so that models coupling more processes can be developed for more complex realizations.

References

Altman SJ, Aminzadeh B, Balhoff MT, Bennett PC, Bryant SL, Cardenas MB, Chaudhary K, Cygan RT, Deng W, Dewers T (2014) Chemical and hydrodynamic mechanisms for long-term geological carbon storage. J Phys Chem C 118:15103–15113

Benson SM, Cole DR (2008) CO2 sequestration in deep sedimentary formations. Elements 4:325–331

Bergman PD, Winter EM (1995) Disposal of carbon dioxide in aquifers in the US. Energy Convers Manag 36:523–526

Casas I, Pablo JD, Giménez J, Torrero ME, Bruno J, Cera E, Finch RJ, Ewing RC (1998) The role of pe, pH, and carbonate on the solubility of UO2 and uraninite under nominally reducing conditions. Geochim Cosmochim Acta 62:2223–2231

Dai S, Ren D, Chou C-L, Finkelman RB, Seredin VV, Zhou Y (2012) Geochemistry of trace elements in Chinese coals: a review of abundances, genetic types, impacts on human health, and industrial utilization. Int J Coal Geol 94:3–21

Dai S, Yang J, Ward CR, Hower JC, Liu H, Garrison TM, French D, O'Keefe JM (2015) Geochemical and mineralogical evidence for a coal-hosted uranium deposit in the Yili Basin, Xinjiang, northwestern China. Ore Geol Rev 70:1–30

Dunn G, Vagenas J, Teo Y, Dunn G, Vagenas J (2010) Uranium recovery by continuous ion exchange of alkaline leachate. Orway Mineral Consultants (WA) Pty Ltd Western Australia orway. com. au Google Scholar

Eliwa AA (2017) Kinetics and thermodynamics of carbonate dissolution process of uranium from Abu-Zeniema wet crude uranium concentrates. J Radioanal Nucl Chem 312:1–11

Gasperikova E, Hoversten G (2008) Gravity monitoring of CO 2 movement during sequestration: model studies. Geophysics 73:WA105–WA112

Harvey OR, Qafoku N, Cantrell KJ, Brown CF (2012) Geochemical Implications of CO2 Leakage Associated with Geologic Storage: A Review. U.S. Department of Energy

Harvey OR, Qafoku NP, Cantrell KJ, Lee G, Amonette JE, Brown CF (2013) Geochemical implications of gas leakage associated with Geologic CO2 Storage—a qualitative review. Environ Sci Technol 47:23–36

Holloway S, Savage D (1993) The potential for aquifer disposal of carbon dioxide in the UK. Energy Convers Manag 34:925–932

Iglauer S (2011) Dissolution trapping of carbon dioxide in reservoir formation brine–a carbon storage mechanism. In: Mass Transfer-Advanced Aspects. InTech

IPCC (2005) Intergovernmental Panel on Climate Change: Special Report on Carbon Dioxide Capture and Storage. Cambridge University Press, Cambridge

Lemieux JM (2011) Review: the potential impact of underground geological storage of carbon dioxide in deep saline aquifers on shallow groundwater resources. Hydrogeol J 19:757–778

Liu C, Zhu J, Che C, Yang H-L, Fan M-Z (2009) Methodologies and results of the latest assessment of coalbed methane resources in China. Nat Gas Ind 11:046

Mason C, Turney W, Thomson B, Lu N, Longmire P, Chisholm-Brause C (1997) Carbonate leaching of uranium from contaminated soils. Environ Sci Technol 31:2707–2711

Shen J, Qin Y, Fu X-H, Chen G, Chen R (2014) Properties of deep coalbed methane reservoir-forming condition and critical depth discussion. Nat Gas Geosci 25:1470–1476

US-DOE-NETL (2015) Carbon Storage Atlas (Fifth Edition). U.S. Deparment of Energy – National Energy Technology Laboratory – Office of Fossil Energy

Wei N, Li X, Wang Y, Zhu Q, Liu S, Liu N, Su X (2015) Geochemical impact of aquifer storage for impure CO2 containing O2 and N2: Tongliao field experiment. Appl Energy 145:198–210

Yang G, Li Y, Atrens A, Yu Y, Wang Y (2017) Numerical Investigation into the Impact of CO2-Water-Rock Interactions on CO2 Injectivity at the Shenhua CCS Demonstration Project, China. Geofluids

Yang W, Maroto-Valer M, Steven MD (2011) Environmental consequences of potential leaks of CO 2 in soil. Energy Procedia 4:3224–3230

Zhang L, Parthasarathy H, Karamalidis A (2017) Investigation on arsenopyrite dissolution and As (III) migration under geologic carbon storage conditions: a numerical simulation approach. Greenh Gases Sci Technol 7(3):460–473

Strain Distribution in Geothermal Energy Piles: A Parametric Study

Rajni Saggu(✉)

Department of Civil Engineering,
Galgotias College of Engineering and Technology,
Greater Noida 201306, India
rajni.saggu@galgotiacollege.edu

Abstract. This work emphasizes on the alteration in pile-soil interaction in case of geothermal energy piles during thermal cycle. The geothermal energy piles are investigated numerically using finite element software Abaqus. To simulate the soil mechanical and thermal response, two user defined material subroutines are used for the soil surrounding the piles. The behaviour of soil is reproduced using CASM; a soil constitutive model which is based on the concepts of critical state soil mechanics. To investigate the additional strains induced in the piles due to the thermal load, parametric analyses are carried out considering the effect of (i) different pile end restraints, (ii) relative densities of the soil, (iii) pile dimensions and (iv) lateral earth pressure coefficient. The analysis results indicate that the axial and radial strains are induced in the pile due to pile expansion during thermal loading. The increase in lateral earth pressure coefficient at interface of pile and soil can be correlated to the thermally induced radial strains. Moreover, the pile response to the thermal cycle can be considered to the governed by soil stiffness and the magnitude of thermal load applied on the pile. Analyses are also performed to investigate the influence of thermal parameters of soil and thermal load on the soil earth pressure coefficient at interface of pile and soil. The lateral earth pressure coefficient increases following the increase in magnitude of thermal load, however the effect of thermal conductivity of soil is not significant.

Keywords: Geothermal · Axial and radial strains
Lateral earth pressure coefficient

1 Introduction

The technology of heat exchanger piles or geothermal energy piles is a novel approach to harness the energy of soil surrounding the piles for building heating in winter and to reject the building heat into the soil in summer (Bourne-Webb et al. 2009). Energy piles experience the thermal as well as mechanical loads and the in depth understanding of the response of these piles requires analysis of pile response against each type of load. The load transfer mechanism of the energy piles involves thermal soil-structure interaction. Experimental, numerical and analytical studies are presented in literature by various researchers.

© Springer Nature Singapore Pte Ltd. 2019
L. Zhan et al. (Eds.): ICEG 2018, ESE, pp. 129–137, 2019.
https://doi.org/10.1007/978-981-13-2227-3_16

According to Wang et al. (2013, 2015), pile temperature is a decisive parameter that affects the load carrying capacity of geothermal energy piles and the shaft resistance increases as a consequence of heating induced radial expansion of the pile installed in unsaturated dense sand. Goode et al. (2014) have noted 20% increase in axial strain for each 1 °C rise in pile temperature for the pile installed in dry Nevada sand. Saggu and Chakraborty (2015) analyzed the pile-soil interaction under constant mechanical and cyclic thermal loading of the piles and reported an increase in pile base displacement after each consecutive thermal cycle. Saggu and Chakraborty (2017) have reported the combined thermo-mechanical behavior of energy piles considering elasto-plastic behaviour of soil and concluded that additional stresses are developed in the piles due to thermal loading. To analyze the geothermal energy pile response under thermal as well as mechanical loading, the loads should be applied separately and alternately so as to study the thermal and mechanical effects, separately (Laloui and Nuth 2006). Under the mechanical loading alone, the pile is under compression and may move into the supporting soil. Conversely, geothermal energy piles may experience uplift as compared to mechanical piles which settle under the constant dead weight of building. The purpose of the present study aims at the understanding of the influence of thermal loading of piles with different pile end conditions on (i) the axial strains in pile, (ii) the radial strains in pile and (iii) effect of thermal load on pile and thermal conductivity of soil on coefficient of lateral earth pressure by numerically investigating the geothermal energy piles considered to be installed in sand under thermal loading. The piles installed in sand while under thermal loading and unloading exhibit expansion and contraction, consequently, the surrounding sand experience both normal and shear loading and as a result, contract or dilate considerably. The lateral earth pressure coefficient, K changes with soil void ratio and the mean effective stress. Thus, the both the axial and radial strains are generated in the pile. Hence, the value of K after thermal loading of pile will be different from K_0 (the lateral earth pressure coefficient at rest). Thus, the ratio of K/K_0 becomes significant to study the soil response under thermal loading of the pile.

The objectives as sated above are accomplished by performing numerical investigation of energy piles under thermal loading only. The mechanical load on the pile is not considered so as to understand the influence of thermal loading, separately. The thermal pile response is analyzed by considering different (i) end conditions of the pile, (ii) the soil relative density (D_R), (iii) the lateral earth pressure coefficient at rest (K_0), (iv) length (L_P) and diameter (B) of the pile, (v) the thermal load (ΔT) on the pile and (vi) the thermal conductivity (k_s) of soil. The finite element (FE) analyses are carried out for axisymmetric model geometries using FE software Abaqus (Abaqus Manual Version 6.11, 2011). The pile is assumed to respond as a linear elastic material and the soil response is simulated by applying a unified soil state parameter model employed for clay and sand CASM (Yu 2007). The CASM is integrated in Abaqus using two user-defined material subroutines for soil; (i) UMAT for describing the mechanical stress-strain behavior and (ii) UMATHT for describing the thermal properties. The temperature change over the entire pile length is applied uniformly as applied by Laloui and Nuth (2006).

2 Finite Element Model and Material Parameters

The axisymmetric FE analyses presented in this study are carried out by creating pile and soil geometries, separately. The concrete pile possessing ultimate compressive strength as 45 MPa is considered for the analyses. The mechanical and thermal material properties of the pile are presented in Table 1. Ottawa sand is considered as soil surrounding the piles. The sand response is simulated through employing a soil critical-state based material constitutive model, CASM. The right side vertical soil boundary is considered at a distance of $15B$ from the interface of pile and soil. The bottom soil boundary is considered at a distance of $1L_P$ from the base of the pile. The right side soil boundary is assumed to be rollers to allow vertical movement of the soil and the bottom soil boundary is fixed against the vertical and horizontal movements. The thermal boundary conditions are applied for (i) heat flow through the bottom and side boundaries of the model, (ii) an initial temperature of 15 °C at the top surface of soil and (iii) zero heat flux along the axis of symmetry.

Table 1. Material parameters used for sand and pile.

Parameter	Value	Reference
Slope of critical state line in e-ln (p') space, λ	0.02	Loukidis (2006)
Slope of unloading-reloading line in e-ln(p') space, κ	0.005	Yu (2006)
Critical state line intercept at 1 kPa pressure, Γ	0.8	Model simulation
Reference state parameter, ξ_R	0.075	Yu (2006)
Model parameter, n	4.5	Model simulation
Slope of critical state line in q-p' space, M_{cc}	1.2	Yu (2006); Loukidis (2006)
Poisson's ratio, υ_s	0.3	Yu (2006)
Shear modulus, G	32.6 MPa	Yu (2006); Murthy et al. (2006)
Bulk modulus, K_b	15 MPa	
Thermal conductivity, k_s	0.274 W/m °C	Tarnawski et al. (2009)
Specific heat, C_s	722 J/°C	
Coefficient of thermal expansion, α_s	10^{-4}/°C	
Elastic and thermal parameters for pile		
Modulus of elasticity, E_c	33.7 GPa	Pile material parameters assumed to be same as concrete
Poisson's ratio, υ_c	0.2	
Thermal conductivity, k_c	2.1 W/m °C	
Specific heat, C_c	800 J/°C	
Coefficient of thermal expansion, α_c	10^{-5}/°C	

The initial temperature of ground is considered as 15 °C (Laloui and Nuth 2006). The uniform thermal change, ΔT is applied along the pile length using a thermal boundary condition for duration of 28 days. The thermal cycle consists of 12 days as heating period and 16 days as cooling period (Laloui and Nuth 2006). The pile-soil model is meshed using CAX4T (four node axisymmetric thermally coupled quadrilateral, bilinear displacement and temperature) elements. A refined mesh with minimum element size (t_s) of 0.075 mm in the soil near the pile-soil interface is used and at the far-field regions, t_s is taken as 0.15 mm. At the interface of pile and soil, a frictional contact is applied by defining a coefficient of friction μ between soil and concrete as 0.55 taking $\mu = \tan(\phi_c)$ in the tangential direction. A hard contact is considered in a direction normal to pile-soil interface. To model heat conduction between pile and soil, a gap conductance value same as the soil thermal conductivity is defined. For the determination of the CASM parameters for Ottawa sand, a FORTRAN code is formulated for drained and undrained triaxial compression test simulations. The model parameters are obtained by comparing the code based simulation results with the experimental data from Sasitharan et al. (1994) for loose sand and Carraro (2006) for dense sand. The tensile stresses and strains are assumed as positive in the analyses. The CASM and thermal parameters for Ottawa sand are presented in Table 1. The thermal constitutive model is integrated in Abaqus software by defining a user-defined material subroutine for soil; UMATHT.

3 Thermal Validation of Finite Element Simulation

The validity of numerical thermal analysis of energy piles is assured by matching the present numerical simulation outcomes with the full scale pile load test results and the numerical simulations results of Laloui and Nuth (2006). They investigated the thermo-mechanical loading of the pile under an axial mechanical load of 1300 kN and thermal load ΔT of 21 °C. The CASM model parameters λ, κ, Γ, ξ_R and n are assumed as same as that of Ottawa sand. Figure 1 shows that the head displacement is comparable with the results obtained from Laloui and Nuth (2006).

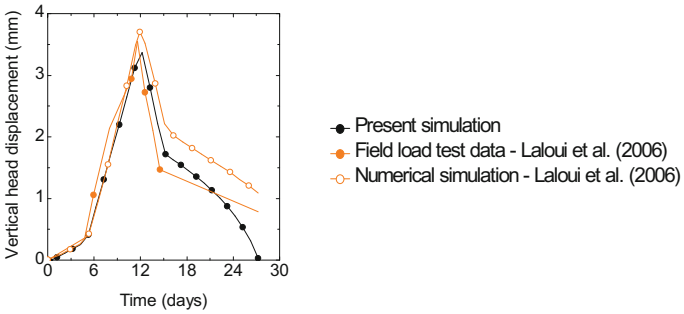

Fig. 1. Comparison of vertical pile head displacement from numerical simulation with the results of (Laloui and Nuth 2006).

4 Axisymmetric Finite Element Simulation

Axisymmetric FE analyses of piles installed in Ottawa sand under the applied thermal loading are performed using software Abaqus. The analysis is performed in two steps consisting of a static step for applying the gravity load for simulating initial geostatic equilibrium and a coupled temperature-displacement step for applying thermal load as temperature change ΔT = 21 °C along the pile length. The thermal load is applied in form of temperature time-history of 28 days constituting 12 days as heating period and 16 days as cooling period (Laloui and Nuth 2006). The piles are analyzed for two pile end conditions (i) both ends free and (ii) both ends restrained. To analyze the piles with both ends free, floating piles installed in a single layer of Ottawa sand are considered. To simulate the pile response with restraint at pile toe, two different soil layers are considered; Ottawa sand along the entire length of the pile and stiff sand as bearing layer with elastic modulus E_s = 4 GPa. The Poisson's ratio (υ_s) = 0.154 is considered for the bearing sand layer. The thermal parameters of stiff sand layer; thermal conductivity k_s = 1.1 W/m °C, specific heat capacity C_s = 784 J/°C and coefficient of thermal expansion $\alpha_s = 1\times10^{-06}$/°C are assumed similar to Laloui and Nuth (2006). The thermal parametric study is performed for (i) ΔT = 21 °C, 35 °C and (ii) k_s = 0.274, 0.5. In the present study, different pile lengths, L_P as 15 m and 20 m and two different pile diameters, B as 0.5 m and 1 m are considered to investigate the effect of pile dimensions on thermo-mechanical response of the piles. The lateral earth pressure coefficient at rest (K_0) is assumed as 0.5 and 1 to simulate anisotropic and isotropic in-situ stress conditions of soil, respectively. The thermal parametric sensitivity analyses are carried out for L_P = 15 m and B = 0.5 m piles, D_R = 50% and K_0 = 0.5, as these piles experience significant variation in results under thermal loading as noted from other analyses. From the analyses, the results are presented in terms of axial strain, radial strains and the K/K_0 at the interface of pile and soil.

5 Results and Discussion

5.1 Axial Strains in Pile

Pile with Both Ends Free. Figure 2(a) shows generation of axial strains along the pile length considering different values of D_R and K_0 of soil and different L_P and B of pile for piles with both ends free to expand or contract under thermal loading or unloading. The results are presented at the end of heating. A pile with top free and soft soil at the base exhibit free expansion while under heating. The magnitude of strain varies along the pile length. The maximum strains are observed at the top and toe of the pile. A decrease in pile strain is observed towards the middle portion of the pile. Piles exhibit higher magnitude of axial strains for D_R = 70% when compared to that for D_R = 50%.

Pile with Both Ends Restrained. Figure 2(b) shows the generation of axial strains in pile considering different values of D_R and K_0 of soil and different L_P and B of pile for piles with both ends restrained. The results are presented at the end of heating.

The magnitude of axial strains shows significant decrease for piles with both ends restrained when compared to the piles with ends free to expand under thermal loading. The axial strains are of same magnitude through the entire pile length except at the pile toe. The nil or negative axial strain at the toe of the pile may be due the heave of the hard bearing soil layer. It may be concluded from Fig. 2 that the axial strains in piles strictly depends on the pile end conditions, relative density of the soil, pile lengths and lateral earth pressure coefficient.

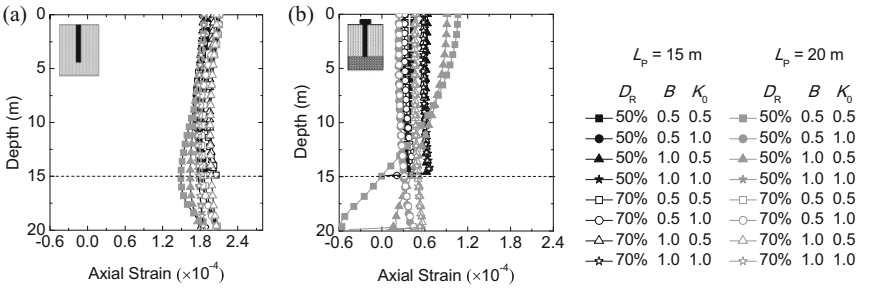

Fig. 2. Axial strain along pile depth for L_P = 15 m and L_P = 20 m for piles (a) with both ends free and (b) both ends restrained

5.2 Radial Strains in Pile

Pile with Both Ends Free. Figure 3(a) shows the generation of radial strains along the pile length considering different values of D_R and K_0 of soil and different L_P and B of pile for piles with both ends free to expand or contract under thermal loading or unloading.. The results are presented at the end of heating. For a pile with free top and soft soil at the base, the axial expansion occurs due to heating and the pile tends to expand in the radial direction too. Hence, high value of radial strain is noted for these piles. The magnitude of radial strain varies along the pile length. The higher radial strains are noted towards the middle portion of pile, however, the radial strain magnitude decreases towards the pile ends. The piles in soil with D_R = 70% show higher radial strain in comparison to those in soil with D_R = 50%.

Pile with Both Ends Restrained. Figure 3(b) shows the radial strains along the pile length considering different values of D_R and K_0 of soil and different L_P and B of pile for piles with both ends restrained. Contrary to the piles with both end free, the magnitude of radial strain is higher for piles with both ends restrained which is may be associated to the expansion of these piles only in radial direction as these piles cannot expand in axial direction. An almost uniform magnitude of radial strain is observed along the length of the pile because of presence of single soil layer along the entire length of the pile; however, a significant increase in radial strain is observed at the toe which is associated to the resistance offered by hard bearing soil to axial expansion of the pile at pile toe. The magnitude of radial strain is higher for the piles in soil with D_R = 50% in comparison to those for D_R = 70%. It may be summarized from Fig. 3

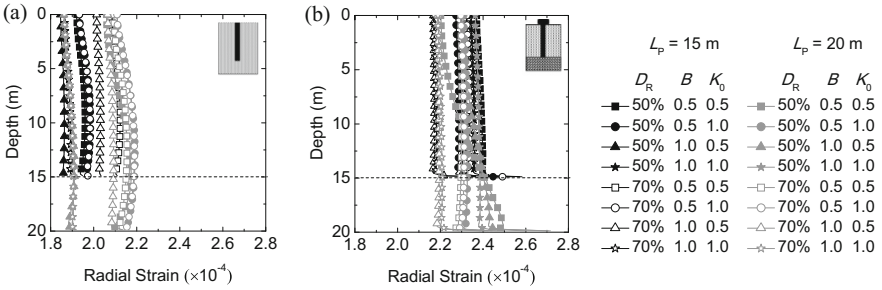

Fig. 3. Radial strain along pile depth for L_P = 15 m and L_P = 20 m for piles with (a) both ends free and (b) both ends restrained

that the radial strains vary with pile end restraint conditions, soil relative density, pile lengths and soil earth pressure coefficient.

6 Thermal Parametric Studies

Figure 4(a) presents the influence of increase in thermal load, ΔT as 21 °C and 35 °C on the K/K_0 values at pile-soil interface for piles with (i) both ends free and (ii) both ends restrained. The results are presented for L_P = 15 m piles. An increased thermal load on the pile results in an increase in K/K_0 for both the cases. The increased magnitude of K/K_0 may be associated to higher thermal expansion of the piles under higher thermal load which results in significant compaction of the soil surrounding the piles. Analysis is also performed to investigate the influence of thermal conductivity of the soil on the K/K_0 for k_s as 0.274 W/m °C and 0.5 W/m °C.

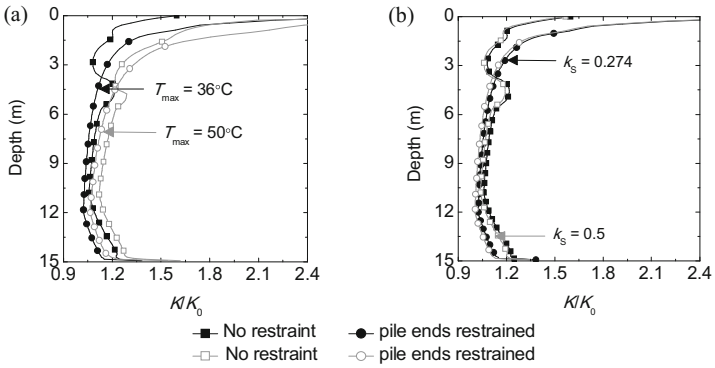

Fig. 4. Effect of variation in (a) thermal load and (b) thermal conductivity of soil on K/K_0

Figures 4(b) shows the effect of change of k_s on the K/K_0. It is observed from the figures that the increased thermal conductivity results in marginal decrease in K/K_0 and the effect is insignificant.

7 Conclusions

The present study has numerically investigated the response of geothermal energy piles installed in sand and subjected to thermal loading using the FE software Abaqus and CASM; a user-defined material subroutine for soil. The analyses have been carried out to analyze the effect of end conditions of the pile, soil relative density, the initial lateral earth pressure coefficient of the soil, the length and diameter of the pile, the thermal load and the thermal conductivity of soil on the axial and radial strain response of the piles. It is concluded from the studies conducted herein that the pile length and relative density of soil play key role in deciding the pile behavior while under thermal loading. All the piles sustain thermally induced axial and radial strains, however, the strain magnitudes are smaller in comparison to free pile strain. The piles with both ends fixed exhibit significant magnitude of radial strain, however, the axial strain magnitudes are insignificant. The parametric sensitivity studies conclude that thermal loads on pile is an important parameter which governs the pile response. The lateral earth pressure coefficient increases following an increase in thermal loading of the pile. The influence of change in soil thermal conductivity is negligible on the lateral earth pressure coefficient.

References

Bourne-Webb PJ, Amatya B, Soga K, Amis T, Davidson C, Payne P (2009) Energy pile test at Lambeth College, London: geotechnical and thermodynamic aspects of pile response to heat cycles. Géotechnique 59(3):237–248

Saggu R, Chakraborty T (2015) Cyclic thermo-mechanical analysis of energy piles in sand. Geotech Geol Eng 33(2):321–342

Saggu R, Chakraborty T (2017) Thermo-mechanical response of geothermal energy piles in sand and parametric study. Int J Geomech 17(9). https://doi.org/10.1061/(ASCE)GM.1943-5622.0000962

Sasitharan S, Robertson PK, Sego DC, Morgenstern NR (1994) State-boundary surface for very loose sand and its practical implications. Can Geotech J 31(3):321–334

Tarnawski VR, Momose T, Leong WH, Bovesecchi G, Coppa P (2009) Thermal conductivity of standard sands. Part I. Dry state conditions. Int J Thermophys 30(3):949–968

Wang B, Bouazza A, Singh RM, Haberfield C (2015) Post temperature effects on shaft capacity of a full scale geothermal energy pile. J Geotech Geoenvironmental Eng 141(4). https://doi.org/10.1061/(ASCE)GT.1943-5606.0001266

Yu HS, Tan SM, Schnaid F (2007) A critical state framework for modelling bonded geomaterials. Geomech Geoengin Int J 2(1):61–74

Yu HS (2006) Plasticity and geotechnics. Springer, New York

Carraro JAH (2006) Mechanical behaviour of silty and clayey sands. Ph.D. thesis, Purdue University, West Lafayette, USA

Goode JC III, Zhang M, McCartney JS (2014) Centrifuge modeling of energy foundations in sand. In: Gaudin C, White D (eds) Proceedings of 8th international conference on physical modelling in geotechnics. Taylor and Francis, London, pp 729–736

Laloui L, Nuth M (2006) Numerical modeling of some features of heat exchanger piles. In: Proceedings of GeoShanghai international conference on Foundation analysis and design: innovative methods (GSP 153), Shanghai, China, pp 189–194

Wang B, Bouazza A, Singh RM, Barry DM, Haberfield C, Chapman G, Baycan S (2013) Field investigation of geothermal energy pile: initial observations. In: Proceedings of the 18th international conference on soil mechanics and geotechnical engineering, pp 3415–3418

Surface Monitoring Strategies at CO_2 Storage Sites

Matthew Myers(✉), Cameron White, Alf Larcher, and Bobby Pejcic

CSIRO Energy, Kensington, WA 6151, Australia
matt.myers@csiro.au

Abstract. Geological CO_2 storage is viewed as a potentially viable strategy for reducing greenhouse gas emissions from point sources such as power plants, fertilizer production facilities and bio-ethanol fermenters, etc. However, for this strategy to be successful at its aim of reducing greenhouse gas emissions, a monitoring strategy is required to ensure that the CO_2 remains in the intended storage reservoir and does not leak. Furthermore, monitoring is required in most jurisdictions around the water as a permitting condition. It is also necessary to provide assurance to the community and other stakeholders that the CO_2 being stored is not affecting the environment. There are many subsurface monitoring techniques including pressure monitoring, 4D seismic, etc.; however, these must be complemented by surface monitoring approaches. Based on our experience monitoring fugitive methane emissions for the gas industry, we have found that mobile surveys using vehicles containing real-time spectroscopic analysis equipment that sample gases from the atmosphere can be used to identify potential leaks. Similarly, this approach could be used for monitoring of the nearby region surrounding a CCS storage site. However, this strategy suffers from several disadvantages such as limited land access, poor wind conditions, variation in leak rate over time and interference from other sources (e.g. agriculture, vehicles and industry) that might preclude the detection of an actual CO_2 leak. Furthermore, this strategy only provides a snapshot of the leak characteristics at a particular time which may or may not be indicative of long term behavior. To complement this approach, fixed site monitoring can be utilized; however, current fixed-site monitoring approaches can be quite expensive. This can lead to a situation where a very limited number of fixed monitoring sites are implemented. Furthermore, the site selected for the fixed monitoring station may be biased or not indicative of the actual overall emissions in the field. To rectify this, a high density of low-cost and reliable sensors is required. This approach would meet regulatory requirements, provide assurance to the community and provide actionable information in the event of a substantial leak. In this paper, we will show that the combined approach of fixed-site and mobile monitoring can each address many of the disadvantages of the other.

Keywords: CCS · Monitoring · Sensors · Greenhouse gases

© Springer Nature Singapore Pte Ltd. 2019
L. Zhan et al. (Eds.): ICEG 2018, ESE, pp. 138–143, 2019.
https://doi.org/10.1007/978-981-13-2227-3_17

1 Introduction

Recently, we conducted baseline surveys of both CO_2 and CH_4 gas concentrations in the North Perth Basin using either vehicle-based mobile or semi-permanent fixed site atmospheric surveys and mobile soil-gas flux chamber measurements [1]. Commercially available IR-based cavity ring-down spectrometers were used for this project. This project focused on CH_4 as it was primarily concerned with tight gas resource development in the northern Perth Basin. Though this study focused on CH_4, CO_2 concentrations were also measured and the techniques and strategies discussed in this paper are equally applicable to both CO_2 and CH_4. With a very long effective path length and stable optical sources/detectors, these systems have sub-ppb resolution for a wide range of concentrations and are very suitable for monitoring fluctuations in background concentrations that might be attributed to sources or sinks of either CO_2 or CH_4 [2].

Mobile surveys, particularly vehicle-based surveys, whether atmospheric and/or soil-gas flux measurements can cover a very large area depending on accessibility. However, this approach only provides data for a particular time at a particular location and may be subject to wind conditions, diurnal cycles, and changes in subsurface conditions over time. As such, this approach may not give a truly representation. Multiple transits at different times of the day and the year can help to provide an understanding of variations over time; however, this approach is obviously limited by the availability of human resources. Fixed monitoring sites have the advantage of providing a long-term picture of the evolution of gas concentration at a particular location. However, fixed monitoring station require a lot of equipment resources to operate and have a limited geographical range. Due to high equipment and operating costs and other practical constraints (e.g. access to field site, availability of power, protection against the elements), the ability to implement fixed monitoring sites can be very limited. Fixed monitoring sites are only able to give information for a fairly localized area (depending on topography and wind conditions).

Soil-gas flux measurements either at a fixed site station or as part of a mobile survey allow for the direct measurement of leak rates by combining flux measurements over the spatial extent of the leak. A concentration ratio approach can be utilized (where a known amount of a tracer gas (e.g. acetylene) is released into the atmosphere at the same location as the leak) and the change in concentration of the gas being studied (i.e. CH_4 or CO_2) relative to the change in the tracer concentration can be used to estimate leak rates [3]. However, this approach requires pinpointing the exact location of the leak. Atmospheric gas mixing models can be utilized to estimate leak rates; however, long-term characterization is necessary for these studies and often many added assumptions need to be considered [4].

This paper outlines a general strategy where both fixed site monitoring and mobile survey methods are utilized to achieve an optimal outcome. The analysis of the data garnered from the monitoring activities is also discussed along with considerations for how to maximize the usefulness of the data.

2 Mobile Surveys

Vehicle based surveys can cover a very large area and as such the background concentration over the study area may vary [5]. For both CO_2 and CH_4, variations in the atmospheric concentration may simply be due to changes in the agricultural landscape over the study area and are important to consider when establishing a baseline for comparison. To identify emission sources, it is important to differentiate between changes over large distances (e.g. changes in the agricultural landscape) compared to changes over short distances (e.g. gas pipeline infrastructure, seeps). If the background concentration is changing, periodically re-establishing baseline conditions or examining the rate of change in the concentration profile can be very useful in identify point-source emissions. Changes in the isotopic composition or the CO_2:CH_4 concentration ratio are also indicators of emission sources. In the scenario that an anomalous reading is obtained, it is important to try to identify the source in real-time. It is very helpful then in these instances to minimize the equipment response time; this can be accomplished by maximizing the gas flow rate in to the spectrometer, minimizing the sampling distance and using a fast sample loop with an external air pump. When an anomalous reading is observed, the vehicle can be stopped immediately or turn around even to try to pinpoint the source location. Wind measurements and soil-gas flux chamber measurements can be very helpful in locating the source location. If an emission source is confirmed and is significant, the site might be a candidate for deployment of a fixed site monitoring station.

3 Fixed Site Monitoring

Due to the significant deployment of resources for a fixed site monitoring station, the location will often be well rationalized. Possible reasons for choosing a particular site might include proximity to relevant surface infrastructure (e.g. oil/gas production or CO_2 injection facilities), subsurface geology (e.g. fractures) or a known emission source. The site selection might also be entirely motivated by the need to acquire baseline data and might be located in an area with no significant rationale or anomalies. Fixed site monitoring stations can either be powered by the electrical grid or with solar panels and battery bank in more remote circumstances (see Fig. 1). Atmospheric sampling is done by continuously pumping air into the spectrometer and soil-gas flux measurements can be conducted by circulating the gas in the flux chamber into the spectrometer in a close loop. An automated multiplexer can be used to switch between atmospheric sampling and soil-flux chamber measurements as well as between multiple flux chambers. Long-term fixed site measurements are useful in characterizing the temporal changes in concentration which can be very helpful in understanding the nature of the emission source and developing a strategy for mitigation. However, changes in temperature and soil-moisture combined with both diurnal and annual changes will inevitably lead to fluctuations in the concentration readings therefore it is important to obtain soil moisture and temperature data to assist with data analysis and

Fig. 1. A solar powered monitoring station for atmospheric and soil-gax flux chamber measurements deployed onto a mobile trailer.

interpretation. If the flux chambers are located near a known seep they can be used to estimate the overall emissions flux from the ground and also to ascertain how the emissions flux varies over time. This data can be very useful in understanding the underlying cause for a seep.

Long-term equipment reliability can also be an issue leading to equipment shut-down or periodically unreliable data. This might be due to extreme weather conditions (e.g. rain, high or low temperatures). In the case of equipment shutdown, it is important to design restart mechanisms that are automated; this is particularly important if the site is in a remote location. Telemetry capabilities to access and control the detection system are particularly useful in maintaining the equipment and improving reliability. The prevalence of unreliable data (i.e. very high concentration readings that cannot be explained by physical phenomena) might be attributed to alignment or curve fitting issues and is often exacerbated by either extreme low or high temperatures. In any case, analysis methods can be incorporated into the processing of the data to identify and compensate for these problematic data points.

4 Data Analysis

For vehicle surveys, flux chamber measurements and atmospheric sampling will need to be separated as their analysis is distinctly different. The reliability and validity of the data can be improved by regular testing of the system using calibration standards. If this is done on a periodic basis during a survey, equipment drift and stability can be assessed. This is particularly important when covering large distances as it is important

to understand whether slowly varying changes in concentration are due to spectrometer drift or due to actual changes in background concentration. Flux chamber measurements are tagged by GPS location and time and the rate of change in concentration can be multiplied by the volume and divided by the surface area to quantify the emissions flux. In an area, where there is a significant seep, it is useful to acquire many flux measurements at locations close to each other and these measurements can be integrated together to provide an estimate for the overall emissions rate for the seep. For atmospheric measurements, the data should be tagged by GPS coordinates as a function of time and periodic wind measurements. It is also useful to tag anomalous data (e.g. sudden transient increases in concentration) with an explanation (e.g. the vehicle passed a field with cattle causing an increase in methane concentration).

For fixed site monitoring stations, there is often a very large amount of data. For baseline monitoring situations, histogram analysis where the data is binned based on concentration and time of day can provide an understanding of diurnal variations in concentration (see Fig. 2). In Fig. 2, it can be easily seen that higher CO_2 concentrations are more prevalent in the early morning and late evening hours. This approach can also be very useful in identifying data that is erroneous as well. This same approach can be used to analyse data on a daily or weekly basis allowing for seasonal variations to be ascertained. If the fixed site location is chosen for monitoring a seep, the flux chamber measurement data can be analysed by quantifying the rate of change in concentration for each flux chamber measurement. Similarly, histogram analysis can be used to understand if the flux is changing over time and whether there are any diurnal or seasonal variations.

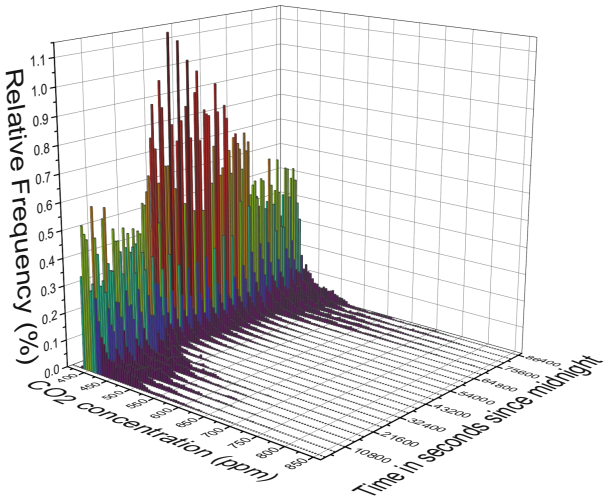

Fig. 2. Histogram of CO_2 data over a period of approximately 3 months

5 Conclusions

A combined approach of mobile monitoring surveys and fixed site stations is probably the optimal approach to maximizing the usefulness and representativeness of an emissions monitoring program. For mobile monitoring surveys, a system with very high concentration resolution is necessary in order to locate possible sources of emission as the survey location might be some distance from the actual source. For fixed site stations, the resolution can be significantly less as small variations in data are likely to not be meaningful. However, low drift and stability are much more important. There is an opportunity for these fixed monitoring sites to develop lower cost technologies that can be deployed on a larger scale without significant resources. Systems with lower power requirements and larger operating temperature ranges characteristics are also much more easily deployed. By using a combination of approaches and technologies, the impact of a monitoring program can be maximized providing vital information to industry, government and the community as a whole.

References

1. Hortle A, Rachakonda PK, George S, Myers M, White C. (2017) Baseline characterisation and monitoring protocols for development of shale and tight gas resources, Northern Perth Basin. APPEA J 57(1):64–78
2. Jongma RT, Boogaarts MGH, Holleman I, Meijer G (1995) Trace gas detection with cavity ring down spectroscopy. Rev Sci Instrum 66(4):2821–2828
3. Mønster JG, Samuelsson J, Kjeldsen P, Rella CW, Scheutz C (2014) Quantifying methane emission from fugitive sources by combining tracer release and downwind measurements–a sensitivity analysis based on multiple field surveys. Waste Manag 34(8):1416–1428
4. Hurry J, Risk D, Lavoie M, Brooks BG, Phillips CL, Gockede M (2016) Atmospheric monitoring and detection of fugitive emissions for enhanced oil recovery. Int J Greenh Gas Control 45:1–8
5. Atherton E, Risk D, Fougere C, Lavoie M, Marshall A, Werring J et al (2017) Mobile measurement of methane emissions from natural gas developments in Northeastern British Columbia, Canada. Atmos Chem Phys 17(20):12405–12420

Tailings and Mine Wastes

(Edited by Jiangfeng Liu and Lingling Zeng)

Effects of Permeable Reactive Barriers for Treating Uranium Mine Pit Water

Nana Li(✉)

CNNC Beijing Research Institute of Uranium Geology, Beijing 100029, China
alina0351@163.com

Abstract. In this study, laboratory-scale Permeable reactive barrier (PRB) reactors were designed with the mixture of non-valent iron, active carbon, hydrated lime and quartz sands as reaction media. The feasibility and effectiveness of treating uranium mine pit water by PRB were tested under 3 different proportions of media through dynamic simulation tests, which came out the optimal proportion of contaminants. The result indicated that the remediation effect of reactor B was the best, whose average removal rate to U was up to 99%, as well as the average value of total α, total β, and ^{226}Ra in effluent were 0.78 Bq/L, 3.52 Bq/L and 0.47 Bq/L respectively. The quality of effluent met the requirement of relevant standards, which indicated that the PRB technology is a feasible method for the treatment of uranium mine pit water.

Keywords: Permeable reactive barriers · Radioactive contamination
Uranium mine pit water

1 Introduction

A large number of radioactive substances release into the environment during the nuclear fuel cycle, which lead to environmental pollution and potential hazards, in which uranium mining and milling industry contributes a lot. The main radioactive contamination caused by THEM lies in radioactive pit water and radon gas.

Uranium mine pit water, wide in distribution and small in scale, contains a certain amount of radionuclides and hazardous chemical elements such as U, Ra, Mn, Zn and so on. It will lead to radioactive contamination, if discharged without treating properly. Block strategy was the main method to uranium mine pit water at present. In fact, this did not solve the problem. This requires an economical, feasible and effective technique to treat uranium mine pit water. In this study, we took PRB technology to solve the problem.

Permeable reactive barrier (PRB) [1] is economical and high efficiency on in suit remediation of polluted groundwater. technology is to set a barrier filled with reactive materials in situ of polluted water. When polluted groundwater flows though the barrier, the radionuclide and other contamination will be removed by adsorption, sedimentation, and oxidation-reduction reaction of pre-designed media. Thus, the polluted groundwater was treated [2].

As a kind of in-situ treatment, PRB technology can process polluted water continuously. With high efficiency and low investment, PRB can be installed and

© Springer Nature Singapore Pte Ltd. 2019
L. Zhan et al. (Eds.): ICEG 2018, ESE, pp. 147–155, 2019.
https://doi.org/10.1007/978-981-13-2227-3_18

constructed easily. In summer, it is particularly suitable for processing uranium mine pit water.

The purpose of this study is to conduct Laboratory-scale PRB reactor, determine optimal proportion of reactive materials, as well as valuate feasibility and effectiveness of PRB in processing pit water.

2 Equipment, Materials and Methods

2.1 Water Samples

The tested water sample was taken from a uranium mine. The chemical properties were measured. As showed in Table 1, it was acidic and with high concentration of Uranium, total α and total β, which were all higher than relevant limits.

Table 1. Properties of uranium mine pit water

pH	U/(μg/L)	Th/(μg/L)	Cs/(μg/L)	Cr/(μg/L)	Cu/(μg/L)	Zn/(μg/L)	Cd/(μg/L)
3.56	3698	0.13	0.87	75.50	3.44	1.39	1.12
In/(μg/L)	Mo/(μg/L)	Ni/(μg/L)	Pb/(μg/L)	Mn/(μg/L)	Total α/(Bq/L)	Total β/(Bq/L)	^{226}Ra/(Bq/L)
0.005	1179	2	1.51	79.96	84.6	14.6	2.41

2.2 Equipment

The designed reactor with height of 50 cm and inside diameter of 10 cm was showed as in Fig. 1.

At the top of the column was filled with quartz sands with height of 10 cm, which can isolate from the air and prevent volatile organic matters from getting out. At the bottom of the column was filled with quartz sands with height of 5 cm, it can play an important role in filtration, buffer of inflow and protection of reactive materials. The middle of the column with the height of 35 cm was the main part of the reactor. The sampling port and wastewater inlet were filled with polyethylene to prevent spilling of reactive materials.

2.3 Reactive Materials

Reactive materials determined the effect of PRB directly. The materials must have good performances in adsorption, degradation and corrosion resistance. With average granularity, they could keep steady for long time without any chemical reactions, by-products. They could not be dissolved in wastewater [3].

Based on all the mentioned principles and lots of investigations, non-valent iron and hydrated lime were chosen as the main materials, and active carbon as assistant material.

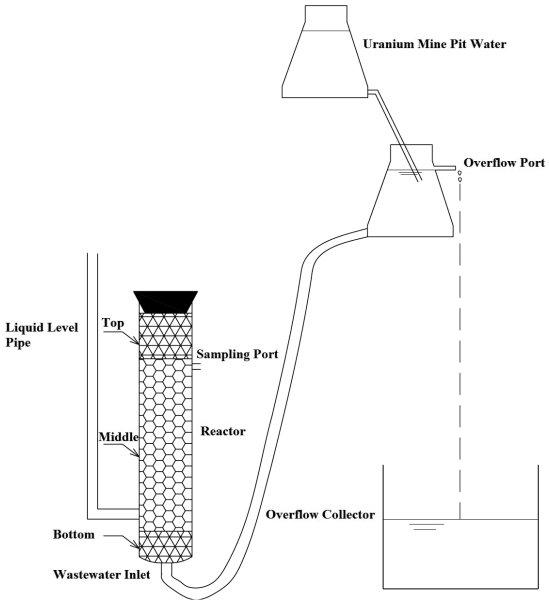

Fig. 1. Schematic diagram of experiment equipment

(1) Main materials

① Fe^0: Non-valent iron, with high performance of deoxidizing, can remove uranium through this oxidation-reduction reaction, which can deoxidize heavy metal and turn into Fe^{2+} itself. The reaction [4] was as follows:

$$Fe^0(s) + UO_2^{2+}(aq) \rightarrow Fe^{2+} + UO_2(s) \quad (1)$$

In addition, it was reported that many other kinds of heavy metal can be removed by Fe^0, such as Cr, Ni, Pb, U, Cu, Co, Cd, Zn, Mo, V and so on.

② Hydrated Lime: The role of hydrated lime is to adjust pH and promote sedimentation of U though reaction (2). Generally speaking, the most suitable condition for sedimentation of U is neutral, which is pH = 5–8.5 [5].

$$2OH^- + UO_2^{2+}(aq) \rightarrow UO_2(OH)_2(s) \quad (2)$$

(2) Assistant material

① Active carbon: Active carbon plays role in physical adsorption, sustaining, and a kind of activator, can speed up the reaction cooperating with non-valent iron.

② Quartz sands: It can play an important role in filtration, buffer, and protecting reactive materials.

2.4 Experimental Scheme

The experiments were conducted in three reactors named A, B and C respectively. Composition of reactive materials in 3 reactors was showed in Table 2. The 3 kinds of reactive materials were mixed up first, then, put into the columns and tamped down to close to the natural aquifer water-bearing stratum. The wastewater was transferred from bottom to upper with the rate of 100–120 cm/d. The treated water was sampled from sampling port, and the sampling was controlled under anaerobic condition strictly. The main parameters were measured including U, pH, ^{226}Ra, Total α, Total β.

Table 2. Configurations of reaction media and parameters of the reactors

Reactors		A	B	C
Composition/mass percentage %	Fe^0	40	50	60
	Hydrated lime	30	30	20
	Active carbon	30	20	20
Flow rate/(L · d^{-1})		2.0	1.8	1.9
Flow velocity/(cm · d^{-1})		115	105	110

2.5 Analysis Methods

The analysis frequency and methods of main parameters were showed in Table 3.

Table 3. Analysis frequency and methods

Items	Sampling frequency	Instrument/methods	Discharge limits	Relevant standards
^{238}U	Once/d	HR-ICP-MS	0.05 mg/L	Regulation for radiation and environment protection in uranium (GB15848-1995)
^{226}Ra	Once/3d	PC-2000	1.11 Bq/L	
Total α	Once/3d	MINI20α, β MULTIDETECTOR	1 Bq/L	Integrated wastewater discharge Standard (GB8978-1996)
Total β	Once/3d		10 Bq/L	
pH	3 times/d	F-33pH/mV/°C Meter	6–9	Integrated wastewater discharge Standard (GB8978-1996)

3 Results and Discussions

3.1 Variation of pH

Changes of pH in effluent of different reactors were showed in Fig. 2. The pH of 3 reactors shows a similar tendency, all presented an increasing trend at first four days, then approached equilibrium for next 14 days, and started decline from 20th day, which

was the results of neutralization reaction between hydrated lime and acid [6]. $Ca(OH)_2$ changes pH of liquid in the reactor, which provides favorable condition for Fe^0 to deoxidize U and other heavy metals. In all, effluent pH of reactor B was more stable than that of reactor A and C.

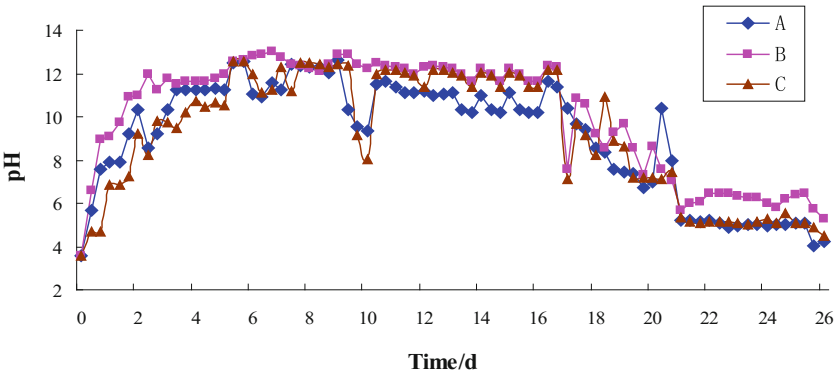

Fig. 2. Changes of pH in effluent of different reactors

3.2 Variation of U

The variation of removal rate of U was showed in Fig. 3, which indicated that the effect of reactor B was the best of 3 reactors and can reached above 99% after stable operation. The concentration of U in outlet water was 7.54 μg/L, meeting the requirements of 0.05 mg/L [7, 8]. Variation of removal rate of U showed same tendency in 3 reactors, all presented a quick upward in first five days, then approached equilibrium for next 12 days, then started decline to about 78%.

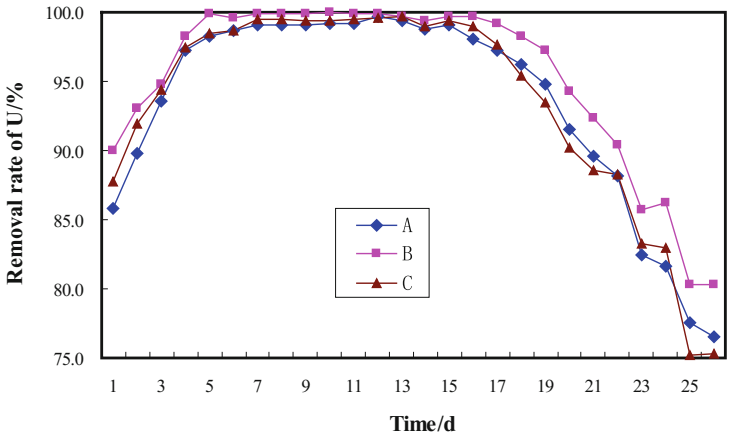

Fig. 3. Changes of removal rates of U in effluent different reactors

The chemical characteristics of U in water are very complex [6]. High removal rate of U in PRB reactor is the result of cooperation of oxidation-reduction reaction, sedimentation, and adsorption.

(1) Function of Fe^0' reduction: Fe^0 can deoxidize UO_2^{2+} to UO_2 which is a kind of sediment, and turn into Fe^{2+} itself. So, Fe^0 can provide electron, in addition, it can form hydrate of ferric oxide, such as $Fe(OH)_2$ and Fe $(OH)_3$, which have high capability of adsorption and agglomeration [9], could adsorb U and get sedimentation together.
(2) Function of $Ca(OH)_2$' sedimentation: The dissolved U in water are mainly U^{6+} in the form of UO_2^{2+}, which can react with OH^- and form $UO_2(OH)_2$, thus U can be removed from waste water. U^{4+} can not be dissolved in water. At the mean time, Ca^{2+} can react with SO_4^{2-} and form $CaSO_4$ which could wrap and absorb U and other heavy metal during sedimentation.
(3) Physical adsorption of active carbon: Active carbon with a lot of acidic and basic groups such as carbonyl group and phenolic hydroxyl group are a kind of porous material and can be used to enhance penetrability in the experiment. The existing of these acidic and basic groups can make active carbon have capability of adsorption, and have catalysis to the oxidation-reduction reaction. Heavy metal can be oxidized by these groups, for example, Fe^{2+} can be oxidized to Fe^{3+}, meanwhile UO_2^{2+} can be deoxidized into UO_2 in the form of solid and would be removed by adsorption further more.

Above all, the removal of U in PRB reactor is the result of cooperation of oxidation-reduction reaction, sedimentation, and adsorption.

3.3 Removal Rates of Heavy Metals

Heavy metal ions with high electric potential are one of most important pollutants in uranium mine pit water. And some heavy metals have high concentration. The oxidation-reduction reaction happens between Fe^0 and heavy metals, thus heavy metals turn to undissolved compounds or elementary substances which would separate out from water [10]. 3 reactors showed good effect in removing heavy metals. Just as showed in the Table 4, the Reactor B had the best efficiency, whose removal rates for Mo, Cd, Th and Mn were 98.85%, 96.52%, 94.66% and 94.66% respectively.

Table 4. Removal rates of heavy metals in effluent in different reactors

Heavy metals		Mo	Cd	In	Pb	Th	Mn
Removal rates/%	A	95.12	89.20	60.00	44.64	67.18	87.17
	B	98.85	96.52	80.00	61.26	94.66	98.87
	C	97.14	95.00	80.00	33.64	77.10	99.30

3.4 Variation of ^{226}Ra

Variation of ^{226}Ra was showed in Fig. 4. The concentrations of ^{226}Ra in effluent of 3 reactors appeared same tendency which declined in first 6 days and reached steady from 7th to 14th, then went up in the reason of using up reaction media.

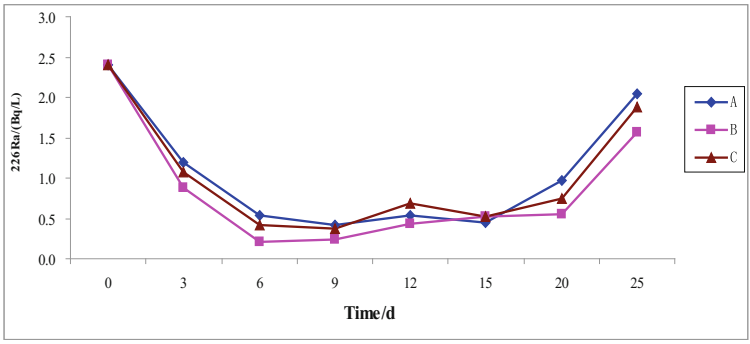

Fig. 4. Changes of ^{226}Ra in effluent in different reactors

The average concentrations of ^{226}Ra in 3 reactors were 0.58 Bq/L, 0.39 Bq/L, 0.55 Bq/L respectively after reaching steady, all of which were lower than the limit of 1.11 Bq/L [7, 8]. Reactor B was the best in removing ^{226}Ra of 3.

3.5 Variations of Total α and Total β

Total α and Total β are two important indexes of water quality which can indicate radioactive level of water. Variations of Total α and Total β were showed in Fig. 5.

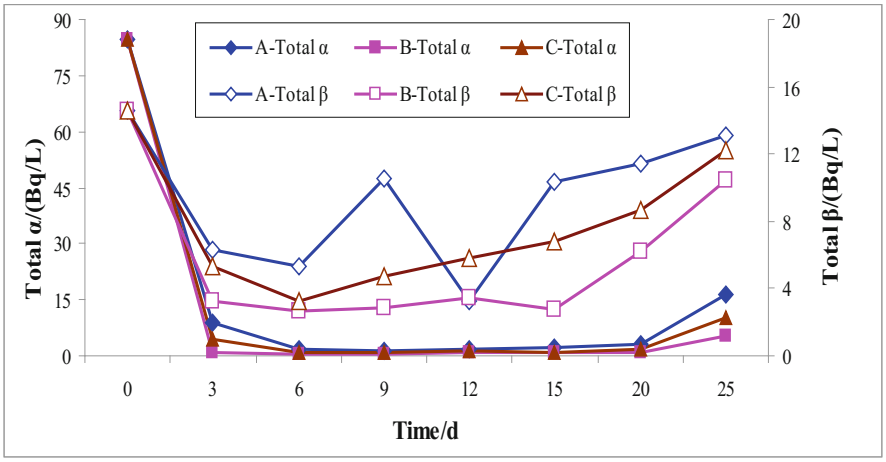

Fig. 5. Changes of total α and total β in effluent in different reactors

As showed in Fig. 5, all of 3 reactors showed good removal effect to both Total α and Total β. The average concentrations of Total α of effluent in 3 reactors were 1.78 Bq/L, 0.68 Bq/L and 0.99 Bq/L respectively after reaching steady, and the average concentrations of Total β of effluent in 3 reactors were 6.35 Bq/L, 2.98 Bq/L, and 4.76 Bq/L respectively. At the same time, the removal effect of reactor B was the steadiest of 3, while reactor A was the most unstable of 3. In all, reactor B had the best removal effect for Total α and Total β with average concentration of effluent 0.68 Bq/L and 2.98 Bq/L respectively, which can meet the requirement of discharge standard for $\alpha \leq 1$ Bq/L [11], 总$\beta \leq 10$ Bq/L [11].

4 Conclusions

(1) PRB technology with Fe^0, Hydrated Lime and Active Carbon as active materials had high performance in removing radioactive contaminations and heavy metals, which indicated that the PRB technology is a feasible method for the treatment of uranium mine pit water.
(2) The optimal proportion of Fe^0, Hydrated Lime and Active Carbon is 5:3:2. Remediation effect of reactor B was the best, whose average removal rate to U was up to 99%, as well as the average value of total α, total β, and ^{226}Ra in effluent were 7.54 μg/L, 0.47 Bq/L, 0.78 Bq/L, 3.52 Bq/L respectively, which can all meet the requirements of relevant standards.
(3) High removal rate of U in PRB reactor is the result of cooperation of oxidation-reduction reaction, sedimentation, and adsorption.
(4) PRB has some disadvantages, such as reactive materials need to be replaced after being used up, the porosity and permeability will decline as time goes on, which will slow down the reaction and lead to blocking. All of these would go against the practical application of PRB. Lots of studies have to be carried out in future to realize the practical application.

References

1. Beitinger E (1998) Permeable treatment walls design, construction and cost. NATO/CCMS pilot study 1998. Special Session, Treatment Walls and Permeable Reactive Barriers, U.S. EPA. Report No.: 542-R-98-003, vol 229, pp 6–161
2. Lou J, Ma XG, Jing CY et al (2008) Application of PRB in treating acid mine drainage. Min Saf Environ Prot 35(3):83–85
3. Zhai B (2005) PRB application in recovery of groundwater pollution. China Environ Prot Ind 2:33–35
4. Simon F-G, Segebade C, Hedrich M (2003) Behavior of uranium in iron-bearing permeable reactive barriers: investigation with 237U as a radioindicator. Sci Total Environ 307 (1/2/3):231–238
5. Shi J (1990) Uranium geochemistry principle, vol 258. Atomic Energy Press, Beijing
6. Lv J, Xiong Z, Yang Y (2007) The feasibility study of using PRB technology to remedy acid seepage water from uranium mill-tailings. J Huaihua Univ 26(2):64–66

7. GB15848-1995 Regulation for radiation and environment protection in uranium
8. GB14586-1995 Environmental management regulation for the decommissioning of military uranium mining and mills
9. Zhao D, Shi H, Xu G et al (2002) Study on the pretreatment of p-Fluoronitrobenzene wastewater by microelectrolysis. Environ Prot Chem Ind 22(1):15–18
10. McRae CW, Blowes DW, Ptacek C (1997) Laboratory - scale investigation of remediation of As and Se using iron oxides. In: Sixth symposium and exhibition on groundwater and soil remediation, Montreal, Canada, March 1997
11. GB8978-1996 Integrated wastewater discharge Standard

Phenomenological Analysis and Physical Interpretation of the Reflection Coefficient of Clays

Andrea Dominijanni(✉), Nicolò Guarena, and Mario Manassero

Department of Structural, Geotechnical and Building Engineering, Politecnico di Torino, Corso Duca degli Abruzzi 24, 10129 Turin, Italy
andrea.dominijanni@polito.it

Abstract. The reflection coefficient, also known as the chemico-osmotic efficiency coefficient, is commonly measured in order to quantify the ability of clays to act as semipermeable porous media. However, it should be pointed out that this parameter is not a soil property, but it rather represents the soil response to hydraulic and chemical stresses, so that it depends on which test is used and may vary significantly when the clay void ratio, the specimen preparation method and/or the chemical composition of the pore solution are changed. A physically sound model is used to assess the flow mechanisms that govern the experimental determination of this parameter, considering also the effects of clay fabric.

Keywords: Bentonite · Chemico-osmosis · Electro-osmosis · Diffusion

1 Introduction

A clay soil is termed "semipermeable" when it is able to generate a water flux in response to a gradient in the chemical composition of the pore solution (chemico-osmosis). This ability of clays is related to the microscopic interactions that occur between the electrically charged solid particles and the ions that are contained in the pore solution. Since these interactions are related to surface phenomena of an electric nature, chemico-osmosis is only relevant in soils that have a high specific surface, such as bentonites, which are used in geosynthetic clay liners, compacted clay or sand-bentonite mixtures, soil-bentonite cutoff wall backfills and highly compacted bentonite buffers for high-level radioactive nuclear waste containment.

The relevance of the semipermeable behaviour of clays is commonly quantified through the laboratory measurement of the reflection coefficient, ω_m. This parameter is also referred to as the "chemico-osmotic efficiency coefficient" or the "membrane efficiency coefficient" (Malusis et al. 2001; Shackelford 2013), although its range of variation is not limited to between 0 and 1 by thermodynamic constraints. However, since the vast majority of ω values typically range from zero, for porous media without semipermeable properties, to unity, for "ideal" semipermeable porous media, the parameter ω_m is normally considered as an efficiency coefficient. For this reason, the

© Springer Nature Singapore Pte Ltd. 2019
L. Zhan et al. (Eds.): ICEG 2018, ESE, pp. 156–163, 2019.
https://doi.org/10.1007/978-981-13-2227-3_19

values of ω_m that are found outside the 0 to 1 range are generally classified as manifestations of "anomalous osmosis" (Yaroshchuk 1995).

This phenomenological parameter is not a soil property, but it rather represents a measurement of the effects that are determined at the macroscopic scale by the water and ion transport mechanisms which occur at the microscopic scale in response to the imposed hydraulic and chemical boundary conditions. For this reason, a physically sound model is proposed with the aim of providing an interpretation of the obtained macroscopic measurements. Before that, the different types of laboratory tests which are used to measure ω_m are compared and the differences between the obtained results are pointed out.

2 Methods for the Measurement of the Reflection Coefficient

Several test configurations have been conceived in order to measure ω_m (Kemper and Rollins 1966; Yaroshchuk 1995; Malusis et al. 2001, Olsen 2003). Shackelford (2013) classified the different types of tests as open or closed hydraulic control systems.

In the case of a closed hydraulic control system, a direct measurement of ω_m is obtained when the porous medium is interposed between two external bulk solutions that have different ion concentrations, and the volumetric flux of water is hindered across the soil. When these conditions are maintained over time, a hydraulic head difference arises between the specimen boundaries under steady-state conditions. The measured global value of the reflection coefficient, ω_{mc}, is therefore given by:

$$\omega_{mc} = \left(\frac{\Delta P}{\Delta \Pi}\right)_{q=0;I=0} \tag{1}$$

where ΔP is the difference in hydraulic pressure across the porous medium, $\Delta\Pi$ is the difference in osmotic pressure across the porous medium, q is the volumetric flux of the salt solution and I is the electrical current flux. For the sake of simplicity, it is assumed that the aqueous solution contains a single diluted 1:1 salt, so that the difference in osmotic pressure can be expressed through the van't Hoff equation as follows (Malusis et al. 2001):

$$\Delta \Pi = 2 \cdot R \cdot T \cdot (c_0 - c_L) \tag{2}$$

where R is the universal gas constant, T is the absolute temperature, and c_0 and c_L are the salt concentrations of the external bulk solutions in contact with the porous medium.

If an open hydraulic control system is adopted, the reflection coefficient is determined on the basis of the results of a double-stage test. In the first stage, a chemically induced liquid flux is evaluated by placing the porous medium between two reservoirs containing salt solutions of different concentration, but under the same hydraulic pressure. During the second stage, the same specimen is permeated with a solution of constant salt concentration, under the effect of an applied hydraulic pressure gradient

(Kemper and Rollins 1966). The measured value of the reflection coefficient, ω_{mo}, is therefore given by:

$$\omega_{mo} = -\frac{(q)_{\Delta P=0;I=0}}{(q)_{\Delta \Pi=0;I=0}} \cdot \frac{\Delta P}{\Delta \Pi}. \tag{3}$$

A further test configuration that needs to be considered is that of a hyperfiltration experiment, in which a constant volumetric flux, q, of a salt solution of concentration c_0 is imposed through the porous medium, and the downstream concentration of the filtrate solution (i.e. the so-called hyperfiltrate), c_L, is measured under steady state conditions (Olsen 2003). In this case, the measured value of the reflection coefficient, ω_{mh}, is estimated as follows:

$$\omega_{mh} = \left(1 - \frac{c_L}{c_0}\right)_{q \to \infty;I=0}. \tag{4}$$

3 Phenomenological Analysis of the Different Types of Measurements of the Reflection Coefficient

A phenomenological comparison between ω_{mc} and ω_{mo} can be established on the basis of the integration of the following water flux equation (Malusis et al. 2001; Dominijanni and Manassero 2012a):

$$q = -\frac{k}{\gamma_w} \cdot \left(\frac{dP}{dx} - \omega \cdot 2 \cdot R \cdot T \frac{dc_s}{dx}\right). \tag{5}$$

where γ_w is the unit weight of water, k is the hydraulic conductivity, ω is the "local" value of the reflection coefficient, P is the virtual hydraulic pressure and c_s is the virtual salt concentration. The phenomenological coefficients k and ω depend on different variables, such as the salt concentration, the clay void ratio and the clay fabric, as will be illustrated in the next part of the paper (Dominijanni and Manassero 2012b; Dominijanni et al. 2017). However, if the changes in void ratio and fabric across the specimen in a single test stage are sufficiently small, the porous medium can be considered macroscopically homogeneous, and k and ω result to be primarily controlled by the salt concentration. Under steady-state conditions, the integration of Eq. 5 provides the following result:

$$q \cdot \gamma_w \cdot \int_0^L \frac{1}{k} \cdot dx = \Delta P - 2 \cdot R \cdot T \cdot \int_{c_L}^{c_0} \omega \cdot dc_s \tag{6}$$

where L is the length of the specimen.

In the case of a closed hydraulic control system, q = 0 and, as a result:

$$\omega_{mc} = \left(\frac{\Delta P}{\Delta \Pi}\right)_{q=0;I=0} = \frac{2 \cdot R \cdot T \cdot \int_{c_L}^{c_0} \omega \cdot dc_s}{\Delta \Pi} = \frac{1}{\Delta c_s} \cdot \int_{c_L}^{c_0} \omega \cdot dc_s = \omega_g \tag{7}$$

where $\Delta c_s = c_0 - c_L$ is the difference in salt concentration across the porous medium and ω_g is the "global" value of the reflection coefficient, that is the integral mean value of ω (Dominijanni et al. 2018).

In the case of an open hydraulic control system, the measured value of the reflection coefficient is given by:

$$\omega_{mo} = -\frac{(q)_{\Delta P=0;I=0}}{(q)_{\Delta \Pi=0;I=0}} \cdot \frac{\Delta P}{\Delta \Pi} = \frac{1}{\Delta c_s} \cdot \int_{c_L}^{c_0} \omega \cdot dc_s \cdot \frac{\left(\int_0^L \frac{1}{k} \cdot dx\right)_{stage2:\Delta \Pi=0}}{\left(\int_0^L \frac{1}{k} \cdot dx\right)_{stageI:\Delta P=0}}. \tag{8}$$

From these results, it may be concluded that ω_{mc} and ω_{mo} would only be the same if the hydraulic conductivity, k, were independent of the salt concentration. However, the dependence of k on the salt concentration may be rather great, due to different phenomena, such as electroviscosity, induced swelling or shrinkage of the clay and clay fabric modification. One way of limiting the influence of the hydraulic conductivity changes on the measurement of ω_{mo} is to permeate the specimen, in the second stage of the test, with a solution that is obtained by mixing equal parts of the solutions that were used in the first testing stage, as suggested by Kemper and Rollins (1966). Under such conditions, the change in k between the two stages of the test is minimized, and it is possible to assume $\omega_{mo} \cong \omega_{mc}$.

The phenomenological analysis of the hyperfiltration method used to estimate the reflection coefficient requires the integration of the following salt mass flux equation (Malusis and Shackelford 2002; Dominijanni and Manassero 2012a):

$$J_s = (1 - \omega) \cdot q \cdot c_s - n \cdot D_\omega^* \frac{dc_s}{dx}. \tag{9}$$

where n is the clay porosity and D_ω^* is the "local" value of the osmotic effective diffusion coefficient. Since $J_s = q \cdot c_L$ in a hyperfiltration test, the integration of Eq. 9 provides the following result (Yaroshchuk 1995):

$$q \cdot L = \int_{c_L}^{c_0} \frac{n \cdot D_\omega^*}{c_L - (1 - \omega(c_s)) \cdot c_s} \cdot dc_s. \tag{10}$$

where the dependency of ω on c_s has been pointed out. When $q \to \infty$, the denominator in the integrand has to tend to zero at the integration limit $c_s = c_0$, which immediately provides the following result:

$$\omega_{mh} = \left(1 - \frac{c_L}{c_0}\right)_{q \to \infty;I=0} = \omega(c_0). \tag{11}$$

Therefore, the so-called limiting rejection is an estimation of the "local" value of the reflection coefficient in correspondence to the salt concentration of the source solution. As a result, this measurement differs in a substantial way from the previous ones, which provide a "global" value of the reflection coefficient that depends on the values that are assumed by the salt concentration at the two boundaries of the porous medium (Dominijanni et al. 2018). Only when the differences in the salt concentration are sufficiently small can the "global" value of the reflection coefficient be compared with the "local" one, and the result of a closed or open hydraulic controlled system can be compared with the result of a hyperfiltration test. However, it should be stressed that ω_{mh} is obtained from an extrapolation of the experimental data to the asymptotic condition of $q \to \infty$ which is commonly affected by a significant uncertainty.

4 Physical Interpretation of the Reflection Coefficient

A physical interpretation of the macroscopic transport parameters of a clay may be derived from a macroscopic transport model that is obtained by upscaling the Navier-Stokes equation for the volumetric flux of the salt solution and the Nernst-Planck equations for the ion mass fluxes (Dominijanni and Manassero 2012b). The obtained macroscopic equations can be expressed as follows:

$$q = -\kappa_m \left(\frac{d\bar{P}}{dx} + F \cdot \bar{c}_{sk} \cdot \frac{d\bar{\Phi}}{dx} \right). \tag{12}$$

$$J_i = q \cdot \bar{c}_i - (n_m \cdot \tau_m) \cdot D_{0,i} \cdot \left(\frac{d\bar{c}_i}{dx} + z_i \cdot \bar{c}_i \cdot \frac{F}{R \cdot T} \cdot \frac{d\bar{\Phi}}{dx} \right) \quad \text{for } i = a, c. \tag{13}$$

$$I = F \cdot \sum_{i}^{a,c} z_i \cdot J_i = 0. \tag{14}$$

where κ_m is the mechanical permeability (which only depends on the matrix tortuosity, the micro-pore size and the micro-pore volume), F is the Faraday constant, $\bar{c}_{sk}$ is the charge concentration of the solid skeleton, with reference to the void volume, n_m is the porosity of the conductive micro-pores, τ_m is the matrix tortuosity associated to the geometry of the interconnected conductive micro-pores, $D_{0,i}$ is the free-solution or aqueous-phase diffusion coefficient of the i-th ion (i = a for anion; i = c for cation), z_i is the electrochemical valence of the i-th ion ($z_a = -1$; $z_c = 1$), $\bar{P}$ is the real hydraulic pressure within the porous medium, $\bar{\Phi}$ is the real electric potential within the porous medium and $\bar{c}_i$ is the real concentration of the i-th ion within the porous medium.

Integration of Eqs. 12–14 requires $\bar{P}$ and $\bar{c}_i$ to be known at the boundaries of the porous medium. These quantities can be derived from the Donnan equations of equilibrium as follows (Dominijanni et al. 2013):

$$\bar{c}_{a,0} = -\bar{c}_{sk}/2 + \sqrt{(\bar{c}_{sk}/2)^2 + c_0^2} \qquad \bar{c}_{a,L} = -\bar{c}_{sk}/2 + \sqrt{(\bar{c}_{sk}/2)^2 + c_L^2} \tag{15}$$

$$\bar{c}_{c,0} = \bar{c}_{a,0} + \bar{c}_{sk} \qquad \bar{c}_{c,L} = \bar{c}_{a,L} + \bar{c}_{sk} \tag{16}$$

$$\bar{P}_0 = P_0 + R \cdot T \cdot \left(\bar{c}_{c,0} + \bar{c}_{a,0} - 2 \cdot c_0\right) \qquad \bar{P}_L = P_L + R \cdot T \cdot \left(\bar{c}_{c,L} + \bar{c}_{a,L} - 2 \cdot c_L\right). \tag{17}$$

For a close hydraulic control system, q = 0 and the combination of Eqs. 13 and 14 yields:

$$\Delta\bar{\Phi} = \frac{R \cdot T}{F} \cdot \left(\frac{D_{0,c} - D_{0,a}}{D_{0,c} + D_{0,a}}\right) \cdot \ln\left(\frac{D_{0,c} \cdot \bar{c}_{c,L} + D_{0,a} \cdot \bar{c}_{a,L}}{D_{0,c} \cdot \bar{c}_{c,0} + D_{0,a} \cdot \bar{c}_{a,0}}\right). \tag{18}$$

In the absence of an electric current flux, the electric potential gradient is generated in response to the diffusion of the ions, which move with different velocities, due to the difference between the free-solution diffusion coefficient of the anion and free-solution diffusion coefficient of the cation.

The measured reflection coefficient can be evaluated as follows:

$$\omega_{mc} = \left(\frac{\Delta P}{\Delta\Pi}\right)_{q=0;I=0} = \frac{\Delta\Pi - \Delta\bar{\Pi} - F \cdot \bar{c}_{sk} \cdot \Delta\bar{\Phi}}{\Delta\Pi} \tag{19}$$

where $\Delta\bar{\Pi} = R \cdot T \cdot (\bar{c}_{c,0} + \bar{c}_{a,0} - \bar{c}_{c,L} - \bar{c}_{a,L})$.

As a result, the physical model shows that two mechanisms contribute to determining the measured reflection coefficient:

1. the ion partition expressed by the term $\Omega_p = (1 - \Delta\bar{\Pi}/\Delta\Pi)$;
2. the diffusion induced electro-osmosis given by term $\Omega_e = (-F \cdot \bar{c}_{sk} \cdot \Delta\bar{\Phi}/\Delta\Pi)$.

While Ω_p is always positive, which means that it is related to a water flux which is directed from the low salt concentration side to the high salt concentration side, the electro-osmotic contribution Ω_e is always negative for $D_{0,a} > D_{0,c}$, so that the sign of $\omega_{m1} = \Omega_p + \Omega_e$ depends on the relative magnitude of the two contributions. Negative osmosis is obtained when $|\Omega_e| > |\Omega_p|$, i.e. when diffusion induced electro-osmosis is dominant over the actual chemical-osmosis that is only related to the ion partition effect. An example of the weights of these contributions is shown in Fig. 1 for a value of $\bar{c}_{sk} = 21.1$ mM, as measured by Dominijanni et al. (2013) on a natural sodium bentonite with a total porosity of 0.81.

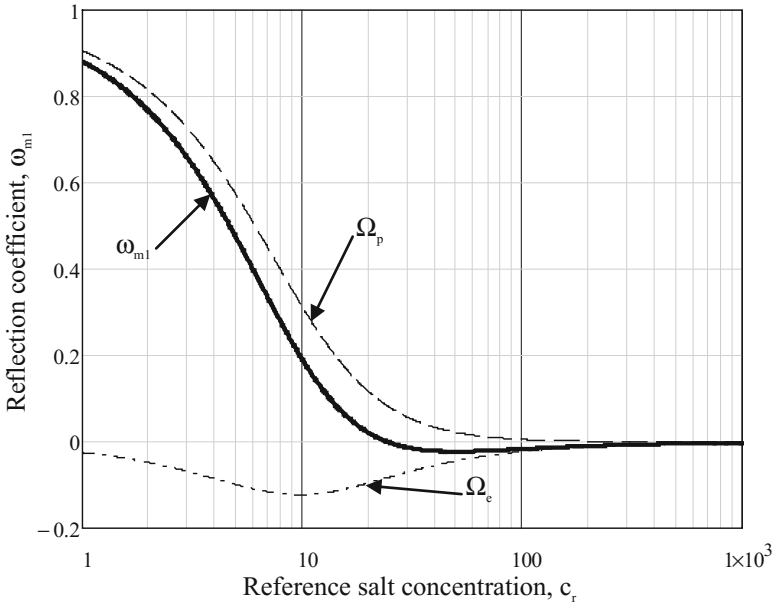

Fig. 1. Measured reflection coefficient, ω_{m1}, and its components Ω_p (ion partition) and Ω_e (electro-osmosis) as a function of the salt concentration c_r, which is related to the boundary salt concentrations as follows: $c_0 = 1.1 \cdot c_r$ and $c_L = 0.9 \cdot c_r$. The salt is sodium chloride (NaCl) and the fixed charge concentration is equal to 21.1 mM, as obtained by Dominijanni et al. 2013

5 Conclusions

The proposed physical interpretation of the reflection coefficient provides an explanation of the microscopic mechanisms that determine the results of experimental tests. In particular, the fixed charge concentration $\bar{c}_{sk}$ appears to be the fundamental material parameter that governs chemical-osmosis.

Dominijanni et al. (2018) showed, for tests conducted on specimens of the same bentonite, but with different void ratios, that the experimental data can be interpreted by assuming

$$\bar{c}_{sk} = \bar{c}'_{sk,0} \Big/ e \tag{20}$$

where $\bar{c}'_{sk,0}$ is the solid charge coefficient, which is mainly controlled by the bentonite fabric, and which can only be assumed constant over the range of relatively low values of salt concentration (i.e. $c_s < 0.1$ M). However, it should be stressed that significant changes in $\bar{c}'_{sk,0}$ are expected in specimens which are prepared with different procedures (e.g. due to the different methods of compaction, salt flushing, hydration and consolidation that are adopted). As a consequence, it is difficult to compare the measured values of the reflection coefficient if they are obtained from different types of tests and different specimen preparation methods.

References

Dominijanni A, Guarena N, Manassero M (2018) Laboratory assessment of the semipermeable properties of a natural sodium bentonite. Can Geotech J (Accepted)

Dominijanni A, Manassero M (2012a) Modelling the swelling and osmotic properties of clay soils. Part I: the phenomenological approach. Int J Eng Sci 51:32–50

Dominijanni A, Manassero M (2012b) Modelling the swelling and osmotic properties of clay soils. Part II: the physical approach. Int J Eng Sci 51:51–73

Dominijanni A, Manassero M, Boffa G, Puma S (2017) Intrinsic and state parameters governing the efficiency of bentonite barriers for contaminant control. In: Springer series in geomechanics and geoengineering, pp 45–56

Dominijanni A, Manassero M, Puma S (2013) Coupled chemical-hydraulic-mechanical behaviour of bentonites. Géotechnique 63(3):191–205

Kemper WD, Rollins JB (1966) Osmotic efficiency coefficients across compacted clays. Soil Sci Soc Am J 30(5):529–534

Malusis MA, Shackelford CD (2002) Coupling effects during steady state solute diffusion through a semipermeable clay membrane. Environ Sci Technol 36(6):1312–1319

Malusis MA, Shackelford CD, Olsen HW (2001) A laboratory apparatus to measure chemico-osmotic efficiency coefficients for clay soils. Geotech Test J 24(3):229–242

Olsen HW (2003) Coupled chemical and liquid fluxes in earthen materials. In: Germaine JT et al (eds) Soil behavior and soft ground construction, vol 119. ASCE, GSP, pp 57–85

Shackelford CD (2013) Membrane behavior in engineered bentonite-based containment barriers: State of the art. In: Proceedings of the international symposium on coupled phenomena in environmental geotechnics. CRC Press/Balkema, London, pp 45–60

Yaroshchuk AE (1995) Osmosis and reverse osmosis in fine-charged diaphragms and membranes. Adv Colloid Interf Sci 60(1–2):1–93

Numerical Model for Electro-Osmotic Drainage in Unsaturated Soils

Liujiang Wang(✉), Sihong Liu, Yaoming Wang, and Chenyang Xue

College of Water Conservancy and Hydropower, Hohai University,
Xikang Road 1, Nanjing 210098, China
15850514642@163.com

Abstract. A numerical model coupling of water flow and electrical transport in a deformable porous medium is developed to simulate the electroosmosis drainage in the unsaturated soil. This model is in accounting for unsaturated-induced nonlinear changes in the physical and geoelectrical properties that take place on the soil, with the additions of two-dimensional consolidation, and an external hydraulic gradient. The exponential relation is used to represent nonlinear changes in the hydraulic and electro-osmotic conductivities, and soil-water retention curve. The algorithm of this model is conducted using finite-element method. The pore water pressure, settlement, moisture content, drainage, and electric potential and current density as a function of time and position within the soil can be obtained. Finally, the proposed numerical solution is verified to be accurate compared with the experimental measurement.

Keywords: Electroosmosis · Drainage · Numerical modelling
Unsaturated soil · Validation

1 Introduction

Over the past few decades, there has been substantial infrastructure development for soft foundations around the world, which calls for time efficient ground improvement technology. Electro-osmosis, among various methods developed for the improvement of these soft foundations, is an alternative method for soil improvement. This method, which involves the application of a potential difference between electrodes and causes the flow of water from the anode towards the cathode, has proven to be a promising method, especially for soils with low permeability.

While various analytical solutions (Esrig 1968; Wan and Mitchell 1976; Feldkamp and Belhomme 1990; Shang 1998; Li et al. 2010; Xu et al. 2011; Wu and Hu 2013; Wang et al. 2013) and numerical simulations (Lewis and Garner 2010; Rittirong and Shang 2008; Zhou et al. 2013; Yuan and Hicks 2013, 2016; Hu et al. 2012; Hu and Wu 2013; Deng and Zhou 2016; Wang et al. 2012, 2016) have been conducted to examine the behaviour of pore water flow within electro-osmotic drainage systems. However, most of these studies focused on fully saturated conditions. For electro-osmotic drainage, the soil water is permitted to drain at the cathode and is prevented from entering the anode, which leads to a decrease of the soil water content. Thus, soil changes from the saturated state into the unsaturated state during the electro-osmotic drainage

© Springer Nature Singapore Pte Ltd. 2019
L. Zhan et al. (Eds.): ICEG 2018, ESE, pp. 164–171, 2019.
https://doi.org/10.1007/978-981-13-2227-3_20

process, especially for soils near the anode. As such, the total drainage and drainage time are overestimated using the analytical and numerical models proposed under fully saturated conditions compared with those under unsaturated conditions.

To our knowledge, fewer mathematic models exist for electro-osmotic drainage in unsaturated soils. Wang et al. (2012) proposed a mathematical model considering the coupling effects of an electrical field, a seepage field and a stress field based on the theory of unsaturated multiphase porous media. Yuan and Hicks (2016) further derived the formulation with consideration of the influence of gas generation in electro-osmosis consolidation. Although both of the mathematic models considered unsaturated flow effects, they were only validated against laboratory tests performed on saturated soil or a 1-D analytical solution for the electro-osmosis consolidation of a saturated soil. The influence of the saturation degree on the electro-osmotic drainage was not well studied. Thus, the objective to this paper is to develop a theoretical model to adequately describe the behaviour of electro-osmotic drainage subject to the effects of unsaturated flow and hydro-mechanical coupling. Then, a time-dependent finite-element method (FEM) model is developed based on the proposed theory, and validated against laboratory experiments performed under unsaturated conditions.

2 Formulation of Governing Equations

The governing equations for the electrical potential and hydraulic head distributions are derived based on the following assumptions. (1) The current due to electrophoresis of the fine-grained particles is negligible. (2) The effect of electrical-chemical reactions is negligible. (3) Flow of fluid due to an electrical and a hydraulic gradient may be superimposed to obtain the total flow. (4) The electrical gradient caused by movement of the ions is negligible compared to the applied electrical field. (5) The pore air pressure in the soil is kept unchanged, and a constant atmospheric pressure is maintained. (6) The constitutive behaviour of the soil is isotropic and linear elastic, and net stress and suction are both taken as independent stress variables. (7) Ohm's law is valid. (8) Darcy's law is valid.

2.1 Balance of Water Mass

According to the above assumption, the fluid flow due to electrical and hydraulic gradients may be superimposed to obtain the total flow as follows:

$$v = v_h + v_{eo} = -\frac{k_w(u_w)}{\gamma_w}\left(\frac{\partial u_w}{\partial x_i} + \gamma_w z\right) - k_{eo}(u_w)\frac{\partial U}{\partial x_i} \tag{1.1}$$

where x_i represents the x-, y-, z-direction; v is the velocity vector of the pore water; v_h and v_{eo} are the hydraulic flow velocity vector and electro-osmotic flow velocity vector, respectively; u_w is the excess pore water pressure; k_w, γ_w and z are the hydraulic permeability for unsaturated soils, the unit weight of water and the elevation, respectively; k_{eo} is the electro-osmotic permeability for unsaturated soils; and U is the electric potential.

Applying the conservation of water mass and considering the deformation of the unsaturated soil, the nonlinear differential equation describing water flow in unsaturated soils during the electro-osmosis is expressed as follows:

$$n\frac{\partial S_r}{\partial u_w}\frac{\partial u_w}{\partial t}+\beta_w\frac{\theta}{\rho_w}\frac{\partial u_w}{\partial t}-S_r\alpha_c\frac{\partial \varepsilon_v}{\partial t}=-\frac{\partial v}{\partial x_i} \tag{1.2}$$

where θ is the volumetric water content; t is the time; ε_v is the bulk strain, $\varepsilon_v = \varepsilon_x + \varepsilon_y + \varepsilon_z$ in the three dimensional problem; S_r is the degree of saturation; ρ_w is the density of water; n is the porosity of the soil mass; $\alpha_c = 1 - K/K_s$ is Biot's hydro-mechanical coupling coefficient ($0 \leq \alpha_c \leq 1$); K is the bulk modulus of the soil skeleton, K_s is the bulk modulus of the soil fabric material; $\beta_w = \partial\rho_w/\partial u_w$ is the compressibility of water; and $\partial S_r/\partial u_w$ is the specific storativity.

The three-dimensional stress-strain relationships related to the normal strains are expressed in an incremental form as:

$$\frac{d\varepsilon_v}{3}=\frac{(1-2\mu)d\bar{p}}{E}+\frac{d(u_a-u_w)}{F} \tag{1.3}$$

in which $\bar{p}$ is the net mean stress ($\sigma - u_a$), σ is the total stress, u_a is the pore air pressure, ($u_a - u_w$) or s is the soil suction, E is the elasticity modulus of the partially saturated porous medium upon a variation of the net normal stresses; and μ is Poisson's ratio. F denotes the elastic modulus of the partially saturated porous medium upon a variation of soil suction, which is a function of stress, while $F < 0$ when the soil mass is collapsible and $F > 0$ when the soil is expansive. If there is no stress change, ε_v is only related to u_w under constant u_a.

The stress state in the soil foundation is related to electro-osmosis dewatering. If there is no loading, the total stress is unchanged, and the net mean stress remains constant according to supposition (5). The pore water moves from the anode to the cathode and discharges from drainage pipe during the process, and the effective stress in the unsaturated soils vary with changes in pore water pressure. On the basis of suppositions (5) and (6), Eq. (1.3) becomes the following:

$$\frac{\partial \varepsilon_v}{\partial t}=-\frac{3}{F}\frac{\partial u_w}{\partial t} \tag{1.4}$$

Substituting Eqs. (1.1) and (1.4) into Eq. (1.2) and neglecting the compressibility of water ($\beta_w = 0$), the electro-osmosis dewatering incorporating hydro-mechanical coupling can be represented in the following form:

$$\left(n\frac{\partial S_r}{\partial u_w}+\frac{3S_r\alpha_c}{F}\right)\frac{\partial u_w}{\partial t}=-\frac{\partial}{\partial x_i}\left(\frac{k_w(u_w)}{\gamma_w}\left(\frac{\partial u_w}{\partial x_i}+\gamma_w z\right)+k_{eo}(u_w)\frac{\partial U}{\partial x_i}\right) \tag{1.5}$$

Based on the relationship between the volumetric water content and the degree of saturation, i.e. $\theta = nS_r$, the degree of saturation, hydraulic permeability of a partially saturated porous medium are assumed to take the following forms (Gardner 1958):

$$S_r(u_w) = \begin{cases} 1 & u_w \geq -\psi_{ae} \\ (1 - S_{rw}) \exp[\alpha_G(u_w + \psi_{ae})] + S_{rw} & u_w < -\psi_{ae} \end{cases} \tag{1.6a}$$

$$k_w(u_w) = \begin{cases} k_s & u_w \geq -\psi_{ae} \\ k_s \exp\left[\beta_G(u_w + \psi_{ae})\right] & u_w < -\psi_{ae} \end{cases} \tag{1.6b}$$

where S_{rw} is the residual water saturation; α_G is the desaturation coefficient; ψ_{ae} is the air-entry value; k_s is the saturated hydraulic permeability; and β_G is the relative exponent for hydraulic permeability.

For the electro-osmotic permeability in unsaturated conditions, only a few tests have been reported. Based on the laboratory data in literature, Tamagnini et al. (2010) suggest that the relative electro-osmotic permeability can be given as a function of the degree of saturation. Thus, we assumed that electro-osmotic permeability also satisfied the relation of exponential function as hydraulic permeability.

$$k_{eo}(u_w) = \begin{cases} k_e & u_w \geq -\psi_{ae} \\ k_e \exp\left[\gamma_G(u_w + \psi_{ae})\right] & u_w < -\psi_{ae} \end{cases} \tag{1.7}$$

where k_e is the electro-osmotic permeability under fully saturated condition; and γ_G is the relative exponent. To facilitate the determination of the soil parameters according to the laboratory experiments, the influence of the change of porosity to the soil-water retention curve, hydraulic and electro-osmotic conductivities was neglected in this study.

2.2 Electric Current Density Balance Equation

According to Ohm's law, the electrical current flow can be expressed by

$$j = -k_\sigma \frac{\partial U}{\partial x_i} \tag{1.8}$$

where k_σ is the electrical conductivity of the soil. The electrical conductivity is a function of the soil mineralogy and pore fluid composition. However, it is evident from experiments that the electrical conductivity of the pore water is greater than that of the bulk soil. The effective electrical conductivity of an unsaturated porous medium can be represented by (Mualem and Friedman 1991):

$$k_\sigma = \chi_{rel}(S_r)k_{\sigma w} + k_{\sigma s} \tag{1.9}$$

where $k_{\sigma s}$ is the electric conductivity of the solid skeleton, $k_{\sigma w}$ is the electric conductivity of the pore water under saturated conditions, and $\chi_{rel}(S_r)$ is the relative electrical conductivity. The variable A is related to the degree of water saturation and can be described by the power law as follows (Mattson et al. 2002):

$$\chi_{rel} = cS_r^d \tag{1.10}$$

where c and d are material parameters.

By applying the conservation of charge, the governing equation for the electric field can be represented as

$$C_p \frac{\partial U}{\partial t} = k_\sigma(u_w) \frac{\partial^2 U}{\partial x_i^2} \tag{1.11}$$

where C_p is the electrical capacitance per unit volume. Neglecting the electrical capacitance of the soil, $C_p = 0$ is assumed in this paper.

2.3 Finite-Element Formulation

The governing equations can be solved by the finite element method. Time integration and the Newton-Raphson methods (Wang et al. 2012; Yuan and Hicks 2013) are used to solve the coupled governing equation system. As shown in Eq. (1.4), the bulk strain increment will be obtained after the pore-water pressure was solved at each time step. Then, using the bulk strain increment in the FEM code for stress-strain analysis, the soil deformation during electro-osmosis can be achieved, and the deformation obtained in this study is not induced by loading but by electro-osmotic drainage only.

3 Validation

The laboratory experiment of electro-osmotic drainage at different initial degrees of saturation was conducted (Sun et al. 2016). The experimental setup is shown in Fig. 1. The soil samples with the initial degrees of saturation 98% (Case 1), 84% (Case 2), and 74% (Case 3) were placed in the EK cell. The EK cell was made of 10-mm-thick Plexiglas with inside dimensions of 200 × 120 × 120 mm (length × width × height). The relevant parameters are shown in Table 1. Based on the proposed numerical solution for a subsurface drainage system with electro-osmosis in unsaturated soils, the behaviours of electro-osmotic drainage are shown in Fig. 2. It can be found that the predicted cumulative water seepage, settlement, and current are close to the experimental measurements. It means that the proposed numerical model can be applied in practical engineering reasonably.

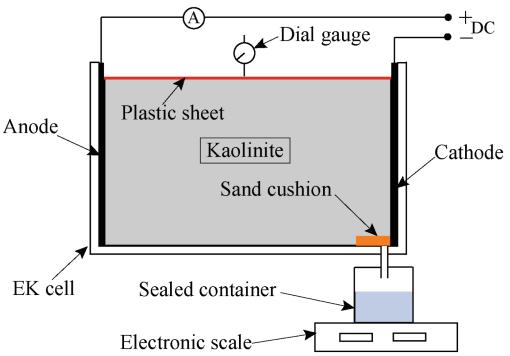

Fig. 1. Layout of the laboratory test

Table 1. Basic parameters for electro-osmotic drainage in the numerical model

Parameter	Value
Saturated hydraulic permeability, k_s: m/s	1.21×10^{-9}
Saturated electro-osmotic permeability, k_e: m^2/s per V	2.23×10^{-9}
Initial porosity, e_0	0.5
Air-entry value, ψ_{ae}: kPa	10
Residual water saturation, S_{rw}	0.45
Desaturation coefficient, α_G: kPa^{-1}	0.001
Relative exponent for hydraulic permeability, β_G: kPa^{-1}	0.001
Relative exponent for hydraulic permeability, γ_G: kPa^{-1}	0.001
Young's modulus, E: kPa	5.0×10^3
Poisson's ratio, μ	0.3
Elastic modulus with respect to suction change, F: kPa	9.0×10^3
Biot's hydro-mechanical coupling coefficient, α_c	0.7
Electric conductivity of the pore water, $k_{\sigma w}$: S/m,	0.033
Constant related to the relative electric conductivity, c	1.3
Constant related to the relative electric conductivity, d	4.0
Applied voltage, U_a: V	30

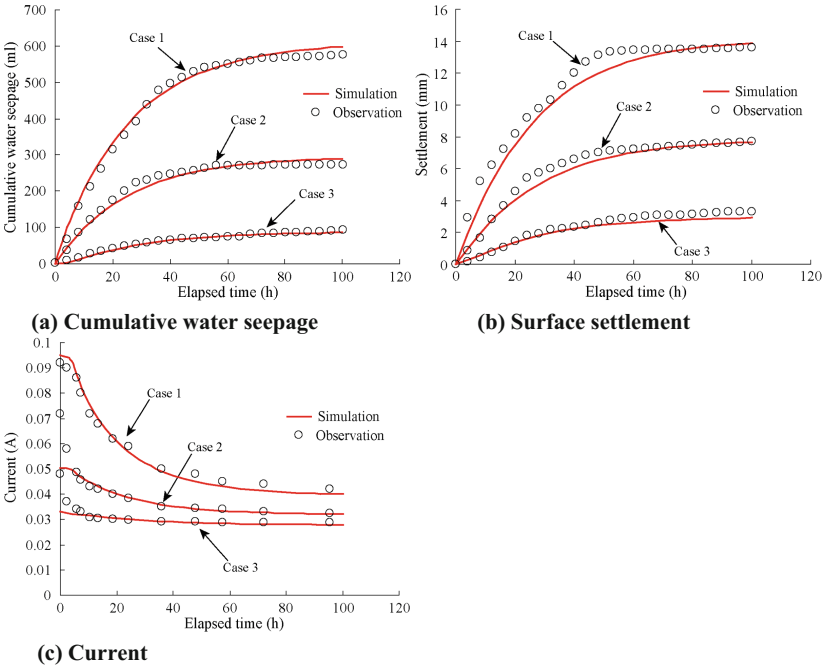

(a) Cumulative water seepage **(b) Surface settlement**

(c) Current

Fig. 2. Comparison between the measured and predicted results

4 Conclusion

A numerical model for electro-osmotic drainage under unsaturated conditions has been proposed; this model can simulate the coupling of water flow and electrical transport in a deformable porous medium. The nonlinear changes of the properties (including electro-osmotic conductivity, hydraulic conductivity, and electrical resistivity) induced by the changes of degree of saturation, and an external hydraulic gradient acting at the boundaries of the soil layer are taken into account. The proposed numerical solution is verified to be accurate compared with the experiments that conducted under different initial degree of saturation.

Acknowledgment. Financial support from the National Natural Science Foundation of China (Grant no. 51509077) and the Fundamental Research Funds for the Central Universities (Grant no. 2016B03514) are gratefully acknowledged.

References

Deng A, Zhou Y (2016) Modeling electroosmosis and surcharge preloading consolidation. I: model formulation. J Geotech Geoenviron Eng 142(4):04015093

Esrig MI (1968) Pore pressures, consolidation, and electrokinetics. J Soil Mech Found Div 94 (4):899–922

Feldkamp JR, Belhomme GM (1990) Large-strain electrokinetic consolidation: theory and experiment in one dimension. Géotechnique 40(4):557–568

Gardner WR (1958) Some steady-state solutions of the unsaturated moisture flow equation with application to evaporation from a water table. Soil Sci 85(4):228–232

Hu L, Wu W, Wu H (2012) Numerical model of electro-osmotic consolidation in clay. Géotechnique 62(6):537–541

Hu L, Wu H (2013) Mathematical model of electro-osmotic consolidation for soft ground improvement. Géotechnique 64(2):155–164

Lewis RW, Garner RW (2010) A finite element solution of coupled electrokinetic and hydrodynamic flow in porous media. Int J Numer Methods Eng 5(1):41–55

Li Y, Gong XN, Lu MM et al (2010) Coupling consolidation theory under combined action of load and electro-osmosis. Chin J Geotech Eng 32(1):77–81

Mualem Y, Friedman S (1991) Theoretical prediction of electrical conductivity in saturated and unsaturated soil. Water Resour Res 27(10):2771–2777

Mattson ED, Bowman RS, Lindgren ER (2002) Electrokinetic ion transport through unsaturated soil: 1. Theory, model development, and testing. J Contam Hydrol 54(1–2):99–120

Rittirong A, Shang JQ (2008) Numerical analysis for electroosmotic consolidation in two-dimensional electric field. In: Proceedings of the 18th international offshore and polar engineering conference, Vancouver, pp 566–572

Shang JQ (1998) Electroosmosis-enhanced preloading consolidation via vertical drains. Can Geotech J 35(35):491–499

Sun YC, Yang JG, Li QM et al (2016) Electro-osmosis tests of unsaturated clays. Sci Technol Eng 16(21):307–312

Tamagnini C, Jommi C, Cattaneo F (2010) A model for coupled electro-hydro-mechanical processes in fine grained soils accounting for gas generation and transport. Anais da Academia Brasileira de Ciencias 82(1):169–193

Wan TY, Mitchell JK (1976) Electro-osmotic consolidation of soils. J Geotech Geoenviron Eng 102(2):473–491

Wang LJ, Liu SH, Wang JB et al (2012) Numerical analysis of electro-osmostic consolidation based on coupled electrical field-seepage field-stress field. Rock Soil Mech 33(6):1904–1911

Wang LJ, Liu SH, Wang ZJ et al (2013) A consolidation theory for one-dimensional large deformation problems under combined action of load and electro-osmosis. Eng Mech 30 (12):91–98

Wu H, Hu L (2013) Analytical solution for axisymmetric electro-osmotic consolidation. Geotechnique 63(12):1074–1079

Wang LJ, Liu SH, Chen SK et al (2016) Numerical simulation of electro-osmostic drainage test based thermo-hydro-mechanical coupling model. J Cent South Univ (Sci Technol) 47(3):889–896

Yuan J, Hicks MA (2013) Large deformation elastic electro-osmosis consolidation of clays. Comput Geotech 54(10):60–68

Yuan J, Hicks MA (2016) Influence of gas generation in electro-osmosis consolidation. Int J Numer Anal Methods Geomech 40(11):1570–1593

Zhou Y, Deng A, Wang C (2013) Finite-difference model for one-dimensional electro-osmotic consolidation. Comput Geotech 54(54):152–165

The Properties of Reinforced Retaining Wall Under Cyclic Loading

Lihua Li[1], Junchao Yang[1,2], Zhi Hu[1(✉)], Henglin Xiao[1], and Yongli Liu[1]

[1] School of Civil Engineering, Architecture and Environment, Hubei University of Technology, Wuhan 430068, China
huzhi@hbut.edu.cn
[2] School of Civil Engineering and Architecture, Wuhan University of Technology, Wuhan 430070, China

Abstract. In this study, waste tires-biaxial geogrids combining reinforced retaining walls were thoroughly investigated using the independently-developed apparatus for simulating cyclic loading. A comparative analysis was conducted between biaxial geogrids, waste tires, geocells, and different layout schemes of tire-geogrids. The dynamic earth pressures and accelerations of different reinforced retaining walls subjected to cyclic loading were investigated to determine the optimal combining scheme of tire-geogrids. The tests demonstrate that the tire-geogrid reinforcement materials are propitious to enhancing anti-seismic performance and the stability of reinforced retaining walls. Additionally, in the scheme of tire-geogrid reinforcement, the effectiveness is better when the space between tires equals to the radius of the tire, which could save 30% of material cost. Under the cyclic load, the dynamic earth pressure and acceleration of the tire-geogrid reinforced retaining wall increase with increasing relative wall height (y/H). The acceleration peaks at the top of the wall. Moreover, the dynamic earth pressure changes with the variations of cyclic loading amplitude, and after reaching its peak value, the growth rate slows down and the value becomes stable.

Keywords: Waste tires · Geogrid · Vehicle load · Reinforced retaining wall
Dynamic earth pressure · Acceleration response

1 Introduction

Waste tires known as "black pollution" in the world are difficult to deal with. How to utilize the enormous waste tires has become a serious international economic and environmental issue. Waste tires have the advantages of high tensile strength, good toughness, anti-wear, aging-resistance and anti-collision. Waste tires reinforcement makes the construction easy and low-cost while adapting to deformation and having long-term stability [1]. What is more, using waste tires is an environmentally sound practice and indestructible [2]. On the other hand, the pull out tests of the tire strips shows a better interlock between tire strip and sand, comparing with the uniaxial and biaxial geogrids [3].

© Springer Nature Singapore Pte Ltd. 2019
L. Zhan et al. (Eds.): ICEG 2018, ESE, pp. 172–180, 2019.
https://doi.org/10.1007/978-981-13-2227-3_21

In geotechnical engineering, the tire-faced retaining wall, sometimes known as "fabric wall", built on National Forest roads, was proved to be low cost and environment-friendly [4]. The grid composed of tread and sidewall of waste tires have been successfully used to improve the bearing capacity of reinforced foundations [5]. To deal with problems from overweight vehicles, more researches of roadbed and their retaining structures under vehicle load are conducted, showing that the traffic loading will accelerate the accumulation of the permanent strain of roadbed [6–9]. A pseudo-static method is proposed to calculate the long-term settlement of the soft subgrade induced by traffic loading [10]. However, the relevant studies on dynamics of reinforced retaining wall are rare.

This paper studies the effect of tires spacing, reinforcement materials and speed on dynamic earth pressure and acceleration of retaining wall. The behavior of optimal tire-geogrid reinforced retaining walls have been studied under cyclic loading tests.

2 Experimental Method and Materials

The test equipment consists of an electro hydraulic servo loading system, a vehicle circulating device and a test box. The servo loading system can simulate vehicle load and the motor can simulate the vehicle speed. A 20 mm-thick layer of standard sand was laid at the bottom of the box to act as foundation.

A reduced-scale (1/5) model is established to simulate the reinforced retaining wall. A Polyethylene film (thickness: 0.24 mm, tensile strength: 0.91 MPa) was used to replace the geocell (thickness: 1.2 mm, tensile strength: 18.49 MPa). A 10 cm diameter, 2 cm thick Polyethylene tire was selected to simulate the 175/65/R14 tire. The biaxial geogrid (size: 30 × 30 mm, tensile strength: 20 kN/m) was replaced by a Polyethylene net (size: 6 × 6 mm, tensile strength: 0.7 kN/m). The steel wire was replaced by high tensile strapping tape to fix tires and geogrids.

The experimental schemes are shown in Table 1. The vehicle load is increased from 20 kPa to 100 kPa and then reduced to 20 kPa with a load increment of 20 kPa. The loading period for each stage is 2 min and rotation speed of wheels are constant.

3 Experimental Contrast of Reinforcement Materials

3.1 Effects on Dynamic Earth Pressure

Figure 1 shows the effect of different reinforcement materials on dynamic earth pressure. The relative wall height is defined by y/H, where H is height of the retaining wall and y is LVDT position from base of the wall. At a distance of 300 mm to the facing panel and y/H = 0.5, the earth pressure peak of tire-geogrid groups (G4 ~ G8) is 17% lower than geocells, and 34% lower than geogrids. The stress diffusion rate (SDR) illustrated in Eq. (1) are applied to evaluate the effectiveness of tire-geogrid schemes with different tire spacing. From Table 2, the observed SDR of G4 shows the highest value. Compared to G4, the SDR of G7 is closer and G7 can save 30% of cost. Therefore, G7 is the optimal combination.

Table 1. Testing program

	Materials	Combinations	Spacing (cm)	Load time (min)	Speed (km/h)
G1	Geogrid	—	20	120	80
G2	Geocell	—	20	120	80
G3	Waste tire	Fully paved	20	120	80
G4	Tire-geogrid	Fully paved	20	120	80
G5	Tire-geogrid	$s_x = s_y = D$	20	120	80
G6	Tire-geogrid	$s_x = 0, s_y = D$	20	120	80
G7	Tire-geogrid	$s_x = s_y = 0.5D$	20	120	80
G8	Tire-geogrid	$s_x = 0, s_y = 0.5D$	20	360	80
G9	Tire-geogrid	$s_x = s_y = 0.5D$	20	360	60
G10	Tire-geogrid	$s_x = s_y = 0.5D$	20	360	100

Note: D = diameter of tire; s_x = x-axils spacing between tires; s_y = y-axils spacing between tires.

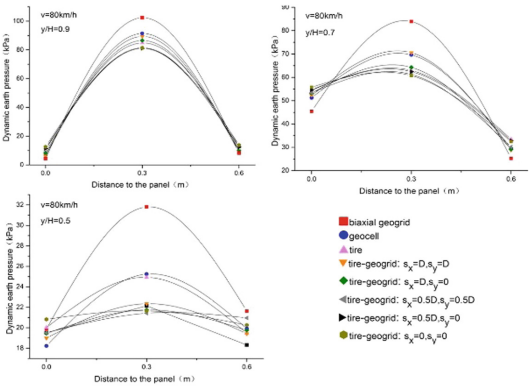

Fig. 1. Dynamic earth pressure peak

Table 2. Stress diffusion rate of tire-geogrid

Stress diffusion rate	y/H = 0.9	y/H = 0.7	y/H = 0.5
Tire-geogrid $s_x = s_y = D$ (G5)	44.7	72.2	96.4
Tire-geogrid $s_x = D, s_y = 0$ (G6)	47.9	76.6	97.8
Tire-geogrid $s_x = s_y = 0.5D$ (G7)	53.2	79.3	98.5
Tire-geogrid $s_x = 0.5D, s_y = 0$ (G8)	53.6	80.3	98.7
Tire-geogrid $s_x = s_y = 0$ (G4)	54.1	81.2	99.1

$$SDR = \frac{P_m - (\sum_1^n |P_n - P_{n-1}| \div n)}{P_m} \quad (1)$$

where, n—The number of test point,
P_n—Earth pressure peak of each test point,
P_m—Maximal vertical load.

3.2 Effects on Acceleration of Reinforced Retaining Wall

Figure 2 shows the relationship between y/H and acceleration peak. The acceleration peak increases with increasing y/H, indicating that the maximum acceleration of the retaining wall occurs at the crest portion of the wall. The acceleration peaks of tire-geogrid (G4-G8) are lower than those of geogrids and geocells, which can reveal better anti-seismic performance of tire-geogrid. The reinforcement performance of tires in tire-geogrids is similar to that of geocells which can enhance the lateral restraint of backfill and improve the stability of retaining walls. The G4 ($s_x = s_y = 0$) shows the best anti-seismic performance, while taking into account its cost, the G7 is a more reasonable choice.

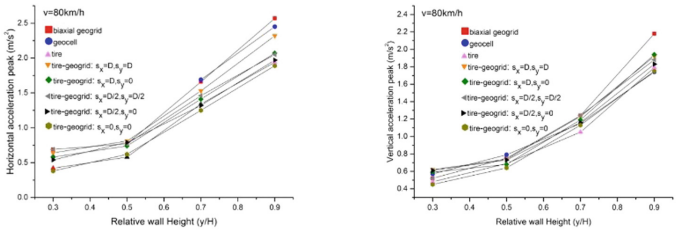

Fig. 2. Acceleration peak of each group: horizontal (left) and vertical (right)

4 The Model Test of Tire-Geogrid Reinforced Retaining Wall

Since the optimal group of tire-geogrids ($s_x = s_y = 0.5D$) was chosen in the last section, the vehicle load tests at different speed (60 km/h, 80 km/h, 100 km/h) were conducted.

4.1 Effect of Different Speed on Dynamic Earth Pressure

Figure 3 shows that dynamic earth pressure increases with increased relative wall height, indicating pressure peak at the top of the retaining wall. The earth pressure also increases with increased vertical load and load time. It is noteworthy that the earth pressure peak suddenly increases when the load time reaches 130 min to 170 min. When the maximum peak is reached, the earth pressure slowly decreases to stable values as the load time increases. Moreover, higher speed generates larger earth pressure peak. Compared with 60 km/h, the groups of 80 km/h and 100 km/h are increased by 12% and 22% respectively.

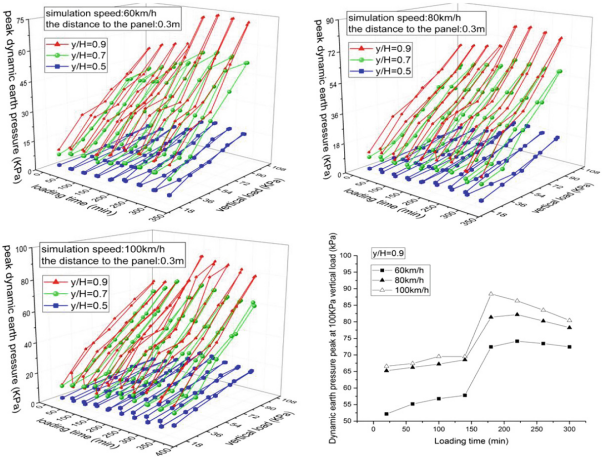

Fig. 3. Dynamic earth pressure of tire-geogrid reinforced retaining wall

When the load time reaches 130 min to 170 min, the rate of speed increase is faster than 4 $\sim$ 5 times the average rate. It is demonstrated that the increase of the number of cyclic loading leads to the repeated compaction of the soil, so that the degree of compaction of soil becomes higher and dynamic earth pressure increase. After the earth pressure peak is reached, the pressure slowly decreases and tends to stabilize. Due to the repeatability and continuity of cyclic loads, the contact between soil and reinforcing material becomes closer after repeated compaction and vibration, to exert sufficiently the reinforcing effect of tire-geogrid.

4.2 Effects of Different Speed on Acceleration

To simplify the presentation of vertical distribution of the acceleration, acceleration amplification factors at different elevation are used. Then, acceleration amplification factors are calculated using the root mean square method (RMS) applied to the acceleration time history for each accelerometer at special elevation, as shown in Eq. (2).

$$RMS = \left[\frac{1}{t_d}\int_0^{t_d} a(t)^2 dt\right]^{\frac{1}{2}} \tag{2}$$

where, $a(t)$—acceleration time history,

t_d—duration of the acceleration record

Figure 4 shows that the acceleration value of the tire-geogrid reinforced retaining wall changes with the load change. It can be seen that the acceleration increases non-linearly with increasing y/H and acceleration peak are amplified more on the top of the wall. The horizontal acceleration is about 80% $\sim$ 90% of vertical acceleration. Acceleration value increases slowly with increasing load time. The acceleration value begins to slow and stabilize after the maximum acceleration peak is reached. Compared

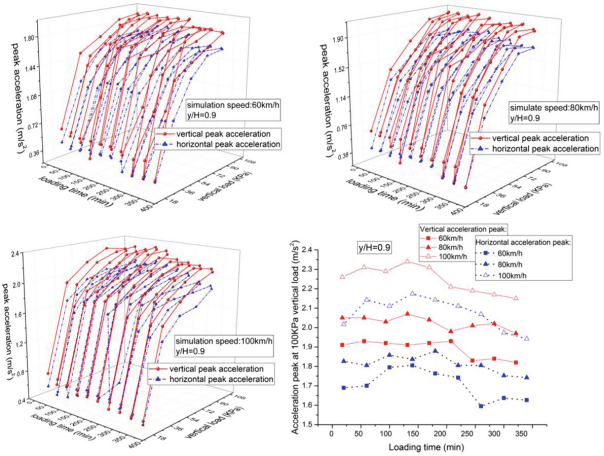

Fig. 4. Acceleration of tire-geogrid reinforced retaining wall

with 60 km/h, the horizontal and vertical maximum acceleration peak of 80 km/h are increased by 5.6% and 8.3%, and those of 100 km/h increased by 21.5% and 21.1%.

The vehicle speed has a corresponding influence on the dynamic earth pressure and the acceleration of reinforced retaining walls, especially on acceleration. With the cyclic load applied repeatedly, the acceleration factor of retaining walls first increased and then reduced slowly to stability. Since the increasing number of cyclic loads leads to compaction of the retaining wall, the stiffness of retaining walls increases and dynamic response of the soil reduces.

According to Figs. 3 and 4, the loading time of 200 min can be presented as the critical time in the vehicle load condition so that in the specified vehicle speed, the accumulation of load time of 200 min enhance stability of earth pressure and acceleration of tire-grid reinforced retaining wall. The time is the key reference value to study the early-age stability and strength of retaining wall.

4.3 Analysis of Function Fitting

According to the dynamic response rules of tire-geogrid reinforced retaining walls under vehicle load, function fitting is applied to analyze the relationship between the acceleration amplification coefficient and relative wall height relative load, and the relationship between the acceleration amplification coefficient and. Under the vehicle load, the acceleration peak increases with the increasing height of the wall, a function relationship similar to the exponential function, as shown in Eq. (3). Figure 5 shows the increase in fitting degree of acceleration amplification coefficient and relative wall height, the fitting parameters being a = 0.13, b = 2.11.

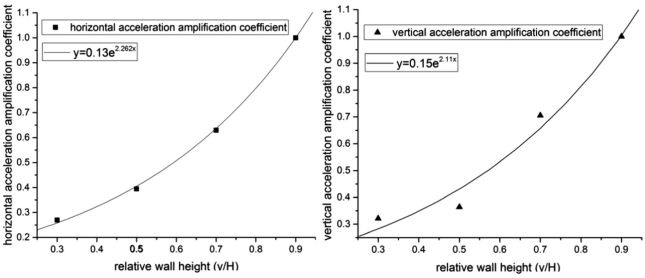

Fig. 5. Function fitting between acceleration amplification coefficient and relative wall height

$$\xi = ae^{b(y/H)} \tag{3}$$

where, ξ—acceleration amplification coefficient,
y/H—relative height of wall,
a, b—fitting parameters.

The acceleration peak increases with increased vertical load, a function relationship similar to the logarithmic function, as shown in Eq. (4). Figure 6 shows the function fitting between acceleration amplification coefficient and relative load.

$$\xi = alog_b(p/p_{max}) \tag{4}$$

where, ξ—acceleration amplification coefficient,
p/p_{max}—relative load,
a, b—fitting parameters.

With the increase of simulated speed, the frequency of vibration of retaining wall increases and the acceleration of the retaining wall is higher. At the same speed, the vertical acceleration is slightly larger than horizontal acceleration.

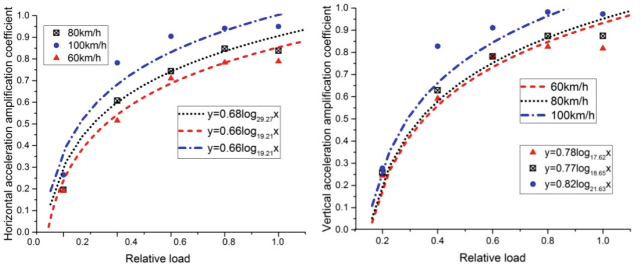

Fig. 6. Function fitting between acceleration amplification coefficient and relative load

Therefore, in the engineering application, the short-term vehicle load has significant influence on retaining walls. In a way, it can improve the compactness and stability of the retaining wall. On the other hand, the long-term vehicle load will cause uneven

settlement at the top of the retaining wall, causing the increase of vehicle load by road surface roughness. The reinforcement effect of tire-geogrids is better than commonly used reinforced materials, thus enhancing the maintenance cycle of the highway.

The acceleration increases with the increase of relative wall height in the form of an exponential function, indicating the maximum acceleration peak is at the top of wall. Hence, in the application of road engineering, more reinforcement measures should be applied within the zone at y/H = 0.7 to enhance the intensity and vibration resistance of top of retaining wall. The measures include increasing layers of reinforcement materials, increasing the length of reinforcement materials and utilizing better backfill.

5 Conclusion

- The performance of tire-geogrid reinforcing is superior to normal reinforcement materials (geocells and geogrids). Compared with biaxial geogrids and geocells, the acceleration peak decreased by approximately 27% and 16%, earth pressure peak decreased by 30% and 13%. The tire-geogrid materials are propitious to enhancing anti-seismic performance and the stability and diffusing the additional stress.
- Based on the dynamic earth pressure and acceleration under vehicle loading, the group spacing $s_x = s_y = 0.5D$ is the optimal scheme, saving 30% of material costs.
- Under the vehicle load, the acceleration of retaining wall increases with increasing the relative wall height and peaks at the top of the wall. The acceleration amplification coefficient increases with relative wall height in form of exponential function.
- The dynamic earth pressure changes with the vehicle load. After reaching its peak value, the increasing rate slows and tends to be stable. The acceleration amplification coefficient increases with relative load in form of logarithmic function.

Acknowledgments. This work was supported by the National Natural Science Foundation of China (No. 51678224, 51708190 and 51778217), National Program on Key Research Project of China (No. 2016YFC0502208) and the Hubei Provincial Science Foundation for Distinguished Young Scholars (No. 2018CFA063).

References

1. Sayao A, Gerscovich D, Medeiros L et al (2009) Scrap tire-an attractive material for gravity retaining walls and soil reinforcement. J Solid Waste Technol Manage 35(3):135–155
2. Kim KS, Yoon YW, Yoon GL (2011) Pullout behavior of cell-type tires in reinforced soil structure. J Civil Eng 15(7):1209–1217
3. Li LH, Chen YJ, Ferreira PMV et al (2017) Experimental investigations on the pull-out behavior of tire strips reinforced sands. Mater 7:707–720
4. Keller GR (2016) Application of geosynthetics on low-volume roads. Transp Geotech 8:119–131
5. Yoon YW, Cheon SH, Kang DS (2014) Bearing capacity and settlement of tire-reinforced sands. Geotext Geomembr 22:104–108
6. Tang LS, Lin PY, Wu K (2011) Response characteristics of dynamic stress of subgrade soil under vehicle loads. Chin J Geotech Eng 33(11):1745–1749

7. Biabani MM, Indraratna B, Ngo NT (2016) Modelling of geocell- reinforced subballast subjected to cyclic loading. Geotext Geomembr 44(1):489–493
8. Zhang F, Lin B, Feng D et al (2017) Permanent deformation of subgrade induced by long-term truck traffic loading in seasonally frozen regions. J Harbin Inst Technol 49(3):120–126
9. Xiong H, Guo L, Cai YQ (2016) Deformation behaviors of sandy subgrade soil under traffic load-induced stress path. Chin J Geotech Eng 38(4):662–669
10. Lv XL, Fang H, Zhang JF (2016) A theoretical solution for long-term settlement of soft subgrade induced by traffic loading. Rock Soil Mech 37(S1):435–440

A Solution to Estimate Stresses in Backfilled Stopes by Considering Self-weight Consolidation and Arching

Jian Zheng(✉) and Li Li

Research Institute of Mining and Environment (RIME UQAT-Polytechnique),
Department of Civil, Geological and Mining Engineering,
École Polytechnique de Montréal, C.P. 6079, succursale Centre-Ville,
Montréal, Québec H3C 3A7, Canada
jian.zheng@polymtl.ca

Abstract. Mine backfilling is an environment friendly solution. It has become a common practice in many underground mines around the world. Despite numerous advantages associated with this practice, efforts are needed to adequately design a retaining structure, called barricade to hold the backfill slurry in the stopes. This requires a good knowledge of the backfill pressures on the barricades. When a slurried backfill is poured in the stope, self-weight consolidation takes place with a quick generation and a slow dissipation of excess pore water pressure (PWP). When the dissipation of excess PWP advances sufficiently, effective stresses can develop in the backfill and shear stresses generate along fill-wall contacts. The shear stresses along the fill-wall contacts tend to reduce the stresses in the backfill and known as arching effect. Until now, the pressure estimation in backfilled stopes has been done mostly by considering only one of the two processes. In this paper, a solution is presented to evaluate the stresses in backfilled stopes by taking into account the self-weight consolidation and arching effect. The proposed solution is validated against numerical modeling performed with PLAXIS2D.

Keywords: Mine backfilling · Barricade · Backfill pressure
Self-weight consolidation · Arching effect

1 Introduction

Every day, a large amount of wastes are produced by mining industry. It is a great challenge to adequately manage these mine wastes. For most case, they are deposited on surface and constitute potential sources of environmental (e.g. acid mine drainage) and geotechnical problems (failure of tailings dams) [1]. However, mine wastes can be used as filling material to fill underground mined-out spaces (stopes). This practice, known as underground mine backfilling, can improve ground stability, increase ore recovery and decrease the amount of mine wastes to be deposited on surface. The environmental impact from mining industry can thus be reduced.

An important issue of mine backfilling is to have a safe and economic design of barricade, a confining structure built at the base of stope near the draw-point to hold the

© Springer Nature Singapore Pte Ltd. 2019
L. Zhan et al. (Eds.): ICEG 2018, ESE, pp. 181–189, 2019.
https://doi.org/10.1007/978-981-13-2227-3_22

fresh slurried backfill in the stope. Failures of barricade in several mines have been reported and often lead to serious consequences. Subsequently, care is needed to the stability and design of barricades. This requires a pressure estimation in backfilled stopes, which needs a full understanding of the hydro-mechanics behavior of the slurried backfill placed in mine stopes.

When a slurried backfill is discharged into a mine stope, the solid particles tend to settle down under the action of their own weight. The backfill thus tends to become denser while the pore water tends to be expelled out of the slurry. As mine backfill made of full tailings usually contains a large portion of fine particles, the permeability is usually small. The pore water cannot drain out quickly and excess pore water pressure (PWP) is generated. In most case, the total PWP at the moment of slurry pour can be as high as the vertical total stress based on the overburden of the backfill. The effective stresses are absent. The vertical and horizontal total stresses are identical and equal to the PWP. The pressures are called hydrostatic, geostatic or isostatic pressure based on overburden.

With time, the drainage and dissipation of excess PWP take place. When the process reaches a degree where the particles contact each other, effective stress can be developed. This drainage and dissipation of the excess PWP are called self-weight consolidation. Gibson [2] is probably the first one to evaluate the evolution of the PWP associated with the self-weight consolidation of accreting deposition of slurried backfill. As the Gibson [2] model is one dimensional consolidation theory without consideration of the effective stresses, it has been directly used to evaluate the pressure evolution in mine backfilled stopes [3, 4].

However, when the dissipation of the excess PWP reaches a degree where the particles of the backfill touch each to other, effective stresses start to develop, leading to the generation of shear stresses along the fill-wall contacts. The shear stresses along the fill-wall contacts tend to decrease the stresses in the backfilled opening, resulting in stresses and pressures less than those based on the overburden solution. This phenomenon is known as arching effect.

The arching theory has been used to estimate the pressures of backfill placed in mine stopes. More representative conditions of mine backfilled stopes have also been considered in the arching theory, such as the 3D geometry [5] and non-uniform stress distribution across the stope width [6]. However, most of the previous studies involving arching effect were conducted by considering dry backfill. Only a few studies were reported by considering submerged backfill in stopes with hydrostatic pressure, a state corresponding to the final steady state at the end of the drainage and dissipation of the excess PWP [7].

The brief literature review given above indicates that most of the existing works on pressure estimation in backfilled openings are devoted to the two extreme cases, either to the beginning or to the end of the self-weight consolidation process. No consideration was given to the intermediate state, in which the excess PWP dissipation and arching development jointly occur.

In this paper, the self-weight consolidation and arching effect during the placement of slurried backfill are jointly considered in evaluating the stresses in backfilled stopes. The excess PWP is first calculated by using the truly analytical solution of the Gibson (1958) model [2], developed by Zheng et al. [4]. The PWP is then introduced into the

arching solution to obtain the effective and total stresses. The proposed solution is validated by numerical modeling conducted with PLAXIS 2D.

2 Proposed Solution

2.1 Self-weight Consolidation of Accreting Deposition of Slurried Backfill

Figure 1 shows a mine stope (with impervious surrounding rock walls) being continuously filled with a slurried backfill. The backfill thickness increases at a filling rate of m (m/h). On the figure, h is the current thickness of the backfill at a given time t (i.e. $h = mt$); H is the final thickness at the end of deposition; B is the width of the stope; x and y are the abscissa and ordinate of the coordinate system, respectively; l is the depth of a layer element to be considered in the solution development; V is the vertical force on the top of the layer element; W is the weight of the layer element, C and S are the compressive and shear forces on the side of the layer element, respectively.

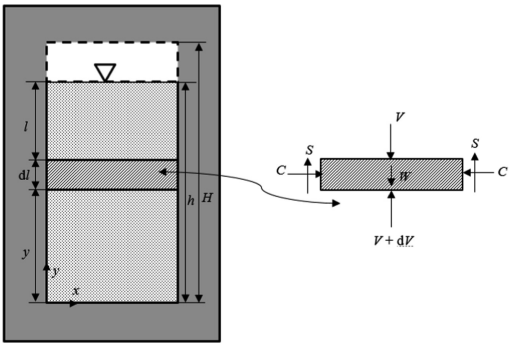

Fig. 1. Accreting deposition of slurried material in a mine stope with a horizontal layer element.

Gibson (1958) gave the following equation to describe the self-weight consolidation of an accreting deposition of slurried backfill:

$$c_v \frac{\partial^2 u}{\partial y^2} = \frac{\partial u}{\partial t} - \gamma' \frac{dh}{dt} \tag{1}$$

where u (kPa) is the excess PWP, c_v (m^2/h) is the consolidation coefficient, t (h) is the deposition time, γ' (kN/m^3) is the submerged unit weight of the backfill.

Solving Eq. (1) leads to the following equation (Gibson [2]):

$$u = \gamma' mt - \gamma' E(\pi c_v t)^{-\frac{1}{2}} \exp\left(\frac{-y^2}{4c_v t}\right) \tag{2}$$

where

$$E = \int_0^{\infty} \xi \tanh\left(\frac{m\xi}{2c_v}\right) \times \cosh\left(\frac{y\xi}{2c_v t}\right) \times \exp\left(-\frac{\xi^2}{4c_v t}\right) d\xi \tag{3}$$

and ξ(m) is an integral variable ($0 < \xi < \infty$).

The derivation of excess PWP leads to an expression as follows:

$$\frac{du}{dy} = -\gamma'(\pi c_v t)^{-\frac{1}{2}} \exp\left(\frac{-y^2}{4c_v t}\right) \times \left[\left(\frac{-y}{2c_v t}\right) \times E + F\right] \tag{4}$$

where

$$F = \int_0^{\infty} \xi \tanh\left(\frac{m\xi}{2c_v}\right) \times \sinh\left(\frac{y\xi}{2c_v t}\right) \times \left(\frac{\xi}{2c_v t}\right) \times \exp\left(-\frac{\xi^2}{4c_v t}\right) d\xi \tag{5}$$

The integral in Eqs. (3) or (5) can be approximated by a summation of series proposed by Goodwin [8]:

$$\int_{-\infty}^{\infty} g(z) \times \exp(-z^2) dz = h_0 \sum_{n=-\infty}^{\infty} g(nh_0) \exp(-n^2 h_0^2) \tag{6}$$

in which, g is a generic function of a variable z; n is a series number; h_0 is step interval of z. Goodwin [8] has shown that high accuracy approximation can be obtained as the value of n is large enough and h_0 is taken between 0 and 1.

Equations (3) and (5) can then be rewritten as follows:

$$E = \frac{h_0}{2} \sum_{n=-\infty}^{\infty} 4c_v t \times (nh_0) \times \tanh\left(\frac{mnh_0\sqrt{t}}{\sqrt{c_v}}\right) \times \cosh\left(\frac{ynh_0}{\sqrt{c_v t}}\right) \times \exp(-n^2 h_0^2) \tag{7}$$

$$F = \frac{h_0}{2} \sum_{n=-\infty}^{\infty} 4c_v t \times (nh_0) \times \tanh\left(\frac{mnh_0\sqrt{t}}{\sqrt{c_v}}\right) \times \sinh\left(\frac{ynh_0}{\sqrt{c_v t}}\right) \times \left(\frac{nh_0}{\sqrt{c_v t}}\right) \times \exp(-n^2 h_0^2) \tag{8}$$

With Eqs. (2) and (7), the excess PWP, u, can be expressed as follows:

$$u = \gamma' mt - \gamma'(\pi c_v t)^{-\frac{1}{2}} \exp\left(\frac{-y^2}{4c_v t}\right) \times \frac{h_0}{2} \sum_{n=-\infty}^{\infty} 4c_v t \times (nh_0) \times \tanh\left(\frac{mnh_0\sqrt{t}}{\sqrt{c_v}}\right) \times \cosh\left(\frac{ynh_0}{\sqrt{c_v t}}\right) \times \exp(-n^2 h_0^2) \tag{9}$$

Equation (9) is the analytical solution of Gibson [2] model proposed by Zheng et al. [4]. In most case, a stable result of u can be obtained when the value of h_0 is taken as 0.3 and n is in the range of −91 to 91.

With Eqs. (4), (7) and (8), the du/dy can be expressed as follows:

$$\frac{du}{dy} = -\gamma'(\pi c_v t)^{-\frac{1}{2}} \exp\left(\frac{-y^2}{4c_v t}\right) \times \left[\left(\frac{-y}{2c_v t}\right) \times \frac{h_0}{2} \sum_{n=-\infty}^{\infty} 4c_v t \times (nh_0) \times \tanh\left(\frac{mnh_0\sqrt{t}}{\sqrt{c_v}}\right) \times \cosh\left(\frac{ynh_0}{\sqrt{c_v t}}\right) \times \exp(-n^2 h_0^2) + \frac{h_0}{2} \sum_{n=-\infty}^{\infty} 4c_v t \times (nh_0) \times \tanh\left(\frac{mnh_0\sqrt{t}}{\sqrt{c_v}}\right) \times \sinh\left(\frac{ynh_0}{\sqrt{c_v t}}\right) \times \left(\frac{nh_0}{\sqrt{c_v t}}\right) \times \exp(-n^2 h_0^2)\right] \tag{10}$$

Equations (10) will be used in the next section to evaluate the stresses in backfilled stopes during the placement of backfill by considering the excess PWP dissipation.

2.2 Arching Consideration

Considering the equilibrium of the isolated layer element (Fig. 1) yields

$$dV + 2S = W \tag{11}$$

The vertical force V can be calculated as follows by assuming a uniformly distributed vertical stress σ_v across the width of stope

$$V = \sigma_v B \tag{12}$$

The weight of the layer element is expressed as follows

$$W = \gamma_{sat} B\, dl \tag{13}$$

where γ_{sat} (kN/m^3) is the unit weight of the saturated backfill; dl is the thickness of the layer element.

The shear force acting on the side of the layer element can be calculated by using the Mohr-Coulomb criterion

$$S = \sigma_h' \tan \delta'\, dl = K\sigma_v' \tan \phi'\, dl \tag{14}$$

where σ_v' (kPa) is the vertical effective stress; σ_h' (kPa) is the horizontal effective stress; δ' (°) is the effective friction angle along the interface between the backfill and rock wall, which is assumed to be equal to the effective internal frictional angle of the backfill ϕ'(°); K is the earth pressure coefficient, which is usually taken as the Rankine's active earth pressure coefficient K_a (= (1 − sinϕ')/(1 + sinϕ')) or Jaky's at-rest earth pressure coefficient K_0 (= 1 − sinϕ') in mine backfilled stopes.

Introducing Eqs. (12), (13) and (14) into Eq. (11) leads to

$$\frac{d\sigma_v'}{dl} + \frac{2K \tan \phi'}{B}\sigma_v' = \gamma' - \frac{du}{dl} \tag{15}$$

The vertical effective stress can be solved from Eq. (15) as follows

$$\sigma_v' = e^{-\frac{2K \tan \phi'}{B}l}\left[\int (\gamma' - \frac{du}{dl})e^{\frac{2K \tan \phi'}{B}l}dl + A\right] \tag{16}$$

where A is an arbitrary constant.

Considering the boundary condition $\sigma_v' = 0$ at $l = 0$ leads to

$$\sigma_v' = e^{-\frac{2K \tan \phi'}{B}l}\int_0^l \left(\gamma' - \frac{du}{dy}\right)e^{\frac{2K \tan \phi'}{B}l}dl \tag{17}$$

Considering $l = h - y$ and $du/dl = -du/dy$, Eq. (17) yields

$$\sigma_v' = e^{-\frac{2K \tan \phi'}{B}l}\int_0^l \left(\gamma' + \frac{du}{dy}\right)e^{\frac{2K \tan \phi'}{B}l}dl \tag{18}$$

Equation (18) constitutes a solution to calculate the vertical effective stress within the slurried backfill during the accreting deposition. The horizontal effective stress can be calculated as $\sigma_h' = K\,\sigma_h'$, while the vertical and horizontal total stresses can then be calculated as follows:

$$\sigma_v = \sigma_v' + u + \gamma_w l = e^{-\frac{2K \tan \phi'}{B}l}\int_0^l \left(\gamma' + \frac{du}{dy}\right)e^{\frac{2K \tan \phi'}{B}l}dl + u + \gamma_w l \tag{19}$$

$$\sigma_h = \sigma_h' + u + \gamma_w l = ke^{-\frac{2K \tan \phi'}{B}l}\int_0^l \left(\gamma' + \frac{du}{dy}\right)e^{\frac{2K \tan \phi'}{B}l}dl + u + \gamma_w l \tag{20}$$

3 Validation of the Proposed Solution by PLAXIS 2D

To evaluate the validation of the proposed solution, numerical simulations were conducted with PLAXIS2D to evaluate the stresses distribution in a backfilled stope.

Figure 2 shows the numerical model of a mine backfilled stope. The stope has a width of $B = 4$ m and filled at a filling rate of $m = 0.5$ m/h to a final height of $H = 12$ m. The slurried backfill is cohesionless and obeys the Mohr-Coulomb criterion; its properties are shown in Fig. 2. The impermeable surrounding rock is elasto-plastic, obeying the Mohr-Coulomb criterion. Its properties are shown in the figure.

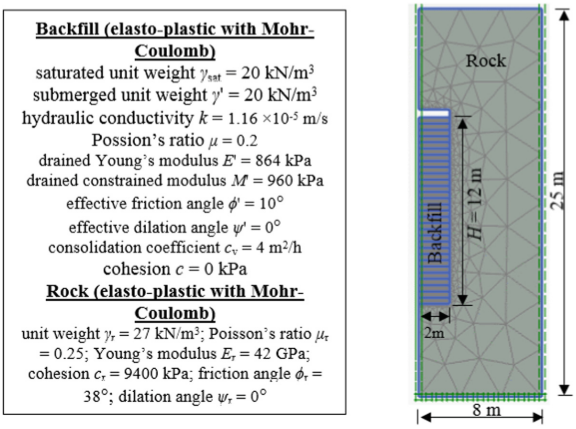

Fig. 2. Numerical model of a backfilled stope filled with a slurried backfill.

As shown in Fig. 2, the symmetry plane was taken into account and the numerical simulations were conducted by considering half of the model. The upper outer boundary of the numerical model is left free in all directions. The bottom of outer boundary is fixed in the horizontal and vertical directions. The two vertical side boundaries are allowed to freely move in the vertical direction but fixed in the horizontal direction. Drainage is only allowed through the top surface of each newly added backfill layer.

An initial stress is first obtained in the rock. The excavation is conducted to form the mine stope, which is then filled with backfill in layers. In practice, the filling is continuous. This can only be approximated in PLAXIS 2D by instantaneous additions of thin layers of backfill. The backfill thickness should be small enough to represent the continuous deposition. Here, the stop is filled to a final height of 12 m with layer thickness of 0.4 m. The waiting time between two consecutive layers is 0.8 h with m = 0.5 m/h.

Figure 3 shows the distribution of the excess PWP (Fig. 3a), effective and total (Fig. 3b) stresses along the height of the backfilled stope at the end of filling operation (at t = 24 h), obtained with the PLAXIS 2D and calculate with the proposed solution (Eqs. 9, 18, 19, and 20) by considering $K = K_a$. The good agreements between the pressures and stresses obtained by the proposed solution using $K = K_a$ and the numerical modeling with PLAXIS 2D indicate that the proposed solution is validated. One can also see that the u obtained by the numerical modeling and calculated with the proposed solution are much smaller than that based on the isostatic pressure solution. This indicates the occurrence of significant dissipation of the excess PWP during the filling operation. In addition, the occurrence of arching effect during the placement of the backfill is illustrated by the non-negligible effective stresses and the calculated total stresses smaller than the isostatic pressure based on the overburden pressure shown in Fig. 3b. Neglecting the excess PWP dissipation and arching effect may thus result in overly conservative and uneconomic design of barricades.

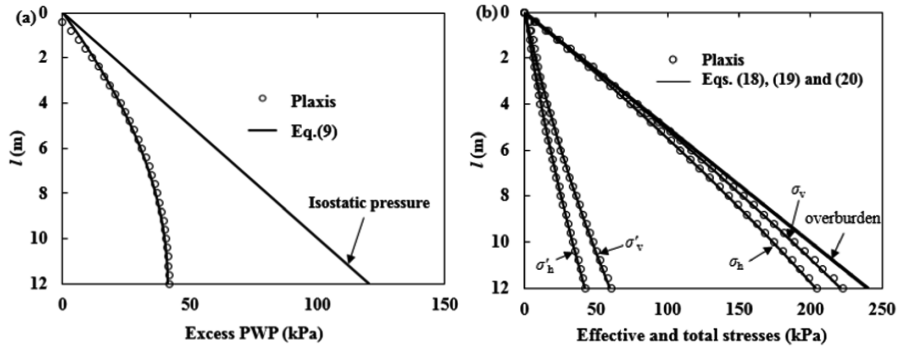

Fig. 3. Distribution of the (a) excess PWP, (b) effective and total stresses along the height of the backfilled stope at the end of the filling operation, obtained by numerical modeling with PLAXIS 2D and calculated with the proposed solution (Eqs. 9, 18, 19, and 20) using $K = K_a$.

4 Conclusion

The safe and economic design of backfill barricades is largely dependent on the reliability and accuracy of the stress estimation in backfilled stopes and pressures on barricades. In this paper, a new solution has been proposed to evaluate the stresses in backfilled stopes during the accreting deposition on an impervious base. Self-weight consolidation and arching effect are jointly considered by calculating the excess PWP in the backfill using the analytical solution of Gibson (1958) model first and then introducing into the arching solution. The proposed solution is validated by numerical simulations conducted with PLAXIS 2D. It thus constitutes a useful tool to calculate the stresses in backfilled stopes. The proposed solution can also be used to evaluate the influence of some key factors (e.g., filling rate, consolidation coefficient, backfill final height, etc.) on the stresses development in backfilled stopes during the filling.

Acknowledgements. The authors would like to acknowledge the financial support from the Natural Sciences and Engineering Research Council of Canada (NSERC 402318), Institut de recherche Robert- Sauvé en santé et en sécurité du travail (IRSST 2013-0029), Fonds de recherche du Québec—Nature et Technologies (FRQNT 2015-MI- 191676), and industrial partners of the Research Institute on Mines and the Environment (RIME UQAT-Polytechnique; http://rime-irme.ca/).

References

1. Bussiere B (2007) Colloquium 2004: Hydrogeotechnical properties of hard rock tailings from metal mines and emerging geoenvironmental disposal approaches. Can Geotech J 44 (9):1019–1052
2. Gibson RE (1958) The progress of consolidation in a clay layer increasing in thickness with time. Geotechnique 8(4):171–182

3. Zheng J, Li L, Mbonimpa M et al (2018a) An analytical solution of Gibson's model for estimating the pore water pressures in accreting deposition of slurried material under one-dimensional self-weight consolidation. Part I: Pervious Base Ind Geotech J 48(1):72–83
4. Zheng J, Li L, Mbonimpa M et al (2018b) An analytical solution of Gibson's model for estimating pore water pressures in accreting deposition of slurried material under one-dimensional self-weight consolidation. Part II: Impervious Base Ind Geotech J 48(1):188–195
5. Li L, Aubertin M, Belem T (2005) Formulation of a three dimensional analytical solution to evaluate stress in backfilled vertical narrow openings. Can Geotech J 42(6):1705–1717. (with Erratum 43(3):338–339)
6. Li L, Aubertin M (2008) An improved analytical solution to estimate the stress state in subvertical backfilled stopes. Can Geotech J 45(10):1487–1496
7. Li L, Aubertin M (2009) Influence of water pressure on the stress state in stopes with cohesionless backfill. Geotech Geol Eng 27(1):1–11
8. Goodwin ET (1949) The evaluation of integrals of the form $\int_{-\infty}^{+\infty} f(x)e^{-x^2}dx$. In: Mathematical proceedings of the Cambridge philosophical society, pp 241–245. Cambridge University

Study on Consolidation Behaviors of Waste Slurry by Using Vacuum Filtration Test

Bin Zhang(✉) and Liangtong Zhan

MOE Key Laboratory of Soft Soils and Geoenvironmental Engineering, Zhejiang University, Hangzhou 310058, China
{zhangjibin, zhanlt}@zju.edu.cn

Abstract. Waste slurry is an inevitable product of construction and is characterized by high water content, high content of fine particles, high void ratio, and extremely low strength. Its treatment requires consideration of the economic and environmental implications. In this paper, vacuum filtration test was conducted indoor to investigate the effect of volume reduction and consolidation behaviors of waste slurry. The monitored parameters included the filtration rate, height of slurry surface, solid content of filtrate, and moisture content of slurry column after testing. The effect of vacuum filtration is remarkable: the volume of slurry (desanding) and slurry (with sand) decreased by 80% and 63.3% respectively after 10 days' test, the filtrate was comparatively clear and the solid content were only 0.17% and 0.14%, and the moisture content of the bottom of the slurry column was reduced to 53.31% and 45.97% respectively, which is equivalent to the moisture content of the soft soil.

Keywords: Vacuum filtration · Waste slurry · Consolidation behaviors

1 Introduction

The process of urbanization in China has been speeding up, and various civil engineering projects, such as super high-rise buildings, large bridges, underground tunnels, subway and so on, have been developed rapidly. During the process of construction, a large amount of waste slurry is produced. Waste slurry has the following characteristics: high water content and fixed components and it is difficult to achieve rapid sedimentation; the stability of slurry colloid is good, and it is difficult to separate naturally by precipitation; waste slurry contains chemical additives and if not handled properly, it will pollute the environment. With the improvement of social environmental awareness, how to handle it has attracted the attention of relevant government departments and researchers.

The frequently-used treatment methods for waste slurry are flocculation sedimentation method, mechanical pressure filtration method, vacuum filtration method and centrifugal separation method. Colin et al. (1995) investigated the distribution of water in sludge dewatering in relation to their mechanical dewatering; Rasteiro et al. (2008) carried out flocculation studies of precipitated calcium carbonate induced by cationic polyacrylamides using light diffraction scattering and evaluated the flocculation mechanisms; Satyamurthy et al. (2012) investigated the effect of polymer conditioning

© Springer Nature Singapore Pte Ltd. 2019
L. Zhan et al. (Eds.): ICEG 2018, ESE, pp. 190–197, 2019.
https://doi.org/10.1007/978-981-13-2227-3_23

on dewatering characteristics of fine sediment slurry using geotextiles. The above research focuses on chemical methods and mechanical methods, however, these two methods have limited disposal capacity and high treatment cost, landfill treatment is still the main terminal disposal way of waste slurry at present.

In recent years, the method of soil-water separation using geotextiles has gradually been applied. Generally, geotextile is used as filtration medium to apply forward pressure or vacuum negative pressure to accelerate the separation of soil and water. This paper carried out experiments on the soil-water separation of waste slurry with vacuum filtration method indoor and investigate the consolidation behaviors of waste slurry under vacuum filtration situation.

2 Test Materials and Apparatus

2.1 Testing Materials

The waste slurry sample was taken from the Xiecun transfer wharf in Hangzhou, China, divided into slurry (with sand) and slurry (desanding), all of which were produced in the construction process of drilling piles. During the processing of desanding, water was added to remove mud from the sand, and sand collected is sold, so the water content of slurry (desanding) is higher than that of the slurry (with sand). After the treatment, the slurry was transported to the Deqing landfill for landfill disposal.

The basic physical properties of slurry were tested before the experiment. In order to analyze the effect of solid particle size on the soil-water separation of slurry, the OMEC LS-909 laser particle size analyzer was used to test the particle size of slurry, the following Table 1 and Fig. 1 gives the basic physical properties and the grain-size distribution curve of the slurry.

Table 1. Physical properties of waste slurry.

Types	Density/g·cm^{-3}	Water content/%	Specific gravity	Sand fraction/%	Silt fraction/%	Clay fraction/%
Slurry (with sand)	1.017	363	2.76	1.34	79.18	19.48
Slurry (desanding)	1.042	727	2.72	0.43	76.42	23.15

2.2 Geotextile

Bourgès-Gastaud et al. (2014) compared the dewatering performance of different geotextiles in the pressure filtration test, and drew the conclusion that there was no connection between the sludge dewatering efficiency and the geotextiles within a certain range of opening size. Therefore, the geotextile common and easy to buy in the market was selected in this test, and its basic characteristics were shown in Table 2.

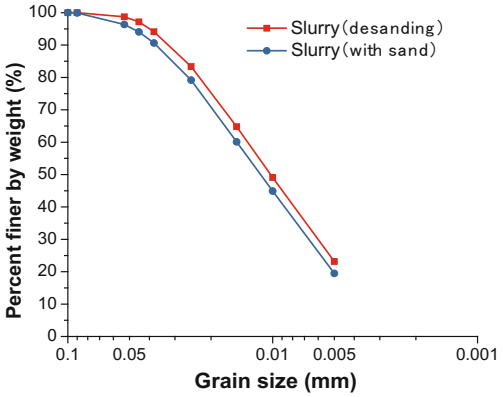

Fig. 1. Grain-size distribution curves for the slurry

Table 2. Characteristics of geotextile

Opening size[a]/μm	Fiber type[a]	Fabrication method[a]
40	Continuous filament	Heat calendered

[a]Data from producer

2.3 Apparatus

The vacuum filtration device used in this test is shown in Fig. 2, which consists of a slurry sample tube, a filter, a filtrate collection chamber, an air-water separator, an electronic scale (measuring range is 3 kg and precision is 0.01 g), a vacuum pump, several vacuum valves and compression-resistant hoses. The inner diameter of the sample tube made of plexiglass is 100 mm, and the height is 400 mm.

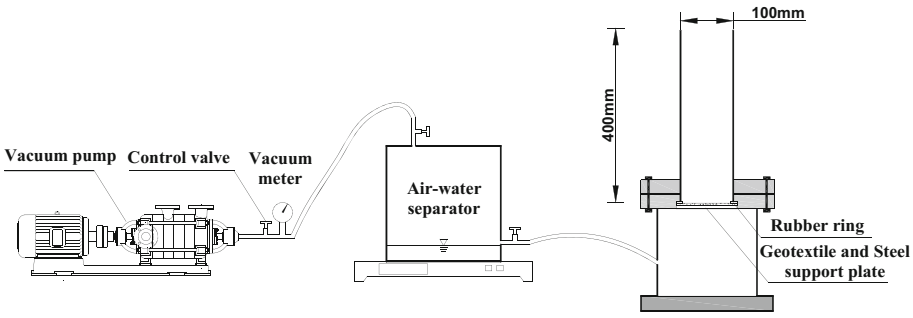

Fig. 2. Vacuum filtration test devices

3 Test Schemes and Procedures

3.1 Test Schemes

This test investigated the consolidation behaviors of two kinds of slurry by using vacuum filtration test. The two groups of test conditions were consistent, and the initial sample height was 300 mm.

Table 3. Test schemes

Schemes	Slurry	Opening size of GTX/μm	Vacuum pressure/kPa
A_1	desanding	40	−65
A_2	with sand	40	−65

3.2 Test Procedures

Before the experiment, the test devices were connected according to Fig. 2, and the sealing performance of the devices were checked, then the following test steps were carried out:

1 The slurry was mixed evenly and divided into 6 portions in each group, then a small amount of slurry was taken in each portions to test the moisture content (taking the average value as the initial water content of the slurry). Then the slurry was poured into the sample tube up to the desired height of approximately 300 mm, and the slurry was stirred at the speed of 300 r/min for 5 min using agitator.
2 Place the air-water separator on the electronic scale. After setting the electronic scale reading to zero, open the vacuum valves and control the vacuum pressure at −65 kPa. During the process of vacuum filtration, the vacuum degree, the quality of filtrate and the height of the sample surface were recorded at intervals.
3 After the experiment, the vacuum valves were closed. A proper amount of filtrate was taken to measure the solids content and then the slurry column was taken from the sample tube; the height of the slurry column was recorded and the moisture content of slurry column along the height was measured.

4 Results and Discussions

In the vacuum filtration test, in addition to the drainage path at the top interface of the slurry, the water in the slurry has two drainage paths, upward drainage path and downward drainage path, due to the existence of vacuum filtration pressure at the bottom of slurry. Besides, the seepage path is shortened, resulting in the rapid discharge of water from the slurry and the consolidation of the slurry. When filtered, the solid-liquid phase moves toward the surface of the filter medium under the effects of gravity, stress (suction caused by vacuum pressure), and shear force caused by liquid phase viscosity. The particles settling in moving fluid are affected by pressure, resistance,

buoyancy, drag, and acceleration force of fluid. Under the combined effect of these forces, coarse particles rapidly deposit on the surface of the filter medium. The filter cake formed fine particles deposit on it and fine particles move to the lower layer through the voids formed by coarse particles (Fan et al. 2015). Thus, at the end of the test, the slurry column was formed.

4.1 Cumulative Amount of Filtrate

The amount of water filtrated reflects the volume reduction and consolidation degree of slurry. From the Fig. 3, it can be seen that the cumulative amount of filtrate of this two kinds of slurry gradually increases with time. At the beginning, the filtration speed is faster due to the combined effect of self-weight sedimentation consolidation and vacuum consolidation. However, after a period, the filtration rate gradually becomes smaller and the amount of filtrate approaches a stable maximum value due to the formation of filter cake. The cumulative filtration quality of this two kinds of slurry was 1407.7 g and 1315.53 g respectively after 10 days test.

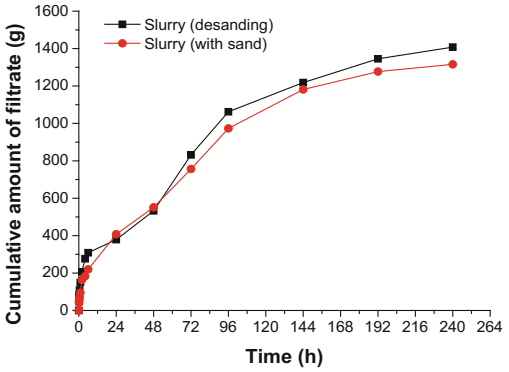

Fig. 3. Cumulative amount of filtrate varies with time

4.2 Height of Slurry Surface

The height of slurry surface changing with time is shown in Fig. 4. It can be observed from the figure, when the application of the vacuum pressure commences, there is a rapid linear decrease in the height slurry because the combined effect of self-weight sedimentation consolidation and vacuum consolidation. Thereafter, the curves gradually becomes flat as the drainage rate decreases. The height of desanding slurry was stable at about 67 mm after 48 h, and the height of the slurry with sand was reduced by about half (about 148 mm) after 96 h, which means the filter cakes were formed after 48 h and 96 h respectively for this two kinds of slurry, and the self-weight sedimentation consolidation and vacuum consolidation were basically completed. After 10 days of testing, the volume of this two kinds of slurry decreased by 80% and 63.3% respectively.

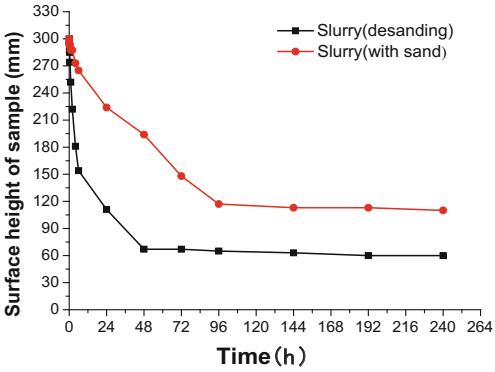

Fig. 4. Height of slurry surface versus time

4.3 Filtration Rate and Solid Content of Filtrate

At the beginning of the test, the filtration rate reached 584.4 $g{\cdot}h^{-1}$ and 486 $g{\cdot}h^{-1}$ respectively. Then, the filtration rate began to decrease remarkably after 15 min and 30 min. In the whole process of vacuum filtration test, the filtration rate of slurry desanding was faster than that of slurry with sand, because the content of particle in the slurry desanding is less than that of slurry with sand, and the filter cake of slurry desanding is thinner than slurry with sand and the permeability of filter cake of slurry desanding is better in the formation process of filter cake. The height of slurry column of these two kinds of slurry is basically unchanged after 48 h and 96 h respectively, and then the vacuum filtration process can be equivalent to the process of falling head permeability test, and the calculation formula for permeability coefficient of the falling head test can be used to calculate the average permeability coefficient of the slurry column. After the experiment, the solid content of filtrate was also measured, as shown in Table 4.

Table 4. Average permeability coefficient of slurry column and solid content of filtrate

Types	Average permeability coefficient/$cm{\cdot}s^{-1}$	Solid content of filtrate/%
Slurry (desanding)	5.1×10^{-7} (48 h–72 h)	0.17
Slurry (with sand)	1.0×10^{-8} (144 h–168 h)	0.14

4.4 Distribution of Moisture Content

Figure 6 shows the distribution of moisture content along the slurry column. The moisture content of the slurry column increases with the increase of height. The moisture content of the bottom of the slurry column was reduced to 53.31% and 45.97% respectively after 10 days of test, which is equivalent to the moisture content of the soft soil. The effect of soil-water separation is obvious, but the water content in the upper part of the slurry column is still large. Besides, the moisture content of slurry

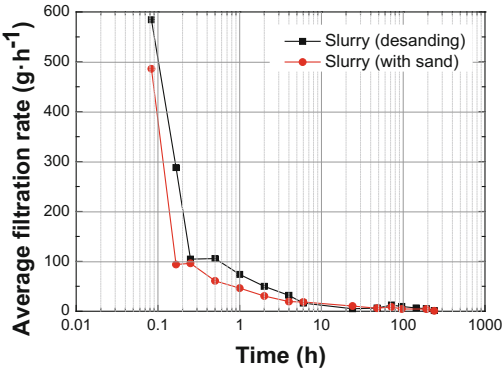

Fig. 5. Filtration rate versus time

column (desanding) is higher than slurry (with sand). The reasons are as follows: the content of particle in the slurry desanding is less than that of slurry with sand, so the drag force is smaller due to the relative velocity of the subsidence of soil particles and the seepage of water is smaller during the process of test. Thus the slurry column formed are relatively loose and the void ratio of slurry column is higher during the process of formation of slurry column. After the seepage of surface water basically finished, the vacuum pressure began to decrease, and the moisture content and consolidation degree of slurry desanding is lower due to the loss of vacuum pressure at the later stage of the test.

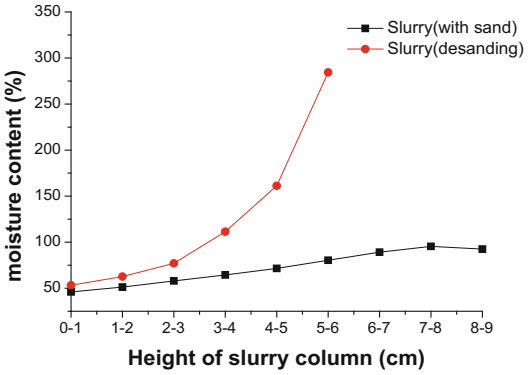

Fig. 6. Distribution of moisture content along slurry column

5 Conclusions

In this study, laboratory tests were conducted to investigate the consolidation behavior of waste slurry. Following is a summary of the findings and conclusions drawn from the study:

1 The particles settling in moving fluid are affected by pressure, resistance, buoyancy, drag, and acceleration force of fluid. Under the combined effect of these forces, coarse particles rapidly deposit on the surface of the filter medium, thus, the filter cake formed and the filtration rate decreased.
2 The more water the slurry contains, the earlier the filter cake formed, the faster the filtration rate, but the consolidation degree is relatively lower due to the loss of vacuum pressure.
3 After 10 days of test, the volume of slurry (desanding) and slurry (with sand) decreased by 80% and 63.3%, and the moisture content of the bottom of the slurry column was reduced to 53.31% and 45.97% respectively, which is equivalent to the moisture content of the soft soil.

References

Colin F, Gazbar S (1995) Distribution of water in sludges in relation to their mechanical dewatering. Water Res 29(8):2000–2005

Rasteiro MG, Garcia FAP, Ferreira P et al (2008) The use of LDS as a tool to evaluate flocculation mechanisms. Chem Eng Process 47(8):1323–1332

Satyamurthy R, Bhatia SK (2012) Effect of polymer conditioning on dewatering characteristics of fine sediment slurry using geotextiles. Geosynthetics Int 16(2):83–96

Bourgès-Gastaud S, Stoltz G, Sidjui F et al (2014) Nonwoven geotextiles to filter clayey sludge: an experimental study. Geotext Geomembr 42(3):214–223

Fan YP, Dong XS, Li H (2015) Dewatering effect of fine coal slurry and filter cake structure based on particle characteristics. Vacuum 114:54–57

Haegeman W, Impe WFV (2015) Filtration performance testing of geotextiles for vacuum consolidation drains. Geosynthetics Int 6(1):41–51

Alam N, Ozdemir O, Hampton MA et al (2011) Dewatering of coal plant tailings: flocculation followed by filtration. Fuel 90(1):26–35

One-Dimensional Model for Sedimentation and Consolidation of Tailings Slurry

Yijie Wang, Dantong Lin, and Liming Hu(✉)

State Key Laboratory of Hydro-Science and Engineering,
Department of Hydraulic Engineering,
Tsinghua University, Beijing, China
gehu@tsinghua.edu.cn

Abstract. The exploitation of mineral resources produces large amount of mine tailings. Usually these tailings are pumped into a sedimentation pond in a slurry state to be stored. However, the process of tailings slurry transformation from the muddy fluid state to the natural sedimentary soil has not been understood adequately. This paper studies the mechanism of tailings sedimentation and consolidation process by model test. The sedimentation and consolidation of muddy soil was carried out in a one-dimensional experimental setup to obtain the tempo-spacial variations of displacement and pore water pressure during the process, and the physical mechanism was further investigated. The deposition process of tailings can be divided into two stages and three zones, which can be distinguished by the change of slurry surface and pore water pressure. The results of this paper can provide new understanding about the mechanism of transformation process of slurry.

Keywords: Tailings · Sedimentation/consolidation theory
One-dimensional model

1 Introduction

Mineral resources and their processing provides a powerful assistance to the national economy and tailings are produced inevitably in the process of mineral exploitation. Tailings are the part of slags that remains after the mineral has been mined and screened to remove the valuable parts. The most common way to treat the tailings is to stockpile them in ponds enclosed by a dam that is also built using tailings. Widespread accidents caused by tailings dams in various mining industries are due to the management and engineering quality issues as well as inadequate understanding of the behaviour and mechanisms of tailings [1].

After the tailings slurry is discharged into the pond, it starts to settle and consolidate under the effect of gravity. During the process, the tailings possess high water content, large void ratio, strong compressibility, and unstable engineering properties. Studies have been conducted in the past to understand the sedimentation and consolidation of slurries. Several researchers opine that there is no effective stress during the sedimentation period and the process is governed by sedimentation theory [2, 3]. Soil structure would develop with time in the sedimentation process [4, 5] and the particles behavior [6], void ratio [7, 8] water content would be different from suspended state.

© Springer Nature Singapore Pte Ltd. 2019
L. Zhan et al. (Eds.): ICEG 2018, ESE, pp. 198–204, 2019.
https://doi.org/10.1007/978-981-13-2227-3_24

In this paper, a polymethyl methacrylate (PMMA) column was used to observe the process of tailings deposition by gravity. The change of the tailings surface shifting was recorded via video, and the pore water pressure was measured by porewater pressure transducers (PPTs). The curve of the tempo-spatial variation of interface between clean water and slurry can be divided into two parts indicating the different mechanisms during the tailings deposition process. The pore water pressure characteristics also showed the transformation during tailings sedimentation and consolidation.

2 Materials and Method

2.1 Tailings

The copper mine tailings were obtained from Bahuerachi, Mexico. Based on the particle sizes, the tailings can be classified into three types, fine tailings, coarse tailings and unclassified tailings. The current test was performed using the fine tailings whose average particle size is under 0.03 mm. A series of laboratory experiments were conducted to investigate the mechanical properties of the tailings including the specific gravity and particle size distribution. The specific gravity and the particle size characteristics of the tailings are summarized in Table 1.

Table 1. Geotechnical properties of fine copper tailings

Material	Fine tailings
Specific gravity	2.764
D_{60} (mm)	0.025
D_{50} (mm)	0.018
D_{30} (mm)	0.009
D_{10} (mm)	0.0019
Coefficient of uniformity, Cu	13.16
Coefficient of curvature, Cc	1.17

2.2 Test Methods

A polymethyl methacrylate (PMMA) column was chosen for the test and the transparent wall made the deposition convenient for observation. The column diameter was 10 cm to reduce the wall friction effect [9] and the height was 150 cm. Five pore water pressure sensors were installed on the wall at heights 0 cm, 30 cm, 60 cm, 90 cm and 120 cm from the base. A soft ruler pasted on the column wall was used to measure the height of the soil-water interface. The actual test setup and the schematic are shown in Fig. 1.

The mass ratio of fine tailings to water was 1:1.6 and the materials were adequately mixed using a mechanical stirrer. The mixture was subsequently injected into the column through a pipe in order to reduce air bubbles and to ensure homogeneity.

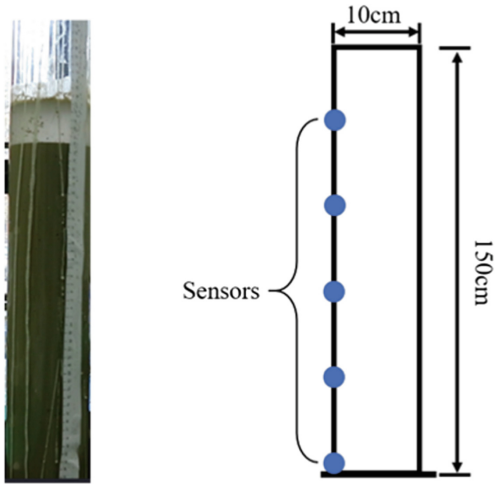

Fig. 1. Experimental setup and schematic used for the tailings deposition study

3 Results and Discussion

3.1 Interface

The height of tailings slurry was 122.5 cm at the beginning of the experiment. Initially, the mixture was stable and the interface of tailings and water could not be distinguished. About 1 min later, the interface between tailings and clear water appeared and kept shifting down. The water above the interface became clearer, with only a small amount of visible floc. There was only one distinct interface and the part below the interface was muddy and indistinguishable. The change in the height of the soil-water interface with time is shown in Fig. 2.

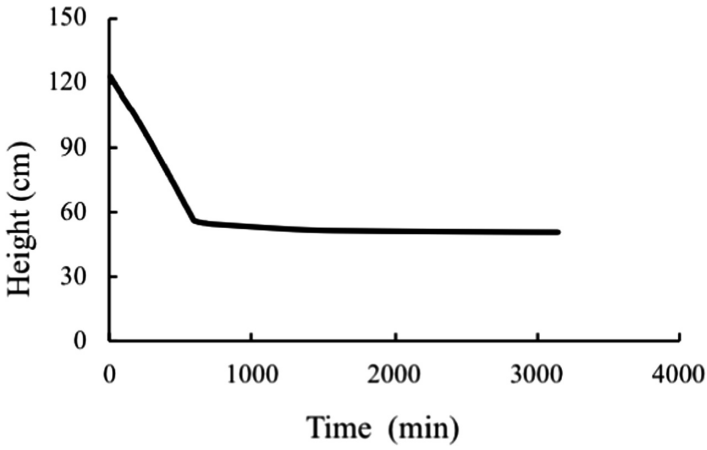

Fig. 2. The change in slurry surface height with time

The curve can be divided into two phases – an initial constant speed followed by an almost constant interface height. At first, the descending speed of the slurry surface is 1 mm per minute. The speed was constant as seen by the inclined straight line portion of the curve. However, after 590 min of the experiment there was an abrupt reduction in the falling speed of the interface which indicated that the tailings slurry reached a different phase. In order to observe the slow change of interface in the second phase, the second part of slurry deposition is plotted in logarithmic scale in Fig. 3 (Fig. 3 started with 591 min). It is a typical consolidation curve of soil and rate of change was not a constant. The experiment lasted about 51 h and eventually the interface dropped to 51 cm.

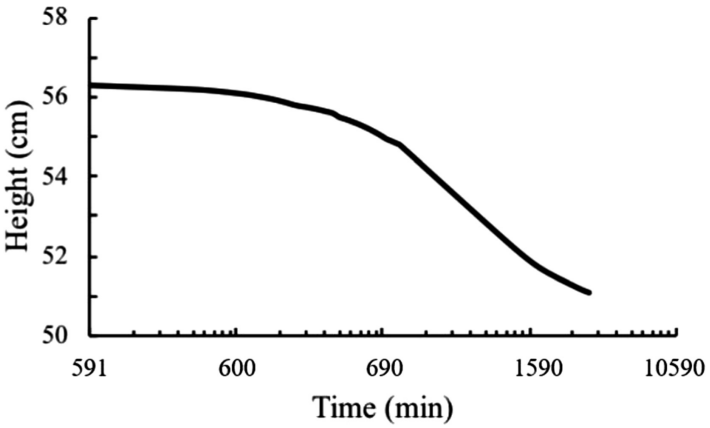

Fig. 3. Slurry surface changed with time in second phase

3.2 Water Pressure

Five pore water pressure sensors, distributed on the column wall at 30 cm intervals, measured the water pressure data every second and the change of pore water pressure are shown in Fig. 4.

The highest line in Fig. 4 represented the sensor at the bottom (0 cm). In the first two hours of deposition, pore water pressure dissipated rapidly. The interface of slurry water was a dividing line. Above the interface was clear water and could be considered as the hydrostatic pressure. Under the interface the water pressure is bigger than hydrostatic pressure but the different locations under the interface had different states of water pressure. If the soil skeleton had been formed, the total pressure would be equal to the sum of effective stress and pore water pressure [10].

It can been seen that the water pressure curves also had turning points. At the initial stage, the water pressure dropped fastest at the bottom and the bottom water pressure came to the turning point first. This is due to the soil skeleton being formed first at the bottom and followed by consolidation.

These was no effective stress for the tailings particles in the initial suspension. However, as the particles sank to the bottom of the column, they made contact with

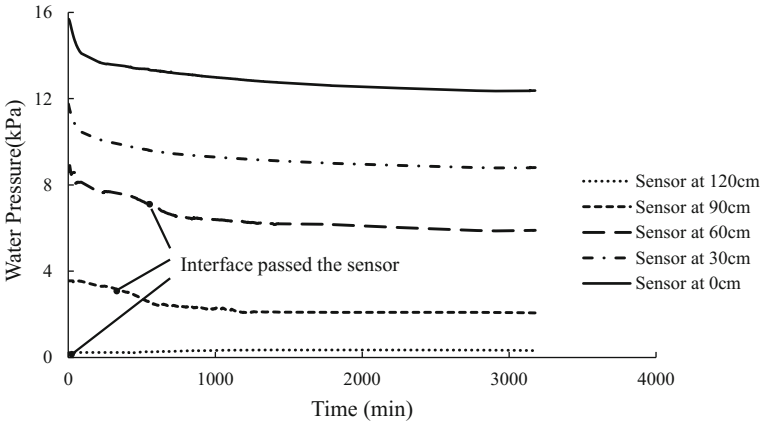

Fig. 4. The change in water pressure with time at different column heights

each other and the effective stress developed. Once the effective stress appeared, this portion of the tailings acted like soil and turned to consolidation instead of sedimentation. The soil skeleton formed at bottom first, and expanded with more particles falling. This could be possibly due to the presence of another interface between the soil skeleton and slurry which could not be observed.

3.3 Void Ratio

After 50 h, the water pressure dissipated smoothly and the surface of tailings was at 51 cm. Utilizing the holes on the column wall, saturated soil samples were extracted from various heights and oven dried at 105 °C. The void ratio at the different heights were calculated and the results are shown in Table 2. The particles at the bottom had longer consolidation time and higher self-weight stress which made the void ratio small.

Table 2. Void ratio at different sampling heights

Sampling height (cm)	Void ratio
50	1.703
30	1.479
0	1.049

3.4 Discussion

According to the above test results, the column can be divided into three regions from top to the bottom - clear water zone, settlement zone and consolidation zone (refer Fig. 5). The interface between clear water zone and settlement zone was distinct and appeared soon after the start of the experiment. Furthermore, this interface dropped at a constant speed of 1 mm/min. The second interface was between the settlement zone

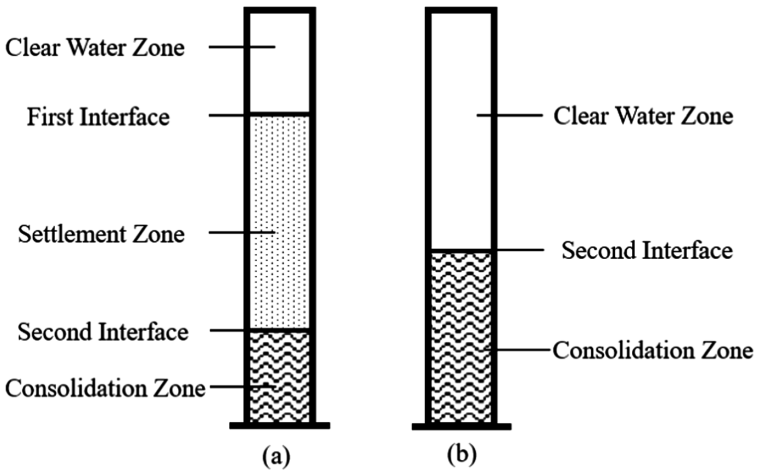

Fig. 5. (a) Division of regions in tailings deposition in first stage (b) Division of regions in tailings deposition in second stage

and consolidation zone but it could not be observed directly. The second interface ascended with particles dropping down. The clear water zone and consolidation zone expanded and the settlement zone shrank with time. Finally, the settlement zone vanished which was the turning point in Fig. 2. We could use the two interfaces as the boundary of settlement zone. When the settlement zone vanished, all the particles were in contact with the neighboring particles and the tailings started to undergo consolidation. The behavior of particles in different zones were different. Particles in the settlement zone were suspended and controlled by the sedimentation theory. The particles in the consolidation zone were squeezed and governed by the consolidation theory. In the clear water zone, the water pressure equaled the static water pressure. In settlement zone, the water pressure was higher than the hydrostatic pressure and equaled the total stress because total stress was borne by the water and slurry was heavier than water. Effective stress was zero in the settlement zone because soil skeleton had not been formed. In the consolidation zone, the total stress was borne by the water and the soil skeleton.

The deposition process of fine tailings slurry under gravity could be divided into two stages from based on the elapsed time because the stable phase of slurry was transient which could be ignored. At first stage, particles were falling to the bottom and formed the soil skeleton. The effective stress appeared at this region. The formed soil skeleton began to discharge pore water pressure under gravity and effective stress developed. The second interface between the settlement zone and consolidation zone dropped under gravity consolidation, but it also ascended as the number of particles increased which indicates that the rate of change of the second interface was not a constant as seen in Fig. 3. In fact, the second interface would ascend in first stage and drop slowly in second stage. The consolidation part would not affect the change rate of settlement.

4 Conclusions

A one-dimensional column study was conducted to observe the process of tailings deposition under gravity. In the experiment, uniform fine tailings slurry could not remain stable and the interface between water and tailings appeared in few minutes. The change of the interface was observed and the water pressure were monitored using PPTs. The following are the summary and conclusions from the study:

1. The process of tailings deposition could be divided into two stages based on the elapsed time. At the first stage, tailing particles dropped to the bottom continuously and the soil skeleton formed. Before the particles reached the bottom, there was no effective stress developed between them and all pressure was borne by water. When the particles reached the bottom and had contact with others particles, the effective stress developed and the stress was borne by pore water and soil skeleton. In the second stage, all particles reached the bottom and the whole system turned to a consolidation process of soil under self-weight.
2. The tailings deposition process could be divided into three regions of space from top to bottom - clear water zone, settlement zone and consolidation zone. The boundaries of these three regions were the two interfaces. The first interface between water and suspended tailings dropped with time at a constant rate. The second interface between suspended tailings and consolidated tailings ascended in first stage and dropped slowly in second stage.

References

1. Azam S, Li Q (2010) Tailings dam failures: a review of the last one hundred years. Geotech News 28(4):50–54
2. Imai G (1981) Experimental studies on sedimentation mechanism and sediment formation of clay materials. Soils Found 21(1):7–20
3. Fitch B (1966) Mechanism of sedimentation. Ind Eng Chem Fund 5(1):129
4. Tan TS, Yong KY, Leong EC et al (1990) Sedimentation of clayey slurry. J Geotech Eng 116(116):885–898
5. Sills G (1998) Development of structure in sedimenting soils. Philos Trans Mathe Phys Eng Sci 356(1747):2515–2534
6. Zhang N, Zhu W (2014) Study of sedimentation and consolidation of soil particles in dredged slurry. Geo-Shanghai, 70–79
7. GuiZhong X, Gao Y, Hong Z et al (2012) Sedimentation behavior of four dredged slurries in China. Mar Georesour Geotechnol 30(2):143–156
8. Dimitrova RS, Yanful EK (2011) Undrained strength of deposited mine tailings beds: effect of water content, effective stress and time of consolidation. Geotech Geol Eng 29(5):935–951
9. He W, Williams D, Shokouhi A (2017) Numerical study of slurry consolidometer tests taking into account the influence of wall friction. Comput Geotech 91:39–47
10. Terzaghi K (1943) Theoretical Soil Mechanics. Wiley, New York

The Effects of Meta-Kaolin on pH, Electric Conductivity (EC) and Ca2+ Ions Consumption of Lime-Treated Laterite

Gideon M. Limunga and Yun-zhi Tan(✉)

China Three Gorges University, Yichang 443002, China
yztan@ctgu.edu.cn

Abstract. Lime treated lateritic soils are among the commonly applied construction materials in tropical and subtropical regions where they are widely distributed, due to the humid climate. However, the long-term performance of this material has been greatly influenced by the changes in the geoenvironment, for instance, under the action of contaminants lime-treated laterite may not perform as well as it would have in their absence. To characterize the changes in the geoenvironment, determining the degree of its acidity or alkalinity i.e. pH has been adopted by most scholars, and it has been shown that pH has a profound effect on the solubility of contaminants. In order to observe these issues experimental setups where established to monitor the effect of aggregate size, and addition of Meta-Kaolin (MK) on pH, Electrical conductivity (EC) and calcium ion (Ca^{2+}) concentration of lime treated laterite. The results show that MK lowers the pH slightly in the short term and tends to maintain a very narrow range in the long term. Moreover, this property significantly influences the erosional and permeability properties. It was also observed that for the same percentage of lime a sample with 5 mm maximum aggregate had a pH slightly higher than the one with 0.5 mm maximum aggregate size sample. Further, a decrease in the amount of Ca2+ concentration, inevitably translates into a decrease in pH values and EC for a lime-laterite mixture.

Keywords: pH · Electrical Conductivity (EC) · Ca^{2+} concentration
Meta-Kaolin · Lime-treated laterite

1 Introduction

Lime treated lateritic soils have earned a wide variety of engineering applications, from embankment fills, highway bases to foundations of structures. Lateritic soils are a group of highly weathered reddish tropical soils, they are rich in iron and aluminum oxides, and contains kaolin as the predominant clay mineral [1–3]. These soils are applied for various purposes in construction, however, in their raw form they are susceptible to deterioration due to their poor geotechnical properties [2]. Hence, the need to improve their properties through stabilization with various agents such as cement, lime, fly ash, silica fumes etc. [1, 3–5].

Lime treatment, whether in form of quicklime or hydrated line can potentially enhance the properties of a soil being stabilized. It can improve the strength, stiffness,

© Springer Nature Singapore Pte Ltd. 2019
L. Zhan et al. (Eds.): ICEG 2018, ESE, pp. 205–211, 2019.
https://doi.org/10.1007/978-981-13-2227-3_25

durability, workability/plasticity, water retention of the raw soil, swelling potential and in-situ compaction [6–8]. Ciancio et al. [7] identified three general phenomenon by which lime-soil reaction could be described viz. cation exchange, pozzolanic reaction and carbonation. In other words, during the initial stages of the reaction, ion exchange takes place thereby causing clay particles to flocculate-agglomerate. Then, in the presence of water the hydration process commences resulting into formation of calcium and aluminum hydrates, which later form cementitious compounds, this is process is commonly referred to as pozzolanic reaction [2, 4, 6, 9]. On the other hand, carbonation results from the reaction between lime-soil and carbon dioxide present in air, it is undesirable because it reduces strength by inhibiting formation of cementitious materials [7]. However, the adequacy of lime-treated laterite in engineering applications may be compromised by other factors such as leaching, environmental contamination, and changes in in-situ conditions, hence, necessitating other additives to be included, in order to improve their resistance to damage, one such additive is meta-kaolin.

Meta-kaolin is a chemical phase that forms upon thermal treatment of kaolinite. Kaolinite's chemical composition is Al2O3:2SiO2. 2H2O and as a result of thermal treatment in the range of 400–500 °C, the water is driven away to form an amorphous alumino-silicate called meta-kaolin. Kaolin clay is raw material used in the production of meta-kaolin (Al2Si2O7) [10, 11]. When Metakaolin reacts with lime it produces, calcium silicate hydrates (CSH) gel. It can also be seen that MK contains alumina, which normally reacts with CH to produce additional alumina-containing phases such as C2ASH8 (gehlenite hydrate), C4AH13 (tetracalcium aluminate hydrate), and C3AH6 [11]. It's noteworthy that MK has received wide acceptance and application in concrete technology due to the various advantages it offers, such as enhanced workability, increased compressive and flexural strength, improved permeability and durability, increased resistance to chemical attack, and reduced shrinkage due to particle packing [11–15]. However, the potential of MK as a geotechnical pozzolan has not been fully exploited, in spite of the fact that it possesses properties of geotechnical significance. Consequently, this current study seeks to investigate the effects of MK on lime-treated laterites.

In order to achieve the underlying aim for this work physicochemical tests were conducted on samples containing laterite with lime and/or MK. These included; pH values, Electrical conductivity (EC), and calcium ions (Ca^{2+}) concentrations. Soil pH is defined as a measure of acidity or alkalinity of the soil water suspension. It is a principal governing factor in the lime treatment process, since the dissolution of reactive alumina and silica from the clay minerals is dependent on the highly alkaline conditions prevailing in the soil solution, resulting from an excess supply of hydroxyl ions from lime dissociation [6, 16]. Evidently, pH can be used to monitor consumption of anions and cations in solution. Boardman et al. [9] defined electrical conductivity as a measure of a solution's ability to conduct electricity that is directly related to the quantity of ions in solution. Hence, it shows the quantity of dissolved solids. Further, dissociation of lime results into two ions viz. calcium ions and hydroxyl ions, thus, monitoring the rate of consumption of these ions gives an indication on the rate of propagation of the reaction.

In summary, the current study sought to establish the effects of MK on pH, EC, and calcium ions concentration of lime treated laterite. In light of the physical and chemical properties of MK which can be useful in geo-technology applications.

2 Materials and Experimental Methods

2.1 Materials

The main materials used for this work were Laterite (LT), lime (L), and Meta-Kaolin (MK). The laterite was sourced from Guili, Guanxi province, China. The commercial hydrated lime (Ca(OH)2) was used. Its natural moisture content being 17%, and constituted of 95% CaCO3, with maximum particles passing an 80 μm sieve opening. While, the Meta-kaolin used was obtained from Metamax, its natural moisture content was 19% and maximum particles passing an 80 μm sieve opening.

2.2 Sample Preparation and Experimental Programs

The laterite soil was air dried to a constant mass; The air-dried soil was then split into two portions, which were crushed using a rubber hammer, separately, and passed through a 0.5 mm and 5 mm sieve openings. From the sieved laterite, samples were prepared as summarized in the experimental program provided in Table 1.1.

Table 1. Summary of the experimental programs

Test		D_{max} (mm)	Materials		Water content (%)	Sample dimension (mm)		Curing period (d)
			Lime-treated	Meta-kaolin		*d*	*h*	
Optimum lime determination	pH EC C_{Ca2+}	0.5, 5	1, 3, 5, 7, 9%	0%	30% + 5% (soaking)	61.8	20	1, 3, 7, 14, 28, 60, 120, 240, 360
Effects of Meta-kaolin	pH EC C_{Ca2+}	0.5, 5	5%	1, 3, 5, 7%	30% + 5% (soaking)	61.8	20	1, 3, 7, 14, 28, 60, 120, 240, 360

For each sample type the pozzolans and laterite were thoroughly mixed in their dry state, afterwards water was added to achieve a target moisture content of 35%, and then mellowed for 24 h prior to compaction.

The samples were then statically compacted to 96% of the maximum dry density i.e. 1.49 g/cm3, using a hydraulic compactor, a mold and 61.8 mm in diameter cylindrical rings (20 mm height). After compaction, samples were cured at 25 °C and 95% relative humidity until the various test ages of 1, 3, 7, 14, 28, 60, 120, 180 and 240 days.

Mettler Toledo, SevenExcellence Multiparameter was used to determine the pH, electric conductivity (EC) and concentration of calcium ions (Ca^{2+}) of the samples in aqueous solution based on the following procedure. At each curing age, 10 g of compacted sample was weighed and pulverized in a mortar with a pestle. Then added to a sealable beaker; 100 ml of deionized water was also added, after which the beakers were sealed and put in a mechanical shaker at room temperature and agitated for 1-h prior to measuring pH, EC, and Ca^{2+}. This procedure was modified from ASTM: D6276-96 and ASTM: 4972-96a.

3 Results and Discussions

There are three major facets addressed herein the effect of aggregate size, Changes in pH, Electrical Conductivity (EC) and concentration of calcium ions (Ca^{2+}) with time, and the influence of MK.

The maximum aggregate size and particle size distribution of laterite have a profound effect on pH, EC and Ca^{2+} concentration, since the specific surface area of the samples normally depends on these factors [5, 6]. As can be observed in Fig. 1, at 5% lime the pH of 5 mm aggregates is slightly higher than that of 0.5 mm aggregates. This entails a slower consumption rate of Ca^{2+} in larger aggregates as compared to finer aggregates with larger specific surface area, hence a much faster rate of reaction. Nevertheless, at higher percentages of lime the pH values coincide, this is due to the excess lime that does not take part in the initial reaction, and thus available as free lime. Additionally, Laterite consists of ferric aggregates that could lead to a formation of a water-lime film around the particles, and since these aggregates are acidic in nature, it can be inferred that as the reaction propagates they dissociate thereby releasing their acidotic ions into the soil that could affect the pH. Boardman et al. [9] discussed the effect of Ion solubility on the pH of soils their work revealed that certain mineral elements such as $Fe(OH)_2$, $Fe(OH)_3$, Fe_2O_3, Al_2O_3 etc. Dissociate at certain pH levels, implying that if the pH is not maintained within a particular range of values, some of these elements will dissolve hence lowering the pH further. Thus, it is imperative to ensure that the pH does not drop below a certain limit, and MK helps to achieve that by maintaining the pH within a narrow range in the long term (see Fig. 3).

The parameters to be measured (viz., pH, EC and Ca^{2+} concentration), where monitored at different curing ages up to 240 days. It was observed that pH decreased with time (see Fig. 2), this was accompanied by a corresponding decrease in EC and Ca^{2+} concentration. The relationships between these parameters can be explained by considering the fact that, as the reactions propagate Ca^{2+} and OH^- ions are consumed to form calcium hydrates and alumino-hydrates. Thereby, reducing the amount of free ions available to affect the pH and conductivity of the solution, these similar phenomenon where reported by other scholars [1, 2, 4, 17–19].

The influence of meta-kaolin on pH, EC and Ca^{2+} concentration of lime treated laterite was achieved by keeping the amount of lime in all the samples constant, then varying the percentages of MK.

In Fig. 3, time dependent relationships are established with respect to pH, for a sample treated with only 5% lime, compared to another one treated with 5% lime and

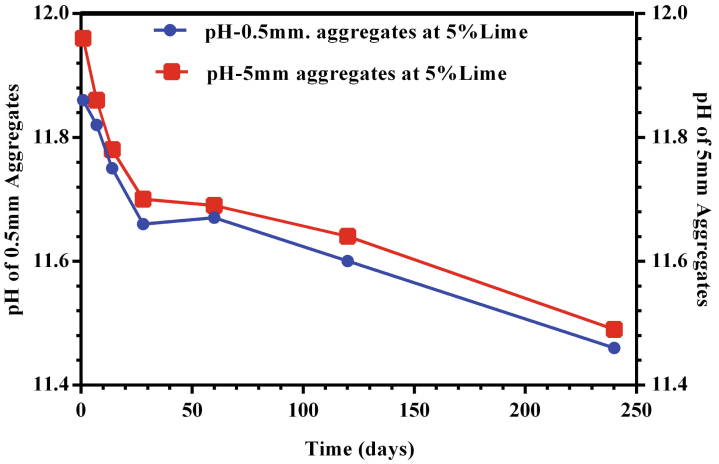

Fig. 1. pH of 0.5 and 5 mm max aggregate size as a function of time 5% lime

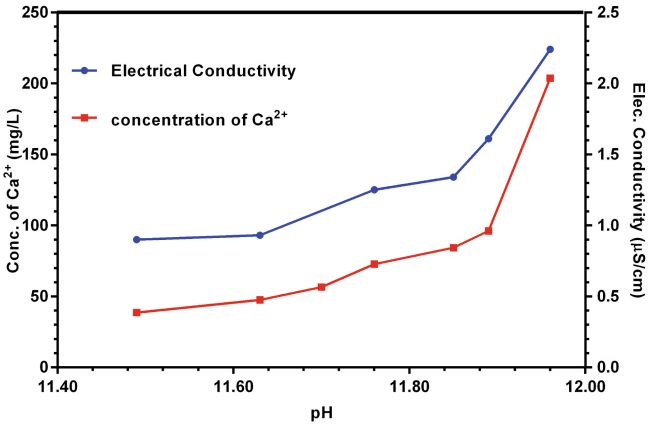

Fig. 2. Variation of Ca^{2+} and EC with pH at 5% Lime content

5% MK. The results show that addition of meta-kaolin has an overall effect of lowering the pH values in comparative terms. It can also be pointed out from the figure that for 5% MK the initial pH is higher than that of samples with lime only. However, between 28 and 180 days the trend is different as the sample treated with lime only shows significantly higher values. Further, when MK is added a sharp drop in the pH values was observed, this can be attributed to the fact that the reaction between MK and lime proceeds at a high rate in the first 7 days of the process [20].

The reaction mechanism between lime treated laterite and MK presents a peculiar phenomenon in that in the early days of curing the cementing of the materials can be more attributed to lime, owing to the slow reactivity of MK, however in the long run Metakaolin slowly enters the process thereby offsetting the reaction path. As presented

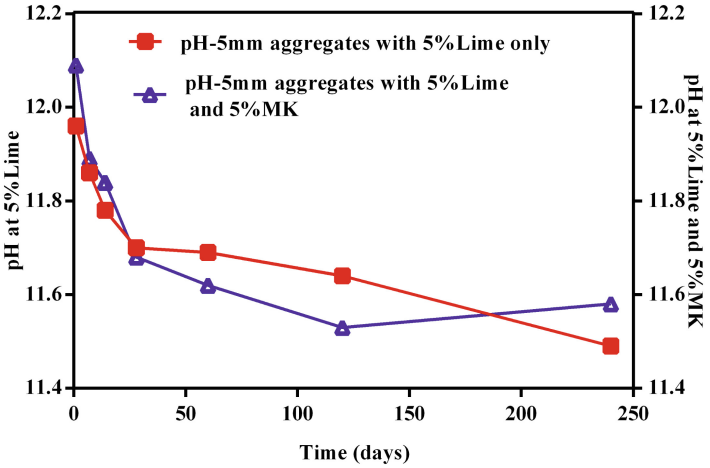

Fig. 3. Effect of Meta-Kaolin on the variation of pH with time

in the figures above (Figs. 1, 2 and 3), it clearly shows that the parameters slowly decline in the absence of MK i.e. in lime treated only. Conversely, the case is different in the presence of MK, while the path for lime treated laterite seems to exhibit the steady decline, the MK path eventually peaks up and begins to rise; as a result, the terminal pH is higher. This coupled with MK's ability to resist dissociation implies that addition of MK ultimately improves the overall strength in the long term, as it maintains the pH within the narrow range.

4 Conclusions

1. The granular aggregates have a slower lime consumption rate as compared to the finer aggregates.
2. A decrease in the amount of Ca^{2+} concentration, inevitably translates into a decrease in pH values and EC for a lime-laterite mixture.
3. When meta-kaolin is added to a lime-treated lateritic soil it generally tends to lower the pH of the sample in the short term, but eventually attains an equilibrium range of pH values. This is in contrast to the behavior of samples treated with lime only, which exhibited a continuous decline in pH values and took longer to reach equilibrium. This demonstrates that MK has the potential to improve the long term strength of lime treated laterite.

References

1. Attoh-Okine NO (1995) Lime treatment of laterite soils and gravels - revisited. Constr Build Mater 9(5):283–287
2. Millogo Y, Morel JC, Traoré K, Ouedraogo R (2012) Microstructure, geotechnical and mechanical characteristics of quicklime-lateritic gravels mixtures used in road construction. Constr Build Mater 26(1):663–669
3. Millogo Y, Hajjaji M, Ouedraogo R, Gomina M (2008) Cement-lateritic gravels mixtures: microstructure and strength characteristics. Constr Build Mater 22(10):2078–2086
4. Arabi M, Wild S (1986) Microstructural development in cured soil-lime composites. J Mater Sci 21(2):497–503
5. Wang Y, Cui Y, Tang AM, Benahmed N (2016) Aggregate size effect on the water retention properties of a lime-treated compacted silt during curing. Appl Clay Sci 11013:1–4
6. Cherian C, Arnepalli DN (2015) A critical appraisal of the role of clay mineralogy in lime stabilization. Int J Geosynth Gr Eng 1:8
7. Ciancio D, Beckett CTS, Carraro JAH (2014) Optimum lime content identification for lime-stabilised rammed earth. Constr Build Mater 53:59–65
8. Al-Mukhtar M, Lasledj A, Alcover JF (2014) Lime consumption of different clayey soils. Appl Clay Sci 95:133–145
9. Boardman DI, Glendinning S, Rogers CDF (2001) Development of stabilisation and solidification in lime-clay mixes. Géotechnique (6):533–543
10. Mathur S Understanding the Benefits of High Reactivity Metakaolin
11. Siddique R, Khan MI (2011) Supplementary Cementing Materials, vol 3. Springer, Heidelberg, p 287
12. Shi Z, Geiker R, De Weerdt K, Østnor TA, Lothenbach B, Winnefeld F et al (2017) Role of calcium on chloride binding in hydrated Portland cement–metakaolin–limestone blends. Cem Concr Res 95:205–216
13. Wianglor K, Sinthupinyo S, Piyaworapaiboon M, Chaipanich A (2017) Effect of alkali-activated metakaolin cement on compressive strength of mortars. Appl Clay Sci 141:272–279
14. Pavlík V, Užáková M (2016) Effect of curing conditions on the properties of lime, lime-metakaolin and lime-zeolite mortars. Constr Build Mater 102:14–25
15. Silva AS, Gameiro A, Grilo J, Veiga R, Velosa A (2014) Long-term behavior of lime-metakaolin pastes at ambient temperature and humid curing condition. Appl Clay Sci 88–89:49–55
16. Rahman M, Nahar TT (2015) Effect of pH on shear strength behavior of granular soil 15(1)
17. Attoh-Okine NO, Fekpe ESK (1996) Strength characteristics modeling of lateritic soils using adaptive neural networks. Constr Build Mater 10(8):577–582
18. Khattab SA, Al-Mukhtar M, Fleureau J-M (2007) Long-term stability characteristics of a lime-treated. J Mater Civ Eng 19(4):358–366
19. Rao SM, Shivananda P (2005) Role of curing temperature in progress of lime-soil reactions. Geotech Geol Eng 23(1):79–85
20. Dojkov I, Stoyanov S, Ninov J, Petrov B (2013) On the consumption of lime by metakaolin, fly ash and kaoline in model systems. J Chem Technol Metall 48(1):54–60

The Effects of Probe Diameter and Penetration Speed on the Miniature Penetrometer Tests

Wei Bai[1,2,3(✉)], Ling Wei Kong[1], and Rong Bing Lin[1]

[1] State Key Laboratory of Geomechanics and Geotechnical Engineering, Institute of Rock and Soil Mechanics, Chinese Academy of Sciences, Wuhan 430071, Hubei, China
william_bai@yeah.net

[2] Key Laboratory of Tianjin Soft Soil Character and Engineering Environment, Tianjin 300381, China

[3] GuangXi Key Laboratory of Geomechanics and Geotechnical Engineering, Guilin University of Technology, Guilin 541004, China

Abstract. The miniature penetrometer tests are often used to investigate the distribution and strength of aggregates in soils. In this work, seven different diameters of probe and three different penetration speeds were used in the miniature penetrometer tests. The results show that: Smaller probe diameter is not suitable for stiffer clay; therefore, determining suitable diametric probes is necessary before conducting miniature penetrometer tests on different types of clay. However, the influence of the probe diameter on penetration can be ignored, if the probe is non-deformed. Faster penetration speed results in larger penetration stress when the penetration speeds are in the range of 8.9 mm/min to 50.5 mm/min. When the probe diameters are in a range of 2.35 to 2.95 mm, the penetration speed will have a significant influence on penetration stress.

Keywords: Miniature penetrometer test · Soil · Probes · Penetration speed

1 Introduction

Fine-grained clay is comprised by aggregates and the physical and mechanical properties of clay are partly determined by sizes, shapes, internal structures, and strength of aggregates. In order to research the distribution and strength of aggregates in clays, scholars have conducted several studies. Shi [1] used a super miniature penetrometer (SMP) to show the strength distribution isocline maps of aggregates. In addition, the SMP was applied to determine the thermal effects of clay strength [2] and structural strength evolution in the drying process [3]. By using a, Feng [4] used a TMS-PRO texture analyzer to measure soil cone index and detect soil structure. Nevertheless, the above-mentioned studies were only present only one probe diameter and one penetration speed. Clays with different water contents present different statements, so penetration resistance may significantly influenced by different probe diameter and penetration speeds. Therefore, quantitative evaluations of the effects of probe diameters and penetration speeds are needed.

© Springer Nature Singapore Pte Ltd. 2019
L. Zhan et al. (Eds.): ICEG 2018, ESE, pp. 212–218, 2019.
https://doi.org/10.1007/978-981-13-2227-3_26

2 Materials and Test Method

2.1 Materials

Soil specimens were taken from Jingmen City, Hubei Province [4]. The soil is yellowish-brown and contained black iron–manganese concretion. The granulometric composition, physical properties, and mineral composition are shown in Table 1. According to the Unified Soil Classification System (USCS), the liquid limit is smaller than 50% and above the A-line, so the group is labeled "CL".

Table 1. Geotechnical properties and Chemical element composition of the fine-grained clay

Properties		Values
Geotechnical properties		
Grain composition	>0.075 (mm)	13.2%
	0.075 ~ 0.005(mm)	57.3%
	0.005 ~ 0.002(mm)	14.5%
	<0.002(mm)	15.0%
Specific gravity		2.72
Liquid limit		42.1%
Plastic limit		20.9%
Plasticity index		21.2
Free swell ratio		42%
Unified Soil Classification System (USCS) classification		CL
Optimum moisture content		15.5%
Maximum dry density		1.86 $g.cm^{-3}$
Mineral compositions (proportion, %)		
Illite		35
Kaolinite		40
Quartz		20
Montmorillonite		5

The sample was prepared using the pressure sample preparation method. The process of sample preparation is illustrated as follows: (a) Crush the soil and put them through a 2 mm sieve. Add water to the sample preparation's moisture content target (Practically, moisture content in the filling roadbeds is slightly higher than the optimum moisture content. The compacted sample moisture content is 17%, which is greater than the optimum moisture content of 15.5%. The dry density is 1.77 g/cm^3 with degree of compaction of 95.2%. And mix them for 30 min, put them into a hermetic bag, and then store them in a wet-protection cylinder for 24 h to make the distribution of soil's humidity uniform. (b) Calculate every required wet soil's quality according to expected dry density and put corresponding quality of wet soil into a well-prepared sample pressure, level the sample surface, and press the sample soil into the preparation

mould with static pressure. After compaction, all the specimens were wrapped with a thin plastic film and stored in curing boxes (20 ± 1 °C) at least 72 h until tested.

2.2 Test Method

(1) The experimental facility
The miniature penetrometer test facility is shown in Fig. 1.

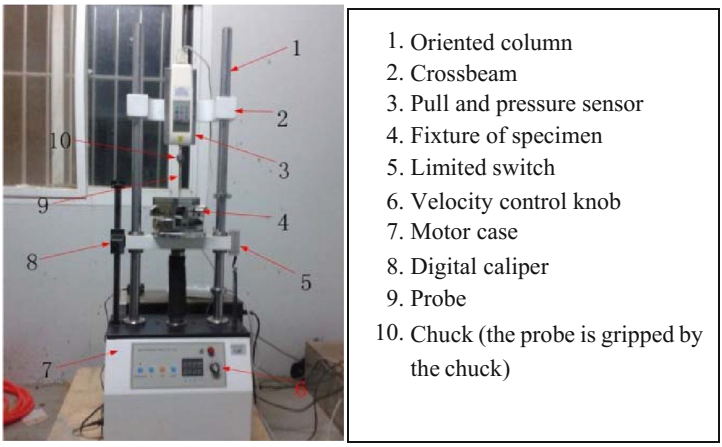

Fig. 1. Miniature penetrometer

The penetration probe is fixed on the bottom of the sensor by a chuck. The infinitely variable speed motor drives the clay sample to increase or decrease at a given rate. A pressure sensor measured the tensile and pressure strength during the process of penetration or pulling out.

(2) Test procedures
Cylindrical probes were used in the test with length of 60 mm. As shown in Fig. 2, seven different diameters are 2.9, 2.65, 2.35, 2.05, 1.75, 1.45, and 1.05 mm. Three types of penetration speeds are 10, 25, and 50 mm/min. The measured speeds are 8.9, 25.2, and 50.5 mm/min. The penetration depth is 8.0 mm.

(3) Data processing method
When the cylindrical probe penetrates into the soil sample vertically at a constant speed, the total resistance R_{ptotal} can be obtained, which consists of tip resistance R_p and penetrated friction f_1. Pulling out of the probe is affected by the force of friction f_2. Approximately, the penetrated friction is equal to the pulled out friction, that is, $f_1 = f_2$. Therefore, the tip resistance R_p is the algebraic difference of the total resistance R_{ptotal} and the friction f_2, that is, $R_p = R_{ptotal} - f_2$.

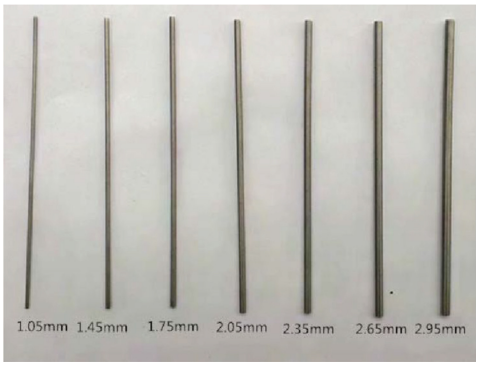

Fig. 2. Photograph of probes

3 Results

3.1 Effects of Probe Diameters on Penetration Stress

Figure 3 illustrates the relationship between the penetration resistance and depth. Larger probe diameters correspond to higher penetration resistance. Therefore, penetration resistance cannot be analyzed and compared directly.

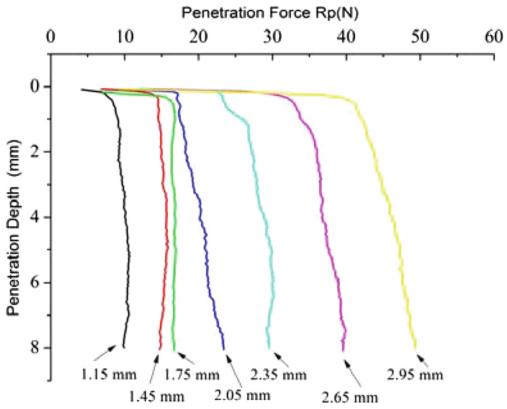

Fig. 3. Relationship between penetration resistance and penetration depth of 7 different diameter probes

Penetration stress can be calculated by penetration resistance obtained from the tests and probe cross-sectional area:

$$P_t = R_p/CSA. \tag{1}$$

P_t is the penetration stress (MPa), R_p is the penetration resistance (N), and *CSA* is the probe sectional area (mm^2).

From Fig. 4, the following observations can be made:

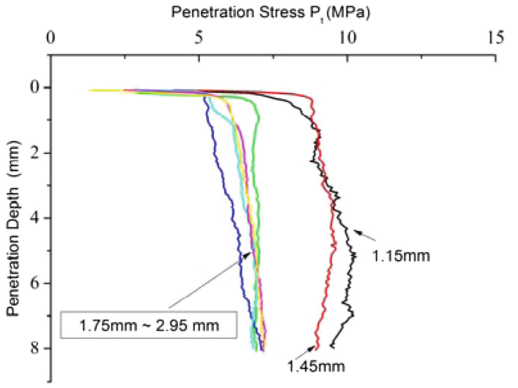

Fig. 4. Variation of the penetration stress with depth of 7 different diameter probes

Firstly, when the probe diameters are 2.95, 2.65, 2.35, 2.05, and 1.75 mm, the penetration curves are almost consistent. The penetration stress increases in the early penetration period (the penetration depth is less than 0.5 mm). In the middle period, penetration stress keeps stable. When the probe is smaller than 1.45 mm, a relatively large amplitude decrease of penetration stress was observed during the early and last penetration periods. Given that soil is homogeneous, the average penetration stress is theoretically unrelated to the probe's cross-sectional area. However, the penetration stresses of the 1.15 mm and 1.45 mm diameter probes are larger than those of probes with diameters of 2.95, 2.65, 2.35, 2.05, and 1.75 mm. In the process of data measurements, the probes deformed in the penetration process and caused large resistance and penetration stress, therefore the penetration of a probe with a diameter smaller than 1.75 mm is unsuitable for a soil sample with 1.77 g/cm^3 dry density and 17% moisture content. Given the limitation of material rigidity in miniature penetrometer tests, a smaller probe diameter leads to higher possibility of penetration stress errors. Therefore, determining suitable diametric probes was necessary before testing of different types of soils.

Secondly, when the probe diameters are within a suitable range (1.75 to 2.95 mm), the penetration stress error will be relatively small at the same penetration speed ($P_{t\max} - P_{t\min}/P_{t\min} < 4\%$). Therefore, at the same speed, the effect of changing probe diameters on the penetration stress is slight.

3.2 Effects of Penetration Speed on Penetration Stress

By calculating the cone penetration based on mollisol, Liyanapathirana [5] found that penetration resistance increases with strain rate and the increase has no immediate relationship with soil fragility. Using ABAQUS of secondary development, Fan [6]

numerically analyzed T-shaped penetrometer penetration mechanism in mollisol and found that penetration speed mainly influences the resistance coefficient of T-shaped probes. By conducting an interior piezocone penetration test at five penetration speeds, Chen [7] proposed that strain rate has an influence on soil samples. Peak intensity is a increasing function of strain rate when the intensity peak is smaller than the influence of strain rate. When the peak intensity is larger than the threshold of strain rate, intensity peak is a decreasing function of the strain rate.

In the miniature penetrometer tests, the influence of penetration speed on penetration stress is shown in Table 2. 8.9 mm/min, 25.2 mm/min, 50.5 mm/min are the measured penetration speed.

Table 2. The effect of penetration speed on penetration stress

Probe diameter (mm)	Average penetration stress P_t (MPa)			
	8.9 mm/min	25.2 mm/min	50.5 mm/min	
1.75	6.48	6.41	6.91	Trial value
	(0.00%)	(−1.08%)	(6.64%)	Rate of change
2.05	6.49	6.60	6.88	Trial value
	(0.00%)	(1.69%)	(6.01%)	Rate of change
2.35	6.25	6.62	6.84	Trial value
	(0.00%)	(5.92%)	(9.44%)	Rate of change
2.65	6.32	6.83	7.09	Trial value
	(0.00%)	(8.07%)	(12.18%)	Rate of change
2.95	5.91	6.91	7.10	Trial value
	(0.00%)	(16.92%)	(20.14%)	Rate of change

When the penetration speeds fall within 8.9 to 50.5 mm/min, faster speeds lead to larger penetration stress. This finding is similar to the results made by Liyanapathirana [5]. When probe diameters are in the range of 2.35 mm to 2.95 mm, penetration speed has a major effect on the penetration stress with the largest increase rates of 16.92% and 20.14% (probe diameter of 2.95 mm), respectively. When the probe diameters are 1.75 and 2.05 mm, penetration speed has a minor influence on penetration stress. As for the probe diameter of 1.75 mm, the average penetration speed is 25.2 mm/min, which is smaller than the trial value of 8.9 mm/min. Thus, when penetration rate is low, a small deformation in the probe will cause a large average penetration stress to some extent.

4 Conclusion

The effects of probe diameter and penetration speed on the miniature penetrometer tests were studied in this work, and the following conclusions were obtained.

(1) The influence of the probe diameter on penetration can be ignored, if the probe is non-deformed.
(2) Smaller probe diameter is not suitable for stiffer clay, therefore, determining suitable diametric probes is necessary before conducting miniature penetrometer tests on different types of clay.
(3) Faster penetration speed results in larger penetration stress when the penetration speeds are in the range of 8.9 mm/min to 50.5 mm/min.
(4) When the probe diameters are in a range of 2.35 to 2.95 mm, the penetration speed will have a significant influence on penetration stress with the largest increase rate of 20.14%.

Acknowledgments. The financial supports from the National Natural Science Foundation of China (Grant No. 51209196, No. 41772339), GuangXi Key Laboratory of Geomechanics and Geotechnical Engineering (14-KF-04) and Key Laboratory of Tianjin Soft Soil Character and Engineering Environment (Grant No. 2014SCEEKL01) are gratefully acknowledged.

References

1. Shi B, Liu ZB, Cai Y (2005) Development of the super mini-penetrometer and its application. Rock Soil Mech 26(8):1211–1215
2. Hong JJ (2013) A study of temperature effect on the structural strength of a clayey soil using the micropenetrometer. Master's thesis, Nanjing University, Nanjing, pp 11–23
3. Wang DY, Tang CS, Li J, Shi B (2014) Super miniature penetration test on structural strength of clayey soil during evaporation. J Eng Geo 22(5):818–823
4. Feng XB, Ding QS, Gong JH, Ren W (2010) A rapid method of construction for soil micro-penetrometer system. Exp Technol Manage 27(12):98–100
5. Liyanapathirana DS (2009) Arbitrary Lagrangian Eulerian based finite element analysis of cone penetration in soft clay. Comput Geotech 36(5):851–860
6. Fan QL, Luan MT, Liu ZG (2009) Numerical simulation of penetration resistance of T-bar penetrometer in soft clay. Rock Soil Mech 30(9):2850–2854
7. Chen TL (2001) Constitutive model of structured clay sand study of parameter determination. PhD Dissertation, Nanjing Hydraulic Research Institute, Nanjing, pp 59–66

Droplet Interaction with Hydrophobic Granular Materials: An Insight with the Lattice Boltzmann Method

Hengyi Kang[1], Sérgio D. N. Lourenço[1(✉)], and Ryan Yan[2]

[1] Department of Civil Engineering, The University of Hong Kong, Kong Kong SAR, China
lourenco@hku.hk

[2] Department of Civil Engineering, University of Auckland, Auckland, New Zealand

Abstract. Water repellent soils, or hydrophobic soils, are described as having delayed wetting of the soil surface and reduced amount of water infiltration, which has been proposed as alternative slope cover materials. The degree of soil water repellency is usually judged by the droplet interaction with the soil surface in the experimental studies. Hence, in this study, the potential capability of the Lattice Boltzmann (LB) method in studying the droplet dynamics on a granular surface with varying wettability is demonstrated, of which the implications to characterizing the soil water repellency are discussed. Simulations are performed on the droplet standing, infiltrating and sliding. On a horizontal surface, LB method can be used to interpret the intrinsic contact angle (CA) at the particle level by simulating the droplet standing with an apparent CA or the time for a droplet to infiltrate. On an inclined surface, LB method helps seek the critical combination of CA and slope angle to trigger the droplet movement, which prevents the accumulation of water on a slope. Therefore, performing the LB simulations within those scenarios will reveal the performance of the water repellent soils in resisting the water infiltration.

Keywords: Soil water repellency · Droplet dynamics · Lattice boltzmann

1 Introduction

Soil water repellency or soil hydrophobicity is defined as a reduction of the affinity between soils and water, so that water cannot spontaneously wet soils [1]. Its natural occurrence results from the coatings of hydrophobic organic matter on the soil particles, which may generate from wild-fires [2] or soil microbiological activities [3]. Soil water repellency can impede the infiltration and facilitate the runoff, so the reduced water supply from rainfall can be detrimental to the growth of plants in agriculture, for instance. However, in geotechnical engineering, the waterproof property may be utilized for reducing the amount of water infiltration and improving the stability of slopes or landfills [4]. Unlike the impermeable shotcrete cover on slopes or the geomembranes in landfills, water-repellent soils are not susceptible to cracks owing to ground deformation. Moreover, synthetic soil water repellency can be controlled, so that they can

© Springer Nature Singapore Pte Ltd. 2019
L. Zhan et al. (Eds.): ICEG 2018, ESE, pp. 219–226, 2019.
https://doi.org/10.1007/978-981-13-2227-3_27

also be used as semi-impermeable barriers, allowing the necessary amount of water for the growth of vegetation to infiltrate. Therefore, investigating the soil water interaction is of practical significance for the potential applications of the synthetic water repellent soils in geotechnical engineering.

The performance of water repellent soils can be revealed from a microscopic perspective by investigating the way in which droplets interact with hydrophobic particles that constitute a granular media. Considering a droplet deposited on a horizontal soil surface, whether the droplet sits above the surface, infiltrates slowly or fast has been used to quantitatively characterize the soil water repellency in the commonly-used sessile drop method (SDM) and the water drop penetration time (WDPT), which respectively takes the liquid-solid apparent CA and the time for completely infiltration as the indicator [5]. On the inclined soil surface, the property of water-repellent soils to trigger a droplet to slide on the inclined soil surface under its own gravity prevents the accumulation of the ponding water, which can be beneficial to maintain the soils in the dry condition. On the contrary, a droplet which gets entrapped on the surface or slides quite slowly will be more likely to result in a ponding situation and may cause severe infiltration. The droplet dynamics can be studied to shed light on the performance of the water repellent soils in resisting water infiltration.

As the droplet interaction with the granular soils develops at the particle-level, multiphase LB method serve as the appropriate tools to study the droplet dynamics [6]. Both the information of the droplet movement above the surface and the microscopic insights into the flows in pores can be retrieved, which compensate for the limitations of experimental studies in observing the pore-scale flows. The objective of this paper is to present the capability of the LB method in studying the droplet standing, infiltrating and sliding dynamics, of which the implications to characterizing the soil water repellency will be discussed.

2 Methodology

The LB method is one popular computational fluid dynamics (CFD) numerical tool, which serves as the appropriate tools for investigating the porous fluid flows. It originates from the kinematic theory and describe the fluid flows in the mesoscale level. The fluid system is treated as groups of molecules residing on a regular lattice, corresponding to several discrete molecular velocities $\boldsymbol{c_i}$. A set of distribution functions related to each $\boldsymbol{c_i}$ are used to represent the statistical information of the molecular movements, from which the macroscopic physical quantities (i.e., pressure and velocity) can be obtained. The governing equation is the discrete Boltzmann equation (DBE), of which the formulation is essentially equivalent to solving the incompressible Naiver-Stokes equation by the artificial compression method [7]. Recently, LB method has been extended to deal with a fluid system with spatially varying density and viscosity [6]. By coupling the LB with the Cahn-Hilliard (CH) equation explicitly tracking the phase field, the coupled LB-CH scheme is capable of addressing a multiphase fluid flow problem, such as the droplet dynamics in this paper.

In the phase-field LB method, the evolution equation for the distribution function g_i with a Bhatnagar-Gross-Krook (BGK) approximation [7] is written as:

$$\frac{\partial g_i}{\partial t} + \boldsymbol{c}_i \cdot \nabla \boldsymbol{g_i} = -\frac{\boldsymbol{1}}{\boldsymbol{\lambda}}\left(\boldsymbol{g_i} - \boldsymbol{g_i^{eq}}\right) + (\boldsymbol{c_i} - \boldsymbol{u}) \cdot [\nabla \boldsymbol{\rho c_s^2}(\boldsymbol{\Gamma}_i(\boldsymbol{u}) - \boldsymbol{\Gamma}_i(\boldsymbol{0}) + \boldsymbol{F}\boldsymbol{\Gamma}_i(\boldsymbol{u})], \quad (1)$$

where λ is the relaxation time factor, g_i^{eq} is the equilibrium distribution function, c_s is the sound of speed and $\boldsymbol{F}$ is the body force. Here, the relationship between λ and the kinematic viscosity v can be written as $v = \lambda c_s^2$. For each LB node, the material properties of viscosity v and density ρ, together with the body force $\boldsymbol{F}$, shall be obtained from the CH equation. By solving the evolution of g_i over the time step δt, the fluid pressure p and velocity $\boldsymbol{u}$ can be easily computed as:

$$\rho \boldsymbol{u} = \sum \boldsymbol{c}_i g_i + \frac{\delta t}{2}\boldsymbol{F}, \quad (2)$$

$$p = \sum g_i + \frac{\delta t}{2}\boldsymbol{u} \cdot \nabla \rho c_s^2. \quad (3)$$

While the LB method handles the hydrodynamic aspect of a multiphase flow problem, the CH equation tracks the evolution of the two immiscible liquid and vapour phases. The system of binary fluids adopts the one-fluid formulation where a phase index field C is defined to describe the phase that occupies each computational cell. The phase index C is around 1 for the liquid phase and is around 0 for the vapour phase. The value gradually changes from 0 to 1 in the interface. The CH equation that models the phase separation is written as:

$$\frac{\partial \boldsymbol{C}}{\partial \boldsymbol{t}} + \nabla \cdot (\boldsymbol{uC}) = \boldsymbol{M}\nabla^2 \boldsymbol{\mu}, \quad (4)$$

where the μ is a functional of the phase index C, termed as chemical potential. M is the rate of the highly non-linear non-Fickian diffusion, which leads to the phase separation and helps maintains a liquid-vapour interface at a stable thickness. While the CH equation provides the viscosity, density and the surface tension force for the LB, it requires the velocity to evaluate the advection term $\nabla \cdot (\boldsymbol{uC})$. With the coupled NS-CH equations, the complex behavior of multiphase flows can be simulated.

Table 1. Modelling parameters.

	Parameters	Values
Droplet	Volume (μL)	10
	Density (kg/m^3)	10^3
	Kinematic viscosity (m^2/s)	2.34×10^{-6}
	Surface tension (mN/m)	72.8
Particle	Diameter (mm)	0.89
	CA (°)	30 – 123

In the next section, the application of this phase-field LB method to modelling various droplet dynamics will be presented. The droplet standing, infiltrating and sliding on a granular soil surface will be simulated. The droplet volume is 10 μL, which is within the range of natural rainfall drops [8]. A layer of 0.89 mm spherical particles that matchs those of medium-sized sands will be used as the substrate. The modelling parameters in this study can be referred to Table 1.

3 Modelling Droplet Dynamics

3.1 Droplet Standing

Placing a droplet onto a soil surface leads to an intricate solid-fluid interaction due to the interplay between the droplet infiltration and spreading. The droplet dynamics is governed by the wettability on the soil particle surfaces, which can be described by the intrinsic CA shown in Fig. 1(a). For a soil is in higher degree of water repellency, the droplet may reach a stable configuration with the particles, standing still above the porous surface in a spherical-cap shape. Figure 1(b) shows an image of the SDM test, involving depositing a droplet on sprinkling particles stuck to a double-sided tape [9]. The apparent CA is the intersection angle between the droplet interface and the base plane, which is directly measured on the soil surface. It is the intrinsic CA that governs the bonding capillary stress, the soil water retention and capillary imbibition in a partially saturated soil. Yet, only the apparent CA on a layer of particles is what can be measured. Therefore, analyzing the relationship between the apparent CA and the intrinsic CA is of great importance, and the objective can be addressed with the LB method.

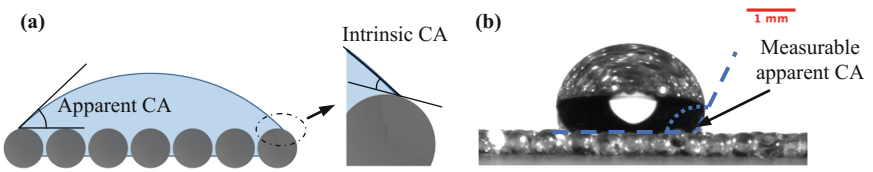

Fig. 1. (a) Sketch of intrinsic CA and apparent CA on a particle layer and (b) Image of the SDM test, showing a 10-μL water drop standing above a layer of hydrophobic glass beads.

Here, the deposition process for 10-μL droplet on a layer of 0.89 mm spheres is simulated with the phase-field LB method described in Sect. 2. Figure 2 presents the temporal evolution of the side projected area A_{proj} of the droplets above the soil surface normalized by the initial projected area A_0, together the representative snapshots. The droplet oscillates and reaches the steady state after the dissipation of the kinematic energy. A significant portion of the droplet with a spherical-cap shape is maintained above the granular surface, converging to a stable apparent CA. For the intrinsic CA as 75°, the apparent CA can be measured from the image at 116.6 ms as 72.5°. By running more tests under different intrinsic CAs, the linkage between the apparent CA and the intrinsic CA can be established.

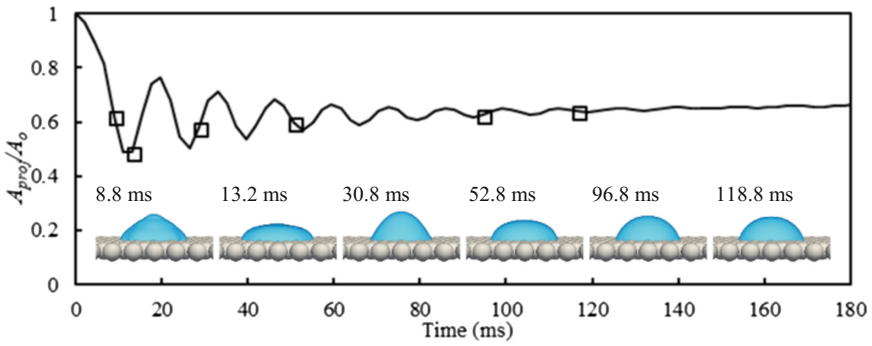

Fig. 2. Normalized projected areas plotted against time for a droplet deposition on the 0.89 mm particle layer with intrinsic CA = 75°. The markers are referring to instants to take the snapshots.

The LB method directly computes the force equilibrium between the pairs of surface tensions and the gravity for a water droplet. Compared to the analytical models assuming an infinitesimal roughness scale relative the droplet size [10], the LB simulation reveals a more realistic droplet configuration with the particles. Within the context of SDM, it provides the opportunity to back analyze the intrinsic CA with the measurable apparent CA.

3.2 Droplet Infiltrating

On a soil surface with reduced wettability, the droplet can still infiltrate but with a much smaller rate. Those soils with reduced wettability are usually termed as 'sub-critical water repellent soils' [11], which may be used as semi-impermeable barriers, allowing the necessary amount of water for the growth of vegetation to infiltrate. In the WDPT test, the time for a water droplet to infiltrate into the soil is used as an indicator of the water repellency. However, this value does not quantitatively reveal the particle-level intrinsic CA. Hence, conducting the LB simulation of the droplet infiltration helps interpreting the results obtained from a WDPT test.

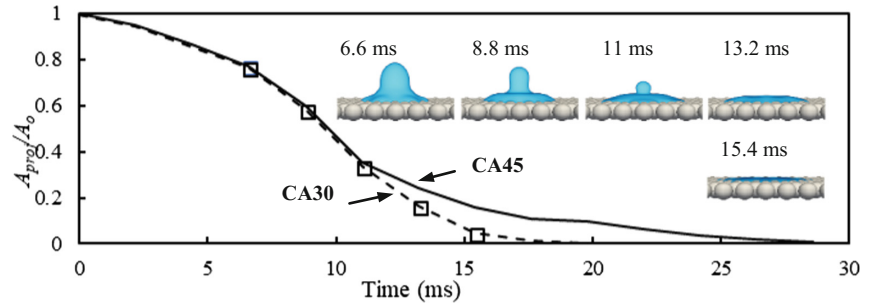

Fig. 3. Normalized projected areas plotted against time for a droplet deposition on the 0.89 mm particle layer with intrinsic CA = 30° (dash line) and 45° (solid line). The markers are referring to instants to take the snapshots.

The droplet infiltration on a layer of 0.89 mm diameter spheres with intrinsic CA = 30° and 45° is simulated. Figure 3 presents the temporal evolution of the A_{proj}/A_0, together the representative snapshots for CA = 30°. Unlike the simulation in Sect. 3.1, the projected area decreases monotonically with time. The infiltration takes 15.4 ms for CA = 30°, and 26.4 ms for CA = 45°. While Sect. 3.1 shows the possibility of back analyzing the intrinsic CA with apparent CA in a relatively higher degree of water repellency, conducing the infiltrating numerical tests under different intrinsic CAs can also help interpreting the intrinsic CA for the 'subcritical water repellent soils'.

3.3 Droplet Sliding

Water droplets slide on an inclined hydrophobic surface with a high CA. One typical example in daily experience is the freely-moving water droplet on a lotus leaf [12]. If an impermeable barrier with high-level waterproof performance is required on a slope, synthetic water-repellent soils as the cover material can be utilized for triggering a droplet to slide on the inclined soil surface under its own gravity. While the study in Sects. 3.1 and 3.2 provide the information on the critical condition to trigger the droplet infiltration, investigating the droplet sliding dynamics can reveal the performance of the soils in preventing the water accumulation on a slope.

Here, a droplet is released near on an 0.89 mm particle layer inclined to 60°, where two intrinsic CAs 104° and 134° are chosen. Since the simulation requires much more time steps, only the two-dimensional analysis is performed. Figure 4 illustrates the evolution of the droplet sliding velocity, from which the effect of intrinsic CA can be identified. The droplet keeps sliding down the slope by pinning and depinning of its interface for the CA = 123°, while the droplet sticks to the granular surface in an asymmetric shape for the CA = 104°. Therefore, the LB method can used to study the critical combination of CA and slope angle [13], which helps determine the required water repellency on a slope.

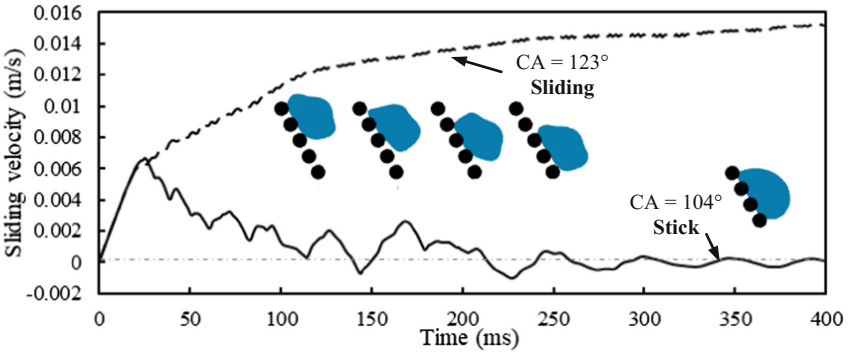

Fig. 4. Siliding velocity plotted against time for a droplet released on an inclined 0.89 mm particle layer with intrinsic CA = 104° (solid line) and 123° (dash line).

4 Conclusion

The paper presents the potential of using the LB method to investigate the droplet dynamics on the water repellent soils. Three aspects of the droplet dynamics are addressed: droplet standing, droplet infiltrating and droplet sliding. On a horizontal surface, a droplet may stand with an apparent CA, or infiltrates into the soils. We demonstrate that LB method helps interpret the intrinsic CA at the particle level in those scenarios. On an inclined surface, the droplet may stick to the surface or slide down the slope. LB method can be used to seek the critical combination of CA and slope angle to trigger the droplet movement, which has practical implications to determine the required water repellency on slopes. In the future, we expect the LB method to be coupled with discrete element method, so that the particle movement can be considered. It will show great potential in modelling the formation mechanism of 'liquid marble' [14], defined as the spontaneous attachment of soil particles to the droplet interfaces. Moreover, the displacement of particles by droplet impacting can be simulated with relations to the splashing erosion [15].

Acknowledgements. This work has been funded by the General Research Fund, Research Grants Council of Hong Kong (17203417: Physically-enhanced water repellency in granular materials). This simulation is conducted in part using the HKU ITS research computing facilities that are supported in part by the Hong Kong UGC Special Equipment Grant (SEG HKU09).

References

1. Doerr SH, Shakesby RA, Walsh R (2000) Soil water repellency: its causes, characteristics and hydro-geomorphological significance. Earth Sci Rev 51(1–4):33–65
2. Debano LF, Krammes JS (1966) Water repellent soils and their relation to wildfire temperatures. Hydrol Sci J 11(2):14–19
3. Jex GW, Bleakley BH, Hubbell DH, Munro LL (1985) High humidity-induced increase in water repellency in some sandy soils 1. Soil Sci Soc Am J 49(5):1177–1182
4. Zheng S, Lourenço SD, Cleall PJ, Chui TFM, Ng AK, Millis SW (2017) Hydrologic behavior of model slopes with synthetic water repellent soils. J Hydrol 554:582–599
5. Leelamanie DAL, Karube J, Yoshida A (2008) Characterizing water repellency indices: Contact angle and water drop penetration time of hydrophobized sand. Soil Sci Plant Nutr 54 (2):179–187
6. Lee T, Liu L (2010) Lattice Boltzmann simulations of micron-scale drop impact on dry surfaces. J Comput Phys 229(20):8045–8063
7. Bhatnagar PL, Gross EP, Krook M (1954) A model for collision processes in gases. I. Small amplitude processes in charged and neutral one-component systems. Phys Rev 94(3):511
8. Hodson MC (1986) Raindrop size distribution. J Climate Appl Meteorol 25(7):1070–1074
9. Bachmann J, Ellies A, Hartge KH (2000) Development and application of a new sessile drop contact angle method to assess soil water repellency. J Hydrol 231:66–75
10. Bachmann J, McHale G (2009) Superhydrophobic surfaces: a model approach to predict contact angle and surface energy of soil particles. Eur J Soil Sci 60(3):420–430
11. Czachor H, Doerr SH, Lichner L (2010) Water retention of repellent and subcritical repellent soils: new insights from model and experimental investigations. J Hydrol 380(1–2):104–111

12. Marmur A (2004) The lotus effect: superhydrophobicity and metastability. Langmuir 20 (9):3517–3519
13. Lv C, Yang C, Hao P, He F, Zheng Q (2010) Sliding of water droplets on microstructured hydrophobic surfaces. Langmuir 26(11):8704–8708
14. Aussillous P, Quéré D (2001) Liquid marbles. Nature 411(6840):924
15. Delon G, Terwagne D, Dorbolo S, Vandewalle N, Caps H (2011) Impact of liquid droplets on granular media. Phys Rev E 84(4):046320

A Numerical Study of the Effect of Wick Drains Applied in Mine Stopes with Paste Fill

Pengyu Yang[1,2(✉)], Li Li[2], and Gengshe Yang[1]

[1] Xi'an University of Science and Technology, Xi'an 710054, China
pengyu.yang@polymtl.ca
[2] Polytechnique Montreal, Montreal H3C 3A7, Canada

Abstract. Paste fill is popularly used in underground mines. A large amount of water is added into fills to facilitate their pipe transportation. Upon placement, the self-weight consolidation in paste fill can lead to the generation of excess pore-water pressures. To avoid excess pressures applied on the retaining structure, filling is usually staged with an undesirable curing interval. Recent numerical analyses conducted by the authors indicated that pre-installing wick drains in backfilled stopes can accelerate the consolidation, and thus enable continuous filling. In previous analyses, however, a zero pressure head was imposed along the wick drains and the effect of third dimension was ignored. These tend to overestimate the fill's consolidation. In this paper, more representative numerical models are performed with GeoStudio, with the three-dimensional drainage around a wick drain converted to an equivalent plane-strain condition. Moreover, the fill permeability in the drift is reduced, compared to that in the stope, to mimic the restricted flow via the drawpoint. The results show that the consolidation of paste fill depends largely on the wick drain layout (spacing). The effect of wick drain size is also evaluated.

Keywords: Paste fill · Wick drains · Modeling · Consolidation

1 Introduction

When applying paste fill in underground mines, a large amount of water is commonly added to produce a flowable mixture for transportation. Before filling, a retaining structure (barricade) is built near the drawpoint to hold the initially saturated fills.

The paste fill possesses a relatively low permeability. Upon placement, the self-weight consolidation occurs within paste fill which can then generate large excess pore-water pressures (PWPs). The resulting excessive stresses may endanger the barricade. As a result, filling is usually staged with an undesirable interval (Thompson et al. 2012). However, such interval may cause pipe clogging and impair the production. To improve the drainage in backfilled stopes, barricades have been built with porous materials or equipped with drain pipes (Potvin et al. 2005).

Recently, Li (2013) has proposed to pre-install wick drains (see Fig. 1) in stopes to accelerate the consolidation of paste fill. Details on the installation of wick drains were also presented. Further analyses conducted by the authors have indicated that applying wick drains in backfilled stopes can facilitate the production by eliminating the filling

© Springer Nature Singapore Pte Ltd. 2019
L. Zhan et al. (Eds.): ICEG 2018, ESE, pp. 227–233, 2019.
https://doi.org/10.1007/978-981-13-2227-3_28

interval (Li and Yang 2015). While providing useful insights on the behaviors of wick drains applied in mine stopes, previous numerical models contain several oversimplifying assumptions. For instance, a zero pressure head is imposed along the wick drains. A uniform fill permeability is used in the stope and drift without considering the reduced third dimension of the drift. These may over predict the drainage and consolidation within fills and thus lead to non-conservative barricade design. The third dimension of wick drains is also ignored. In the following, more representative numerical analysis is conducted by converting the three-dimensional (3D) drainage around a band drain to an equivalent plane-strain condition.

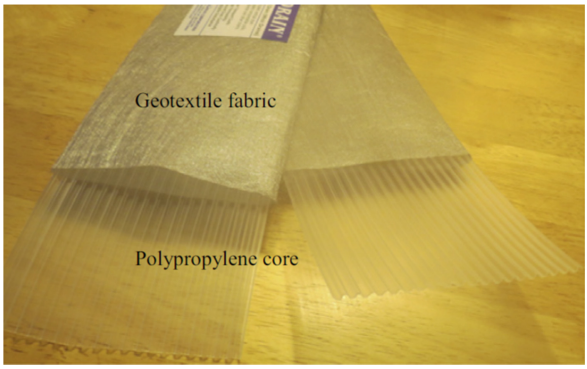

Fig. 1. Wick drains consisting of geotextile fabric and polypropylene core (AMERDRAIN®) (Reproduced with permission from Li and Yang 2015).

2 Equivalent Plan-Strain Permeability

In 3D condition, the equivalent diameter d_e of a wick drain (rectangular in cross section) can be obtained by considering the "perimeter equivalence" (Hansbo 1979):

$$d_e = \frac{2(t+w)}{\pi} \tag{1}$$

where t is the thickness of the wick drain and w its width.

Applying Eq. 1 converts the flow around a band drain to an equivalent axisymmetric (AX) radial flow around a circular drain. The latter is more of simplicity, and its corresponding theory of consolidation has been widely applied in geotechnical engineering (e.g. Hansbo 1981, Indraratna and Redana 1997).

To obtain the same degree of consolidation for AX and plane-strain (PS) conditions, the AX hydraulic conductivity of fill k_{ax} can be converted to an equivalent PS value of fill k_{ps}. For simplicity, such conversion is commonly done by changing only the hydraulic conductivity of soils in two conditions while keeping the size of drains the same (i.e. AX drain diameter equals to PS drain thickness; Hird et al. 1992):

$$\frac{k_{ps}}{k_{ax}} = \frac{0.67}{[\ln(n) - 0.75]} \tag{2}$$

where n (=D/d_e) is the ratio of drain spacing D to the equivalent drain diameter d_e.

3 Numerical Simulations

3.1 Numerical Model

The "Coupled Stress/PWP" analysis type of SIGMA/W (Geo-Slope 2007) is used. Figure 2 shows the numerical model of a backfilled stope with one pre-installed wick drain (spaced at 10 m). Filling is done at a rising rate of 0.1 m/h for a stope of 30 m high and 10 m wide. The height of the drift is 5 m. The thickness t of wick drain is 4 mm and its width w is 100 mm, corresponding to a PS drain with equivalent thickness d_e of 66 mm (based on Eq. 1). No hydraulic boundary condition is imposed along the wick drain. In the drift, five drain points are modeled at the end of paste fill to drain water from the consolidating fills, with each wick drain (one or more) passing through each drain point (see Fig. 2). The mesh of the fill (in stope and drift) is 0.25 × 0.25 m. The top of the backfilled stope is left open while other outer boundaries are fixed.

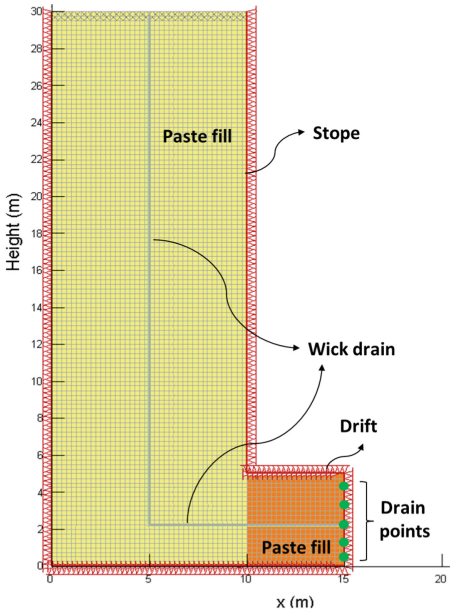

Fig. 2. Numerical model of a typical backfilled mine stope with one pre-installed wick drain.

The hydraulic functions of paste fill are plotted in Fig. 3; these are based on laboratory data reported for tailings (Godbout et al. 2007). The saturated hydraulic conductivity of paste fill k_{ax} in AX condition is 1×10^{-7} m/s, so its equivalent value k_{ps} in PS condition is obtained by Eq. 2. The hydraulic conductivity of fills gradually decreases as they consolidate; this can be approximated by the *k*-modifier function provided by SIGMA/W (see Li and Yang 2015). The horizontal permeability k_x of the wick drain is kept the same as that of the initial k_{ps} of paste fill, while its vertical value k_y is taken as 1×10^{-5} m/s (to be representative of the well/drain resistance; Geo-Slope 2007).

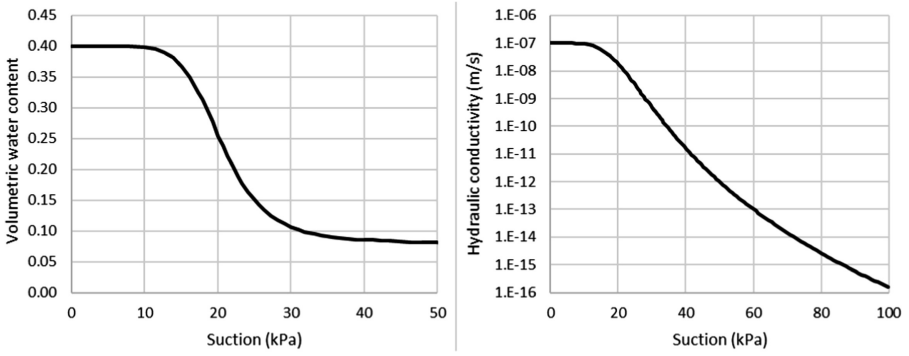

Fig. 3. Hydraulic functions of paste backfill used for numerical simulations.

The paste fill is modeled as a Mohr-Coulomb elastoplastic material. Table 1 shows the cases of simulations. The mechanical properties of wick drain are identical to the paste fill so that the former does not affect the mechanical response of the latter.

Table 1. Characteristics of simulation cases (paste fill: $k_{ax} = 1 \times 10^{-7}$ m/s; wick drain: $t = 4$ mm, k_x = initial k_{ps}, $k_y = 1 \times 10^{-5}$ m/s; wick drain and fill: Poisson's ratio $v = 0.334$, internal friction angle $\phi' = 30°$, Young's modulus $E = 5000$ kPa, effective cohesion $c' = 0$, dilation angle $\psi = 0$, unit weight $\gamma = 20$ kN/m^3, coefficient of compressibility $m_v = 0.0002$ kPa^{-1})

Case no.	Wick drain spacing D (m)	Wick drain width w (mm)	d_e (mm)[a]	k_{ps} (m/s)[b]	k_{drift} (m/s)[c]
1	10	100	66	1.57×10^{-8}	$k_{ps}/4 = 3.93 \times 10^{-9}$
2	2	100	66	2.52×10^{-8}	$k_{ps}/4 = 6.30 \times 10^{-9}$
3	10	200	130	1.86×10^{-8}	$k_{ps}/4 = 3.93 \times 10^{-9}$
4	10	100	66	1.57×10^{-8}	$k_{ps}/1 = 1.57 \times 10^{-8}$

[a]d_e is obtained by Eq. 1; [b]k_{ps} is estimated by Eq. 2; [c]considering a ratio of 4 or 1 between the stope length and the drift width (Fahey et al. 2009; Yang and Li 2017).

In 3D, the flow via drawpoint is restricted due to the reduced third dimension of drift, in relative to stope. For 2D modeling, such effect is simulated by reducing the permeability k_{drift} of fill in the drift (see also Fahey et al. 2009; Yang and Li 2017).

3.2 Results

Figure 4 illustrates the PWP contours of backfilled stopes at the end of filling, for different layouts of wick drains. Figures 4b and c indicate the progressive reduction of PWPs due to the introduction of wick drains, which is more profound around the wick drain as the depth increases. As seen from the 50 kPa contour lines shown in Fig. 4b and c, at the end of filling, the upward drainage inside the wick drain occurs. Small unsaturated zones are present around the wick drains at the top surface of the consolidating fills. Figure 4 also illustrates that increasing the number of wick drains from 1 to 5 (reduced spacing from 10 to 2 m) would significantly accelerate the consolidation of paste fills. As the spacing of wick drains decreases, the PWPs reduce throughout the stope and drift (particularly around wick drains).

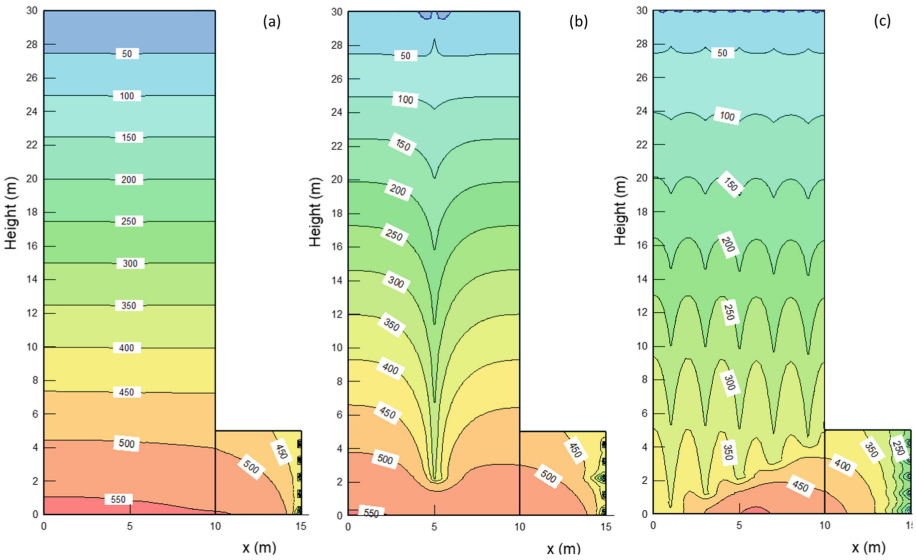

Fig. 4. PWP contours of backfilled stopes at the end of filling with: (a) no wick drain, (b) one and (c) five wick drains spaced at 10 (Case 1) and 2 m (Case 2) respectively.

The effect of the wick drain width (w) on the distribution of PWP has also be investigated. Figure 5 shows the PWP distributions across the height of 5 m (from the stope base) in backfilled stopes at the end of filling, for different widths of wick drain. These results indicate that doubling the width of a wick drain only leads to small reduction in PWP.

Figure 6 demonstrates the PWP distributions across the bottom of the backfilled stope and drift at the end of filling, for different values of k_{drift}. For Cases 1 and 4, the

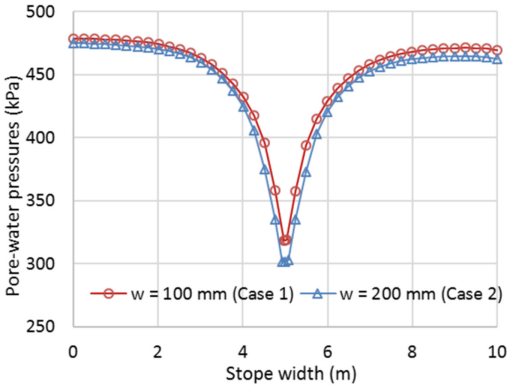

Fig. 5. Distributions of PWP in backfilled stopes (across the height of 5 m) at the end of filling, for different widths of wick drain (Cases 1 and 3).

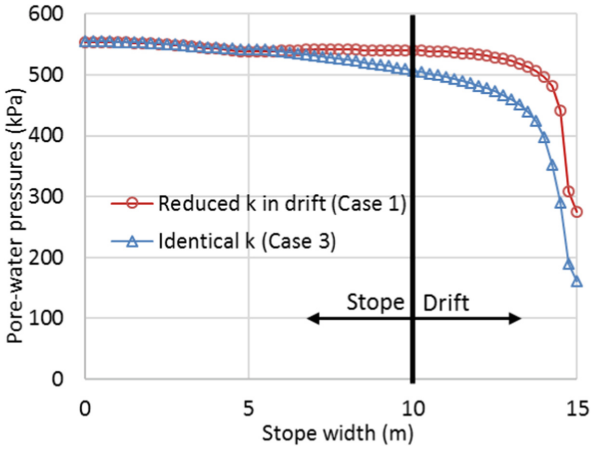

Fig. 6. Distributions of PWP along the bottom of the backfilled stope and drift at the end of filling, for different permeability k_{drift} (Cases 1 and 4).

values of PWP are almost identical on the left-hand side of the stope center. On the right-hand side, the PWPs are seen to be much larger in the case of reduced k_{drift}, particularly for areas in the drift. Thus, a narrower drift and a smaller k_{drift} can results in higher PWP on the barricade.

4 Concluding Remarks

Introducing wick drains in backfilled stopes can accelerate the fills consolidation. Such process is numerically simulated in a more realistic manner using GeoStudio, with the 3D drainage around a wick drain converted to an equivalent plane-strain case. The progressive reduction of PWP near wick drains is modeled. The results indicate that the

degree of consolidation of paste fill depends mainly on the layout of wick drains; their size nonetheless has relatively small effect.

Additional results (not shown here) indicate that the use of wick drain could largely impact the post-filling ponding on the top surface of fill. Other factors being studied include the rising rate of backfill, wick drain resistance, and clogging of wick drains. Three-dimensional modeling is also required to better investigate the hydromechanical behavior of backfilled stope with pre-installed wick drains.

Acknowledgements. The authors acknowledge the support of the NSERC (402318), IRSST (2013-0029), FRQNT (2015-MI-191676), Mitacs Elevate Postdoctoral Fellowship (IT08484), and industrial partners of Research Institute on Mines and Environment (RIME UQAT-Polytechnique; http://rime-irme.ca/en).

References

Fahey M, Helinski M, Fourie A (2009) Some aspects of the mechanics of arching in backfilled stopes. Can Geotech J 46(11):1322–1336

Geo-Slope: Stress-Deformation Modeling with SIGMA/W, GEO-SLOPE International Ltd., Calgary (2007)

Godbout J, Bussière B, Aubertin M, Belem T (2007) Evolution of cemented paste backfill saturated hydraulic conductivity at early curing time. In: 60th canadian geotechnical conference, Ottawa, Canada

Hansbo S (1979) Consolidation of clay by band-shaped prefabricated drains. Ground Eng 12 (5):16–25

Hansbo S: Consolidation of fine-grained soils by prefabricated drains. In: 10th international conference on soil mechanics and foundation engineering, vol. 3, pp. 677–682. AA. Balkema, Rotterdam, The Netherlands (1981)

Hird CC, Pyrah IC, Russell D (1992) Finite element modelling of vertical drains beneath embankments on soft ground. Géotechnique 42(3):499–511

Indraratna B, Redana IW (1997) Plane strain modeling of smear effects associated with vertical drains. J Geotech Eng 123(5):474–478

Li L (2013) A new concept of backfill design - application of wick drains in backfilled stopes. Int J Min Sci Technol 23:763–770

Li L, Yang PY (2015) A numerical evaluation of continuous backfilling in cemented paste backfilled stope through an application of wickdrains. Int J Min Sci Technol 25(6):897–904

Potvin Y, Thomas E, Fourie A (2005) Handbook on Mine Fill. ACG, Perth, Australia

Thompson BD, Grabinsky MW, Bawden WF (2012) In situ measurements of cemented paste backfill at Cayeli Mine. Can Geotech J 49(7):755–772

Yang P, Li L (2017) Evolution of water table and pore-water pressure in stopes with submerged hydraulic fill. Int J Geomech 17(9):04017052

Check for updates

Effect of Additives on Consistency Limits of Red Mud Waste: A Comparative Study

N. Gangadhara Reddy(✉) and B. Hanumantha Rao

School of Infrastructure, IIT Bhubaneswar, Argul, Jatni 752050, Odisha, India
{gnll, bhrao}@iitbbs.ac.in

Abstract. Knowledge of consistency limits is considered important in predicting the engineering properties (viz., swelling, shrinkage, strength, etc.) as well as for identifying and classifying the geomaterials. Determination of these consistency indices becomes even more imperative when selecting geomaterials (soil or waste) as a resource material for constructing earthen structures. This paper focuses on evaluating the consistency limits (or Atterberg's limits such as liquid limit, plastic limit, and plasticity index) of red mud waste admixed with oxalic acid, gypsum, sodium silicate, and the combination of fly ash and gypsum additives in different proportions, in a comprehensive way. The results show significant variations in the value of Atterberg's limits of ameliorated red mud waste vis-à-vis with that of raw waste. It has been inferred that the results reported in the study are of great help in asserting the suitability of the red mud waste in geotechnical engineering applications.

Keywords: Consistency limits · Red mud · Chemical additives
Waste utilization

1 Introduction

Problems arise in the disposal and management of a large quantity of wastes, in addition to the environmental considerations, are compelling to utilize these materials for the development of infrastructure. Red mud is one of the waste materials obtained as a by-product by aluminium companies in the Bayer's process. Its huge quantity of generation is increasingly becoming unmanageable to dispose it and thereby, becoming a cause of concern to the environment because it is highly alkaline in nature. Recent studies have brought out that the waste possesses very good geotechnical properties, resemble that of conventional soils [1, 2] and thus, it received the attention to consider as a potential resource material for the civil engineering applications.

A typical consistency limits for the untreated red mud waste reported by research fraternity range from 25 to 66%, 17.5 to 40%, and 4 to 32% of liquid limit (w_L), plastic limit (w_{PL}), and plasticity index (w_{PI}), respectively [1, 3–7]. Many of the studies classify the red mud as inorganic low plasticity silt, ML, [2, 4, 6, 8]. It has also been found from the literature that the waste exhibits plastic behavior, analogous to clayey soils, even when it does not constitute with any clay type minerals [1, 6]. However, studies related to investigating the geotechnical properties including index and strength are very limited, that too most of them remained confined to untreated waste.

© Springer Nature Singapore Pte Ltd. 2019
L. Zhan et al. (Eds.): ICEG 2018, ESE, pp. 234–241, 2019.
https://doi.org/10.1007/978-981-13-2227-3_29

Modification by mechanical stabilization or alteration by chemical treatment is a common technique of enhancing the strength and stability of weak or problematic soils. The stabilization or treatment can, in turn, enable the poor soil performing superior so that it could qualify to be chosen in geotechnical engineering applications. In general, ordinary Portland cement is extensively being employed for the purpose of soil modification or stabilization. However, the carbonation process subsequent to the admixture of cement leads to the release of CO_2 and create other environmental complications such as pollution of soil and water. In this context, studies have highlighted that treating with additives such as fly ash or organic chemicals, either alone or in their combination, in predetermined proportions is beneficial [9]. The stabilization or treatment, usually, in addition to changing the engineering properties also alters the index properties due to cementation or hydration process which takes place with the addition of an additive(s).

As such, the establishment of index properties becomes vital as they often are the basis for asserting suitability of a soil/waste for constructing earthen structures and concurrently, in assessing other engineering properties. However, many studies on the red mud suggest that neutralization or treatment is mandatory in order to reduce its alkalinity levels (i.e. pH) to a well acceptable level specified by codes and standards [10, 11]. Generally, soils having high clay content can, in turn, show high plasticity indices, within the pH levels varying from 5 to 9. On the other hand, the red mud predominantly contains silt sized particles shows less to moderate plasticity index values, even though alkalinity levels are significantly high i.e. above 11 [1, 2, 12, 13].

Many studies show that the red mud is a non-toxic material [14–16]. USEPA also doesn't classify it as a toxic material rather it suggests neutralizing the waste for lowering the alkalinity levels. Thus, neutralization or treatment of the red mud becomes a major issue. Generally, pH between 8 to 9 is acceptable [2, 16] because at this pH value heavy metals get precipitated or turned into oxidation form and thereby, will not get released into ecosystem [10, 11, 16]. Additives such as gypsum and oxalic acid are commonly preferred to reduce the pH. In addition, researchers also advocated alkali activation to stabilize the red mud using sodium silicates and sodium hydroxide [17].

The objective of this paper is to establish the consistency limits of the red mud waste after suitably ameliorating with a variety of additives. In the present study, additives such as oxalic acid (an organic acid), gypsum (commercial grade), sodium silicate (chemical solution) and the combination of fly ash (waste material) and gypsum have been chosen for admixing with the red mud. The findings reported in the study have had significant applications in the range from classifying the red mud waste to understanding the possible effect of additives on various engineering properties to assessing the feasibility of the red mud for beneficial reuse in geotechnical engineering applications.

2 Materials and Methods

Red mud used in the present study was collected from NALCOs Alumina Refinery factory disposal pond located at Damanjodi of Koraput district, Odisha, India.

2.1 Physical Properties

The size analysis and specific gravity of the red mud were determined in accordance with the ASTM standards. It has been observed that the red mud predominantly consists of fine particles in the range of silt size (66%), followed by clay and sand sizes of 29% and 5%, respectively. The specific gravity of the waste is measured as 3.05. The high value is due to the presence of oxides and mineral groups belonging to Fe family. The value of specific gravity measured is confirming to the results of Reddy and Rao (2018), Rao and Reddy (2017) [2, 12] on the same source red mud waste. The results obtained are presented in Table 1. Based on USCS, the red mud waste can be classified as silt of low plasticity soil (ML).

Table 1. Physical and geotechnical properties of the raw red mud waste

Property	Value
pH range	10.7–11.5
w_L, w_P, and w_{PI} (%)	41, 36, & 5
Sand, silt, and clay fraction (%)	5, 66, & 29
Specific gravity	3.05
Classification (USCS)	ML type

2.2 Sample Preparation and Procedures

Atterberg's limits of the raw and ameliorated red mud were determined using Casagrande apparatus following the guidelines of ASTM D 4318-17 standard [18]. The raw material passing 425 μm was taken by dry weight basis according to their designated proportions. To this dry material, distilled water was added in the desired quantity and mixed thoroughly until homogenous paste form is attained. The prepared sample was then kept in zip lock bags and stored in a humidity chamber for homogenization for a period of 18 h at room temperature. The prepared sample is then transferred to the Casagrande apparatus for determination of the liquid limit. The tests are carried at a uniform drop blow rate of 2 cycles/second. The water content is determined corresponds to 25 numbers of blows by plotting the number of blows versus water content on a semi-log graph. The plastic limit of red mud is determined by making a thread of about 3 mm diameter (hand rolling) of the homogenized sample on a smooth glass plate.

The consistency indices in terms of water content were obtained for different combinations such as (a) red mud (RM) + oxalic acid (OA), (b) red mud + gypsum ($CaSO_4{\cdot}2H_2O$) (GP), (c) red mud + sodium silicate (Na_2SiO_3) (SS), and (d) red mud + fly ash (FA) + gypsum, respectively. The consistency limits measured on the raw red mud are listed in Table 1.

3 Results and Discussion

It has been reported that the physical properties of the raw red mud are considerably influenced by the amount of water present in it. Upon the addition of water, the red mud quickly turns into a slurry form, offering practically no resistance to flow. Therefore, in all practical scenarios, this limit of water content has a great significance in understanding the behavior of red mud waste.

Figures 1, 2, 3 and 4 shows the variations in consistency indices measured on the raw red mud and that of admixed with different additives in varying proportions.

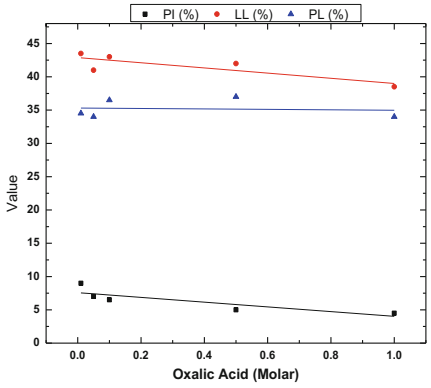

Fig. 1. Influence of oxalic acid treatment on the consistency indices of the red mud waste

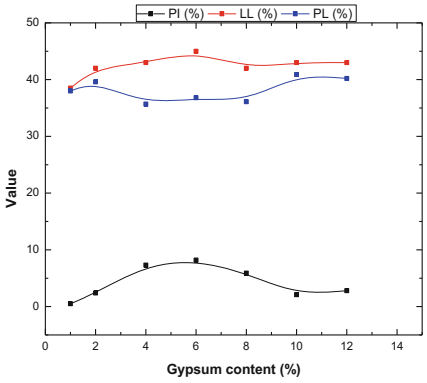

Fig. 2. Influence of gypsum treatment on the consistency indices of the red mud waste

Evidently, the addition of oxalic acid steadily decreased (refer to Fig. 1) all the three consistency limits of the red mud. However, the decrease in the magnitude is noticed to be marginal. Whereas the treatment with gypsum additive caused to increase w_L & w_{PI} and decrease in w_P slightly up to the gypsum content of 6% and beyond this value, the response became reverse, as depicted in Fig. 2. On the other hand, SS admixture to the red mud seems to have negligibly decreased w_{PI} with a slight increase in w_L & w_P, as depicted in Fig. 3. Overall, it can be observed from the Figs. 1, 2 and 3 that the gypsum treatment, as compared with the oxalic acid and sodium silicate, lead to the red mud exhibiting greater plasticity behavior, as the values of w_{PI} measured found to be falling in the range of 1–9%. It is seen from the Fig. 2 that the value of w_{PI} over the GP content of 4 to 8% are higher than that of raw RM. While the range of water content over which SS & OA admixed samples showed plasticity behavior is just measured as 3–5%, which incidentally are lesser as compared to raw RM (i.e. 5%) as well as that of GP treated samples.

In addition, Atterberg's limits were also measured on the red mud waste admixed with fly ash & gypsum in varying proportions. The results obtained are shown in Fig. 4. A simple observation of Fig. 4 reveals that the influence of fly ash in altering the consistency indices appears to be more prominent over the gypsum additive. Evidently, the values of w_L, w_P and w_{PI} remained almost the same for the whole range of gypsum

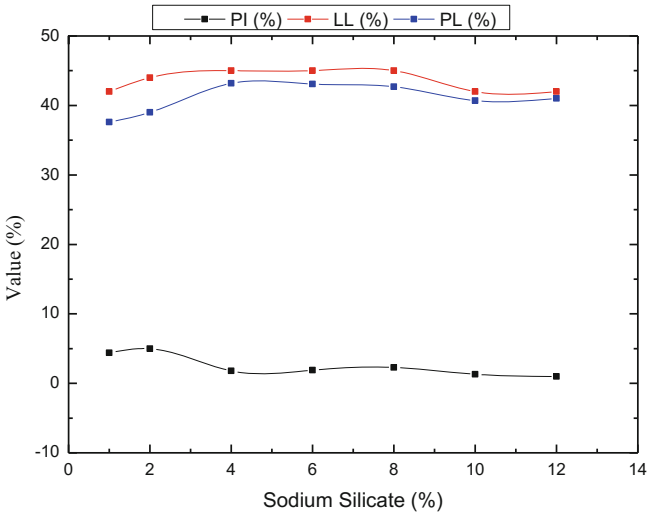

Fig. 3. Influence of sodium silicate treatment on the consistency indices of the red mud waste

content from 2 to 8%. While, with an increase in fly ash content, both w_L and w_P decreased and w_{PI} has increased.

It can also be noticed from Fig. 4 corresponding to a particular fly ash proportion, the change in values of Atterberg's limits over the gypsum content from 2 to 8% is trivial. Importantly, w_{PI} is quite low (<3% less than that of raw red mud) when the admixed fly ash content is less than 20% and increased considerably (exceeding the raw red mud) with its further addition. Generally, the specifications of different codes and standards highlight that soil/waste exhibiting lower w_{PI} are good resource materials to be selected for earthen construction (viz., roads, pavements, etc). It can be inferred from the results that the addition of fly ash up to 20% would be ideal in a stabilization point of view.

From Figs. 1 and 2, it can be witnessed that the addition of OA and SS does not seem to change the plasticity properties of the red mud waste significantly. This finding well corroborates with the results of Rai et al. [11] and Li and Rutherford [19], who also have asserted that oxalic acid being an organic acid does not affect plasticity properties of the red mud waste. Thus, it can be highlighted that the stabilization of RM using these two additives is particularly beneficial. In this regard, Newson et al. [1] have reported that the acid treatment (HNO_3) causes breakdown of hydroxysodalite bonds causing to change marginally the mechanical properties, only, of treated red mud waste. At low percentage of SS, some sodium ions might be adsorbed to the red mud particles. This way the net negative charge of the red mud decreases. At higher concentrations, SS might be resulting in adsorption of positively charged sodium ions causing to decrease in the net negative charge of the particle. These could have a possible influence on the liquid limit and plastic limit, overall leading to a decrease in the plasticity index of the red mud.

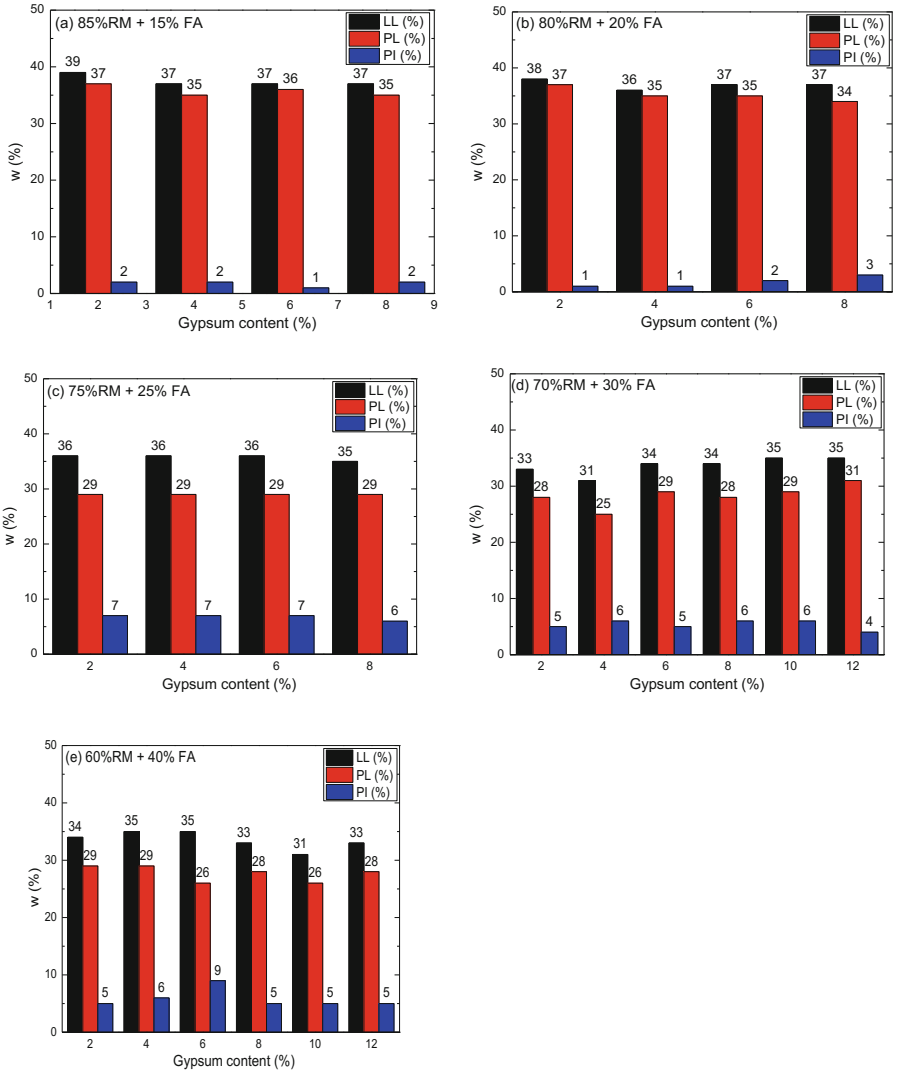

Fig. 4. Variations in Atterberg's limits of red mud admixed with fly ash and gypsum in varying proportions

4 Conclusions

In the present study, consistency indices of the red mud waste were measured after admixing it with a variety of additives in different proportions. It has been observed from the results that the addition of chemicals such as oxalic acid and sodium silicate does not significantly affect the plasticity properties of the red mud waste. While the treatment with gypsum alone and the combination of gypsum & fly ash have altered the plasticity properties of the red mud waste. As such, the samples ameliorated with

sodium silicate alone and the combination of RM: FA: GP in 80%:20%:4% showed least w_{PI} values, confirming that the red mud has a potential to become a beneficial material in geotechnical engineering applications.

Acknowledgments. The research work presented in the paper was carried out with the financial support provided by DST-SEB, Govt. of India. Authors greatly acknowledge and thank the DST-SERB, Government of India, for the financial support for carrying out this research work.

References

1. Newson T, Dyer T, Adam C, Sharp S (2006) Effect of structure on the geotechnical properties of bauxite residue. J Geotech Geoenvironmental Eng 132(2):143–151
2. Reddy NG, Rao BH (2018) Compaction and consolidation behaviour of untreated and treated waste of Indian red mud. Geotech Res 5(2):106–121
3. Reddy NG, Rao BH (2016) Evaluation of the compaction characteristics of untreated and treated red mud. Geotech Spec Publ 272:23–32
4. Reddy NG, Rao BH (2018) Characterization of settled particles of the red mud waste exposed to different aqueous environmental conditions. Indian Geotech J, 15 pages
5. Kirkpatrick DB (1996) Red mud product development. Light Metals, In: Proceedings of the technical sessions at the 125th TMS annual meeting; TMS light metals committee, pp. 75–80
6. Somogyi F (1976) Dewatering and drainage of red mud tailings. PhD Dissertation, Department of Civil Engineering; University of Michigan; Ann Arbor, MI; 291 pages
7. Villar LFS, Campos TMP, Azevedo RF, Zornberg JG (2009) Influence of laboratory techniques on the geotechnical characterization of mining and industrial wastes. In: 17th International Conference on Soil Mechanics and Geotechnical Engineering, pp. 186–189, Alexandria, Egypt
8. Gore MS, Gilbert RB, McMillan I, Isovitsch PSL (2016) Geotechnical characterization of compacted bauxite residue for use in levees. Geotech Spec Publ 270:299–310
9. Cheshomi A, Eshaghi A, Hassanpour J (2017) Effect of lime and fly ash on swelling percentage and Atterberg limits of sulfate-bearing clay. Appl Clay Sci 135:190–198
10. Khaitan S, Dzombak D, Lowry GV (2009) Chemistry of the acid neutralization capacity of bauxite residue. Environ Eng Sci 26(5):873–881
11. Rai S, Wasewar KL, Mukhopadhyay J, Yoo CK, Uslu H (2012) Neutralization and utilization of red mud for its better waste management. Arch Environ Sci 6:13–33
12. Rao BH, Reddy NG (2017) Zeta potential and particle size characteristics of red mud waste. In: Babu GLS, et al (eds) Geoenvironmental practices and sustainability, developments in geotechnical engineering, pp. 69–89, Springer, Singapore
13. Gräfe M, Power G, Klauber C (2011) Bauxite residue issues: III. Alkalinity Assoc Chem Hydrometall 108:60–79
14. Paramguru RK, Rath PC, Misra VN (2004) Trends in red mud utilization - a review. Miner Process Extr Metall Rev 26(1):1–29
15. Rubinos DA, Barral MT (2013) Fractionation and mobility of metals in bauxite red mud. Environ Sci Pollut Res 20:7787–7802
16. Panda I, Jain S, Das SK, Jayabalan R (2017) Characterization of red mud as a structural fill and embankment material using bioremediation. Int Biodeterior Biodegrad 119:368–376

17. Choo H, Lim S, Lee W, Lee C (2016) Compressive strength of one-part alkali activated fly ash using red mud as alkali supplier. Constr Build Mater 125:21–28
18. ASTM D4318-17 (2017) Standard test methods for liquid limit, plastic limit, and plasticity index of soils, ASTM International, West Conshohocken, PA
19. Li LY, Rutherford GK (1996) Effect of bauxite properties on the settling of red mud. Int J Miner Process 48:169–182

Optimization of Disposal Areas by Studying of the Mining Rock Waste Granulometry of an Iron Mine

Christ Jesus Barriga Paria(✉), Hernani Mota de Lima, and Eleonardo Lucas Pereira

Universidade Federal de Ouro Preto,
Ouro Preto, 35400-000 Minas Gerais, Brazil
cjbarriga_87@hotmail.com

Abstract. Usually, the values of the resistance parameters of the material disposed in the mine waste rock piles differ from those that were used in the design phase, so it becomes necessary to know how the resistance parameters are affected by the change in granulometry. The present work aims to evaluate the variations of the geotechnical properties and the effect that causes the scale of the granulometry in the behavior of the sterile rock. An extensive experimental program, including laboratory testing techniques and the use of sophisticated equipment, starting with the knowledge of its characteristics, in a vision to improve the implementation of the experimental program, always under international standards, samples obtained from tests were used of physical characterization. The methodology accompanying the behavior of a sample of mine waste rock deposited in sterile waste pile to which was artificially modifying their granulometry unchanged the original design of the granulometric curve was subjecting each specimen tests direct shear to ob tain resistance parameters based on these modifications. The friction angle obtained for these new granulometric correlations was made by processing data with an empirically known relative compactness which highlighted the influence of these parameters of the sterile rock. Impressions and proposals were witnessed and certified quality by their consistency and reproducibility for different granulometries comprised proposals artificially, by its granular material characteristic studied strength parameters obtained from the test run shear it turned proper technique. It is concluded that there is a very close relationship between the reduction of the granulometry and decrease in the value of the angle of friction being these proportional, there being a dependence on the resistance to shear and its diameter of the grain. It is worth highlighting that by carrying out a good analysis and design of a sterile waste pile knowing the correct values of the resistance parameters for its real granulometry, the project will be oriented towards safety and contributing to the reduction of deposit areas, so that the environmental impact will then be minimized.

Keywords: Shear strength · Mine waste rock · Particle size

© Springer Nature Singapore Pte Ltd. 2019
L. Zhan et al. (Eds.): ICEG 2018, ESE, pp. 242–252, 2019.
https://doi.org/10.1007/978-981-13-2227-3_30

1 Introduction

An analysis of the behavior of granular soils can allow the evaluation of waste rock dumps in a mining, for this will be based on the properties of the material and their coincidences in what the work is focused on. Specific techniques were used for the evaluation, applying methods for granular soils to justify the effect of compactness and its plasticity limit. One of the observations that can be made in the work and has justified a deep chemical analysis is that the behavior of granular soils such as sand and material under study although physically similar, differ highly in their mineralogical compositions, the high content of iron in the samples.

In general, the particles have random characteristics and different grain sizes, which together form granular soils irregularly. Therefore, the type of particle that forms this soil, and the density index (DI), known as relative density (CR) and the disposition of the particles will be the most important factors that influence the shear strength of a mass of granular soil. Individual forces and displacements that occur at each point of contact govern the behavior of granular soils as dependent on external forces. The horizontal component of the force between its particles develops transmitted stresses at very large contact points during the shear strength of these soils. It must occur on the ground to be mobilized the resistance to sharp deformations, and the related movement among the main agents of this action.

Large amounts of waste rock called franc or marginal mineral form Waste rock dumps, which are generally large structures. In the case of open pit mines, the procedures for obtaining the ore with a substantial economic value can generate large quantities of sterile rock which, when disposed of without control, can be sources of landslides at a terrifying scale. Many studies and tests must be carried out to obtain the properties of the material and in this way avoid accidents of this magnitude and ensure the chemical and physical stability of the sterile rock deposits.

In this context, the study of the behavior of the sterile rock based on its particle size associated with the resistance parameters is interesting, mainly through the analysis to quantify the influence of the size of the particles in the friction angle of the material of waste rock material.

2 Materials and Methods

2.1 Study Location

The study consisted of characterization tests and direct shear made in the Technology Center of Applied Geotechnics (CTGA) Geotechnical Center (NUGEO) of the Federal University of Ouro Preto (UFOP).

The trial of this research program was developed from the use of a sample originating from an iron mine located in the Iron Quadrangle, have been collected randomly from a representative point of the sterile pile. To determine the physical and chemical characteristics of the sterile was adopted methodically regulatory procedures according to the Brazilian Association of Technical Standards (ABNT) and when the absence of

these, international procedures, such as the American Testing Company and Materials (ASTM).

2.2 Experimental Program

Sterile characterization tests were carefully performed to determine the grain size, grain density, maximum and minimum of voids and direct shear test. The latter aimed to obtain the strength parameters. The direct shear test was chosen by the characteristics of the material under study. The ease of direct shear access and manipulation contribute to the choice of the test.

2.2.1 Comminution of Sterile Sample, Identify and Build Size Distribution Curves

The evaluation of the sterile grain size is of fundamental importance in waste piles project, due to condition various geotechnical properties of granular materials, such as arrangement of grains, permeability and shear strength, the latter object of study of this work. Thus, it becomes necessary to obtain the initial particle size distribution of the obtained sterile sample for subsequent construction of curve prepared for an analysis of the influence of the particle size in sterile strength parameters used in the study.

Granulometric classification of the sample obtained in the field based on the Brazilian NBR 7181 (ABNT 1984) was established. First there was the screening to determine the coarser fractions of the sample and sizes of similar grains to the gravel and sand, with the use of traditional screens available in the laboratory with a maximum opening of 75 mm and the minimum aperture of 38 μm. To obtain the percentages of fines, represented by silts and clays did not take place the conventional sedimentation procedure. We opted for particle size by laser diffraction, measuring the grain size distributions by measuring the angular variation in the intensity of scattered

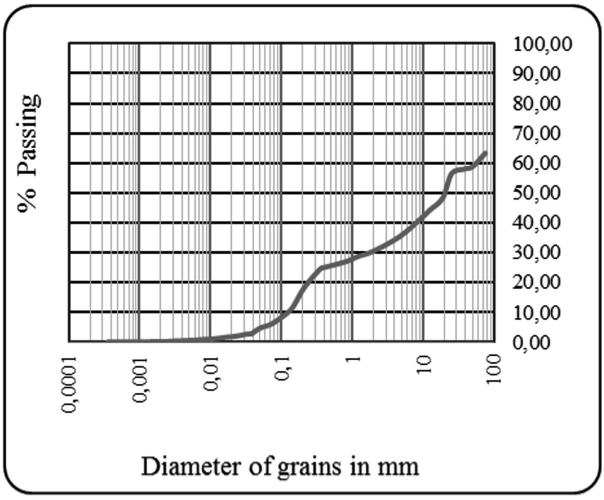

Fig. 1. Granulometric curve of the obtained sterile field.

light as a laser beam interacts with the sample dispersed particles. large particles scatter light at small angles to the beam, and smaller particles scatter light at large angles. The particle size of the sterile curve is shown in Fig. 1.

Since the purpose of this research incorporates especially an evaluation of scale effect, sterile was then brought to the crusher for reducing the particle size so as to achieve the endurance tests in smaller particle size samples.

The jaw crusher with an approximate opening of 18 mm was used for primary crushing.

After passing through the primary crushing, then part of the material was again crushed by a roll crusher, adjusted to an approximate opening of approximately 7 mm.

As a final process step, a part of the comminuted material on the roll crusher was brought to grinding by a ball mill with load for obtaining fine particle size fraction.

The reproduction of gradation curves had the principle to maintain the proportion of graduation sterile, for smaller particle size materials, adapting them for testing in large, conventional shear boxes. In the case of large equipment (described in this chapter), its shear box has dimensions of 200 mm × 200 mm and 50 mm sample height. In order to obtain a behavior in which burst itself is characterized by the formation of a continuous shear surface in the mass of material, avoiding the sterile shear grain, only the material in the sieve bolt 3/4″ was used. Thus, the greater equivalent diameter of the particle brought to shear box was 19 mm.

Therefore, we used the original material as a reference for obtaining the other curves, considering only part of the curve corresponding to the representation of grains smaller than 19 mm. The other curves were constructed considering the same feature of the original curve, graphically obtained through parallelization. They longitudinally distributed with equal spacing, and then through the analytical method to obtain the through-held weights and percentages for each of the different grain size ranges.

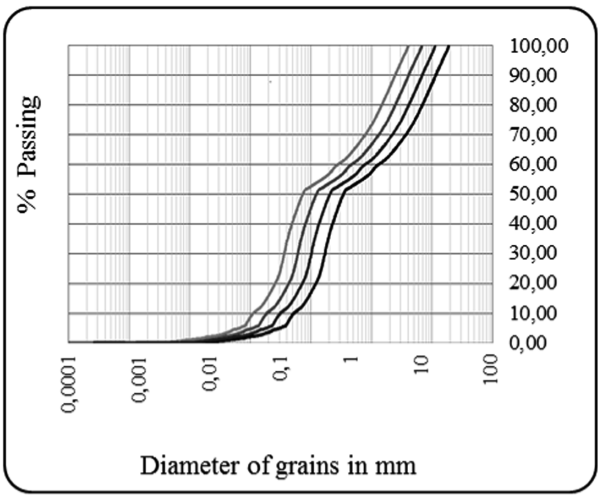

Fig. 2. Granulometric curves of sterile samples artificially structured.

Figure 2 shows four curves, with the latter, called EMF-03, with particle size of premeditated material so stay 50% retained on # 200 sieve (75 micron opening). Thus, all samples were to behave like granular most keenly.

The samples were artificially and structures were identified by 3 letters followed by two numbers. The three letters refer to the Iron Ore Barren, and subsequent algorithms correspond to variation in particle size of the sterile. Held an opposite procedure of particle size analysis, as graphically, critically, it managed to get the values of the cumulative percentages, then get analytically those of retained percentages values accumulated and partial, reaching at the end, the necessary weights the plots. The percentage represented by the curves presented above, are shown in Table 1 (ASTM).

Table 2 shows, from the granulometric analyzes of samples, the values of the characteristic diameters D10, D30, D50 and D90 and the value of the non-uniformity

Table 1. Particle size distribution according to ASTM

Scale		EMF-00 (%)	EMF-01 (%)	EMF-02 (%)	EMF-03 (%)
Grave		26,63	–	–	–
Sand	G	10,27	31,15	23,93	14,38
	M	11,07	13,82	16,71	22,51
	F	39,22	34,44	22,16	12,89
Silt		11,55	18,6	34,42	45,74
Clay		1,12	1,67	2,23	3,38
Colloid		0,14	0,32	0,55	1,1

Table 2. Summary of Product Characteristics grain size of samples

SAMPLE	D60 (mm)	D30 (mm)	D10 (mm)	CNU	CC
EMF-00	1,40	0,170	0,055	25,5	0,4
EMF-01	0,79	0,100	0,030	26,3	0,4
EMF-02	0,47	0,061	0,020	23,5	0,4
EMF-03	0,28	0,036	0,012	23,3	0,4

coefficient (CNU) and curvature (CC). These values were obtained in order to verify how the grain size of the samples, based on the characteristic diameters, interferes with the friction angle.

It is observed that non-uniformity coefficient (CNU) for all samples is above 15, characterizing materials and slaughtered granulometric curves, occupying a larger region, with different diameters, which is typical non-uniform materials.

Although classical classification attribute granular soils as possessing curvature coefficient (CC) between 1 and 3, the sterile studied show a reasonable degree. Despite the D30 value approaches regarding D10, there is a growing when evaluating D50.

After all, we tried to work with a well-distributed particle size, to produce a distribution proportionally equivalent to the original sample, as already highlighted in the chapter of the experimental program.

2.2.2 Density and Voids Ratio

The tests were conducted in accordance with auditing standards: NBR 6508 (ABNT 1984) "Determination of mass specific soil grains which pass on the 4.8 mm sieve" and NBR 6458 (ABNT 1984) "Determination of mass specific gravel grains retained on the 4.8 mm sieve."

The procedures of NBR 12004 standards (ABNT 1990), "Solo - Determination of the maximum void ratio of non-cohesive soils" and NBR 12051 (ABNT 1991), "Solo - Determination of minimum soil voids non-cohesive" out to obtain the maximum specific mass and a minimum of granular materials, knowing the density of the material grains, to obtain the minimum and maximum void ratios, respectively.

In theory, it calculated the value of the void ratio to a relative compactness (CR) of

Table 3. Dry Densities of each sample for CR = 50%

Sample	e_{max}	e_{min}	e	ρ_s g/cm^3	ρ_d g/cm^3
EMF-0	0,83	0,24	0,53	3,938	2,568
EMF-1	0,9	0,25	0,57	3,96	2,516
EMF-2	0,86	0,24	0,55	3,952	2,549
EMF-3	1,00	0,32	0,66	4,096	2,467

50%. Each sample had a different void ratio since their maximum and minimum void ratios are also different. So it is not possible to establish a correlation due to the void ratio, but the relative compactness.

The summary of the values obtained for these samples are shown in Table 3.

Obtaining these values was essential for molding sample, as highlighted in the previous chapter, therefore, from the knowledge of the value of the dry density and the mold volume, it was calculated the value of the mass used in each mold to the different samples.

2.3 Shear Strength Tests

To evaluate the behavior of artificially structured samples, conventional direct shear tests were performed (Fig. 3) and large size (Fig. 4), in compact servo-controlled equipment. The experimental procedures involved series of test samples under different confining tensions following the D3080/D3080 M-11 ASTM standards.

Next is shown the graphs obtained in the shear tests for each sample corresponding to the tests made in Great Porte Equipment Figs. 5, 6, 7 and 8.

The obtained friction angles are highlighted in Table 4.

Fig. 3. View of the compact conventional direct shear equipment.

Fig. 4. View of direct shear equipment of large size automated.

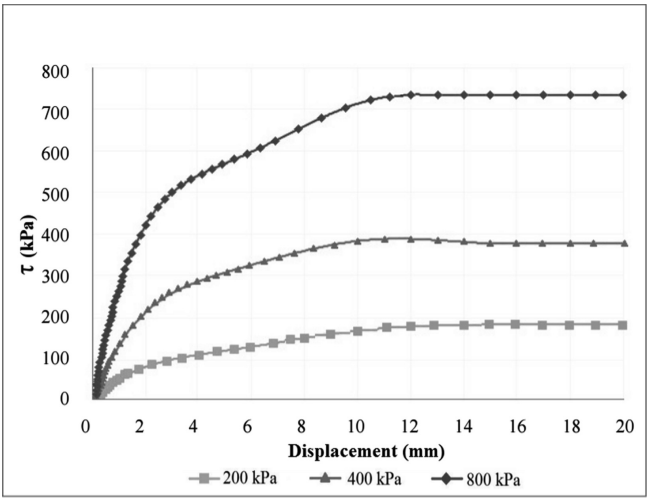

Fig. 5. Relationship between Shear Stress and Displacement sample EMF-00. Large size test.

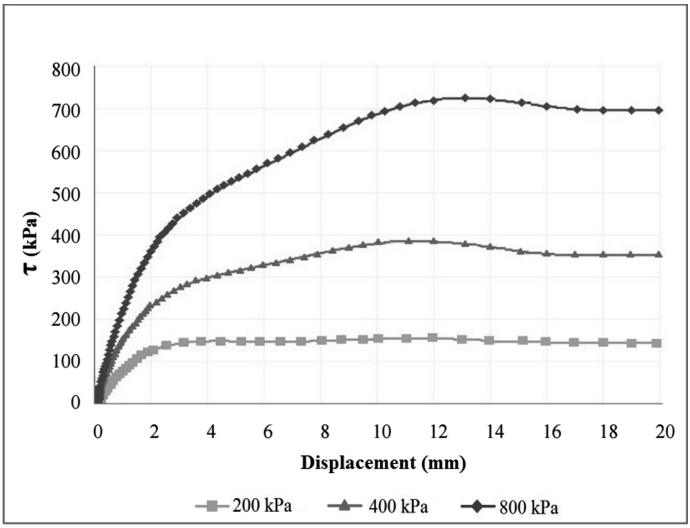

Fig. 6. Relationship between Shear Stress and Displacement sample EMF-01. Large size test.

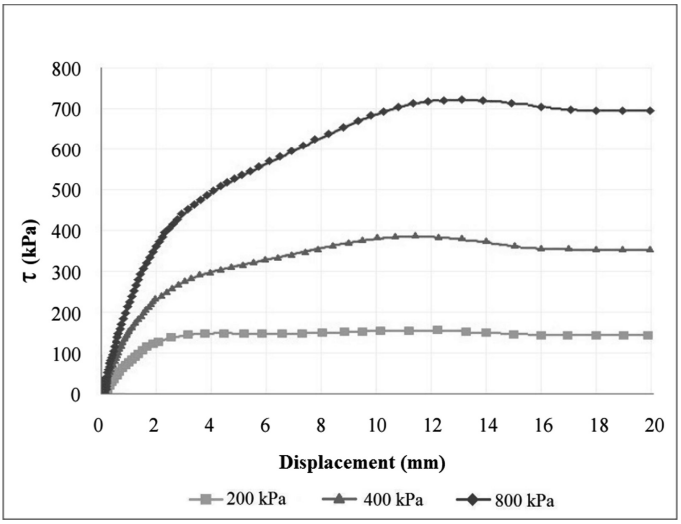

Fig. 7. Relationship between Shear Stress and Displacement sample EMF-02. Large size test.

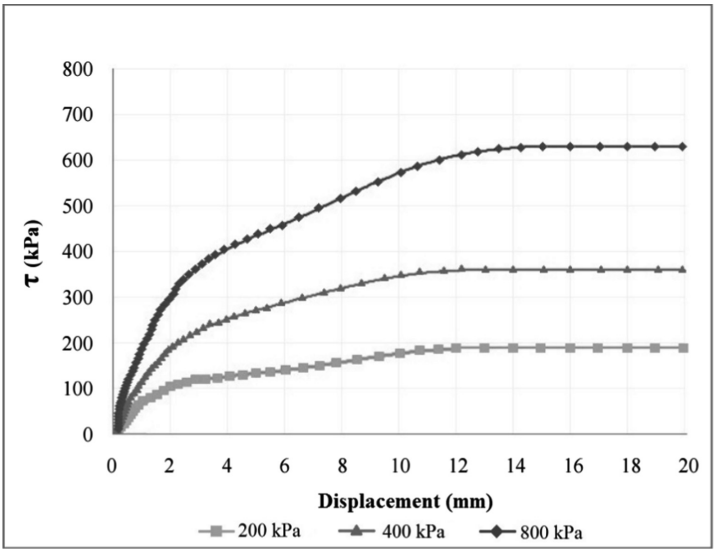

Fig. 8. Relationship between Shear Stress and Displacement sample EMF-03. Great Port test.

Table 4. Effective friction angle values (ϕ')

SAMPLE	Friction Angle (ϕ') (o)	
	Great port equipment	Conventional equipment
EMF-00	42,83	–
EMF-01	42,38	41,93
EMF-02	41,95	41,53
EMF-03	40,36	41,37

3 Analysis of Results

The increase of the EMF-00 sample resistance in large test can also be attributed to the higher iron content present. Thus, both the granulometry and the high iron content (shown on the high value of the specific mass of grains) contributed to the increased value of the friction angle of the original sample.

It must be further noted that the samples EMF-01, 02-EMF and EMF-03 were obtained and built considering the same feature of the original curve, graphically obtained through parallelization. Therefore, as already highlighted in this paper, the original sample was comminuted by crushing. The crushing operation produces abrasion between the grains of the material, which can influence the shape and roughness of the grains. The process may generate less rough and angular grains, thereby contributing to the reduction of surface friction, which leads consequently to a reduction of the friction angle. Materials consisting of angular grains tend to have greater than compounds meshing soil rounded particles. Thus, angular grains tend to have higher friction angles.

The linearity expressed in the test with conventional equipment can be related to the unique behavior experienced during shearing for all samples. It is noteworthy that even with the exclusion of the EMF-00 sample the finest sample (EMF-03) has grains with a maximum diameter of 4 mm, corresponding to one fifth of the CP time. The dilatant performance was observed for all samples tested. In the large scale test, whereas the amount of CP should be at least 6 times the diameter of the largest grain of the material to be tested, the EMF-sample 03 is perfectly aligned with the North American standard procedures. It is observed that only for this sample when comparing the two devices, the obtained friction angle was greater for the conventional assay (41, 37º) than for large ones (40, 36º).

4 Conclusions

Two automated direct shear equipment, a conventional and a large, were used during the research. Tools were consistent with the data acquisition system and insertion consistent data, and the software used was judged very helpful. These are mechanism that contribute to precision in data collection and reduction potential reading error sources. Technological advances implemented in the large apparatus, to improve the

operation were significant, according to the terms of the American Society for Testing and Materials.

The execution of shear tests at large especially for determining the resistance of sterile parameters proved to be a consistent tool when applied to granular sterile. The agreement and the reproducibility of the results for the different samples with different grain sizes, attested and measured the quality of impressions and proposals made.

The results of trials conducted in conventional equipment were more conservative when compared to the results of the extensive equipment. It was perceived friction angles keep a smaller amplitude difference between the equivalent angles to each reduction in particle size of the waste material studied.

However, it is clear that a reassessment of the maximum grain diameter to be used for a given height of the CP. The effect of grain size during the shear was observed, particularly in conventional equipment, whose samples showed shear during expansion.

The effect of working range in determining the friction angle of the sterile object of this research, it became evident, both in the conventional test as the large test. The dependence between particle size of the samples sterile and the sterile shear resistance was realized by decreasing the tendency of the friction angle with the reduced diameter of its particles.

Finally, it is emphasized that for a proper assessment of the project, with regard to the geotechnical behavior of sterile, are relevant studies of this nature, since many structures are scaled from trials with reduced particle sizes compared to those present in field. In general, when this is done, the outcome of the project is moving in the sense of security, because if conservative design parameters based structures. However, although evaluated, looking for a study of the effect of scale, structures that require smaller disposition areas may be proposed, generating as a result, significantly less environmental impact.

References

ABNT: Associação Brasileira de Normas Técnicas (1990) NBR 12004: Solo - Determinação do índice de vazios máximo de solos não-coesivos. Rio de Janeiro

ABNT: Associação Brasileira de Normas Técnicas (1991) NBR 12051: Solo - Determinação do índice de vazios mínimo de solos não-coesivos. Rio de Janeiro

ASTM: American Society for Testing and Materials (2011) D3080/D3080 M: Direct shear test of soils under consolidated drained conditions. Washington, D. C., USA

ASTM: American Society for Testing and Materials (2007) D422-36: Standard Test Method for Particle-Size Analysis of Soils (Withdrawn 2016). Washington, D. C., USA

ASTM: American Society for Testing and Materials (2006) D4253–00: Standard test methods for maximum index density and unit weight of soils using a vibratory table. Washington, D. C., USA

ASTM: American Society for Testing and Materials (2014) D854-14: Standard test methods for Specific Gravity of Soil Solids by Water Pycnometer. Washington, D. C., USA

Head KH (1994) Manual of soil laboratory testing, vol 2, 2nd edn. Pentech Press. London

Technological Characterization of Tailings from Iron and Gold Mining with a Geoenvironmental Focus for Reuse in Geotechnical Application

Thaís Guimarães dos Santos[1(✉)], Luís Fernando Ribeiro Martins[1], and Evelin Rodriguez Sosa[2]

[1] University of Brasilia, Brasilia, Brazil
thaisguimaraess@hotmail.com
[2] Central University "Marta Abreu" of Las Villas, Santa Clara, Cuba

Abstract. The use of mining tailings to stabilize the materials normally used in civil works is already a fairly common practice. Tailings are commonly used in landfill layers, in the construction of houses where they replace conventional materials, as well as their use as a filler in the cement industry, among other applications. Thus reducing the exploitation of the deposits and preserving the environment. However, while studies show improvement in mechanical behavior in soils with the addition of tailings, they can also act to contaminate soil and water resulting from excess heavy metals. In this context, the present research aims to evaluate the mobility and availability of the metals present in the tailings. The iron reject studied comes from the Iron Quadrangle and the gold is from northwestern Minas Gerais, Brazil. The studies covered the physical and geochemical-environmental characterization of the material. With the results, it was possible to know the characteristics of these materials when they are in contact with water as a means of dissolution, allowing the evaluation of the influence of such aspects on the behavior of the mixtures and to evaluate the potential use of these materials in civil works.

Keywords: Metal · Mobility · Disponibility

1 Introduction

Mining, complemented by steelmaking, is one of the essential activities in the development of the modern world. In this context, Brazil, due to its mineral diversity and territorial extension, holds a prominent position in the world scenario when it comes to reserves and production of mineral goods. Mainly metallic mineral goods [1].

Despite the great economic importance of the mining industry, this represents a potentially degrading agent of the physical environment to which it is inserted. With the production of iron and gold, it is not different, with the greatest environmental impacts arising from these productions being the large volume of waste generated in the beneficiation process [2].

© Springer Nature Singapore Pte Ltd. 2019
L. Zhan et al. (Eds.): ICEG 2018, ESE, pp. 253–260, 2019.
https://doi.org/10.1007/978-981-13-2227-3_31

The tailings, however, can still contain expressive metallic contents and can be returned to the production process. In addition, tailings can contain materials with potential uses in civil works, which would mitigate damage to the environment. However, the evaluation of reuse of mining tailings is not trivial. The studies should not only evaluate the mechanical behavior of the new materials in face of the possible requests that may be submitted, but also investigate the interaction of the tailings with the environment. The present study is aimed at evaluating the potential reuse of iron and gold residues in geotechnical applications, but giving a geoenvironmental approach, in order to verify the availability and mobility of the metals present in the tailings.

2 Reuse of Iron Mining Rejection in Civil Construction

Brazil occupies a prominent position in the world scenario in what concerns the reserves and production of iron ore. As a consequence of the large volumes produced, this is also the mineral good responsible for the largest volume of mining waste generated in the country [3].

Based on the scientific literature, it was verified the existence of researches related to the characterization of mining tailings in order to reuse them in civil works. Among the possible uses of iron tailings found are:

- Incorporated to cement for use in base and sub-base layers of highways [4].
- Filler in asphalt mixtures [2].
- In the production of concrete elements for paving [5].
- As a stabilizing material mixed to a lateritic soil in the northeastern region of Brazil for use in base and sub-base layers of highways [6].
- Incorporation in cement, concrete, mortar and ceramics manufacturing and use in paving works [2].
- As alternative material for road infrastructure in the base layer of pavements [7].

Also noteworthy are studies carried out with the reject of the Monjolo pile, from the Quadrilátero Ferrífero (MG), performed pro Gratão et al. [8] and Echeverri [9].

Gratão et al. [8] studied the reuse of the iron reject from the Monjolo drainage of the Quadrilátero Ferrífero for use in road works by means of mixtures of tailings (25% and 50% by mass) with a latosol (HB9) from the Federal District. The authors verified that the results obtained in the tests of non-confined compression demonstrate an increase in the values of resistance to simple compression with the increase of the content of mixed mixed to the soil.

Echeverri [9] evaluated the use of iron ore tailings from the Monjolo pile in the Quadrilátero Ferrífero as a filter in land works, mainly for dams, replacing the natural sand found in the rivers and dunes. The author found that the properties of resistance and durability of this waste can be considered as a good material to be used in filters of dams.

It is verified that the tailings of the processes of iron processing have an important potential of use in works of paving, based, mainly, on their granulometric characteristics.

For the gold tailings, studies prove its potential use for the production of sulfuric acid for the manufacture of fertilizers [10].

Studies for gold reject are still limited due to economic and environmental issues. We highlight the current Brazilian scenario of reprocessing of refusals due to the low levels currently recorded in the country. And environmental issues such as the presence of sulfide minerals that are likely to cause environmental problems.

In spite of numerous studies in the area, the rejects present a great variability of properties. This occurs because of the natural geological heterogeneity of the mineral goods and the various processes that the ores can be submitted, that can alter even the physico-chemical of the surface of the particles. In this way, the studies on the reuse of tailings are not exhausted.

3 Methodology

The studied wastes were collected from the state of Minas Gerais, Brazil. The tailing of iron comes from the Monjolo tailings pile, in the iron quadrilateral, which is one of the largest reserves of mineral goods in the world. The tailing of gold comes from the northwest region of the state of Minas Gerais, of the Santo Antônio dam. Both were collected in the waste pipes.

The characterization of the metallic wastes was carried out using the methodology developed by Sosa [11], which involves physical, mineralogical, chemical, geochemical and geoenvironmental. Described below.

3.1 Physical Characterization

The physical characterization of the tailings has the purpose of obtaining texture, prognosis of its nature, in addition to the indication of a large number of geotechnical characteristics such as strength, permeability, compaction characteristics, estimation of parameters for filters, capillarity, amplitude of chemical reactions. The texture affects soil properties such as hydraulic conductivity and moisture retention, thus having an important effect on the transport and retention capacity of metals.

The tests carried out for the physical characterization of the wastes were carried out according to NBR 7181 “Soil - Granulometric Analysis” [12] and specific mass of grains, which were performed using the PENTAPYC 5200e “Quantachrome Instruments” model pentapicnometer.

3.2 Mineralogical Characterization

The purpose of the mineralogical characterization is to identify the minerals present in the tailings and thus to allow the evaluation of the physical and chemical behavior, allowing the optimum use of the resources.

For the mineralogical knowledge of the tailings, the technique of Difratometry of rays X (XRD).

3.3 Chemical and Geochemical Characterization

The purpose of the chemical and geochemical characterization was the qualitative and quantitative analysis of the chemical species present in the tailings, interaction of the particles, to verify the mobility potential of the metals in the tailings and in the aqueous medium.

The chemical analyzes were performed using the Plasma Optical Emission Spectrometry (ICP) technique. The pH was measured using 4 g of residue and adding 10 mL of deionized water, maintaining the ratio of 1: 2.5 (w/v). Samples were agitated for half an hour at low speed followed by 30 min rest and separation of the liquid extract by centrifugation and filtration. After the process, measurements were taken.

For extraction with $CaCl_2$, 4 g of residue was used and 10 ml of (0.01 M) $CaCl_2$ was added, also maintaining the ratio 1: 2.5 (w/v). Samples were agitated for half an hour at low speed followed by 30 min rest and separation of the liquid extract by centrifugation and filtration. After the process, the filtrate was sent for analysis in ICP.

The extraction with meteoric water was done by weighing 1 g of waste and 50 ml of meteoric water (distilled water with HCl) of pH 6.0 ± 0.1, the average pH of the Brazilian rainfall. The samples were agitated for one hour at low speed followed by 30 min rest and separation of the liquid extract by centrifugation and filtration. After the process, the filtrate was sent for analysis in ICP.

4 Results

In Fig. 1 are the grain size curves of iron and gold tailings.

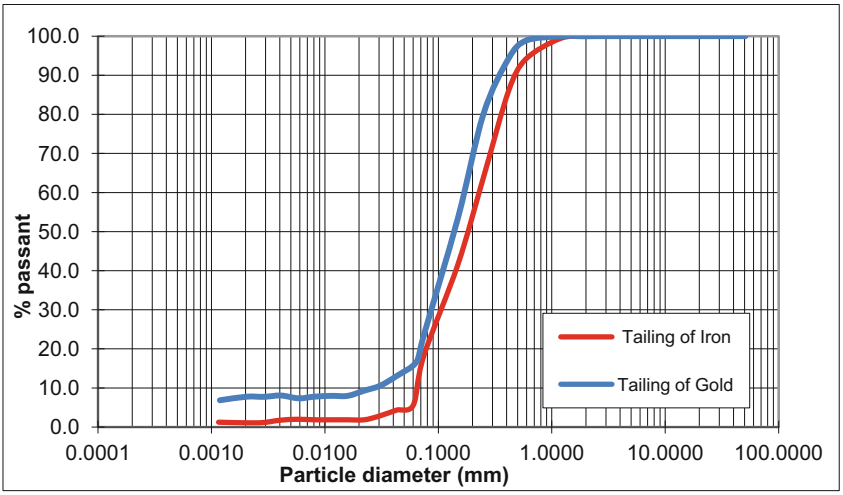

Fig. 1. Size distribution curves of the tailing

The tailing of iron is in the granulometric range of the medium to thin sands. The tailing of gold is located in the granulometric range of the fine sands, since the gold finds widespread in the mineral body, being necessary greater comminution of the ore to expose the gold for collection. Both are non-uniform.

The iron waste has granulometry that falls under DNIT 141 "Paving - Granulometrically Stabilized Base - Service Specification" for less intense traffic [13]. Already the gold waste presents thinner than allowed.

Also according to the particle size analysis obtained, both tailings have the potential to be used as soil-cement, according to DNIT 143 "Paving - Base of soil-cement - Service specification" [14].

The specific masses of the grain of the tailings were 3.49 g/cm^3 for the tailing of iron and 3.22 g/cm^3 for the tailing of gold.

The mineral analyses performed by the XRD indicate that the tailings of iron presents quartz and hematite.

The results of XRD for the tailings of gold identified the minerals quartz, hematite, kaolinite, goethite, anastasis, rutile, pyrite, calcite, dolomite, montmorillonite, sepiolite and ferroactinolite. Calcite and dolomite being the minerals responsible for the high pH verified, described later.

The result of the XRD of the gold waste does not indicate the presence of arsenopyrite, a trace mineral of the mine that has a correlation with gold [15]. However, the possible presence of this mineral in the tailing cannot be ruled out. It is known that ray X diffraction presents the limitation of not guaranteeing the identification of minerals in small amounts in the samples.

The results of the chemical analysis of the tailings are presented below (Table 1).

Table 1. Chemical analysis of tailings

Chemical elements	Tailing of Iron		Tailing of Gold	
	mg/Kg	%	mg/Kg	%
Al	3,265.190	0.327	24.345,950	2.435
As	36.057	0.004	25,847	0.003
Ba	49.078	0.005	2.616,519	0.262
Ca	12,581.380	1.258	72.657,543	7.266
Cd	77.123	0.008	63,624	0.006
Co	1.002	0.002	228,647	0.023
Cr	1.502	0.004	79,529	0.008
Cu	256.287	0.026	97,921	0.010
Fe	334,572.000	33.457	166.922,353	16.692
K	3,028.850	0.303	14.598,623	1.460
Mg	776.234	0.001	35.311,071	0.001
Mn	660.134	0.078	3.836,301	3.531
Mo	26.041	0.066	25,350	0.384
Na	35.056	0.003	99,412	0.003

(*continued*)

Table 1. (*continued*)

Chemical elements	Tailing of Iron		Tailing of Gold	
	mg/Kg	%	mg/Kg	%
Ni	54.364	0.005	65,115	0.010
P	211.837	0.021	15,035.980	1.504
Pb	194.157	0.019	40.759	0.004
Se	497.042	0.005	40.759	0.004
Si	35,414.268	3.541	15,527.356	1.553
Sr	7.512	0.001	1,595.559	0.160
Ti	135.215	0.014	69,588.260	6.959
Zn	144.730	0.014	421.009	0.042
Zr	31.550	0.003	1,307.265	0.131

Among the metals identified in the tailings, there are some that can act as environmental contaminants, such as aluminum (Al), arsenic (As), barium (Ba), cadmium (Cd), chromium (Cr), copper (Cu), iron (Fe), manganese (Mn), lead (Pb), selenium (Se) and zinc (Zn). However, only the quantification of these elements is not enough to determine the possible contamination of the environment by the tailings, it is necessary the study of the mobility of these metals, which is closely linked with the chemical speciation. For example, the solid species tend to have less mobility than the colloidal and dissolved forms.

The pH values of the tailings are 7.40 and 9.16 for the iron and gold tailings, respectively, indicating basic pH. Values of pH above six favor the retention of metals in the porous medium, which decreases the mobility of metals in solution [16]. However, it should be noted that in the gold residue there is pyrite, detected by XRD and there is a likelihood of containing arsenopyrite. These minerals, when exposed to environmental conditions, oxidize, generating acid mine drainage (DAM), as well as the dissolution of a number of other metals present in the tailings, such as Al, Mn, Cu, As, Zn, Pb and Cd These elements can be solubilized and mobilized in drainage waters and can be absorbed at toxic levels by plants and incorporated into the trophic chain [17]. This is one of the most serious environmental impacts associated with the mining activity, besides the fact that arsenic is an element that presents potential for toxicity.

For the simple extractions with $\mathbf{CaCl_2}$ and meteoric water, only the elements Al, As, Ba, Cd, Cr, Cu, Fe, Mn, Pb, Se and Zn were analyzed, see Table 2.

Table 2. Simple Extraction with $CaCl_2$ and rainwater

Chemical elements	Extraction with $CaCl_2$		Extraction with rainwater	
	Tailing of Iron	Tailing of Gold	Tailing of Iron	Tailing of Gold
	ml/L	ml/L	ml/L	ml/L
Al	0,457	0,643	0,450	6,400
As	0,060	0,064	0,240	0,385

(*continued*)

Table 2. (*continued*)

Chemical elements	Extraction with $CaCl_2$		Extraction with rainwater	
	Tailing of Iron	Tailing of Gold	Tailing of Iron	Tailing of Gold
	ml/L	ml/L	ml/L	ml/L
Ba	0,124	1,588	0,130	1,840
Cd	0,079	0,083	0,010	N.I
Cr	0,011	0,004	0,045	0,040
Cu	0,022	0,024	0,125	0,185
Fe	0,020	N.I	3,750	17,800
Mn	0,156	0,010	1,000	1,345
Pb	0,028	0,015	0,180	0,190
Se	0,021	0,077	0,255	0,270
Zn	0,209	0,311	0,730	2,230

N.I - Not identified

The extractor with 0.01 M $\mathbf{CaCl_2}$ must extract the species that correspond to the fraction with soluble and exchangeable properties. These fractions are the ones that allow greater availability of the metals in soil, greater phytoabsorbability, being formed by free ions in solution, soluble complexes and metals connected electrostatically to the ion exchange sites existing in the surfaces of the colloids of the soil. In both extractions the low capacity of transfer of metals to the aqueous medium was verified. Except for Cr, Fe, Mn and Pb, all other metals present more mobility in the gold waste than in the iron ore.

5 Conclusions

The iron and gold tailings are sand and fall within Brazilian paving standards, however, the chemical analysis identified metals harmful to the environment in both tailings. However, pH and geoenvironmental studies realized, although simple, provide an indication of the low mobility and availability of metals in contact with water as a means of dissolution, which makes feasible the reuse of these in geotechnical works.

However, for the reuse certification of the material, it is indicated to perform a more complex extraction as sequential extractions to understand the chemical speciation of the materials and to analyze the availability of living organisms.

Undoubtedly, mining tailings, in general, can be reused in geotechnical works, based mainly on their granulometric characteristics as aggregates. In this sense, the research carried out here presents an important step in relation to the environmental characterization of mineral tailings.

References

1. Salomons W (1995) Environmental impacts of metals derived from mining activities: process, predictions, prevention. J Geochem Explor 52(1):523
2. Andrade LCR (2014) Caracterização de rejeitos de mineração de ferro, in natura e segregados, para aplicação como material de construção civil. Dissertação de Mestrado, Departamento de Engenharia Civil, Universidade Federal de Viçosa, Viçosa, MG, 96p
3. Instituto De Pesquisa Econômica Aplicada (2012) Diagnóstico dos Resíduos Sólidos Urbanos. IPEA, Brasília, Brasil, vol 1, 77p
4. Xu S (2013) Research on application of iron tailings on road base. In: Advanced Materials Research, vol 743, pp 54–57
5. Toffolo RVM, Sant´Ana FJN, Batista JOS, Silva SN, Cury AA, Peixoto RAF (2014) Viabilidade técnica de elementos de concreto para pavimentação produzidos com rejeito de barragem de minério de ferro. In: Anais do 56º Congresso Brasileiro Do Concreto - CBC2014–56CBC
6. Dantas AAN (2015) Caracterização Caracterização de resíduos oriundos do beneficiamento do minério de ferro para uso em pavimentação. 88 pp, Dissertação de mestrado em Engenharia Civil. Universiade Federal do Rio Grande do Norte, Natal
7. Bastos LAC (2013) Utilização de rejeito de barragem de minério de ferro como matéria prima para infraestrutura rodoviária. Dissertação de mestrado, Núcleo de Geotecnia da Escola de Minas da Universidade Federal de Ouro Preto, Universidade de Ouro Preto, Ouro Preto, MG, 97p
8. Gratão LS, Pereira EL, Ribeiro LFM (2006) Utilização de um rejeito de mineração como alternativa para estabilização de um solo tropical da região Centro-oeste. IIgeojovem 2006
9. Echeverri J (2012) Aplicabilidade dos Rejeitos de Mineração de Ferro para Utilização em Filtros de Barragens. Dissertação de Mestrado, Departamento de Engenharia Civil, Universidade de Brasília, Brasília, DF, 112p
10. Oliveira Júnior GG (2011) Desenvolvimento de uma rota de processo de dessulfurização de rejeitos de um minério aurífero sulfetado. Dissertação de mestrado, Departamento de Engenharia de Minas, Universidade Federal de Minas Gerais, Belo Horizonte, MG, 71p
11. Sosa ER (2016) Caracterização e aproveitamento dos rejeitos oriundos de processos hidrometalúrgicos do níquel e cobalto com um enfoque geoambiental. Tese de Doutorado em Geotecnia. Departamento de Engenharia Civil e Ambiental, Universidade de Brasília, Brasília, DF, 170p
12. Associação brasileira de normas técnicas (2016) NBR-7181: Solo – Análise Granulométrica. Brasil
13. Departamento Nacional De Infraestruturas De Transporte (2010) DNIT: 141 Pavimentação – Base estabilizada granulometricamente - Especificação de serviço. Brasil
14. Departamento Nacional De Infraestruturas De Transporte (2010) DNIT 143: Pavimentação – Base de solo-cimento - Especificação de serviço. Brasil
15. Daitx EC, Zarnado A (2000) Estudo Petrográfico e Minerográfico de Rochas da Mina Morro do Ouro. (Paracatu, MG). 2vol. Programa Parceria RPM/Fundusnep
16. Sodré FF, Lenzi E, Costa AC (2001) Utilização de modelos físico-químicos de adsorção no estudo do comportamento do cobre em solos argilosos. Química Nova, São Paulo 24 (3):324–330
17. Mello JWV, Abrahão WAP (1998) Geoquímica da drenagem ácida. In: Dias LE, Mello JWV (eds) Recuperação de áreas degradadas. Universidade Federal de Viçosa, Viçosa, pp 45–57

Biogeotechnical Engineering

(Edited by Jia He, Yongfu Xu, and Jiangnan Chen)

A Model for Aerobic Biochemical Degradation of Municipal Solid Waste

Diankun Xiao, Wenjie Xu(✉), Liangtong Zhan, and Yunmin Chen

Zhejiang University, Hangzhou, China
wenjiexu@zju.edu.cn

Abstract. Based on the principles of electron currents conservation and mass conservation, this paper considers the two kinds biochemical reactions of organic aerobic oxidation and simultaneous nitrification-denitrification under the condition of aerobic degradation of municipal solid waste (MSW). Select rapid degradation cellulose (RDC), slow degradation cellulose (SDC), total sugar, fat, protein, and microorganisms as the limiting substrates, and write an aerobic biochemical reaction stoichiometric equation that can reflect the mass linkages among various substances. First-order kinetic equations were used to describe the kinetic behavior of biodegradable organics in the process of aerobic degradation, meanwhile the effects of temperature, water content, and oxygen concentration on the aerobic degradation rate of organic matter were also considered. The microorganism decay was described using a first-order kinetic equation. A model with a clear physical meaning and capable of simulating the time-varying process of aerobic degradation of MSW has been established. The robustness of the model still requires instance validation.

Keywords: Electron currents conservation · Organic aerobic oxidation
Simultaneous nitrification denitrification · First-order kinetic

1 Introduction

There are many disposal methods for MSW such as landfill, composting, and incineration. Anaerobic landfilling is the main disposal method, however, which has the shortcomings such as slow degradation and reduced service performance in the late landfill period. At this time, aerobic degradation measures such as ventilation with oxygen can effectively accelerate the stabilization of landfill degradation.

Zhou [1] has identified that in the process of waste aerobic reaction, there are mainly three types of biochemical reactions: one is the aerobic oxidation of organic substances, the reaction mainly consumes oxygen to remove organic pollutants; the second is an aerobic nitration reaction, and the reaction is mainly consumed oxygen converts ammonia nitrogen to nitrate nitrogen; the third type is denitrification, which converts nitrate nitrogen to nitrogen while consuming large amounts of organics.

The existing formulas of aerobic biochemical reaction can't effectively express three types of reaction processes during the aerobic degradation of MSW, and can't clearly establish the conversion relationship between various materials. Thus, it is

© Springer Nature Singapore Pte Ltd. 2019
L. Zhan et al. (Eds.): ICEG 2018, ESE, pp. 263–271, 2019.
https://doi.org/10.1007/978-981-13-2227-3_32

imperative to establish a set of aerobic biodegradation model with clear physical meanings and capable of linking changes among various materials.

2 Biochemical Stoichiometric Equations

McCarty [2] proposed a method for establishing a biochemical stoichiometric equation based on microorganisms as a medium. The method requires three kinds of semi-reactions, one is electron donor, such as sugars, fats, proteins; one is electron acceptor, including oxygen, nitrate, nitrogen, carbon dioxide; the rest is used for cells synthesize. Assuming that the electron donor is used to synthesize the cell is f_s, and the rest is related to energy release, then the overall equation can be obtained.

Based on McCarty's semi-reaction theory, Zhou [3] uses the electron acceptor f_s for cell synthesis as a basic parameter to establish the semi-reaction equations, and using the above formulas to synthesize the three major biochemical reaction stoichiometric equations in the aerobic degradation process of MSW.

According to McCarty's semi-reaction theory and the construction of Zhou's biochemical reaction stoichiometric equations, based on the principles of "conservation of electron currents" and mass conservation, various organics are used as electron donors, and O_2 is used as electron acceptor, one can write the general formulas of the electronic stoichiometric equations for the three types aerobic degradation biochemical reactions with 1 mol electron is considered.

2.1 Aerobic Oxidation of Organics

The aerobic oxidation of organic matter refers to the redox reaction of organics with oxygen. Hoover and Porges [4], Symons and McKinney [5] found that aerobic microorganisms can be represented by $C_5H_7O_2N$, which are widely used by following scholars, and will be expressed here. So the stoichiometric formula can be written as follows:

$$\begin{aligned}&\tfrac{1}{r}C_aH_bO_cN_d + \tfrac{1-f_s}{4}O_2 + \tfrac{f_s}{20}NH_4^+ + \tfrac{f_s}{20}HCO_3^- + \tfrac{d}{r}H^+ \\ &= \tfrac{d}{r}NH_4^+ + \tfrac{f_s}{20}C_5H_7O_2N + (\tfrac{5}{r} - \tfrac{f_s}{5})CO_2 + (\tfrac{1}{2} - \tfrac{f_s}{20} - \tfrac{2a-c}{r}]H_2O\end{aligned} \tag{1}$$

$$\begin{aligned}&\tfrac{1}{q}C_aH_bO_c + \tfrac{1-f_s}{4}O_2 + \tfrac{f_s}{20}NH_4^+ + \tfrac{f_s}{20}HCO_3^- \\ &= \tfrac{f_s}{20}C_5H_7O_2N + (\tfrac{a}{q} - \tfrac{f_s}{5})CO_2 + (\tfrac{1}{2} - \tfrac{f_s}{20} - \tfrac{2a-c}{q})H_2O\end{aligned} \tag{2}$$

Where $r = 4a + b - 2c - 3d$, $q = 4a + b - 2c$, a, b, c, d are the number of atoms of each element in the molecular formula based on the unit mass of substrates; f_s represents the component for cell synthesis.

2.2 Aerobic Nitration

Nitrification refers to the biochemical reaction of oxidizing $NH_3 - N$ to $NO_X - N$ (e.g. $NO_3 - N$, $NO_2 - N$). This process is performed by nitrite bacteria and nitrate bacteria, including two steps of nitrosation and nitration.

The nitro-nitrogen pathway equation is written as follows:

$$\frac{1-f_s}{4}O_2 + \frac{5+2f_s}{40}NH_4^+ + \frac{f_s}{4}HCO_3^- = \frac{f_s}{20}C_5H_7O_2N + \frac{1}{8}NO_3^- + \frac{5-4f_s}{20}H^+ + \frac{5+6f_s}{40}H_2O \quad (3)$$

The nitroso-nitrogen pathway equation is written as follows:

$$\frac{1-f_s}{4}O_2 + \frac{10+3f_s}{60}NH_4^+ + \frac{f_s}{4}HCO_3^- = \frac{f_s}{20}C_5H_7O_2N + \frac{1}{6}NO_2^- + \frac{5-3f_s}{15}H^+ + \frac{10+9f_s}{60}H_2O \quad (4)$$

2.3 Anaerobic Denitrification

Denitrification refers to the biology reaction of $NO_X - N$ and other nitrogen oxides as electron acceptors that are reduced to nitrogen or other gaseous oxides under anaerobic or anoxic conditions (dissolved oxygen < 0.3 − 0.5 mg/L). This process is done by denitrifying bacteria. For simplicity, we only write equations about $NO_3 - N$ here. The denitrifying bacteria uses $NO_3 - N$ as a nitrogen source, and the complete denitrification reaction equation can be written as:

$$\begin{aligned}&\tfrac{1}{r}C_aH_bO_cN_d + \tfrac{28-23f_s}{140}NO_3^- + (\tfrac{28-23f_s}{140} + \tfrac{d}{r})H^+ = \tfrac{f_s}{28}C_5H_7O_2N \\ &+ \tfrac{1-f_s}{10}N_2\uparrow + (\tfrac{a}{r} - \tfrac{5f_s}{28})CO_2 + (\tfrac{84-29f_s}{140} - \tfrac{2a-c}{r})H_2O + \tfrac{d}{r}NH_4^+\end{aligned} \quad (5)$$

$$\begin{aligned}&\tfrac{1}{q}C_aH_bO_c + \tfrac{28-23f_s}{140}NO_3^- + \tfrac{28-23f_s}{140}H^+ = \tfrac{f_s}{28}C_5H_7O_2N \\ &+ \tfrac{1-f_s}{10}N_2\uparrow + (\tfrac{a}{q} - \tfrac{5f_s}{28})CO_2 + (\tfrac{84-29f_s}{140} - \tfrac{2a-c}{q})H_2O\end{aligned} \quad (6)$$

When the microbial molecular formula is determined, the equation coefficients becomes a function of f_s, and the determination of f_s directly determines the coefficients of all stoichiometric equation, which is very useful in aerobic design and operation of MSW. The determination of f_s here can be obtained from inversion of the test data.

3 Aerobic Biodegradation Model

3.1 Biochemical Molecular Stoichiometric Equations

Stombaugh [6], Komilis [7] etc. uses kinetic equations such as first-order kinetics and Monod equations to simulate the aerobic biodegradation process. However, due to the lack of a complete chemical equation, it is difficult to establish the relationship between various materials. The biodegradable organics in MSW mainly include sugar, cellulose, lignin, protein, and fat. Chen [8] chose cellulose, sugar, protein, fat, and methane bacteria as limiting substrates when establishing an anaerobic biodegradation model.

The first-order kinetic equation was used to describe the degradation process and achieved good results. Here, with reference to his research method, the rapid degradation cellulose (abbreviated as RDC:$C_6H_{10}O_5$), slow degradation cellulose (SDC: $C_6H_{10}O_5$), total sugar ($C_6H_{10}O_5$), fat ($C_{55}H_{104}O_6$), protein ($C_{46}H_{77}O_{17}N_{12}S$), and microorganisms ($C_5H_7O_2N$: the general name of aerobic bacteria, nitrifying bacteria and denitrifying bacteria) are selected as limiting substrates. For ease of study, the aerobic nitration equation and anaerobic denitrification reaction are combined together according to the ratio of 1:1, which is called the simultaneous nitrification-denitrification equation. Refer to the three types of biochemical stoichiometric reactions in Sect. 2, we can write two kinds of biochemical reactions: aerobic oxidation and simultaneous nitrification-denitrification molecular equations of various limiting substances, limiting substrate coefficient is 1.

RDC oxidation equation:

$$C_6H_{10}O_5 + 6(1-f_s)O_2 + \frac{6f_s}{5}NH_4HCO_3 = \frac{6f_s}{5}C_5H_7O_2N + (6 - \frac{24f_s}{5})CO_2 + (5 - \frac{6f_s}{5})H_2O \tag{7}$$

SDC oxidation reaction equation:

$$C_6H_{10}O_5 + 6(1-f_s)O_2 + \frac{6f_s}{5}NH_4HCO_3 = \frac{6f_s}{5}C_5H_7O_2N + (6 - \frac{24f_s}{5})CO_2 + (5 - \frac{6f_s}{5})H_2O \tag{8}$$

Total sugar oxidation reaction equation:

$$C_6H_{10}O_5 + 6(1-f_s)O_2 + \frac{6f_s}{5}NH_4HCO_3 = \frac{6f_s}{5}C_5H_7O_2N + (6 - \frac{24f_s}{5})CO_2 + (5 - \frac{6f_s}{5})H_2O \tag{9}$$

Fat oxidation reaction equation:

$$C_{55}H_{104}O_6 + 78(1-f_s)O_2 + \frac{78f_s}{5}NH_4HCO_3 = \frac{78f_s}{5}C_5H_7O_2N + (55 - \frac{312f_s}{5})CO_2 + (52 - \frac{78f_s}{5})H_2O \tag{10}$$

Protein oxidation reaction equation:

$$C_{46}H_{77}O_{17}N_{12}S + \tfrac{189(1-f_s)}{4}O_2 + \tfrac{189f_s}{20}NH_4HCO_3 = \tfrac{189f_s}{20}C_5H_7O_2N + 12NH_3 \bullet H_2O + \tfrac{230-189f_s}{5}CO_2 + H_2S + \tfrac{150-189f_s}{20}H_2O \tag{11}$$

RDC simultaneous nitrification-denitrification equation (nitro nitrogen pathway):

$$C_6H_{10}O_5 + (6-6f_s)O_2 + 6f_sNH_4HCO_3 + (3 - \tfrac{24f_s}{5})NH_3 \bullet H_2O = \tfrac{72f_s}{35}C_5H_7O_2N + \tfrac{12-12f_s}{5}N_2 \uparrow + (\tfrac{138f_s}{35} - \tfrac{9}{5})HNO_3 + (6 - \tfrac{30f_s}{7})CO_2 + (\tfrac{67}{5} - \tfrac{174f_s}{35})H_2O \quad (12)$$

SDC simultaneous nitrification-denitrification equation (nitro nitrogen pathway):

$$C_6H_{10}O_5 + (6-6f_s)O_2 + 6f_sNH_4HCO_3 + (3 - \tfrac{24f_s}{5})NH_3 \bullet H_2O = \tfrac{72f_s}{35}C_5H_7O_2N + \tfrac{12-12f_s}{5}N_2 \uparrow + (\tfrac{138f_s}{35} - \tfrac{9}{5})HNO_3 + (6 - \tfrac{30f_s}{7})CO_2 + (\tfrac{67}{5} - \tfrac{174f_s}{35})H_2O \quad (13)$$

Total sugar simultaneous nitrification-denitrification equation (nitro nitrogen pathway):

$$C_6H_{10}O_5 + (6-6f_s)O_2 + 6f_sNH_4HCO_3 + (3 - \tfrac{24f_s}{5})NH_3 \bullet H_2O = \tfrac{72f_s}{35}C_5H_7O_2N + \tfrac{12-12f_s}{5}N_2 \uparrow + (\tfrac{138f_s}{35} - \tfrac{9}{5})HNO_3 + (6 - \tfrac{30f_s}{7})CO_2 + (\tfrac{67}{5} - \tfrac{174f_s}{35})H_2O \quad (14)$$

Fat simultaneous nitrification-denitrification equation (nitro nitrogen pathway):

$$C_{55}H_{104}O_6 + (78 - 78f_s)O_2 + 78f_sNH_4HCO_3 + (39 - \tfrac{312f_s}{5})NH_3 \bullet H_2O = \tfrac{936f_s}{35}C_5H_7O_2N + \tfrac{156-156f_s}{5}N_2 \uparrow + (\tfrac{1794f_s}{35} - \tfrac{117}{5})HNO_3 + (55 - \tfrac{390f_s}{7})CO_2 + (\tfrac{806}{5} - \tfrac{2262f_s}{35})H_2O \quad (15)$$

Protein simultaneous nitrification-denitrification equation (nitro nitrogen pathway):

$$C_{46}H_{77}O_{17}N_{12}S + \tfrac{189(1-f_s)}{4}O_2 + \tfrac{189f_s}{4}NH_4HCO_3 + \tfrac{465-1512f_s}{40}NH_3 \bullet H_2O = \tfrac{81f_s}{5}C_5H_7O_2N + \tfrac{189(1-f_s)}{10}N_2 \uparrow + \tfrac{184-135f_s}{4}CO_2 + \tfrac{1242f_s-567}{40}HNO_3 + H_2S + \tfrac{1473-972f_s}{20}H_2O \quad (16)$$

Microorganism decay:

$$C_5H_7O_2N + 5O_2 = 5CO_2 + 2H_2O + NH_3 \quad (17)$$

3.2 Dynamic Model

Imitate the writing of Chen [8] anaerobic model, the aerobic degradation of organics here adopts a first-order kinetic model. When the biodegradation reaches equilibrium, the mass balance equation of organics is:

$$\frac{dS_i}{dt} = \beta_i \sum_{j=1}^{m} C_{j,i}\phi_j\varphi_j \quad (18)$$

Where, β_i is concentration conversion factor of the ith substance, if it is a liquid solute substance, that is $1/\theta$, θ is volumetric moisture content, other material is 1; $C_{j,i}$ represents conversion ratio coefficient, which can be calculated from $C = C_c \bullet C_m$, among them C_c is the mass conservation equation coefficient matrix, with the negative of the reactants, the product is positive, the limiting substrate coefficient is −1, if it is not involved in the reaction, it is 0; C_m is the quality coefficient matrix, $m_{j,i}$ represents the molar mass ratio of material i to the limiting substrate in the jth chemical reaction; ϕ_j is a competitive factor that represents the biochemical reaction of the same limiting substrate; φ_j is the reaction rate of the j group chemical reactions when it reacts independently, which is related to the concentration of reactants, temperature, moisture content, oxygen concentration, and the like.

The above biochemical molecular stoichiometric Eqs. (7–17) involved a total of 14 substances, followed by RDC, SDC, total sugar, fat, protein, microorganism, ammonium bicarbonate, ammonia ($NH_3 \bullet H_2O$), nitric acid, and sulfur hydrogen, oxygen, carbon dioxide, nitrogen, water.

Previous scholars have shown that the aerobic reaction rate is related to temperature, water content, oxygen concentration, and limiting substrate concentration. The limiting substrates aerobic oxidation reaction rate of Eqs. (7–11) can be expressed by the following formula:

$$R_j = \varphi_j = -k_{mTOj} \bullet f(T) \bullet f(C_{water}) \bullet f(C_{O2}) \bullet S_j \tag{19}$$

The limiting substrates simultaneous nitrification-denitrification reaction rate of Eqs. (12–16) can be expressed by the following formula:

$$R_j = \varphi_j = -k_{mTNj} \bullet f(T) \bullet f(C_{water}) \bullet f(C_{O2}) \bullet S_j \tag{20}$$

In the formula, K_{mTOj} is first-order reaction kinetics degradation rate constants for aerobic oxidation of the jth limiting substrates at the reference temperature T_m, d^{-1}; K_{mTNj} is first-order reaction kinetics degradation rate constant for simultaneous nitration-denitrification of the jth limiting substrates at reference temperature T_m, d^{-1}; R_j is the reaction rate of the limiting substrate; S_j is limiting substrate concentration; $f(T)$ is temperature influence function; $f(C_{water})$ is water content influence function; $f(C_{O2})$ is oxygen content influence function; C_{water} is moisture content, water quality/total quality; C_{O2} is oxygen content, volume fraction.

Here, the reference temperature is set to 20 °C and the temperature influence function can be expressed as formula (21).

$$f(T) = 1.066^{(T-20)} - 1.21^{(T-60)} \tag{21}$$

The effect of moisture content is mainly reflected in the use of nutrients by microorganisms and their effect on the air-permeable space. The following formula can be used to express the influence of water content.

$$f(C_{water}) = \frac{1}{e^{(-17.684C_{water}+7.0622)}+1} \tag{22}$$

The adjustment of the oxygen content (volume fraction) to the reaction rate can be expressed by the following formula.

$$f(C_{O2}) = \frac{C_{O2}}{C_{O2}+2\%} \tag{23}$$

The microorganisms decay uses a first-order kinetic formula to describe:

$$R_9 = \theta K_d f_{Td} S_5 \tag{24}$$

$$f_{Td} = \begin{cases} \exp[-\lambda_d (T - T_s)^2] (T < T_s) \\ 1 (T \geq T_s) \end{cases} \tag{25}$$

Here, f_{Td} is the effect function of temperature on the microorganisms decay rate, λ_d is temperature effect parameter.

It is possible to write the change rate of each substance in MSW:

$$\frac{dS_i}{dt} = \beta_i \sum_{j=1}^{m} C_{j,i}\phi_j\varphi_j = \beta_i \sum_{j=1}^{m} C_{j,i} \bullet \phi_j \bullet k_{mTj} \bullet f(T) \bullet f(C_{water}) \bullet f(C_{O2}) \bullet S_j \tag{26}$$

According to the mass conservation principle, the mass change rate of solid, water and gas in unit MSW can be obtained as follows.

Solid:

$$f_{Td} = \sum_{i=1}^{5} \frac{dS_i}{dt} \tag{27}$$

Water:

$$f_{wd} = \frac{dS_{14}}{dt} \tag{28}$$

Gas:

$$f_{gd} = \sum_{i=10}^{13} \frac{dS_i}{dt} \tag{29}$$

The undetermined parameters include first-order reaction kinetics degradation rate constants K_{mTOj} for aerobic oxidation of the five limiting substrates at the reference temperature T_m, and first-order reaction kinetics degradation rate constants K_{mTNj} for simultaneous nitration-denitrification of the five limiting substrates at the reference temperature T_m, competition factors ϕ_j for biochemical reactions of the same limiting substrates, and components of electron donors f_s for cell synthesis.

So far, this model can be used to perform aerobic biodegradation simulation and get the change amount of each substance over time with initial variables and parameters of MSW be provided. The change of each substance is taken as the source and sink of biodegradation of MSW and further coupled with the deformation of waste solid skeleton, the migration of pore fluid, the migration of liquid phase solute, the migration of pore gas, and the heat conduction differential equations to simulate the process of MSW aerobic degradation.

4 Conclusions

According to the principles of electron currents and mass conservation, two types of reactions, oxidation of organics and simultaneous nitrification-denitrification under aerobic conditions were considered. A set of MSW aerobic biochemical reaction stoichiometric formulas with a clear physical meaning and closely related mass was established.

The first-order kinetic equations were used to describe the aerobic dynamics degradation of MSW. RDC, SDC, total sugar, fats, proteins, and microorganisms were selected as the limiting substrates, and the relationship between the mass of various substances over time was established. At the same time, the effects of temperature, moisture content, and oxygen concentration on the aerobic degradation of organic matter were considered.

Model robustness still requires case demonstration; part of the model parameters to be determined is difficult to obtain, such as the competition factors of the same limiting substrate; no consideration of initial C/N ratio effect.

Acknowledgement. The authors would like to acknowledge the financial supports from the National Science Foundation of China (NSFC) (51508504), the major science and technology project of Zhejiang Province (2015C03021), the Fundamental Research Funds for the Central Universities (2017FZA4018).

References

1. Zhou SQ (2005) Biochemical reaction mechanism of landfill leachate simultaneous aerobic and anaerobic biological treatment. J Shihezi Univ (Nat Sci) 23(3):276–279
2. McCarty PL (1972) Stoichiometry of biological reactions. Prog Water Technol 7:157–172
3. Zhou SQ (2001) Theoretical stoichiometry of biological denitrifications. Environ Technol 22:869–880

4. Hoover SR, Porges N (1952) Assimilation of dairy wastes by activated sludge: II. The equation of synthesis and rate of oxygen utilization. Sewage Ind Waste 24(3):306–312
5. Symons JM, Mckinney RE (1958) The biochemistry of nitrogen in the synthesis of activated sludge. Sewage Ind Waste 30(7):874–890
6. Stombaugh DP, Nokes SE (1996) Development of a biologically based aerobic composting simulation model. Am Soc Agricult Eng 39(1):239–250
7. Komilis DP (2006) A kinetic analysis of solid waste composting at optimal conditions. Waste Manag 26:82–91
8. Yunmin C (2014) A fundamental theory of environmental geotechnics and its application. Chin J Geotech Eng 36(1):1–46

A Modeling Study of the Bio-geochemical Processes in Microbially Induced Calcite Precipitation

Xuerui Wang(✉) and Udo Nackenhorst

Institute of Mechanics and Computational Mechanics,
Leibniz Universität Hannover, Appelstraße. 9a, Hannover, Germany
xuerui.wang@ibnm.uni-hannover.de

Abstract. Microbially induced calcite precipitation *(MICP)* offers potential for the development of innovative and environmental friendly techniques for soil improvement. The main purpose of this study is deepening the understanding of bio-geochemical processes involved in MICP by means of numerical modelling. In this paper a coupled bio-geochemo-hydraulic model considering multispecies bio-reactive transport is presented. Generally, this model is based on the theory of porous media, continuum mechanics and solved by finite element method *(FEM)*. Utilizing this model a numerical case study is performed. It is estimated that this model is able to predict a rational bio-geochemical behavior of MICP. Besides, sensitivity analysis regarding the relevant model parameters has been performed to identify key factors in the MICP processes.

Keywords: MICP · Bioremediation · Biogeochemical · Coupled model
Multispecies

1 Introduction

Microbially induced calcite precipitation *(MICP)* provides potential solutions to a wide range of problems in geotechnical engineering, e.g. reinforcement of soft underground, soil erosion control, slope stabilisation and remediation of heavy metal and nuclides contamination according to the observations, MICP can significantly improve soil properties in terms of porosity, permeability reduction and increase of strength. Utilization of bio-geochemical processes to improve soil properties is usually called bio-mediated soil improvement method or biogrout process (DeJong et al. 2013). Compared to conventional soil improvement methods using cement/chemical grouts, which are highly energy consuming and can cause pollution of ground and ground water, biogrout processes are more environmental friendly. By applying MICP in biogrout process, specific bacteria species (e.g. *Sporosarcina pasteurii*), urea and calcium-enriched solution are injected into the soil sequently. By use of urea as the energy source for the metabolic activity, bacteria process enzyme urease that cause catalysed hydrolysis of urea. As consequence of the hydrolysis of urea, ammonium and carbonate ion are produced (Eq. 1). In the presence of calcium, calcium carbonate is formed and by an oversaturated state calcite can precipitate (Eq. 2).

© Springer Nature Singapore Pte Ltd. 2019
L. Zhan et al. (Eds.): ICEG 2018, ESE, pp. 272–279, 2019.
https://doi.org/10.1007/978-981-13-2227-3_33

$$CO(NH_2)_2 + 2H_2O \xrightarrow{bacteria} 2NH_4^+ + CO_3^{2-} \quad (1)$$

$$CO_3^{2-} + Ca^{2+} \rightarrow CaCO_3 \quad (2)$$

Until now, soil improvement via MICP can only be demonstrated in the laboratory, the most application challenges are related to the design and control of MICP process (Martinez et al. 2011; van Wijngaarden et al. 2011). Therefore, numerical modelling should be performed to predict MICP behaviour and to get better understanding of the main mechanisms involved in MICP.

Generally MICP in soil can be considered as microorganisms induced mechanisms that affects the transport process and cause a series of coupled chemo-physical interactions in porous media. To analyse MICP involved bio-geochemical processes in soil a reactive mass transport model serves as an essential tool (Steefel et al. 2005). Recently several biogrout models particularly addressed to MICP in soil have been proposed (Barkouki et al. 2011; van Wijngaarden et al. 2011; Barkouki et al. 2014).

The objective of this paper is a numerical analysis of the relevant bio-geochemical processes involved in MICP based on a related modelling framework. A first goal is to identify the most sensitive factors and conditions within the bio-geochemical processes in MICP.

2 Theoretical Background

Generally the equations to describe MICP process in soil are based on the theory of porous media and continuum mechanics and derived from the macroscopic balance equations, complemented by proper constitutive equations. In the considered problem, the porous medium is assumed as full saturated with one liquid phase, advective and diffusive transport of multi chemical species is considered. Bacteria are assumed to be suspended in the liquid phase. The chemical resultant calcite (Eq. 2) is assumed to precipitate instantaneously and present only in solid phase. Other chemical reactants and resultants (urea, calcium, and ammonium) are assumed to be dissolved and only present in liquid phase. Besides, urea and calcium are considered as a single species with equivalent molar mass, because they are consumed to be injected equimolarly and consumed in the same ratio in the reactions. The spatial and temporal evolution of aqueous species is governed by an advection-diffusion-dispersion-reaction equation,

$$\frac{\partial(\phi C_i)}{\partial t} = \nabla \cdot (\phi \mathbf{D}_i \nabla C_i) - \nabla \cdot (\mathbf{v} C_i) + R_i. \quad (3)$$

In this equation C_i is the concentration of species i. Subscript i stands for different bio-chemical components ($i = r$ for $urea + Ca^{2+}$, $i = p$, stands for NH_4^+ and $i = bac$ for bacteria), ϕ is the porosity, $\mathbf{D}$ is the diffusion-dispersion tensor, $\mathbf{v}$ is the advection velocity vector. The reaction term is considered as source/sink term R_i in the transport equation. It is assumed that bacterial and aqueous chemical species are perfectly

miscible in the pore water. Therefore the advection velocity of all species can be governed by the same fluid velocity (in Eq. 3). This velocity is derived from Darcy's law,

$$\mathbf{v} = -\frac{k}{\mu}(\nabla p - \rho_l \mathbf{g}), \tag{4}$$

where k is the permeability, μ is the viscosity, ρ_l is the density of fluid and $\mathbf{g}$ is gravity acceleration vector. Regarding the bio-chemical reaction, an overall reaction model (van Paassen 2009) is adopted. In this model an overall kinetic rate k_{rea} is defined according to Michaels-Menten kinetics and is dependent on urease activity U and the urea concentration C_r,

$$k_{rea} = U\frac{C_r}{C_r + K_m}\exp\left(-\frac{t}{t_d}\right), \tag{5}$$

where K_m is the half saturation constant and t_d is the exponential time constant. Furthermore U is a factor depending on the bacterial activity,

$$U = u_{sp} C_{bac}. \tag{6}$$

In this equation u_{sp} defines the specific urease activity and C_{bac} is the bacterial concentration.

Usually before MICP treatment bacteria will be cultivated in the laboratory to get the desired concentration and activity, afterwards bacterial will be injected into the soil. Therefore during the injection and cementation phase of MICP bacteria decay predominates and a decrease of bacteria activity is expected. For that reason bacteria growth is neglected in the model. Bacteria decay is considered by applying a constant bacteria decay rate k_d. The time rate of the evolution of bacteria concentration is then given by,

$$\frac{\partial C_{bac}}{\partial t} = k_d C_{bac}. \tag{7}$$

By adopting the overall reaction model and related stoichiometry, the reaction term in (Eq. 3) for each aqueous bio-chemical component can be expressed as,

$$R_r = -k_{rea}\phi m_r;\ R_p = 2k_{rea}\phi m_p;\ R_{bac} = -k_d \phi C_{bac}, \tag{8}$$

where m_i is the molar mass. The solid component calcite R_c is assumed to be immobile, the increase of calcite is calculated directly at the corresponding node, e.g. the concentration of calcite at the current time step t_n at node j is given by,

$$C_{cj}^{t_n} = C_{cj}^{t_{n-1}} + k_{rea} m_c \phi \Delta t, \tag{9}$$

where $C_{cj}^{t_{n-1}}$ is the concentration of calcite at the previous time step.

These equations have been implemented in the finite element code OpenGeoSys *(OGS)*, which was developed specifically to address multi-phase and multi-physical problems in porous media (Kolditz et al. 2012).

3 Numerical Case Studies

3.1 Model Description

A 2D geometrical model (Fig. 1(a)) of 30 × 15 cm has been set up to simulate a laboratory injection test on a thin sand sample. Five representative points are selected for plotting results. The sand sample is assumed to initially contain a homogeneous suspended bacteria density of 3 OD (the optical density measured at a wavelength of 600 μm). Chemical solution of urea and calcium concentration of 1.1 kmol/m^3 is injected at the top of the sample at a constant injection flow velocity of 3.0×10^{-6} m/s. The total duration of the injection is assumed to be 72 h. Common material parameters representative for silty sand (Table 1) are assigned in the model. The value of reaction parameters in the biogrout model summarized in Table 2 have been obtained from the related literature (van Paassen 2009; van Wijngaarden et al. 2016; Fauriel and Laloui 2012).

Table 1. Material parameters used in the modelling

Porosity (−)	ϕ	0.6
Permeability (m^2)	k	1×10^{-12}
Viscosity (Pa s)	μ	0.001
Diffusion coefficient (m^2/s)	D	2×10^{-9}
Molar mass (g/mol)	m_r, m_p, m_c	136, 18, 100

Table 2. Reaction parameters in the biogrout model

Half-saturation constant (−)	K_m	0.01
Specific urea activity (mol/m^{3}sOD)	u_{sp}	2×10^{-7}
Decay rate (t^{-1})	k_d	1×10^{-6}
Time constant (s)	t_d	28800

3.2 Numerical Results

The propagation of the injection front is illustrated in (Fig. 1(b) and (c)). The injection front is driven by advection and diffusion due to the advective flow and concentration gradient respectively. After 1 h of injection, the front reached an axial position of around 11 cm. After 4 h of injection, the front can already reach the bottom of the sample. The numerical results also indicate that with the constant injection velocity of 3.0×10^{-6} m/s a homogeneous distribution of urea and calcium solute with constant concentration of 1.1 kmol/m^3 can be achieved after 17 h of injection in the sample, although they are consumed continuously in the bio-chemical reactions (Eq. 1).

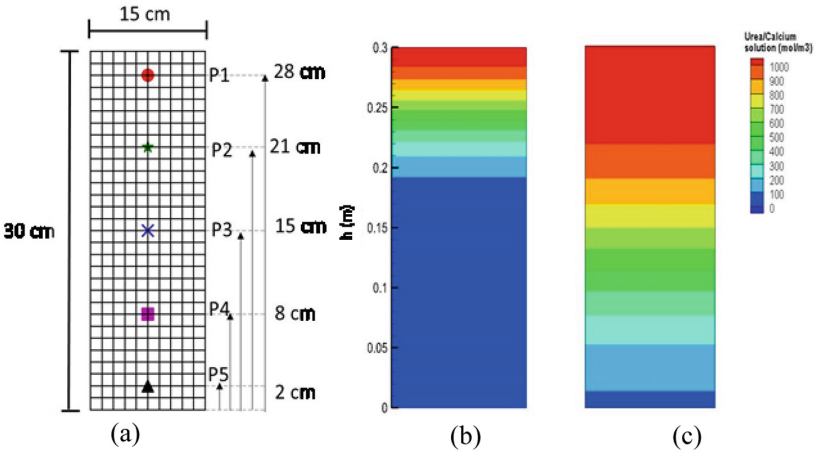

Fig. 1. (a) Model geometry and mesh; distribution of urea calcium concentration after 1 h (b) and after 4 h (c) of injection

The time evolution of the main reactants, i.e. urea/calcium solution and bacteria, the production of calcite at the representative points (Fig. 1) are illustrated in Fig. 2. The continuous injection causes a progressive increase of urea/calcium concentration at each node. In the contrary, the chemical reaction does not cause an obvious reduction in the urea/calcium concentration due to the continuous supply. The maximal concentration of urea/calcium solution at each point has been reached already after 17 h of injection. The continuous decrease of bacteria concentration is caused by the bacteria decay. Bacteria distribute always homogeneously in the sample. Initially there is no calcite present in the sample. At the early injection stage, the reaction rate is quite high and cause a sharp increase of the precipitated calcite concentration. The calcite concentration at positions near to the bottom remains lower than that at the positions close to the top, even though after 17 h the urea/calcium concentration remains overall constant at 1.1 kmol/m^3. The axial gradient of the calcite concentration in the sample reveals the time effects in the reaction system. As aforementioned, the reaction kinetic is dependent on the concentration of urea (Eq. 5). At the early injection stage, the concentration of urea at the lower points is much less than that at the upper points causing a slower precipitation of calcite in the lower area. Due to the decreased reaction activity over time as a consequence of bacterial decay, in the late injection phase even by the constant urea supply the concentration in the area near to bottom is obviously less than near to the top. Besides, the majority of the precipitated calcite attaches to the surface of solid gains and thus is immobile. Therefore, a homogenous distribution of calcite concentration is not expected to be obtained under the considered injection strategy.

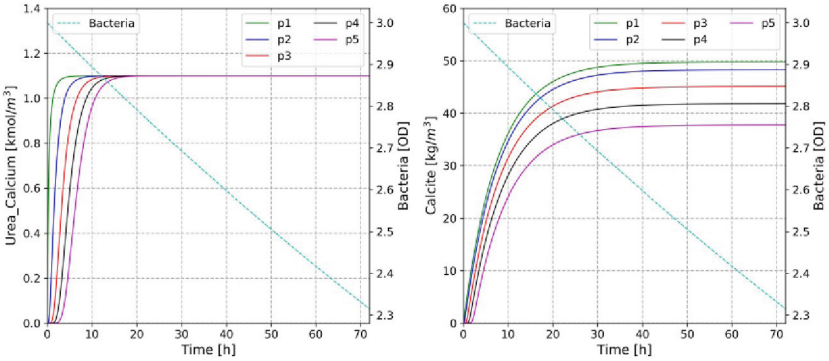

Fig. 2. Temporal evolution of the bacteria concentration at point p1, the urea/calcium solution concentration (left) and the precipitated calcite concentration (right) at the representative points

3.3 Sensitivity Analysis

With the consideration that the value of the reaction parameters in the biogrout model (Table 2) usually depend on several different factors, e.g. temperature, PH value, oxygen concentration etc. and therefore are difficult to determine, a sensitivity analysis is performed by variation of parameters. The computed calcite and bacteria concentration at 72 h by using different values for k_d, t_d and u_{sp} at point P1 is shown in Fig. 3. The reference value is the result using the parameters given in Table 1. The increase of the bacteria decay rate (k_d) causes significant decrease of bacteria concentration (dashed line). However, its effects on the calcite concentration is slightly. Only a small decrease of calcite concentration by increasing of decay rate can be observed. In the contrary, both u_{sp} and t_d have significant effects on the calcite concentration. Increasing u_{sp} causes an approximate linear increase in the calcite concentration, at high values the effects of u_{sp} is more significant than t_d.

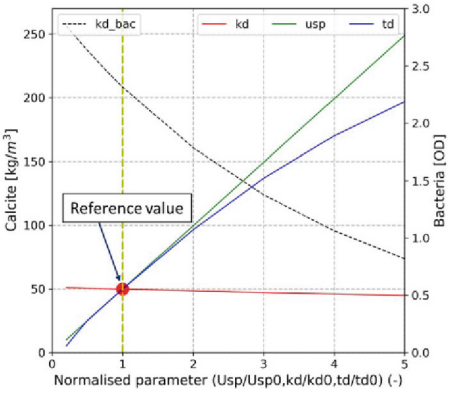

Fig. 3. The concentration of the precipitated calcite and bacteria at point P1 after 72 h of injection by applying of different model parameters.

4 Conclusion

A numerical study on the bio-geochemical features of MICP in porous media is presented. The development of the mathematical formulation for the coupled bio-geochemo-hydraulic model is based on a continuum approach and the macroscopic mass conversation of the multi-components. To address the bio-geochemical processes of MICP an overall bio-reactive model has been adopted by defining an overall kinetics. The bio-reactive model has been coupled with the hydraulic model. Thus the transport of each component is governed by both advection and diffusion processes. The numerical model has been applied to simulate an injection test on a sand sample. The numerical results indicate that the model is able to reproduce the main bio-geochemical processes of MICP. Besides, a sensitivity analysis with regard to different parameters of the bio-reactive model has been performed, which is of great interest for the design of laboratory and in situ tests as well as for the applications. The presented model can be applied to simulate different application strategies of MICP in porous media by adapting the corresponding initial and boundary conditions as well as injection strategy. In addition, the model can be extended to analyze further issues related to MICP process in porous media, e.g. effects of the attachment of chemical components on the solid grain, MICP induced variation of porosity and permeability.

References

Barkouki T, Martinez B, Mortensen B, Weathers T, DeJong J, Spycher N et al (2011) Forward and inverse bio-geochemical modeling of microbially induced calcium carbonate precipitation in half-meter column experiments. Transp Porous Med 90:23–29

Barkouki TH, Martinez BC, Mortensen BM, Weathers TS, De Jong JD, Ginn TR, Spycher NF, Smith RW, Fujita Y (2014, September) Forward and inverse bio-geochemical modeling of microbially induced calcite precipitation in half-meter column experiments. http://doi.org/10.1007/s11242-011-9804-z

DeJong JT et al (2013) Biogechemical processes and geotechnical applications: process, opportunities and challenges. Geotechnique 63(4):287–301

Fauriel S, Laloui L (2012) A bio-chemo-hydro-mechanical model for microbially induced calcite precipitation in soils. Comput Geotech 46:104–120. https://doi.org/10.1016/j.compgeo.2012.05.017

Kolditz O, Bauer S, Bilke L, Böttcher N, Delfs JO, Fischer T, Zehner B (2012) OpenGeoSys: an open-source initiative for numerical simulation of thermo-hydro-mechanical/chemical (THM/C) processes in porous media. Environ Earth Sci 67(2):589–599. https://doi.org/10.1007/s12665-012-1546-x

Steefel CI, DePaolo DJ, Lichtner PC (2005) Reactive transport modeling: an essential tool and a new paradigm for the earth sciences. Earth Planet Sci Lett 240:539–558

Martinez BC, Barkouki TH, DeJong JD, Ginn TR (2011) Upscaling of microbial induced calcite precipitation in 0.5mcolumns: experimental and modeling results. In: Han J, Alzamora DA (eds) Advances on geotechnical engineering. Geotechnical Special Publications. Proceedings of geo-frontiers, 13–16 March 2011, Dallas, Texas

van Paassen LA (2009) Biogrout, ground improvement by microbial induced carbonate precipitation. PhD thesis, Delft University of Technology

van Wijngaarden WK, Vermolen FJ, van Meurs GAM, Vuik C (2011) Modelling biogrout: a new ground improvement method based on microbial-induced carbonate precipitation. Transp Porous Media 87(2):397–420

van Wijngaarden WK, van Paassen LA, Vermolen FJ, van Meurs GAM, Vuik C (2016) A reactive transport model for biogrout compared to experimental data. Transp Porous Media 111(3):627–648. https://doi.org/10.1007/s11242-015-0615-5

Arsenic Removal from Contaminated Soil by Phytoremediation Combined with Chemical Immobilization

Saki Arita and Masahiko Katoh(✉)

Department of Agricultural Chemistry, Meiji University, Kanagawa, Japan
mkatoh@meiji.ac.jp

Abstract. We have designed a new phytoremediation technique called phytosuction separation (PS-S). To date, it has indicated that the PS-S can remove antimony 69–533 times higher than that removed by phytoextraction (PE). However, it should be deeply investigated that PS-S can effectively remove the metalloid other than antimony. Arsenic-contaminated soil was used in this study. Ferryhydrite synthesized in the laboratory was used as an immobilization material. Four treatments for PS-S were prepared changing the amount of contaminated soil put in the pot: 1.6, 1.0, 0.5, 0.2 cm soil depth, respectively. The removal ratios of PS-S system were higher than that of PE despite the soil depth of PS-S system. The removal ratios of PS-S system increased with the decrease in the soil depth, indicating that the PS-S system could remove arsenic from less than 0.5 cm soil layer. This study indicates that the PS-S system can remove arsenic from the contaminated soil compared with PE, and it can be more effective with more shallow soil layer.

Keywords: Arsenic removal · Phytoremediation · Phytosuction separation
Soil pollution · Soil remediation

1 Introduction

Phytoremediation is a generic term for remediation technique using plant. Phytoremediation is an eco-friendly and cost-effective approach to soil remediation, which can be divided into several categories depending on its function (Ensley 2000). Phytoextraction (PE) is the most effective and promising phytoremediation method for removing toxic metals and/or metalloids from contaminated soil. PE can extract toxic metal and/or metalloid from contaminated soil absorbing them from plant root system. However, it has a crucial disadvantage; i.e., it requires long periods for the removal of toxic metal and/or metalloid from contaminated soil, even when using a hyperaccumulator that can accumulate toxic metal and/metalloid at high concentration (Freitas et al. 2013).

We have designed a new phytoremediation technique called phytosuction separation (PS-S), in which a material that can immobilize toxic metal and/or metalloid is placed onto contaminated soil and plants are grown on the upper layer of this material. Toxic metal and/or metalloid in the soil are transported toward the upper layer by the

© Springer Nature Singapore Pte Ltd. 2019
L. Zhan et al. (Eds.): ICEG 2018, ESE, pp. 280–285, 2019.
https://doi.org/10.1007/978-981-13-2227-3_34

water suction effect of the roots and immobilized by the material and then removed from the contaminated soil. Thus, the PS-S system can reduce the period for metal and/or metalloid removal compared with the PE system because metal and/or metalloid absorbing by the root system is unnecessary. In previous, our research group has indicated that the PS-S can remove lead and antimony at 8–25 and 69–533 times higher than that removed by PE, respectively (Katoh et al. 2016). Furthermore, it demonstrates that the metalloid, particularly existing oxyanion, could be effectively removed by PS-S system compared with metal, particularly existing cation. This is because of differences of mobility between metal cation and metalloid oxyanion in soil. However, it should be deeply investigated that whether the metalloid other than antimony can be effectively removed by PS-S system. In addition, the important factor of removal efficiency by the PS-S system is the mobility of toxic metal and/or metalloid. Thus, it should be understood the relationship between the soil depth in which the PS-S system can remove the metalloid and the removal efficiency of metalloid. The aims of this study were (1) to investigate whether arsenic in the contaminated soil could be effectively removed by the PS-S compared with the PE and (2) to evaluate the soil depth in which PS-S can remove metalloid effectively.

2 Materials and Methods

2.1 Soil and Immobilization Material

The arsenic-contaminated soil used in the present study was obtained from tunnel construction in the central part of Honshu island, Japan. The air-dried soil sample was passed through a 2-mm sieve prior to chemical analysis and cultivation test. Chemical properties of soil were shown in Table 1. Commercial soil suitable for cultivation was used as the planting soil in the PS-S experiment (Table 1).

Table 1. Physicochemical properties of soil used in this study (on the basis of air-dried weight)

Soil	Sand (%)	Silt (%)	Clay (%)	pH	EC (mS/m)	Arsenic (mg/kg)	
						Water-soluble	Total
Contaminated	62	36	2	8.9	7.2	2.03	338
Non contaminated	45	48	7	5.7	9.2	0.02	9.3

Ferrihydrite was used as an immobilization material and obtained by the neutralization and precipitation of a 1.24 mol L^{-1} $Fe(NO_3)_3$ $9H_2O$ solution using 5 mol L^{-1} NaOH (Richmond et al. 2004).

2.2 Phytosuction Separation

Acrylic pots (65 × 65 × 95 mm high) with 25 holes at the bottom were used for cultivation test. The detail of PS-S system was referred in Katoh et al. (2016). In brief, the PS-S system has three layers: contaminated soil layer, immobilization material

layer, and planting soil layer from the bottom of pot. The fertilizer was mixed with the planting soil, and guinea grass (Panicum maximum J.) was grown in the planting soil. Each layer was separated by a nylon mesh sheet. Sufficient pure water was added to each pot to maintain to 50% of water-holding capacity of soil every two to three days. This experimental design allowed the water to flow from the lower parts toward the upper parts. Three pots were prepared for each treatment. The plants were grown for 13 weeks at a controlled temperature (25 °C) with a 14-h photoperiod using a 40-W horticultural lamp.

2.3 Treatment of Cultivation Test

Four treatments for the PS-S were prepared changing the amount of contaminated soil put in the pot: 100, 60, 30, 10 g/pot, respectively, which were corresponded to 1.6, 1.0, 0.5, 0.2 cm soil depth, respectively (Hereafter referred as PS-S-1.6, PS-S-1.0, PS-S-0.5, and PS-S-0.2, respectively). The ferrihydrite was put on the contaminated soil at an amount that can immobilize arsenic in the contaminated soil even if all the arsenic in the contaminated soil migrates to the material layer. 100 g of planting soil was putted on the material layer. The PE treatment using the 100 g contaminated soil was also prepared for control.

2.4 Analytical Methods

After 13 weeks of plant growth, the aboveground of plant was cut, and the shoot length (from the surface of the soil to the furthest leaf tip) was measured. The shoot samples were dried at 80 °C for 48 h to obtain a constant weight and then weighed and ground. The total arsenic concentrations were determined in the dried, ground shoot samples, and the uptake of arsenic by the shoots was calculated to measure the amount of arsenic removed by PE. To analyze the effectiveness of PS-S, samples of the immobilization material were carefully collected from the pots without mixing and were air dried. The total arsenic concentrations in the immobilization material were determined after sieving at 0.425 mm. The amounts of arsenic in the immobilization materials were treated as the amounts of arsenic removed by PS-S. The contaminated soil was used to extract water-soluble arsenic after sieving at 2 mm.

3 Results and Discussion

3.1 Shoot Biomass of Plant

The shoot biomass of guinea grass grown in the planting soil for 13 weeks was shown in Table 2. Both shoot length and dried weight in the PE were significantly lower than those in all the PS-S treatments. In the PE treatment, the plant was grown in the contaminated soil, directly. Thus, the arsenic toxicity to plant was responsible for the suppression of plant growth. In contrast, the plant growth in all the PS-S treatments was higher than in PE, but those were different between the treatments; the plant growth was higher in PS-S-0.5 and PS-S-1.0 than PS-S-0.2 and PS-S-1.6. In PS-S-0.2 and

PS-S-1.6, the coefficients of variation for plant growth were high. This was attributed to the differences of plant growth between the pots; the plant growth in some pots was suppressed. The suppression of plant growth in such treatments would result from the toxicity of arsenic that migrated from the contaminated soil and not immobilized by the material layer. The arsenic concentration of plant in these pots was higher in PS-S-0.2 and PS-S-1.6 than PS-S-0.5 and PS-S-1.0 (data not shown). This would be because variations of each pot of PS-S system make arsenic migration not prevent completely regardless of soil depth. Thus, the improvement of PS-S system should be necessary to completely prevent arsenic migration into the planting soil in the material layer.

Table 2. Shoot biomass of guinea grass grown in soil for 13 weeks

Treatment	Shoot length (cm)	Shoot weight (g/plant-DW)
PS-S-0.2	29.1 ± 25.8	0.11 ± 0.20
PS-S-0.5	42.5 ± 24.5	0.26 ± 0.31
PS-S-1.0	61.8 ± 8.7	0.33 ± 0.17
PS-S-1.6	21.9 ± 20.3	0.10 ± 0.17
PE	7.8 ± 3.7	0.004 ± 0.006

3.2 Arsenic Removal by PS-S System

The ratio of arsenic removal by PS-S system to water-soluble arsenic in the contaminated soil was shown in Fig. 1. The ratio (hereafter, referred as removal ratio) was calculated on the basis of amount of arsenic removed by PS-S or PE and the amount of water-soluble arsenic in the contaminated soil before cultivation. The amount of arsenic removed by PE was based on the amount of arsenic uptake by plant, and it for PS-S was the amount of arsenic in the material after the cultivation test.

Comparing with PE, the removal ratios in all the PS-S treatments were greatly higher. The removal ratios were 0.7% for PE and 38% for PS-S-1.6. The amount of contaminated soil was same (100 g/pot). Thus, it demonstrates that PS-S system could greatly remove arsenic from the contaminated soil at 54 times higher than PE. The removal efficiency for arsenic was compatible with the case of antimony (Katoh et al. 2016), suggesting that the PS-S system can effectively remove arsenic at the same level as in the case of antimony.

Comparing within the PS-S system, the removal ratios increased with the decrease in the soil depth; the highest ratio was observed in PS-S-0.2 (192%), and the lowest was PS-S-1.6 (38%). This indicates that the PS-S system could effectively remove arsenic from less than 0.5 cm soil layer although it could remove arsenic from more than 0.5 cm soil layer compared with PE. The removal ratio in PS-S-0.2 exceeded 100%. Arsenic can occur in various different phases in soil, including dissolved in the soil solution, or bound to metal oxides and organic matter. The water-soluble arsenic fraction appears to be at equilibrium for each of the arsenic phases. Thus, as arsenic is removed by the PS-S system, it would continue to be added to the water-soluble fraction from each arsenic phase, resulting in the removal ratio of arsenic of over 100%.

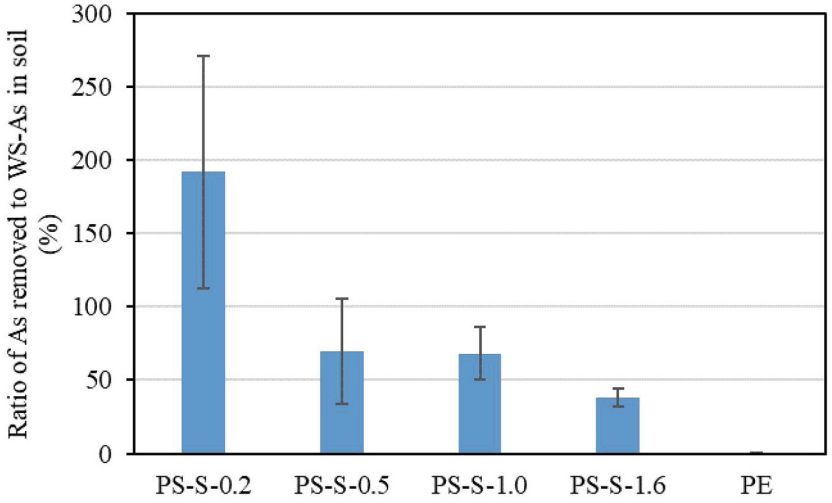

Fig. 1. Ratio of arsenic removal by PS-S system to water-soluble arsenic in the contaminated soil before cultivation

3.3 Water-Soluble Arsenic in Contaminated Soil After Cultivation

The amount of water-soluble arsenic in the contaminated soil after the cultivation was shown in Fig. 2. The amount of water-soluble arsenic in PS-S-1.6 was the same level as it before the cultivation. However, they became lower with the decrease in the soil depth, and it was 1.1 mg/kg in PS-S-0.2, which was corresponded to 54% of it before the cultivation. These results indicate that the PS-S system can remove arsenic from the

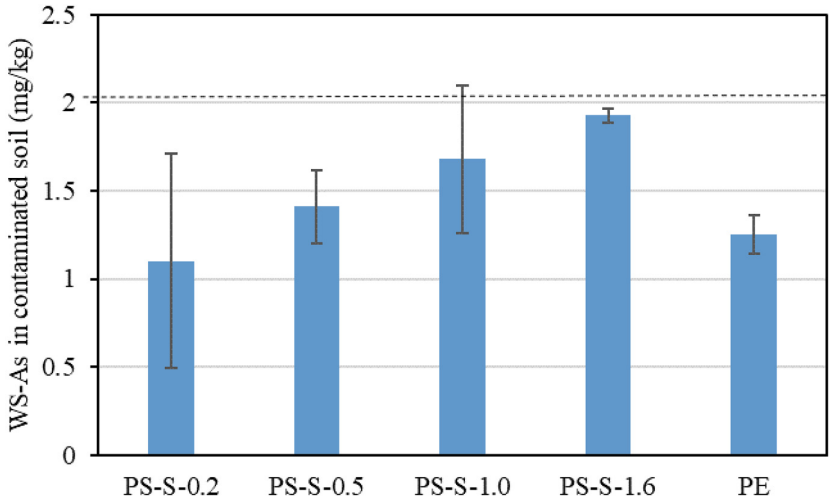

Fig. 2. Water-soluble arsenic in the contaminated soil after the cultivation. Broken line in the figure indicates its level before the cultivation

contaminated soil more effectively with more shallow soil layer. The amount of water-soluble arsenic in PE also became lower than that before the cultivation, and it was the same level as that in PS-S-0.5 despite the removal ratio in PE was greatly low compared with all the PS-S treatments (Fig. 1). The reason was not clear, but it might be explained for the rhizosphere effect. The exudation from the plant root changes the redox potential, microbial activities, and chemical speciation of elements. Thus, the rhizosphere effect might change the arsenic phases in the contaminated soil during the cultivation, which might make the arsenic phases more insoluble.

4 Conclusion

This study investigated whether arsenic in the contaminated soil could be effectively removed by the PS-S compared with the PE and evaluated the soil depth in which PS-S can remove metalloid effectively. Both shoot length and dried weight in all the PS-S treatments were significantly higher than that in PE; however, plant biomass was different between the PS-S treatments due to the arsenic migration. Thus, the improvement of PS-S system should be necessary to completely prevent arsenic migration into the planting soil in the material layer. Comparing within the PS-S system, the removal ratios increased with the decrease in the soil depth, indicating that the PS-S system could remove arsenic from less than 0.5 cm soil layer although it could remove arsenic from more than 0.5 cm soil layer compared with PE. The amount of water-soluble arsenic became lower with the decrease in the soil depth, and it was 1.1 mg/kg in PS-S-0.2, which was corresponded to 54% of it before the cultivation. This study indicates that the PS-S system can remove arsenic from the contaminated soil compared with PE, and it can be more effectively with more shallow soil layer.

References

Ensley BD (2000) In: Raskin I, Ensley BD (eds) Phytoremediation of toxic metals. Willey, New York

Freitas EV, Nascimento CW, Souza A, Silva FB (2013) Citric acid-assisted phytoextraction of lead: a field experiment. Chemosphere 92:213–217

Katoh M, Hashimoto K, Sato T (2016) Lead and antimony removal from contaminated soil by phytoremediation combined with an immobilization material. CLEAN–Soil Air Water 44:1717–1724

Richmond WR, Loan M, Morton J, Parkinson GM (2004) Arsenic removal from aqueous solution via ferrihydrite crystallization control. Environ Sci Technol 38:2368–2372

Deformation and Saturated Permeability Characteristics of Bentonite-Sand Mixtures Saturated on Salt Solution

Wenjing Sun[1,2,3(✉)] and Cheng Liu[1]

[1] Civil Engineering Department, Shanghai University, Shanghai 200444, China
wjsun@shu.edu.cn
[2] Institute for the Conservation of Cultural Heritage, Shanghai University, Shanghai 200444, China
[3] State Key Laboratory of Geomechanics and Geotechnical Engineering, Institute of Rock and Soil Mechanics, Chinese Academy of Sciences, Wuhan 430071, China

Abstract. Bentonite-sand mixture is often used as the artificial engineering barriers for the high-level radioactive waste repository and the anti-seepage barriers in civil geotechnical engineering, and it is very important to study its deformation and permeability characteristics in evaluating the service performance and durability. The compression test was used to obtain the compression deformation characteristics and saturated hydraulic conductivity of the mixtures with different sand content saturated on salt solution of different concentrations. The concepts of the actual effective stress p_e and the montmorillonite void ratio e_m are introduced, and the change rules of e_m-p_e relationships and the e_m-k relationships of the mixtures with different sand content saturated on salt solution of different concentrations are summarized.

Keywords: Bentonite-sand mixtures · Saturated hydraulic conductivity
Salt solution concentration · Montmorillonite void ratio · True effective stress

1 Introduction

Bentonite has been selected as an ideal matrix for artificial engineering barrier and anti-seepage barrier of civil geotechnical engineering structures (Ye et al. 2010) because of its high expansibility, low permeability and excellent adsorption capacity. In view of the engineering cost, the bentonite-sand mixture is generally used as the engineering barrier in actual projects. Infiltration of ground water with different chemical compositions can cause the change of the pore structure of the mixture. Once the anti-seepage effect of the bentonite-sand mixtures is weakened or lost, the pollutants will spread to the biosphere. Therefore, it is very necessary to study the deformation and saturated permeability of the mixtures saturated on salt solution.

Scholars at home and abroad have studied the deformation and saturated hydraulic conductivity of the mixtures with different types of bentonite as the base material. Zhu et al. (2013) conducted permeability test of GMZ01 bentonite, indicating that the saturated hydraulic conductivity of pure bentonite increases with the increase of salt

© Springer Nature Singapore Pte Ltd. 2019
L. Zhan et al. (Eds.): ICEG 2018, ESE, pp. 286–292, 2019.
https://doi.org/10.1007/978-981-13-2227-3_35

concentration. Studds et al. (1998) conducted permeability test about GMZ01 bentonite of pure bentonite and the mixtures with 80%, 90% sand content saturated on salt solution of different concentrations, and it is concluded that the swelling characteristic of the mixtures is similar to that in pure bentonite at a low stress, while the swelling characteristic of the mixtures changed at a high stress, or soaked in the high concentration salt solutions.

At present, less research results have been reported of the swelling and saturated permeability of the bentonite-sand mixtures at the full range of sand content saturated on the salt solution of different concentrations. In this paper, the swelling tests of the mixtures with different sand content saturated on salt solution of different concentrations were carried out, and then the compression tests of the saturated mixtures were conducted in order to obtain the saturated permeability by the indirect method, and finally the swelling and saturated hydraulic conductivity characteristics of the mixtures are analyzed.

2 Experiments and Methodology

2.1 Materials

The basic physical index of bentonite and sand are reported in Table 1. Bentonite and sand were mixed by weight ratio of 70:30, 30:70, and 100:0, respectively and the compressed specimens with dry density of 1.5 g/cm^3 and the initial water content of 15% were prepared. NaCl salt solutions of different concentrations were prepared at 0 mol/L, 0.1 mol/L, 0.5 mol/L and 1 mol/L by using NaCl particles and distilled water in the test.

Table 1. Basic physical index of bentonite and sand

Bentonite	Index	Sand	Index
Particle density ρ_s (g/cm^3)	2.71	Particle density ρ_s (g/cm^3)	2.65
Liquid limit w_L (%)	153.4	Average particle size D_{50} (mm)	0.34
Plastic limit w_p (%)	26.8	Non-uniform coefficient C_u	1.97
Montmorillonite content (%)	45.8	Minimum dry density ρ_{dmin}	1.35
Expansion index (ml/g)	12.5	Compression index C_c	0.08

2.2 Testing Method and Procedure

Under the vertical load of 25 kPa, the swelling deformation tests saturated on the salt solution of different concentrations were carried out. After the completion of swelling deformation test, a series of compression test on the saturated mixtures were conducted in accordance with the ASTM-D2435 test standard. And according to Terzaghi's one-dimensional consolidation theory, the saturated hydraulic conductivity was calculated by the indirect method.

3 Test Results and Analysis

3.1 Deformation Characteristics

Figure 1 shows the relationship between void ratio e and vertical stress σ_v of saturated bentonite-sand mixtures with the same sand content saturated on NaCl salt solution of different concentrations. It can be seen from Fig. 1(a) that the void ratio of the pure bentonite increases after saturated by NaCl salt solutions and the increase amplitude in the void ratio gradually decreases with the increase of the concentration of NaCl solution. When the concentration of salt solution is 0.5 mol/L and 1 mol/L, the void ratio of the pure bentonite after saturation seems almost unchanged. When the sand content is 70%, the void ratio of the finally saturated mixtures soaked in NaCl salt solution of different concentrations is basically consistent with the initial void ratio, as shown in Fig. 1(b). The results show that the NaCl concentration has little effect on the void ratio of the mixtures at the higher sand content of 70%.

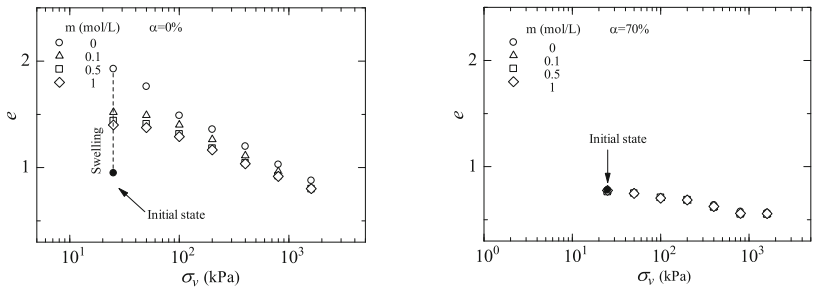

(a) $\alpha = 0$ % (b) $\alpha = 70$ %

Fig. 1. e-lgσ_v relationship of the mixtures with the same sand content saturated on NaCl salt solution of different concentrations.

Sun et al. (2009) introduced the montmorillonite void ratio e_m, which characterized the amount of water absorbed by montmorillonite per unit volume after full wetting. The montmorillonite void ratio e_m can be expressed as follow:

$$e_{\mathrm{m}} = \frac{e_f \rho_m}{\rho(1-\alpha)\beta} \tag{1}$$

where ρ is the specific gravity of the mixtures, e_f is the void ratio at full saturation, ρ_m is montmorillonite specific gravity, α is the sand content, and β is the montmorillonite content in bentonite.

For the pure bentonite saturated with salt solution, the effective stress is composed of three parts: the vertical effective stress (σ_v-u_w), osmotic stress (p_π) and electrochemical stress (A-R) (Rao et al. 2017). The effective stress borne by bentonite saturated with salt solution is defined as the true effective stress, as indicated as follows,

$$p_e = (\sigma_v - u_w) + p_\pi + (A - R) \tag{2}$$

where σ_v is the vertical stress; u_w is the pore water pressure; σ_v-u_w is the vertical effective stress; (A-R) is the electrochemical stress, which is proved small and negligible in Rao et al. (2017); p_π is the osmotic stress acting on the pure bentonite (Xu et al. 2014), and is expressed as:

$$p_\pi = \pi\left(\frac{p}{\pi}\right)^{D_S - 2} \tag{3}$$

where *Ds* is a parameter to describe the roughness of the surface of the material; π represents osmotic suction in pore water, and the Van's Hoff formula (4) is used to calculate π.

$$\pi = vRTm\varphi \tag{4}$$

where v is the number of ions contained in the salt molecule (NaCl: v = 2); R is the constant of gas, R = 8.3145 J/mol · K; T is the absolute temperature, the unit is K; m is the molar concentration of the solution, and the unit is mol/L.

When the bentonite is mixed with sand, the osmotic stress acting on the bentonite-sand mixtures can be expressed as $(1 - \alpha)\, p_\pi$. The true effective stress of the mixtures can be calculated by formula (5).

$$p_e = (\sigma_v - u_w) + (1 - \alpha)p_\pi \tag{5}$$

The montmorillonite void ratio e_m and the true effective stress p_e are used to analyze the compression curves of pure bentonite and the mixtures with 30% and 70% sand content. It is shown from Fig. 2 that the relationship between void ratio e and vertical stress σ_v of the bentonite-sand mixtures saturated on NaCl salt solution of different concentrations can be normalized by the relationship between true effective stress p_e and the montmorillonite void ratio e_m on concentration. When the sand content of the mixtures is 0% (pure bentonite) and 30%, the e_m-p_e relationship represents the straight line. With the increase of sand content, the e_m-p_e relationship of the mixtures begins to deviate from the line when true effective stress is greater than a special value, and the special vertical stress is called the true effective deviation stress p_{es}.

The critical sand content of bentonite-sand mixtures is introduced by Sun et al. (2009). When the sand content is less than this value, the sand particles cannot contact each other, that is, the sand skeleton will not form, but when the sand content is greater than the critical sand content, the sand skeleton can be formed under the relatively high vertical stress. The critical sand content can be calculated by Eq. (6).

$$\alpha_s = \frac{\beta\rho_s + \frac{(1-\beta)\rho_m\rho_s}{\rho_{nm}}}{e_{smax}\rho_m + \beta\rho_s + \frac{(1-\beta)\rho_m\rho_s}{\rho_{nm}}} \tag{6}$$

where e_{smax} is the largest sand void ratio; ρ_s is sand specific gravity; and ρ_{nm} is non montmorillonite specific gravity.

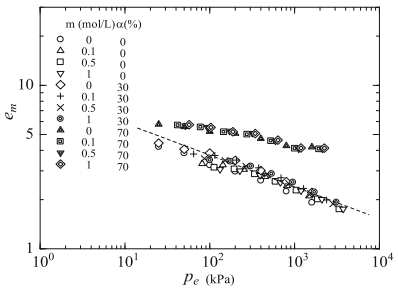

Fig. 2. lge_m-lgp_e relationship of the mixtures with different sand content saturated on NaCl salt solutions with different concentrations

When the sand content of the mixtures is less than critical sand content α_s, the sand skeleton of the mixtures will not form, and the sand particles are suspended in bentonite. The external force on the bentonite-sand mixtures is only borne by bentonite, and the sample is easier to be compressed. With the increase of sand content, the sand skeleton is formed under certain stress. At this time, the sand skeleton and bentonite bear external force together, and the sample is not easy to be compressed. Therefore, the slope of the e_m-p_e linear relationship of the mixtures with the high sand content is less than that of the mixtures with the small sand content.

3.2 Permeability Properties

On the basis of the consolidation test, the hydraulic conductivity of the bentonite-sand mixtures is calculated by indirect method. Figure 3 shows the relationship between the montmorillonite void ratio e_m and the hydraulic conductivity k of pure bentonite and the mixtures with 30% and 70% sand content saturated on salt solution of different concentrations. Here shows only the lge_m-lg$k$ relationship of the mixtures with 0 mol/L and 1 mol/L NaCl concentration. Figure 3 shows the linear correlation between the montmorillonite void ratio and hydraulic conductivity of the pure bentonite and the mixtures with 30% sand content saturated on salt solution of different concentrations, and the deviation occurs when the sand content is 70%. The main reason is that the hydraulic conductivity of bentonite mainly depends on the montmorillonite when sand content of the mixtures is small, so the hydraulic conductivity k has a unique linear relationship with the montmorillonite void ratio e_m. When the montmorillonite void ratio is at the same, compared with the mixtures with a sand content less than α_s, the mixtures with the high sand content of 70% is more dense and the hydraulic conductivity is smaller, therefore the lge_m-lg$k$ relationship deviates from the linear relationship.

Figure 4 shows the lge_m-lg$k$ relationships of the bentonite-sand mixtures saturated on salt solution of different concentrations. As we can see from Fig. 4, the lge_m-lg$k$ of the mixtures with less sand than the critical sand content shows the linear relationship. With the increase of NaCl solution concentration, the slope of the linear relationship becomes larger and when the montmorillonite void ratio is the same, which is the same as the conclusion of Ye et al. (2014).

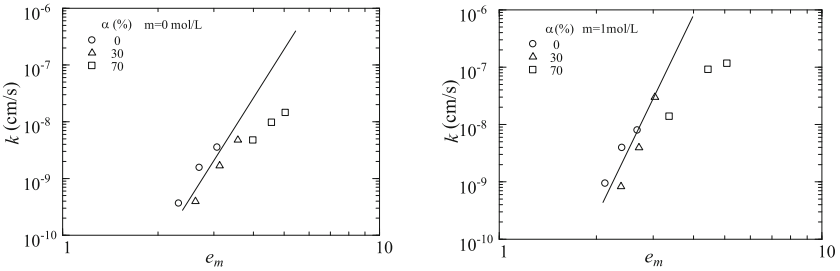

(a) m = 0 mol/L (b) m = 1 mol/L

Fig. 3. lge_m-lg$k$ relationships of the mixtures saturated on NaCl salt solution of different concentrations.

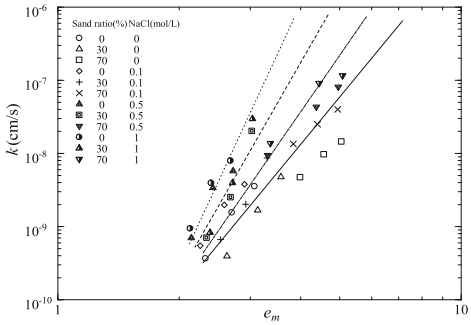

Fig. 4. lge_m-lg$k$ relationship of the mixtures samples with different sand content saturated on NaCl salt solution of different concentrations

As the concentration of NaCl solution increases, the slope of lge_m-lg$k$ relationship line increases gradually, which is related to the decrease of diffusion double layer thickness caused by the increase of concentration. According to the diffusion double layer theory, the thickness of the electric double layer is inversely proportional to the valence of ions and the square root of the ion concentration. With the increase of concentration of salt solution, the binding water content in bentonite decreases, which makes the thickness of DDL decrease and the effective porosity increases, which leads to the increase of permeability (Guimaraes et al. 2013).

4 Conclusions

In this paper, the swelling deformation and compression tests of the bentonite-sand mixtures with 0%, 30% and 70% sand content saturated on salt solution of different concentrations were carried out. It is summarized as follows: The sand content and the concentration of salt solution have larger effect on the deformation and permeability characteristics of the mixtures. The montmorillonite void ratio and the true effective

stress can better summary the law of the deformation and permeability of the mixtures with different sand content saturated on NaCl salt solution of different concentrations.

Acknowledgements. The authors are grateful to the National Sciences Foundation of China (Grant No. 41572284) and the Open Research Fund of State Key Laboratory of Geomechanics and Geotechnical Engineering, Institute of Rock and Soil Mechanics, Chinese Academy of Sciences (Grant No. Z013008) for the financial supports. At the same time, The authors thank the support of Shanghai Key Innovative Team of Cultural Heritage Conservation.

References

Ye WM, Chen YG, Chen B et al (2010) Advances on the knowledge of the buffer/backfill properties of heavily-compacted GMZ bentonite. Eng Geol 116(1):12–20

Studds PG, Stewart DI, Cousens TW (1998) The effects of salt solutions on the properties of bentonite-sand mixtures. Clay Miner 33(4):651–660

Sun DA, Cui HB, Sun WJ (2009) Swelling of compacted sand-bentonite mixtures. Appl Clay Sci 43(3):485–492

Rao S, Deepak GB, Rao PR et al (2017) Influence of physico-chemical components on the consolidation behavior of soft kaolinites. Acta Geotech 12(2):1–11

Xu Y, Xiang G, Jiang H et al (2014) Role of osmotic suction in volume change of clays in salt solution. Appl Clay Sci 101:354–361

Ye WM, Zhang F, Chen B et al (2014) Effects of salt solutions on the hydro-mechanical behavior of compacted GMZ01 Bentonite. Environ Earth Sci 72(7):2621–2630

Guimaraes L, Gens A, Sanchez M (2013) A chemo-mechanical constitutive model accounting for cation exchange in expansive clays. Geotechnique 63(3):221–234

Modelling the Effects of Thermal Gradient on Microbe Facilitated Mineral Precipitation Kinetics in Subsurface Flow Conditions

Shakil A. Masum(✉) and Hywel R. Thomas

Geoenvironmental Research Centre, Cardiff University, Cardiff CF24 3AA, UK
masumsal@cardiff.ac.uk

Abstract. Deep geological sequestration of anthropogenic carbon dioxide is a plausible way to reduce global greenhouse gas impacts. Long-term containment of sequestered CO2 can be achieved by preventing leakage and by ensuring further entrapments such as solubility-trapping and mineral-trapping. These processes can be enhanced by involving subsurface microbial community that restrict flows by forming biofilms and/favours biomineralization. For example, ureolytic bacteria, *Sporosarcina pasteurii*, catalyzes urea hydrolysis and accelerate calcite precipitations in presence of dissolved calcium ions. However, subsurface flows and reactions are complex and often involve multiple phases, chemicals and minerals as well as pressure and thermal gradients. These complex coupled behaviours are challenging and limitedly attempted.

Within the scope of an ongoing study, a coupled numerical model has been developed under a THCM framework including subsurface microbial processes and associated bio-geochemical reactions. The model deals with liquid flow, multicomponent gas flows, dissolved chemicals and suspended microbes flows in liquid phase, heat flow, biofilms and minerals growths, mechanical deformations and geochemical/bio-geochemical reactions. In this paper, the coupled microbial model has been used to investigate the effects of thermal gradient on microbial growth and mineral precipitation as well as their overall impacts on the flow properties of the medium.

Keywords: Coupled · Modelling · Biofilm · Thermal · Biomineralization

1 Introduction

Sequestration of anthropogenic carbon dioxide in deep geological formations, such as, saline aquifers, un-mineable coal seams is an effective means to reduce global greenhouse gas effects. Long-term containment of sequestered carbon is essential for a viable engineering solution. Trapping of labile carbon into solid carbonate minerals or Mineral-trapping (Mitchell et al. 2010) is a useful method to ensure such containment. Inorganic carbon can also be contained as aqueous phases in the formation solution or via solubility-trapping (Mitchell et al. 2010). Calcium, which is an abundantly available cation in the surface and subsurface waters (Stumm and Morgan 1996) can aid mineralization of carbonates into calcite ($CaCO_3$) during mineral-trapping (Mitchell et al. 2010). Formation of $CaCO_3$ takes place in presence of sufficient Ca^{2+} ions, suitable

© Springer Nature Singapore Pte Ltd. 2019
L. Zhan et al. (Eds.): ICEG 2018, ESE, pp. 293–301, 2019.
https://doi.org/10.1007/978-981-13-2227-3_36

nucleation substrates and at elevated pH levels (Stumm and Morgan 1996; Mitchell et al. 2010). Precipitation of $CaCO_3$ occurs once its saturation in solution is exceeded. A novel strategy to achieve and/to enhance the mineralization is by involving subsurface microbial community, also known as microbially induced calcite precipitation or MICP. Biofilm forming bacteria such as *S. pasteurii* enzymatically hydrolyses urea $[CO(NH_2)_2]$ and influences the saturation state (Ω) of surrounding fluids to accelerate $CaCO_3$ precipitation. The overall reaction:

$$CO(NH_2)_2 + 2H_2O \rightarrow 2NH_4^+ + CO_3^{2-} \quad \text{(R1)}$$

$$Ca^{2+} + CO_3^{2-} \leftrightarrow CaCO_3(s) \quad \text{(R2)}$$

Ureolytic bacteria release urease enzyme and the ureolysis (R1) results into production of ammonium, inorganic carbon and elevated pH that favours calcite precipitation. MICP has been investigated as a potential mechanism for sealing fractures, controlling flows (De Muynck et al. 2010), radionuclides co-precipitation (Mitchell and Ferris 2005) etc. Laboratory experiments and numerical models of MICP processes are often carried out at isothermal conditions; although, temperature variations influences both microbial growth (Zwietering et al. 1991; Ratkowsky et al. 1983) and calcite precipitation (Lopez et al. 2009; Appelo and Postma 2005) kinetics.

In this paper, biofilm growth and calcite precipitation under non-isothermal conditions have been investigated via numerical modelling approach. To study subsurface microbial processes, a coupled model (Masum and Thomas 2018) has been developed under a Thermal-Hydraulic-Chemical-Mechanical (THCM) framework. The model deals with liquid flow, multicomponent gas flows, dissolved chemicals and suspended microbes flows in liquid phase, heat flow, biofilms and minerals growths, mechanical deformations and geochemical/bio-geochemical reactions. However, in this article, the focus has been limited to biofilm and mineral growth, heat flow and geochemical reactions in a saturated porous medium. The kinetic reactions of ureolysis (R1) and calcite precipitation (R2) have been estimated using the geochemical model Phreeqc (Parkhurst and Appelo 1999), which is linked with the coupled transport model. The effects of mineral growth and biofilm accumulation on the porous media flow properties are also demonstrated.

2 Model Setup

In a previous paper (Masum and Thomas 2018), developments of the coupled microbial model including theoretical formulation, numerical implementation and incorporation of the geochemical model with the transport model have been described in details. The model was presented for isothermal condition. In the current paper, the model has been extended to non-isothermal conditions and mass conservations of mineral phases has been included. The governing equations, relevant to this paper, have been described below. Following assumptions have been made for necessary simplifications in this work: Biofilm and mineral phases are impermeable and immobile. Diffusion of chemicals due to thermal gradient or Soret effect is negligible. Heat

transfers only via conduction and the contribution of biofilm phase on the overall heat content is insignificant.

2.1 Governing Equations

The mass balance equation of an immobile phase (k) is:

$$\frac{\partial}{\partial t}(c_k) = s_k,\ k \in \{b, m\}, \tag{1}$$

where b and m represent biofilm and mineral phases, respectively. c_k is the concentration, *i.e.*, amount of biofilm/minerals per unit volume of the porous media and it is related to their volumetric content (θ_k): $c_k = \theta_k \rho_k$. Here ρ_k is the mass density of the k^{th} phase. s_k is the sink/source term.

The transport of i^{th} chemical species in a multicomponent system is given by:

$$\frac{\partial\left(\theta_l c_d^i\right)}{\partial t} = \nabla\left(\theta_l D_d^* \nabla c_d^i\right) + \nabla\left(\theta_l c_d^i v_l\right) + s_d^i \tag{2}$$

where c_d^i is the concentration and D_d^* is the hydrodynamic dispersion coefficient of the i^{th} component in the liquid phase. v_l is the liquid phase velocity and S_d^i is the total sink/source of the i^{th} component. Estimation of the hydrodynamic dispersion coefficient has been detailed in Masum and Thomas (2018).

The heat transport equation is based on the conservation of energy principle which dictates that the temporal derivative of heat content (Ψ) is equal to the spatial derivative of heat flux (Q). Therefore, in absence of an external sink/source:

$$\partial\Psi/\partial t = -\nabla Q. \tag{3}$$

The heat content is considered as the sum of soil heat storage capacity:

$$\Psi = H_c T \tag{4}$$

where H_c is the heat capacity and it is calculated as:

$$H_c = (1-n)C_{ps}\rho_s + C_{pl}\theta_l\rho_l + C_{pm(T)}\theta_m\rho_m. \tag{5}$$

Here C_{ps}, C_{pl} and C_{pm} are the specific heat capacities of solid, liquid and mineral phases, respectively and ρ_s is the solid density. Heat capacity of natural (C_{pm}) calcites as a function of temperature was measured by Jacobs et al. (1981) and proposed the following relationship, valid between 298 < T < 775 K:

$$C_{pm(T)} = -184.79 + 0.32322T - 3688200T^{-2} - \left(1.2974 \times 10^{-4}\right)T^2 + 3883.5T^{-1/2} \tag{6}$$

Considering heat conduction is the dominant method of flow, heat flux can be expressed as:

$$Q = -\lambda_{(T)} \nabla T. \tag{7}$$

Here $\lambda_{(T)}$ is the thermal conductivity as a function of temperature (W/mK). Birch and Clark (1940) suggested that the reciprocal of thermal conductivity is a liner function of temperature:

$$\lambda_{(T)}^{-1} = a_0 + a_1 T. \tag{8}$$

Here a_0 (m °C/W) and a_1 (m/W) are fitting parameters and T is in degree centigrade.

2.2 Sink/Source Terms

s_b combines the microbial biomass growth (r_{subs}) and the decay (r_{decay}) rate. Microbes mainly grow by metabolising growth-limiting substrates. In absence of a suitable electron acceptor, substrate metabolism rate is explained by the Monod's kinetic as:

$$r_{subs} = k_{+(T)} \left(\frac{c_d^s}{K_s' + c_d^s} \right) c_b. \tag{9}$$

Here c_d^s is the substrate concentration ($i = s$ in Eq. (2)) and K_s' is the Monod half-saturation constants of substrate. $k_{+(T)}$ is a temperature dependent substrate utilisation rate. Ratkowsky et al. (1983) proposed that:

$$k_{+(T)} = b'(T - T_{min})\{1 - \exp[c'(T - T_{max})]\} \tag{10}$$

where b' and c' are Ratkowsky parameters. T_{min} and T_{max} are the minimum and the maximum of a biokinetic temperature range, respectively.

Biomass decay is expressed using a first-order rate as follows:

$$r_{decay} = k_- c_b. \tag{11}$$

Here k_- is the endogenous decay or cell death rate.

s_d^i evaluates the total loss or gain of the i^{th} chemical component in the liquid phase. Microbial activities, geochemical reactions and external supply or removal conditions may influence this term. For example, biofilm phase acts as a sink for substrates which is considered as a dissolved chemical species. The loss of substrates ($i = s$ in Eq. (2)) from the solution is calculated by:

$$s_d^s = -r_{subs}/Y \tag{12}$$

where Y is the growth yield *i.e.* the amount of biomass created per unit mole of substrate (Bethke 2008). Similarly, ureolysis reduces the amount of urea in the solution and the sink ($i = u$ in Eq. (2)), can be calculated, following Zhang and Klapper (2010) as:

$$s_d^u = k_u \theta_b c_d^u \tag{13}$$

where k_{urea} is the maximum rate of urease activity.

s_m estimates the changes of mineral concentration due to precipitation and dissolution reactions. In this paper, the kinetic precipitation of calcite is calculated as (Appelo and Postma 2005):

$$s_m = k_c(A/V)(\Omega - 1). \tag{14}$$

Here k_c is the precipitation rate constant, A is the calcite surface area, V is the solution volume. In this case, $(A/V) = 1\,\mathrm{m}^2/\mathrm{m}^3$ has been considered. Ω is the saturation ratio. For $\Omega = 1$ the system is in equilibrium, $\Omega > 1$ supersaturation and $\Omega < 1$ subsaturation. Please note that the precipitation calcite reduces the amount of calcium and carbonates in the solution, and therefore, the s_d^i of these chemicals.

2.3 Effects of Mineral and Biofilm Growth on Porous Media Flow Properties

The relationship between volumetric contents of liquid (θ_l), biofilm (θ_b), mineral (θ_m) phases and total porosity (n_0) is given by:

$$\theta_l + \theta_b + \theta_m = n_0 \tag{15}$$

Biofilm growth and mineral precipitation alter the total porosity. Therefore:

$$n = n_0 - (\theta_b + \theta_m). \tag{16}$$

Here n is the active porosity where fluids and chemicals flow takes place.

3 Application

In this section, the effects of temperature on microbial growth and mineral precipitation are demonstrated and the consequent impact on the overall porosity of the medium is also investigated. A 1.0 m by 0.1 m saturated sandstone core is used in this simulation. The core has been exposed to a heat source to create a thermal gradient. To begin with, uniform distributions of ureolytic bacteria (*S. pasteurii*), a growth-limiting substrate and a solution of urea and calcium chloride; across the sample has been considered. To observe the effects of temperature, explicitly, on these processes further supply or boundary conditions of these components have been ignored during the simulation. The sample domain is discretized into 100 quadrilateral elements. The simulation is carried out for 12 h. The kinetic reactions (R1 & R2) have been calculated via Phreeqc (version 2.0) and using the standard database *Phreeqc.dat* (Phreeqc Homepage 2018).

3.1 Initial and Boundary Conditions

Initial concentration of the biofilm $c_{b(x,0)} = 1.0\ \text{kg/m}^3$. Concentration of the glucose substrate $c^s_{d(x,0)}$, urea $(c^u_{d(x,0)})$, and calcium $(c^{Ca}_{d(x,0)})$ are 20.0 mM, 20 mM and 10.0 mM, respectively. Initially the core contained no calcite, $c^c_{m(x,0)} = 0.0$. Initial pH 7.0 and temperature 298 K. At the left boundary, *i.e.* x = 0, a fixed temperature of 313 K is applied.

3.2 Results and Discussion

The simulation parameters are listed in Table 1. Figure 1 presents the results of temperature, pH, chemicals, minerals and porosity evolution at x = 0 and 0.25 m and Fig. 2 presents some of their profiles across the length. Figures 1a and 2a results show that temperature of the sandstone core increases due to the applied heat at the left boundary. Biofilm growth (Fig. 1c) is observed to occur at various rates in the sample. Since the initial substrate concentration is uniform across the sample and no boundary is applied during the simulation, the higher biofilm growth (Fig. 2b) at the vicinity of the heat source is due to the rise in temperature. However, away from the heat source, temperature increases gradually which results into slower biofilm growth. The rate of ureolysis (Eq. 13) increases with biofilm concentration. The results in Fig. 1b indicate higher rate of ureolysis closer to the heat source where biofilm concentration is also high. Since ureolysis elevates the pH level and accelerates calcite precipitation in presence of sufficient calcium ion (R2), solution pH (Fig. 1a) closer to the left

Table 1. Parameter values for the non-isothermal simulation

Parameters	Values	Comments
n_0	0.25	
b'	$2.76 \times 10^{-2}\ \text{K}^{-1}\ \text{h}^{-0.5}$	Kovářová et al. (1996)
c'	$1.12\ \text{K}^{-1}$	Kovářová et al. (1996)
T_{min}	275.7 K	Kovářová et al. (1996)
T_{max}	315.2 K	Kovářová et al. (1996)
Y	0.628 kg/kg	Beyenal et al. (2003)
K'_s	$26.9 \times 10^{-3}\ \text{kg/m}^3$	Beyenal et al. (2003)
k_-	$3.18 \times 10^{-7}\ \text{s}^{-1}$	Taylor and Jaffé (1990)
ρ_s	$2650\ \text{kg/m}^3$	Peyton (1995)
ρ_b	$65\ \text{kg/m}^3$	
ρ_m	$2710\ \text{kg/m}^3$	
C_{ps}	750 W/mK	Thomas et al. (2013)
C_{pl}	4180 W/mK	Thomas et al. (2013)
a_0	0.3514 m °C/W	Eppelbaum et al. (2014)
a_1	3.795×10^{-4} m/W	Eppelbaum et al. (2014)
k_u	$1.15 \times 10^{-6}\ \text{s}^{-1}$	Zhang and Klapper (2010)
k_c	$7.76 \times 10^{-7}\ \text{mol/m}^2\text{/s}$	Appelo and Postma (2005)

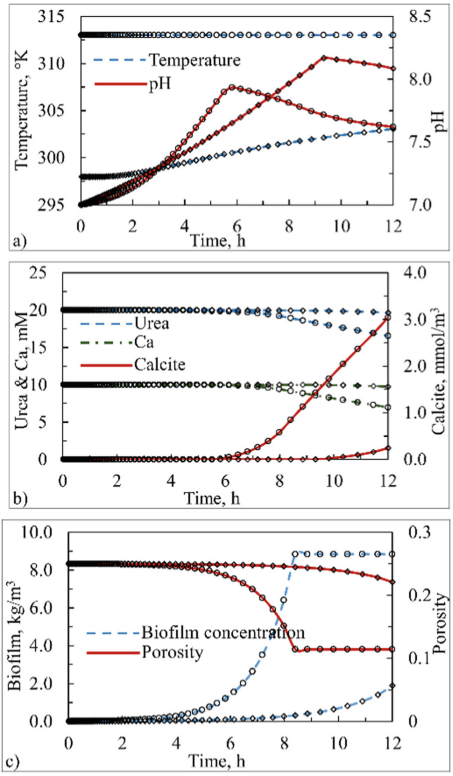

Fig. 1. Evolution of (a) Temperature & pH; (b) Urea, Calcite & Ca; (c) Biofilm concentration & of porosity in the sandstone core. Symbols (○) and (◇) represent results at x = 0 and 0.25 m, respectively.

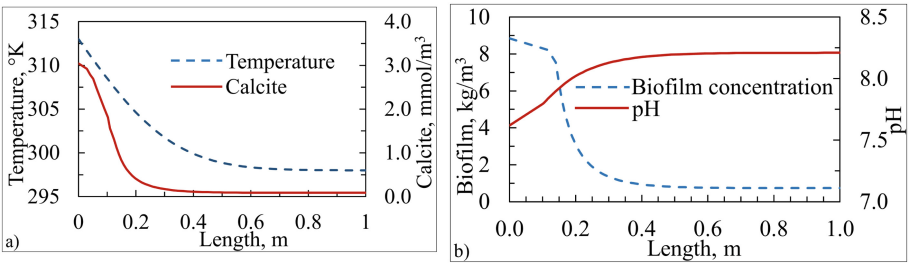

Fig. 2. Profiles of (a) calcite & temperature; (b) Biofilm concentration & pH in the sandstone core at the end of simulation period.

boundary increases rapidly causing higher amount of calcite to precipitate (Fig. 1b) than that of far from the heat boundary. Figure 2a shows the correlation between temperature and calcite precipitations across the sandstone core. Lopez et al. (2009) observed similar behaviour on temperature dependent calcite precipitations. Loss of calcium ions (Fig. 1b) in the solution follows the calcite precipitation. The formation of calcite crystals and its precipitation reduces solution pH which is clearly visible in Figs. 1a and 2b. The overall impacts of biofilm growth and mineral precipitations on the sandstone porosity is presented in Fig. 1c. After around 8.5 h the core porosity at the left boundary reduces to the minimum, which is mainly due to the loss of porosity associated with the biofilm volume. Since the volumetric content of mineral phase is significantly smaller than that of the biofilm phase.

Acknowledgment. Funding to support this research was provided by Welsh Government and HEFCW through Ser Cymru National Research Network for Low Carbon, Energy and the Environment (NRN-LCEE) via *Geo-Carb-Cymru* Cluster.

References

Appelo CAJ, Postma D (2005) Geochemistry, groundwater and pollution, 2nd edn. A.A. Balkema Publishers, Amsterdam

Bethke CM (2008) Geochemical and biogeochemical reaction modelling, 2nd edn. Cambridge University Press, New York

Beyenal H, Chen SN, Lewandowski Z (2003) The double substrate growth kinetics of Pseudomonas aeruginosa. Enzyme Microb Technol 32:92–98

Birch F, Clark H (1940) The thermal conductivity of rocks and its dependence upon temperature and composition. Am J Sci 238(8):529–558

De Muynck W, De Belie N, Verstraete W (2010) Microbial carbonate precipitation in construction materials: a review. Ecol Eng 36(2):118–136

Eppelbaum L, Kutasov I, Pilchin A (2014) Thermal properties of rocks and density of fluids. In: Applied geothermics. Lecture notes in earth system sciences. Springer, Heidelberg, pp 99–149

Jacobs GK, Kerrick DM, Krupka KM (1981) The high-temperature heat capacity of natural calcite (CaCO3). Phys Chem Miner 7(2):55–59

Kovářová K, Zehnder AJB, Egli T (1996) Temperature-dependent growth kinetics of escherichia coli ML 30 in glucose-limited continuous culture. J Bacteriol 178(15):4530–4539

Lopez O, Zuddas P, Faivre D (2009) The influence of temperature and seawater composition on calcite crystal growth mechanisms and kinetics: implications for Mg incorporation in calcite lattice. Geochimia et Cosmochimia Acta 73:337–347

Masum SA, Thomas HR (2018) Modelling coupled microbial processes in the subsurface: model development, verification, evaluation and application. Adv Water Resour 116:1–17

Mitchell AC, Ferris FG (2005) The coprecipitation of Sr into calcite precipitates induced by bacterial ureolysis in artificial groundwater: temperature and kinetic dependence. Geochimia et Cosmochimia Acta 69(17):4199–4210

Mitchell AC, Dideriksen K, Spangler LH, Cunningham AB, Gerlach R (2010) Microbially enhanced carbon capture and storage by mineral-trapping and solubility-trapping. Environ Sci Technol 44:5270–5276

Parkhurst DL, Appelo CAJ (1999) User's guide to PHREEQC (version 2). United States Geological Survey, USA

Peyton BM (1995) Effects of shear stress and substrate loading rate on Pseudomonas aeruginosa biofilm thickness and density. Water Res 30(1):29–36

Ratkowsky DA, Lowry RK, McMeekin TA, Stokes AN, Chandler RE (1983) Model for bacterial culture growth rate throughout the entire biokinetic temperature range. J Bacteriol 154 (3):1222–1226

Stumm W, Morgan JJ (1996) Aquatic chemistry, 3rd edn. Wiley, New York

Taylor SW, Jaffé PR (1990) Substrate and biomass transport in a porous medium. Water Resour Res 26(9):2181–2194

Thomas HR, Vardon PJ, Cleall PJ (2013) Three-dimensional behaviour of a prototype radioactive waste repository in fractured granitic rock. Can Geotech J 51(3):246–259

Zhang T, Klapper I (2010) Mathematical model of biofilm induced calcite precipitation. Water Sci Technol 61(11):2957–2964

Zwietering MH, De Koos JT, Hasenack BE, De Wit JC, van't Riet K (1991) Modelling of bacterial growth as a function of temperature. Appl Environ Microbiol 57(4):1094–1101

PHREEQC Homepage. https://wwwbrr.cr.usgs.gov/pro-jects/GWC_coupled/phreeqc/. Accessed 10 Apr 2018

The Comparison of Microbiologically-Induced Calcium Carbonate Precipitation and Magnesium Carbonate Precipitation

Xiaohao Sun(✉) and Linchang Miao(✉)

Institute of Geotechnical Engineering,
Southeast University, 210096 Nanjing, China
sunxiaol4hao@126.com, Lc.miao@seu.edu.cn

Abstract. Similar to calcium carbonate, magnesium carbonate also has a cementing character, and the strength of magnetite ore is much higher than calcium ore. In this paper, firstly, the effects of different ions, such as the concentration of Ca^{2+} and Mg^{2+}, on the urease activity of Sporosarcina pasteurii were researched. Then the productive rates for calcium carbonate and magnesium carbonate were comparatively analyzed. Finally, with adding various amounts of urea to medium, the productive rates for magnesium carbonate were compared. The results show that the increase in the magnesium ion enhances urease activity, while calcium with high concentration significantly impairs it. Under the same conditions, productive rate for magnesium carbonate is smaller than its calcium counterpart. However, the method adding urea to the medium significantly promotes to form precipitation, and with higher urea concentration, more magnesium precipitation is got. Therefore, the presented method can solve the problem that insufficient magnesium precipitation cannot solidify sands, which acts as a guide for the magnesium carbonate sand solidification technology.

Keywords: Sporosarcina pasteurii · Calcium carbonate
Magnesium carbonate · Productivity rate

1 Introduction

It is widely recognized that microorganisms contribute to precipitation of a variety of minerals [1]. Many studies have been revealed about the precipitation of various minerals in microbial cultures because this biogeochemical technology is here to stay [2–4]. Carbonate precipitation is an important aspect of biomineralization and has been investigated extensively due to its wide range of technological implications [4]. Specifically, the precipitation production by bacteria has led to the applied exploration of the process in the field of construction materials and ground reinforcement including conservation of ancient masonry buildings and improving the compressive strength of ground foundations [5–7].

Magnesium carbonate has a cementing character the same as calcium carbonate. Besides, the fact needed to be noticed that the strength of magnesite ore is larger than that of calcium ore. Therefore, researches on magnesite precipitation produced via MICP technology are meaningful. However, few studies were focused on it. In this

© Springer Nature Singapore Pte Ltd. 2019
L. Zhan et al. (Eds.): ICEG 2018, ESE, pp. 302–308, 2019.
https://doi.org/10.1007/978-981-13-2227-3_37

paper, the effect of magnesium ion on MICP technology was emphasized. The influences of concentration of Ca^{2+} and Mg^{2+} on urease activity were analysed. Apart from that, the comparative tests of productive rates between calcium carbonate and magnesium carbonate were conducted, as well as the comparison of productive rates for magnesium precipitation with different amounts of urea.

2 Materials and Methods

In the paper, the bacterium, Sporosarcina pasteurii (S. pasteurii ATCC 11859), was cultured on Luria Bertani medium, which consisted of yeast extract (15.0 g/L), polypeptone (10.0 g/L), NaCl (10.0 g/L), and distilled water. All bacteria used in experiments were cultured for 48 h, which meant that they were in the stable stage.

2.1 Measurement of Urease Activity

The urease activity could be indirectly gotten by measuring conductivity of solution per minute, as the amount of urea hydrolyzed was in proportion to the change on the conductivity of solution [8]. With 3 ml of bacterial solution combining with 27 ml of urea solution, the change on conductivity in 5 min was monitored via electrical conductivity meter in 20 °C. The average change on conductivity per minute (μs/min) was calculated, then it was converted into the amount hydrolyzed by urea per minute (M urea hydrolysed/min), which was defined as urease activity in the paper. The bacteria cultured for 48 h-culture were inoculated into nutrient solution at 1% with initial pH of 7 and urease activity was monitored every three hours with 30 °C. The whole experimental process was conducted in a bacteria-free operating environment, meaning in a closed system.

2.2 The Effects of Different Ions on Urease Activity

Calcium ion was a key factor to MICP reaction and thus it was necessary to study the effect of concentration of it on urease activity. Calcium acetate was used as the raw material of the production of calcium carbonate, as sand column solidified by using calcium acetate could own higher uniformity compared with using calcium chloride and calcium nitrate [9]. The concentration of calcium acetate in solution varied: 0, 0.3, 0.6, 0.9, 1.2, 1.5, or 1.8 M, and the absorbance of bacterial solution (OD_{600}) was 0.5, 1.0 or 1.5. In the reaction process, calcium ion and carbonate ion were integrated to form calcium precipitation, affecting the conductivity. It was unpractical to use conductivity to calculate urease activity because the calcium ion would affect the monitoring results of conductivity. To avoid the phenomena, the Berthelot color principle was utilized to determine the concentration of NH_4^+-N in 5 min. After centrifugation, the supernatant of the sample was taken and diluted to an appropriate concentration, and then 2 mL of the diluted sample was added to cuvette and 0.1 mL was also added. After that, the absorbance value at 425 nm was determined by spectrophotometer. Therefore, the concentration of NH_4^+-N in the sample could be calculated according to the calibration line and dilution ratio. According to urea hydrolysis reaction, 1 mol urea

was hydrolyzed into 2 mol NH_4^+, and thus corresponding urease activity could be obtained within 5 min. As for magnesium ion, magnesium acetate was used as raw material to form magnesium carbonate precipitate, and the same method as investigating the effect of calcium ion on urease activity was adopted to study the effect of concentration of magnesium ion on urease activity. All experiments were conducted in a bacteria-free operating environment.

2.2.1 Comparison of Productive Rates Between Calcium and Magnesium Precipitation

S. pasteurii was utilized for microbiologically-induced precipitation tests, and calcium acetate was used as the raw material to form calcium precipitate, as well as magnesium acetate for magnesium precipitate. The bacterial solution with OD_{600} of 1.02 was added to gelling solution (urea and calcium acetate or magnesium acetate solution) and pH was maintained at 7. The concentration of calcium acetate, magnesium acetate and urea were all 0.5 M and temperature varied from 20 °C, 25 °C, to 30 °C. The productive rates were calculated in 2nd, 4th and 6th day. The whole experimental process was conducted in a closed system.

2.2.2 Comparison of Magnesium Precipitation with Various Amounts of Urea

The eventual purpose of microbiologically-induced magnesium precipitation tests was the applications of practical engineering with magnesium carbonate. However, compared with calcium precipitation, magnesium precipitation was much smaller under the same conditions. With the view of addressing the issue, the method that adding urea to medium was proposed, in which urea was decomposed to CO_3^{2-} in advance, and the CO_3^{2-} then combined with Mg^{2+} to form precipitation once bacterial medium was added to gelling solution. It meant that the partial slow biological precipitation process was divided into two parts and the first one part proceeded in advance before gelling solution was added to medium. As a result, the formation of magnesium precipitation was dramatically accelerated.

The bacterial solution with OD_{600} of 0.98 and pH at 7 was used in tests. The concentration of calcium acetate and urea were both 0.5 M and temperature was varied from 20 °C to 30 °C. The productive rates of magnesium precipitation were gain in 2nd, 4th and 6th day. The whole experimental process was conducted in a closed system.

3 Results and Discussions

3.1 The Effects of Different Ions on Urease Activity

The changes in urease activity with increase in concentration of calcium ion were shown in Fig. 1. From the Fig. 1, the urease activity declined significantly from 0 to 1.8 M. Hence, high concentration of calcium chloride had a significant inhibitory effect on urease activity. With 1.2 M of concentration of calcium ion, the urease activity dropped by nearly one third no matter which bacterial solution was used and the urease

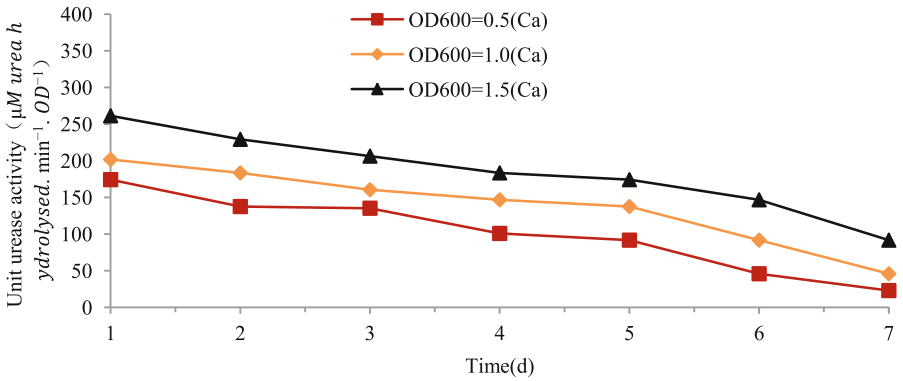

Fig. 1. The effect of concentration of calcium ion and magnesium ion on urease activity

activity went down by almost half with 1.8 M. The experimental conclusions were consistent with Whiffin's [8] observation results with calcium nitrate despite different calcium source. Therefore, the increase in concentration of calcium ion enabled to augment the production of calcium precipitation, but it could not be too high while considering the urease activity.

The changes in urease activity with various magnesium ion were shown in Fig. 2. The urease activity went up with the increase in concentration of magnesium ion, except that the magnesium ion with extremely high concentration had negative impact on urease activity. With the OD_{600} being 1.5, the urease activity climbed the optimum state. Therefore, it could be concluded that magnesium ion enabled to promote urease activity, but urease activity was restrained obviously with extremely high concentration of magnesium ion. This was probably because too much salt in the solution could inhibit the strain response of the bacteria. Therefore, it was necessary and useful to increase the salt content to enhance urease activity, but the concentration of magnesium ion needed to be controlled in the experiment.

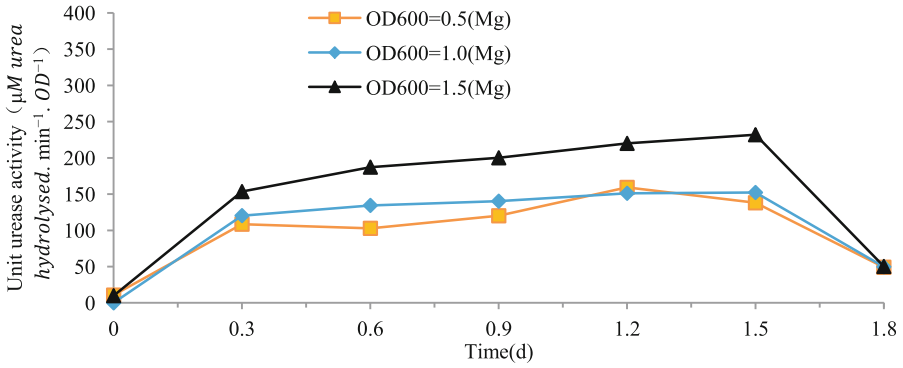

Fig. 2. The effect of concentration of magnesium ion on urease activity

3.2 Microbiologically-Induced Precipitation Tests

3.2.1 Comparison of Productive Rates Between Calcium and Magnesium Precipitation

The productive rates were calculated in 2nd, 4th and 6th day, as shown in Table 1. The data were the average values after conducting three times repeat tests. From Table 1, it could be easily found that under the same conditions, the magnesium carbonate with magnesium acetate as the raw material for precipitation had definitely lower productive rates, in contrast of calcium carbonate. In particular, the productive rate of calcium carbonate was up to 25.4% in 30 °C in the 6th day, while that of magnesium carbonate was only 13.3%. One of the reasons was that the solubility of magnesium carbonate in such conditions was about 1×10^{-2}, however, the solubility of calcium carbonate was only around 1×10^{-3}, almost an order of magnitude less than its magnesium counterpart. It was also the reason why the magnesium precipitation could hardly be gain in the first day no matter which temperature was set. Another reason was that magnesium carbonate would be hydrolysed slightly to generate magnesium hydroxide. With the same amount of substance, the amount of magnesium hydroxide was distinctly less than that of calcium carbonate.

Table 1. The comparison of productive rates

Raw material	Days	20 °C	25 °C	30 °C
Calcium acetate	2	9.5%	9.5%	22.3%
	4	11.8%	12.3%	23.6%
	6	14.9%	17.8%	25.4%
Magnesium acetate	2	/	/	/
	4	1.1%	3.7%	5.9%
	6	7.3%	11.2%	13.3%

3.2.2 Comparison of Productive Rates with Different Amounts of Urea

Similar to comparative tests between calcium and magnesium precipitation, temperature was varied from 20 °C to 30 °C and the productive rates were calculated in 2nd, 4th and 6th day, as shown in Table 2. The data were also the average values after conducting three times repeat tests. When urea was added to the medium, it was decomposed to CO_3^{2-} in advance with the strain growing and reproducing. Once the gelling solution was mixed with the bacterial solution, a large amount of magnesium precipitation was generated soon. No matter how much urea was added, the precipitation was formed in the beginning, which relieved significantly the problem of insufficient precipitation got in the 2nd day with no urea added. From Table 2, it was obvious that groups with higher urea concentration, such as 20 g/L, had more magnesium precipitation in the 2nd day than other groups with lower urea concentration or even no urea. After that, urea in gelling solution allowed bacteria to continue to generate CO_3^{2-}, which meant that increasingly more sediment was obtained. The eventual productive rates of magnesium carbonate with higher concentration of urea were larger than the other two groups regardless of temperature.

Table 2. The productive rates of magnesium carbonate with different urea amounts.

Urea concentration	Days	20 °C	25 °C	30 °C
0 g/L	2	/	/	/
	4	1.0%	3.1%	4.5%
	6	6.3%	11.8%	12.2%
10 g/L	2	9.4%	10.1%	17.4%
	4	10.7%	11.3%	18.2%
	6	12.6%	14.5%	27.5%
20 g/L	2	12.3%	14.5%	19.9%
	4	14.8%	15.2%	21.7%
	6	17.6%	19.1%	28.4%

It was concluded that the method, adding urea to the bacteria solution, could accelerate MICP reaction and promote more precipitation to be formed. Therefore, such method allowed for obtaining more magnesium precipitation, which was helpful to solve the problem that insufficient precipitation could not solidify sands or repair cracks completely in low temperature.

4 Conclusions

In the paper, the effects of two different ions, such as calcium or magnesium ion, on the urease activity were analyzed and the productive rates of calcium carbonate and magnesium precipitation were comparably studied. The conclusions are as follows:

The increase in the magnesium ion can enhance urease activity, but the concentration should not be too high. However, the calcium ion with high concentration has a significant inhibitory impact on urease activity. Under the same conditions, the productive rates of magnesium carbonate are much smaller than that of calcium carbonate regardless of temperature and time, but the method that adding urea to medium makes the formation of precipitation available in the beginning and promotes more precipitation to be got eventually. Moreover, the higher concentration of urea, the larger productive rates of magnesium carbonate get. Therefore, such method can solve the problem of insufficient precipitation in low temperature.

Acknowledgments. This work was supported by the National Natural Science Foundation of China (No. 51578147) and Scientific Research Foundation of Graduate School of Southeast University (No. YBJJ1846).

References

1. Ehrlich HL (2002) Geomicrobiology, 4th edn. Marcel Dekker, New York
2. Lith YV, Warthmann R, Vasconcelos C et al (2003) Microbial fossilization in carbonate sediments: a result of the bacterial surface involvement in dolomite precipitation. Sedimentology 50(2):237–245

3. Martínalgarra A (2006) Carbonate and phosphate precipitation by chromohalobacter marismortui. Geomicrobiol J 23(1):1–13
4. Wijngaarden WKV, Vermolen FJ, Meurs GAMV et al (2011) Modelling biogrout: a new ground improvement method based on microbial-induced carbonate precipitation. Transp Porous Media 87(2):397–420
5. Harkes MP, Paassen LAV, Booster JL et al (2010) Fixation and distribution of bacterial activity in sand to induce carbonate precipitation for ground reinforcement. Ecol Eng 36 (2):112–117
6. Paassen LAV, Ghose R, Linden TJMVD et al (2010) Quantifying bio-mediated ground improvement by ureolysis: a large scale biogrout experiment. J Geotech Geoenvironmental Eng 136(12):1721–1728
7. Botter G, Basu NB, Zanardo S et al (2010) Stochastic modeling of nutrient losses in streams: interactions of climatic, hydrologic, and biogeochemical controls. Water Resour Res 46 (8):416–428
8. Whiffin VS (2004) Microbial CaCO3 Precipitation for the Production of Biocement. Murdoch University, Perth
9. Zhang Y, Guo HX, Cheng XH (2015) Role of calcium sources in the strength and microstructure of microbial mortar. Constr Build Mater 77:160–167

Use of Bionanocementation as a Technique in Increasing Resistance of Sandy Soil

Bruna Bilhar Dall Agnol(✉) and Antonio Thome

PPGEng, University of Passo Fundo, Passo Fundo, RS, Brazil
brunab_d@hotmail.com

Abstract. With the increase in population and infrastructure, the search for areas for occupation has increased significantly. Therefore, there is also an increase in the environmental impacts associated with the bad use of the soil, thus making these soils need an improvement for their use. Soil improvement techniques used involve the addition of mechanical energy and/or synthetic materials. However, the bionanocementation technique has the purpose of improving the mechanical properties in a sustainable way. Biocementation is the formation of calcium carbonate that binds the soil particles by microorganisms metabolism. It only occurs when the microorganisms have a source of calcium and urea and the potential for biocementation. The objective of this work was evaluate the increase in mechanical strength, through the technique of bionanocementation, in sandy soil with different concentrations of calcium (20, 30 and 40 g/L). Calcium substrate was supplied at nano and micro scale. Four different treatments were performed in the experiment: SN−B; SN+B; CN−B and CN+B. Biochemical test of urease production, CO_2 evolution test, compression strength test and MEV and EDS were performed. During the study, we observed that the product at nano scale was already in $CaCO_3$, making the treatments with nutrient medium CN did not obtain good results. The CPs with nutrient medium SN stood out in the trials, as well as the treatments that had no bioaumentation. In addition, the results with higher concentration (40 g/L) stood out.

Keywords: Bionanocementation · Precipitation of CaCO3 · Bioestimulation

1 Introduction

With the population increase, the demand for infrastructure in the world increased as well as investment in this area, since the availability of soil on which it can be built is decreasing. The development ends up disabling large areas of land besides devaluing real estate and limiting urban development. In this context studies and remediation techniques for the improvement of these areas arise, making possible their use later execution of activities as previously developed (Rebechi 2007).

Biogeotechnology is a new branch in geotechnical engineering, it works mainly with the application of biological methods to geotechnical problems. Currently biogeotechnologies are mainly the use of plants or vegetation cover for erosion control, slope protection, soil permeability reduction. This technology has the advantages of low investment cost and maintenance cost. In addition to these applications,

© Springer Nature Singapore Pte Ltd. 2019
L. Zhan et al. (Eds.): ICEG 2018, ESE, pp. 309–316, 2019.
https://doi.org/10.1007/978-981-13-2227-3_38

the potential use of microorganisms for this area has been shown to be efficient in the technique of soil biocementation (Ivanov and Chu 2008).

The objective of this study is to evaluate the increase in the mechanical strength of a coastal sandy soil using the bionanocementation technique with different substrate concentrations.

2 Methodology

The research was carried out in the Laboratory of Environmental Geotechnics at the Technological Center (CETEC) and in the Laboratories of Environmental Engineering Teaching at the University of Passo Fundo, Campus I.

2.1 Urease Test

The biochemical test of urease production used to determine if a bacterium produces the enzyme urease, which hydrolyzes urea. The test was performed by placing a loop of the bacteria on the surface of the medium in test tubes that is at neutral pH and then 1 g of urea is placed and the tubes are shaken thereafter. When the test is positive the ammonia formation alkalinizes the culture medium leaving it of pink color. When the result is negative, the medium becomes yellow.

2.2 Molding of the Specimens

Three specimens were assembled for each treatment suggested; A Blank sample was used only in the Evolution of CO_2. The control variables of the experiment were the use of culture media with nanosubstrate (CN) or with calcium acetate (NS), substrate in macro scale. In addition, three different concentrations were used for CN and SN, being 20, 30 and 40 g/L. Another control in the experiment is the use of bioaumentation (+B or −B).

The response variable for the experiment was the amount of CO_2 evolved from the microbial process. The resistance obtained in the compression test was used in the comparison of the specimens that have nanosubstrate and those that have calcium acetate as substrate for the microorganism. In addition, SEM/EDX results were compared with the literature.

Sand soil used. The sandy soil used in the survey comes from the coastal region of the Municipality of Osorio (RS) - Brazil. It is classified as fine quartz sand. This material is a fine sand of uniform granulometry.

Bioestimulation: Nutrient media. The medium used as a base was proposed by Lee (2003), with good results for the precipitation of $CaCO_3$. The composition for the preparation of the medium consists of 15 g of calcium acetate, 4 g of yeast extract, 5 g of glucose and 10 g of urea for each 1000 ml of distilled water, having a pH of 8. three different concentrations of calcium acetate for the nano-free medium (SN), and three different concentrations for the medium with nano (CN), which is the base medium, but with nanosubstrate instead of calcium acetate. The nanosubstrate used in the research

was purchased by importing company SkySpring Nanomaterials located in Texas, United States of America.

2.3 Evaluation of CO_2

The technique of evaluation of CO_2 or respirometry is used to quantify the metabolic activity of the microorganisms in the soil during the bionanocementation process. The methodology was define by Bartha and Pramer (1965). This procedure is based on the uptake of CO_2 released by microbial metabolism. Monitoring of carbon dioxide production was perform every 48 h for a period of 49 days, with all experimental units being maintained at room temperature.

2.4 Compression Test

For the evaluation of the resistance of the specimens after the evolution of CO_2 the compression test was performing. This test is the most used for the evaluation of mechanical characteristics of soils. It enables us to evaluate the influence of different parameters on soil resistance. The test specimens for this test are 50 mm in diameter and 100 mm in height, 2:1 ratio indicate in the standard for resistance test.

2.5 SEM/EDX

Electronic Scanning Electron Microscope (SEM) is an equipment generally used for microstructural analysis of solid materials. It is a complex equipment, but despite this, it provides good results and easy interpretation, these results are high resolution images. The Energy Dispersive X-ray Detector, EDX is an essential accessory in the microscopic characterization study of materials. An electron beam is incident on the analyzed material that causes the energy levels of an atom to change temporarily, when those levels return to the previous position release energy emitted at wavelength of x-rays and it is possible to identify the element present in the sample.

3 Results and Discussions

Urease Test
The test had a positive result, as shown below, where the color of the medium became pink immediately after sowing of the bacteria present in the soil and remained in the 24 h indicated for observation (Fig. 1).

Evaluation of CO_2
The respirometry test was followed for a period of 49 days. In microbiology, the moment of stabilization of the CO_2 evolution curve, that is, the microbiological activity is stopping or there will be no more reactions in the medium. When related to this experiment, when the curve reaches the stabilization, it means that it will no longer occur bionanocementation.

Fig. 1. Positive result for the urease test.

In Fig. 2 it can be observed that there are four specimens that stand out with better results. These specimens (CP's) are SN−B (40); SN−B (30); SN+B (40) and SN+B (30), respectively. As observed, the specimens that stand out are those that do not have nanoparticles in the nutrient medium used in bioestimulation.

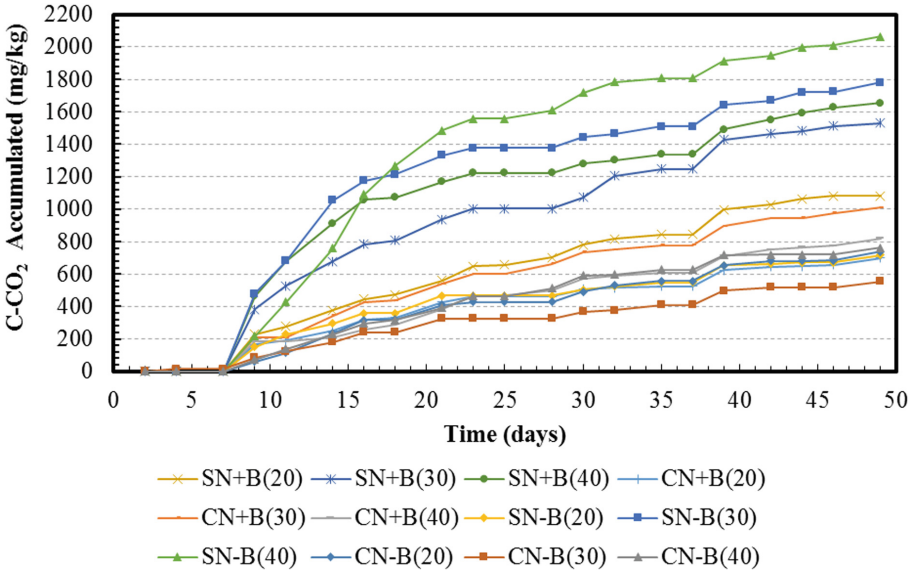

Fig. 2. CO_2 Evaluation results.

In addition, the first two to stand out are the −B, showing that the bioestimulation of native microorganisms is more efficient than the addition of endogenous microorganisms. The higher the concentration of calcium inserted, the greater the formation of bionanocementation, this can be observed in the results, since the most concentrated bodies of evidence were highlighted in the evaluation of CO_2.

Compression Test

In the comparison between the treatments in relation to the addition of microorganisms or not, for the resistance results the treatment without addition of microorganisms was highlighted. It can conclude that there may have been competition between the added microorganisms and the native microorganisms of the soil, thus not reaching expected values. In the comparing the CN and SN treatments, it can be observed that the SN treatment stands out, this may have occurred due to the failure to use the product at a nano scale.

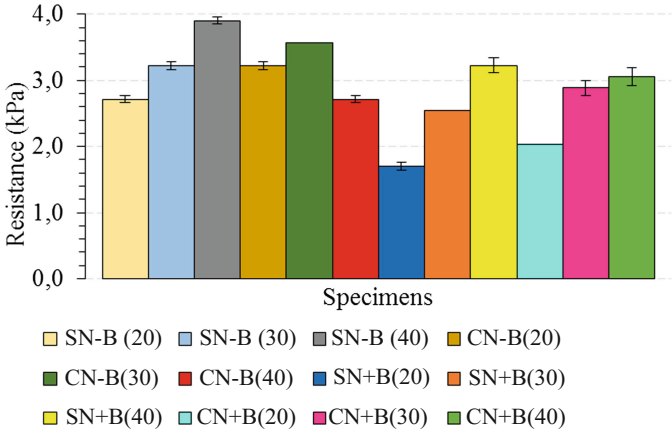

All the results of resistance presented have error bar, but as the results variance was very low it is not possible to see the bars well, only in some results the bars are more visible. This may have occurred because of the low resistance values read, the load cell used had a sensitivity of 0.1 kgf, but it is not sufficient, other ways of measuring this resistance are necessary for the best evaluate of the experiment.

SEM/EDX

The samples sent to MEV and EDS were those of 40 g/L of medium, and the best results were obtained in CO_2 evaluation and compression test (Table 1).

Amostra 1. It can be seen that the formation of $CaCO_3$ was low. This is evidenced in EDX results which show that the percentage of Calcium in the sample analyzed is 0.1% (Fig. 3).

Amostra 2. The compounds found in this sample are not the same as the first, since the equipment automatically reads what is in the sample. The percentage of calcium found in Sample 2 is 0.1% as well. In addition, by the image taken in the SEM the crystals formed are very small (Fig. 4).

Table 1. Sample labels for de SEM/EDX evaluation.

Sample label	Original sample label	Concentration
Amostra 1	SN+B	40 g/L
Amostra 2	CN+B	40 g/L
Amostra 3	SN−B	40 g/L
Amostra 4	CN−B	40 g/L

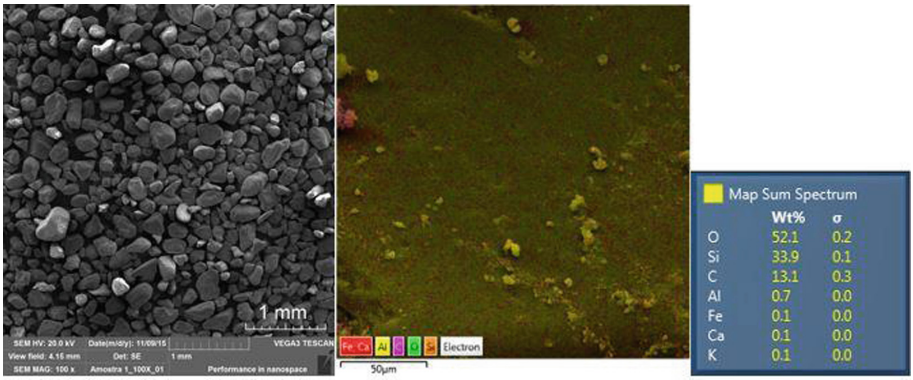

Fig. 3. SEM/EDX results for Amostra 1.

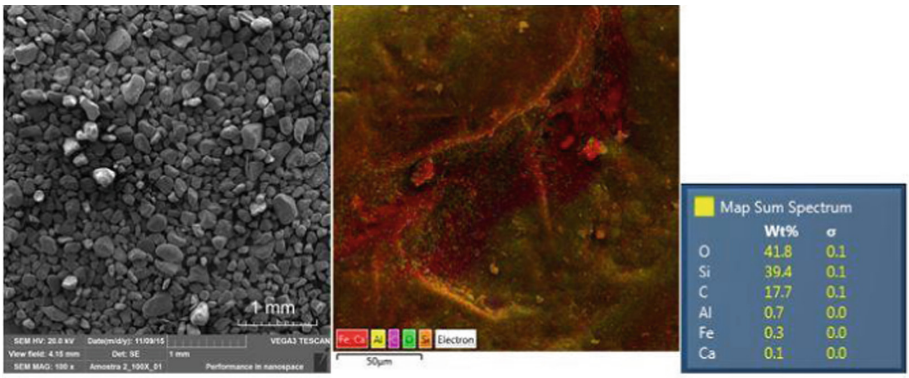

Fig. 4. SEM/EDX results for Amostra 2.

Amostra 3. It is possible to observe a percentage of 0.8% of calcium in the sample, in addition, it was possible to see from the result of the MEV the crystals of $CaCO_3$ in the enlargement of the sample, which are larger than those observed in Amostra 2 and Amostra 1 (Fig. 5).

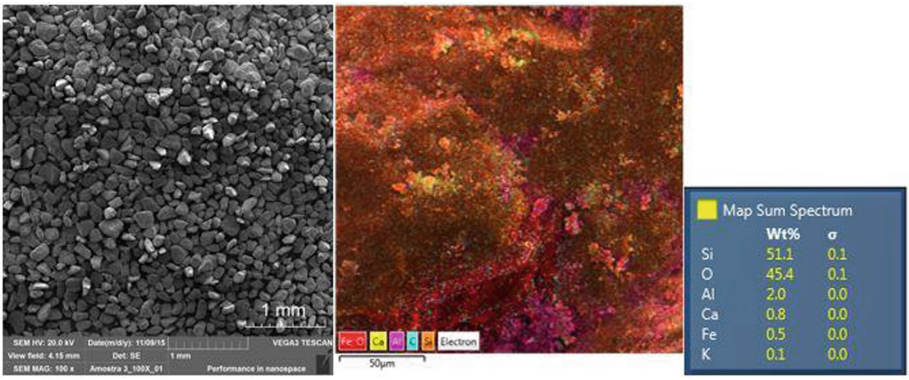

Fig. 5. SEM/EDX results for Amostra 2.

Amostra 4. In the SEM results, it is possible to observe the formation of agglomerates that are identified with the layers as Calcium or Iron, but in the results of the EDX, the percentage of Calcium found in the sample was 0.4% (Fig. 6).

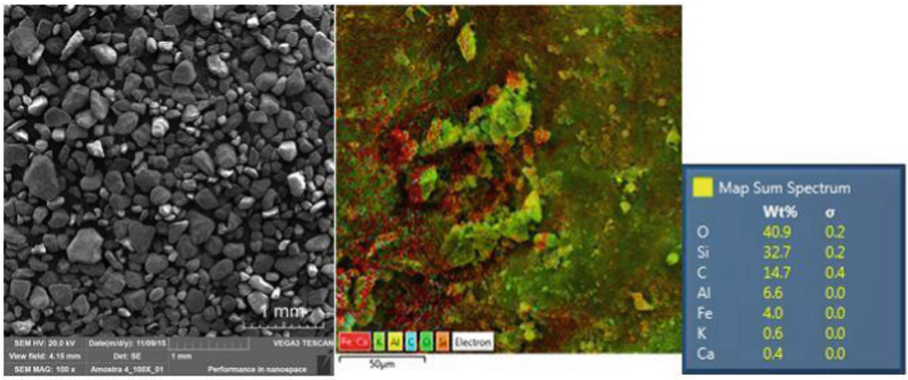

Fig. 6. SEM/EDX results for Amostra 2.

4 Conclusion

From the tests carried out, it was possible to conclude that native soil microorganisms such as microorganisms added to the soil as bioaumentation have the capacity to precipitate $CaCO_3$, as evidenced in the biochemical test, CO_2 evolution and resistance test. The media used for the CN and SN specimens had the same base, their only difference was the calcium source, as the medium used in the CN test bodies was nano$CaCO_3$, their results did not stand out. It was concluded that bioestimulation with this product is not indicated and further studies are required with different calcium source compounds rather than $CaCO_3$. From the comparison between the concentrations of the medium used in the bioestimulation that the highest concentrations stood

out in the majority of the results; From the measured resistances it was possible to show that the bionanocementation for this research was not as efficient as expected.

References

Rebechi MRL (2007) Bioremediagao na descontaminagao de um solo residual de basalto contaminado com oleo diesel e biodiesel. Passo Fundo, Dissertajao, 112 p. Programa de Pos Graduajao em Engenharia. Universidade de Passo Fundo

Inavov V, Chu J (2008) Applications of microorganisms to geotechnical engineering. Environ Sci Biotechnol 7:139–153

Bartha R, Pramer D (1965) Features of flask and method for measurement the persistence and biological affects of pesticides in soil. Soil Sci 100:68–70

Compacted Sewage Sludge as a Barrier for Tailing Impoundment: The Microbial Functional Diversity in the Compacted Sludge Specimen

Qing Zhang[1,2(✉)], Huyuan Zhang[1], and Jinfang Wang[1]

[1] Key Laboratory of Mechanics on Disaster and Environment in Western China, Lanzhou University, Ministry of Education, Lanzhou 730000, China
m35t@163.com, zhanghuyuan@lzu.edu.cn
[2] School of Geography and Environmental Engineering, Lanzhou City University, Lanzhou 730070, China

Abstract. In order to study the feasibility and microbial mechanism of sludge barrier for acid mine drainage (AMD), the microbial functional diversity in the compacted sludge with different seepage conditions (the distilled water (DW), the pH2.1 sulfuric acid and the simulate AMD) was studied using Biolog and Most Probable Number (MPN) testing system. The results showed that the average well color development (AWCD), the Shannon index (H), the Evenness index (E), the number of positive Ecoplate wells (S), the total bacteria (TB), and the sulfate reducing bacteria (SRB) quantity differed between different seepage conditions. Compared with the DW seepage condition, the acidity and AMD condition had the lower AWCD, S, H, E values which showed the latter inhibition effect be stronger. The seepage conditions changed the microbial quantity of carbon utilization and ability to utilize the single carbon source. So the property of the microbial functional diversity in the compacted sludge might indicate the microbial differences under the different seepage conditions in this study.

Keywords: Acid Mine Drainage (AMD) · Compacted Sludge Reducing barrier · Microbial functional diversity Sulfate Reducing Bacteria (SRB)

1 Introduction

According to statistics, the total tailing accumulation of China was 5 billion tons, accounting for about 40% of the industrial solid waste, and increases every year by 400 to 500 million tons, for the most part of which currently stored in the earth's surface. Such a lot tailings, brought great hidden troubles to the environmental safety [1]. The pollution of the tailings dumps mainly came from heavy metals and acidity of the acid mine drainage (AMD) because of their oxidation [2, 3]. Mature way to control the pollution of tailings, general was to design the encapsulating facilities according to the principle of geotechnical engineering, in the appropriate area for landfill disposal [4].

© Springer Nature Singapore Pte Ltd. 2019
L. Zhan et al. (Eds.): ICEG 2018, ESE, pp. 317–323, 2019.
https://doi.org/10.1007/978-981-13-2227-3_39

From bioreactor principle, to use the sulfate reducing bacteria (SRB) passive bioreactor dealing with all kinds of sewage (especially AMD), was a hot issue of academic studies over the years [5]. Tailings reducing barrier, using activated sludge, was actually to transplant the bioreactor to the internal encapsulating facilities. Tailings oxidation was a slow process; formation and diffusion of permeant liquid could last for decades or even hundreds of years. Accordingly, in the Sewage sludge, microbial growth and reproduction could also be long-term to maintain the sludge anaerobic reducing condition. From the years, microbial barrier of the nature long-term service work coincided with the characteristics of tailings whose slow release of pollutants. In addition, the sludge microbial reproduction and growth was spontaneous, without external supplies, and also needed no special engineering maintenance measures [6].

Research on the relationship between microbial species and heavy metal fixation, mainly revolved the sulfate reducing bacteria (SRB) [2]. In recent years, scholars had also made great advances in this field [5, 7–11]. However, the researches focused on microbial remediation of heavy metal pollution, mainly focus on some particular microbe, and were under the condition of pure culture to analysis reducing fixation effect of heavy metals. Natural microbial communities in sludge, including sulfate-reducing bacteria fell in interactions: cooperative or competitive. The studies of the patterns of these microbes in mixed culture, at present, were few and unsystematic [5, 12], besides of radiation resistant bacteria and thermophilic bacteria [13, 14] had been reported.

The purpose of this paper was to study the microbial functional diversity in the compacted sludge column under the simulate AMD seepage condition.

2 Materials and Methods

The sewage sludge used in this study was sampled from Yanerwan municipal sewage water treatment plant in Lanzhou, Gansu province, China. As per reference [15], the sludge was air-dried, ground and passed through 0.5-mm sieve for biochemical and geotechnical tests. Specimens were compacted for the hydraulic conductivity test in a flexible-wall permeameter. Three different solutions were used to simulate acid pore water and used as the permeant liquid: the synthetic AMD, the distilled water (DW), and the pH 2.1 sulfuric acidic water (SA).

The hydraulic conductivity was 7.8×10^{-10} cm s^{-1} with DW seepage condition, 7.6×10^{-10} cm s^{-1} with SA seepage condition and 6.8×10^{-10} cm s^{-1} with AMD seepage condition respectively at the first day and then decreased from the baseline value of 3.7×10^{-10} to 3.5×10^{-11} cm s^{-1} which was nearly impermeable. At the time of the 41st day seepage, the cells of the flexible-wall permeameter were opened and the sewage sludge specimens were taken out to be kept in 4 °C refrigerator. Then some of the fresh sludge specimens were diluted with aseptic water to test Cultivable SRB enumeration and total bacteria enumeration. Others were extracted for the community level functional diversity analysis.

Culturable SRB enumeration was performed with sludge solutions using the Most Probable Number technique (MPN) as per ASTM (2009) [16]. SRB were cultivated under anaerobic conditions using the SRB testing tubes (Watest KBC-SRB)

(Zhengzhou Water Testing Tech. Co. Ltd., P.R. of China). Tubes (three replicates per dilution) were inoculated and incubated at 30 °C for 7d under anaerobic conditions. Total bacteria enumeration was also performed using the MPN technique. The sludge solutions were cultivated under anaerobic conditions using the Total bacteria testing tubes (Watest KBC-BT) (Zhengzhou Water Testing Tech. Co. Ltd. P.R. of China). Tubes (three replicates per dilution) were inoculated and incubated at 37 °C for 24 h under anaerobic conditions.

Biolog Eco plates were used for the test of the community level functional diversity (Biolog Inc., Hayward, CA, USA). Samples of 10 g (wet weight) of the compacted sewage sludge were weighed into 200 mL pyrex tubes, suspended in 100 mL of aseptic NaCl solution (0.145 M) and shaken at 150 rev min^{-1} for 15 min. The suspensions were then further diluted to 10^{-2} After 10–15 min standing, aliquots of 150 μL of the extracts were added to each well in the microplates which contained three replicates of one sample because the plates contained 96 wells with three sets of 31 substrates plus one control. And the plates were incubated in the dark at 25 °C for 10 days. The Biolog Eco plates were read at 0 h, once every 12 h for 10 days with a VAMAX Microplate Reader at 595 nm (Microlog Rel 3.5 software). The readings for 0 h and for the control wells were subtracted from all subsequent readings to correct for potential color development due to added organic matter. The absorbance of the 31 substrates was used to calculate the average well color development (AWCD) [17].

$$\mathrm{AWCD} = \left(\sum \frac{C - R}{31}\right) \tag{1}$$

Where C was the absorbance of the 31 substrates wells; R was absorbance of the control wells). The values of AWCD were plotted against the incubation period of the plate. The Shannon index ($H = -\sum \mathrm{PilnPi}$, Pi was the ratio between relative absorbance of each well (C-R) and the total absorbance of 31 substrates.) and the Evenness index ($E = \frac{H}{\ln S}$, S, number of positive EcoPlate wells) of bacterial communities were calculated based on the EcoPlate readings after 144 h of incubation.

The data on the sewage sludge characteristic, the AWCD, the Shannon index, the principal component (PC) analysis were statistically analyzed using the SPSS for Windows 19.0. Mean values were compared using the analysis of variance (ANOVA).

3 Results and Discussion

The AWCD on the Biolog EcoPlate inoculated with sludge specimen sampled from the untreated sludge column was the highest compared with those from the seepage conditions (Fig. 1). For 144 h incubation, there was significant difference among the samples from the four treatments. The AWCD in the sludge specimen with AMD seepage was the lowest. Then that with the SA seepage was lower than that with the DW seepage condition. And the AWCD in the untreated sludge specimen was the highest significantly. At 144 h, the untreated sludge specimen readings showed significantly higher AWCD, Shannon index (H), Evenness index (E), and Number of

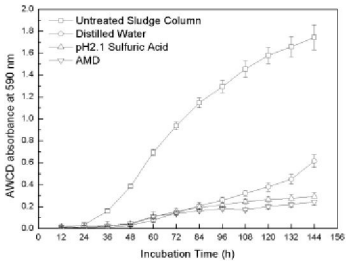

Fig. 1. Average well color development (AWCD) of Biolog EcoPlate inoculated with sludge specimen under different seepage conditions.

positive EcoPlate wells (S) compared with that under different seepage conditions. The readings of the sludge specimen with DW seepage condition were significantly higher than those with SA or AMD seepage conditions. However, there were no significant difference between the sludge specimens with SA seepage and those with AMD seepage (Table 1).

Table 1. Analysis of microbial community Average well color development (AWCD), Shannon index (H), Evenness index (E), and Number of positive EcoPlate wells (S) as determined by Biolog EcoPlates inoculated with sludge specimen under different seepage conditions

Sludge specimen	S	H	E	AWCD
Untreated	79	2.95a	0.67a	1.74a
With DW seepage	69	1.06b	0.25b	0.62b
With SA seepage	56	0.66c	0.17c	0.29c
With AMD seepage	54	0.63c	0.15c	0.25c

Means within the same column and followed by the different letter were significantly different from each other based on ANOVA at $P < 0.05$.

According to different sewage sludge specimens utilization of different carbon sources on Biolog Ecoplate, the readings at 144 h were analyzed by principal component analysis (PCA) to determine the microbial functional structure. The first (PC1), the second (PC2) and the third (PC3) principal components explained 67.6%, 11.9%, 5.1% of the data variances respectively (Fig. 2). The PC1 and PC2 scores biplot (Fig. 2A) showed the untreated sludge column specimen clustered to the first quadrant, the sludge specimen with pH2.1 sulfuric acid seepage condition clustered to the second quadrant, while that with distilled water or AMD seepage condition clustered to the third quadrant. The biplot between PC1 and PC3 scores (Fig. 2B) showed the untreated sludge column specimen clustered to the first quadrant, the sludge specimen with DW seepage condition clustered in the second quadrant, while that with SA or AMD condition lay in the third quadrant. The biplot between PC2 and PC3 scores (Fig. 2C) showed the untreated sludge column clustered to the first quadrant, the specimen with

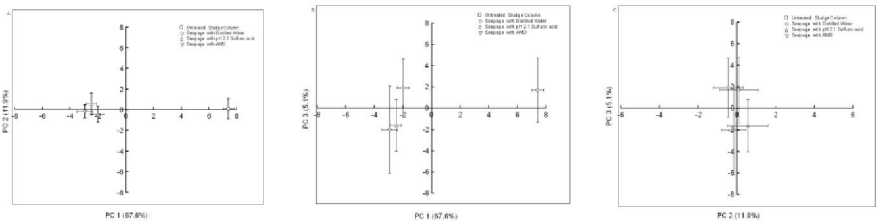

Fig. 2. Principal component analysis (PCA) of the carbon substrates utilization data of 4 sludge specimen with different seepage conditions (distilled water, pH2.1 sulfuric acid, AMD or untreated), incubated with the Biolog EcoPlate at 144 h A. PC1 and PC2 scores biplot B. PC1 and PC3 scores biplot C. PC2 and PC3 scores biplot.

DW seepage condition clustered to the second quadrant, while that with AMD or SA seepage condition clustered to the third or fourth quadrant respectively.

The carbon substrates on the Biolog Ecoplate utilized by the microbial functional community in the sludge specimen incubation at 144 h, which discreted the different specimen with different seepage conditions along the PC1, PC2 and PC3 axes, were 9 Carbohydrates, 4 Amino acids, 2 Carboxylic acids, 3 Polymer, 1Phenolic acid and 3 Amines, that was, 22 substrates contributed to the PC1. As for PC2, 1 Carboxylic acid was consisted in, mean while another 1 Carboxylic acid contributed to PC3.

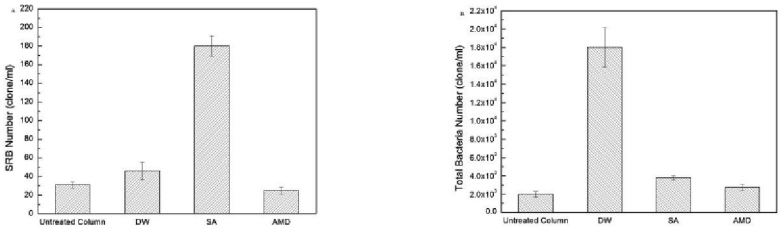

Fig. 3. Sulfate reduce bacteria (SRB) or total bacteria quantity in different sludge specimen with different seepage: Distilled water (DW), pH 2.1 Sulfuric acid (SA), AMD or in the untreated sludge column A. Sulfate reducing bacteria (SRB) quantity in the sludge specimens B. Total bacteria quantities in the sludge specimen

The sulfate reducing bacteria (SRB) quantity in the sludge specimens were showed in Fig. 3A. Among different seepage conditions, sludge with pH 2.1 sulfuric acid permeant (SA) showed the highest SRB quantity, 180 clones mL^{-1}, 578.3% of that in the untreated sludge column while that with AMD permeant showed the lowest SRB quantity, 25 clones mL^{-1}, 80.3% of that in the untreated sludge column. The total bacteria quantities in the sludge specimen were showed in Fig. 3B. The sludge specimen with DW permeant showed the highest total bacteria quantity, 1.8×10^4 clones mL^{-1}, while the untreated sludge column showed the lowest, 2.0×10^3 clones mL^{-1}. The total bacteria quantity in the sludge with AMD seepage condition was 137.5% of that in the untreated sludge column, while that with SA seepage condition is 190%.

Table 2. Pearson correlation analysis of the SRB quantity, Total Bacteria (TB), AWCD, S, H, and E in the different sludge columns

Correlation coefficient matrix	Pearson correlation					
	SRB	TB	AWCD	S	H	E
SRB	1.000	−0.155	−0.248	−0.045	−0.256	−0.255
TB	−0.155	1.000	0.046	0.172	0.051	0.054
AWCD	−0.248	0.046	1.000	0.868**	0.992**	0.990**
S	−0.045	0.172	0.868**	1.000	0.866**	0.862**
H	−0.256	−0.155	0.992**	0.866**	1.000	1.000**
E	−0.255	0.054	0.990**	0.862**	1.000**	1.000

**$p < 0.01$

As shown in Table 2, there was no correlation between SRB quantities; Total bacteria quantities (TB) and the microbial community level functional diversity data (AWCD, S, H and E).

4 Conclusions

According to Biolog data and MPN data, with different seepage conditions, the AWCD, S, H, E and SRB, TB quantity changed compared with those of the untreated compacted sludge; and the acidity and AMD condition had the lower AWCD, S, H, E values. It showed the latter inhibition effect was stronger; the seepage conditions change the microbial quantity of carbon utilization and ability to utilize the single carbon source. So the characteries of the microbial functional diversity in the compacted sludge might indicate the microbial differences under the different seepage conditions in this study.

Acknowledgements. This work was supported by the Doctoral Program of Higher Education of China (No. 20110211110025) and the Natural Science Foundation of Gansu Provincial Science & Technology Planning Project, China (No. 18JR3RA222).

References

1. MEP of China (2010) The guide to the emergency management of tailings (Trial). MEP, Beijing
2. Lottermoser BG (2007) Mine wastes-characterization, treatment, environmental impacts, 2nd edn. Springer, Heidelberg, New York
3. Rodriguez L (2009) Heavy metal distribution and chemical speciation in tailings and soils around a Pb-Zn mine in Spain. J Environ Manag 90:1106–1116
4. Blight G (2010) Geotechnical engineering for mine waste storage facilities. Tayor & Francis, London

5. Neculita CM, Zagury GJ, Bussiere B (2007) Passive treatment of acid mine drainage in bioreactors using sulfate-reducing bacteria: Critical review and research needs. J Environ Qual 36:1–16
6. Wang B, Zhang H, Fan Z et al (2010) Compacted sewage sludge as a barrier for tailing impoundment. Environ Earth Sci 61:931–937
7. Bai H, Kang Y, Quan HE et al (2013) Treatment of acid mine drainage by sulfate reducing bacteria with iron in bench scale runs. Biores Tech 128:818–822
8. Wang J, Li SJ, Chen TH et al (2012) Effects of heavy metals on the performance of anaerobic sulfidogenic reactor using rape straw as carbon source. Environ Earth Sci 67:2161–2167
9. Zhou Q, Chen YZ, Yang M et al (2013) Enhanced bioremediation of heavy metal from effluent by sulfate-reducing bacteria with copper-iron bimetallic particles support. Biores Tech 136:413–417
10. Tang Q, Gu F, Zhang Y et al (2018) Impact of biological clogging on the barrier performance of landfill liners. J Environ Manag 222:44–53
11. Tang Q, Gu F, Gao YF et al (2018) Desorption characteristics of Cr(III), Mn(II) and Ni(II) in contaminated soil using citric acid and citric acid containing wastewater. Soils Found (JGS) 58(1):50–64
12. Brim H (2006) Deinococcus radiodurans engineered for complete toluene degradation facilitates Cr(VI) reduction. Microb, 152:2469–2477
13. Möller C, Van Heerden E (2006) Isolation of a soluble and membrane-associated Fe(III) reductase from the thermophile, Thermus scotoductus (SA-01). FEMS Microb Lett 265:237–243
14. Opperman DJ (2007) Aerobic Cr(VI) reduction by Thermus scotoductus strain SA-01. J Appl Microb 103:1907–1913
15. Zhang H, Zhang Q, Yang B et al (2014) Compacted sewage sludge as a barrier for tailings: the heavy metal speciation and total organic carbon content in the compacted sludge specimen. PLoS ONE 9:e100932
16. ASTM (2009) Standard methods for sulfate-reducing bacteria in water and water-formed deposits, in D4412-84, ASTM International, West Conshohocken
17. Moynahan OS, Zabinski CA, Gannon JE (2002) Microbial community structure and carbon-utilization diversity in a mine tailings revegetation study. Rest. Eco. 10:77–87

Complex Conductivity and Shear Wave Velocity Responses of Sand-Calcite Mixture

Junnan Cao[1], Chi Zhang[2], and Bate Bate[3](✉)

[1] Department of Civil, Architectural and Environmental Engineering, Missouri University of Science and Technology, Rolla, MO, USA
jcg83@mst.edu
[2] College of Liberal Arts and Sciences – Geology, University of Kansas, Lawrence, USA
chizhang@ku.edu
[3] Institute of Geotechnical Engineering, College of Civil Engineering and Architecture, Zhejiang University, 866 Yuhangtang Road, Hangzhou, China
batebate@zju.edu.cn

Abstract. Size and distribution of precipitated particles significantly influence the efficiency of ground improvement by introducing fine particles in the original soil matrix mechanically, chemically, or biologically. However, direct measurement of these fine particles poses challenges to the existing non-destructive methods. Recent advancement in low-frequency (0.01–100 Hz) complex conductivity showed promising results in obtaining the size and accumulation pattern of fine particles distributed in coarse-grained soils. In this study, low-frequency complex conductivity measurements were conducted to monitor the spectral induced polarization (SIP) responses of Ottawa 50–70 sand mixed with eggshell powder at sieve size between No. 80 and 140. Vertical stresses of 5, 25, 50 and 100 kPa were progressively added to the sample. Shear wave velocity (V_s) was also monitored by bender element technique. Relaxation frequency of imaginary conductivity increased with the increment of vertical stress, which was attributed to crack generation of eggshell as vertical stress increased. The calculated particle size at 5 kPa from complex conductivity measurement was close to the size of eggshell powder used, suggesting the accuracy of the prediction of SIP method. Shear wave velocity detected increment of stiffness of the mixture as stress increased.

Keywords: Spectral induced polarization · Complex conductivity
Sand-eggshell mixture · Shear wave velocity · Size

1 Introduction

Spectral induced polarization (SIP) is a noninvasive geophysical method to investigate the conduction and polarization mechanisms of porous media, with applications of monitoring the process of calcite precipitation (Wu et al., 2011), iron corrosion (Wu et al., 2005), and biofilm formation and mineral precipitation in porous media (Zhang et al., 2012). The imaginary conductivity of SIP can be used as a proxy of the size and the distribution of precipitated particles. Both have major influences over the

© Springer Nature Singapore Pte Ltd. 2019
L. Zhan et al. (Eds.): ICEG 2018, ESE, pp. 324–331, 2019.
https://doi.org/10.1007/978-981-13-2227-3_40

mechanical properties of geo-materials. In addition, the distribution pattern of the precipitated particles, i.e., suspended in pore fluid (pore-filling) or coated on large grain surfaces (whether or not at grain-contacting points) also play a significant role. SIP, as a promising tool to detect both size and distribution, could yield valuable information of the engineering properties. Successful application of SIP could provide valuable tool for in-situ monitoring of heterogeneous and multiphase evolution processes, such as microbial induced calcite precipitation (MICP) and ground improvement by lime treatment. Bender element, as another non-destructive method, is widely used to measure the shear wave velocity, which is related to the initial tangent shear modulus. Shear wave velocity could vary significantly with different precipitated particle sizes and distribution patterns, especially in MICP (Weil et al., 2012).

Since both SIP and shear wave velocity are related to the particle size and distribution, the relationship between complex conductivity and shear wave velocity can be investigated. In this study, the low-frequency complex conductivity is applied to monitor the induced polarization responses of Ottawa 50–70 sand-eggshell (100%) mixture. Particle sizes are estimated from imaginary conductivity. And shear wave velocities are detected from bender element at different vertical stresses. The influence of calcite particles on both complex conductivity and shear wave velocity are elucidated.

2 Background

2.1 Spectral Induced Polarization (SIP)

Low-frequency (typically less than 1 kHz) complex conductivity (σ^*), which is measured through two current electrodes (to generate sinusoid, positioned at both ends of the sample) and two potential electrodes (to receive responding sinusoid, located between the current electrodes), can be generally expressed as

$$\sigma^*(\omega) = \sigma'(\omega) + i\,\sigma''(\omega) \tag{1}$$

where ω is the angular frequency, σ' is the real conductivity, representing the conduction (energy loss) component, and σ'' is the imaginary conductivity, representing the polarization (energy storage) part, $i = \sqrt{-1}$.

For saturated porous media at low frequencies (<1000 Hz), σ^* can be written as

$$\sigma^* = \sigma_{el} + \sigma^*_{surf}(\omega) = \sigma_{el} + \sigma'_{surf}(\omega) + i\,\sigma''_{surf}(\omega) \tag{2}$$

where σ_{el} is the frequency independent electrolytic conductivity of the interconnected pore space, $\sigma'_{surf}(\omega)$ and $\sigma''_{surf}(\omega)$ are frequency dependent real and imaginary components of the complex surface conductivity σ^*_{surf}, respectively.

Cole-Cole model (Cole and Cole 1941; Pelton et al., 1978; Wu et al., 2010), as one of the most popular phenomenological models, is typically used in soil to describe the complex conductivity. The mean relaxation time τ ($= 2\pi f_{peak}$, f_{peak} is the peak

frequency obtained from imaginary conductivity vs. frequency curves) in the model is related to the particle diameter d. The relationship is defined by Schwarz (1962):

$$\tau = \frac{d^2}{8D_s} \tag{3}$$

where D_s is the diffusion coefficient (m^2/s).

2.2 Bender Element Testing System

Bender element (BE) is a non-destructive testing (NDT) method typically used in geotechnical engineering to evaluate the shear wave velocity (V_s) of a geomaterial, which is related to the initial tangent shear modulus (G_0) by:

$$G_0 = \rho V_s^2 \tag{4}$$

The BE testing system consisted of five pairs of bender elements, signal generation and data acquisition systems: a function waveform generator (33210A, Agilent), a filter conditioner (3364, Krohn-Hite), a linear amplifier and an oscilloscope (54622A, Agilent) (Fig. 1).

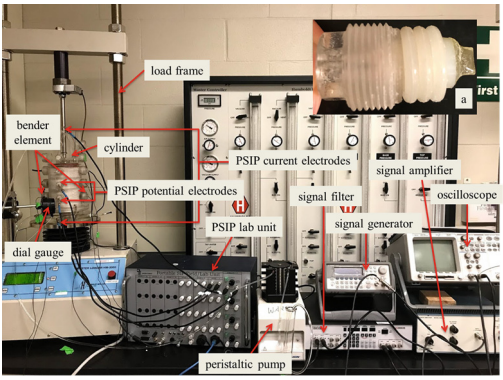

Fig. 1. Experimental setup with PSIP lab unit and BE testing system; inset: a bender element unit.

The method of BE construction is similar to that in Kang et al. (2014). A brief description was given below. The piezoceramic BE plate (Piezo Systems, Inc.) was cut into the dimensions of 12.7 mm × 8.0 mm × 0.6 mm (length × width × thickness) before directly connected to a coaxial cable, coated at least three layers of polyurethane as the electrical isolator and waterproofing, and fixed in a nylon spacer (inner diameter × height = 12.7 mm × 15.88 mm) by epoxy (Fig. 1a). The parallel type connection was adopted to minimize the electromagnetic coupling (Lee and Santamarina, 2005).

The tip of BE was extruded to the top of nylon spacer (inner diameter × height = 0.95 cm ×2.22 cm) 5 mm (Fig. 1a). The extruded portion was coated with epoxy for protection and covered with plastic wrap to minimize crosstalk (Zhu et al., 2018).

The tip-to-tip distance (L, m) was selected as the travel distance between sender and receiver BEs. The first arrival time (t_c, s) was determined using the zero-crossing point with the x-axis of the half peak before the first major peak. Therefore, the shear wave velocity (m/s) is

$$V_s = \frac{L}{t_c} \tag{5}$$

3 Materials and Experimental Methods

Ottawa 50–70 silica sand (U.S. Silica Holdings Inc., Chicago, IL) and eggshell powder (extracted from fresh eggs from a grocery store) were used in this study. D_{50} of Ottawa sand is 0.26 mm and e_{max} = 0.87, e_{min} = 0.55. The total organic carbon (TOC) of eggshell powder is 2.77% (Shimadzu, SSM-5000A).

Both Ottawa 50–70 sand and eggshell were firstly washed with deionized water three times, and then oven-dried (100 °C) for at least 24 h. Before packing, the inner surface of SIP/BE column was flashed three times with deionized water and 70% alcohol, respectively. Eggshell were grounded into powders using a coffee grinder (Hamilton Beach, model#: 80335) after removing the inner membranes. The particle size of sieved eggshell powder is between 0.18 mm – 0.106 mm. The inner diameter of sample cylinder (Fig. 1) was 10 cm and the total length was 30 cm. Mixture of 1575.4 g sand and 522.1 g eggshell powder was compacted into cylinder. The initial void ratio of pure sand was 1.094. The final height of the mixed sample was 15.85 cm, yielding a void ratio (e) of 0.582 and porosity (n) of 36.8%. After packing the porous media, a solution of 2.5 mM $CaCl_2$ (ACROS ORGANICS, CAS: 10043-52-4) (conductivity = 548 μS/cm) were flushed into the sample from the bottom of the column through a peristaltic pump. The flow rate was kept at 10 ml/min by the pump. After the soil was fully saturated, the fluid flow was stopped and four vertical loads (5, 25, 50 and 100 kPa) were progressively added on the top of the sample via the load frame (Master loader HM-3000, Humboldt MFG. CO., Norridge, IL). Meanwhile, settlements of the sample under each vertical load were measured by a dial gauge (Humboldt MFG. CO., accuracy = 0.0001 inch). It was found that void ratio slightly decreased from 0.582 to 0.579 as vertical stress increased from 5 to 100 kPa.

4 Results and Discussion

The changing of real and imaginary conductivities with frequencies at 5, 25, 50 and 100 kPa vertical stresses were shown in Fig. 2. It can be observed that (1) real conductivity (σ') varies from 8.4 to 9.8 mS/m in the frequency range of 0.05–100 Hz under

all vertical stresses; (2) imaginary conductivity curves of 25 and 50 kPa were similar with each other; (3) two peak frequencies were detected on 25 and 50 kPa curves. They were around 1 and 0.1 Hz, respectively; (4) One peak frequency was observed on both 5 ($\approx$ 0.1 Hz) and 100 kPa ($\approx$ 2.5 Hz) curves over the tested frequency range from 0.01 to 100 Hz; (5) Major peak frequency increased with the increment of vertical stress.

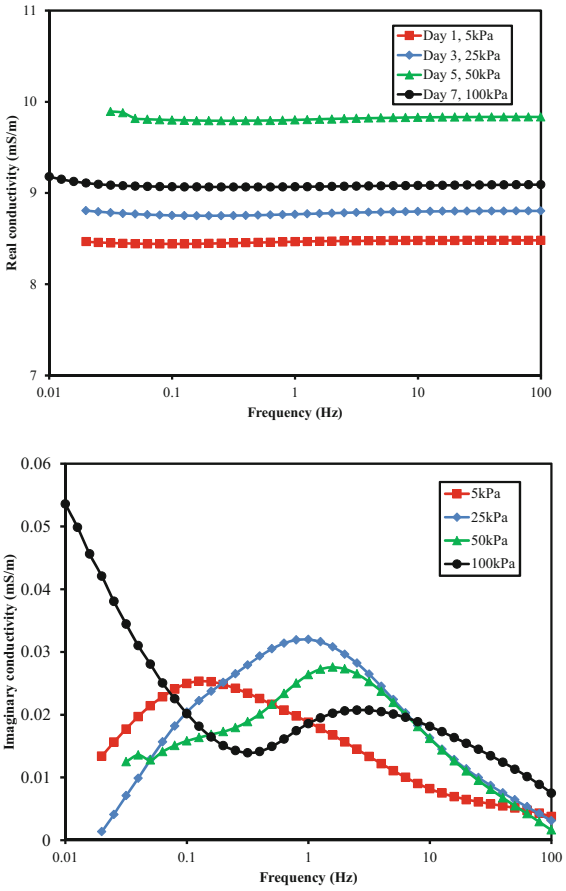

Fig. 2. Tested spectral (a) real and (b) imaginary conductivities.

Ribeiro et al., (2008) found that the diffusion coefficient (D_s) of $CaCl_2$ solution (0.005–0.1 mol/l) was 1.335 $\times$ 10^{-9} m^2/s at 25 °C. Their experimental results showed that diffusion coefficient decreased with the increment of $CaCl_2$ concentration. Therefore, substituting D_s = 1.335 $\times$ 10^{-9} m^2/s into Eq. 3, the particle diameters at different vertical stresses for this study could be calculated (Table 1). The obtained value at peak frequency $\approx$ 0.1 Hz was similar to the size of the individual eggshell particle. Major peak frequency increased with the increment of vertical stress.

This might due to the crushing of eggshells caused by the stress concentration at particle contacts under vertical loads. More cracks and smaller particle sizes would occur with the increment of vertical stress, which caused the major peak frequency shifting to the right direction (Fig. 2b). Particle size $\geq$0.412 mm was detected at 100 kPa (Table 1). This might due to the attachment of eggshell powder on the surface of Ottawa sand (electrostatic attraction) forming relatively larger particles. This conclusion could be substantiated by the increased BE results shown in Fig. 3 (see discussion later).

Table 1. Estimated mean particle sizes of sand and eggshell powder using Eq. 3.

Vertical stress (kPa)	Time (day)	Peak frequency (Hz)	Relaxation time (s)	Particle size (mm)
5	1	0.126	1.263	0.116
25	3	1	0.159	0.041
		0.1	1.592	0.130
50	5	1.58	0.100	0.033
		0.1	1.592	0.130
100	7	2.512	0.063	0.026
		$\leq$ 0.010	$\geq$ 15.915	$\geq$ 0.412

Outflow fluid conductivities (σ_f) increased from 728.3 to 820.7 μS/cm at day 1 to day 5 and decreased to 798.9 μS/cm at day 7. This had the similar trend with real conductivity (Fig. 2a). The slight increment of σ_f was postulated to be the leaching of the dissolved ions remaining in the eggshell, which is often nutrient enriched. According to Archie's law (1942), real conductivity (σ') was affected by the fluid conductivity and porosity. But the test results showed that the fluid conductivity was the major influential factor of the real conductivity in this study. In addition, surface conductance played a secondary role in influencing the real conductivity due to the small specific area of Ottawa 50-70 sand and eggshell powder, which located in the range of fine sand.

Figure 3 presented the values of shear wave velocity at different vertical stresses. V_s increased with the increment of vertical stress. The maximum V_s value was 189.2 m/s. The slope of V_s increment between 50–100 kPa is the largest compared to those at 5–25 kPa and 25–50 kPa.

Robertson et al. (1995) measured the shear wave velocity of in-situ Ottawa sand (C109) (e_{min} = 0.500, e_{max} = 0.820, D_{50} = 0.35 mm) when it consolidated from loose condition to the void ratio locating at the critical state line, K_0 = 0.4. The results at 5, 25, 50 and 100 kPa were selected and also plotted in Fig. 3. Santamarina and Cho (2001) reported that the critical state effective friction angle φ' of Ottawa sand was 34 °. Based on the Jaky's equation, $K_0 = 1 - \sin \varphi'$, the calculated K_0 value of this study was 0.44, which was similar with the value of Robertson et al. (1995). It can be observed from Fig. 3 that the slope of V_s increment between adjacent vertical loads increased more mildly compared to those of this study. In addition, comparing the V_s

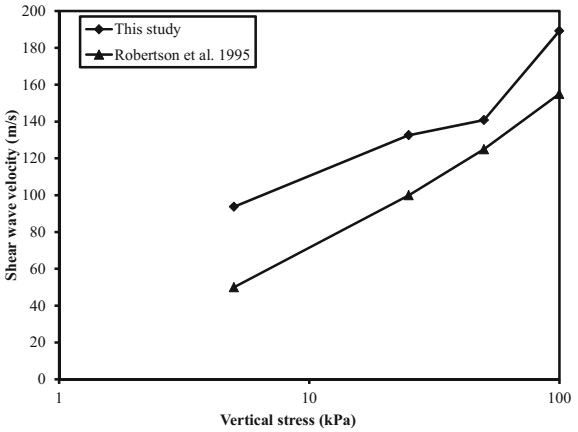

Fig. 3. Shear wave velocity vs. vertical stress.

values of the two curves, shear wave velocities of this study were larger than those of Robertson et al. at four vertical stresses. These could probably be attributed to the effects of calcite from eggshell powders used in this study.

5 Summary

Low-frequency complex conductivity was applied to monitor the induced polarization responses of a mixture of Ottawa 50–70 sand and eggshell powder (sieve size 80–140). Vertical stresses were added progressively on top of the soil sample following the sequence of 5, 25, 50 and 100 kPa. Particle sizes were calculated from the results of imaginary conductivities. Shear wave velocity was monitored by bender element technique. The following observations are made:

(1) Real conductivity was primarily influenced by the fluid conductivity;
(2) Estimated particle size from imaginary conductivity at 5 kPa was similar to the size of eggshell powder used in this study;
(3) Peak frequency changing with vertical stress might due to the generation of cracks on eggshells.
(4) Shear wave velocity result probably reflected the effects of calcite from eggshell powders on Ottawa sand;
(5) SIP can detect both size and precipitated particle distribution, and could provide valuable information for in-situ monitoring of heterogeneous and multiphase evolution processes, such as MICP.

References

Cole KS, Cole RH (1941) Dispersion and absorption in dielectrics I. alternating current characteristics. J Chem Phys 9(4):341–351

Kang X, Kang G-C, Bate B (2014) Measurement of stiffness anisotropy in kaolinite using bender element tests in a floating wall consolidometer. Geotech Test J 37:869–883

Lee J-S, Santamarina JC (2005) Bender Elements: Performance and Signal Interpretation. J Geotech Geoenviron Eng 131(9):1063–1070

Pelton WH, Ward SH, Hallof PG, Sill WR, Nelson PH (1978) Mineral discrimination and removal of inductive coupling with multifrequency IP. Geophys 43:588–609

Ribeiro AC, Barros MCF, Teles ASN, Valente AJM, Lobo VMM, Sobral AJFN, Esteso MA (2008) Diffusion coefficients and electrical conductivities for calcium chloride aqueous solutions at 298.15 K and 310.15 K. Electrochim Acta 54:192–196

Robertson PK, Sasitharan S, Cunning JC, Sego DC (1995) Shear-wave velocity to evaluate in-situ state of Ottawa sand. J Geotech Eng 121(3):262–273

Santamarina JC, Cho GC (2001) Determination of critical state parameters in sandy soils-Simple procedure. Geotech Test J 24(2):185–192

Schwarz G (1962) A theory of the low-frequency dielectric dispersion of colloidal particles in electrolyte solution[1, 2]. J Phys Chem 66:2636–2642

Weil MH, DeJong JT, Martinez BC, Mortensen BM (2012) Seismic and resistivity measurements for real-time monitoring of microbially induced calcite precipitation in sand. Geotech Test J 35:330–341

Wu Y, Ajo-Franklin J, Spycher N, Hubbard S, Zhang G, Williams K, Taylor J, Fujita Y, Smith R (2011) Geophysical monitoring and reactive transport modeling of ureolytically-driven calcium carbonate precipitation. Geochem Trans 12(1):7

Wu Y, Hubbard S, Williams KH, Ajo-Franklin J (2010) On the complex conductivity signatures of calcite precipitation. J Geophys Res, 115: G00G04

Wu Y, Slater LD, Korte N (2005) Effect of precipitation on low frequency electrical properties of zerovalent iron columns. Environ Sci Technol 39(23):9197–9204

Zhang C, Slater L, Redden G, Fujita Y, Johnson T, Fox D (2012) Spectral induced polarization signatures of hydroxide adsorption and mineral precipitation in porous media. Environ Sci Technol 46:4357–4364

Zhu J, Cao JN, Bate B, Khayat KH (2018) Determination of mortar setting times using shear wave velocity evolution curves measured by the bender element technique. Cem Concr Res 106:1–11

Diversity of Bacterial Structure Community in the Compacted Sewage Sludge as a Barrier for Tailings

Qing Zhang[1,2(✉)], Huyuan Zhang[2], and Jinfang Wang[2]

[1] School of Geography and Environmental Engineering, Lanzhou City University, Lanzhou 730070, China
m35t@163.com

[2] Key Laboratory of Mechanics on Disaster and Environment in Western China, Lanzhou University, Ministry of Education, Lanzhou 730000, China
zhanghuyuan@lzu.edu.cn

Abstract. Compacted sewage sludge (CSS), also known as reducing barrier, can be used as barrier for tailings of mines. CSS is an effective means to isolate and eliminate acid mine drainage (AMD) produced by tailings. We studied the dynamics of bacterial community structure diversity over 75 days in the CSS. Samples were taken from two seepage conditions: pH 2.1 sulfuric acid water (SA) and the synthetic AMD. Deionized water (DW) was used as control. We used PCR-DGGE technique, which is denaturing gradient gel electrophoresis. The results indicated that *Clostridiales, Bacillaceae,* and *Carnobacteriaceae* dominated in the CSS samples with different relative abundance ranged from 46.26% to 10.25% at the start point (SP) of seepage, the 41st day (T1) of seepage or at the 75th day (T2) of seepage, under different seepage conditions (DW, SA and AMD). By redundancy analysis on the influences between environmental factors and microbial-community, microbial- mechanisms differed.

Keywords: Compacted sewage sludge
Microbial community structure diversity
PCR- Denaturing Gradient Gel Electrophoresis (PCR-DGGE)
Acid mine drainage (AMD) · Heavy metals potential mobility

1 Introduction

Large amounts of tailings and tailings pollution incidents caused prominent social and environmental problems and accounted for a lot of environmental risk. New technologies to control the associated problems, such as heavy metals, acidic drainage, were required to solve the increasingly serious pollution from tailings. Acid Mine Drainage (AMD), characteristic of higher heavy metals contents and acidity but lower organic matters content, produced by the gradual oxidation of tailings, was harmful to underground water and human health. In case the formation and leaching of AMD, the compacted sewage sludge (CSS) barrier was designed to meet the requirement of tailings landfill known as reducing barrier, with lower permeability and variable carbon

© Springer Nature Singapore Pte Ltd. 2019
L. Zhan et al. (Eds.): ICEG 2018, ESE, pp. 332–339, 2019.
https://doi.org/10.1007/978-981-13-2227-3_41

sources and microbial species for the cover or liner of tailings innovatively [1]. And Zhang et al. [2] found that as the aspect of environmental risk, the CSS was feasible to be the barrier for tailings.

Tailings oxidation was a slow process, and AMD formation and diffusion could last for decades, even centuries [3]. The tailings CSS encapsulation barrier actually transplanted the micro-bioreactors to the encapsulation facility inside. We need to know what the microorganisms changed with time.

At present, the microbe researches had been widely used in mine leaching [4], environment restoration theory [5] and so on. However, most of the researches were only for the bacteria cultured from isolation which accounted for a very small fraction of the total bacteria number, up to 1%, in the living environment. Denaturing Gradient Gel Electrophoresis (DGGE) was a technique developed in recent years. The biggest advantage of that was there was no procedure of isolation and culture for microorganisms, but extracting DNA directly, thus avoiding of parochialism in microorganisms culture techniques.

The objectives of our research were (1) to analyze microbial community structure diversity and its dynamics in the CSS samples under two different seepage conditions (pH 2.1 sulfuric acid water (SA) and the synthetic AMD with deionized water (DW) as control) in the different periods (41st Day and 75th Day) by DGGE technique; (2) to illuminate the relations between the microbial community structure diversity and the differently environmental factors; (3) to help the further studies find functional bacteria and genes which functioned in the CSS barrier for tailings.

2 Materials and Methods

Based on Zhang et al. [2], the sewage sludge was collected from Yanerwan municipal sewage water treatment plant in Lanzhou, Gansu province, China. The sewage sludge powder was set in a flexible-wall permeameter. DW, SA and AMD were prepared to be the permeant liquids.

The hydraulic conductivity kept in the state of nearly impermeable. At the time of the 41st day (T1) and the 75th day (T2) respectively, the cells of the flexible-wall permeameter were opened and the sludge samples were taken out. Some were air-dried, ground, passed through 0.5-mm sieve for Cd, Cu, Fe, Ni, and Zn speciation tests, others were kept in the −20 °C refrigerator for analysis of bacterial community structure and diversity by DGGE.

Total genomic DNA in the CSS were extracted using rapid extraction kit of sludge genomic DNA (Mobio^{TM} DNA Kit, USA). Taking samples genomic DNA as templates, hypervariable region sequences of 16S rDNA were amplified using two universal primers: GC-338F and 518R bacterial.

16S rDNA sequences of the most similar to type strain with Blast program for homology in GenBank were accessed (http://www.ncbi.nlm.nih.gov/BLAST). And then Phylogenetic tree with Neighbor-joining method, bootstrap index was 1000, was constructed employing Molecular Evolutionary Genetics Analysis (MEGA 5) software. The Redundancy analysis (RDA) was performed by CANOCO 4.5 (Biometris, Wageningen, Netherlands) to explain our data. Ordination triplots including the

environmental variables, CSS samples and 29 bacterial species were used to explain our data. A dendrogram analysis of the DGGE fingerprints was constructed based on the Dice similarity coefficient using unweighted pair group method clustering with the Quantity One software.

3 Results and Discussion

29 dominant bands were isolated successfully for DGGE sequencing. From the bands quantity, location and grey degree on the DGGE gel, the microbial community structure difference was detected.

Figure 1 presented the DGGE profiles hierarchical cluster analysis of different sludge samples calculated by Dice similarity and showed the similarities among different samples. The sludge samples with SA seepage showed more similarity to that with AMD seepage condition at Time1. The sludge samples at start point (SP) showed less similarity to others.

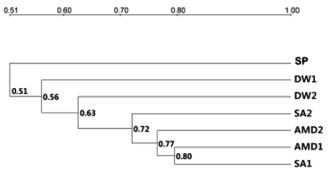

Fig. 1. Dendrogram representation of the DGGE profiles hierarchical cluster analysis. The bold letters represented different CSS samples at Time1 (T1) and Time2 (T2) under different seepage conditions.

In total, from the GenBank analysis, 29 clones matched the similar strains. And the phylogenetic tree analysis was presented in Fig. 2. Among the 29 similar strains, 72.4% belonged to *Firmicutes*, 13.8% belonged to *Actinobacteria*, 10.3% belonged to *Proteobacteria*, 3.5% belonged to *Bacteria, Candidatus Saccharibacteria*.

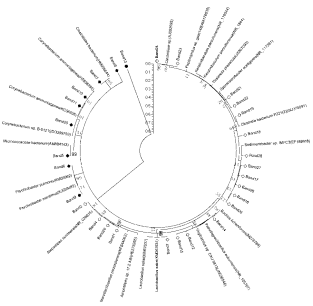

Fig. 2. Phylogenetic tree of DGGE sequences obtained from 16S rDNA amplification fragments

Bacteria in *Firmicutes* were Gram-positive, having thicker cell wall and Peptidoglycan layer, lower G + C content. Most could produce endospores, which resisted to water shortages and extreme environmental conditions, such as higher heavy metals content and lower pH degree, thus could adapt to the harsh environment better. It's a reason that *Firmicutes* occupied 72.4% of 29 strains in the seepage conditions. Rodrigues et al. [6] used 16S rDNA sequencing to analyze the bacterial communities in a Brazilian copper mine soil samples and found bacteria in *Firmicutes* dominate in the slope soil samples. The results of Sauvain et al. [7] inferred the potential role for transport and deposition of trace metals in lake sediments to endospore-forming *Firmicutes*.

Bacteria in *Actinobacteria* were Gram-positive, having higher G + C content. Most of them had the substrate mycelium and aerial hypha, and could produce spores. Most of these bacteria were Saprophytes, widely distributed in soil, generally aerobic. *Actinomycetes* were capable of producing antibiotics, which accounted for 56% of more than 2000 kinds of antibiotics discovered in the world. They were popular in the mine. Research showed that microbial antibiotic resistance was often coupled with microbial resistance to high concentrations of heavy metal ions [8]. And this kind of bacteria, often populated in the acidic ecosystem, might have special ways deal with heavy metals [9]. The research of Luo et al. [10] indicated that *Actinobacteria* and *Firmicutes* were positively correlated with As and Sb concentration in an As and Sb contaminated mine field by metagenomic method.

Proteobacteria was the largest group of the bacteria, including many pathogens, such as *Escherichia coli, Salmonella* and *Helicobacter*, also containing a lot of nitrogen-fixing bacteria. Bacteria in *Proteobacteria* were all Gram negative, whose outer membrane mainly composed of lipopolysaccharides. *Proteobacteria* had many types of metabolism, most of which were obligate or facultative anaerobic and heterotrophic. Some species could store energy through photosynthesis, because of purple pigments, which were known as purple bacteria. Based on rRNA sequences, *Proteobacteria* could be classified into five categories —*α-Proteobacteria*, *β-Proteobacteria*, *X-Proteobacteria*, *δ-Proteobacteria* and *ε-Proteobacteria*.

Batacteria in *Proteobacteria* played an important role in the degradation of pollutants, in which most of the species were saprophytic heterotrophic bacteria and, in addition, also included a lot of ammonia-oxidizing bacteria, nitrite-oxidizing bacteria and denitrifying bacteria. Islam et al. [11] researched the microbial diversity in Uranium mine, India, by PCR-DGGE, and found *Proteobacteria* bacteria was one of the predominant groups in the site of high Total Organic Carbon and different content of heavy metals, U, Cu, Cr, Zn, etc. The research of Zhan et al. [12] indicated that in a copper mine tailings during ecological restoration periods, *Proteobacteria* bacteria were the main free-living nitrogen-fixing microorganisms.

Among 29 strains, there were 12 families: *Carnobacteriaceae*, 17.2% of the total, *Bacillaceae*, 10.3%, *Clostridiales Family XI. Incertae Sedis*, 17.2%, *Clostridiales*, *Clostridiaceae*, 13.8%, *Lactobacillaceae*, 3.4%, *Peptoniphilaceae*, 3.4%, *Ruminococcaceae*, 6.9%; *Micrococcineae*, 3.4%, *Corynebacteriaceae*, 10.3%, *Moraxellaceae*, 6.9%, *Caulobacteraceae* and one uncertain family bacteria, 3.4% individually; and there were 19 Genus: *Alkalibacterium*, *Atopostipes*, *Marinilactibacillus*, *Pseudogracilibacillus*, *Bacillus*, *Virgibacillus*, *Sedimentibacter*, *Sporanaerobacter*, *Tissierella*,

Clostridia, *Keratinibaculum*, *Lactobacillus*, *Peptoniphilus*, *Ruminiclostridium*, *Micrococcaceae*, *Corynebacterium*, *Psychrobacter*, *Brevundimonas*, one uncertain Genus.

Candidatus Saccharibacteria Phylum known as *TM7 phylum sp. canine oral taxon 237* in this study, was very popular in the wastewater, sludge, soils, animals and many sources human related. TM7 phylum was only described in the 16S rRNA gene sequence and genome data. And a lot needed us to enrich the knowledge of this enigmatic group [13].

As shown in Fig. 3, at the start point of seepage, *Clostridiales* dominated in the CSS samples and its relative abundance was 39.69%. At T1 (41st seepage day), under DW seepage condition, *Clostridiales* dominated in the CSS samples with the relative abundance of 34.17%; under SA seepage condition, *Clostridiales* dominated; under AMD seepage condition, *Clostridiales* dominated in the CSS sample and its relative abundance was 41.86%. At T2 (75th seepage day), under DW seepage condition, *Carnobacteriaceae* dominated in the CSS samples with the relative abundance of 43.54%; under SA seepage condition, *Clostridiales* dominated; under AMD seepage condition, *Clostridiales* also dominated in the CSS sample and its relative abundance was 35.42%. Chen et al. [14] researched the microbial community diversity by pyrosequencing analysis in a simulated experiment of natural pyrite oxidative dissolution which could produce AMD. The results showed at the early stage, a newly proposed genus, *Tumebacillus* dominated in the system; at the middle stage, *Alicyclobacillus* dominated while *Tumebacillus* was the 2nd abundant population; in the end, *Ferroplasma* dominated while its the 10th at the early stage.

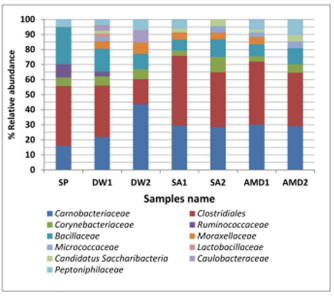

Fig. 3. Relative abundances (%) of dominant lineages in different CSS samples at Time1 (T1) and Time2 (T2) under different seepage conditions

According to Zhang et al. [2], the heavy metals potential mobility decreased at T2 compared to that at T1 in the CSS samples under the synthetic AMD seepage condition. That was, the environmental risk of combination between CSS and synthetic AMD was the lowest.

pH in the CSS samples at SP was 6.35, however, that under DW seepage condition at T1 was 6.91, at T2 that also was 6.91. Under the seepage condition of SA, pH was

5.82 and 5.80 respectively at T1 and T2. And under AMD seepage conditions, pH was 5.85 and 5.80 at T1 and T2 respectively. It indicated that the acid buffer capacity in the CSS functioned.

Redundancy analysis (RDA) on the influences between environmental factors (pH and heavy metals potential mobility in the CSS samples) and microbial community structure diversity or the different CSS samples as a whole was shown in Fig. 4. The results indicated that, through Monte Carlo permutation tests, all axis were significant ($P < 0.01$). First two axes of RDA plot represented 45.9% and 21.2% of the total variance of the DGGE data respectively with accordance to high species-environment correlation values: 0.921 for axis 1 and 0.931 for axis 2. The axis 1 had negative relations to the potential mobility of Cd and Cu while positive relations to the potential mobility of Fe, Zn and to pH. The axis 2 had negative relation to the Fe and Ni while had positive relations to the potential mobility of Cu, Zn and to the pH. Liu et al. [15] researched the microbial diversity patterns affected by the extreme and different geochemical environmental factors in the copper tailings impoundment which produced AMD. And the results showed that the microbial diversity patterns had significantly correlation with pH; the simplest microbial diversity pattern was with the extreme acidic condition; the microbial diversity was more complicated in the neutral environmental condition. Kuang et al. [16] researched 59 microbial communities in variable AMD sites of Southeast China by a bar-coded 16S rRNA pyrosequencing technology. The results also showed pH was the key environmental factor which affected the microbial community structures and linage abundance. Chen et al. [17] found Proteobacteria-related sequences dominated primary tailings, slightly acidic tailings and extremely acidic tailings while Ferroplasma-related sequences dominated extremely acidic tailings and orange-coloured oxidized tailings with relative abundance ranging from 28% to 58%. Our results also showed this trend, however, it was affected by the different heavy metals potential mobility.

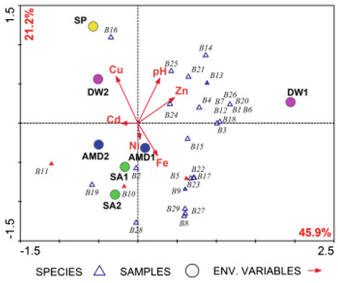

Fig. 4. RDA triplot analysis based on binary data of bacterial community structure diversity, CSS samples and environmental factors in the CSS. The arrows indicated the direction of maximum correlation, and the length of the arrow reflected the strength of the correlation.

4 Conclusions

The results indicated that *Clostridiales*, *Bacillaceae* and *Carnobacteriaceae* dominated in the CSS samples ranged from 46.26% to 10.25%. RDA on the influences of environmental factors showed that the bacteria such as *Carnobacteriaceae*, *Bacillaceae*, *Clostridiales Family XI. Incertae Sedis*, *Clostridiaceae*, *Lactobacillaceae*, *Peptoniphilaceae*, *Ruminococcaceae*, *Moraxellaceae*, *Caulobacteraceae*, *Corynebacteriaceae* had positive relation to Zn potential mobility and pH; *Carnobacteriaceae*, *Bacillaceae*, *Clostridiales Family XI. Incertae Sedis*, *Clostridiaceae*, *Micrococcineae*, *Moraxellaceae*, uncertain family bacteria (Band 8) had positive relation with Fe potential mobility; *Carnobacteriaceae*, *Clostridiaceae*, *Corynebacteriaceae* had positive relation to Cd and Ni potential mobility; and that *Ruminococcaceae* had positive relation to Cu potential mobility.

Acknowledgements. The research was supported by the Doctoral Program of Higher Education of China (No. 20110211110025) and the Natural Science Foundation of Gansu Provincial Science & Technology Planning Project, China (No.18JR3RA222).

References

1. Wang B, Zhang H, Fan Z et al (2010) Compacted sewage sludge as a barrier for tailing impoundment. Envir Earth Sci 61:931–937
2. Zhang H, Zhang Q, Yang B, et al (2014) Compacted sewage sludge as a barrier for tailings: the heavy metal speciation and total organic carbon content in the compacted sludge specimen. Plos One 9(6):e100932
3. Lottermoser B (2007) Mine wastes-characterization, treatment, environmental impacts, 2nd Edition, Springer Heidelberg, New York
4. Vera M, Schippers A, Sand W (2013) Progress in bioleaching: fundamentals and mechanisms of bacterial metal sulfide oxidation-part A. Appl Microb Biotech 97:7529–7541
5. Paul D, Pandey G, Pandey J et al (2005) Accessing microbial diversity for bioremediation and environmental restoration. Trends Biotech 23:135–142
6. Rodrigues V, Torres T, Ottoboni L (2014) Bacterial diversity assessment in soil of an active Brazilian copper mine using high-throughput sequencing of 16S rDNA amplicons. Antonie Van Leeuwenhoek Inter. J Gen Mole Microb 106:879–890
7. Sauvain L (2014) Bacterial communities in trace metal contaminated lake sediments are dominated by endospore-forming bacteria. Aquatic Sci 76:S33–S46
8. Seiler C, Berendonk T (2012). Heavy metal driven co-selection of antibiotic resistance in soil and water bodies impacted by agriculture and aquaculture. Frontiers Microb 3(69):399
9. Remenar M (2014) Actinobacteria occurrence and their metabolic characteristics in the nickel-contaminated soil sample. Biologia 69:1453–1463
10. Luo J, Bai Y, Liang J, et al (2014) Metagenomic approach reveals variation of microbes with arsenic and antimony metabolism genes from highly contaminated soil. Plos One 9(10): e108185
11. Islam E, Paul D, Sar P (2014) Microbial diversity in uranium deposits from Jaduguda and Bagjata uranium mines, India as revealed by Clone Library and Denaturing Gradient Gel Electrophoresis analyses. Geomicrob J 31: 862–874

12. Zhan J, Sun Q (2011) Diversity of free-living nitrogen-fixing microorganisms in wastelands of copper mine tailings during the process of natural ecological restoration. J Environ. Sci.-China 23: 476–487
13. Ferrari B, Winsley T, Ji M, et al (2014) Insights into the distribution and abundance of the ubiquitous candidatus saccharibacteria phylum following tag pyrosequencing. Sci. Rep. 4 (2):3957
14. Chen Y (2014) Biogeochemical processes governing natural pyrite oxidation and release of acid metalliferous drainage. Environ Sci Tech 48: 5537–5545
15. Liu J (2014) Correlating microbial diversity patterns with geochemistry in an extreme and heterogeneous environment of mine tailings. App Environ Microbiol 80: 3677–3686
16. Kuang J (2013) Contemporary environmental variation determines microbial diversity patterns in acid mine drainage. ISME J 7:1038–1050
17. Chen L (2013) Shifts in microbial community composition and function in the acidification of a lead/zinc mine tailings. Environ Microbiol 15: 2431–2444

Enriching Indigenous Ureolytic Bacteria in Coastal Beach Sand

Yi-Jie Wang, Xiao-Le Han, and Ning-Jun Jiang(✉)

Department of Civil and Environment Engineering,
University of Hawaii at Manoa, Honolulu, HI 96822, USA
jiangn@hawaii.edu

Abstract. In this study, a series of enrichment tests were conducted to investigate the effectiveness of two enriching media on the indigenous ureolytic bacteria in Hawaiian coastal beach sand. Sand collected from the intertidal zone of the Kailua Beach was used in the study, which was subjected to the erosion action of wave and tide periodically. Two media applied were YE (yeast extract only) and YEU medium (yeast extract with urea). Shaking incubation test was conducted up to 72 h to stimulate the indigenous ureolytic bacteria. The pH, ammonium concentration, ureolytic activity, and viable bacterial colony number of the enriched bacterial solution were measured at 6 h, 12 h, 24 h, 48 h and 72 h respectively. Results show that the primary stimulation occurred within the first 48 h. The concentration of ammonium ions and ureolytic activity were significantly increased and the viable bacterial colony number was slightly decreased at the end of the enrichment. These observations indicate that the ureolytic bacteria resided in the intertidal zone can be enriched effectively.

Keywords: Ureolytic bacteria · Coastal erosion · Enrichment ureolytic activity

1 Introduction

Coastal erosion is a common problem along the shoreline areas worldwide, which has an impact on 70% of the Earth's sandy beach environment [1]. The runup elevations of waves and the morphology of the fronting beach are the two important factors that may cause the coastal erosion [2]. According to recent studies [3, 4], Coastal erosion has a globally devastating impact on community life and can be induced by various ecological and physical factors. Therefore, it is necessary to develop an efficient way to mitigate the coastal erosion.

Based on the origins of coastal erosion, different erosion control methods have been developed. Artificial beach nourishment method has been applied for decades, which can offer protection against storms and beach erosion [5]. Some other geotechnical methods are also utilized such as geotextile tube technology [6], coastal cells [7] and massive sea block system [8]. However, these methods are limited in scope and difficult to maintain a sound ecosystem. Some researchers also attempt to mitigate erosion using ecological-based methods [9, 10], though their effectiveness in short-term is questionable.

© Springer Nature Singapore Pte Ltd. 2019
L. Zhan et al. (Eds.): ICEG 2018, ESE, pp. 340–347, 2019.
https://doi.org/10.1007/978-981-13-2227-3_42

Ureolytic-driven bio-cementation has been studied in civil and environmental engineering in recent years [11–14]. It involves the hydrolysis of urea by urease enzyme produced by ureolytic bacteria. When calcium is available, calcium carbonate precipitation is generated, which can cement granular coastal sand particles. Ureolytic-driven bio-cementation can be achieved through either exogenous bio-augmentation or indigenous bio-stimulation. Since introducing exogenous microorganisms may threat the local environment and ecosystem, the indigenous bio-stimulation method is preferred for the sensitive coastal environment.

In this study, efforts were taken to stimulate indigenous ureolytic bacteria capable of inducing bio-cementation from coastal beach sand. Both selective and generic media was used to facilitate the enrichment. Shaking incubation tests were conducted by mixing the beach sand (1 g) with the enrichment media (50 mL). The pH, ammonium concentration, ureolytic activity, and viable bacterial colony number of the enriched bacterial solutions were measured.

2 Materials and Methods

2.1 Soil and Enrichment Media

In this study, the calcareous sand was sourced from the intertidal zone of the Kailua beach, on the east shore of the O'ahu Island, Hawaii. Twigs, roots and shells were immediately removed. The collected soil samples were stored at 4 °C prior to use, as most microorganisms are able to maintain their activities at this temperature. The particle size distribution of the beach sand is shown in Fig. 1. One gram of sand was used for each test.

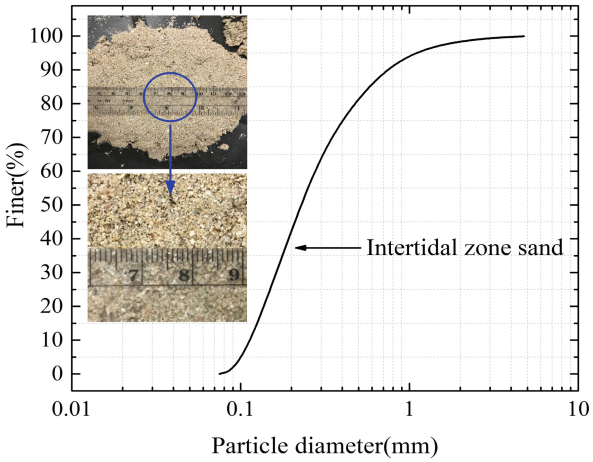

Fig. 1. Particle size distribution curve for intertidal zone sand

Two media prepared in this test were YEU and YU. YEU (20 g yeast extract, 170 mM urea dissolved in 1 L distilled water) was a selective medium, which was reported to be able to effectively stimulate ureolytic bacteria [15]. YE (20 g yeast extract dissolved in 1 L distilled water) was a generic medium, which could support most non-fastidious bacteria. Raw chemicals were autoclaved at 121 °C, 17–20 psi for 35–40 min before used to prepare the enrichment media.

2.2 Shaking Incubation Test for Indigenous Bacteria Enrichment

The shaking incubation test was conducted at 30 °C ambient temperature under aerobic condition inside conical-bottom centrifuge tubes (50 mL). A tiny hole was drilled on the centrifuge tube cap to allow air circulation. Fresh coastal beach sand (1 g) was firstly mixed with the enrichment medium (50 mL) and then subjected to horizontal shaking at 200 rpm in a shaking incubator for 72 h. The test was conducted in triplicate to ensure the results were reliable.

2.3 Testing Measurements

During the shaking incubation tests, the pH, concentration of ammonium, ureolytic activity, and viable bacterial colony number of the enriched bacterial solution were measured at 6 h, 12 h, 24 h, 48 h, and 72 h, respectively. Traceable® handheld pH and EC meters were used to measure the solution pH and EC by inserting the probes into the supernatant. The probes were disinfected by 70% ethanol prior to the measurement. The ureolytic activity was determined by the increase of EC value measured at the 1st and 9th minute after 1 mL enriched bacterial solution was mixed with 9 mL urea solution (1.5 M). The ammonium concentration of the enriched bacterial solution was determined spectrophotometrically by a modified Nessler Method [16]. The number of viable bacterial colonies was measured by the plate counting method. The enriched bacterial solution (100 μL) was spread on the solid YE agar medium (20 g yeast extract, 15 g agar in 1 L distilled water) inside the petri dish and then incubated overnight for counting.

3 Results and Discussion

3.1 pH

The pH is an indication of the acidity of the enriched bacterial solution. The variations of pH of the two enriched bacterial solutions with time are shown in Fig. 2. In general, pH change was divided into three stages, as marked in the graph. Within the first 12 h (stage 1), pH dropped from 7.7 to 7.3 for YEU and from 6.9 to 6.4 for YE. This was due to the bacterial respiration process in the enrichment solution. The main byproduct of aerobic respiration from bacteria was carbon dioxide, which led to the decrease of pH when dissolved in the water. The respiration process was also verified by the viable bacterial colony number results, which will be discussed later.

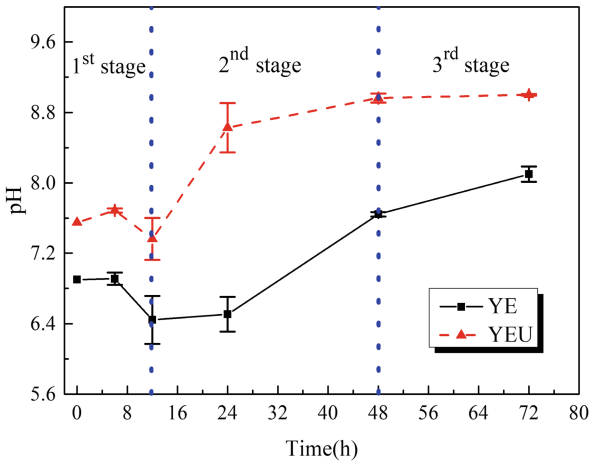

Fig. 2. Variation of pH with time

For the YE medium, the pH increased from 6.4 to 8.1 at stage 2 and 3, which was attributed to the degradation process (the breakdown of organic nitrogenous compounds from yeast extract by microorganisms). In this process, ammonium was excreted as a waste product, which led to the increase.

For the YEU medium, pH increased from 7.3 to 9.0 at stage 2 and 3, which was attributed to the combined effects of the respiration, degradation and ammonification process. The ammonification process could be demonstrated by the following chemical reaction (Eq. (3.1)).

$$CO(NH_2)_2 + 2H_2O \rightarrow 2NH_4^+ + CO_3^{2-} \tag{3.1}$$

3.2 Ammonium Concentration

The variations of ammonium concentration ($c[NH_4^+]$) of the two enriched bacterial solutions with time are presented in Fig. 3. At all the time, compared with the YE medium, $c[NH_4^+]$ of the YEU enriched bacterial solution was approximately 3 to 4 times larger.

More specifically, $c[NH_4^+]$ increased marginally from 0.5 mM to 3.4 mM for the YE medium and from 2.9 mM to 22 mM for the YEU medium at stage 1 (0–12 h). At stage 2 (12–48 h), $c[NH_4^+]$ increased dramatically to 101 mM and 284 mM, respectively. The increase for the YE bacterial solution was caused by the degradation process, while urea hydrolysis accounted for the sharp increase in the YEU bacterial solution. At stage 3 (48–72 h), the uptrend gradually slowed down, which was due to the stagnation of bacteria growth (in both YE and YEU) and the depletion of urea (only YEU).

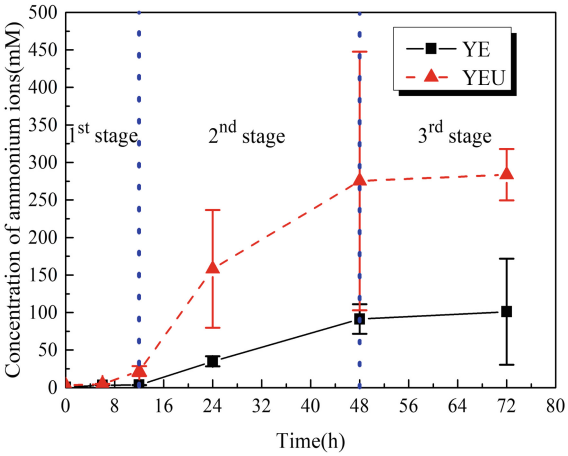

Fig. 3. Evolution of concentration of ammonium ions with time

3.3 Ureolytic Activity

The hydrolysis of urea liberated ions from non-ionic substrates (see Eq. (3.1)), which can lead to the increase of EC and the rate at which EC increases was proportional to the solution ureolytic activity. A calibration curve was made to converse the EC value (μS) to the amount of completed hydrolyzed urea(mM) [15]. The ureolytic activity of the two enriched bacterial solutions was shown in Fig. 4. A slight increase in the ureolytic activity at stage 1 was observed in the YEU enriched bacterial solution which was followed by a significant increase at stage 2, indicating massive urease enzyme production. Nevertheless, such increase slowed down after 48 h because of the depletion of urea and stagnation of bacteria growth, which was in accord with the pH and c[NH_4^+] results. Compared with the YEU enriched bacterial solution, there is little build-up of ureolytic activity in the YE bacterial solution at all stages, suggesting few ureolytic bacteria were enriched when the generic YE medium was used.

3.4 Viable Bacterial Colony Number

Viable bacterial colony number was obtained through the plating counting method in this study. It is a more accurate method to estimate actual live bacteria number while the optical density method (OD_{600}) only gives total number of both live and dead bacteria. The variations of viable bacterial colony number is shown in Fig. 5. In both enrichment media, the colony amount was around 3×10^6 cfu per gram soil initially but went up to 6×10^9 cfu per gram soil at 24 h. This phenomenon indicated that most bacteria reproduced from the beginning of the stage 1 to the middle of the stage 2. Accordingly, the decrease of pH in this stage was mainly resulted from the respiration process.

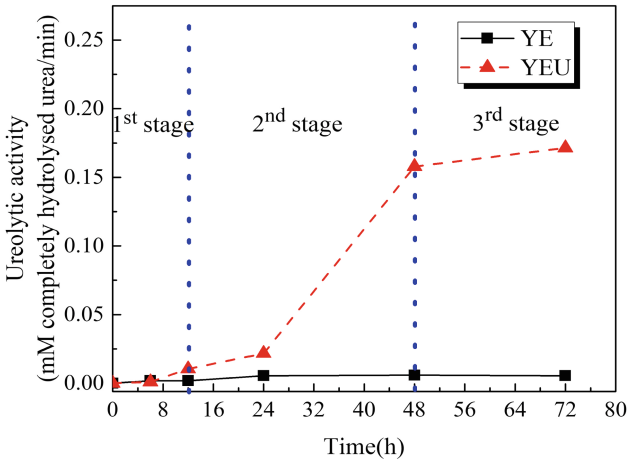

Fig. 4. Variations of ureolytic activity with time

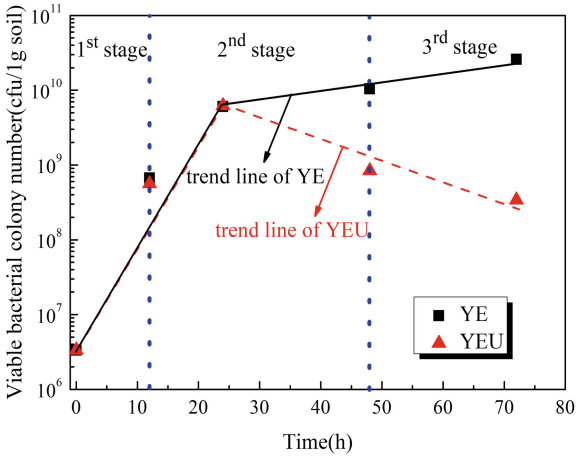

Fig. 5. Variation of viable bacterial colony number with time

From 24 h to the end of the test, a decrease from 6×10^9 to 3.4×10^8 of viable bacterial colony number was observed in the YEU enriched bacterial solution. This was because that the alkaline condition caused by the hydrolysis of urea inhibited further reproduction of ureolytic bacteria. For the YE medium, the general culture media could support the growth of most bacteria. Without the potential inhibition effect as the YEU medium, the number continued rising at a relatively slow rate at the stage 2 and 3.

4 Conclusion

The following conclusions can be drawn from this study

(1) In the presence of the YEU medium (a selective medium), the ureolytic bacteria can be stimulated significantly. The YE media is not effective at stimulating ureolytic bacteria. The enrichment process can be divided into three stages: 0–12 h, 12–48 h, and 48–72 h. The primary stimulation occurred at the late first stage and the second stage.
(2) The pH dropped slightly at stage 1 which was ascribed to the bacterial respiration and then increased significantly at stage 2 and 3 because of the degradation and ammonification process.
(3) The ureolytic activity increased marginally at stage 1 and then followed by a significant increase at stage 2, indicating that massive urease enzymes were produced during the second stage.
(4) The viable bacterial colony number reflected the amount of the enriched bacteria in the solution. It increased simultaneously from 0 to 24 h for both YE and YEU. A decrease was observed for YEU after 24 h, while the number continued increasing slowly for YE.

References

1. Bird ECF (1985) Coastline changes. a global review. Wiley, Chichester
2. Ruggiero P, Komar PD, McDougal WG, Marra JJ, Beach RA (2001) Wave runup, extreme water levels and the erosion of properties backing beaches. J Coast Res 17(2):407–419
3. Fletcher CH, Romine BM, Genz AS, Barbee MM, Dyer M, Anderson TR, Richmond BM (2011) National assessment of shoreline change: historical shoreline change in the Hawaiian Islands. Director 51(3):ix–xvi(8)
4. Romine BM, Fletcher CH, Barbee MM, Anderson TR, Frazer LN (2013) Are beach erosion rates and sea-level rise related in Hawaii. Global Planet Change 108:149–157
5. Finkl CW (1981) Beach nourishment, a practical method of erosion control. Geo-Mar Lett 1(2):155
6. Shin EC, Oh YI (2007) Coastal erosion prevention by geotextile tube technology. Geotext Geomembr 25(4–5):264–277
7. Van Rijn LC (2011) Coastal erosion and control. Ocean Coast Manag 54(12):867–887
8. Wheeler JL (1992) U.S. Patent No. 5,129,756. Washington, DC: U.S. Patent and Trademark Office
9. Gedan KB, Kirwan ML, Wolanski E, Barbier EB, Silliman BR (2011) The present and future role of coastal wetland vegetation in protecting shorelines: answering recent challenges to the paradigm. Clim Change 106(1):7–29
10. Meyer DL, Townsend EC, Thayer GW (1997) Stabilization and erosion control value of oyster cultch for intertidal marsh. Restor Ecol 5(1):93–99
11. Mortensen BM, Haber MJ, DeJong JT, Caslake LF, Nelson DC (2011) Effects of environmental factors on microbial induced calcium carbonate precipitation. J Appl Microbiol 111(2):338–349

12. Jiang NJ, Yoshioka H, Yamamoto K, Soga K (2016) Ureolytic activities of a urease-producing bacterium and purified urease enzyme in the anoxic condition: implication for subseafloor sand production control by microbially induced carbonate precipitation (MICP). Ecol Eng 90:96–104
13. Jiang NJ, Soga K, Kuo M (2016) Microbially induced carbonate precipitation for seepage-induced internal erosion control in sand–clay mixtures. J Geotech Geoenvironmental Eng 143(3):04016100
14. Keykha HA, Asadi A, Huat BB, Kawasaki S (2018) Microbial induced calcite precipitation by Sporosarcina pasteurii and Sporosarcina aquimarina. Environ Geotech, 1–5
15. Whiffin VS (2004) Microbial $CaCO_3$ precipitation for the production of biocement (Doctoral dissertation, Murdoch University)
16. Greenberg AE, Clesceri LS, Eaton AD (1992) Standard methods for the examination of water and wastewater, 18th edn. EPS Group. Inc., Hanover, Maryland

Influence of Physical and Biochemical Composition of Three Cellulose Fibers on Cracking of Soil

Rishita Boddu[1,2], Min Hong[1], Yongkang Deng[1], Fengjiao Chen[1], Ankit Garg[1], Sanandam Bordoloi[1], and Viroon Kamchoom[3(✉)]

[1] Shantou University, Guangdong, China
[2] Mahindra École Centrale, Hyderabad, India
[3] Faculty of Engineering, King Mongkut's Institute of Technology Ladkrabang, Bangkok 10520, Thailand
viroon.ka@kmitl.ac.th

Abstract. Different soil improvement techniques have been used to intensify the engineering properties of soil. Three different lignocellulose fiber-reinforced (jute, coir and water hyacinth (WH)) have been explored on the desiccation potential of compacted clayey silt coil. The experimental methodology involved the mixing of fibers with soil at requisite amount and subjecting them to natural environment with controlled irrigating. The controlled irrigation comprised of 15 wetting/drying cycles for 105 days. Parameters like matric suction and water content were focused upon and recorded along with the surface crack formation. The data obtained from the field experiments were analyzed using the Artificial Neural Network (ANN) approach, which is developed in house using C++ language. From the analysis, it can be comprehended that coir is more effective as a reinforcement due to its multifilament nature and higher lignin content which is suitable in resisting crack formation. Further, optimization analysis and sensitivity analysis suggested mechanism of cracking for each fiber.

Keywords: Desiccation cracks · Lignocellulose fibers · Crack intensity factor Soil water retention · ANN

1 Introduction

The contribution of the environment friendly natural fibers as reinforcements in soil have a lot of potential in improving infrastructures, stability of soils as well as irrigation systems [1–3]. Determination of the influence of plant, tree and roots on the stability of earth slopes brought fiber reinforced soils into the spot light in 1970's [4]. Lignocellulose fibers have also been subjected to discussion as the idea of natural fibers was being improvised. Natural lignocellulose materials are suitable for temporary shallow soil reinforcement and soil erosion control in compacted earth structures. Desiccation cracks, which are measured by Crack Intensity Factor (CIF) have been analyzed by the addition of potential fibers [5–7].

Desiccation cracks could majorly affect the soil structures due to increase in infiltration rate and pore water pressure by preferential flows [8–10]. Desiccation cracks

© Springer Nature Singapore Pte Ltd. 2019
L. Zhan et al. (Eds.): ICEG 2018, ESE, pp. 348–355, 2019.
https://doi.org/10.1007/978-981-13-2227-3_43

prove to be highly necessary for the stability and seepage analysis of slopes. Studies have suggested the development of tensile stress by the formation of weak planes as the soil dries. The tensile stress is derived from matric suction which is a function of moisture content of soil, number and amplitude of drying/wetting cycles, soil mineralogy and compaction state [11–13]. Physical characteristics differ for each kind of fiber [6] and the mechanism of cracking which takes place in these fiber-reinforced soils is still not known. To improve and understand the knowledge of the occurrence of cracking, physical characteristics of fibers is used. The mechanism of cracking in fiber reinforced soil can give a deeper insight on improvement in theoretical model development.

The aim of this paper is to study mechanism of cracking in fiber reinforced soil by investigating and quantifying the interactive effects of CIF with soil-water retention properties like water content and matric suction. Artificial Neural Networks (ANN) approach is adopted as it has the ability to understand the simultaneous effects of water content and matric suction through analysis like sensitivity analysis, optimization analysis and uncertainty analysis. ANN code, developed in C++ language, is used to generate models to carry out the aforementioned analysis. Field monitoring studies are executed to verify this study experimentally.

2 Materials and Methods

2.1 Soil and Fibers

The natural fibers utilized for the experiments are lignocellulose materials as they have cellulose, lignin and hemicellulose biopolymers which primarily determines properties like tensile strength, bio-degradation resistance etc. [14]. Hence, determining their biochemical composition is of utmost importance and have been determined by procedures given by Jenkins (1930), TAPPI Test Methods (1996), Goering and Van Soest (1970) and ASTM E1755-01 (2007). According to IS-1670-(1991) and IS-2720-Part 3-(1980) tensile strength at breakage, elastic Young's modulus and specific gravity of tested fibers are determined. The Table 1 shown below depicts some physical and chemical properties of each fiber type which have been expressed in mean and standard error of mean. The soil used for the experimental procedure is taken from a local hill site located at Indian Institute of Technology (IIT) Guwahati, India. Application of various test procedures including ASM-D422-63-07, ASTM- D4318-10 and ASTM- D1557-15 on soil revealed that the soil contains 50% silt, 25% each of sand and clay. The shrinkage, plastic and liquid limits obtained were 19%, 24% and 42% respectively.

The soil has been classified as low plastic inorganic silt (ML) by unified soil classification system (USCS; ASTM D2487-11). The maximum dry density and optimum moisture content is 1650 kg/m^3 and 17% (by mass) according to standard Proctor's test (ASTM D1557). Other engineering properties of the soil have been listed in Table 1.

Table 1. Properties of soil and natural fibers

Soil Properties	Values
Specific Gravity	2.58
Grain Size Analysis (%)	
Coarse Sand (4.75mm-2mm)	0
Medium Sand (2mm-0.425mm)	7
Fine Sand (0.425mm-0.075mm)	19
Silt (0.075mm-0.002mm)	50
Clay (<0.002mm)	24
Consistency Limits (%)	
Liquid Limit	42
Plastic Limit	24
Shrinkage Index	21.30
Plasticity Index	18
Compaction Study	
Optimum Moisture Content (%)	17
Maximum Dry Density (g/cc)	1.69
Shear Parameters	
Cohesion (kPa)	16.40
Angle of Internal Friction	14.40°

	Properties	Coir	Jute	WH
Bio-chemical composition	Cellulose (%)	43.4	60	45.58
	Lignin (%)	38.3	15.9	11.3
	Hemicellulose (%)	14.7	22.1	21
	Ash (%)	2	1	11.20
Physical properties	Moisture content (%)	7	10	12
	Specific gravity (g/cc)	1.24	1.12	0.7
	Breaking tensile strength (MPa)	150	500	312.5
	Elongation at break (%)	26	10	13.6

2.2 Experimental Programme and Procedures

A schematic test setup has been depicted in Fig. 1. All the test soils were compacted in a Poly Vinyl Chloride (PVC) mold with diameter of 290 mm and height of 250 m as its dimensions. To prevent loss of soil particle, it was placed on a perforated base plate with a filter paper. All the test soils were compacted to 0.9MDD by the application of 60 kN vertical compaction force [15]. The final height of the sample was 170 mm and for each type of soil (unreinforced; reinforced by coir, jute and WH), three replicates were prepared (12 molds in total).

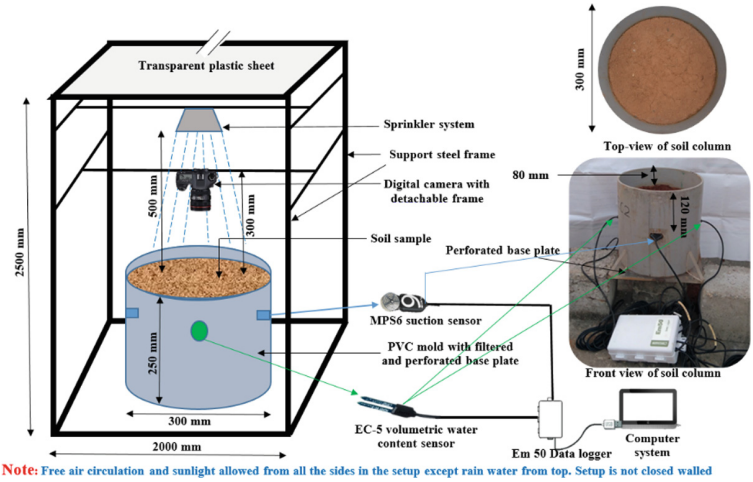

Fig. 1. Schematic representation of typical column set up containing soil mixed with fibers

The prepared samples were subjected to natural environment by being placed in an open steel frame with transparent roof for the entire monitoring period. Controlled irrigation was achieved by attaching a sprinkler system on top of the soil column. To facilitate the study of crack development patterns, a digital camera (model: Canon EOS 700d) with adjustable frame was installed on top of the soil column which is shown in Fig. 2. One MPS-6 sensor and one EC-5 sensor installed diametrically at 40 mm soil depth, were used to measure matric suction and water content respectively. A total of 15 drying cycles have been conducted in 105-day monitoring period.

2.3 Parameter Setting for ANN

70% of the data has been assigned to ANN for training, 15% for testing and 15% for validation. Models of CIF as a function of matric suction and water content for different types of soils (unreinforced; reinforced by coir, jute and WH) were developed using Statistica modelling program by an in-house developed code in ANN. For this approach, a three-layer feed forward neural network is employed.

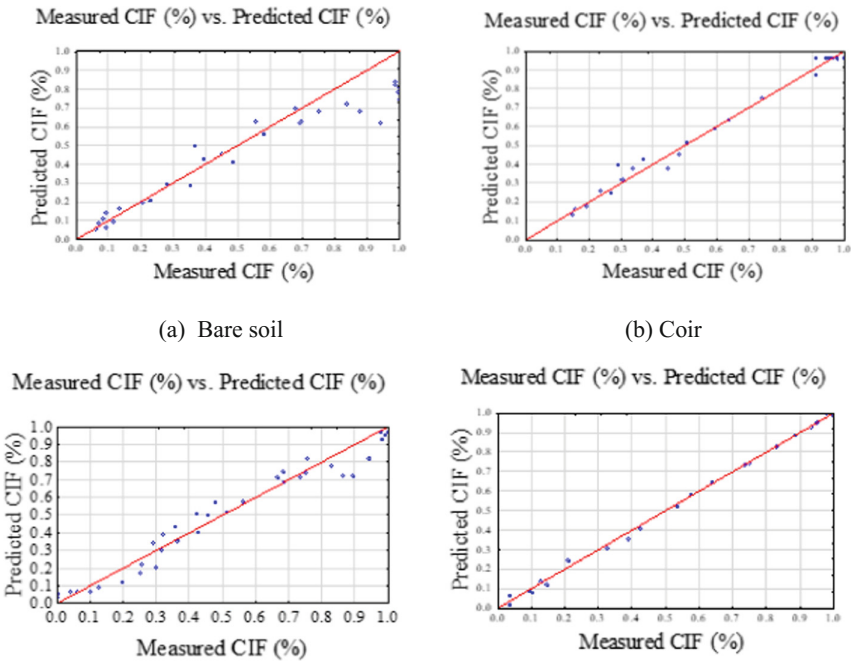

(a) Bare soil (b) Coir

(c) Jute (d) WH

Fig. 2. Performance analysis for CIF models on testing and training data

3 Results and Discussions

The Fig. 2 shown above represents the plots between training and testing data of CIF models generated by model development in ANN. The main purpose of performance analysis is to obtain a clear image of the accuracy of the model generated. It can be concluded that the normalized CIF models generated are reasonably accurate as the measured and computed values are similar.

3.1 3D Plots

As the fibers are added into the soil, the increase in influence of water content is expected to be seen. In Fig. 3, it can be also inferred that to obtain minimum CIF, the suction required in bare soil and jute soil is comparatively less than the other two. For minimum CIF, the threshold water content (normalized) is at 0.5 whereas for coir and WH fiber-reinforced soils, it is at 0.8 and 0.6 respectively. Coir has the ability to retain more water when it is mixed with soil and hence a high value of threshold water content is observed.

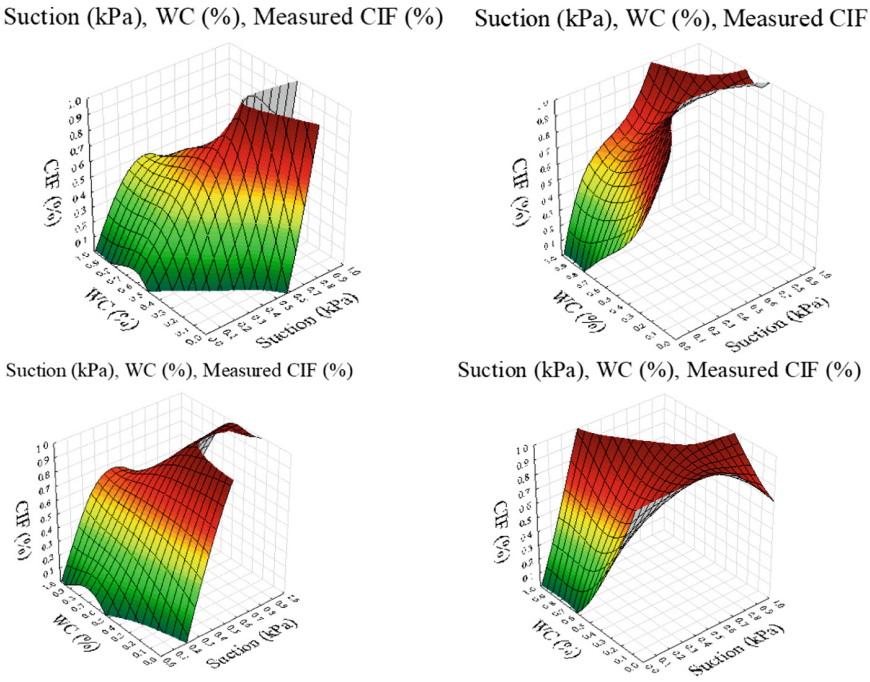

Fig. 3. 3D plots depicting the influence of matric suction and water content on CIF

3.2 Sensitivity Analysis

Sensitivity analysis provides accurate correlations between model parameters and even gives the effect of changing parameters when given a fitted model with model parameter for each predictor. The main parameters in this experiment include CIF, water content and matric suctions. Figure 4(a) shows the absolute values and Fig. 4(b) shows the percentages of the contributions of matric suction and water content. From Fig. 4(b), when bare soil and other fiber-reinforced soils are compared, it can be seen that there is significant increase in the water holding capacity of the soil when fibers are added to soil. This might be due to the fibers because they possess bio-polymers which have free hydroxyl group, through which, they absorb water molecules into the fiber [16].

As coir has the advantage of mobilizing its tensile strength as it is a multifilament fiber. This advantage plays a crucial role in coir's ability to resist crack formation [6]. Even though coir has a lower tensile strength than jute and WH, it is observed that the dependence of CIF on water content is the highest in the case of coir.

Networks	Sensitivity analysis Samples: Train, Test, Validation	
	Suction	WC
BARE	37	1
WH	4858	237
JUTE	2	2
COIR	265	4

(a)

Networks	Sensitivity analysis Samples: Train, Test, Validation	
	Suction (%)	WC (%)
BARE	99	1
WH	95	5
JUTE	71	29
COIR	99	1

(b)

Fig. 4. Sensitivity analysis showing contributions of suction, and water content to CIF

4 Conclusion

Lignocellulose materials have been extremely significant in improvising the soil-water retention properties of soil. The main aim of this paper is to examine the crack intensity factor (CIF) of bare soil and fiber-reinforced soils (reinforced with jute, coir and WH) with respect to matric suction and water content. These fibers showcase various properties like higher surface roughness and greater moisture absorption capacity, which are highly beneficial for various applications like slope stability etc. Field monitoring was carried out for 105 days which includes 9 drying/wetting cycles. This is followed by the creation of CIF models with respect to matric suction and water content using ANN.

Data obtained from experiments and analysis exhibit that the addition of lignocellulose materials to soils increases the soil water retention capacity significantly. This is likely due to the bio-polymer in each type of fiber which contain free hydroxyl groups. Results also show that coir reinforced soil has higher water retention capacity than jute or WH because of its porous nature. The sensitivity analysis reveals the mechanism of cracking in which the driving force (suction) and the resisting force (water content and tensile strength of fiber) play an important role. The 3D plots also suggest that coir is suitable to be used as cover material for slopes or as landfill cover because it provides the lowest cracking, However, various field monitoring studies are essential to strongly recommend the utilization of lignocellulose fiber-reinforced soils in slopes or landfill covers.

References

1. Anggraini V, Asadi A, Huat BB, Nahazanan H (2015) Effects of coir fibers on tensile and compressive strength of lime treated soft soil. Measurement 59:372–381
2. Pourakbar S, Asadi A, Huat BB, Fasihnikoutalab MH (2015) Stabilization of clayey soil using ultrafine palm oil fuel ash (POFA) and cement. Transp Geotech 3:24–35

3. Blasón S, Correia JAFDO, Apetre N, Arcari A, De Jesus AMP, Moreira PMGP, Fernández-Canteli A (2016) Proposal of a fatigue crack propagation model taking into account crack closure effects using a modified CCS crack growth model. Procedia Struct Integrity 1:110–117
4. Waldron LJ (1977) The shear resistance of root-permeated homogeneous and stratified soil 1. Soil Sci Soc Am J 41(5):843–849
5. Li X, Zhou W, Liu F, Zhu GZ, Shamsuzzoha M, Celler K, Shao YT (2017) About materials science. J Mater Res 32(12/28)
6. Bordoloi S, Garg A, Sreedeep S, Lin P, Mei G (2018) Investigation of cracking and water availability of soil-biochar composite synthesized from invasive weed water hyacinth. Bioresour Technol
7. Campbell CA, Biederbeck VO, Zentner RP, Lafond GP (1991) Effect of crop rotations and cultural practices on soil organic matter, microbial biomass and respiration in a thin Black Chernozem. Can J Soil Sci 71(3):363–376
8. Ahmad M, Lee SS, Lee SE, Al-Wabel MI, Tsang DC, Ok YS (2017) Biochar-induced changes in soil properties affected immobilization/mobilization of metals/metalloids in contaminated soils. J Soils Sediments 17(3):717–730
9. Krisnanto S, Rahardjo H, Fredlund DG, Leong EC (2014) Mapping of cracked soils and lateral water flow characteristics through a network of cracks. Eng Geol 172:12–25
10. Yesiller N, Miller CJ, Inci G, Yaldo K (2000) Desiccation and cracking behavior of three compacted landfill liner soils. Eng Geol 57(1–2):105–121
11. Costa S, Kodikara J, Shannon B (2013) Salient factors controlling desiccation cracking of clay in laboratory experiments. Géotechnique 63(1):18. https://doi.org/10.1680/geot.9.p.105
12. Cui YJ, Tang CS, Tang AM, Ta AN (2014) Investigation of soil desiccation cracking using an environmental chamber. Italian Geotechnical Journal. 1:9–20
13. Costa S, Kodikara J, Barbour SL, Fredlund DG (2017) Theoretical analysis of desiccation crack spacing of a thin, long soil layer. Acta Geotechnica 1–11. https://doi.org/10.1007/s11440-017-0602-9
14. Hearle JW, Morton WE (2008) Physical properties of textile fibers. Elsevier
15. Reddy BV, Jagadish KS (1993) The static compaction of soils. Geotechnique 43(2)
16. Pejic BM, Kostic MM, Skundric PD, Praskalo JZ (2008) The effects of hemicelluloses and lignin removal on water uptake behavior of hemp fibers. Bioresour Technol 99(15):7152–7159. https://doi.org/10.1016/j.biortech.2007.12.073

Methane Oxidizing Bacteria and Its Potential Application of Methane Emission Control in Landfills

Wenjing Sun[1,3], Xiaoyang Liu[1], and Xueping Chen[2,3](✉)

[1] Civil Engineering Department, Shanghai University, Shanghai 200444, China
[2] School of Environmental and Chemical Engineering, Shanghai University, Shanghai 200444, China
xpchen@shu.edu.cn
[3] Institute for the Conservation of Cultural Heritage, Shanghai 200444, China

Abstract. A large amount of methane gas released during the service of a landfill will not only cause the greenhouse effect, but it may also cause an explosion when the methane reaches a certain concentration in the air or soil. In the background of promoting energy conservation and environmental protection, it is of great significance to effectively reduce the methane release content in landfills, ensure the normal service of landfill and the safety of people's life and property. The mechanism of methane oxidation by methane oxidizing bacteria is reviewed and the factors affecting the efficiency of methane oxidizing bacteria to oxidize methane are analyzed in order to reduce the emission reduction of hazardous gases in the landfill and provide a reference for the design of other new landfills.

Keywords: Methane oxidizing bacteria · Landfill · Greenhouse effect
Emission reduction · Biodegradation

1 Research Background

After the second industrial revolution, the world economic level has been developed rapidly. The growing population has led to the continuous growth of solid waste. There are three basic technologies for solid waste treatment, namely landfill, composting and incineration, but landfill is still the first choice in many parts of the world.

Landfill gas may be released for a long time after the landfill is closed, which is produced by anaerobic degradation of organic matter in municipal solid waste and mainly composed of carbon dioxide, methane and some volatile organic compounds. Although the concentration of methane gas is lower than that of carbon dioxide, research shows that methane in the atmosphere is an important greenhouse gas second only to CO_2, with a contribution to the greenhouse effect of about 26% (Zheng 2013). It is estimated that the annual methane emission to atmosphere is between 0.5 billion and 0.6 billion tons. The amount of methane released annually by the landfill accounts for about 6%–12% of the total methane emission worldwide.

© Springer Nature Singapore Pte Ltd. 2019
L. Zhan et al. (Eds.): ICEG 2018, ESE, pp. 356–362, 2019.
https://doi.org/10.1007/978-981-13-2227-3_44

Methane is not only a greenhouse gas but also flammable and explosive. When the methane released in the landfill reaches a certain concentration in the air, it is very easy to cause a series of major accidents, such as the explosion and collapse of the landfill, even the casualties and property loss. For example, there have been 20 explosions and fires caused by methane in the United States, resulting in the tragedy of 5 deaths (Han et al. 2000). Therefore, in order to ensure the safe service of landfills and safety of the people's life and property, it is very necessary and urgent to apply methane oxidizing bacteria to the overlying layer of landfill to reduce the greenhouse effect caused by methane emission.

Because the establishment of methane collection system is expensive, especially for the old landfill, it is not economical to install the new gas gathering system. Some old landfill sites are not set up gas collection system. Even if a gas collection system is set up, the methane released by the landfill cannot be completely collected. In the methods of methane emission reduction, Methane oxidizing bacteria reduces methane content by biodegradation, which is considered to be an important global methane sink and plays a vital role in maintaining the relative stability of the global methane content. Studies show that 90% of methane can be oxidized by methane oxidizing bacteria before entering the atmosphere (Gupta et al. 2013). The oxidation efficiency of methane oxidizing bacteria is closely related to temperature, pH value, water content, density and depth of overburden and so on.

In conclusion, applying methane oxidizing bacteria to the landfill overlay can effectively reduce the greenhouse effect caused by methane emissions. According to the survival conditions of methane oxidizing bacteria, it is very important to control the indexes of the overlying soil and improve the efficiency of methane oxidation bacteria to degrade methane gas, which is of great importance to solve the environmental problems.

2 The Mechanism of Methane Oxidation and the Classification of Methane Oxidation Bacteria

Methane oxidizing bacteria are a class of bacteria with methane as the only carbon source and energy. According to the use of the oxygen in the environment as the electron acceptor, methane oxidizing bacteria can be divided into aerobic methane oxidizing bacteria and anaerobic methane oxidizing bacteria.

The mechanism of oxidation of methane by aerobic methane oxidizing bacteria is relatively complicated. It is believed that this approach can be divided into two stages: the first phase is activated by methane monooxygenase (MMO) to generate methanol by CH_4, and then methanol to formaldehyde; the second stage is mainly through the serine pathway or the monophosphate monophosphate pathway to assimilate methanol to the microbial biomass or to oxidize it to formic acid, and finally the formic acid is oxidized to CO_2 (Han 2008). Oxidation process is as follows

$$CH_4 \rightarrow CH_3OH \rightarrow HCHO \rightarrow HCOOH \rightarrow CO_2 \quad (1)$$

Figure 1 clearly describes the process of the two stages. In methane oxidizing bacteria cells, MMO is the first key enzyme to use methane. MMO oxidize methane to methanol under the action of molecular oxygen; methanol is oxidized to formaldehyde under the action of methanol dehydrogenase (MDH); then cells are synthesized through the serine cycle or pentose phosphoric acid pathway, and at the same time, the formaldehyde dehydrogenase (FADH) and the methylene dehydrogenase (FADH) are used. Under the action of formic dehydrogenase (FDH), formaldehyde is further oxidized to formic acid, CO_2 and H_2O, and to provide a reducible coenzyme NADH for cell metabolism (Han 2008). CO_2 is the final product of CH_4 deep oxidation.

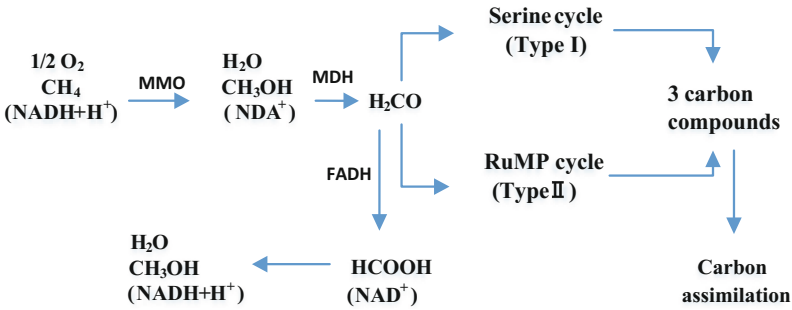

Fig. 1. Mechanism of methane oxidation by aerobic methane oxidizing bacteria (Han 2008)

$$CH_4 + 2O_2 \rightarrow 2H_2O + CO_2 \quad (2)$$

In quantitative terms, the methane of 1 mol will be oxidized by 2 mol oxygen to produce 1 mol carbon dioxide and 1 mol water.

As early as 1960s, some methane oxidizing bacteria had been found to oxidize methane under anaerobic conditions (Dunfield et al. 2007), but the mechanism of methane oxidation by anaerobic methane oxidizing bacteria is also complex. At present, there are three ways in the environment: anaerobic methane oxidation coupled with sulfate reduction, anaerobic methane oxidation coupled with nitrate reduction and anaerobic methane oxidation coupled metal ion reduction. Morn et al. (2008) also proposed a new methanogenic pathway: methylation pathway. The reaction process is expressed as follows:

$$CH_4 + 1/3HCO_3^- + 5/3H^+ + 4/3HS^- \rightarrow 4/3H_3CSH + H_2O \quad (3)$$

$$4/3H_3CSH + SO_4^{2-} \rightarrow 4/3HCO_3^- + 7/3HS^- + 5/3H^+ \quad (4)$$

That is, methane oxidizing bacteria uses HS^- and methane to form CH_3SH, and CH_3SH is used to produce HCO_3^- and HS by desulphurization bacteria (Moran et al. 2008).

In addition to methane oxidation, methane oxidizing bacteria can significantly reduce the concentration of organic compounds in landfill leachate, such as degradation of toxic halogenated hydrocarbons and polycyclic aromatic hydrocarbons in sewage. Therefore, from the point of view of industrial utilization and ecological protection, methane oxidizing bacteria is of great research value.

Bowman et al. (1993) divided methane oxidizing bacteria into Type I, Type II and Type X. Their difference lies in the different methods and ways of assimilating formaldehyde in bacteria. Type I assimilates formaldehyde by monophosphate pathway to assimilate formaldehyde as cell component; Type II uses serine pathway to assimilate formaldehyde as cell component; Type X is similar to Type I, and C assimilation by RuMP pathway (Bowman 1993). The methane oxidizing bacteria in the garbage samples can be classified as Methylocaldum, Methylobacterium and Methylocystis, and the dominant strains were Methylocaldum belonging to Type I (Zhang 2012). The following are several examples of methane oxidizing bacteria found in landfills (see Table 1).

Table 1. Methane oxidizing bacteria found in landfills

Type	Genus	Source	Literature
Type I	Methylocaldum	A municipal solid waste landfill site in Hebei province	Zhang et al. (2012)
Type II	Methylocystis	A municipal solid waste landfill in Hangzhou	Guo et al. (2008)
Type I	Methylobacter	A municipal solid waste landfill in Hangzhou	Yu et al. (2008)
Type II	Methylocystis	Landfill in Northern Germany	Gebert (2008)

3 Factors Affecting the Efficiency of Methane Oxidation by Methane Oxidizing Bacteria

The research shows that the physical properties of the landfills, such as temperature, moisture content and pH value, are very closely related to the efficiency of methane oxidation by methane oxidizing bacteria. Therefore, it is of great theoretical and practical significance to study the effects of different physical properties of the overburden on the methane oxidation capacity of methane oxidizing bacteria.

3.1 Water Content

The water content in the soil has a great influence on the activity of methane oxidizing bacteria. When the soil water content is low to a certain value, the metabolism of methane oxidizing bacteria will be reduced, and even the methane oxidizing bacteria will be dormant. Ding and Cai (2003b) found that the influence of water content on the

methane oxidation efficiency of methane oxidizing bacteria depends on the soil quality. Boeckx et al. (1996) described that the water content of the soil could change the permeability of the soil, thus affecting the efficiency of methane oxidation by methane oxidizing bacteria.

3.2 Thickness of Biological Cover Layer

Yang et al. (2010) studied the effect of the thickness of different biological cover layers on methane oxidation in the landfill and found that the efficiency of methane oxidation by methane oxidizing bacteria was different with the depth of the cover layer. From the economic ecological coupling benefit, the oxidation efficiency of methane was the best when the thickness of the landfill cover was 30 cm. The methane oxidation rate of 100% can be reached for a long time.

3.3 CH_4 Concentration and O_2 Concentration

During the service process of landfills, the concentration of methane released from landfills will be changed with the change of service life. Cai (2014) studied the efficiency of methane oxidation by methane oxidizing bacteria under different methane concentration in laboratory conditions. It is found that methane can be completely consumed by methane oxidizing bacteria in 12 h when CH_4 concentration is less than 5%. Methane oxidizing bacteria can still achieve better effects when methane concentration is high. It only takes a long time, for example, for methane with a concentration of about 20% and methane oxidizing bacteria can be eliminated more than 90% in 48 h. As for oxygen, Czepiel et al. (1996) found that the oxygen concentration had a significant effect on the rate of methane oxidation. When the oxygen concentration was below 3%, the rate of methane oxidation was basically zero, so the ideal oxidation rate of methane can only be achieved if a certain amount of oxygen is guaranteed.

3.4 Temperature and PH Value

The effect of temperature and pH value on the oxidation efficiency of methane is mainly manifested by affecting the activity of enzymes in methane oxidizing bacteria. As the monooxygenase of methane oxidizing bacteria is easily inactivated during the purification process, it is very difficult to study the response mechanism of methane oxidizing bacteria to temperature change. There are few reports on the mechanism of methane oxidizing bacteria (Ding and Cai 2003a). Although the studies are fewer, it is not difficult to find that the efficiency of methane oxidation by methane oxidizing bacteria increases in a certain temperature range, but when the temperature is too high, the activity of the monooxygenase will be reduced and even inactivated, thus the effect of methane oxidation will be affected. The pH value over high and low will reduce the activity of monooxygenase and even deactivate the enzyme, which will affect the oxidation efficiency of methane.

3.5 Nitrogen Source

Nitrogen source is essential for the growth and reproduction of methane oxidizing bacteria. Wang et al. (2003) described that the effect of inorganic nitrogen input on the oxidation of soil CH_4 depended on the type of methane oxidizing bacteria, the species and quantity of nitrogen, and the soil condition (Wang et al. 2003). The study of Fei and Wang (2008) and Wei (2015) found that the oxidation of methane to methane by methane oxidizing bacteria was inhibited when the concentration of nitrogen source was higher than a certain value.

It can be seen that there are many factors affecting the efficiency of methane oxidation. When methane oxidizing bacteria is used in landfill, the effects of various factors on the activity of methane oxidizing bacteria should be taken into consideration. Only in this way can the methane oxidizing bacteria be used to ensure the efficiency of methane oxidation.

4 Conclusion and Prospect

At present, the study of methane oxidizers is limited to the screening of bacteria in the laboratory and the study of the efficiency of methane degradation. However, considering the effects of vegetation coverage and the density of overburden, there are few examples of using methane oxidizing bacteria in landfills to achieve emission reduction.

In natural environment, landfill will be affected by natural conditions such as wind, sun and rain, and the physical properties of the overlying layer will be changed under the condition of dry and wet circulation, which will affect the activity of methane oxidizing bacteria. The research and engineering application of methane oxidizing bacteria will be promising on the basis of previous research if we control the density, pH value, water content and oxygen supply of the overlying soil and combine with the study of ecology.

If the real natural conditions are simulated in the laboratory and the cracking of the overlying soil is studied, to some degree, it can provide a theoretical analysis for the large scope of the methane oxidizing bacteria in the landfill. In addition, sensors are added to the landfill to monitor the methane concentration in the landfill in real time and take necessary measures to control it in time which may provide a new idea for the formulation of energy conservation and atmospheric protection schemes.

Acknowledgement. The authors are grateful to the support of Shanghai Key Innovative Team of Cultural Heritage Conservation, and the National Sciences Foundation of China (Grant No. 41572284).

References

Zheng SW, Tang W, Gu Y et al (2013) Estimation and control of methane emissions in landfills. Environ Sci Manag 38(7):45–49

Han HF, Jin MT, Chi CJ et al (2000) On applicable urban domestic refuse treatment technologies in China. Environ Pollut Prev 21(6):40–41

Han B (2008) Methanogenic bacteria, molecular ecology study on methanotrophs and fundermantal research on the applications ofmethanotrophs. Tsinghua University

Dunfield PF, Yuryev A, Senin P et al (2007) Methane oxidation by an extremely acidophilic bacterium of the phylum verrucomicrobia. Nature 450:879–882

Moran JJ, Beal EJ, Vrentas JM et al (2008) Methyl sulfides as intermediates in the anaerobic oxidation of methane. Environ Microbiol 10(1):162–173

Bowman JP (1993) Revised taxonomy of the methanotrophs: description of Methylobacter gen. nov. emendation of Methylococcus, validation of Methylosinus and Methylocystis species, and a proposal that the family Methylococcaceae includes only the group I methanotrophs. Int J Syst Bacteriol 43(4):735–753

Zhang W, Yue B, Huang QF et al (2012) Community analysis of methane oxidizing bacteria in municipal solid waste semi-aerobic landfill. Chin J Ecol Environ 8:1462–1467

Guo M, He PJ, Lv F et al (2008) Type II methanotrophs community structure in the cover soils of landfill. Chin Environ Sci 28(6):536–541

Yu T, He PJ, Lv F et al (2008) Effect of operational modes on community structure of type I methanotroph in the cover soil of municipal solid waste landfill. Environ Sci 29(10):2987–2992

Gebert J, Stralis-Pavese N, Alawi M, Bodrossy L (2008) Analysis of methanotrophic communities in landfill biofilters using. Environ Microbiol 10(5):1175–1188

Ding WX, Cai ZC (2003a) Mechanism of methane oxidation by methanotrophs and effect of soil moisture content on their activity. Chin J Eco-Agric 11(1):94–97

Boeckx P, Cleemput OV, Villaralvo I (1996) Methane emission from a landfill and the methane oxidizing capacity of its covering soil. Soil Biol Biochem 28(10–11):1397–1405

Yang WJ, Dong SK, Zhang XF et al (2010) Effect of bio-cover thicknesses on methane oxidation in landfill. Environ Pollut Prev 32(7):20–24

Cai CH (2014) Experimental study on performance and its influencing factors of methane degradation by methanotrophs. Henan Polytechnic University

Czepiel PM, Mosher B, Crill PM, Harriss RC (1996) Quantifying the effect of oxidation on landfill methane emissions. J Geophys Res-Atmos 101(D11):16721–16729

Ding WX, Cai ZC (2003b) Effect of temperature on atmospheric CH_4 oxidation in soils. J Ecol 22(3):54–58

Wang ZP, Hu CS, Yang JR (2003) Effect of inorganic nitrogen on CH_4 oxidation in soils. J Appl Ecol 14(2):305–309

Fei PA, Wang Q (2008) Analysis on the mechanism and influence factors of methane oxidation in landfill soil covers. Renew Energ 26(1):97–101

Wei WP, Deng H, Li GX et al (2015) Screening and culture condition of a type II methanotroph. Appl Environ Biol 21(3):455–463

Microbial Induced Solidification of Municipal Solid Waste Incineration Fly Ash

Guiwei Wang[1], Hui Xu[2(✉)], Xiaoqing Ding[2], Yanxu Gao[2], Ping Chen[2], and Xiufang Hu[1]

[1] College of Life Science, Zhejiang Sci-Tech University, Hangzhou 310018, People's Republic of China
[2] School of Civil Engineering and Architecture, Zhejiang Sci-Tech University, Hangzhou 310018, People's Republic of China
xuhui@zstu.edu.cn

Abstract. To investigate the applicability of microbial induced calcite precipitation (MICP) to the solidification of municipal solid waste incineration (MSWI) fly ash, the following work are carried out. Firstly, three ureolytic strains, UR1, UR2 and UR3, were isolated and identified as *Sphingobacterium cladoniae*, *Bacillus aryabhattai* and *Raoultella ornithinolytica*, respectively. Secondly, the fly ash samples were solidified by the above three strains, and the case with strain UR2 displayed largest unconfined compressive strength of 0.740 MPa. Lastly, heavy metal leaching test was carried out for the solidified samples. The immobilization ratios for Cu, Pb, and Cd were in the range of 41–77%. The case with UR1 displayed higher immobilization ratios for Cu, Cr, and Cd, and UR2 exhibited higher immobilization ratio for Pb. Overall, strains UR1 and UR2 provide promising use for the solidification of MSWI fly ash.

Keywords: MSWI fly ash · Heavy metal · Immobilization rate
Microbial induced calcite precipitation (MICP)

1 Introduction

In China, it is estimated that 200 million tons of municipal solid waste are generated annually since 2015, accounting for about 30% of the total world production. Municipal solid waste incineration (MSWI) is one of the most widely used methods, with 4 million tons fly ash produced annually. MSWI fly ash is a kind of hazardous waste due to that the pollutants (e.g., heavy metals) exceed the limits in the identification standard for hazardous wastes [1]. Therefore, fly ash is becoming a vital environmental problem remained to be solved.

MSWI fly ash can be treated in several ways, including chemical stabilization, cement solidification and thermal separation [2–4], but all of them are short of efficient technology, effective cost or friendly environment. Recently, microbial induced calcite precipitation (MICP) has a potential use for solidification of the fly ash and immobilization of the metals, because of its characterization of sustainable and eco-friendly approach for the solidification and stabilization of porous materials.

© Springer Nature Singapore Pte Ltd. 2019
L. Zhan et al. (Eds.): ICEG 2018, ESE, pp. 363–368, 2019.
https://doi.org/10.1007/978-981-13-2227-3_45

Some bacteria synthesize urease to hydrolyze urea and produce NH_3 and CO_2. The released NH_3 subsequently increases the pH, leading to the accumulation of $CaCO_3$. Calcium carbonate precipitation, performed by bacteria to provide nucleation sites, has been observed in numerous environments [5]. This MICP process offers an efficient way to sequester inorganic substance, including heavy metals. The calcite precipitation induced by bacteria provide a protective film to prevent corrosion on mild steel and a novel approach to preserve the frescos [6]. *Sporosarcina pasteurii*, *Bacillus sphaericus*, and *Myxococcus xanthus* were reported for the restoration of construction materials, sequestration of metals and radionuclides [7].

In this paper, the primary objective was to assess the potential application of MICP technique in treating the MSWI fly ash. Subject involves the following specific contents: Firstly, three ureolytic bacterias, UR1, UR2 and UR3, were isolated from the rhizosphere soil of *Salviae miltiorrhizae* in the campous garden (Zhejiang Sci-Tech University), *Sporosarcina pasteurii* ATCC 11859 from the China General Microbiological Culture Collection Center (CGMCC). The 16S rRNA molecular identification test was carried out on the above isolated bacterias. Secondly, unconfined compressive strength were tested to evaluate the solidification capacity of the MICP treated fly ash. Lastly, leaching concentrations of heavy metals were tested to evaluate the stabilization capacity of the fly ash after MICP treatment.

2 Materials and Methods

Three ureolytic bacterias, UR1, UR2 and UR3, were isolated from the rhizosphere soil of *Salviae miltiorrhizae* in the campous garden (Zhejiang Sci-Tech University), *Sporosarcina pasteurii* ATCC 11859 from the China General Microbiological Culture Collection Center (CGMCC). In the following experiments, the bacterias were cultured for 24 h in NH_4-YE medium at 30 °C and 220 g. The NH_4-YE medium contained 20 g/l yeast extract, and 10 g/l $(NH_4)_2SO_4$ [8].

2.1 Identification of the Bacterias

Genomic DNA extraction, amplification and sequencing of the 16S rRNA gene were performed as described previously [9]. The 16S rRNA gene sequence was aligned with the closely related bacteria deposited in the GenBank, EMBL and DDBJ databases. Phylogenetic trees were constructed by three methods: the neighbour-joining (mega version 3.1), maximum parsimony and maximum likelihood (phylip version 3.65) methods.

2.2 Solidification of the MSWI Fly Ash

MSWI fly ash was collected from an energy-to-waste facility (Hangzhou, China) and pretreated with lime and active carbon. The treated fly ash were mixed with the culture of bacterias (1:0.3, w/v). The mixture was filled into a cylindrical mould of 36 mm in diameter and 80 mm in height and retain moisture for 7 days. The fly ash treated with the same volume of liquid medium was selected as the control group (UR0).

2.3 Unconfined Compressive Strength of the Solidified MSWI Fly Ash

After curing for 24 h, the moulding cylinder was removed and then continued curing for another 6 days. Subsequently, the unconfined compression test was conducted on the solidified sample by using a servo mechanical press (CMT4000, China). The servo mechanical press can supply a maximum force of 30 kN with an accuracy of 1 N and a loading rate of 2 mm/min.

2.4 Immobilization of Heavy Metals of the Solidified MSWI Fly Ash

After the completion of the unconfined compression test, the sample was collected and dried at the temperature of 105 ± 5 °C for 24 h, and then pulverized by a rubber mallet. Subsequently, The immobilization ratio of metals in the solidified fly ash was assessed. A dried cylindrical sample of 100 g was leached using 1000 ml distilled water for 8 h at 25 °C and 110 g, then resting for 16 h. The eluate was filtered and used for determination of the metal content using ICP-MS (7700X, Agilent, America).

3 Results

3.1 Identification of the Isolated Bacteria

Based on the 16S rRNA gene sequence, UR1 shared 99% maximum homology with *Sphingobacterium cladoniae*. The phylogenetic trees showed that UR1 was grouped together with *S. cladoniae* in one cluster (Fig. 1). Therefore, it was identified as *S. cladoniae*. The other bacterias, UR2 and UR3, were identified as *Bacillus aryabhattai* and *Raoultella ornithinolytica*, respectively.

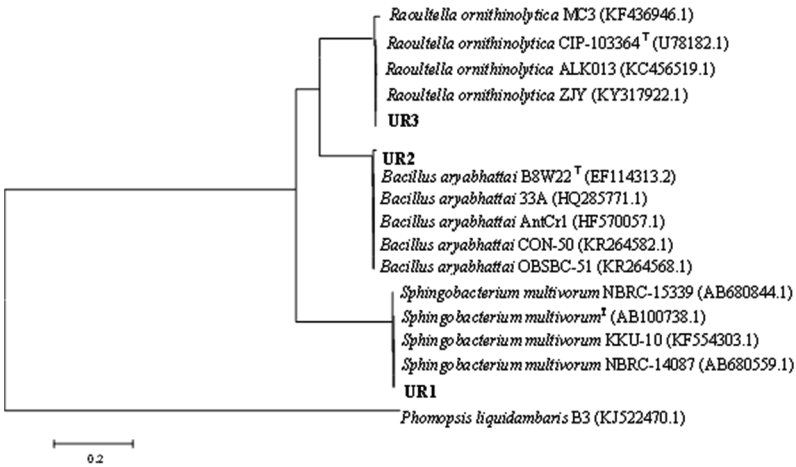

Fig. 1. Phylogenetic trees of th bacterias based on 16S rDNA sequences (The scale of 0.2 means 20% differences between two sequences).

3.2 Solidification of MSWI Fly Ash

All the above bacterias were used to solidify the fly ash. The effects of the bacterias on the compressive strengths and immobilization ratio of heavy metals for the treated MSWI fly ash are shown in the following.

Unconfined Compressive Strength of Solidified MSWI Fly Ash. Figure 2 shows the unconfined compressive strengths of the fly ashes solidified with four bacterias. Firstly, unconfined compressive strengths of the solidified fly ash ranged from 0.527 to 0.740 MPa, and the sample treated with UR2 had the largest compressive strength of 0.740 MPa. Secondly, the samples treated with UR1, UR2, UR3 and *S. pasteurii* showed 17.24%, 40.50%, 8.68% and 2.91% higher in unconfined compressive strength than the control group UR0. Urease activity from the ureolytic bacteria can promote the deposition of carbonate, thus enhancing the compressive strength. So the compressive strength is positively correlated with urease activity.

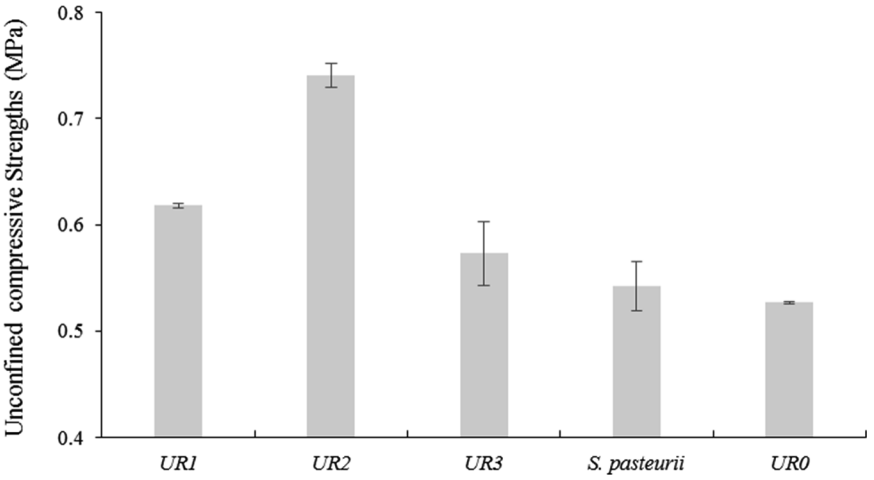

Fig. 2. Unconfined compressive strengths of the treated MSWI fly ashes

Immobilization of Heavy Metals in the MSWI Fly Ash. The immobilization ratio of the heavy metals from the MSWI fly ash is shown in Fig. 3. Most bacterias significantly fixed the heavy metals Cu, Pb, and Cd with a immobilization ratio of 41%–77%. Lower immobilization ratios were obtained for Hg and Cr. UR1 showed the highest immobilization ratio for Cr (55%), Cd (54%) and Cu (77%). For Pb, UR2 presented the highest immobilization ratio (63%), followed by UR1 (61%). However, UR1 presented the lowest immobilization ratio for Hg (19%), UR2 for Cr (12%), and *S. pasteurii* for Pb (29%) and Cd (16%). The immobilization of heavy metals induced by MICP process could be explained as follows. Firstly, urease activity could influence biosorption of heavy metals, cementation with ureolytic bacteria was effective for immobilization fly ash and preventing particle dispersion [8]. Secondly, polysaccharide

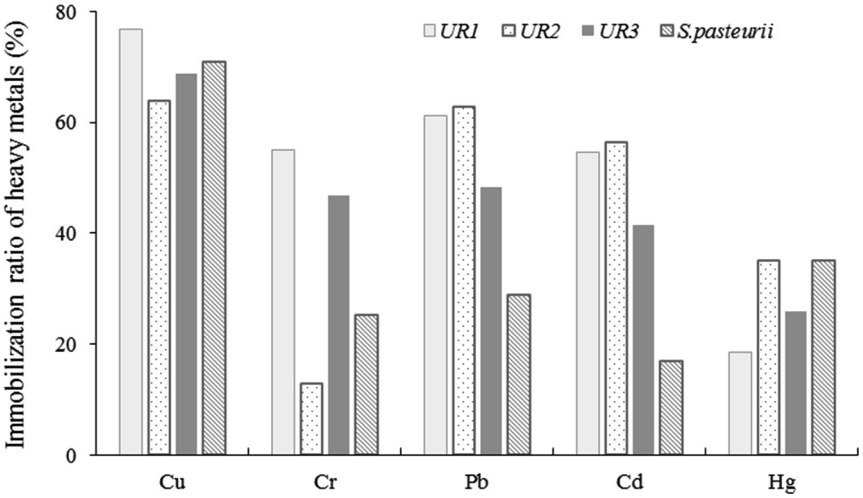

Fig. 3. Immobilization ratio of heavy metals for the treated MSWI fly ashes

secreted by the ureolytic bacteria also plays a significant roles in biosorption of heavy metals [9].

4 Conclusions

Three ureolytic bacteria were isolated and identified in the laboratory of college of life science of the Zhejiang Sci-Tech University, namely *Sphingobacterium cladoniae* UR1, *Bacillus aryabhattai* UR2 and *Raoultella ornithinolytica* UR3. MSWI fly ash solidified with strain UR2 displayed the largest unconfined compressive strengths. Strain UR1 displayed higher immobilization ratios for Cr, Pb, Cd, and Cu. Overall, strains UR1 and UR2 provide promising use for the solidification of MSWI fly ash. This study is a part of broader on-going study funded by the natural science foundation of China with the goal to isolate bacterias and put forward corresponding operation process to efficiently solidify the MSWI fly ash.

Acknowledgements. We are grateful to Dr. Greg Duns for his valuable comments on the paper.

References

1. Tian H, Gao J, Lu L et al (2012) Temporal trends and spatial variation characteristics of hazardous air pollutant emission inventory from municipal solid waste incineration in China. Environ Sci Technol 46(18):10364–10371
2. Zacco A, Borgese L, Gianoncelli A, Struis RPW, Depero JLE, Bontempi E (2014) Review of fly ash inertisation treatments and recycling. Environ Chem Lett 12(1):153–175
3. Wang CP, Li FZ, Zhou MK, Chen Y, Chen X (2015) Effect of cement-MSWI fly ash hydration on the stabilization/solidification of Pb and Cd. Mater Res Innov 19(1):1161–1166

4. Tang Q, Liu Y, Gu F, Zhou T (2016) Solidification/stabilization of fly ash from a municipal solid waste incineration facility using Portland cement. Adv Math Sci Eng 106(1):11–21
5. Wang J, Van Tittelboom K, De Belie N et al (2012) Use of silica gel or polyurethane immobilized bacteria for self-healing concrete. Constr Build Mater 26(1):532–540
6. Helmi FM, Elmitwalli HR, Elnagdy SM et al (2016) Calcium carbonate precipitation induced by ureolytic bacteria *Bacillus licheniformis*. Ecol Eng 90(1):367–371
7. Kang CH, Choi JH, Noh JG et al (2014) Microbially induced calcite precipitation-based sequestration of strontium by *Sporosarcina pasteurii* WJ-2. Appl Biochem Biotechnol 174 (7):2482–2491
8. González I, Vázquez MA, Romero-Baena AJ et al (2017) Stabilization of fly ash using cementing bacteria. Assessment of cementation and trace element mobilization. J Hazard Mater 25(1):316–321
9. Dimopoulou M, Vuillemin M, Campbell-Sills H et al (2014) Exopolysaccharide (EPS) synthesis by Oenococcus oeni: from genes to phenotypes. PLoS ONE 9(6):e98898

Modelling Impact of Biomass Growth on Flow Regimes in Porous Media

Peter Cleall(✉), Jose J. Munoz-Criollo, and Michael Harbottle

School of Engineering, Cardiff University, Cardiff, UK
cleall@cardiff.ac.uk

Abstract. Numerical modelling of changes in the flow regimes in soil due to bioclogging of the pore space are considered. Biomass growth dynamics are described by the Monod equation and changes in hydraulic conductivity due to the accumulation of biomass within the pore space are represented by a theoretical model of pore space clogging. The model is validated by comparison with results from experiments performed using the bacterium *Beijerinckia indica* within sand columns with model parameters determined from independent experimental work. The model is then applied to investigate flow diversion within heterogeneous systems composed of a number of regions made up different sand fractions. Finally, the potential of using controlled biomass growth to engineer flow within heterogeneous porous media is considered.

Keywords: Bioclogging · Flow control · Numerical modelling
Porous media

1 Introduction

The potential for microorganisms to effect the geo and bio chemistry of soils is well known. Baveye et al. [1] review many of the key mechanisms by which microorganic processes impact the permeability of soils and other porous media. In more recent years the potential to harness bacterial processes has been explored with a number of applications identified including, for example, biocementation of soils [2] and maintenance of pavement material to reduce changes in pore space [3]. In this study the potential to engineer these bio processes to control flow in porous media is considered.

Bacteria undergo successive cycles of growth and decay which are largely controlled by the availability of substrates (nutrients) within the pore fluid and on soil solids. A number of approaches have been proposed that link the relationship between changes in biomass content in a soil and fluid flow within the pore space. Such approaches address the impact of spatial distribution and growth dynamics of the biomas by considering biofilms, micro-colonies, flow regimes or a combination of these factors [4–7].

In many modelling approaches the presence of bacteria within a porous material is described by combining transport equations, to represent the movement and supply of a substrate to provide nutrients to the bacteria, with a Monod based approach to represent the growth dynamics. Often an approach based on Richard's equation to describe fluid flow is used with an advection-diffusion based equation for chemical species flow.

© Springer Nature Singapore Pte Ltd. 2019
L. Zhan et al. (Eds.): ICEG 2018, ESE, pp. 369–376, 2019.
https://doi.org/10.1007/978-981-13-2227-3_46

Bradford et al. [8] provide a summary of modelling techniques typically used for representing the growth of microorganisms in soil.

In this study a model describing changes in the flow properties of soil that links ground water flow, transport of a nutrient substrate and a model of microorganism growth is presented. Following the development of the theoretical framework the model is validated with experimental data produced by others [9]. Finally, the model is then applied to investigate the effects of bacterial clogging in a 2D heterogeneous porous domain and the potential for novel engineered flow diversion explored.

2 Theoretical and Numerical Formulation

This section presents a model which describes biomass growth and decay in porous materials and considers water flow, substrate (nutrient) transport and bioclogging of the pore structure leading to variations in hydraulic conductivity. The model is based upon three governing equations: Richard's equation - which describes pore liquid flow in unsaturated porous materials; a transport equation that represents advection diffusion and use of nutrient substrate; and the Monod equation- which represents bacterial growth under the influence of a limiting substance. These are each described in the following sections followed by details of the numerical formulation adopted to allow consideration of initial value problems.

2.1 Richard's Equation

Richards unsaturated flow equation is adopted and can be expressed as:

$$\frac{\partial \theta_{tw}}{\partial t} - \nabla \cdot K(e) \nabla h - \frac{\partial K(e)}{\partial z} = 0 \tag{1}$$

where θ_{tw} (m^3/m^3) is the total moisture content, h (m) is the pressure head and $K(e)$ (m/s) is the effective hydraulic conductivity. This "mixed" form has been adopted as it has been found to result in reduced mass balance errors in numerical solution of initial value problems [10].

Equation (1) includes two primary variables, θ_{tw} and h, and is modified during temporal discretization of the system equations to allow expression in terms of pressure head only.

2.2 Chemical Transport Equation

The transport of conservative chemicals through an unsaturated porous medium is described here using the convection dispersion equation [11]:

$$\frac{\partial \left(\theta_{fw} C\right)}{\partial t} = \frac{\partial}{\partial x}\left(\theta_{fw} D \frac{\partial C}{\partial x} - qC\right) + \varphi S \tag{2}$$

where C (mg/cm^3) is the solution concentration, θ_{fw} is the free water content (the water available to flow in the soil), S (mg/cm^3 s) is the substrate consumption rate in the pore space, ϕ (cm^3/cm^3) is the soil porosity, D (m^2/s) is the substrate dispersion coefficient, q (m/s) is the volumetric fluid flux density given by Darcy's law:

$$q = -K(e)\frac{\partial h}{\partial z} - K(e) \tag{3}$$

The sink term, S, of Eq. (2) represents bacterial consumption of substrate.

2.3 Monod Equation

The Monod equation, a mathematical model for the growth of microorganisms [11], is adopted here and relates microbial growth rate with substrate concentration and is expressed as:

$$\frac{\partial M}{\partial t} = YS - bM \tag{4}$$

where M (mg/cm^3) is the bacterial concentration in the pore space, Y (mg/mg) is yield coefficient and b (1/s) is decay rate. The amount of substrate utilized by the bacteria, S, is defined as:

$$S = Mq_m\left(\frac{C}{K_s + C}\right) \tag{5}$$

where q_m (mg substrate/mg biomass) is the maximum specific substrate utilization rate, K_s (mg/cm^3) is a half velocity constant.

The biomass saturation, S_b, is defined as the volume fraction of pore space occupied by biomass. It is obtained from the concentration of biomass in the pore space as:

$$S_b = \frac{M}{\rho_b} \tag{6}$$

where ρ_b (mg/cm^3) is the biomass dry density.

The relationship between total moisture content, θ_{tw}, the free water content θ_{fw} and biomass saturation, S_b, is defined as:

$$\theta_{tw} = \theta_{fw} + S_b.\varphi \tag{7}$$

where φ is the porosity.

2.4 Bioclogging Model

The effective hydraulic conductivity is defined as:

$$K(e) = K_{sat} K_r \tag{8}$$

where K_{sat} (m/s) is the soil's saturated hydraulic conductivity, K_r (nondimensional) is the soil relative hydraulic conductivity.

Here a theoretical relationship proposed by Vandevivere [14] for relative hydraulic conductivity based on biomass concentration is adopted:

$$K_r = \gamma(1 - S_b)^2 + (1 - \gamma)\frac{k_c}{k_c + S_b(1 - k_c)} \tag{9}$$

where k_c is the relative hydraulic conductivity of the plug and γ is defined as:

$$\gamma = \exp\left[-0.5\left(\frac{S_b}{S_{bc}}\right)^2\right] \tag{10}$$

and S_{bc} is the critical biomass saturation factor.

2.5 Numerical Formulation

A numerical solution of the coupled transient system defined by Eq. (1) and (2) is developed, with the finite element method, utilizing linear elements, applied to achieve spatial discretisation. The Petrov-Galerkin and Galerkin methods are selected respectively for the chemical transport Eq. (1) and Richard's Eq. (2). Temporal discretisation is achieved via the finite difference method. The Pickard iterative method is implemented to obtain solution of the non-linear system. Further details are provided in [15].

3 Model Validation

As reported in [15] experimental results from a series of sand columns experiments undertaken by [9] have been used to allow validation of the model presented here. [9] studied bioclogging processes in sands of various grain size fractions via a number of one dimensional column experiments. The experiments considered here used two homogeneous particle size fractions of 150 and 300 μm. The bacterium *B. indica* was selected by [9] because of its reported capacity to yield significant quantities of exopolysaccharide (EPS) material. Sand fractions were prepared in 2.6 cm inner diameter and 20 cm long acrylic tubes. The sand columns were prepared via wet pluviation with dry, sterile sand being poured into a bacterial suspension. Each experiment was repeated in six identical columns. With three control columns prepared with a bacterial suspension containing autoclaved cells and three columns prepared using live cells. A nutrient solution containing 30.0 g/l of glucose in a nitrogen free media was supplied via a peristaltic pump for 16 min per day. Experimental

observation of flow rates and pressure indicated that the nutrient supply system applied a constant pressure head and an initial flow rate of 2.5 ml/min. This resulted in 40 ml of nutrient solution being introduced into each column per day. [9] reported 1.53×10^6 to 1.66×10^6 cells/g dry sand in the prepared columns. Hydraulic conductivity was measured every 2 to 3 days. The complete experimental methodology and results are reported in [9].

The model was applied, using the parameters listed in Tables 1 and 2, to consider a 20 cm long one-dimensional domain with initial homogeneous biomass concentration of 500 mg/L (void space). Based upon experimentally observed behavior a production of 7.8×10^{-11} grams of EPS per cell based was assumed. Based on the experimental methodology initial and boundary conditions are selected resulting in a pressure head of 1 cm applied at the top of the sand column (outlet) and a uniform initial pressure head (1 cm) and substrate concentration (zero). Following the experimental testing regime the inlet pressure is varied to represent periods of nutrient flow (16 min per day) the pressure applied is selected to provide an initial flow rate of 2.5 ml/min during each period of nutrient supply. Flow rates will subsequently vary during each period as biomass growth results in bioclogging and changes in conductivity. A value of 0.83 has been used for Y in the Monod equation based on a theoretical maximum yield estimated from the assumption that *B. indica* consumes all available glucose ($C_6H_{12}O_6$) to produce EPS ($C_{40}H_{53}O_{29}$), with glucose molecules converted to EPS molecules at a ratio of 20:3.

Table 1. Properties of sand fractions [9] and pressure head difference (Δh) between inlet and outlet required for reported flow rate.

Sand fraction (μm)	K_{sat} (cm/s)	φ	Δh (cm)
300	3.2×10^{-2}	0.408	24.9
150	4.1×10^{-3}	0.42	58.3

Table 2. Model parameters. († from Ohashi and Harada (1994))

Parameter	Value	Parameter	Value
Y	0.83	ρ_b	1×10^2 †
q_m	2×10^{-5}	α	0.04
K_s	0.1	D	1×10^{-5}
b	6×10^{-7}		

Results for the column experiments, (measured hydraulic conductivity of the whole column) for 150 and 300 μm fractions reported by [9], are shown in Fig. 1 along with numerical results obtained by the proposed numerical model. It can be seen that the model is able to capture the decrease in hydraulic conductivity due to an increase in biomass saturation. The variation in conductivity after each flow period is a consequence of biomass decay resulting in a small increase in hydraulic conductivity during the periods without feeding (it is assumed that the EPS dissolves in the liquid when its

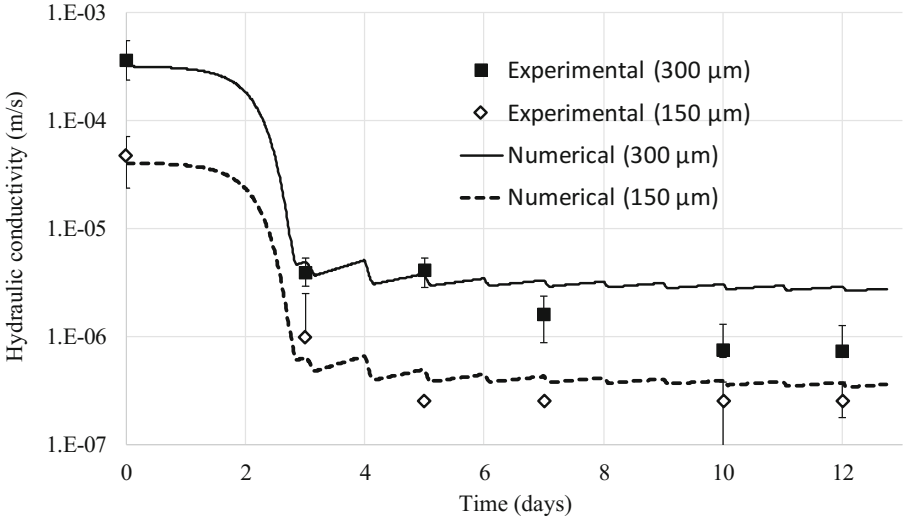

Fig. 1. Experimental observations in 150 and 300 μm sand fraction columns compared with numerical results.

bacterium dies). After a number of cycles the growth and decay of rates reach a pseudo equilibrium.

4 Flow Diversion

The impact of the spatial distribution of biomass and growth dynamics on the flow processes of a heterogeneous porous media are explored via analysis of a 1 m x 1 m two dimensional soil domain composed of three sand fractions distributed in four sections as shown in Fig. 2, sections S1, S2 and S3 are 0.8 m high and one third of the width of the domain. Material parameters are as defined in Table 2. A fixed flow of 0.75 cm^3/s at the inlet is considered with biomass only present is section S1. An initial zero concentration of substrate is considered in all simulations. A third kind boundary condition is maintained at the domain's inlet and an open boundary condition is kept at the domains outlet (S1, S2 and S3).

After an initial period to allow steady flow conditions to become established the domain is continually flushed with substrate (with an external concentration of 30 mg/l) from the bottom allowing the bacteria to grow freely in the domain sections initially populated with biomass. As a consequence the pore space populated with bacteria experiences a reduction in both hydraulic conductivity and volumetric flow as illustrated in Fig. 3, increasing the flow passing through the remaining sections in order to maintain the prescribed constant total flow. It can be seen that by controlling the presence of bacteria and the supply of substrates to different fractions of the soil that the hydraulic flow regime can be engineered and controlled.

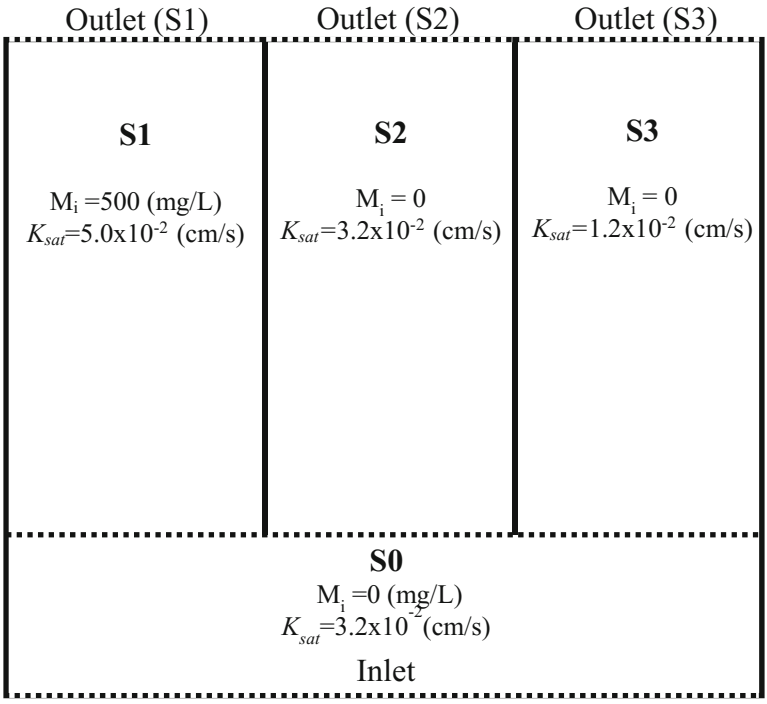

Fig. 2. Heterogeneous porous domain (1 × 1 m).

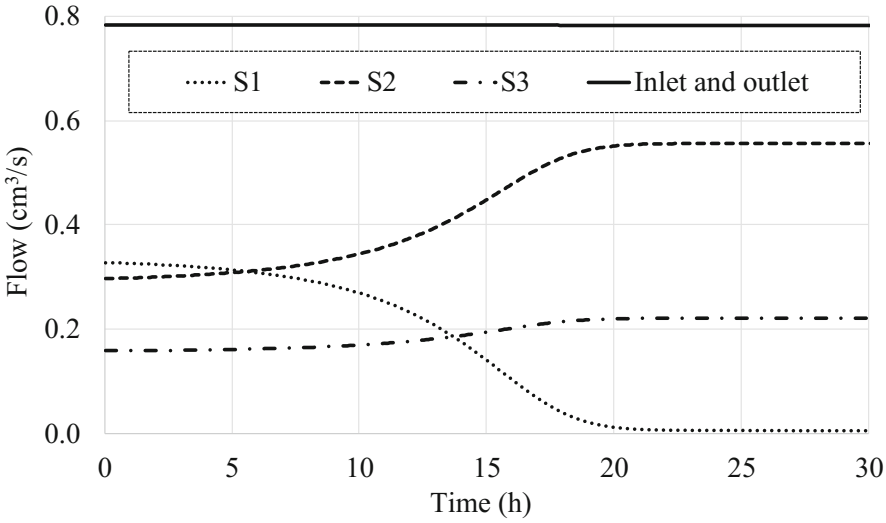

Fig. 3. Flow distribution at outlet of sections S1, S2 and S3 (see Fig. 2)

5 Conclusions

This paper presents a numerical model to describe the impact of biomass growth on flow regimes in porous media. The numerical model was successfully validated against experimental data reported by others (9) of one-dimensional flow in sand columns containing different sizes of sand grains, inoculated with *B. indica* and supplied with a nutrient substrate. The model was then used to explore the effects of bio-clogging in a two-dimensional heterogeneous porous domain and the potential for flow diversion illustrated.

Acknowledgements. This research was funded by the Natural Environment Research Council (NERC) Grant NE/L013908/1 "In situ recovery of resources from waste repositories".

References

1. Baveye P et al (1998) Environmental impact and mechanisms of the biological clogging of saturated soils and aquifer materials. Crit Rev Env Sci Tech 28(2):123–191
2. Ivanov V, Chu J (2008) Application of microorganisms to geotechnical engineering for bioclogging and biocementation of soil in situ. Rev Environ Sci Bio/Tech 7(2):139–153
3. Kia A et al (2017) Clogging in permeable concrete: a review. J Environ Manag 193:221–233
4. Taylor SW, Jaffé PR (1990) Biofilm growth and the related changes in the physical properties of a porous medium: 1. Exp Invest Water Resour Res 26(9):2153–2159
5. Vandevivere P et al (1995) Microbial clogging of saturated soils and aquifer materials: evaluation of mathematical models. Water Resour Res 31(9):2173–2180
6. Clement TP et al (1996) Macroscopic models for predicting changes in saturated porous media properties caused by microbial growth. Ground Water 34(5):934–942
7. Purcell EM (1977) Life at low reynolds number. Am J Phys 45(1):3–11
8. Bradford SA et al (2014) Modeling microorganism transport and survival in the subsurface. J Environ Qual 43(2):421–440. https://doi.org/10.2134/jeq2013.05.0212
9. Alshiblawi P Investigating of bioclogging in homogenous and heterogeneous uncontaminated and contaminated sands. Ph.D. thesis, Cardiff University. http://orca.cf.ac.uk/92494/
10. Celia MA et al (1990) A general mass-conservative numerical solution for the unsaturated flow equation. Water Resour Res 26(7):1483–1496
11. Porro I, Wierenga PJ (1993) Transient and steady-state solute transport through a large unsaturated soil column. Ground Water 31(2):193–200
12. Corman A, Pave A (1983) On parameter estimation of monod's bacterial growth model from batch culture data. J Gener Appl Microbiol 29(2):91–101
13. Van Genuchten M (1980) A closed-form equation for predicting the hydraulic conductivity of unsaturated soils. Soil Sci Soc Am J 44(5):892–898
14. Vandevivere P et al (1995) Microbial clogging of saturated soils and aquifer materials: evaluation of mathematical models. Water Resour Res 31(9):2173–2180
15. Munoz-Criollo JJ, Cleall PJ, Harbottle MJ (2017) Coupled biomass growth and flow in unsaturated soil. In: 2nd Symposium on Coupled Phenomena in Environment Geotechnics (CPEG2)

Role of Plant Health Parameters in Understanding Spatial Heterogeneity of Hydraulic Conductivity of Vegetated Soil: A Case Study of Urban Green Infrastructure Monitoring

Ankit Garg[1], Vinay Kumar Gadi[2(✉)], Siraj Hossain[2], Abhinav[3], Ravi Karangat[2], Sreedeep Sekharan[2], and Lingaraj Sahoo[2]

[1] Shantou University, Guangdong, China
[2] Indian Institute of Technology Guwahati, Assam, India
vinay.gadi@iitg.ernet.in
[3] Indian Institute of Technology Patna, Bihar, India

Abstract. Development of green infrastructure is widely adopted as a key strategy for enhancing socio-ecological benefits in urban areas. Generally, four categories of vegetation exist in urban green infrastructure. Those are (i) vegetated soil under tree shade during entire daylight period, (ii) vegetated soil under tree shade during 3–4 h of daylight period, (iii) vegetated soil under light during entire daylight period and (iv) soil surface covered by mix grass and shredded leaves. Previous studies have shown that presence of vegetation may influence hydraulic conductivity. The main factors those govern such influence are found to be growth of vegetation, which is directly related to photosynthesis and stomatal conductance. Stomatal conductance is the measure of passage of carbon dioxide or water vapor through stomata of leaf. The objective of this study is to investigate role of plant health parameters in understanding spatial heterogeneity of hydraulic conductivity in urban green infrastructure. Field monitoring of mix vegetated soil was conducted for about three months. Plant health is investigated in terms of vegetation growth and stomatal conductance. Stomatal conductance and hydraulic conductivity were measured in 150 locations in selected site once every month. Stomatal conductance was measured using an electronic sensor (leaf porometer). Mini disk infiltrometer was used to measure hydraulic conductivity. Stomatal conductance of mix grass under light for longer duration (around 8 h) was found to be higher than that under light for shorter duration (3–4 h) and shade. Hydraulic conductivity of mix grass cover under shade was found to be relatively low. As compared to stomatal conductance, preferential flow is found to be more dominant in governing the hydraulic conductivity.

Keywords: Stomatal conductance · Vegetation growth
Hydraulic conductivity

© Springer Nature Singapore Pte Ltd. 2019
L. Zhan et al. (Eds.): ICEG 2018, ESE, pp. 377–384, 2019.
https://doi.org/10.1007/978-981-13-2227-3_47

1 Introduction

Hydraulic conductivity of vegetated soil is important property that governs runoff, ground water recharge and slope stability [1, 2]. It is also vital to understand the long-term performance of sustainable drainage systems (i.e., urban green infrastructure; [3]). Suction induced in root zone [4] due to evaporation or evapotranspiration and preferential flow around the root govern the hydraulic conductivity. It is evident that hydraulic conductivity of vegetated soil is affected by vegetation density and shredded leaves [5]. Previous studies show that hydraulic conductivity of vegetated soil could be higher [6] or lower [7] than that of bare soil. In addition, it was reported by Leung et al. [2] that, hydraulic conductivity may vary for different vegetation depending on the stomatal conductance. It can be explained by using Monteith modification of Penman equation [2]. Higher stomatal conductance induces greater evapotranspiration. Greater evapotranspiration induces higher suction [2]. Such higher suction implies less hydraulic conductivity [1].

Mix vegetated soil is found to widely exist in the urban areas as part of green infrastructure (lawns, biofilters and green roofs) to provide socio-ecological benefits [8] and also storm water management [9]. Generally four categories of vegetated soil occur in mix vegetated soil. Those are (i) vegetated soil under tree shade during entire daylight period, (ii) vegetated soil under tree shade during 3–4 h of daylight period, (iii) vegetated soil under light during entire daylight period and (iv) soil surface covered by mix grass and shredded leaves. Gadi et al. 2017 shows that, hydraulic conductivity through these four categories could be different. However, stomatal conductance was not measured in their study. In addition, the hydraulic conductivity tests were conducted only once after vegetation density is reached to 100%. Further growth of vegetation may increase or decrease the hydraulic conductivity due to changes in (1) preferential flow and (2) variation in soil suction. Vegetation density (m^2/m^2) is defined as projected area of vegetation to per unit area [5]. Furthermore, influence of stomatal conductance and vegetation growth was rarely investigated collectively. Such collective investigation is vital to understand the spatial variation of hydraulic conductivity in urban green infrastructure and storm management. The objective of this study is to investigate the influence of plant health parameters on spatial heterogeneity of hydraulic conductivity in mix vegetated soil (i.e., urban green infrastructure).

2 Materials and Methods

2.1 Site Description

Field testing site was selected within campus of Indian Institute of Technology (IIT) Guwahati, which is located in North Eastern part of India near banks of River Brahmaputra. Mixed vegetation consists of *Pongamia Pinnata* tree and several grass species. Mix grass cover contains *Poacea* and *Bauhinia purpurea* species. Field monitoring was conducted on mix grass cover to better understand the spatial variation of stomatal conductance, and hydraulic conductivity.

2.2 Soil Properties

Four disturbed soil samples were collected from different locations at testing site. In situ dry density at four locations was observed to vary between 1315 kg/m^3 and 1387 kg/m^3, with an average value of 1351 kg/m^3 (approximately equal to 78% of dry density. The gravel, sand, and silt and clay contents were found to be 0%, 98.6% and 1.4%. Based on the measured particle size distribution, the soil in the selected site is classified as poorly graded sand (SP; [10]), according to unified soil classification system (USCS). Saturated hydraulic conductivity was found to be 3.7×10^{-4} m/s.

2.3 Overview of Testing Site Consisting Mixed Vegetation

Poacea and *Bauhinia purpurea* species were selected based on (i) broad availability in sub-tropical regions and (ii) drought tolerance ability, which is preferable for bio engineered slope stabilization [5]. *Pongamia pinnata* is selected based on its wide spread presence in sub-tropical regions. It was recognized as the landscape resource [5]. Area of mix grass cover selected for the present study is marked in Fig. 1a (6 m × 5 m). Non-uniformity in shoot length of vegetation in the study site can be seen in Fig. 1a.

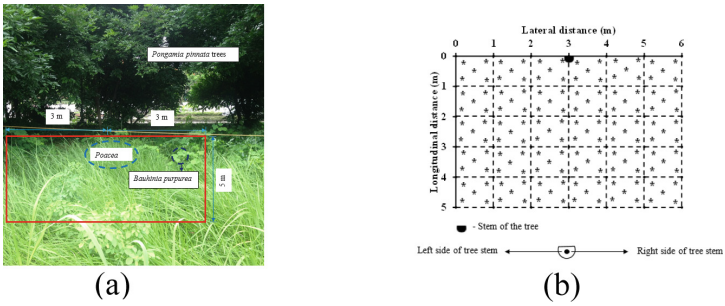

Fig. 1. (a) Overview of mix vegetation in test site and (b) Categorization of selected site into small grids for quantifying spatial variation of stomatal conductance and hydraulic conductivity

2.4 Instrumentation on the Vegetated Soil

Typical layout showing locations (150 measurements), where stomatal conductance and hydraulic conductivity were measured is shown in Fig. 1b. The selected area in the field is categorized into small grids for measuring stomatal conductance and hydraulic conductivity. The selected grid size was determined based on trial measurements of stomatal conductance and hydraulic conductivity. Stomatal conductance was measured using leaf porometer. Leaf porometer [11] allows the leaf in contact with the two known conductance elements. The stomatal conductance is estimated from the difference in humidity between leaf, two sensors and desiccant [12]. Hydraulic conductivity in mix grass cover was measured using mini disk infiltrometer (MDI; [13]). Ghestem et al. [14] showed that, diameter of fine root may decrease and become 40% of its

original diameter, when radiant energy is maximum. Hence, significant preferential flow occurs through soil-root interface during afternoon. Hydraulic conductivity measurements were performed during afternoon to take the preferential flow into account.

2.5 Field Monitoring Programme

The field monitoring programme for quantifying the stomatal conductance and vegetation growth influence on hydraulic conductivity in mixed vegetation site was conducted from 1st May 2017 to 31st July 2017. It is evident that, stomatal conductance and hydraulic conductivity are quite uncertain spatially. To quantify the spatial uncertainty, stomatal conductance and hydraulic conductivity were measured at 150 pints (refer to asterisk (*) in Fig. 1b) once every month. Previous studies show that, stomatal conductance can be influenced by leaf age [5]. Hence, leaves of approximately similar age were considered for the present study. The mix grass growth in the site was started in April month. The mix grass exist on the site in the previous months was wilted due to season change. In addition, tree leaves were also shredded due to season change. The grass shoots selected to measure stomatal conductance were marked for identification in field monitoring period. A series of hydraulic conductivity experiments were performed at designated locations. Hydraulic conductivity was measured using Zhang [15] approach. The Van Genuchten parameters (n and α) were adopted from Carsel and Perish [16] for calculation, which are established using soil water retention curve of bare soil. However, these parameters may not be same for bare soil and vegetated soil [2, 5]. As the main focus of present study is to improve the working knowledge on hydraulic conductivity spatial variation, Van Genuchten parameters of bare soil were adopted. Rainfall depths during May, June and July were found to be 214 mm, 326 mm and 285 mm, respectively. This shows that the tests were conducted during wet period.

3 Results and Discussions

3.1 Vegetation Cover Change During Monitoring Period

Figure 2a, b and c shows the overview of variation in surface area of the selected site during field monitoring period. Figure 2a shows the image captured on 31 May 2017. Typically, four categories of mix grass can be observed during monitoring period (Marked in Fig. 2a). Those are (a) mix grass under tree shade during entire daylight period, (b) mix grass under tree shade during 3–4 h of daylight period, (c) mix grass under light during entire daylight period and (d) surface covered by mix grass and shredded leaves. The proportions of these four categories of mix grass were found to vary with time. Majority area of site is found to cover with *Poacea* during May. *Bauhinia purpurea* is also observed in relatively small area. Figure 2(b) and (c) shows the images of mix grass cover at the end of June 2017 and July 2017. *Poacea* and *Bauhinia purpurea* are found to keep on growing during June and July. Significant area covered by *Bauhinia purpurea* was observed at the end of July. In addition, *Pongamia*

a – Mix grass under tree shade during entire daylight period
b – Mix grass under tree shade during 3 – 4 hours of daylight period
c- Mix grass under light during entire daylight period
d- Surface covered by mix grass and shredded leaves
* Dimensions of marked boundaries are not to the scale

Fig. 2. Mix vegetated soil at the end of three different months: (a) 31 May 2017 (b) 30 June 2017 (c) 31 July 2017

pinnata plants were found to grow within 1 m longitudinal distance in left side of tree stem during June and July.

3.2 Spatial Variation of Stomatal Conductance

Figure 3a, c and e illustrates the spatial variation of stomatal conductance range for three months. Contours were used for illustrating the stomatal conductance. Stomatal conductance is found to vary between 42 mmol/m^{2}s to 510 mmol/m^{2}s. Stomatal conductance was observed to be uncertain spatially. Figure 3a shows spatial variation of stomatal conductance at the end of May. Stomatal conductance of mix grass under light for longer duration (8 h) is observed to be higher than that under light for shorter duration (3–4 h) and shade. Furthermore, stomatal conductance is higher at greater longitudinal distance from tree stem as compared to that near the tree stem. This may be due to absence of shade at Spatial variation of stomatal conductance at the end of June is shown in Fig. 3c. An increase in stomatal conductance over entire area in the selected site was found during June. This is due to growth of *Bauhinia purpurea*, *Poacea* and *Pongamia pinnata* during June. Such growth indicates presence of young shoots, which implies relatively higher stomatal conductance [17]. Trend of variation of stomatal conductance with respect to four categories of mix grass at the end of June is similar to that at the end of May. Figure 3e shows spatial variation of stomatal conductance at the end of July. Unlike to June, stomatal conductance is observed decrease during July. One reason for this may be due to significant increase in *Bauhinia purpurea* during July. Such increase in *Bauhinia purpurea* implies raise in area of mix grass cover under shade. A difference of 17%–350% in stomatal conductance is found between mix grass under shade and light. Results reported by Gross et al. [18] also showed such difference could be up to 450% could be possible. This revealed to be attributed to the relatively low radiant energy under shade [18].

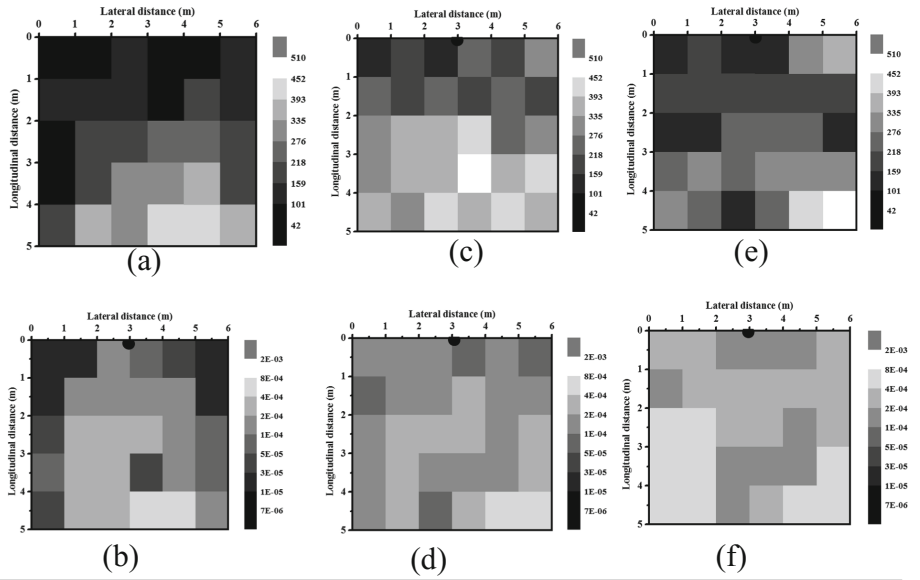

Fig. 3. Spatial variation of stomatal conductance and hydraulic conductivity ranges at the end of: (a) & (b) May 2017; (c) & (d) 30 June 2017; (e) & (f) 31 July 2017

3.3 Spatial Variation of Hydraulic Conductivity

Figure 3b, d and f illustrates spatial variation of hydraulic conductivity range in mix vegetated soil for three months. Range of hydraulic conductivity is found between 7×10^{-6} cm/s and 2×10^{-3} cm/s. Figure 3b shows spatial variation of hydraulic conductivity at the end of May. Hydraulic conductivity of mix grass cover under shade is found to be relatively low among the four categories of mix grass cover. Such low hydraulic conductivity may be attributed to presence of tree roots. Root water uptake through tree roots may induce relatively higher suction as compared to that by mix grass [4]. Higher suction implies less hydraulic conductivity. Although the vegetation densities in both side of tree stem are similar, hydraulic conductivity in right side of tree stem is higher than that in left side within 1 m longitudinal distance. Reason for this may be the presence of greater area covered by mix grass cover in right side of tree stem as compared to that in left side of tree stem, which implies higher preferential flow [5]. This reason may also be attributed to the difference between hydraulic conductivity of grass under light for 3–4 h in left side and right side of tree stem. Hydraulic conductivity through mix grass cover under light during entire daylight period is found to be highest among four categories of mix grass cover. One reason for this may be, higher preferential flow due to presence of mix grass in relatively greater area [5].

Figure 3d shows spatial variation of hydraulic conductivity at the end of June. An increase in hydraulic conductivity can be found in three categories mix grass cover (i.e., mix grass under tree shade, mix grass under tree shade and surface covered by mix grass and shredded leaves). Any increase in hydraulic conductivity through mix grass under light is not found. This may be due to enhanced root water uptake (and stomatal Fig. 3f shows the spatial variation of hydraulic conductivity at the end of July. An increase in hydraulic conductivity is found in three categories of mix grass cover (i.e., mix grass under tree shade during entire daylight period, mix grass under tree shade during 3–4 h of daylight period and surface covered by mix grass and shredded leaves). Any increase in hydraulic conductivity through mix grass under light during entire daylight period is not found. Unlike to previous months, hydraulic conductivity through mix grass within 2 m lateral distance is found to increase during July. Any increase in hydraulic conductivity through mix grass under light during entire daylight period is not found. It can be observed that, larger stomatal conductance exhibits relatively higher hydraulic conductivity through mix grass under light during daylight period. This shows that, preferential flow effect around roots dominates the effect of higher suction induced due to greater stomatal conductance. In addition, lower stomatal conductance exhibits relatively less hydraulic conductivity through mix grass under shade during entire day. This shows that, suction induced due to tree roots dominates the effect of stomatal conductance.

4 Conclusions

The case study explored the spatial variation of hydraulic conductivity in a natural urban green infrastructure containing soil vegetated with mixed species. Spatial variation of hydraulic conductivity was interpreted using plant health parameters (stomatal conductance and vegetation growth). Stomatal conductance was found to vary between 42 mmol/m^{2}s to 510 mmol/m^{2}s. Whereas, hydraulic conductivity was found to vary between 7×10^{-6} cm/s and 2×10^{-3} cm/s.

Stomatal conductance of mix grass under light for longer duration (during entire daylight period) is observed to be higher than that under light for shorter duration (3–4 h) and shade. Presence of young shoots (newly grown mix grass) increase the stomatal conductance. However, excess growth of vegetation accommodates shade on the mix grass, which reduces stomatal conductance. Hydraulic conductivity of mix grass cover under shade was found to be relatively low. This may be attributed to presence of tree roots. Hydraulic conductivity of mix grass cover increases under shade with growth. This may be due to raise in preferential flow with mix grass growth. Whereas, any increase in hydraulic conductivity with growth for mix grass under light during entire day was not found. As compared to stomatal conductance, preferential flow is found to be more dominant in governing the hydraulic conductivity. Further, interaction between plant health parameters and hydraulic conductivity among each category of mix grass needs to be explored. In addition, long term monitoring with consideration of various vegetation species and seasonal variation can be helpful.

References

1. Leung AK, Garg A, Coo JL, Ng CWW, Hau BCH (2015) Effects of the roots of Cynodon dactylon and Schefflera heptaphylla on water infiltration rate and soil hydraulic conductivity. Hydrol Process 29(15):3342–3354
2. Leung AK, Garg A, Ng CWW (2015) Effects of plant roots on soil-water retention and induced suction in vegetated soil. Eng Geol 193:183–197
3. Berretta C, Poë S, Stovin V (2014) Moisture content behaviour in extensive green roofs during dry periods: the influence of vegetation and substrate characteristics. J Hydrol 511:374–386
4. Garg A, Coo JL, Ng CWW (2015) Field study on influence of root characteristics on soil suction distribution in slopes vegetated with Cynodon dactylon and Schefflera heptaphylla. Earth Surf Proc Land 40(12):1631–1643
5. Gadi VK, Tang YR, Das A, Monga C, Garg A, Berretta C, Sahoo L (2017) Spatial and temporal variation of hydraulic conductivity and vegetation growth in green infrastructures using infiltrometer and visual technique. CATENA 155:20–29
6. Mitchell AR, Ellsworth TR, Meek BD (1995) Effect of root systems on preferential flow in swelling soil. Commun Soil Sci Plan 26(15–16):2655–2666
7. Huat BB, Ali FH, Low TH (2006) Water infiltration characteristics of unsaturated soil slope and its effect on suction and stability. Geotech Geol Eng 24(5):1293–1306
8. Meerow S, Newell JP (2017) Spatial planning for multifunctional green infrastructure: growing resilience in Detroit. Landscape Urban Plan 159:62–75
9. Palla A, Berretta C, Lanza LG, La Barbera P (2008) Modelling storm water control operated by green roofs at the urban catchment scale. In: 11th International Conference on Urban Drainage, Edinburgh, Scotland, UK
10. A.S.T.M. D2487-11 (2011) Standard Practice for Classification of Soils for Engineering Purpose (Unified Soil Classification System). Annual Book of ASTM Standards (2011)
11. Decagon Devices (2006) Leaf porometer. Operator's manual. Version 1.0. Decagon Devices. Inc. Pullman, WA
12. Jones HG (2013) Plants and microclimate: a quantitative approach to environmental plant physiology. Cambridge University Press (2013)
13. Decagon Devices (2012) Minidisk Infiltrometer User's Manual Version 10. Pullman, WA (2012)
14. Ghestem M, Sidle RC, Stokes A (2011) The influence of plant root systems on subsurface flow: implications for slope stability. Bioscience 61(11):869–879
15. Zhang R (1997) Determination of soil sorptivity and hydraulic conductivity from the disk infiltrometer. Soil Sci Soc Am J 61(4):1024–1030
16. Carsel RF, Parrish RS (1988) Developing joint probability distributions of soil water retention characteristics. Water Resour Res 24(5):755–769
17. Zeiger E, Farquhar GD, Cowan IR (1987) Stomatal function. Stanford University Press, Stanford
18. Gross K, Homlicher A, Weinreich A, Wagner E (1996) Effect of shade on stomatal conductance, net photosynthesis, photochemical efficiency and growth of oak saplings. Annales des sciences forestières, EDP Sci 53(2–3):279–290

Root Morphology and Mechanical Characteristics of Himalayan (Indian) Native Plant Species

Tarun Semwal[1], Shyam K. Masakapalli[2], and Venkata Uday Kala[1(✉)]

[1] School of Engineering, Indian Institute of Technology Mandi, Mandi 175005, Himachal Pradesh, India
semwaltarun@gmail.com, udaylll2@gmail.com, uday@iitmandi.ac.in

[2] School of Basic Science, Indian Institute of Technology Mandi, Mandi 175005, Himachal Pradesh, India
shaym@iitmandi.ac.in

Abstract. Vegetation improves the soil stability by virtue of its mechanical and hydrological characteristics that are governed by its root morphology. Root network supports the friction between the roots and soil thereby increasing the pull-out resistance and also imparts additional cohesion by induced suction characteristics. Therefore, in order to mitigate landslides and to achieve soil stability, it is needful to have adequate knowledge about root traits. Several researchers evaluated root tensile strength for different species by adopting different mechanisms but it appears from literature that no common clamping arrangement has been developed and it has been modified as per the testing requirement to meet the problems due to root crushing, breaking and slipping at clamps. In the present study, architectural and mechanical characteristics of two Himalayan tree species namely Deodar, Amla and Pine roots were determined. A novel and robust technique for gripping of roots has been developed for testing tensile strength of roots. The effect of diameter on the tensile strength of roots has been shown along with the variation of root network characteristics of plants that were grown under same environmental conditions.

Keywords: Vegetation · Root morphology · Soil stability · Landslide

1 Introduction

Landslides are cause of concern in Asia, since the Himalayan region attaches great importance to mutual development for countries such as India, China and Nepal under the One Belt One Road framework of China [11]. Mostly, landslides occur as a result of triggering mechanisms, such as rainfall, earthquakes, changes in vegetation patterns and man-made activities. The development of vegetation cover for stabilizing the slopes has been employed from several centuries [4, 9, 19]; it is very beneficial for environment eco-friendly and development of the ecosystem. However, these vegetation cover and slope stability are equally inter-related to each other by the ability of the plant growth on the slopes and also due to the interaction between soil and plant root,

© Springer Nature Singapore Pte Ltd. 2019
L. Zhan et al. (Eds.): ICEG 2018, ESE, pp. 385–392, 2019.
https://doi.org/10.1007/978-981-13-2227-3_48

mainly depends on the soil type and plant coverage [19]. The mechanical characteristics of the plants roots are strong in tension whereas, soils are strong in compression and weak in tension. When the soil's shear, roots mobilize their tensile strength whereby, the stresses that develop in the soil matrix are transferred to root fiber via, interface friction along the root system [19, 20] Soil strength can be increased using mechanical reinforcing and also due to the removal of water by transpiration using plant roots [2]. The magnitude of root reinforcement mainly depends on morphological characteristics of the root system [7, 10, 16], root tensile strength using perpendicular model, root modulus values, root tortuosity, the interface friction between the soil matrix and root fiber and orientation of roots to the principal direction of strain [13, 15]. However, this number of plant species in the Himalayan region studied remains restricted.

This study aims at quantifying the tensile strength of plant roots of two species, viz Deodar (*Cedrus Deodara*) and Amla (*Phyllanthus emblica*) grown in plant nursery and a tree roots of Pine (*Pinus*), grown in nature, all of them being typical Himalayan region plant species. Therefore, root tensile strength and root distribution parameters have been depicted in order to improve our knowledge on root properties variability in natural and controlled growth and possibly contribute in controlling the soil mass movements.

2 Materials and Methodology

2.1 Sampling

Deodar and Amla Plant Samples: The plants were collected from the Bioengineering section of plant nursery of IIT Mandi, Himachal Pradesh, India. Around 50 plant species of nearly 2 years of age were taken for the present study. Plants were taken to the laboratory where roots were extracted carefully from the soil by soaking in water gently, so as to prevent any damage to the roots. Roots were then washed properly to remove soil and wiped with a dry filter paper to remove water from the surface. Clear images of dried roots are then captured to carry out image analysis and later determining tensile strength (methodologies discussed in subsequent sections).

Pine Root Samples: Some pine roots have been extracted from a slided younger pine tree, in a recent landslide before it has been replanted. The roots were chosen for the testing purpose, by considering the 150 mm as constant for all of the specimens; with the help of root cutters, the roots were cut and sealed in a plastic bag to prevent the moisture loss. These roots were washed to remove the soil and then sealed in plastic bags to maintain the moisture at −20 °C. Finally, plant roots were tested to check their mechanical strength using Universal Testing Machine Apparatus (UTM). However, due to soil stuck in root matrix of the slided tree, images could not be captured for Image analysis.

2.2 Root Image Analysis

Root images were taken with a high-resolution camera to study the root network characteristics (see Fig. 1). Images were analyzed using Digital Imaging of Root Traits (DIRT [6]), to extract the root architecture parameters. After separating the roots from the shoot portion of the plant using a sharp root cutter, the main root of about 150 mm was separated from the root system to carry out tensile strength testing. Whereas, roots of Pine tree were collected directly from site and their diameter were carefully determined by digital Vernier calipers, before determining their tensile strength.

Fig. 1. Root image used for root morphology

2.3 Tensile Strength Testing

Keeping in view of the various aspects of testing of plant roots, a novel clamping arrangement has been developed such that the root samples can be tested in UTM with the special arrangement of grips controlled by pneumatic pressure attached along with rubber block and sandpaper over it, in order to provide the cushion to prevent the crushing and also slippage of root from the clamps respectively. The clamps are fixed with the root specimen and pneumatic pressure is applied to hold the specimen in position during the test. The apparatus consists of the load cell (1000 kg) and optical encoder of 0.01 mm resolution, which were used for data acquisition directly through the system attached to it (see Fig. 2). The gauge length of the specimen was fixed as 50 mm and strain rate of loading was set to 10 mm/min [1, 2, 5, 8, 16, 20]. The diameter of Deodar plant root specimens for testing was in the range of 0.5–3.5 mm, whereas that of pine root specimens were divided into two groups from 3.5–7.9 mm and 8.1–15.9 mm, by measuring the average diameter of the specimen taken at different locations along the length. The following specimens further moved for testing, till the breakage was observed. Specimens, which break in the middle or near were taken into consideration and others, those were failed near or at the clamps were rejected.

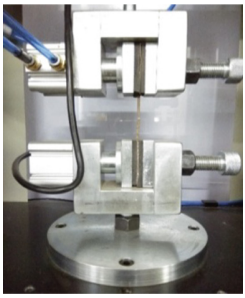

Fig. 2. Testing procedure under UTM apparatus

3 Results

3.1 Image Analysis

The high clarity images of the roots have been captured by a digital camera (Canon EOS 80D). In order to get scale of the image, the images have been captured in white background surrounded by a graph sheet. The scale of the image can be obtained by averaging the scale obtained by inferring the graph sheet in all sides, digitally. These images with the scale were given as input into the DIRT tool, which converts the cleaned images to threshold images in order to analyze the desired root architectural parameters. The real and threshold images of Amla and Deodar plant roots are shown in Table 1. Different root network parameters such as root area, network depth, length, volume was extracted using DIRT and compared with that of Amla plant roots [20] as shown in Table 2 to understand the variation of these parameters among the species.

3.2 Root Tensile Strength

The effect of diameter of deodar and pine roots specimens on their tensile strength (see Fig. 3). The results depicted that the root tensile strength decreases with increasing diameter, in accordance with [1, 2]. It was observed that the tensile strength of roots finer than 4 mm diameter were more likely to follow strong power relation with diameter whereas roots thicker than 4 mm were found to have weak relation (refer, Fig. 3), shown by two zones. Deodar roots have higher R-square value in comparison to that of Amla [20] and Pine roots. The lower value for pine roots are in the accordance with [23]. Though the relationship between the diameter and tensile strength could not be generalized in species, [19, 23] attributes these variations to the variation in physical, chemical and biological contents of the roots. Further analysis on more species with their physic-chemical-biological compositions is required to be carried out for proper explanation of strength-diameter relation across the different species. It was also observed that the thicker diameter pine root specimens have lesser tensile strength; the results range from 3–8 MPa compared to the thinner diameter of Deodar and Amla root specimens ranges from 5–15 MPa and 6–20 MPa respectively and it has been shown in Table 3.

Table 1. Real and threshold images

Plant name	Real image	Cleaned image using DIRT	Threshold image using DIRT
Deodar *(Cedrus deodara)*			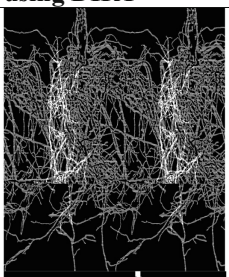
Amla *(Phyllanthus emblica)*			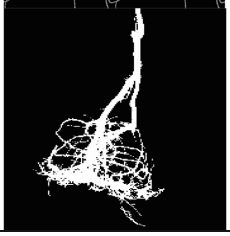

Table 2. Results showing the deodar plant root architecture parameters

Root network parameters	Deodar plant roots	Amla plant roots
	Average value	Average value
Average Root Width (cm)	0.085	0.043
Network Depth (cm)	36.93	200.7
Maximum Number of Roots	51.5	41
Network Width (cm)	20.72	120
Median Number of Roots	32.5	24
Network Area (cm^2)	178.88	3749.69
Network Perimeter (cm)	4336.93	19243.1
Network Surface Area (cm^2)	701.43	1523.58
Network Length (cm)	2508.83	11259.6
Network Volume (cm^3)	20.16	21.36
Network Width to Depth Ratio	1.04	0.59

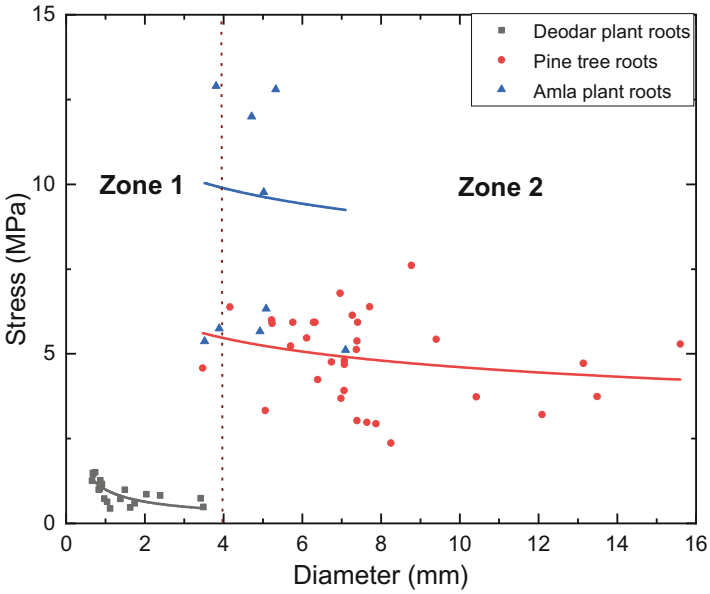

Fig. 3. Relationship between tensile strength and diameter for different plant species.

Table 3. Variation of tensile strength upon diameter variation

	Diameter (mm)	Tensile strength (MPa)
Deodar plant roots	0.60–3.60	4.0–15.0
Pine tree roots	3.40–7.90	2.90–6.80
	8.10–15.60	5.21–8.49
Amla plant roots	3.52–7.09	5.37–21.3

4 Discussion

Earlier researchers depicted that the gripping arrangement has been the most problematic condition for testing the root tensile strength [1, 3, 6, 8, 23]. Researchers modified the gripping arrangement according to the requirement of tests and root types, which created the heterogeneity in testing process and results incomparable. To prevent damage of roots during testing due to improper clamping, rubber grips fixed with sandpaper were attached to pneumatic clamps. The arrangement has been observed to work effectively for different species, diameters and strain rates.

There are several physic-chemical-biological factors that may affect the tensile strength of roots and diameter is influencing parameter among them. Thicker diameter root may spread over the larger surface area into the soil but imparts lesser tensile strength when compared to thinner diameter roots. This suggests the suitability of plant species at different points on slopes. In spite of having the same age and environmental

conditions, different plants of same species may show different root network characteristics and tensile strength. This spread of roots may due to physical, chemical and biological composition of in-situ soils.

5 Conclusion

A novel and robust technique for gripping of roots has been developed for testing tensile strength of roots. DIRT is an effective image analysis tool to extract the root architecture parameters. The data presented in the study expands on the existing body of knowledge regarding root tensile strength of the plant roots of Deodar, Amla and Mandi region pine roots. The results depicted that the root diameter is also a parameter that affects the mechanical strength; as root diameter increases, the tensile strength decreases. The tensile strength may also be affected due to the physical, morphological, chemical and biological composition of roots. The engineering benefits of the bio-engineering plant root can only have obtained from the optimization of tensile strength and root architecture parameters.

Acknowledgment. We sincerely acknowledge Science and Engineering Research Board, Department of Science and Technology (SERB-DST) for providing funds for research grant.

References

1. Cofie P, Koolen AJ (2001) Test speed and other factors affecting the measurements of tree root properties used in soil reinforcement models. Soil Tillage Res 63:51–56
2. De Baets S, Poesen J, Reubens B, Wemans K, De Baerdemaeker J, Muys B (2008) Root tensile strength and root distribution of typical Mediterranean plant species and their contribution to soil shear strength. Plant Soil 305:207–226
3. Edward FG, Jason G (2011) Quercus virginiana root attributes and lateral stability after planting at different depths. Urban Forestry Urban Greening 10:3–9
4. Evette A, Labonne S, Rey F, Liebault F, Jancke O, Girel J (2009) History of bioengineering techniques for erosion control in rivers in Western Europe. Environ Manage 43:972–984
5. Ali F (2010) Use of vegetation for slope protection: Root mechanical properties of some tropical plants. Int J Phys Sci 5(5):496–506
6. Galkovskyi T, Mileyko Y, Bucksch A, Moore B, Symonova O, Price CA, Topp CN, Anjali S, Pascuzzi I, Zurek PR, Fang S, Harer J, Benfey PN, Weitz JS: GiA roots: software for the high throughput analysis of plant root system architecture. BMC Plant Biol (2012)
7. Ghestem M, Veylon G, Bernard A, Vanel Q, Stokes A (2014) Influence of plant root system morphology and architectural traits on soil shear resistance. Plant Soil 377:43–61
8. Giadrossich F, Schwarz M, Cohen D, Cislaghi A, Vergani C, Hubble T, Phillips C, Stokes A (2017) Methods to measure the mechanical behaviour of tree roots: a review. Ecol Eng 109 (B):256–271
9. Huat BBK, Kazemian S (2010) Study of root theories in green tropical slope stability. Electron J Geotech Eng 15:1825–1834
10. Mickovski SB, Van Beek LPH (2009) Root morphology and effects on soil reinforcement and slope stability of young vetiver (Vetiveria zizanioides) plants grown in semi-arid climate. Plant Soil 324:43–56

11. Pale S: The new silk road: a wealth of opportunities in Nepal. New Eastern Outlook (2017). https://journal-neo.org/2017/03/19/the-new-silk-road-a-wealth-of-opportunities-for-nepal
12. Dlapa P, Chrenková K, Mataix-Solera J, Šimkovic I (2012) Soil profile improvement as a by-product of gully stabilization measures. Catena **92**, 155–161
13. Preti F, Giadrossich F (2009) Root reinforcement and slope bioengineering stabilization by Spanish Broom (Spartium junceum L.). Hydrol Earth Syst Sci 13:1713–1726
14. Rees SW, Ali N (2011) Tree induced soil suction and slope stability. Int J Geomech Geoeng 7(2):103–113
15. Reubens B, Poesen J, Danjon F, Geudens G, Muys B (2007) The role of fine and coarse roots in shallow slope stability and soil erosion control with a focus on root system architecture: a review. Trees 21:385–402
16. Saifuddin M, Osman N (2014) Evaluation of hydro-mechanical properties and root architecture of plants for soil reinforcement. Curr Sci 107(5):10–15
17. Schmidt KM, Roering JJ, Stock JD, Dietrich WE, Montgomery DR, Schaub T (2001) The variability of root cohesion as an influence on shallow landslide susceptibility in the Oregon Coast Range. Can Geotech J 38:995–1024
18. Schwarz M, Cohen D, Or D (2012) Spatial characterization of root reinforcement at stand scale: theory and case study. Geomorphology 171–172:190–200
19. Stokes A, Atger C, Bengough A, Fourcaud T, Sidle R (2009) Desirable plant root traits for protecting natural and engineered slopes against landslides. Plant Soil 324:1–30
20. Tarun S, Naresh M, Manushree V, Shyam KM, Uday KV (2017) Study of mechanical characteristics of plant roots for achieving soil stability. In: Proceedings of IGC – 2017. Springer, (in Press)
21. Vergani C, Chiaradia EA, Bischetti GB, Chiaradia EA, Bischetti GB (2012) Variability in the tensile resistance of roots in Alpine forest tree species. Ecol Eng 46:43–56
22. Watson A, Phillips C, Marden M (1999) Root strength, growth, and rates of decay: root reinforcement changes of two tree species and their contribution to slope stability. Plant Soil 217:39–47
23. Zhang CB, Chen L, Jiang J (2014) Why fine tree roots are stronger than thicker roots: the role of cellulose and lignin in relation to slope stability. Geomorphology 206:196–202

Spatial Heterogeneity of Hydraulic Conductivity in Green Infrastructure Due to Presence of Wilted and Live Grass: A Field Study

Vinay Kumar Gadi[1], Siraj Hossain[1], Gitanjali Deka[1], Ankit Garg[2], Ravi Karangat[1], Sreedeep Sekharan[1(✉)], and Lingaraj Sahoo[1]

[1] Indian Institute of Technology Guwahati, Guwahati, Assam, India
srees@iitg.ernet.in
[2] Shantou University, Shantou, Guangdong, China

Abstract. Spatial variation of hydraulic conductivity governs the performance of green infrastructure. Previous studies show that, hydraulic conductivity of vegetated soil may vary by 400% due to presence of vegetation. However, spatial variation of hydraulic of wilted grass in the vicinity of a tree was rarely studied previously. The objective of this study is to investigate spatial variation of hydraulic conductivity of wilted mix grass in the vicinity of a tree. Field monitoring was conducted for two months in the site consisting live grass and wilted grass. The selected site consists of (i) mix grass cover under tree shade during entire daylight period, (ii) mix grass cover under tree shade during 3–4 h of daylight period, (iii) mix grass cover under light during entire daylight period and (iv) soil surface covered by mix grass and shredded leaves. Hydraulic conductivity was measured at 150 locations in the selected site using mini disk infiltrometer. Hydraulic conductivity of wilted and live grass near the tree stem (i.e., under tree shade during entire daylight period) was found to be lower than that away from tree stem. In addition, hydraulic conductivity of wilted and live grass under light during entire daylight period was found to be higher than that under shade for 3–4 h of daylight period. Furthermore, hydraulic conductivity of wilted grass was found to be lower than that of live grass in case of all the selected categories. The obtained results help to analyze the performance of green infrastructure accurately.

Keywords: Hydraulic conductivity · Green infrastructure · Wilted grass

1 Introduction

Urban green space (mix grass in urban areas) improves the well-being of residents [1]. Urban green spaces were widely established to enhance ecosystem balance [2]. Biofiltration units contain mix grass troughs, which infiltrate rain water and reduces runoff [3]. In addition, mix grass improves stability of natural or man-made embankments and land fill system [4, 5]. This shows mix grass has great implications in green infrastructure. Hydraulic conductivity of vegetated soil is an important parameter,

© Springer Nature Singapore Pte Ltd. 2019
L. Zhan et al. (Eds.): ICEG 2018, ESE, pp. 393–400, 2019.
https://doi.org/10.1007/978-981-13-2227-3_49

which governs infiltration, runoff and slope stability [6, 7] in green infrastructure. Evaporation or evapotranspiration induced suction and preferential flow around the plant roots affect the hydraulic conductivity in vegetated soil [8]. Hydraulic conductivity may increase [9] or decrease [10] up to 400% due to presence of plant roots. In addition, hydraulic conductivity plays vital role in long term performance of green infrastructure [11].

Hydraulic conductivity of vegetated soil was explored extensively by previous researchers [6, 11]. However, few studies exist on spatial variation of hydraulic conductivity in mix vegetated soil [12]. Recent study [12] investigated spatial variation of hydraulic conductivity of mix grass cover exists in the vicinity of a tree. In addition, variation of hydraulic conductivity due to vegetation growth was monitored in their study. Although influence of vegetation growth was considered, spatial variation of hydraulic conductivity in completely wilted grass was rarely investigated. Furthermore, spatial variation of hydraulic conductivity was rarely studied when grass density is 100%. Grass density is defined as the ratio of area covered by the grass to the surface of soil considered [13]. It is evident that, mix grass may wilt due to drought stress or aging effect [14]. In such case, suction present in the soil may change due to variation of shade condition. These changes may alter the hydraulic conductivity [8]. This shows that variation due to presence of wilted grass is vital to analyze green infrastructure accurately.

The main objective of the present study is to investigate spatial variation of hydraulic conductivity of wilted grass in the tree vicinity. Field was monitored for a period of two months during which, hydraulic conductivity was measured in live grass as well as wilted grass. Study site was completely covered by the grass and shredded leaves (i.e., 100% grass density) during monitoring period. Hydraulic conductivities of live and wilted mix grass were compared and interpreted.

2 Materials and Methods

2.1 Site Description

Pongamia Pinnata tree vicinity, which is located in IITG was selected for testing (see Fig. 1). Mix grass (i.e., combination of *Poacea* and *Bauhinia purpuria*) exists in the vicinity of *Pongamia Pinnata* tree vicinity. Field monitoring was conducted in the vicinity of *Pongamia Pinnata* tree to understand spatial variation of hydraulic conductivity due to presence of live and wilted mix grass.

2.2 Soil Properties

Six disturbed soil samples were collected from distinct locations in the vicinity of tree. Average in situ dry density at six locations was found to be 76% of maximum dry density (i.e., 1334 kg/m^3). The clay and silt, sand and gravel contents were observed to be 2%, 98% and 0%, respectively. Soil in the tree vicinity is classified as SP (poorly graded sand; [15]) according to United Soil Classification System (USCS) provisions. Saturated hydraulic conductivity was found to be $2.8 \pm 0.7 \times 10^{-4}$ m/s.

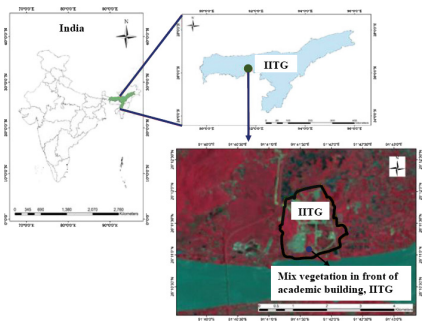

Fig. 1. Location of monitoring site in India (after Gadi et al. [13])

2.3 Overview of Testing Site Consisting Mix Vegetation

Bauhinia purpuria species and *Poacea* were adopted for current study based on (i) broad existence in subtropical regions [16] and (ii) water stress tolerance (i.e., drought) ability [17]. *Pongamia pinnata* tree vicinity is selected due to its wide spread presence in urban areas of subtropical regions [14]. In addition, the ornamental values of selected species were widely recognized [18]. The monitored area in tree vicinity is marked in Fig. 2a.

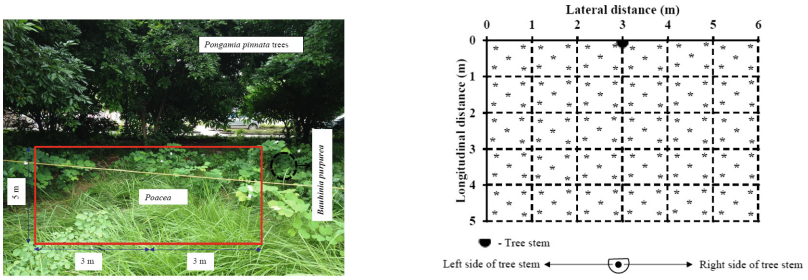

Fig. 2. (a) Overview of mix grass in the vicinity of a tree and (b) site categorization for monitoring spatial variation of hydraulic conductivity

2.4 Instrumentation on the Vegetated Soil

Figure 2b shows the typical layout of measurement locations of hydraulic conductivity. Trail experiments were conducted to understand the significance of variability of hydraulic conductivity in the selected site. The selected area is categorized into small grids based on the trail experiments. Mini disk infiltrometer (MDI; [19]) was used to measure hydraulic conductivity in mix grass. Overview of MDI (left) and (right) measurement of hydraulic conductivity in mix grass is shown in Fig. 3. It should be noted that, MDI measures hydraulic conductivity in relatively small area. Hence, large number of measurements are required in for field monitoring.

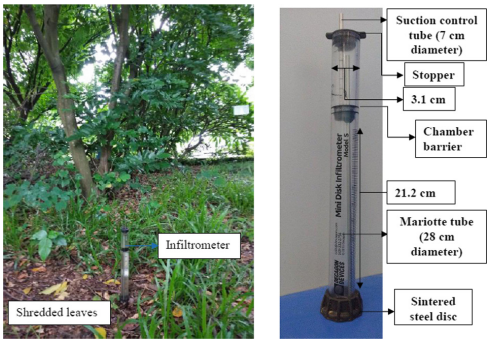

Fig. 3. Measurement of hydraulic conductivity in mix grass cover

A good contact between ground and sintered disk was maintained by placing MDI firmly in the measurement location to allow axis symmetric flow. Air bubbles accumulated in sintered disk were removed by boiling it frequently to measure hydraulic conductivity accurately. Previous researchers show that, diameter of fine roots may be reduced by 60% under relatively high radiant energy. This reduction causes preferential flow around roots. Hydraulic conductivity was measured during afternoon to take preferential flow into account.

2.5 Field Monitoring Programme

The field monitoring programme was conducted to understand the spatial variation of hydraulic conductivity in the selected site. The vicinity of *Pongamia pinnata* was instrumented for two months as shown in Fig. 3. The hydraulic conductivity was measured at 150 points (presented with asterisk (*) Fig. 2(b)). Hydraulic conductivity was measured once every month. Suction was adjusted according to Zhang [20] guidelines. Infiltration was allowed through vegetated soil under a specified suction. The Van Genuchten parameters (i.e., α and n) were adopted from Carsel and Parrish [21] for hydraulic conductivity measurement, which were established from soil water characteristic curve of bare soil. However, soil water characteristic curve of bare soil may be dissimilar to that of rooted soil [7]. As the main objective of current study is to improve the working knowledge on difference between hydraulic conductivity of live and wilted vegetation. Hence, parameters of bare soil water characteristic curve would be suffice the purpose of this study.

3 Results and Discussions

3.1 Vegetation Cover During Field Monitoring Period

Figure 4(a) and (b) depicts the overview of tree vicinity with live and wilted mix grass. Figure 4a shows the image captured on 30 May 2017. Typically, four mix grass categories were found during monitoring period (Marked in Fig. 4a). Those are (a) mix

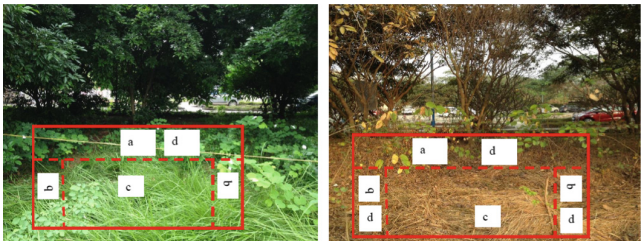

(a) (b)

a – Mix grass under tree shade during entire daylight period
b – Mix grass under tree shade during 3 – 4 hours of daylight period
c- Mix grass under light during entire daylight period
d- Surface covered by mix grass and shredded leaves
* Dimensions of marked boundaries are not to the scale

Fig. 4. Various categories of mix grass in the selected site

grass under shade of tree during entire daylight period, (b) mix grass under shade of tree during 3–4 h of daylight period, (c) mix grass under light during entire daylight period and (d) surface covered by mix grass and shredded leaves. Mix grass exist in the above mentioned four categories is alive during May' 2017 (see Fig. 4a). Whereas, those are completely wilted at the end of February' 2018 (see Fig. 4b). It should be noted that *Pongamia pinnata* plants also exist within 1 m radial distance near to the tree.

3.2 Spatial Variation of Hydraulic Conductivity

Figure 5 shows the spatial variation of hydraulic conductivity in the mix vegetated soil during monitoring period. Range of hydraulic conductivity is observed to vary between

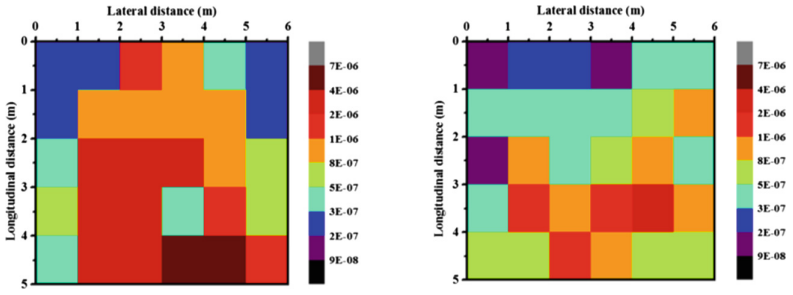

Colour scale indicates hydraulic conductivity (m/sec)
- Stem of the tree

Fig. 5. Spatial variation of hydraulic conductivity due to presence of (a) live mix grass and (b) completely wilted mix grass

9×10^{-8} m/s and 7×10^{-6} m/s. Figure 5(a) depicts the spatial variation of hydraulic conductivity at the end of May' 2017. Hydraulic conductivity of mix grass cover under shade during daylight period is observed to be low as compared to that of other categories in site. Reason for such low hydraulic conductivity may be root water uptake through tree roots.

Tree roots induce large suction, which implies reduction in hydraulic conductivity [8]. Furthermore, Hydraulic conductivity of above mentioned category of mix grass is observed to be higher in right side as compared to that in left of tree stem. This may be due to presence of Pongamia pinnata plants near to tree stem. Existence of these Pongamia pinnata implies preferential flow around the roots [22]. Hydraulic conductivity of mix grass cover under tree shade during 3–4 h of daylight period is observed to be higher than that near to the tree stem. This may due to preferential flow around the roots of live mix grass. Whereas, preferential flow would not be significant near the tree stem. This is because only shredded leaves were found over 80% area near the tree stem. Hydraulic conductivity of mix grass cover under tree shade during 3–4 h is found to be higher in right side as compared to that in left side of tree stem. Reason for this may be self-shade of *Pongamia pinnata* plants and mix grass exists in right side of tree stem. Such self-shade induces relatively less suction in root zone [8]. In addition, hydraulic conductivity is observed to be highest through mix grass under light during daylight period. This may be also due to presence of self-shade due to large shoot length of mix grass.

Figure 5(b) depicts the spatial variation of hydraulic conductivity at the end of February' 2018 (i.e., when vegetation is wilted). Similar to the live vegetation case, Hydraulic conductivity of wilted grass under tree shade in left side of tree stem is less than that in right side of tree stem. It is evident that tree leaves also shredded completely at the end of February' 2018. Area under shade would not be uniform in such case. This non-uniformity of shade may be reason for the difference between hydraulic conductivity in right side and left side. In addition, Hydraulic conductivity of wilted grass cover under tree shade during 3–4 h is found to be higher in right side as compared to that in left side of tree stem. This may also be due to variation in area under shade of wilted mix grass. Hydraulic conductivity is found to be highest through of wilted mix grass under light during entire daylight period. Reason for this may be self-shade of wilted grass.

Hydraulic conductivity of wilted grass under tree shade over entire daylight period is observed to be less than that of live grass cover in the same condition. This may be due to shredding of tree leaves. Entire area may not be under tree shade due to shredding of leaves. In such case, relatively more suction may be induced due to evapotranspiration [8]. Hydraulic conductivity through wilted grass under tree shade during 3–4 h of daylight period is observed to be lower than that of live grass in the same condition. In addition, Hydraulic conductivity through wilted grass under light during entire daylight period is observed to be lower than that of live grass in the same condition. Reason for this may be relatively high suction induced in wilted mix grass cover [6].

4 Conclusions

This study explored the spatial variation of hydraulic conductivity of wilted mix grass in the vicinity of tree. In addition, hydraulic conductivity of live grass was also measured for comparison. Hydraulic conductivity of live grass under tree shade during entire daylight period is lower than that of live mix grass under light during (i) entire daylight period and (ii) 3–4 h in a daylight period. This can be attributed to relatively high suction, which was induced due to presence of tree roots. Maximum hydraulic conductivity occurs through mix grass under light during entire daylight period. Possible reason for this may be self-shade of mix grass. The above mentioned trend of variation of is found in case of wilted mix grass also. Self-shade may cause relatively high hydraulic conductivity through wilted grass under shade during 3–4 h and wilted grass under light during entire daylight period. Hydraulic conductivity through wilted grass under (i) tree shade and (ii) light is lower than that of live grass under those conditions. Non-uniform shade condition due to shredding of tree leaves could be possible reason for relatively lower hydraulic conductivity of wilted mix grass. The results obtained can be useful to estimate runoff from urban green infrastructure similar to the studied one. Further studies are required to understand the spatial variation of hydraulic conductivity of vegetated soil in various types of soil.

References

1. Groenewegen PP, Van den Berg AE, De Vries S, Verheij RA (2006) Vitamin G: effects of green space on health, well-being, and social safety. BMC Public Health 6(1):149
2. Jenerette GD, Harlan SL, Stefanov WL, Martin CA (2011) Ecosystem services and urban heat riskscape moderation: water, green spaces, and social inequality in Phoenix, USA. Ecol Appl 21(7):2637–2651
3. Le Coustumer S, Fletcher TD, Deletic A, Barraud S, Lewis JF (2009) Hydraulic performance of biofilter systems for stormwater management: influences of design and operation. J Hydrol 376(1–2):16–23
4. Gadi VK, Bordoloi S, Garg A, Sahoo L, Berretta C, Sekharan S (2017) Effect of shoot parameters on cracking in vegetated soil. Environ Geotech 1–8
5. Gadi VK, Manogaran IP, Garg A, Berretta C, Sreedeep S (2017) A novel color analysis technique for differentiation of mix grass cover under shade and without shade in green infrastructures. Adv Civ Eng Mater 6(1):564–582
6. Leung AK, Garg A, Ng CWW (2015) Effects of plant roots on soil-water retention and induced suction in vegetated soil. Eng Geol 193:183–197
7. Leung AK, Garg A, Coo JL, Ng CWW, Hau BCH (2015) Effects of the roots of Cynodon dactylon and Schefflera heptaphylla on water infiltration rate and soil hydraulic conductivity. Hydrol Process 29(15):3342–3354
8. Gadi VK, Bordoloi S, Garg A, Kobayashi Y, Sahoo L (2016) Improving and correcting unsaturated soil hydraulic properties with plant parameters for agriculture and bioengineered slopes. Rhizosphere 1:58–78
9. Van Noordwijk M, Heinen M, Hairiah K (1991) Old tree root channels in acid soils in the humid tropics: important for crop root penetration, water infiltration and nitrogen management. In: plant-soil interactions at low pH. Springer Netherlands, pp 423–430

10. Gish TJ, Jury WA (1983) Effect of plant roots and root channels on solute transport. Trans ASAE 26(2):440–0444
11. Garg A, Coo JL, Ng CWW (2015) Field study on influence of root characteristics on soil suction distribution in slopes vegetated with Cynodon dactylon and Schefflera heptaphylla. Earth Surf Process Land 40(12):1631–1643
12. Gadi VK, Tang YR, Das A, Monga C, Garg A, Berretta C, Sahoo L (2017) Spatial and temporal variation of hydraulic conductivity and vegetation growth in green infrastructures using infiltrometer and visual technique. CATENA 155:20–29
13. Gadi VK, Garg A, Prakash S, Wei L, Andriyas S (2018) A non-intrusive image analysis technique for measurement of heterogeneity in grass species around tree vicinity in a green infrastructure. Measurement 114:132–143
14. Wright STC (1979) The effect of 6-benzyladenine and leaf ageing treatment on the levels of stress-induced ethylene emanating from wilted wheat leaves. Planta 144(2):179–188
15. A.S.T.M., D2487-11 (2011) Standard Practice for Classification of Soils for Engineering Purpose (Unified Soil Classification System). Annual book of ASTM standards
16. Au DWT, Hodgkiss IJ, Vrijmoed LL (1992) Fungi and cellulolytic activity associated with decomposition of Bauhinia purpurea leaf litter in a polluted and unpolluted Hong Kong waterway. Can J Bot 70(5):1071–1079
17. Cai ZQ, Poorter L, Cao KF, Bongers F (2007) Seedling growth strategies in Bauhinia species: comparing lianas and trees. Ann Bot 100(4):831–838
18. Zhang Y, Yuan X, Teng W, Chen C, Liu H, Wu J (2015) Karyotype diversity analysis and nuclear genome size estimation for Pennisetum Rich.(Poaceae) ornamental grasses reveal genetic relationship and chromosomal evolution. Sci Hortic 193:22–31
19. Decagon Devices (2012) Minidisk Infiltrometer User's Manual Version 10. Decagon Devices, Pullman
20. Zhang R (1997) Determination of soil sorptivity and hydraulic conductivity from the disk infiltrometer. Soil Sci Soc Am J 61(4):1024–1030
21. Carsel RF, Parrish RS (1988) Developing joint probability distributions of soil water retention characteristics. Water Resour Res 24(5):755–769
22. Ghestem M, Sidle RC, Stokes A (2011) The influence of plant root systems on subsurface flow: implications for slope stability. Bioscience 61(11):869–879

Evaluation of Hydraulic Conductivity of Lateritic Soil Treated with Bacillus *Coagulans* for Use in Waste Containment Applications

K. J. Osinubi, P. Yohanna, A. O. Eberemu(✉), and T. S. Ijimdiya

Department of Civil Engineering, Ahmadu Bello University, Zaria, Kaduna State, Nigeria
aeberemu@yahoo.com

Abstract. Microbial-induced calcite precipitation (MICP) is a green and sustainable soil improvement technique where chemical reaction network managed and controlled by microbes alter the engineering properties of the soil. This research focused on evaluating the potentials of Bacillus *coagulans* for improving the hydraulic property of lateritic soil intended for use in a waste containment facility. Soil samples were treated with Bacillus *coagulans* at one-third (1/3) pore volume in stepped suspension density of 0, 1.5E + 08, 6.0E + 08, 12.0E + 08, 18.0E + 08 and 24.0E + 08/ml, respectively. Soil samples were prepared at moulding water contents of –2, 0, +2 and +4% relative to optimum moisture content and compacted using the British Standard light (BSL) or standard Proctor energy. Cementation reagent was injected into the soil after compaction by gravity. Results show a marginal decrease in hydraulic conductivity values with increase in Bacillus *coagulans* suspension density, while it generally increased with increase in moulding water content with a slight decrease at optimum moisture content (OMC). The degree of saturation of the specimens initially increased and thereafter decreased with varying Bacillus *coagulans* suspension density. However, the degree of saturation increased with moulding water content from –2% to 0% relative to optimum moisture content (OMC) and thereafter decreased. The hydraulic conductivity values of the treated soil did not meet the maximum regulatory 1×10^9 m/s required for its use as liner and cover material in waste containment system. However, higher compaction energy is recommended to achieve the desired result.

Keywords: Bacillus *coagulans* · Degree of saturation · Hydraulic conductivity Lateritic soil · Microbial-induced calcite precipitation (MICP)

1 Introduction

Bio-cementation is a technology by which microorganisms are used to improve the geotechnical properties of soils through the production of soil particle binding materials (calcite), as a result of the introduction of bacteria and cementation reagents into the soil. The soil cementation materials are mostly carbonates, silicates, phosphates, sulphides and hydroxides [1]. Bio-cementation generally leads to reduction in the pore

© Springer Nature Singapore Pte Ltd. 2019
L. Zhan et al. (Eds.): ICEG 2018, ESE, pp. 401–409, 2019.
https://doi.org/10.1007/978-981-13-2227-3_50

spaces within the soil matrix and hence reduces significantly the permeability of the strengthened soil [2]. The mechanism of reduction in permeability of soils hinders the free flow of fluid and contaminant that pollute groundwater. The behaviour of microbial-induced calcite precipitation (MICP) improved soil favours its suitability for use as liners and covers in engineered municipal solid waste containment facilities.

The overdependence on the modern technologically improved geosynthentic materials for the construction of landfill hydraulic barriers has promoted high cost of construction of engineering landfill in developing and underdeveloped countries. MICP is a promising technique that can be used for the containment of various contaminants and heavy metals. The presence of lead in soil may be reduced by its chelation with the MICP product, which is the mechanism responsible for lead immobilization [3, 4]. Microbial-induced calcium carbonate precipitation of radionuclide and contaminant metals into calcite is a competitive co-precipitation reaction in which suitable divalent cations are incorporated into the calcite lattice [5, 6]. The great promise of the use of biological treatments has been demonstrated in many fields. Microbes have been used in environmental applications, including, Bio remediated aeolian sand [7], stabilization of metals [8], development of biological shields for zonal remediation [9], environmental stabilization of contaminated soils [10], and encapsulation of hazardous and other contaminants in natural soils and acid mine tailings. Microbial enhanced oil recovery (MEOR) uses microbes to increase the efficiency of pumping and production in lower yield oil reservoirs [11]. Researchers have even reported the use of microbes to remediate cracks in concrete structures [12, 13].

The suitability of lateritic soils for use in bio-cementation is based on its large pore throat size which enables free movement of the microbes within the soil to enhance bio-cementation and bio-clogging of the soil. [14] Suggested that the optimum range of grain size for the bio-cementation process is between 50 and 400 μm as bacterial activity cannot take place in very fine soils, while large amounts of calcites are required to promote effective improvements in very coarse soils. Bacteria with size ranging from 0.3 to 2 μm can move freely within sandy soil with particle size of 0.05 to 2.0 mm [15]. [16] Reported that significant amounts of silt and clay in soil would have inhibitory effect on bacteria's movement. This study was aimed at the evaluation of the effect of soil microbes (Bacillus *coagulans)* on the geotechnical properties of compacted lateritic soil to be uses as hydraulic barrier in municipal solid waste containment system.

2 Materials and Methods

2.1 Materials

Soil Sample: The soil sample used for this study was collected from an erosion site in Abagana (68°24'31''N and 27°52'11''E), Njikoka Local Government Area of Anambra state, South East Nigeria.

Microorganism: The urease positive Bacillus *coagulans* classified as ATCC 8038 [17] by the American Type Culture Collection (ATCC) was used in this study. The microorganism is a rod shaped gram positive bacterium.

Cementation Reagent: Cementation reagent used contains 3 g of Nutrient broth, 20 g of urea, 10 g of NH_4Cl, 2.12 g of $NaHCO_3$ and 2.8 g $CaCl_2$ per litre of distilled water in accordance with that described by [18].

Index Property: The natural lateritic soil was classified as A-4(2) soil based on AASHTO classification system [19] and SC soil based on Unified Soil Classification System (USCS) [20]. A summary of the properties of the natural soil is given in Table 1.

Table 1. Properties of the natural lateritic soil

Property	Quantity
Percentage Passing No. 200 Sieve	35.4
Natural Moisture Content, %	11.3
Liquid Limit, %	37.5
Plastic Limit, %	19.3
Plasticity Index, %	18.2
AASHTO Classification	A-4(2)
USCS	SC
Maximum Dry Density, Mg/m^3	1.83
Optimum Moisture Content, %	15.3
Coefficient of permeability (m/s)	
–2% relative to OMC	3.66×10^{-7}
0% relative to OMC	6.52×10^{-9}
+2% relative to OMC	3.84×10^{-8}
+4% relative to OMC	6.93×10^{-8}
Colour	Reddish brown

2.2 Methods

Isolation of Bacterium Species: The bacterium was isolated from the soil by serial dilution (1 g of soil was dissolved in 9 ml of sterile distilled water to produce a soil suspension). The isolates was stored at a temperature of 4 °C in nutrient medium prior to its classification and characterization.

The Culture Medium and Growth Condition: The procedure adopted was in accordance with that described by [18]. Bacillus *coagulans* ATCC 8038 was used throughout the study Medium (Tris ± YE). For stock and pilot cultures contained the following ingredients per liter of distilled water: Tris ± HCl, 130 mM (pH 9.0); $(NH_4)2SO_4$, 10 g; and yeast extract, 20 g; to which 1.5% agar was added to obtain a solid medium for the stock culture. Individual ingredients was autoclaved separately and

mixed afterward to avoid precipitation. $CaCO_3$ precipitation experiments was carried out in liquid medium (urea ± $CaCl_2$) containing the following per litre of distilled water: nutrient broth (Bacto), 3 g; urea, 20 g; NH_4Cl, 10 g; and $NaHCO_3$, 2.12 g (equivalent to 25.2 mM). The pH of the medium was adjusted to 6.0 with 6 N HCl prior to autoclaving. 10 ml of filter sterilized solution containing 2.80 g $CaCl_2$ was added afterward and the final pH of the medium was measured. Bacillus *coagulans* was grown at 30 °C under aerobic conditions for stock and pilot cultures. Broth cultures was incubated in a water bath shaker (Lab-line, Model 3540) operated at 200 rpm. Cell concentration was determined by viable cell counting on Tris ± YE plates.

Index Properties: Laboratory experiments were carried out to determine the index properties of the natural and treated soil in accordance with British Standards [21] and [22], respectively. Soil samples were passed through No. 4 sieve (4.76 mm aperture) prior to treatment.

Compaction: Compaction tests were carried out in accordance with [21] to determine the compaction characteristics of the natural soil. Specimens were compacted with British Standard light (BSL) or standard Proctor energy.

Permeability: The permeability test (falling head method) was carried out in accordance with [21]. A relatively short sample was connected to a stand pipe which provided both the water and the means of measuring the quantity of water flowing through the sample [23]. Soil samples were treated with Bacillus *coagulans* at one-third (1/3) pore volume as recommended by [24] before compaction. The soil was treated with bacteria in stepped suspension density of 0, 1.5E + 08, 6.0E + 08, 12.0E + 08, 18.0E + 08 and 24.0E + 08/ml, respectively. Soil specimens were prepared at moulding water contents of –2, 0, +2 and +4% relative to optimum moisture content and compacted using BSL energy. Cementation reagent which composition is given in Sect. 2.1 was injected in three cycles into the compaction soil. The compacted specimens in the moulds were soaked in a water tank for about 24–48 h to allow for full saturation. The specimens were permeated with water until the rates of inflow and outflow were almost equal and the computed hydraulic conductivities were reasonably equal within equal time intervals. Side wall leakage was ignored as recommended by [25]. After saturation, the specimens were then set up to determine the coefficient of permeability, k.

3 Results and Discussion

Particle Size Distribution (Dry Sieving): The particle size distribution curves for natural and the treated soils are shown in Fig. 1.

Test results show that the introduction of Bacillus *coagulans* and cementation reagent significantly improved the gradation characteristics of the lateritic soil by reducing the fines fraction through flocculation and agglomeration. Percentage fines decreased from 8% for the natural soil at 0.0E + 08 m/l to 4.8% at 24.0E + 08/ml Bacillus *coagulans* suspension density. With increase in Bacillus *coagulans* suspension density the quantity of free silt and clay progressively reduced and coarser materials were formed.

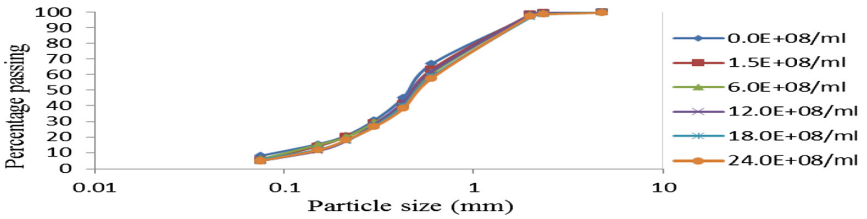

Fig. 1. Particle size distribution of lateritic soil – Bacillus *coagulans* suspension mixtures

A greater density of bacteria resulted in greater enzyme activities that produced more nucleation sites for MICP [7]. The MICP process resulted in the formation of intra granular cemented particles with larger particle sizes. The reported reduction in fines content with increase in Bacillus *coagulans* suspension density may be presumed to be associated with increase in activity level of the microbes as reported by [26] and large soil pore throat which paved way for easy movement of the microbes (Bacillus *coagulans)* and cementation reagent needed for effective soil improvement (calcite formation).

Effect of Bacillus *coagulans* Suspension Density on Hydraulic Conductivity: Hydraulic conductivity with Bacillus *coagulans* suspension density and moulding water content relative to optimum moisture content (OMC) are shown in Figs. 2 and 3, respectively. Results show a decrease in hydraulic conductivity with higher Bacillus *coagulans* suspension density up to 24.0E + 08/ml. The hydraulic conductivity values decreased from 1.59×10^{-7} m/s for the natural soil to a minimum value of 1.89×10^{-9} m/s when treated with 24.0E + 08/ml of Bacillus *coagulans* suspension density, prepared and compacted at –2% of OMC. Similar trend of decrease in hydraulic conductivity was recorded for specimens compacted at OMC, +2 and +4 OMC (see Fig. 2). The decrease in the hydraulic conductivity could be due to microbial urease hydrolyses of urea which produced dissolved ammonium and inorganic carbon, and carbondioxide (CO_2). The ammonia produced and released into the soil specimens increased the pH, and led to accumulation of insoluble calcium trioxocarbonate IV ($CaCO_3$) in a calcium rich environment [27, 28]. [7] Studied the improvement of geomechanical properties of bioremediated aeolian sand and reported that precipitated $CaCO_3$ reduced the pore volume in the specimens.

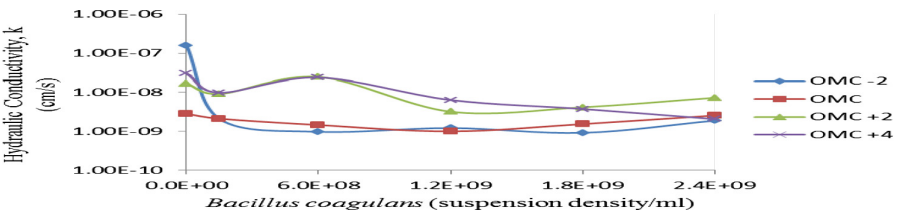

Fig. 2. Variation of hydraulic conductivity of lateritic soil with Bacillus *coagulans* suspension density

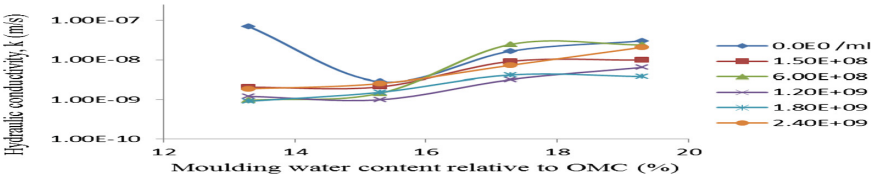

Fig. 3. Variation of hydraulic conductivity of lateritic soil – Bacillus *coagulans* mixtures with moulding water content relative to optimum moisture content.

Also, the reduction in hydraulic conductivity with increase in Bacillus *coagulans* suspension density could be associated with the geometric compatibility of the soil with microbes as reported by researchers [14, 16, 26, 29]. Larger pore throat allows for the easy movement of the microbes and cement reagent within the soil structure needed for the uniform calcite formation. Biofilm formation, biogas generation and the formation of other extracellular polymeric substances (EPS) as biogeochemical processes generate organic solids that occupy a portion of the pore space with a soft, ductile, elastomeric-like material that decreases the soil pore size which may have eventually caused the changes, and thereafter reduced hydraulic conductivity of the soil as reported by [30].

The hydraulic conductivity values recorded in this study did not meet the regulatory maximum value of 1×10^9m/s for landfill application. The effect of moulding water content relative to OMC on hydraulic conductivity of the compacted soil showed a slight increase from –2% OMC to OMC and thereafter much greater increase for all samples. The lowest hydraulic conductivity values were recorded for soil specimens compacted at –2% OMC (see Fig. 3). The increase in hydraulic conductivity with increase in moulding water content could be due to the reduction in pore spaces to be filled by the cementation reagent formed as well as the density of the compacted soil where increasing moulding water replaced the soil particles and enhanced the free flow of water within the soil structure. As the density of the specimen decreased, the voids within the soil matrix increased which led to the increase in hydraulic conductivity.

Effect of Bacillus *Coagulans* Suspension Density on Degree of Saturation: The influence of bacteria density and moulding water content relative to OMC on degree of saturation was examined and presented in Figs. 4 and 5, respectively.

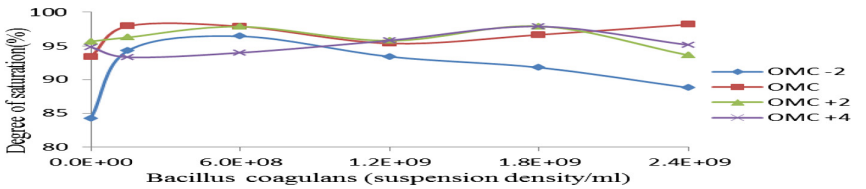

Fig. 4. Variation of degree of saturation of lateritic soil with *Bacillus coagulans* suspension density

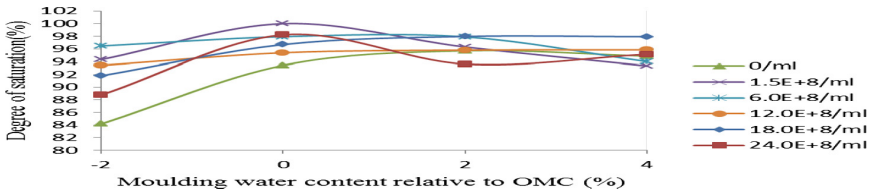

Fig. 5. Variation of degree of saturation of lateritic soil – Bacillus *coagulans* mixtures with moulding water content relative to optimum moisture content.

A general trend of decrease in degree of saturation was recorded with increase in *Bacillus coagulans* suspension density. As the Bacillus *coagulans* suspension density increased more calcite were presumed formed that stiffened the soil and progressively reduced the amount of moisture content in the soil at moulding water content relative to optimum varied from –2% to +4% OMC, An initial increase in degree of saturation was recorded and thereafter decreased with increase in the moulding water content (see Fig. 5). The decrease could be associated with the decrease in the density of the compacted soil where increasing moulding water replaced the soil particles and facilitated ease of free flow of water within the soil structure. Work on the cementation of sand at various degrees of saturations was studied by [31] and it was reported that sample treated at 20% saturation recorded lower $CaCO_3$ crystals, less than half that precipitated at 100% saturation. The changes in hydraulic properties with change in degree of saturation could be attributed to the partially saturated condition (lower degree of saturation) in which air bubbles occupies the center points of the pores spaces within the soil matrix and the total surface area of the soil grains is covered with adsorbed solution, mostly concentrated at the interparticle connection points (corner) leading to the formation of menisci shape [31, 32]. In such conditions crystal precipitation occurs predominantly at the contact points of the soil grains only. This scenario presumed that crystals formation varies in size and location according to the distribution of pore solution, which is influenced by the saturation conditions.

4 Conclusion

The study evaluated the potential of Bacillus *coagulans* as an agent for the improvement of the hydraulic property of lateritic soil intended for use in waste containment application. Marginal decrease in the hydraulic conductivity of lateritic soil was recorded. However, hydraulic conductivity generally increased with increase in moulding water content. The degree of saturation of specimens initially increased to a peak value and thereafter decreased with varying Bacillus *coagulans* suspension density. Also, the degree of saturation increased with moulding water content from –2 to 0% relative to optimum moisture content and there after decreased. Lateritic soil treated with Bacillus *coagulans* suspension density up to 24.0E + 08/ml did not meet the maximum regulatory value of 1×10^9m/s for use as liner and cover material in waste containment system. However, higher compaction energy is recommended to

achieve the desired result. Further investigation should be carried out on microstructure of the treated soil in order to establish the behaviour of the material at the micro level.

References

1. Ivanov V, Chu J (2008) Applications of microorganisms to geotechnical engineering for bioclogging and biocementation of soil in situ. Rev Environ Sci Biotechnol 7:139–153
2. Paassen LAV, Daza CM, Staal M, Sorokin DY, Willem VDZ, Mark CML (2010) Potential soil reinforcement by biological denitrification. J Ecol Eng 36:168–175
3. Achal V, Pan X, Özyurt N (2011) Improved strength and durability of fly ash-amended concrete by microbial calcite precipitation. Ecol Eng 37:554–559
4. Achal V, Pan X, Zhang D, Fu Q (2012) Bioremediation of Pb-contaminated soil based on microbially induced calcite precipitation. J Microbiol Biotechnol 22(2):244–247
5. Li L, Qian CX, Cheng L, Wang RX (2010) A laboratory investigation of microbe-inducing CaCO3 precipitate treatment in Cd2 + contaminated soil. J Soils Sediments 10:248–254. https://doi.org/10.1007/s11368-009-0089-6
6. Hamdan N, Kavazanjian Jr E, Rittmann BE (2011) Sequestration of radionuclides and metal contaminants through microbially-induced carbonate precipitation. In: Pan-Am CGS geotechnical conference
7. Chi L, De Y, Shihui L, Tuanjie Z, Siriguleng B, Yu G, Lin L (2017) Improvement of geomechanical properties of bioremediated aeolian sand. Geomicrobiol J. https://doi.org/10.1080/01490451.2017.1338798
8. Etemadi O, Petrisor IG, Kim D, Wan M-W, Yen TF (2003) Stabilization of metals in subsurface by biopolymers: laboratory drainage flow studies. Soil Sedimen Contamination 12(5):647–661
9. Yang ICY, Li Y, Yen TF (1993) Subsurface application of slime-forming bacteria in soil matrices. In: Hinchee et al. (eds) Applied biotechnology for site remediation, pp 268–274
10. Khachatoorian R, Petrisor IB, Kwan C-C, Yen TF (2003) Biopolymer plugging effect: laboratory-pressurized pumping flow studies. J Pet Sci Eng 38(1–2):13–21
11. DeJong JT, Fritzges MB, Nüsslein K (2006) Microbially induced cementation to control sand response to undrained shear. J Geotech Geoenviron Eng 132(11):1381–1392
12. Ramakrishnan V, Bang SS, Deo, KS (1998) A novel technique for repairing cracks in high performance concrete using bacteria. In: Proceedings of the international conference on HPHSC, Perth, Australia, pp 597–618
13. Ramachandran SK, Ramakrishnan V, Bang SS (2001) Remediation of concrete using micro-organisms. ACI Mater J 98(1):3–9
14. Rebata-Landa V (2007) Microbial activity in sediments: effects on soil behaviour. Georgia institution of technology, Ph.d. thesis
15. Maier RM, Pepper IL, Gerba CP (2009) Environmental microbiology, 2nd edn. Elsevier, China, p 366
16. Ng Wei-Soon, Lee Min-Lee, Hii Siew-Ling (2012) An overview of the factors affecting microbial-induced calcite precipitation and its potential application in soil improvement. World Acad Sci Eng Technol 6:683–689
17. ATCC (2013): American Type Culture Collection P.O Box 1549 Manassas, VA 20108 USA. http://www.atcc.org
18. Stocks-Fischer S, Galinat JK, Bang SS (1999) Microbiological precipitation of $CaCO_3$. Soil Biol Biochem 31(11):1563–1571

19. AASHTO (1986) Standard specification for transportation, Materials and methods of sampling and testing, 14th Edn Amsterdam association of state highway and transportation officia, Washington D.C
20. ASTM (1992) Annual Book of Standards, vol 04(08) American Society for Testing and Materials, Philadelphia
21. BS 1377 (1990) Method of testing soils for civil engineering purpose. British Standard Institute, BSI, London
22. BS 1924 (1990) Method of test for stabilized soils. British Standard Institute, BSI, London (1990)
23. Head KH (1992) Manual of Soil Laboratory Testing. 2 Pentech Press, Plymouth
24. Rowshanbakhta K, Khamehchiyana M, Sajedib RH, Nikudela MR (2016) Effect of injected bacterial suspension volume and relative density on carbonate precipitation resulting from microbial treatment. J Ecol Eng 89:49–55
25. Daniel DE (1994) State of the art: laboratory hydraulic conductivity test for saturated soils, hydraulic conductivity and waste contaminant transport in soil. In: Daniel DE, Trautwein SJ (eds) ASTM STP 1142. American Society for Testing and Materials, Philadelphia
26. DeJong JT, Mortensen BM, Martinez BC, Nelson C (2010) Bio-mediated soil improvement. Ecol Eng 36:197–210
27. Rong H, Qian C (2013) Microstructure evolution of sandstone cemented by microbe cement using x-ray computed tomography. J Wuhan Univ Technol Mater Sci 28(6):1134–1139
28. Karim R, Mashaallah K, Reza HS, Mohammad RN (2016) Effect of injected bacterial suspension volume and relative density on carbonate precipitation resulting from microbial treatment. J Ecol Eng 89:49–55
29. Madigan MT, Martinko JM (2003) Brock biology of microorganisms, 11 edn. Prentice Hall, Upper Saddle River, p 992
30. Dejong JT, Soga K, Kavazanjian E et al (2013) Biogeochemical processes and geotechnical applications: progress. Opportunities Chall Geotech 63(4):287–301. https://doi.org/10.1680/geot.sip13.p.017
31. Cheng L, Ralf CR, Mohamed AS (2013) Cementation of sand soil by microbially induced calcite precipitation at various degrees of saturation. Can Geotech J 50:81–90. https://doi.org/10.1139/cgj-2012-0023
32. Tuller M, Or D, Dudley LM (1999) Adsorption and capillary condensation in porous media: liquid retention and interfacial configurations in angular pores. J Water Res Res 35(7):1949–1964

Unconfined Compressive Strength of Bacillus *Pumilus* Treated Lateritic Soil

Kolawole J. Osinubi[1], John E. Sani[2], Adrian O. Eberemu[1(✉)], Thomas S. Ijimdiya[1], and Sabo E. Yakubu[3]

[1] Department of Civil Engineering, Ahmadu Bello University, Zaria, Nigeria
aeberemu@yahoo.com
[2] Department of Civil Engineering, Nigerian Defence Academy, Kaduna, Nigeria
[3] Department of Microbiology, Ahmadu Bello University, Zaria, Nigeria

Abstract. The study considered the use of Bacillus *pumilus* to trigger microbial-induced calcite precipitation (MICP) process for the improvement of the unconfined compressive strength (UCS) of lateritic soil to be used as a hydraulic barrier in waste containment application. The lateritic soil was treated with stepped Bacillus *pumilus* suspension densities of 0, 1.5×10^8, 6.0×10^8, 12×10^8, 18×10^8 and 24×10^8 cells/ml, respectively. Specimens were prepared at moulding water contents –2, 0, 2 and 4% relative to the optimum moisture content (OMC) that simulate field variation in moisture and compacted with British Standard light (or standard Proctor) energy. The UCS values increased with higher Bacillus *pumilus* suspension densities and moulding water content. Peak UCS values of 1159.08, 1169.52, 1298.27 and 1884.58 kN/m^2 were obtained at 6.0×10^8/ml, 24.0×10^8/ml, 6.0×10^8/ml and 18×10^8/ml Bacillus *pumilus* suspension densities for specimens prepared at –2%, 0%, +2% and +4% relative to OMC, respectively. A compaction plane of acceptable zones for UCS based on regulatory value (i.e., > 200 kN/m^2) gave 6.0×10^8/ml Bacillus *pumilus* suspension density as optimum treatment for lateritic soil to be used in waste containment application.

Keywords: Bacillus *pumilus* · Lateritic soil
Microbial-induced calcite precipitate
Unconfined compressive strength · Waste containment

1 Introduction

Soil improvement techniques require evolution in order to ensure effective and efficient improvement, and at the same time possess sustainable and environment friendly characteristics. Chemical grouts available in the market such as Portland cement, lime, asphalt and sodium silicate, have proven successful in soil improvement [1, 2]. However, the use of these artificial injection formulas often modifies the pH level of soil, contaminates soil and groundwater attributed to their toxic and hazardous characteristics [1, 3].

In order to ensure the structural integrity of a constructed landfill facility, compacted soils for the liner and cover systems requires adequate strength [4]. Adequate

© Springer Nature Singapore Pte Ltd. 2019
L. Zhan et al. (Eds.): ICEG 2018, ESE, pp. 410–418, 2019.
https://doi.org/10.1007/978-981-13-2227-3_51

shear strength of liner or cover system must be such that it can support the overburden imposed by the waste and the self weight of the liners and cover itself. The shear strength of compacted clay depends on the density as well as the compaction water content. Clays compacted dry of optimum are initially stronger than when compacted wet of optimum. The strength of the compacted soil is a parameter of importance in the design of liners in waste containment facilities. Daniel and Wu [4] recommended a minimum 200 kN/m^2 for the design of compacted clay liners.

In underdeveloped countries like Nigeria, municipal solid wastes (MSWs) generated are usually disposed into geological formations like valleys, gorges and even lowland plains without any cover. They are left to decompose under natural condition of temperature and rainfall and sometimes these wastes are burnt. However, most of these waste dump sites are closer to streams and rivers (sources of water for humans, terrestrial and aquatic animals) into which decomposing solid wastes and their toxic leachate are washed down when rain falls. In addition, the structural integrity of these geological formations use as natural barriers in these dump sites cannot be guaranteed as they often contain fissures and cracks under natural weathering conditions which promotes easy migration of leachate into the underground water thereby contaminating it [5, 6].

The aim of this work is to assess the unconfined compressive strength of lateritic soil treated with *B. pumilus* in microbial-induced calcite precipitate (MICP) process on the soil to be used as a hydraulic barrier in waste containment application.

2 Materials and Methods

2.1 Materials

2.1.1 Soil

The lateritic soil used for this study was collected by method of disturbed sampling from an erosion susceptible site in Abagana (6°24'31"N and 6°52'11"E), Njikoka Local Government Area of Anambra state, South East Nigeria. The soil samples were collected at a depth of 1.5 m below the natural earth surface to avoid the influence of organic matter. The particle size distribution curve for the natural soil is shown in Fig. 1.

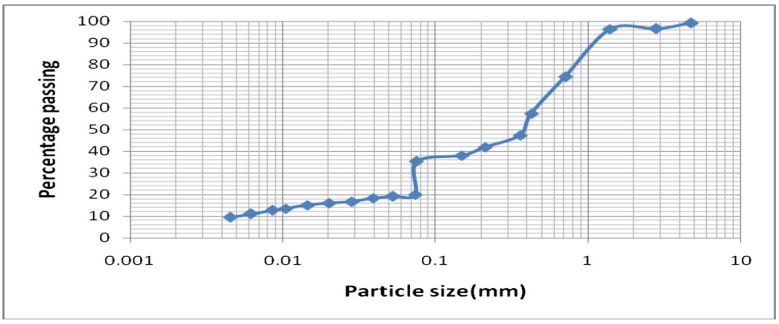

Fig. 1. Particle size distribution curve of the natural lateritic soil

2.1.2 Microorganisms

The Bacillus *pumilus* classified as ATCC 27142 according to American Type Culture Collection (ATCC) was used in the study. The bacteria was cultured in a liquid media consisting of 3 g Nutrient Broth, 20 g of Urea, 10 g of NH_4Cl, 2.12 g $NaHCO_3$ per litre of glass distilled water;, with a pH measured at 9.7. The liquid media were sterilized by autoclaving for 20 min at 121 °C. Bacillus *pumilus* suspensions were prepared in stepped densities of 0 cells/ml (which is the control), 1.5×10^8 cells/ml, 6.0×10^8 cells/ml, 12.0×10^8 cells/ml, 18.0×10^8 cells/ml and 24.0×10^8 cells/ml, respectively, for the treatment of each soil sample.

The role of Bacillus *pumilus* was to produce enzyme urease through its metabolic activity under proper cultivation process. The enzyme urease triggered the MICP biochemical reaction by hydrolyzing urea ($CO(NH_2)_2$) through the following reaction:

$$CO(NH_2)_2 + 3H_2O \rightarrow 2NH_4^+ + HCO_3^- + OH^- \quad (1)$$

The ammonium (NH_4^+) increased the pH and caused the bicarbonate (HCO_3^-) to precipitate with calcium ion (Ca^{2+}) from the calcium chloride supplied in order to form the calcium calcite ($CaCO_3$):

$$Ca^{2+} + HCO_3^- + OH^- \rightarrow CaCO_3 + H_2O \quad (2)$$

The calcite generated is responsible for cementing and clogging the soil specimens. Bio-cementation is achieved when the calcite crystals precipitate on the surface or form bonds between the existing soil grains. This process minimizes the movement of the soil grains, enhancing its strength and stiffness properties [7].

2.1.3 Cementation Reagents

Cementation reagents served as the raw materials for calcite formation in the MICP process. The cementation reagents used in this study are 20 g of urea ($CO(NH_2)_2$) and 2.8 g of calcium chloride ($CaCl_2$). The cementation reagents also contained 3 g nutrient broth, 10 g ammonium chloride (NH_4Cl), and 2.12 g sodium bicarbonate ($NaHCO_3$) per litre of deionized water [3, 8–10].

2.2 Methods

2.2.1 Compaction

Air-dried soil samples passing through British Standard (BS) sieve with 4.76 mm aperture was used. British Standard light, BSL (or standard Proctor) energy was derived from 2.5 kg rammer falling through 30 cm onto three layers in a standard 1000 cm^3 mould, each receiving 27 uniformly distributed blows.

2.2.2 MICP Treatment

Premixing method was adopted in this study and the natural soil was mixed at −2, 0, 2 and 4% relative to optimum moisture content (OMC). The soils were mixed with 1/3 pore volume of the various Bacillus *pumilus* suspensions densities as stated above. Pore volume is the difference between the degree of saturation of fully saturated soil and the

degree of saturation of an unsaturated soil at the compactive effort used. 1/3 of the pore volume was used to measure the volume of bacteria to be used for all treatment at varying moulding water content. The equivalent 1/3 pore volume of the bacteria was deducted from the moulding water content (i.e., −2, 0, 2 and 4% relative to OMC) and mixed to obtain the total moulding water content before being used to mix the soil samples together with water containing 1/3 pore volume of Bacillus *pumilus* suspensions densities as recommended by [11]. The mixture was placed in sealed polythene bag for 12 h to facilitate the proper migration of the *B. pumilus* within the soil mass. Thereafter, compaction was carried out using the BSL energy level. The cementation reagent was introduced into the specimen in the compaction mould, until it was saturated and dripped from the bottom of the mould. The reagent was introduced on the surface of the specimen and allowed to percolate through the soil, 2/3 pore volume of the cementation reagent is adequate to saturate the soil sample. The cementation reagent was introduced to specimens containing the stepped densities of Bacillus *pumilus* suspensions considered at six hour interval for two days.

2.2.3 Unconfined Compressive Strength

The compacted specimens already saturated with stepped densities of Bacillus *pumilus* suspension were extruded from the standard 1,000 cm^3 compaction moulds using a cylindrical steel mould with height of 76.2 mm and internal diameter of 38.1 mm. The specimens were initially cured for 24 h at a constant temperature of 25 ± 2 °C and relative humidity of 100% to enhance calcite formation within the soil before being sealed in polythene bags for 7 days curing period. Thereafter, the specimens were placed in a load frame driven at a constant strain of 0.10%/min until failure occurred. Three specimens were used for each test and the average result was taken.

2.2.4 Microanalysis

Scanning electron microscope (SEM) analysis was used to identify the morphological features of the natural and treated soil. The test was carried out using a Phenom World Pro desktop scanning electron microscope. The sample was placed in a motorized tilt and rotation sample holder and controlled by a dedicated motion control pro suite application which initiates an endless 360° compucentric rotation with a pseudo-eucentric tilting adapted focus ranging from 10^o to 45^o. The motorized tilt and rotation sample holder allows analysis of the sample from all visible sides and enables a unique 3D image of the sample.

3 Results and Discussion

3.1 Index Properties of the Natural Lateritic Soil

The soil used is classified as SC according to the Unified Soil Classification System, USCS [12] and A-4(3) soil according to [13]. Detailed index properties are contained in [14].

3.2 Effect of Moulding Water Content on Unconfined Compressive Strength

Minimum unconfined compression strength (UCS) value of 200 kN/m^2 is recommended to support the bearing stress in a landfill. The variation of UCS with moulding water content is shown in Fig. 2. Generally, the UCS of the mixtures increased with increase in moulding water content for all Bacillus *pumilus* suspension densities considered except for the natural soil that recorded a decrease at higher moulding water content.

The UCS values of the natural soil increased from 517.11, 663.1, 937.29 and 845.81 kN/m^2 at moulding water content of 10.4, 12.4, 14.4 and 16.4%, respectively, to peak values of 1138.19, 1169.52, 1232.17 and 1884.58 kN/m^2 at moulding water content of 10.4, 12.4, 14.4 and 16.4% for Bacillus *pumilus* suspension densities of 24.0 $\times$ 10^8 cells/ml, 24.0 $\times$ 10^8 cells/ml, 24.0 $\times$ 10^8 cells/ml and 18.0 $\times$ 10^8 cells/ml, respectively.

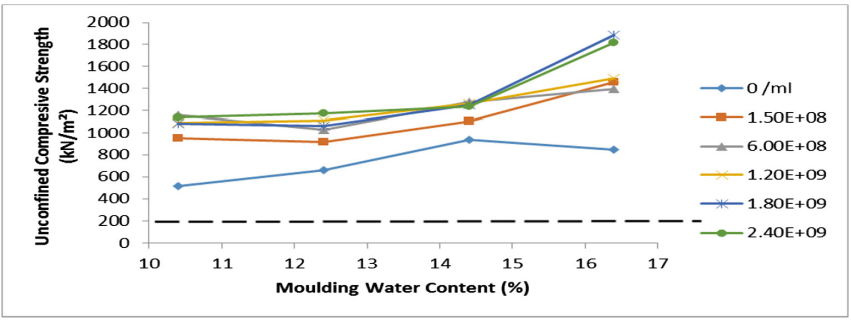

Fig. 2. Variation of unconfined compressive strength of lateritic soil - Bacillus *pumilus* suspension mixtures with moulding water content

The increase in UCS values with higher bacterial suspension density is consistent with the findings reported by [15–20]. The calcite generated during the MICP process was responsible for cementing and clogging the soil specimens. Bio-cementation is achieved when the calcite crystals precipitate on the surface form bridges between the existing soil grains. These calcite crystals bond and stiffen the soil particles hence increasing the unconfined compressive strength of the soil [7].

3.3 Effect of Bacillus *Pumilus* on Unconfined Compressive Strength

The variation of unconfined compression strength (UCS) of lateritic soil with water content relative to optimum (OMC) at stepped Bacillus *pumilus* suspension densities is shown in Fig. 3. Generally, the UCS of the mixtures increased with increase in water content relative to OMC and Bacillus *pumilus* suspension density. Higher UCS values were achieved at higher water content relative to optimum of +4% OMC

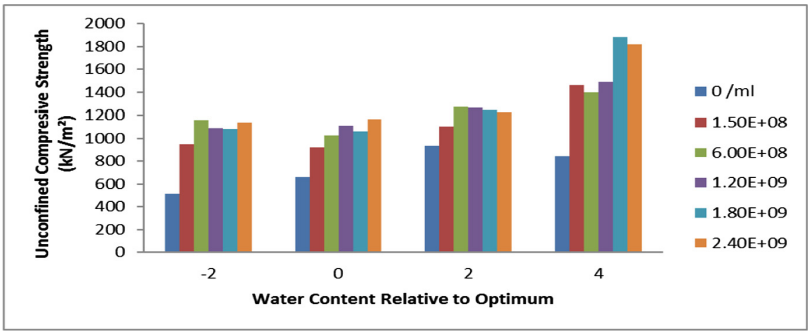

Fig. 3. Variation of unconfined compressive strength of lateritic soil - Bacillus *pumilus* suspension mixtures with water content relative to optimum

Table 1. Two-way analysis of variance results for unconfined compressive strength of lateritic soil - Bacillus *pumilus* suspension mixture

Property	Source of variation	F_{CAL}	P-value	F_{CRIT}
UCS	Moulding water content	18.95458	2.31E–05	3.287382
	B. pumilus suspension	11.46849	0.000108	2.901295

F_{CAL} = F calculate, P-value = Probability of failure while F_{CRIT} = F critical obtained from F "Distribution" table

A two-way analysis of variance (ANOVA) for unconfined compressive strength (UCS) of lateritic soil- Bacillus *pumilus* suspension mixtures is summarized in Table 1. The results showed that moulding water content (F_{CAL} = 18.95458 > F_{CRIT} = 3.287382) and Bacillus *pumilus* suspension density(F_{CAL} = 11.46849 > F_{CRIT} = 2.901295) significantly influenced UCS with the effect of moulding water content being more pronounced than that of Bacillus *pumilus* suspension density.

3.4 Acceptable Compaction Planes

Compaction planes as described by [21] were delineated for UCS values above the minimum regulatory 200 kN/m^2 for Bacillus *pumilus* suspension densities considered. This was developed by relating the moulding water content to the average dry density of specimens recorded during the compaction process. The compaction planes on which the regulatory UCS criterion is satisfied are depicted in Fig. 4.

The Acceptable Zone (AZ) for the natural lateritic soil was obtained at moulding water contents in the range 10.4–14.4% (see Fig. 4a), while it was achieved in the range 10.4–16.4% for 6.0 × 10^8/ml Bacillus *pumilus* suspension density. The AZ for the optimally treated soil is shown in Fig. 4b. The plots of AZs showed that beyond 6.0 × 10^8 cells/ml Bacillus *pumilus* suspension density, wider zones could be achieved because the range of moulding water content in the AZ of the optimally treated soil is wider when compared with that of the natural lateritic soil.

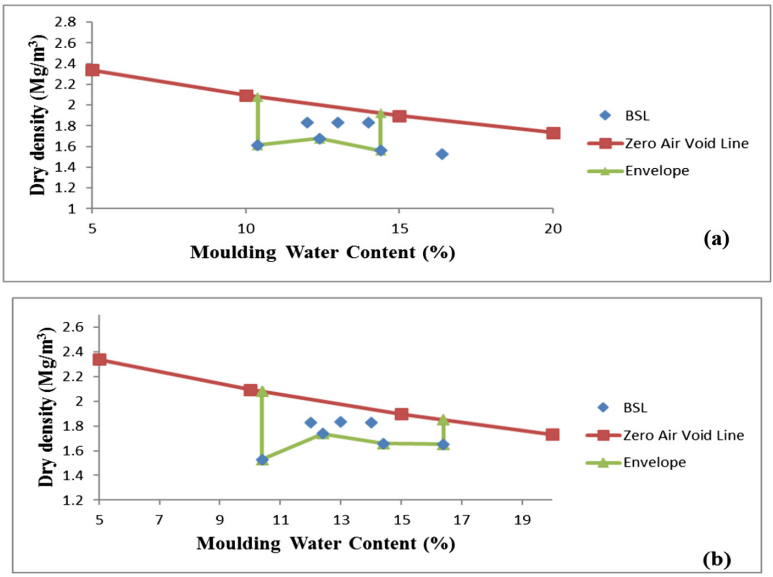

Fig. 4. Acceptable zone (compaction plane) for unconfined compressive strength for lateritic soil – Bacillus *pumilus* mixture for: (a) 0, (i.e., the natural soil) (b) 6.0 × 10^8 cells/ml

3.5 Micrographs of Specimens

The micrograph of the natural lateritic soil (see Plate 1) shows a scaly-like surface morphology on the surfaces. It shows an inter-grain porosity induced by drying and microstructure alteration. This is consistent with the findings reported by [22, 23]. The micrograph of lateritic soil treated with 24.0 × 10^8 cells/ml Bacillus *pumilus* suspension density and cementation reagent (see Plate 2) indicates that improved bonding between the soil particles was caused by calcite precipitate formed within the soil matrix that was responsible for cementing and clogging the soil particles. Physically deposited calcite precipitate formed can be observed on the surface (see Plate 2). The

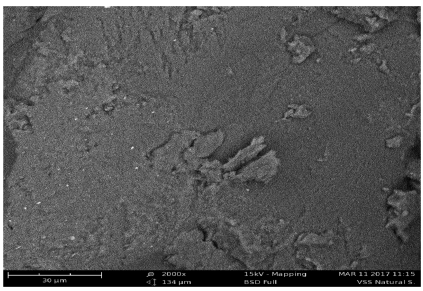

Plate I: Micrograph of the natural lateritic soil cured for 7 days

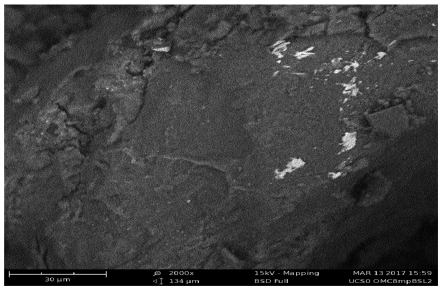

Plate II: Micrograph of lateritic soil –24.0 × 10^8 cells/ml Bacillus *pumilus* cured for 7 days

formation of cementitious product of calcite precipitate covering the soil grains and filling the inter-aggregate pores could be responsible for the improved strength recorded in agreement with the findings reported by [24, 25].

4 Conclusion

Laboratory tests were carried out to evaluate the suitability of the shear strength of lateritic soil treated with Bacillus *pumilus* for use in municipal solid waste containment facilities. Specimens prepared at moulding water contents –2, 0, +2 and –4% of the OMC were compacted with BSL (or standard Proctor) energy. Specimens of lateritic soil – Bacillus *pumilus* suspension mixtures produced satisfactory UCS values for all the treatments and all the moulding water contents considered. Bacillus *pumilus* enhanced the strength of the natural lateritic soil with a peak value of 1884.58 kN/m^2 recorded at Bacillus *pumilus* suspension density of 18.0×10^8 cells/ml and 4% moulding water content relative to OMC. Statistical analysis results showed that moulding water content and Bacillus *B. pumilus* suspension density significantly influenced UCS values. Micro-structural changes were observed on the micrograph of the treated soil. A compaction plane of acceptable zones for UCS based on regulatory value (i.e., > 200 kN/m^2) gave 6.0×10^8 cells/ml Bacillus *B. pumilus* suspension density as optimum treatment for the treatment of lateritic soil when used in waste containment application.

References

1. Karol RH (2003) Chemical grouting and soil stabilization, 3rd edn. M. Dekker, New York
2. Basha EA, Hashim R, Mahmud HB, Muntohar AS (2005) Stabilization of residual soil with rice husk ash and cement. Constr Build Mater 19:448–453
3. DeJong JT, Fritzges MB, Nüsslein K (2006) Microbially induced cementation to control sand response to undrined shear. J Geotech Geoenviron Eng 132:1381–1392
4. Daniel DE, Wu YK (1993) Compacted clay liners and covers for arid sites. J Geotech Eng ASCE 119(2):223–237
5. Daniel DE, Liljestrand HM (1984) Effect of landfill leachate on natural liner system), Geotechnical Engineering Report, GR 83-6 (Geotechnical Engineering Centre, University of Texas, Austin, Tex.) 86
6. Ozcoban MS, Tufekci N, Tutus S, Sahin U, Celik SO (2006) Leachate removal rate and the effect of leachate on the hydraulic conductivity of natural (undisturbed) clay. J Sci Ind Res 65:264–269
7. Harkes MP, Van Paassen LA, Booster JL, Whiffin VS, Van Loosdrecht MCM (2010) Fixation and distribution of bacterial activity in sand to induce carbonate precipitation for ground reinforcement. Ecol Eng 36(2):112–117
8. Stocks-Fischer S, Galinat JK, Bang SS (1999) Microbiological precipitation of $CaCO_3$. Soil Biol Biochem 31(11):1563–1571
9. Stoner DL, Watson SM, Stedtfeld RD, Meakin P, Griffel LK, Tyler TL, Pegram LM, Barnes JM, Deason VA (2005) Application of stereo lithographic custom models for studying the impact of biofilms and mineral precipitation on fluid flow. Appl Environ Microbiol 71(12):8721–8728

10. Qabany AA, Mortensen B, Martinez B, Soga K, Dejong J (2011) Microbial carbonate precipitation correlation of s-wave velocity with calcite precipitation. Geo-Frontiers 2011, pp 3993–4001
11. Soon N, Lee L, Khun T, Ling H (2014) Factors affecting improvement in engineering properties of residual soil through microbial-induced calcite precipitation. ASCE J Geotech Geoenviron Eng 140(5): 04014006 1–11. https://doi.org/10.1061/(ASCE)GT.1943-5606.0001089
12. ASTM (1992): Annual Book of Standards, vol 04.08, American Society for Testing and Materials, Philadelphia
13. AASHTO (1986) Standard Specifications for Transport Materials and Methods of Sampling and *Testing*. In: 14th Edition, American Association of State Highway and Transportation Officials (AASHTO), Washington, D.C Clay. J Geotech Geoenviron Eng ASCE 127(1):67–75
14. Osinubi KJ, Eberemu AO, Ijimdiya TS, Sani JE, Yakubu SE (2018) Volumetric shrinkage of compacted lateritic soil treated with bacillus *pumilus*. In: Farid A, Chen H (eds) Proceedings of GeoShanghai 2018 international conference: geoenvironment and geohazard. GSIC 2018, pp 315–324. Springer, Singapore. https://doi.org/10.1007/978-981-13-0128-5_36
15. Yasuhara H, Hayashi K, Okamura M (2011) Evolution in mechanical and hydraulic properties of calcite-cemented sand mediated by biocatalyst. In: Proceedings of geo-frontiers 2011: advances in geotechnical engineering, Dallas TX, ASCE, Geotechnical special publication 211, pp 3984–3992
16. Park S, Choi S, Kim W, Lee J (2014a) Effect of microbially induced calcite precipitation on strength of cemented sand. In: Proceedings new frontiers in geotechnical engineering 2014: technical papers, ASCE, Geotechnical special publication 234, pp 47–56
17. Park S, Choi S, Nam I (2014b) Effect of plant-induced calcite precipitation on the strength of sand. ASCE J Mater Civ Eng 26(8): 06014017 1–5. https://doi.org/10.1061/(ASCE)GT.1943-5533.0001029
18. Li B, Chu J, Whittle A (2016) Biotreatment of fine-grained soil through the bioencapsulation method. In: Proceedings of Geo-Chicago 2016: technical papers, ASCE, Geotechnical special publication 269, pp 25–32
19. Putra H, Yasuhara H, Kinoshita N, Neupane D, Lu C-W (2016) Effect of magnesium as substitute material in enzyme-mediated calcite precipitation for soil-improvement technique. Front Bioeng Biotechnol 4:37. https://doi.org/10.3389/fbioe.2016.00037
20. Osinubi KJ, Eberemu AO, Ijimdiya ST, Yakubu, SE, Sani JE (2017) Potential use of *bacillus pumilus* in microbial-induced calcite precipitation improvement of lateritic soil. In: Proceedings of the 2nd symposium on coupled phenomena in environmental geotechnics (CPEG2), Leeds, UK
21. Daniel DE, Benson CH (1990) Water content density criteria for compacted soil liners. J Geotech Eng ASCE 116(12):1811–1830
22. Romero E, Simms PH (2008) Investigation in unsaturated soils: a review with special attention to contribution of mercury intrusion porosimetry and environmental scanning electron microscopy. J Geotech Geol Eng 8:1–23
23. Etim RK, Eberemu AO, Osinubi KJ (2017) Stabilization of black cotton soil with lime and iron ore tailings admixture. Transp Geotech 10(2017):85–95. https://doi.org/10.1016/j.trgeo.2017.01.002
24. Wei-Soon Ng, Lee M-L, Hii S-L (2012) An overview of the factors affecting microbial-induced calcite precipitation and its potential application in soil improvement. World academy of science, engineering and technology, vol 6, pp 683–689
25. Hanifi C, Waleed S, Ibrahim HK (2015) Bacterail calcium carbonate precipitation in peat. Arab J Sci Eng 40:2251–2260. https://doi.org/10.1007/s13369-015-1760-4

Evaluation of the Strength of Compacted Lateritic Soil Treated with *Sporosarcina Pasteurii*

Kolawole J. Osinubi[1], Emmanuel W. Gadzama[1], Adrian O. Eberemu[1(✉)], Thomas S. Ijimdiya[1], and Sabo E. Yakubu[2]

[1] Department of Civil Engineering, Ahmadu Bello University, Zaria, Nigeria
aeberemu@yahoo.com
[2] Department of Microbiology, Ahmadu Bello University, Zaria, Nigeria

Abstract. This work evaluates the strength of a tropical residual lateritic soil treated with *Sporosarcina pasteurii* (a microorganism cultured from the soil) in stepped densities of suspension of 0/ml, 1.50×10^8/ml, 6.0×10^8/ml, 1.20×10^9/ml, 1.80×10^9/ml and 2.40×10^9/ml, respectively and cured for 12 h in polythene bags at 24 ± 2 °C. Specimens were prepared at moulding water contents between –2% and +4% relative to optimum moisture content (OMC) and compacted with British Standard light (BSL) energy (or standard Proctor). The compacted soil specimens were then permeated under gravity with a cementation reagent consisting of 20 g of Urea, 10 g of NH_4Cl, 3 g of Nutrient broth, 2.8 g of $CaCl_2$ and 2.12 g of $NaHCO_3$ per litre of de ionized water to initiate microbial-induced calcite precipitation (MICP). Permeation was carried out in three cycles with 2/3 pore volume each, specimens were extruded 24 h after the last permeation and cured for another 48 h before subjection to unconfined compressive strength (UCS) test. Results obtained showed a general decrease in UCS values with higher moulding water content regardless of the density of *S.pasteurii* suspension. Peak UCS values were recorded for specimens prepared at –2% relative to OMC for all densities of *S.pasteurii* suspension. *S.pasteurii* suspension density of 1.20×10^9/ml, can be considered the optimal treatment of the lateritic soil, which recorded a peak UCS value of 2232 kN/m^2 that underscores its efficacy in strength improvement.

Keywords: Lateritic soil · Microbial induced calcite precipitation *Sporosarcina pasteurii* · Unconfined compressive strength

1 Introduction

One of the major concerns of a geotechnical engineer is the improvement of soil engineering properties (Sotoudehfar et al. 2016). Due to soil heterogeneous nature, not all soils normally meet their engineering requirements in their place of origin (Jayanthiand Singh 2016). The vital role played by microorganisms during the process of soil formation has been well acknowledged in literature (Schulz et al. 2013), but the role played by microbial activities in the improvement of the engineering properties of soils had been neglected until the discovery of microbial-induced calcite precipitation (MICP).

© Springer Nature Singapore Pte Ltd. 2019
L. Zhan et al. (Eds.): ICEG 2018, ESE, pp. 419–428, 2019.
https://doi.org/10.1007/978-981-13-2227-3_52

Recently, multi-disciplinary research between geotechnical engineers and microbiologist resulted in the discovery of a new frontier of knowledge called geo-biology. This discovery has prompted engineers to consider soil not only as a construction material but also as an ecosystem in which the engineering properties of soil can be improved through MICP process (Mujah et al. 2017). Achal and Mukherjee (2015) reported MICP as being a promising way of imitating nature's sustainable ways; it is relatively new and possible alternative ground improvement technique with many years of exciting research opportunities lying ahead to completely improve on the laboratory studies into field scale. Furthermore, MICP has been reported to be a promising eco-friendly and more sustainable ground improvement technique (Dejong et al. 2010; Mujah et al. 2017; Wang et al. 2017)

Ivanov and Chu (2008) reported that when using MICP technique for soil improvement the factors to consider should include the screening and identification of suitable microorganisms for different applications and environments, the void spaces (pore throat) available within the soil, cost effectiveness, the optimization of microbial activity *in situ,* etc. Martinez et al. (2013) reported that the most important factor for achieving uniform calcium carbonate precipitation is the distribution of microbes. On the other hand, Hommel et al. (2016) concluded that although the distribution of microbes is a prerequisite in MICP, it is of lesser influence in achieving an engineered MICP relative to injection strategy. Burbank et al. (2013), also reported that indigenous bacteria could be used to induce calcite precipitation and significantly increase liquefaction resistance of sands. This study aimed to evaluate the strength of compacted lateritic soil when treated with *S.pasteurii* for use as a subgrade material.

2 Materials and Methods

2.1 Materials

2.1.1 Soil

The soil used in this study is a lateritic soil obtained from an erosion prone site located in Abagana (Latitude 6°10′15″ N and Longitude 6°58′10″ E), Anambra State, Nigeria. Disturbed method of sampling was used to collect soil samples at depths between 0.5 m and 3.0 m.

2.1.2 Bacteria

The species of bacteria used in this study is *S.pasteurii,* which was screened and cultured from the soil sample.

2.1.3 Cementation Reagent

The composition of the cementation reagent used include: 20 g of Urea, 10 g of NH_4Cl, 3 g of Nutrient broth, 2.8 g of $CaCl_2$ and 2.12 g of $NaHCO_3$ per liter of de-ionized water. The reagent was used in studies reported by Stocks-Fischer et al. (1999) and Al-Qabany et al. (2011).

2.2 Methods

2.2.1 Bacteria Culture/Growth Medium

The bacteria was identified using the of the bacteria was the conventional biochemical confirmatory test outlined in Monica (1995). Bacteria were cultured in an Ammonium-Yeast Extract media described by Mortensen et al. (2011) and Feng et al. (2014). The bacteria *S. pasteurii* was isolated from soil inoculated on media containing 20 g yeast extract, 10 g ammonium chloride, 2 g urea 0.1 g nickel all in 1litre distilled water and NaOH which was used to adjust the pH of the media to 9.0. The media was poured in an aliquot amount of 10 ml per culture bottle corked with foil paper autoclave at 121 °C per 1.1 kg pressure for a period of 15 min, and incubated at 37 °C for a period of 24–48 h for further proper isolation, identification and characterization as isolated urease producing organisms. Biochemical confirmatory tests were conducted on the cultured microorganisms.

2.2.2 Bacteria Cell Concentration

The density of bacteria cell was varied in stepped *S. pasteurii* suspension of 0/ml, 1.5×10^8/ml, 6.0×10^8/ml, 1.2×10^9/ml, 1.8×10^9/ml and 2.4×10^9/ml, respectively. The maximum volume of microorganisms mixed with the soil was one-third (1/3) of the pore volume as recommended by Rowshanbakht et al. (2016).

2.2.3 Index Properties

Determination of the natural moisture content, specific gravity, and particle size distribution were in accordance with procedures outlined in BS 1377:1990.

2.2.4 Atterberg Limits

Soil samples passing through BS No. 40 sieve (425 μm aperture) was used for Atterberg limits tests which consist of liquid limit, plastic limit and plasticity index. The samples were treated with varying densities of the microorganism at the optimum moisture content (OMC) of the soil for British Standard light effort and then treated with the cementation reagent in three cycles each with 2/3 pore volume within a 24-hour period. The treated soil samples were air-dried at room temperature before conducting Atterberg limit tests in accordance with the procedure outlined in BS 1377:1990.

2.2.5 Compaction

Compaction was carried out in accordance with the method outlined in BS 1377 (1990) to obtain the optimum moisture content (OMC). Compaction was done using the British Standard light (BSL) effort (or standard Proctor).

2.2.6 Preparation of Specimens

3000 g of the pulverized air-dried soil sample passed through BS No.4 sieve (4.76 mm aperture) was mixed thoroughly at moulding water contents between –2% and +4% relative to optimum moisture content (OMC) each containing 1/3 of its pore volume as the bacterial densities. Specimens were, cured for 12 h in sealed polythene bags at 24 ± 2°C for hydration and distribution of the microorganisms within the soil before

compaction with BSL energy. This was followed with the permeation of the specimens with the cementation reagent described in Sect. 2.1.3 in three circles with 2/3 of their pore volume each under gravity to initiate the MICP process.

2.2.7 Unconfined Compressive Strength

The treated specimens were cured in the moulds for 24 h before they were extruded. The extruded specimens were further cured in the laboratory at ambient room temperature of 24 ± 2 °C for 24 h after which they were sealed in polyethene bags for another 24 h before crushing to failure using the UCS machine at a controlled strain of 0.02%/min. (Head 1994). Specimens tested had an average height to diameter ratio of 2:1. Crushing of specimens was carried out in triplicates with the average result obtained used.

3 Results and Discussion

3.1 Physical Properties of the Natural Soil

The index properties of the natural soil summarized in Table 1 show that the soil classifies as an A-4(3) soil according to AASHTO (1986) and SC according to Unified Soil Classification System (ASTM 1992). The X-Ray Diffraction analysis of the natural soil revealed kaolinite as the dominant clay mineral.

Table 1. Physical properties of the natural lateritic soil

Property	Quantity
Natural moisture content (%)	11.3
Percent Passing No. 200 Sieve (%)	36.0
Liquid Limit (%)	44.0
Plastic Limit (%)	21.6
Plasticity Index (%)	22.5
Cation Exchange Capacity (Meq)	5.50
Specific Gravity	2.62
AASHTO classification	A – 4(3)
USCS	SC
Colour	Reddish brown
Dominant Clay Mineral	Kaolinite

3.2 Particle Size Distribution

The particle size distribution curve of the natural lateritic soil shown in Fig. 1 indicates that about 36% of the material passed through No 200 sieve. It was also observed that the natural soil has about 64.0% sand content, 14.0% silt content and 22.0% clay content. From the results of the particle size distribution, the geometric compatibility requirements may have been met for effective MICP since the clay content is not relatively much compared to the sand content.

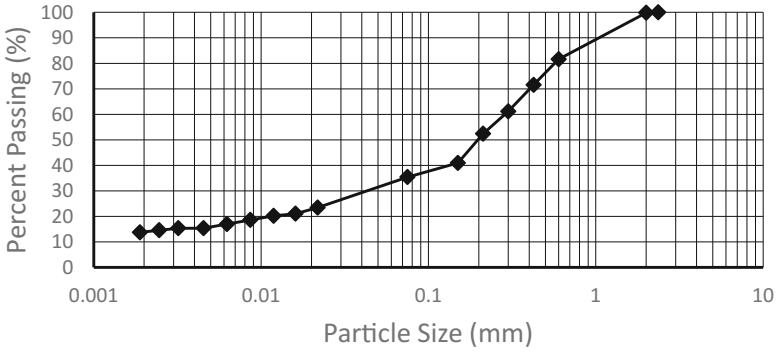

Fig. 1. Particle size distribution curve for the natural lateritic soil

3.3 Atterberg Limits

The variation of Atterberg limits (liquid limit, plastic limit and plasticity index) with varying bacteria densities is shown in Fig. 2. The liquid limit (LL) and plasticity index (PI) values initially increased from 44.0% and 22.5% for the natural soil to peak values of 50.5% and 34.7% at 1.20×10^9/ml and 1.5×10^8/ml *S. pasteurii* suspension density, respectively. Thereafter, LL and PI values generally decreased to 49.5% and 32.1%, respectively, at 2.4×10^9/ml *S. Pasteurii* suspension density.

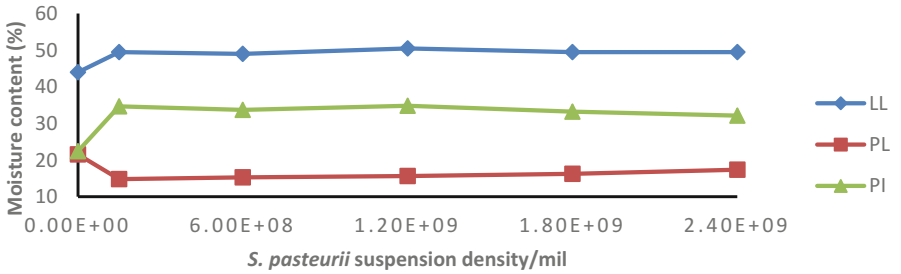

Fig. 2. Variation of Atterberg limits of lateritic soil with *S. pasteurii* suspension density

The initial increase in LL and PI values could probably be due to the presence of calcite deposited in the soil voids that changed the chemistry and behaviour of the lateritic soil-calcite mixture; and resulted to higher demand of water for hydration. The subsequent decrease in LL and PI values could be due to the deposition of higher quantities of non-plastic calcite with higher *S.pasteurii* suspension density that reduced the plasticity of the soil-calcite mixture. Furthermore, cation exchange reaction could have occurred between clay minerals within the soil and calcite formed; since the combined composition of the soil-calcite mixture contains multivalent cations Ca^{2+}, Al^{3+}, Fe^{3+}, etc. that promote the flocculation of clay particles as reported by (Coka 2001; Eberemu 2013; Fehervari et al. 2016). The results recorded show that the

improvement of lateritic soil with *S.pasteurii* produced results in the order: Plastic Limit > Plasticity Index > Liquid Limit.

3.4 Unconfined Compressive Strength

The variation of unconfined compressive strength with *S.pasteurii* suspension density is shown in Fig. 3. The UCS initially increased with increase in *S. pasteurii* suspension density up to 1.2×10^9 organisms/ml and thereafter decreased. This was so because uniform concentration of cementation reagent was applied to all the soil specimens containing different *S. pasteurii* suspension density; it is therefore expected that the urease activities offered by the different suspension densities could have been the only factor that can impact on the calcite crystals precipitation pattern. The UCS also decreased with increased moulding water content irrespective of the *S. pasteurii* suspension density. The highest strength improvement ratio of the treated soil when compared to the natural soil is about 2.39 recorded at *S.pasteurii* suspension density of 1.2×10^9 organisms/ml. It was observed that irrespective of the *S. pasteurii* suspension density used, specimens prepared at –2% OMC recorded the highest UCS values. The increase in strength with increased *S. pasteurii* suspension density could probably be due to the formation of calcites at the inter particle surface of the soil which bridged the particles thus resulting in higher strength values. Dejong et al. (2010) reported two explanations with regard to the distribution of calcite precipitation within the pore space during MICP process, this include a uniform and preferential distribution of calcite precipitate. In the uniform distribution, equal sizes of calcite precipitates are distributed around the soil grains which produces relatively small bonding between the soil grains, thereby offering less strength resistance by the soil grains. This is suspected to have occurred for the specimens prepared at moulding water contents wet of the optimum moisture content. Furthermore, on the wet side of optimum, soil particles are more saturated and would not absorb as much cementation reagent leading the formation of less calcite hence reduced bonding strength. In the preferential distribution, the calcite precipitates are distributed at the particle to particle contact of the soil grain which results in contributing directly to the improvement in strength and stiffness of the soil; this may have occurred in the specimens prepared at moulding water contents dry

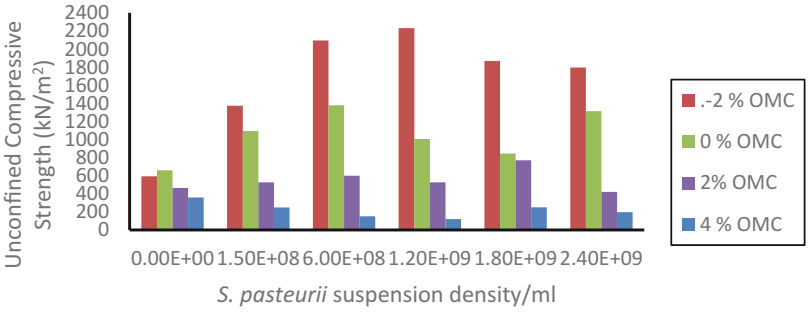

Fig. 3. Variation of unconfined compressive strength lateritic soil prepared at varying moulding water content relative to optimum with *S.pasteurii* suspension density

of optimum and optimum moisture contents respectively. Also particles at this state are less saturated and would absorb more cementation reagent leading the formation of more calcite hence increased bonding strength. This trend is in agreement with results reported by Cheng et al. (2013).

Furthermore, the voids that existed within the soil especially at lower moulding water content may have enhanced easy and increased flow path of the cementation reagent through the soil; this could have led to the formation of more calcite hence the increased strength. It was reported by Choi et al. (2017), that the particle sizes of bio-cements are less viscous and can permeate through porous soil to seal available pores, resulting in the formation of more calcite and subsequently leading to strength gain. The results of this study are in agreement with the findings reported by Cheng et al. (2012; 2013; 2017) and Mujah *et al*. (2017).

3.5 Scanning Electron Microscopy

Micrographs of the scanning electron microscopy (SEM) carried out on the natural and the treated specimens are shown on Plate 1. The micrograph of the natural soil (see Plate 1a) shows micro pores/fissures (red circles); which may have been sealed by the formation of calcite within the micro pores/fissures through bio cementation and bio clogging since they are absent on Plate 1b. The qualitative deduction made from the morphology of SEM in Plates 1a and b is in agreement with observations reported by Cheng *et al*. (2012; 2013; 2017) who reported that not all the calcite crystals formed in the soil pores during MICP necessarily contribute to the improvement in strength of the soil but rather only those forming effective bridges linking the various soil inter-particles as seen in plate 1b.

a) Natural lateritic soil (b) Treated Lateritic soil (1.2 x 10^9/ ml *S.pasteurii* suspension density

Plate I: Micrographs of lateritic soil at x 1000 magnification

3.6 Conclusion

Based on the results of the study carried out, the following conclusions can be drawn:

1. The results of this study have shown the importance of moulding water content relative to optimum in improving the unconfined compressive strength of A-4(3) lateritic soil treated with *S. pasteurii*. It also indicates that optimal performance of this stabilization method is possible while reducing the need for water.
2. Bio-cementation using MICP improved the unconfined compressive strength of A-4 (3) lateritic soil, especially when specimens were prepared at moulding water content dry of optimum or at the optimum moisture content.
3. The peak unconfined compressive strength of 2232.28 kN/m^2 was recorded at *S. pasteurii* suspension density of 1.20 $\times$ 10^9/ml.

Recommendation

An optimal *S. pasteurii* suspension density of 1.20 $\times$ 10^9/ml is recommended for the treatment of lateritic soil classified as A-4(3) soil foruse as a subgrade material.

References

AASHTO (1986) Standard Specifications for Transport Materials and Methods of Sampling and Testing. In: 14th Edition, American Association of State Highway and Transport Officials (AASHTO), Washington, D.C clay. J Geotech Geoenviron Eng ASCE 127(1):67–75

Achal V, Mukherjee A (2015) A review of microbial precipitation for sustainable construction. Constr Build Mater 93:1224–1235. https://doi.org/10.1016/j.conbuildmat.2015.04.051

Al Qabany A, Mortensen B, Martinez B, Soga K, DeJong J.T (2011) Microbial carbonate precipitation: correlation of s-wave velocity with calcite precipitation. In: Proceedings of geo-frontiers 2011: advances in geotechnical engineering, Dallas TX. ASCE, Geotechnical Special Publication 211, pp 3993–4001

ASTM (1992): Annual book of ASTM standards, vol 04(8), Philadephia

BS 1377 (1990). *Method of Testing Soils for Civil Engineering Purpose*. British Standard Institute, BSI, London

Burbank M, Weaver T, Lewis R, Williams T, Williams B, Crawford R (2013) 'Geotechnical tests of sands following bioinduced calcite precipitation catalysed by indigenous bacteria. ASCE J Geotech Geoenviron Eng 139(6):928–936. https://doi.org/10.1061/(ASCE)GT.1943-5606.0000781

Cheng L, Cord-Ruwisch R (2012) In situ soil cementation with ureolytic bacteria by Surface percolation. Ecol Eng 42:54–72. https://doi.org/10.1016/j.ecoleng.2012.01.013

Cheng L, Cord-Ruwisch R, Shahin MA (2013) Cementation of sand soil by microbially induced calcite precipitation at various saturation degrees. Can Geotech J 50:81–90

Cheng L, Shahin MA, Cord-Ruwisch R (2017) Surface percolation for soil improvement by bio cementation utilizing in situ enriched indigenous aerobic and anaerobic ureolytic soil microorganisms. Geomicrobiol J 34(6): 546–556. https://doi.org/10.1080/01490451.20161232766

Choi SG, Chu J, Brown RC, Wang K, Wen Z (2017) Sustainable biocement production via microbially induced calcium carbonate precipitation: use of limestone and acetic acid derived from pyrolysis of lignocellulosic biomass. ACS Sustain Chem Eng 5:5183−5190. https://doi.org/10.1021/acssuschemeng.7b00521

Coka E (2001) Use of class C fly ashes for the stabilization of an expansive soil. ASCE J Geotech Geoenviron Eng 127(7):568–573

Dejong JT, Mortensen BM, Martinez BC, Nelson DC (2010) Bio-mediated soil improvement. Ecol Eng 36:197–210. https://doi.org/10.1016/j.ecoleng.2008.12.029

Eberemu AO (2013) Evaluation of bagasse ash treated lateritic soil as a potential barrier material in waste containment application. Acta Geotech. https://doi.org/10.1007/s11440-012-0204-5

Fehervari A, Gates WP, Patti AF, Turney TW, Bouazza A, Rowe R.K (2016) Potential hydraulic barrier performance of cyclic organic carbonate modified bentonite complexes against hypersalinity. Geotext Geomemb 44:748e–760. http://dx.doi.org/10.1016/j.geotexmem.2016.06.002

Feng K, Montoya BM, Evans TM (2014) Numerical investigation of microbial induced cemented sand mechanical behaviour. In: Proceedings of geo-congress 2014: technical papers, ASCE, geotechnical special publication 234, pp 1644–1653

Head KH (1994) Manual of soil laboratory testing. Permeability, Shear Strength, and Compressibility Tests, vol 2. Pentech Press, London

Hommel J, Lauchnor E, Gerlach R, Cunningham AB, Ebigbo A, Helmig R, Class H (2016) Investigating the influence of the initial biomass distribution and injection strategies on biofilm-mediated calcite precipitation in porous media. Transp Porous Media 114:557. https://doi.org/10.1007/s11242-015-0617-3

Ivanov V, Chu J (2008) Application of microorganisms to geotechnical engineering for bioclogging and biocementation of soil in situ. Rev Environ Sci Biotechnol 7(2):139–153. https://doi.org/10.1007/s11157-007-9126-3

Jayanthi, PNV, Singh, DN (2016) Utilization of sustainable materials for soil stabilization: state-of-the-art. Adv Civil Eng Mater 5(1):46–79. https://doi.org/10.1520/acem20150013. ISSN 2165-3984

Martinez BC, Dejong JT, Ginn TR, Montoya BM, Barkouki TH, Hunt C, Tanyu B, Major D (2013) Experimental optimization of microbial-induced carbonate precipitation for soil improvement. ASCE J Geotech Geoenviron Eng 139(4):587–598. https://doi.org/10.1061/(ASCE)GT.1943-5606.0000787

Monica C (1995) Medical Laboratory Manual for Tropical Countries, vol. II. Elsevier Health Sciences, London, p 520

Mortenson BM, Haber MJ, Dejong JT, Caslake LF, Nelson DC (2011) Effects of environmental factors on microbial-induced calcite precipitation. Appl Microbiol 111(2):338–349. https://doi.org/10.1111/j1365-2672-2011.05065x

Mujah D, Shahin MA, Cheng L (2017) State-of-the-art review of biocementation by microbially induced calcite precipitation (MICP) for soil stabilization. Geomicrobiol J. https://doi.org/10.1080/01490451.2016.1225866

Rowshanbakht K, Kamehchiyan M, Sajedi RH, Nikudel MR (2016) Effects of injected bacterial suspension volume and relative density on carbonate precipitation resulting from microbial treatment. Ecol Eng 89:49– 55. https://doi.org/10.1016/j.ecoleng.2016.01.010

Schulz S, Brankatschk R, Dümig A, Kögel-Knabner I, Schloter M, Zeyer J (2013) The role of microorganisms at different stages of ecosystem development for soil formation. Biogeosciences 10:3983–3996, https://doi.org/10.5194/bg-10-3983-2013

Sotoudehfar AR, sadeghi MM, Mokhtari E, Shafiei F (2016) Assessment of the parameters influencing microbial calcite precipitation in injection experiments using taguchi methodology. Geomicrobiol J 33(2): 163–172. https://doi.org/10.1080/01490451.2015.1025316

Stocks-Fischer S, Galinat JK, Bang SS (1999) Microbiological precipitation of $CaCo_3$. Soil Biol Biochem 31(11): 1563–1571. PII: S00 3 8–07 1 7(99)0 0 08 2–6

Wang Z, Zhang N, Cai G, Jin Y, Ding N, Shen D (2017) Review of ground improvement using microbial induced carbonate precipitation (MICP). Marine Geores Geotechnol. https://doi.org/10.1080/1064119x.2017.1297877

Physical Modelling of Mitigating Methane Emission from Biochar Modified MSW Landfill Cover

Abraham C. F. Chiu(✉) and Y. Xiao

Key Laboratory of Ministry of Education for Geomechanics and Embankment Engineering, Hohai University, Nanjing 210098, China
acf.chiu@gmail.com

Abstract. In this study a laboratory column test has been conducted on a compacted soil modified by a rice-stalk derived biochar to model its methane mitigation capability as a municipal solid waste (MSW) landfill cover material. Preliminary test results showed that gas adsorption was the principal mechanism that reduced the methane emission in the early stage of soil column test. As time passed, microbial methane oxidation became the dominant mechanism over gas adsorption to reduce methane emission. Besides, it was found that the most active zone for methane oxidation was the top 250 mm where the availability of oxygen was adequate for the aerobic activity of methane-oxidising bacteria.

Keywords: MSW landfill cover · Biochar · Methane oxidation
Adsorption · Silt

1 Introduction

Soil cover is a conventional barrier to mitigate landfill gas emissions from municipal solid waste (MSW) landfills. Methane is a major component of landfill gas and it is also a more harmful greenhouse gas than carbon dioxide. Thus, bio-cover has been recently developed to oxidise methane (i.e. reduce methane emission) using the methanotrophic bacteria (Huber-Humer et al. 2009, Stern et al. 2007). Scheutz et al. (2009) presented a review of microbial methane oxidation in different bio-cover systems and pointed out that soil texture, water content, gas supply (methane and oxygen), temperature and nutrients are key influencing factors for methane oxidation in landfill cover soils.

Past studies have shown that soils modified by organic rich materials such as compost and sewage sludge possess higher microbial methane consumption because they have more nutrients, higher water retention capacity and increased porosities (Bohn et al. 2011, Huber-Humer et al. 2008). Biochar is an organic material produced from biomass through pyrolysis. Its highly porous structure and high organic matter content can favour the microbial activity. Based on the results of wood derived bio-chars, recent studies have shown that biohar is a potential soil amendment material to enhance gas adsorption and methane oxidation in the bio-cover (Sadasivam and Reddy 2015, Reddy et al. 2014). Furthermore, Yargicoglu et al. (2015) showed that the physical and chemical properties of biochar can be influenced significantly by the

© Springer Nature Singapore Pte Ltd. 2019
L. Zhan et al. (Eds.): ICEG 2018, ESE, pp. 429–434, 2019.
https://doi.org/10.1007/978-981-13-2227-3_53

feedstock and production process. Thus, it is interested to investigate the methane mitigation capability of soil modified by biochars derived from different feedstocks.

2 Materials and Methodology

2.1 Tested Materials

The tested soil is a fine-grained soil. The basic physical properties were determined in accordance with the procedures given in GB/T 50123-1999 (Ministry of Construction P.R. China 1999). The specific gravity is 2.62. The soil consists of 20% of sand and 80% of silt. The liquid limit and plasticity index are 27% and 9, respectively. The soil is classified as silt of low plasticity (ML) according to the Unified Soil Classification System (USCS). The maximum dry density and optimum water content obtained from the standard compaction test are 1760 kg/m^3 and 16%, respectively. Biochar used in this study was derived from the rice straw, which was pyrolysed at a temperature of 500 °C. The sample has been grinded mechanically by the manufacturer and the maximum grain size is below 2 mm. The specific gravity of the biochar is 0.69. The specific area per unit weight is 118 m^2/g. The organic matter content is 61%. The modified soil samples were prepared by mixing thoroughly the air-dried biochar and soil to achieve a biochar content of 20% of dry mass of soil. The grain sizes of the modified soil consist of 40% sand and 60% silt. On the other hand, addition of biochar increases significantly the liquid limit and plasticity index of modified soil and the modified soil is classified as silt of high plasticity (MH). The maximum dry density and optimum water content of the modified soil are 1220 kg/m^3 and 33%, respectively.

2.2 Soil Column Test

A soil column was used to model the mitigation of methane emission of biochar-modified soil cover under a constant methane flux. Figure 1 depicts the schematic layout of the soil column. It was made of plexiglass with a height of 1050 mm and an internal diameter of 200 mm. There was two gas supply and flow control systems: (1) two gas cylinders of CH_4 and CO_2 and mass flow controllers (with a precision of 0.1 mL/min.) were connected to the bottom of column, and (2) an air compressor and a flowmeter (with a precision of 0.01 mL/min.) were connected to the top of column. The first gas control system was used to supply a constant flux of CH_4 and CO_2 (same mole fraction in the gas mixture) from the bottom of column, while the second one was used to supply a constant flux of air at the top of column.

The soil column consists of two layers: a bottom 100 mm of gravel and a top 800 mm of biochar-modified soil. The modified soil was compacted to a dry density of 1040 kg/m^3 at an initial water content of 30%, which corresponds to 85% of its maximum dry density. The water content and pore air pressure at different height of column were monitored using the Decagon EC-5 water content sensor and U-tube manometer, respectively. The locations of the sensors are depicted in Fig. 1. The column was placed inside a temperature controlled chamber during the test.

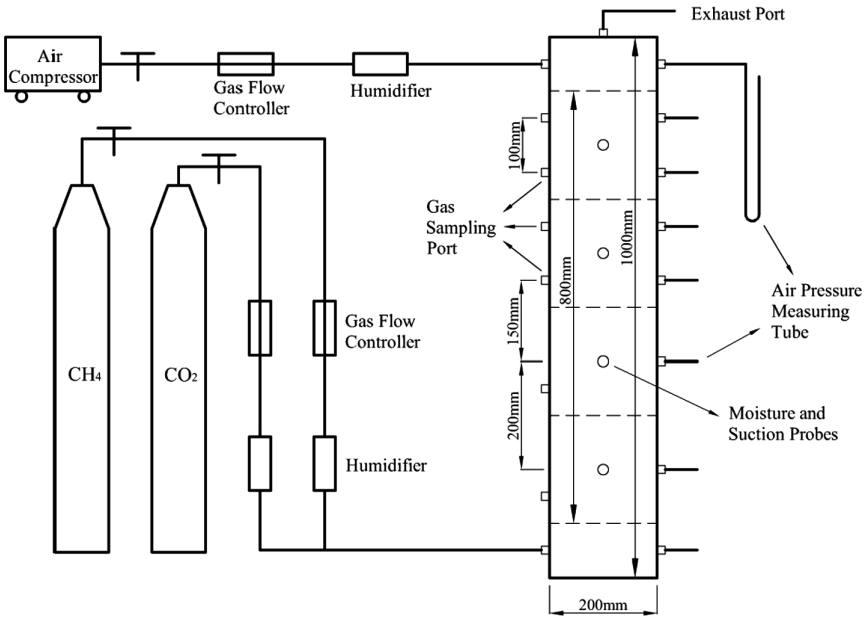

Fig. 1. Schematic layout of laboratory soil column test

During the column test, the flow of methane and carbon dioxide was controlled to a rate of 6.0 mL/min. to simulate a methane flux of 196 g/m^2/day from the bottom of column. On the other hand, an air flow rate of 100 mL/min. was applied at the top of column to provide oxygen for methane oxidation. The methane flux tested in this study is based on the results presented in Scheutz et al. (2009), in which the methane generation rate for a MSW landfill of 20 m depth is about 200 to 300 g/m^2/day for a period between 10 and 15 years after its operation.

Each day 3 mL of gas sample was collected at each gas sampling port (refer to Fig. 1) and also at the top exhaust port. Thereafter, gas chromatography was used to determine the volume fractions of each gas component at different depths of the column. In other words, the spatial distribution of gas components was obtained. The monitoring was conducted for a period of 18 days. The methane flux at the top of column ($flux_{out}$) was determined by

$$flux_{out} = flux_{out(gas)} \cdot C_{CH_4} \tag{1}$$

where $flux_{out(gas)}$ = measured flux of all gas components at the top of column (mL/min.), C_{CH4} = concentration of methane at the top of column. The removal rate of methane (R) is determined by

$$R = \frac{flux_{in} - flux_{out}}{flux_{in}} \cdot 100 \tag{2}$$

where $flux_{in}$ = methane flux at the bottom of column (mL/min.).

3 Test Results and Discussion

Figures 2 and 3 show the distributions of methane, carbon dioxide, oxygen and nitrogen along the height of column after a test period of 1 day and 13 days, respectively. It should be noted that the gas distribution has reached a steady value after a test period of 13 days. It is observed from the figures that the diffusion depth of air is around 250 mm from the top of the column. In other words, oxygen is adequate for the aerobic activity of methane-oxidising bacteria for only the top 250 mm of the column. The results are consistent with the findings reported in the literature (Kightley et al. 1995, De Visscher et al. 1999, Scheutz et al. 2009).

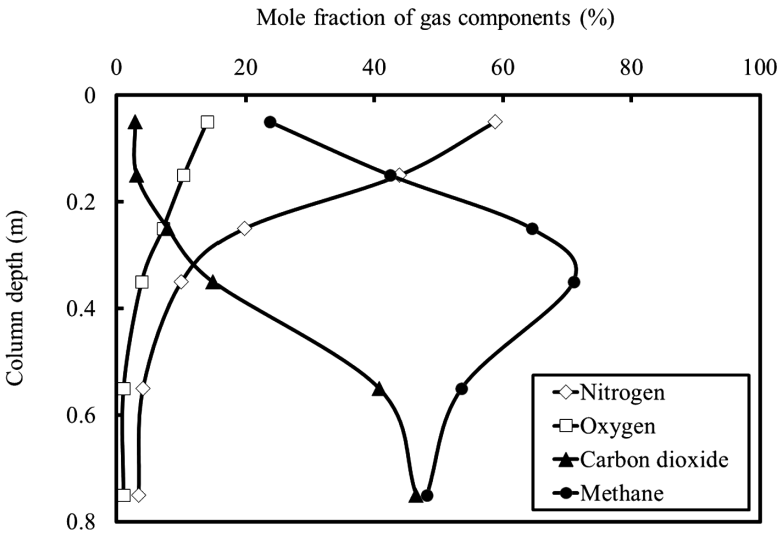

Fig. 2. Variation of gas composition with depth in column test after 1 day of test

Two different mechanisms: gas absorption and microbial methane oxidation are used to interpret the change of compositions of carbon dioxide and methane over time. It is apparent that the gas compositions for the top 250 mm of soil column change over time: both oxygen and methane concentration decrease, but carbon dioxide concentration increases. As depicted in Fig. 2, the concentration of carbon dioxide is significantly lower than that of the methane for the whole column depth after one day of test. It is because the maximum adsorption of carbon dioxide is higher than that of methane resulting in a lower concentration during the initial stage of test. Thus, gas adsorption may be considered as the principal mitigation mechanism for carbon dioxide and methane emission during the initial stage of test.

After reaching the maximum adsorptive capacity of the two gases, Fig. 3 shows that the concentration of methane is slightly lower than that of carbon dioxide in the top 250 mm of soil column after 13 days of testing. Thus, it is suggested that microbial methane oxidation may become the principal mitigation mechanism for methane emission in the long run.

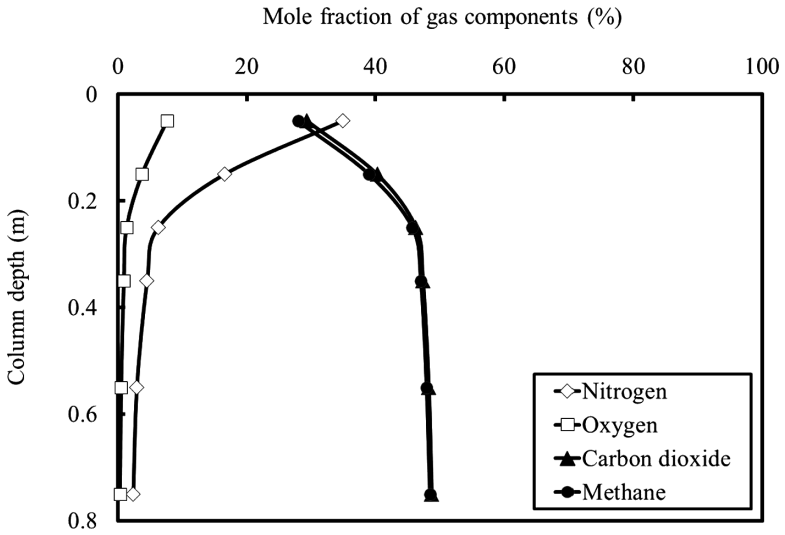

Fig. 3. Variation of gas composition with depth in soil column after 13 days of test

Based on Eqs. (1) and (2), the methane removal rate during the column test was calculated. Figure 4 depicts the variation of methane reduction rate and temperature with time in the column test. It is observed that the amount of methane removal has reached a steady value of 10% after 12 days of test. Besides, the figure also shows that the methane removal rate is quite sensitive to the temperature. As the temperature of the

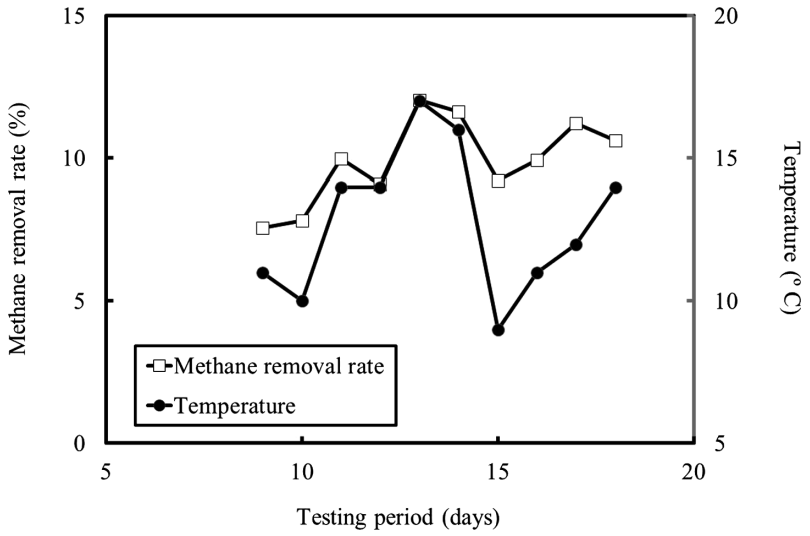

Fig. 4. Variation of methane removal rate and temperature with time in column test

soil column drops from 17 °C to 9 °C between 13th and 15th days of the test, the methane removal rate drops from 12% to 9%.

4 Conclusions

A laboratory soil column test was conducted on a fine-grained soil modified by a rich-straw derived biochar to study its methane mitigation capability as a soil cover. The preliminary test results showed that the mitigation of methane emission using the biochar modified soil is controlled by two mechanisms: gas adsorption and microbial methane oxidation. In the early stage of the column test, gas absorption is the principal mechanism to reduce the emission of carbon dioxide and methane. As the adsorptive capacity of carbon dioxide is higher than than of methane, the removal rate of carbon dioxide is higher than that of methane in the early stage of the test. As time passes, microbial methane oxidation becomes the dominant mechanism to control the mitigation of methane emission. It is found that the methane removal rate has reached a steady value of 10% after running the column test for 11 days. Besides, it is also observed that the microbial methane oxidation is sensitive to the change of temperature.

Acknowledgement. The research is financially supported by the Fundamental Research Funds for the Central Universities of China (Grant No. 2017B00914).

References

Bohn S, Brunke P, Gebert J et al (2011) Improving the aeration of critical fine-grained landfill top cover material by vegetation to increase the microbial methane oxidation efficiency. Waste Manage 31:854–863

De Visscher A, Thomas D, Boeckx P et al (1999) Methane oxidation in simulated landfill cover soil environments. Environ Sci Technol 1999:1854–1859

Huber-Humer M, Gebert J, Hilger H (2008) Biotic systems to mitigate landfill methane emissions. Waste Manage Res 26:33–46

Huber-Humer M, Roder S, Lechner PF (2009) Approaches to assess biocover performance on landfills. Waste Manage 29:2092–2104

Kightley D, Nedwell DB, Cooper M (1995) Capacity for methane oxidation in landfill cover soils measured in laboratory-scale soil microcosms. Appl Environ Microbiol 1995:592–610

Ministry of Construction P.R. China (1999) Standard for soil test method. GB/T 50123-1999, Beijing. (In Chinese)

Reddy KR, Yargicoglu EN, Yue D et al (2014) Enhanced microbial methane oxidation in landfill cover soil amended with biochar. J Geotech Geoenviron Eng 140(9):04014047

Sadasivam BY, Reddy KR (2015) Adsorption and transport of methane in landfill cover soil amended with waste-wood biochars. J Environ Manage 158:11–23

Scheutz C, Kjeldsen P, Bogner JE et al (2009) Microbial methane oxidation processes and technologies for migration of landfill gas emissions. Waste Manage Res 27:409–455

Stern JC, Chanton J, Abichou T et al (2007) Use of biologically active cover to reduce landfill methane emissions and enhance methane oxidation. Waste Manage 27:1248–1258

Yargicoglu EN, Sadasivam BY, Reddy KR, Spokas K (2015) Physical and chemical characterization of waste wood derived biochars. Waste Manage 36:256–268

Geoenvironmental Risk Assessment, Management and Sustainability

(Edited by Shuai Zhang and Chaosheng Tang)

Municipal Solid Waste Disposal in Hangzhou, China

Xiao Bing Xu[1(✉)], Da Ni[1], Si Fa Xu[1], Ji Wu Lan[2], and Hui Xu[3]

[1] Institute of Geotechnical Engineering,
Zhejiang University of Technology, Hangzhou, China
xiaobingxu@zjut.edu.cn
[2] MOE Key Laboratory of Soft Soils and Geoenvironmental Engineering,
Institute of Geotechnical Engineering, Zhejiang University, Hangzhou, China
[3] School of Civil Engineering and Architecture, Zhejiang Sci-Tech University,
Hangzhou, China

Abstract. Hangzhou is one of the eight pilot cities for the sorting, collection and disposal of municipal solid waste (MSW) in China. An overview of current status and future plan of MSW disposal in Hangzhou is carried out. The sorting ratio of MSW was estimated to be less than 25% in 2016. It imposes heavy burden on government's plan of increasing the incineration ratio from 40% to 80% and composting 200 tons of food waste daily in 2020. Through comparison of the landfills, incineration plants and composting plants in Hangzhou, the current standards for the pollution control of MSW disposal facilities are discussed. The risk evaluation during the design period and the monitoring data disclosure during the operation period are suggested to be the mandatory provisions in the future revision of these standards. The work conducted in this paper would provide reference for other cities facing the problem of MSW disposal during the fast urbanization process.

Keywords: Municipal solid waste · Landfill · Incineration · Compost
Pollution

1 Introduction

China is undergoing rapid urbanization, and the urbanization portion is about 57.35% in 2016 (NBS 2016). Municipal solid waste (MSW) disposal is one of the key concerns for city development. Hangzhou, the provincial capital of Zhejiang province, has a population of about 9.18 million by the end of 2016. The total amount of MSW generated in Hangzhou is about 3.78 million tons in 2016 (ZJOL 2017). The increasing rate of MSW generation in Hangzhou is about 10% from 2006 to 2016. Though Hangzhou has been chosen as one of the eight pilot cities for the sorting, collection and

The work was supported by the Zhejiang Provincial Natural Science Foundation of China (Grant Nos. LY17E080021 and LY15E080021) and the National Natural Science Foundation of China (Grant Nos. 51708508, 41502276 and 41402249).

© Springer Nature Singapore Pte Ltd. 2019
L. Zhan et al. (Eds.): ICEG 2018, ESE, pp. 437–445, 2019.
https://doi.org/10.1007/978-981-13-2227-3_54

disposal of MSW in China, it still faces many problems for MSW. Firstly, increasing amount of MSW generated in Hangzhou imposes heavy burden on the demand of more disposal facilities. Secondly, the sorting ratio during MSW collection is still very low (<25%) (ZJOL 2017). Therefore, it's difficult for the choice of proper disposal methods such as landfilling, incineration and composting. Furthermore, for each kind of disposal method, the top concern for citizens is still pollution control. For example, more than five thousand people protested the plan and construction of an incineration plant in Hangzhou in 2014, as the Environmental Impact Assessment (EIA) and the approval process are questionable (Gan 2016).

Wilson et al. (2012) summarized three key hardware components for waste management. The first two hardware components are related to the protection of environment and public health: (i) maintaining healthy conditions in cities through a good waste collection service, and (ii) protection of the environment throughout the waste chain, especially during waste treatment and disposal. This paper focuses on the effect of the three main MSW disposal methods in Hangzhou (i.e., landfilling, incineration and composting) on the protection of environment and public health. The current standards for the pollution control of MSW disposal are discussed.

2 MSW Generation and Collection in Hangzhou

As mentioned above, about 3.78 million tons of MSW is generated in 2016 for Hangzhou. The generation is estimated to be about 4.4 million tons in 2020 (ZJOL 2017). In this study, waste composition of MSW in Hangzhou was determined through manual sorting. Ten samples were collected from MSW in garbage trucks. After manual sorting, waste components were dried at an oven temperature of 60 °C for 48 h to prevent ignition loss of organic matters, and the moisture content of each component were measured. The portion of each component and the moisture content are shown in Table 1. It indicates that MSW in Hangzhou is high food waste content (59.4%, kg/kg, wet basis) MSW. The average moisture content of MSW is about 70.2% (kg/kg, wet basis).

Table 1. Composition of MSW in Hangzhou

Component	Portion (kg/kg, %)		Moisture content (kg/kg, %)
	Wet basis	Dry basis	Wet basis
Food	59.4	33.9	83.0
Paper & Cardboard	13.5	16.8	63.0
Rubber & Plastic	18.0	28.5	53.0
Textile	2.0	2.6	62.0
Wood	1.1	2.5	30.0
Tile	1.6	4.8	12.2
Glass	1.7	5.0	11.3
Metal	0.6	1.8	6.37
Soil & dust	2.1	4.2	41.0

Four types of waste including food waste, recyclable waste, hazardous waste and other waste are suggested to be collected separately in Hangzhou. However, the number of residential community applying source-separating is still very low. Furthermore, the actual source-separating results in the residential community are not satisfying. Institute of Environmental Health Sciences in Hangzhou investigated 618 bags of MSW from transfer stations and residential communities (ZJOL 2015). Among these, 286 bags of MSW were from dustbins for food waste. 276 bags of MSW were from dustbins for other waste. The rest 56 bags of MSW were mixed waste without source-separating. The investigation results indicate that food waste, paper, rubber & plastic and textile account for 71.43%, 12.41%, 8.5% and 4.16%, respectively, in dustbins for food waste. The portions of food waste, paper, rubber & plastic and textile are 34.68%, 28.72%, 20.17% and 6.74%, respectively, in dustbins for other waste. For mixed waste, the portions of waste components are close to the results of this study (Table 1).

In Hangzhou, about 60% of MSW generated is collected and transported into disposal facilities directly. The rest 40% of MSW is still transported into transfer station for preliminary compression and dewatering first. The current status of MSW disposal facilities in Hangzhou is summarized in the following section.

3 MSW Disposal in Hangzhou

The disposal methods of MSW in Hangzhou are shown in Fig. 1. The mixed MSW without source-separating is disposed in incineration plants and landfills. For source-separated MSW, food waste is disposed in landfills and composting plants. Recyclable and hazardous waste is disposed in qualified recycling companies and hazardous waste treatment companies, respectively. Other waste also has two disposal ways including incineration and landfilling. Currently, about 60% of MSW is disposed in landfills, and the rest are mainly disposed in incineration plants.

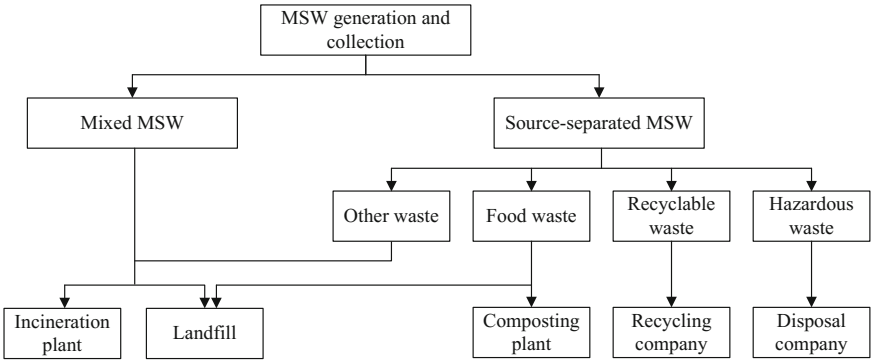

Fig. 1. MSW disposal in Hangzhou

According to HZPB (2014), Hangzhou is divided into five regions for MSW collection and disposal. The MSW disposal facilities in Hangzhou are shown in Table 2. It indicates that there's only Tianziling landfill available for MSW disposal now. Inning Sect. 6 landfill has been closed. According to SC (2011), for the city with scarce land

Table 2. MSW disposal facilities in Hangzhou

Type	Site	Capacity	Service life	Waste to energy
Landfill	Tianziling Gongshu District	1st stage: 6 million m^3 9 million tons	1994–2007	About 1.8×10^5 kW·h/day
		2nd stage: 22 million m^3 5000 ton/day	2007 ~	
Landfill	Inning Sect. 6 Xiaoshan District	0.62 million m^3 2.3 million tons	2007 ~ 2016	No
Incineration plant	Jinjiang A Yuhang District	600 ton/day	1998 ~ 2017	About 7.88×10^7 kW·h/year
	Nengda Jianggan District	800 ton/day	2002 ~ 2015	–
	Lvneng Binjiang District	450 ton/day (Expanded to 1400 ton/day)	2006.8 ~ Under expansion	–
	Jinjiang B Xiaoshan District	1200 ton/day (Expanded to 1800 ton/day)	2007.7 ~ Under expansion	About 1.5×10^8 kW·h/year
	Jiangdong Xiaoshan District	1st stage: 1200 ton/day 2nd stage: 600 ton/day	2015.12 ~	–
	Jiufeng Yuhang District	3000 ton/day	2017.6 ~	About 3.76×10^8 kW·h/year
	Fuyang Fuyang District	1000 ton/day	–	–
	Tianziling Gongshu District	–	Under design	–
Composting plant	Tianziling Gongshu District	1st stage: 200 ton/day food waste and 20 ton/day kitchen oil	2015.4 ~	–
		2nd stage: 250 ton/day food waste	2016.1 ~	
	Linpu Xiaoshan District	400 ton/day food waste	2017.7 ~	About 4.03×10^6 m^3/year biogas and 3×10^4 ton/year biodiesel

resource and high population density, incineration is suggested for MSW disposal rather than landfilling. Therefore, as shown in Table 2, Hangzhou tends to dispose much more MSW in incineration plants. Two incineration plants including Jinjiang A and Nengda have been relocated (as Jiufeng and Jiangdong, respectively) with updated technologies and larger capacity. Two incineration plants including Lvneng and Jinjiang B are under expansion. Fuyang district of Hangzhou also has an incineration plant which may be expanded and updated in the near future. A new Tianziling incineration plant is under plan and design. Now all the residual waste leaving the incineration plants are sent to Tianziling landfill. Based on source-separating, more food waste tends to be disposed. There are two composting plants including Tianziling and Linpu. However, as mentioned above, the actual source-separating is not satisfying, and the two composting plants don't have enough food waste to ensure the running at full capacity. For example, Linpu composting plant has a capacity of 400 ton/day. However, it disposes only 60 ton/day now.

The future plan of MSW disposal in Hangzhou is shown in Fig. 2 (HZG 2014). The daily disposal capacity will reach 10^4 tons in 2020, among which 85% will be disposed in incineration plants. Food waste sorted for composting will reach 200 ton/day which can generate 10 million kWh/year of electricity. According to the standard GB/T18750-2008, the moisture content and ash content of MSW into incinerator should be less than 50% and 25%, respectively. And the lower heating value is suggested to be larger than 4.18 MJ/kg. Therefore, Hangzhou requires better source-separating of MSW and larger incineration plants under stricter standards.

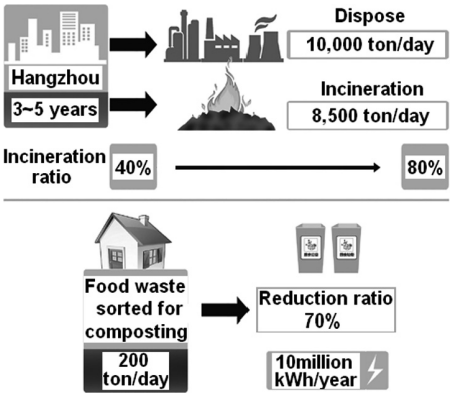

Fig. 2. Future plan of MSW disposal in Hangzhou (HZG 2014)

4 Standards for Pollution Control

Three EIA reports for landfill, incineration plant and composting plant, respectively, were studied. The laws, technical guidelines, policies, codes and standards for pollution control referenced in these three reports were summarized in five groups including general prevention and control of pollution, public participation, industrial standards

Table 3. Laws, technical guidelines, policies, codes and standards for MSW disposal

Type	Title	Tianziling landfill 2nd stage[a]	Jiufeng incineration plant[b]	Tianziling composting plant[c]
Pollution prevention and control	Environmental Protection Law of the PRC	√	–	–
	Soil Pollution Prevention and Control Law of the PRC (Draft Version)	–	–	–
	Water Pollution Prevention and Control Law of the PRC	√	–	–
	Air Pollution Prevention and Control Law of the PRC	√	–	–
	Environmental Noise Pollution Prevention and Control Law of the PRC	√	–	–
	Solid Waste Pollution Prevention and Control Law of the PRC	√	–	–
	Environmental Impact Assessment Law of the PRC	√	√	–
	Environmental Protection Ordinance for Construction Projects	√	√	–
	Technical Guidelines for Environmental Impact Assessment	–	√	–
	Technical Guidelines for Environmental Risk Assessment on Projects	√	√	–
	Municipal Solid Waste Disposal and Pollution Control Technology Policy	√	–	–
Public participation	Measures of Public Participation in Environmental Protection	–	–	–
	Interim Measures of Public Participation in Environmental Impact Assessment	–	√	–
Industrial standards	Technical Code for Municipal Solid Waste Sanitary Landfill	√	–	–
	Standard for Pollution Control on the Landfill Site of Municipal Solid Waste	√	–	–
	Technical Code for Projects of Municipal Solid Waste Incineration	–	–	–
	Standard for Pollution Control on the Municipal Solid Waste Incineration	–	–	–

(*continued*)

Table 3. (*continued*)

Type	Title	Tianziling landfill 2nd stage[a]	Jiufeng incineration plant[b]	Tianziling composting plant[c]
	Technical Code for the Composting of Municipal Solid Waste	–	–	–
Environment quality standards	Quality Standard for Ground Water	√	√	√
	Environmental Quality Standards for Surface Water	√	√	–
	Ambient Air Quality Standards	√	√	–
	Environmental Quality Standards for Soils	–	√	
	Environmental Quality Standard for Noise	√	√	√
Emission standards	Standard for Pollution Control on the Landfill Site of Municipal Solid Waste	√	√	√
	Standard for Pollution Control on the Municipal Solid Waste Incineration	–	√	–
	Emission Standards for Odor Pollutants	√	√	√
	Emission Standards for Industrial Enterprises Noise at Boundary	√	√	√
	The Reuse of Urban Recycling Water-Water Quality Standard for Industrial Uses	–	√	–

Note: [a] information from ESRDIZP (2003); [b] information from SCIESMEP and HECLCZP (2014); [c] information from HECLCZP (2013).

for MSW disposal facilities, environmental quality standards and emission standards. Table 3 indicates that:

(i) For different types of MSW disposal facilities, the contents of EIA reports opened to the public are not prepared in a unified framework. For example, the EIA report of Tianziling composting plant contained the least laws, technical guidelines, policies, codes and standards related to pollution control. EIA reports of Jiufeng incineration plant and Tianziling composting plant even don't mention the industrial standards for the design, construction and operating of their own type of MSW disposal facility.

(ii) Much stricter requirements of the prevention and control of soil pollution will be imposed on MSW disposal. The draft version of Soil Pollution Prevention and Control Law of the People's Republic of China (PRC) is under review now. The Environmental Quality Standards for Soils is still the 1995 version and requires revision accordingly in future.

(iii) There is a lack of the standard for pollution control on MSW composting. Considering more food waste disposed in composting plants, the standard should be drafted as soon as possible.

(iv) The risk evaluation during the design period should be considered for landfilling and composting. Zhang (2017) summarized the main risks for MSW disposal facilities in Hangzhou (Fig. 3). Currently, the risk evaluation for different types of accidents is only required in the Standard for Pollution Control on the Municipal Solid Waste Incineration.

According to the EIA reports of disposal facilities, the environmental monitoring data should be opened to public during the operation of facilities. However, monitoring and measuring results from the third-party environmental protection organization reveal that the excessive discharge of pollutants is common for MSW disposal facilities in China. For example, WEC and FNERI (2016) investigated 231 MSW incineration plants. They found that many incineration plants didn't open their monitoring data and excessive discharge of pollutants was severe.

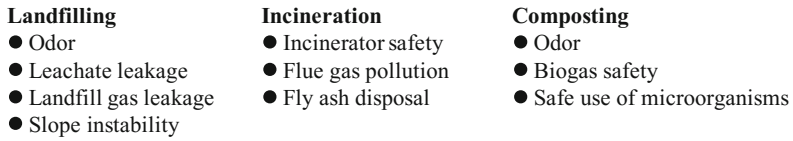

Fig. 3. Risks during the operation of MSW disposal facilities in Hangzhou (Zhang 2017)

5 Conclusions

MSW in Hangzhou is high food waste content (about 59.4%, kg/kg, wet basis) MSW. Its average moisture content is about 70.2% (kg/kg, wet basis). Better source-separating is required in order to increase the ratio of incineration for MSW disposal in Hangzhou.

There are one landfill, five incineration plants and two composting plants available for MSW disposal in Hangzhou now. The remains of MSW after incineration and composting still require landfilling. Therefore, Tianziling landfill is of vital importance for Hangzhou. As it will soon reach the designed capacity, a 3rd stage expansion can be planed.

The risk evaluation during the design period and the monitoring data disclosure during the operation period should be the mandatory provisions in the future revision of relevant standards. Stricter supervision from the government is required.

References

ESRDIZP (Environmental Science Research and Design Institute of Zhejiang Province) (2003). EIA report of the second MSW landfill in Hangzhou (in Chinese)

Gan J (2016) How to avoid NIMBY conflict of municipal solid waste incineration power plant: a case study of Hangzhou Jiufeng Project. Environ Sanitation Eng 24(4):87–88 (in Chinese)

HECLCZP (Huanke Environmental Consulting Limited Company of Zhejiang Province) (2013). EIA report of the 1st stage food waste composting project in Hangzhou (in Chinese)

HZG (Hangzhou Government) (2014) Implementation suggestions of municipal solid waste disposal in Hangzhou-Hangzhenbanhan (2014) 160 (in Chinese)

HZPB (Hangzhou Planning Bureau) (2014) Planning of environmental health in Hangzhou 2008–2020 (in Chinese)

NBS (National Bureau of Statistics of the People's Republic of China) (2017) National economy and society developed statistical bulletin 2016 (in Chinese)

SC (The State Council of the People's Republic of China) (2011) Official notice on municipal solid waste disposal-Guofa (2011) (in Chinese)

SCIESMEP (South China Institute of Environmental Sciences. MEP), HECLCZP (Huanke Environmental Consulting Limited Company of Zhejiang Province) (2014) EIA report of Jiufeng MSW incineration project in Hangzhou (in Chinese)

Wilson DC, Rodic L, Scheinberg A, Velis CA, Alabaster G (2012) Comparative analysis of solid waste management in 20 cities. Waste Manage Res 30(3):237–254

Zhang SK (2017) Risk management of solid waste disposal in Hangzhou. In: 2017 Forum on solid waste disposal and city safety. Invited Lecture (in Chinese)

ZJOL (Zhejiang Online) (2015) http://zjnews.zjol.com.cn/system/2015/12/19/020959344.shtml (in Chinese)

ZJOL (Zhejiang Online) (2017) http://js.zjol.com.cn/ycxw_zxtf/201701/t20170113_2829038.shtml (in Chinese)

WEC (Wuhu Ecology Center), FNERI (Friends of Nature Environmental Research Institute) (2016) Information disclosure and emission reports of 231 MSW incineration plants in China (in Chinese)

Qualitative Evaluation of Methods Applied to Sustainable Remediation

A. B. Braun(✉), A. W. da S. Trentin, and A. Thomé

University of Passo Fundo, Passo Fundo, Brazil
adelibeatrizbraun@hotmail.com

Abstract. This study aimed to define a method applied to remediation of contaminated sites that best represents sustainability. We identified the methods developed and applied in the world scenario and analyzed them as to the satisfaction of nine decision criteria established by the authors to verify the sustainability in the approach of methods. Eight methods of sustainability assessment in remediation of contaminated sites were identified, and a tendency in the graphical representation for decision-making was observed regarding the structures of identified methods. Regarding the criteria, the participation of the different stakeholders in the remediation project obtained the best performance, being approached in all the analyzed methods. In this context, ITRC method obtained the best performance among the analyzed methods. It is concluded that this type of analysis, through the satisfaction of criteria in approach of the methods, provides a more detailed understanding of contributions of different methods to sustainable results.

Keywords: Contamination · Remediation techniques · Sustainable remediation Methodologies · Sustainability

1 Introduction

Sustainable remediation has variable definitions, but there is a common consensus on its broad purpose to reduce environmental, economic, and social impacts by controlling the associated risks and long-term benefits of remediation projects (Holland et al. 2011; Cundy et al. 2013). Therefore, sustainable remediation implies in coordination between the consumption of resources needed for remediation and the benefits achieved in terms of economic viability, conservation of natural resources and biodiversity, and the improvement of quality of life in neighboring communities of the area (Forum 2009; Slenders et al. 2017).

However, sustainable remediation is still an issue that is in phase of adequacy for its effective use and incorporation in the context of the management of contaminated sites, and the discussion of its approach has gradually evolved over the years (Pollard et al. 2004; Bardos et al. 2011; Reddy and Adams 2015; Hou et al. 2016). While countries such as the United States and the United Kingdom, for example, already have high rates of awareness and adoption of sustainable remediation, developing countries, in addition to being less aware, also have low rates of adoption of sustainability in the remediation of contaminated sites (Hou et al. 2016).

© Springer Nature Singapore Pte Ltd. 2019
L. Zhan et al. (Eds.): ICEG 2018, ESE, pp. 446–452, 2019.
https://doi.org/10.1007/978-981-13-2227-3_55

There are still many obstacles to be overcome in the practical context of sustainable remediation, and there is still no universally accepted and accepted method for assessing sustainability with respect to remediation processes in contaminated sites (Reddy and Adams 2015). This suggests that further improvements and studies are possible, aiming at a more detailed understanding of the effective contributions of the theme in achieving sustainable results (Ridsdale and Noble 2016).

This study proposed to define a methodology applied to remediation of contaminated sites that best represents sustainability, based on the identification and description of the methods applied to the sustainable remediation that is being developed in the world scenario, as well as in the characterization of the identified methods, and analysis in relation to pre-defined's decision criteria.

2 Methodology

The identification of these methods in world scenario was carried out through a systematic literature review, with searches in pages of world-wide network of computers and in databases of scientific journals, such as Web Of Science, Scopus, Science Direct and Google Scholar.

In next step, it was analyzed how sustainability is represented and addressed in identified methods, in order to verify how much each approach to sustainability. The basis for such analysis was principles identified in literature, and to guide analysis of content of methods listed, all principles were operationalized as decision criteria (Table 1). The order presented in Table 1 did not take into account the importance of the criteria for sustainability, moreover all criteria were considered equally important.

Documentary analysis and thematic analysis were used as mechanisms for evaluation of methods regarding the satisfaction of criteria, as presented by Bowen (2009). This research strategy basically involves a superficial examination, followed by a complete reading, and ending with interpretation of content, in view of proposed objective, being linked to this stage of research, since, it is proposed an evaluation of the content of the methods related to its relationship with decision criteria, for subsequent selection.

The results were presented qualitatively and quantitatively. The qualitative analysis was based on each decision criterion being totally satisfied (TS), partially satisfied (PS), or not satisfied (NS) in relation to each method analyzed, according to the approach used by Ridsdale and Noble (2016). For one criterion to be fully satisfied, it was considered that method explicitly addressed the criterion, and provided guidance or guidance on the issue. For the criterion to be partially satisfied, it was considered that question was approached in a complementary way to the method. For criterion not to be satisfied, there was no approach to the question in the general context of method.

The quantitative analysis was performed by assigning a numerical scale of 2, 1 and 0 to levels of satisfaction of the TS, PS and NS criteria, respectively. This assignment of values was weighted until the analysis was representative of results, therefore, it was considered that value of the level of satisfaction TS is twice PS and NS is null, that is, the TS level prevails in the analysis, but the importance of PS level is also considered.

Table 1. Principles and decision criteria for analysis and selection of methods

Principles	Decision criteria
Assessment of the central elements of green remediation	C1: The method addresses and evaluates elements such as energy, air, water resources, materials and waste, and land and ecosystem during the remediation process
Guarantee of intergenerational equity	C2: The method addresses the adoption of measures that minimize energy consumption and the use of natural resources, and that maximize the reuse of materials, guaranteeing the needs of future generations
Evaluation of remediation options	C3: The method is supported by comparing different available remedial options
Lifecycle approach	C4: The method refers to life-cycle thinking, with a view to immediate and long-term sufficiency
Concern about the future use of the area	C5: The method considers the possibility of future use of the area, at the beginning of the project, in the evaluation of correction alternatives, and in the application of the remediation process
Consideration and Integration of the sustainability tripod	C6: The method facilitates the inclusion and analysis of the social, economic and environmental aspects of sustainability throughout the remediation process
Protection of human health and the environment in general	C7: The method takes into account the elimination of unacceptable risks associated with the protection of human health and the environment, ensuring the integrity of the people directly involved in the remediation process and communities neighboring the area
Involvement of stakeholders	C8: The method addresses the involvement of affected communities, users in the area or interested in the solution, and/or considers their integration into the remediation process
Registration and documentation of the decision-making process	C9: The method provides the assumptions and data used to achieve the final remediation strategy, with a clear approach and to easy understanding and replication

This assessment resulted in score that describes the level of satisfaction of criteria for each method analyzed.

The information was organized in a spreadsheet for classification, grouping and conducting a comparative analysis between methods and criteria. The criteria and methods with highest scores were analyzed and discussed. For classification purposes, the score obtained was first considered. In case of a tie of scores, the highest number of TS criteria was followed, followed by PS, and finally the NS, and, in case of a new tie, the position of criterion or method was considered in analysis worksheet, not taking into account which criteria are favorable or preferred as regards sustainability.

3 Results and Discussion

Sustainability assessment methods are systematic ways that help in making decisions regarding environmental, social and economic aspects. In addition, they contribute to evaluation of metrics and tools by which sustainability of a remediation project is analyzed (Reddy and Adams 2015).

In the world scenario, eight methods applied to sustainable remediation were identified, linked to agencies and organizations that work on development of methods for analysis of sustainability in remediation of contaminated sites. Methods developed by (1) the Environmental Protection Agency of the United States of America (USEPA); (2) American Society for Testing and Materials (ASTM); (3) Interstate Technology and Regulatory Council (ITRC); (4) Network for Industrially Contaminated Land in Europe (NICOLE); and the groups associated with Sustainable Remediation Forums (SuRFs), (5) United States (SuRF-US), (6) United Kingdom (SuRF-UK), (7) Australia and New Zealand (USEPA 2012; ASTM 2013; ITRC 2011; NICOLE 2010; Holland et al. 2011; SuRF-UK 2010; Smith and Nadebaum 2016; Huang et al. 2011).

Regarding the analysis of these methods according criteria presented in the methodology to diagnose degree of sustainability in approach of each method, the results indicate a great variability among criteria, which is perceived in function that no decision criterion was fully satisfied by all methods, in addition to which no method met all criteria completely.

The classifications, in relation to criteria and framing of methods regarding the satisfaction of latter and their corresponding punctuation, are listed in Fig. 1 and in Table 2, respectively. For satisfaction of criteria a color scale was defined, the colors dark green, light green and red for criteria TS, PS and NS, respectively.

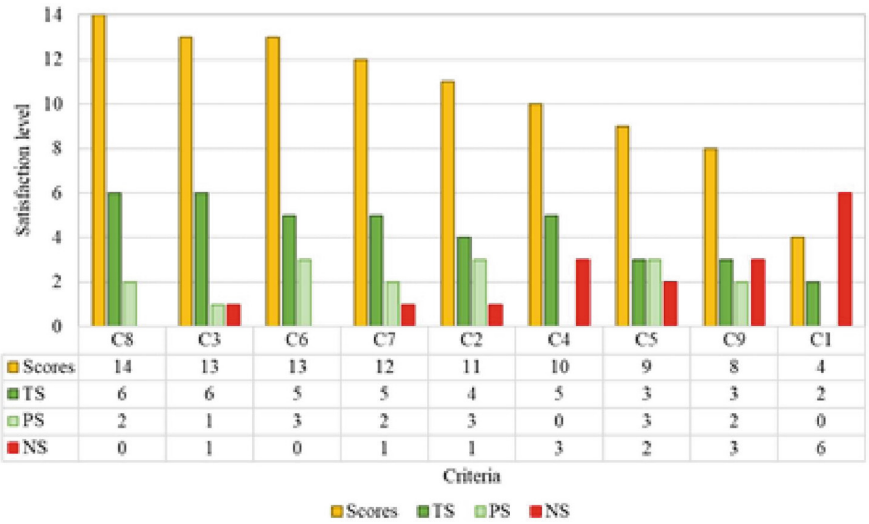

Fig. 1. Classification of criteria in relation to punctuation and satisfaction levels by methods

Table 2. Classification of methods of punctuation and level of satisfaction of criteria

Classification	*Methods*	*Scores*	*TS*	*PS*	*NS*
1st	ITRC	15	7	1	1
2nd	ASTM	15	6	3	0
3rd	SuRF-UK	13	6	1	2
4th	SuRF-US	12	6	0	3
5th	NICOLE	11	5	1	3
6th	USEPA	11	4	3	2
7th	SuRF-ANZ	10	3	4	2
8th	SuRF-Taiwan	7	2	3	4

The "C8" criterion, which involves participation of stakeholders in remediation project, obtained the best performance among methods since it was addressed in all methods analyzed. The methods in general have described the importance of collaboration and involvement of a wide range of stakeholders in remediation project, whether directly involved in process or local community affected by action.

In addition, they emphasized in a very expressive way that the consultative, collaborative and dialogue processes promoted among stakeholders and incorporation of local concerns into decision-making, help in management of uncertainties, generate legitimacy and public confidence and improve results.

The involvement of interested parties throughout remediation process is already a very promoted concept and identified in literature as a critical aspect and of great relevance in process of management and selection of the remediation technology that will be applied (Bonano et al. 2000; Hou et al. 2014).

In the last position is criterion of evaluation of central elements of green and sustainable remediation (C1), which obtained less approach in the methods, this in function that, although some methods incorporate green remediation, the great majority are labeled sustainability with integration of both environmental, social and economic elements on process.

In this context of criteria's analysis, considering the levels of criteria's satisfaction, the method that stands out, according to Table 2, is the ITRC, with 15 points and 7 criteria totally satisfied (TS). In sequence, the ASTM method appears, also with 15 points, but totally satisfying 6 decision criteria, and partially satisfying 3 criteria, addressing in some way all the criteria. The best performance of the ITRC and ASTM methods is due to the dedicated efforts in developing a method that integrates the sustainability approaches during throughout the remediation process.

In third and fourth place are SuRF-UK and SuRF-US methods, also with six totally satisfied criteria. SuRFs are of great importance in scenario of sustainable remediation, according to Ridsdale and Noble (2016), the first coalition specifically dedicated to this approach, and its prominence in the context of development of methods for application of sustainability in remediation of contaminated sites.

Given the conditions considered, ITRC method, presenting 15 points and satisfying seven of nine criteria analyzed, corresponds the methods which best represents the

premises and sustainability discourse, towards the conditions and context of analysis considered in this study.

4 Conclusions

While it is possible to highlight different challenges related to adoption of sustainable remediation concepts, it is concluded that a consensus is emerging on global scenario for a more solid incorporation of sustainable approach into remediation projects with a view to reducing impacts of process and maximization of the long-term benefits of contaminated sites.

Therefore, identifying, describing and analyzing methods applied to sustainable remediation have proved essential for a better understanding of what can be a sustainable remediation process, and thus indicate the information needed to evaluate attributes of sustainability in this context.

The methods share many common definitions and principles, indicating a broad understanding of sustainable remediation between countries and organizations. In a broad sense, sustainable remediation is approached as process that seeks to evaluate and integrate in a balanced way environmental, social and economic element in remediation project in order to find ideal remediation option.

However, there is still great variability in the way sustainability is represented in remediation methods, since, in addition to the fact that no criteria have been fully met, neither method has fully met all criteria, which indicates a space for further studies and improvements.

References

ASTM (2013) ASTM E2876-13 - standard guide for integrating sustainable objectives into cleanup. American Society for Testing and Materials. ASTM Internacional, West Conshohocken

Bardos P, Bone B, Boyle R, Ellis D, Evans F, Harries ND, Smith JWN (2011) Applying sustainable development principles to contaminated land management using the SuRF-UK framework. Rem J [s.l.] 21(2):77–100

Bonano EJ, Apostolakis GE, Salter PF, Ghassemi A, Jennings S (2000) Application of risk assessment and decision analysis to the evaluation, ranking and selection of environmental remediation alternatives. J Hazardous Mater [s.l.] 71(1–3):35–57

Bowen GA (2009) Document analysis as a qualitative research method. Qual Res J [s.l.] 9(2):27–40

Cundy AB, Bardos RP, Church A, Puschenreiter M, Friesl-Hanl W, Müller I, Neu S, Mench M, Witters N, Vangronsveld J (2013) Developing principles of sustainability and stakeholder engagement for "gentle" remediation approaches: the European context. J Environ Manag [s.l.] 129:283–291

DoD (2010) Guidelines for Consideration of Sustainability in Remediation of Contaminated Sites. Department of Defence http://www.defence.gov.au/estatemanagement/governance/Policy/Environment/Contamination/Docs/Toolbox/SustainabilityRemediationGuidelines.pdf. Accessed 10 Jan 2018

Forum US (2009) Sustainable remediation. Sustainable Remediation white paper-Integrating sustainable principles, practices, and metrics into remediation projects. Rem J [s.l.] 19(3):5–114

Gibson B, Hassan S, Holtz S, Tansey J, Whitelaw G (2005) Sustainability assessment: criteria and processes. Earthscan, London, p 268

Holland KS, Lewis RE, Tipton K, Karnis S, Dona C, Petrovskis E, Bull LP, Taege D, Hook C (2011) Framework for integrating sustainability into remediation projects. Rem J 21(3):7–38

Hou D, Al-Tabbaa A, Chen H, Mamic I (2014) Factor analysis and structural equation modelling of sustainable behaviour in contaminated land remediation. J Cleaner Prod [s.l.] 84:439–449

Hou D, Guthrie P, Rigby M (2016) Assessing the trend in sustainable remediation: A questionnaire survey of remediation professionals in various countries. J Environ Manage 15 (184):18–26

Huang IB, Keisler J, Linkov I (2011) Multi-criteria decision analysis in environmental sciences: ten years of applications and trends. Sci Total Enviro [s.l.] 409(19):3578–3594

ITRC (2011) Green and Sustainable Remediation: A Practical Framework. GSR-2. Interstate Technology and Regulatory Council www.itrcweb.org. Accessed 01 Out 2018

Levy Y, Ellis TJ (2006) A system approach to conduct an effective literature review in support of information systems research. Inform Sci J 9:181–212

NICOLE (2010) NICOLE Road Map for Sustainable Remediation. Network for Industrially Contaminated Land in Europe http://www.nicole.org. Accessed 01 Out 2018

Pollard SJT, Brookes A, Earl N, Lowe J, Kearney T, Nathanail CP (2004) Integrating decision tools for the sustainable management of land contamination. Sci Total Environ [s.l.] 325(1–3):15–28

Reddy KR, Adams JA (2015) Sustainable remediation of contaminated sites. Momentum Press, LLC, New York, 268p

Ridsdale DR, Noble BF (2016) Assessing sustainable remediation frameworks using sustainability principles. J Environ Manag [s.l.] 184:36–44

Rizzo E, Bardos P, Pizzol L, Critto A, Giubilato E, Marcomini A, Albano C, Darmendrail D, Döberl G, Harclerode M, Harries N, Nathanail P, Pachon C, Rodriguez A, Slenders H, Smith G (2016) Comparison of international approaches to sustainable remediation. J Environ Manag [s.l.] 184:4–17

Slenders HL, Bakker L, Bardos P, Verburg R, Alphenaar A, Darmendrail D, Nadebaum P (2017) There are more than three reasons to consider sustainable remediation, a dutch perspective. Rem J 27(2):77–97

Smith G, Nadebaum P (2016) The evolution of sustainable remediation in Australia and New Zealand: a storyline. J Environ Manag [s.l.] 184:27–35

SuRF-UK (2010) A Framework for Assessing the Sustainability of Soil and Groundwater Remediation. Sustainable Remediation Forum from United Kingdom. AIRE, London www.claire.co.uk/SuRFuk. Accessed 01 Out 2018

USEPA (2012) Methodology for Understanding and Reducing a Project's Environmental Footprint. US Environmental Protection Agency www.cluin.org/greenremediation/methodology. Accessed 01 Out 2018

Stability Analysis of the Refuse Dam in Xiaping MSW Landfill, China

Shi Yu Zhao(✉), Han Ke, Sheng Ze Lan, Shuai Zhang, and Jie Hu

MOE Key Laboratory of Soft Soils and Geoenvironmental Engineering, Institute of Geotechnical Engineering, Zhejiang University, Hangzhou 310058, China
elena_zsy@163.com

Abstract. Landfilling remains one of the main municipal solid waste (MSW) disposal methods worldwide. And the refuse dam is one of the most important facilities to ensure the safety of landfill. Therefore, it is of great significance to evaluate the safety of the refuse dam. This study aims to analyze the stability of the refuse dam using the finite element method based on PLAXIS3D. The landfill is replaced by the equivalent load applied, which is calculated by three methods including static earth pressure at rest, PLAXIS2D simulation and retaining wall with gentle back surface methods. And the calculation results of above-mentioned methods are compared and the reasons for the different results are explained. The results showed that the calculation of factor of safety by static earth pressure at rest method is the most reliable. And the alarm water level corresponding to the safety coefficient 1.35 is –4.85 m.

Keywords: Landfill · Stability analysis · PLAXIS · Retaining wall
MSW

1 Introduction

As landfilling or dumping is the most common method of solid waste disposal, waste dumps are widespread throughout the world [1–4]. Due to unsound siting, construction and maintenance of waste dumps, many dump landslides have occurred and usually lead to disastrous consequences [3]. The deadliest event in history killed 278 people in Manila, Philippines, in 2000, and the second deadliest event killed 143 people in Bandung, Indonesia in 2005 [3]. And the refuse dam is one of the most important facilities to ensure the safety of landfill. Therefore, it is of great significance to evaluate the safety of the refuse dam.

The aim of this study is to analyze the stability of the refuse dam using the finite element software PLAXIS3D. Because PLAXID3D can only consider the safety factor of the whole field, it is incapable of only evaluating the safety of the refuse dam. Therefore, the landfill is replaced by the equivalent load applied, which is calculated by three methods including static earth pressure at rest, PLAXIS2D simulating and retaining wall with gentle back surface methods. And the calculation results of above-mentioned methods are compared and analyzed to choose the best method.

© Springer Nature Singapore Pte Ltd. 2019
L. Zhan et al. (Eds.): ICEG 2018, ESE, pp. 453–460, 2019.
https://doi.org/10.1007/978-981-13-2227-3_56

2 Study Area

Xiaping MSW landfill is one of the first batch of large sanitary landfills, of which the capacity and design service life were 47 million m^3 and 30 years respectively. It is the important urban infrastructure to solve domestic refuse of Shenzhen city.

It is located in Xiaping Valley of Qingshui River in Luohu District and belongs to typical valley type landfill. The first-stage project covers an area of 634 thousand $m^2$and the designed capacity is 14.93 million m^3, which is about 2.5 times the actual landfills of 5.83 million m^3 in "12•20" landslide, Guangming New District, Shenzhen, China [5] If catastrophic landslide occurs, it will cause immeasurable loss.

And the refuse dam is one of the most important facilities to ensure the safety of landfill. As shown in Fig. 1b, the dam is downstream of the first-stage project. It is homogeneous clay dam reinforced by the slide-resistant piles. The average height of dam is about 15 m, and the dam foundation is basically flush with the original ground.

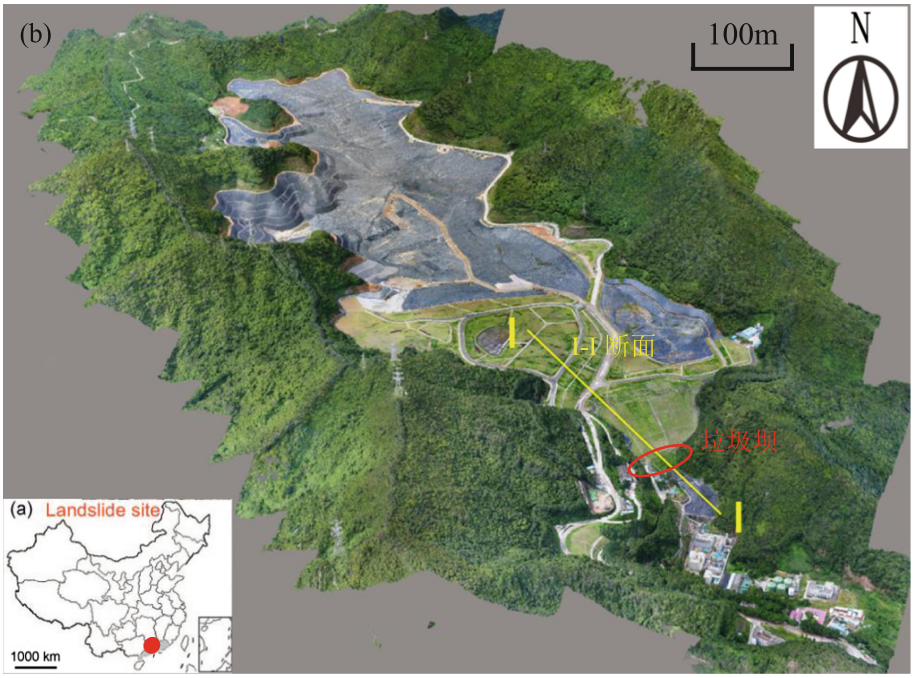

Fig. 1. Landfill remote sensing images, modified from an aerial photo taken on May 21, 2018.

3 Static Stability Calculation Analysis of Refuse Dam

3.1 The Software Introduction

PLAXIS 2D/3D adopts the fem strength reduction method when analyzing the stability. The strength reduction is to decrease slope rock mass shear strength parameter

gradually in the ideal elastoplastic finite element calculation until its broken state, at the same time getting the strength reserve safety coefficient ω of slope [6].

3.2 Stability Analysis

The main steps to analyze the stability of the refuse dam using PLAXIS are as follows:

(1) As shown in Fig. 1b, the I-I section are selected to build the 3D finite element model for calculating and analyzing typical sections. Figure 2 showed the profile map of the refuse dam and internal reinforcement of the refuse dam. Table 1 showed calculation parameters of dam materials.

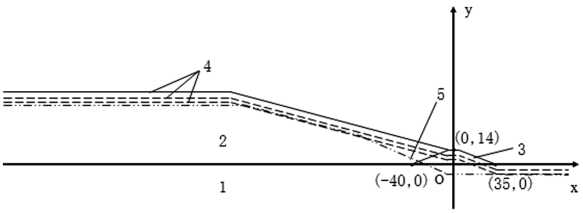

Fig. 2. The profile map of the refuse dam.

(2) The bottom surface of the model is fixed end constraint, that is, x, y and z direction constraints are applied. Both the left and right sides of the model apply X-direction displacement constraints. The displacement constraint in the Y-direction is applied before and after the model. The upper part of the model is free end without displacement constraint.
(3) Because the left side of the model is close to the center of the garbage dump, according to the symmetry, there should be no lateral seepage flow and undrained. As the right side extends out to the field area, there is no such symmetry and it is set as drainage. The front and the back of the extension end take the default drainage condition. And the bottom does not drain.
(4) According to the finite element analysis model established in Fig. 3, the model is meshed. The analysis model is divided into 42,953 units and 58,811 nodes. In the calculation, the point on the soil layer near the ground on the refuse dam is selected as the calculation stress point, and the grid near the center of the model is optimized to improve the calculation accuracy of nearby units.
(5) As shown in Fig. 2, three calculated water levels are set: the first water level is about –9 m. Due to the calculation needs, this water level at the dam baffle is higher than the current water level. The second water level rises to the bottom of the reverse pressure layer, which is about –5 m. In extreme rainfall conditions, the third water level is about 0 m.
(6) Because PLAXID3D can only consider the safety factor of the whole field, it is incapable of only evaluating the safety of the refuse dam. Therefore, the ultimate

Table 1. Calculation parameters of dam materials.

Serial number	Name of soil	Constitutive model	Effective cohesion c' (kN/m^2)	Effective internal friction Angle φ'(°)
1	Bedrock	Linear elastic	–	–
2	MSW	Mohr-Coulomb	20	25
3	Refuse dam	Mohr-Coulomb	10	28

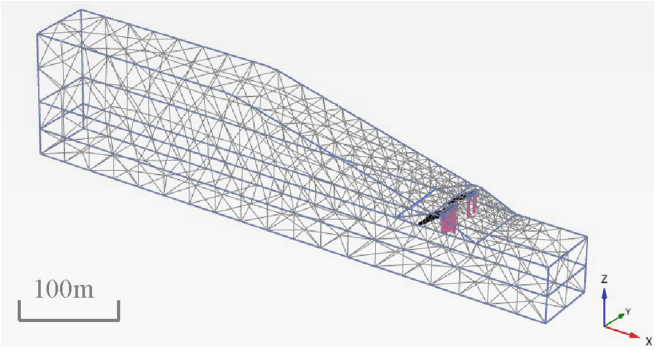

Fig. 3. Finite element model grid diagram of the refuse dam.

force equilibrium analysis is used to obtain the surface force of the dam. Then the landfill is replaced by the equivalent load applied in 3D model, which is calculated by three methods including static earth pressure at rest, PLAXIS2D simulating and retaining wall with gentle back surface.

(7) According to the data, the construction of Xiaping landfill started in August 2010 and stopped in August 2016. In order to simulate the actual situation of the site, the calculation is carried out in the following five steps: Initial geostress equilibrium (K_0 process); Simulation of natural consolidation of soil layer, in other words, the consolidation of the soil layer to the hyperstatic pore water pressure has dissipated; simulation of the process of landfill dumping, and consolidation and drainage process of foundation after stopping dumping; Simulation of different water levels.

3.3 Comparison

The following three methods of calculating the stress applied to the refuse dam are introduced:

(1) Assuming that the dam body does not move at all, the static earth pressure at rest method is used to simulate the load applied to the dam, and the soil and water are calculated respectively.

(2) Retaining wall with gentle back surface refers to the retaining wall of the second failure surface that may appear in the filling when the active limit equilibrium is

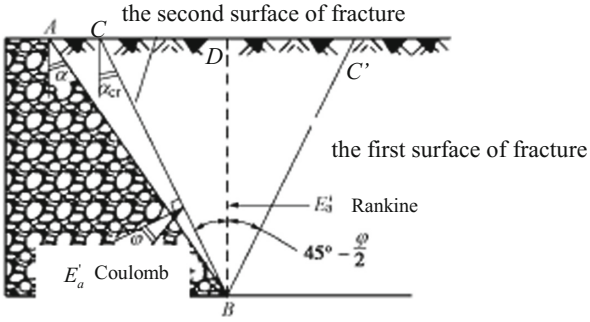

Fig. 4. Substantially planar retaining wall and Coulomb and Rankine earth pressures.

reached. When the backing of wall is relatively flat, that is, the inclination angle α is greater than the critical inclination angle α_{cr} (angle of rupture), and the roughness of the backing is greater(the friction angle between the earth filling and the backing of wall is close to or equal to the internal friction angle of the earth filling, the sliding wedge may not slide along the AB surface of the backing, but along the BC (the first surface of fracture) and BC' (the second surface of fracture) sliding surfaces shown in Fig. 4, and both sliding surfaces occur in the earth filling behind the wall when the retaining wall moves forward until the wedge behind the wall is broken. And the conditions for generating the second fracture surface are related to such factors as the inclination angle of the backing of wall α, the friction angle between the earth filling and the backing of wall δ, internal friction angle of the earth filling φ and the slope angle of the filling surface β. Using the rigid-body equilibrium theory, it can be proved that the angle of rupture can be determined by the following equation when $\delta = \varphi$:

$$\alpha_{cr} = 45^\circ - \frac{\varphi}{2} + \frac{\beta}{2} - \frac{1}{2} acr \sin\left(\frac{\sin \beta}{\sin \varphi}\right) \tag{1}$$

Because the slope angle is small, the surface of the filing is approximately horizontal ($\beta = 0$):

$$\alpha_{cr} = 45^\circ - \frac{\varphi}{2} \tag{2}$$

In this paper, the earth pressure applied to the refuse dam is calculated according to the Coulomb earth pressure.

(3) The soil pressure applied to the dam is calculated using PLAXIS2D finite element software, and the calculation process is basically consistent with that of PLAXIS3D. The model established is shown in Fig. 2.

4 Calculation Results

4.1 Comparison of Stress Calculation Results

In order to facilitate the analysis, Fig. 5a selects the high H as the vertical coordinate and the horizontal stress σ_x as the horizontal coordinate. In this way, the graph curve is consistent with the stress curve considering the stress direction, which is easy to observe and compare.

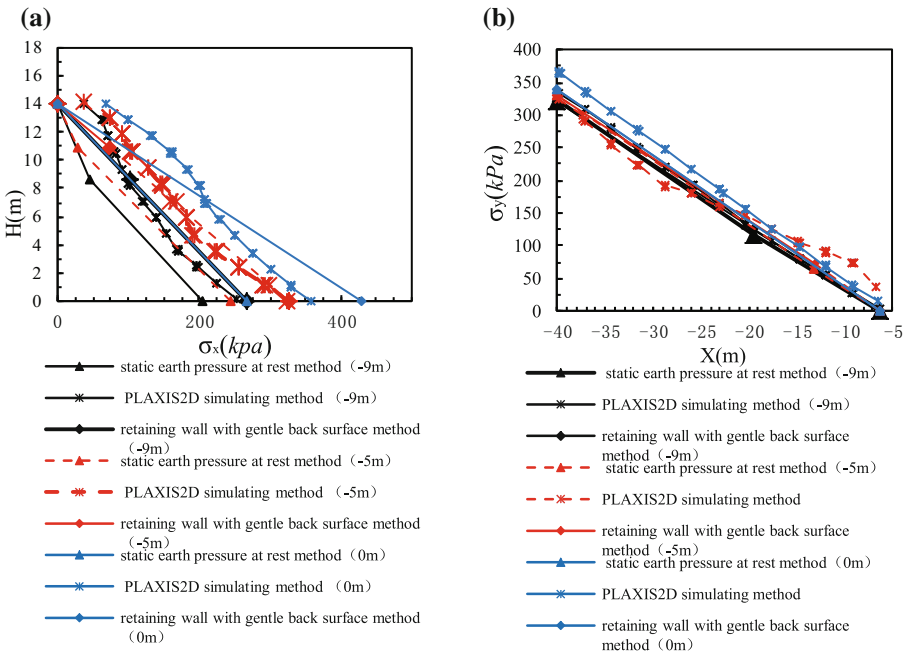

Fig. 5 a. The horizontal stress calculated by three methods varies with depth. b. The vertical stress calculated by three methods varies with the horizontal distance.

Compared with the above stress calculation results, it can be found that there is no significant difference in the calculation results of various methods of vertical stress σ_y. However, there is a large gap in horizontal stress, in which the horizontal stress calculated by the static earth pressure at rest method is smaller than that of the other two methods.

First of all, the reason why the calculation result of static earth pressure at rest method is relatively small is that the existence of the second fracture surface and the influence of slope angle of the filling are not considered. Then, the results of the other methods are different because the load on the surface of the filing is assumed to be zero in the retaining wall with gentle back surface theory. Finally, there is little difference in the results of the other methods, which proves that PLAXIS2D is likely to be applied in calculating earth pressure with the retaining wall with gentle back surface theory, and

the calculation of the retaining wall with gentle back surface method is close to the actual situation.

4.2 Mode of Failure

The calculation process of strength reduction will generate additional displacement, so the total displacement has no physical significance, but the incremental displacement of the failure step shows the failure mechanism. With the increase of the number of iterations in the calculation of the safety coefficient, the displacement value will continuously expand, and the displacement cloud map will tend to a stable shape (the most likely mode of failure). Figure 6 is the displacement cloud diagram at full water level.

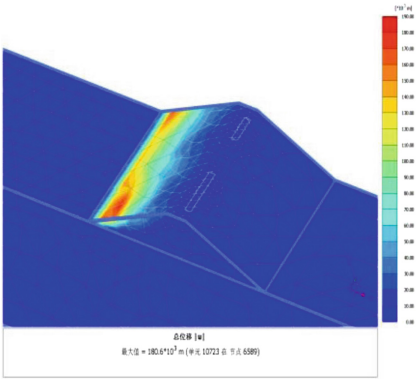

Fig. 6. Displacement cloud map at full water level.

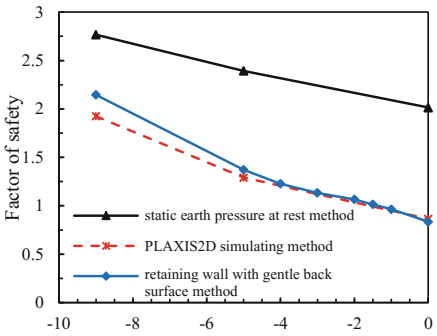

Fig. 7. The safety factor of different working conditions is calculated by different methods.

It can be seen from Fig. 6 that the failure modes of the three calculated water levels are basically the same, all of which are caused by the large displacement at the left bottom of the refuse dam and the local unstability.

4.3 Factor of Safety

As shown in Fig. 7, the results of PLAXIS2D simulation are more similar to those obtained by the retaining wall with gentle back surface method than static earth pressure at rest method. And the results of PLAXIS2D method and the retaining wall with gentle back surface method are very similar in the case of high water level. Thus the calculation of safety factor by static earth pressure at rest method is more reliable. In addition, it can be obtained by interpolation: the alarm water level corresponding to the safety coefficient 1.35 is –4.85 m.

5 Conclusions

This paper analyzed the stability of the refuse dam using the finite element software PLAXIS3D. The landfill is replaced by the equivalent load applied, which is calculated by three methods including static earth pressure at rest, PLAXIS2D simulation and retaining wall with gentle back surface methods. And the calculation results of above-mentioned methods are compared and the reasons for the different results are explained. The following conclusions can be drawn:

(1) It is feasible to use PLAXIS3D to analyze the static stability of the refuse dam of Xiaping landfill in Luohu District, Shenzhen, China and calculate the safety coefficient of the dam.
(2) The reason why the calculation result of static earth pressure at rest method is relatively small is that the existence of the second fracture surface and the influence of slope angle of the filling are not considered. The results of the other methods are different because the load on the surface of the filing is assumed to be zero in the retaining wall with gentle back surface theory. There is little difference in the results of the other methods, which proves that PLAXIS2D is likely to be applied in calculating earth pressure with the retaining wall with gentle back surface theory, and the calculation of the retaining wall with gentle back surface method is close to the actual situation.
(3) The results obtained PLAXIS2D method and the retaining wall with gentle back surface method are very similar in the case of high water level. Thus the calculation of safety factor by static earth pressure at rest method is more reliable. In addition, it can be obtained by interpolation: the alarm water level corresponding to the safety coefficient 1.35 is –4.85 m.

References

1. Jafari N H, Stark T D, Merry S, (2013) The July 10 2000 Payatas landfill slope failure. Int J Geoeng Case History 2(3):208–228
2. Lavigne F, Issmer P, Gomez C, Davies TA, Hadmoko DS, Iskandarsyah TYW, Gaillard JC, Fort M, Texier P, Heng MB, Pratomo I (2014) The 21 February 2005, catastrophic waste avalanche at Leuwigajah dumpsite, Bandung. Indonesia. Geoenviron. Disasters 1(1):1–12
3. Omraci K, Merrien-Soukatchoff V, Tisot JP, Piguet JP, Nickel-SLN L (2003) Stability analysis of lateritic waste deposits. Eng Geol 68(3):189–199
4. Steiakakis E, Kavouridis K, Monopolis D (2009) Large scale failure of the externaliste dump at the "South Field" lignite mine, Northern Greece. Eng Geol 104(3):269–279
5. Zhan L T, Zhang Z, Chen Y M, et al (2018) The 2015 Shenzhen catastrophic landslide in a construction waste dump: Reconstitution of dump structure and failure mechanisms via geotechnical investigations. Eng Geol (2018)
6. Dawson E M, Roth W H, Drescher A (1999) Slope stability analysis by strength reduction. Geotechnique 49(6):835–840

The Effect of Climate Change on Alpine Mountain Hazards Chain: A Case Study in Tianmo Ravine, Tibet, China

Jiao Wang[1,2], Yifei Cui[3(✉)], Clarence E. Choi[3,4], and Charles W. W. Ng[3]

[1] Key Laboratory of Mountain Hazards and Earth Surface Process, Institute of Mountain Hazards and Environment, Chinese Academy of Sciences, Chengdu 610041, China
[2] University of Chinese Academy of Sciences, Beijing 100049, China
[3] Department of Civil and Environmental Engineering, Hong Kong University of Science and Technology, Clear Water Bay, Hong Kong SAR
yifeicui@ust.hk
[4] The HKUST Jockey Club Institute for Advanced Study, Clear Water Bay, Hong Kong SAR

Abstract. Mountain hazards behave a relatively high incidence under regional climate change condition. This compound hazard is often initiated by environment and climate change. A combination of glacial melting and rainfall-induced compound disaster event happened in Tianmo Ravine, Bomi County, Tibet, China on 25 July and 4 September 2010, separately. The debris flow with 450,000 m^3 volume transported along gully and then flushed into Parlung Tsangpo River in the deposition zone, resulting in a destruction of 400 m length section of the G318 highway from Bomi County to Lhasa. A detailed interpretation of this disaster was conducted using unique and high-resolution images obtained through remote sensing. The source material, terrain condition, and climate condition were analyzed to have a comprehensive understanding of environmental background for hazard initiation. It is concluded that the occurring of this disaster event is the comprehensive result of multiple factors led by the climate change. Abundant antecedent precipitation, melting of the glacier, and the instability of soil caused by wetting-drying cycles, led to the occurrence of the Tianmo Ravine disaster. Based on taking various factors into account synthetically, the comprehensive hazards pattern is named using "Mountain hazards pattern in glacial alpine region under climate change (MH-GA-CC)". The climate is the special factor feature that should be taken into account emphatically. The study here provides a scientific base pattern for the future risk assessment of glacial alpine areas under regional climate change background.

Keywords: Climate change · Mountain hazards chain · Debris flow

© Springer Nature Singapore Pte Ltd. 2019
L. Zhan et al. (Eds.): ICEG 2018, ESE, pp. 461–470, 2019.
https://doi.org/10.1007/978-981-13-2227-3_57

1 Introduction

Glacial debris flows in the high mountain landscapes are an important geomorphic process that may pose significant hazard to communities and infrastructure in mountain areas. The debris material originated from steep moraines, talus slopes, destabilized rock glacier tongues, and fluvioglacial deposits within channels (Evans and Delaney 2015). Once mobilized, debris flows consist of fast flowing mixture of sediment and water, behaves high velocity and mobility (Iverson 1997). During the deposition stage, when debris flows entering rivers from tributaries can significantly alter the morphological settings (Gregory et al. 1985), the formation of debris dams will lead to catastrophic flooding and fluvial erosion in riverbank (Choi et al. 2017). This compound disaster will cause extensive loss of life and property, and damage to ecological environment (Cui 2014).

The increased frequency and magnitude of extreme weather events is becoming one of the major causes of disasters (Yilmaz 2017). Challenges include how climate variables, such as temperature and rainfall, affect compound geo-hazards in glacierized mountains. This study aims to comprehend the disaster characteristics and the hazard causal factors by using a case study from the Tianmo Watershed, near the Parlung Tsangpo River in Tibet, China. An in-depth analysis of the disaster events of mountain hazards is conducted to understand the causes and effects of disasters and provide lessons for disaster prevention and mitigation in the process of mountain society development.

2 Watershed Background

The Tianmo Watershed, as a tributary to the Parlung Tsangpo River, is located in Bomi County, Southeast Tibet of China (Fig. 1). This ravine covered an area of 17.8 km^2 with a maximum elevation difference of 3141 m (Wei et al. 2018). Geological investigation indicated that the area in the whole Tianmo gully is located in a strong ductile deformation zone, and is mainly composed of gneissic lithology belonging to a pre-Sinian system which forms the source of rock boulder of the debris flows (Deng et al. 2017; Wei et al. 2018). Because of the obstruction of Tibet Plateau for the Indian monsoon, abundant precipitation can last up to six months (from May to October), and the mean annual rainfall intensity reached approximately 880 mm in the Parlung Tsangpo (Fu and Fletcher 1985). In addition to rainfall, additional sources of runoff in the watershed will be provided by snow-melt and glacial recession because of rising temperature under global climate warming. Meanwhile, an abundance of glacier till also deposited because of glacier recession in this watershed. So the large-scale debris flows take place frequently in the tributaries of Parlung Tsangpo basin due to the ideal conditions of the combination of thick deposits, ample rainfall and runoff. Only in 2010, two large-scale debris flows occurred in the Tianmo Valley (Choi et al. 2018).

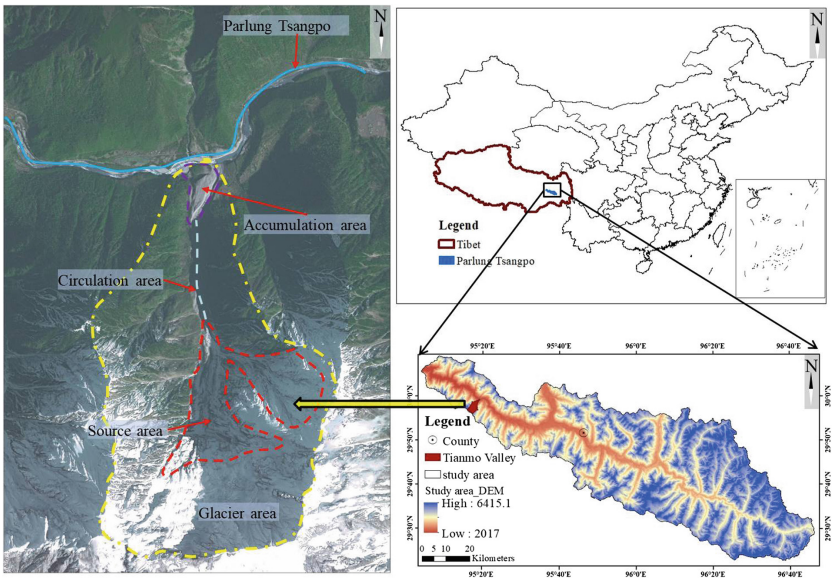

Fig. 1. Geographical location and High-resolution image of Tianmo Watershed (Modified from Choi et al. 2018)

3 Compound Disaster Characteristics

During July 25, 2010, a medium-scale debris flows with 900,000 m^3 total deposited material occurred in Tianmo gully (DF1). This debris flow blocked the Parlung River but breached quickly. This debris flow also destroyed the section of G318 highway with 450 m length, and the north bank of Parlung Tsangpo river was seriously eroded by the outbreak flood and retreated about 110 m (Wei et al. 2018).

Furthermore, on 4th September in the same year, another debris flow (DF2) with deposition about of 450,000 m^3 into the Parlung Tsangpo River took place in Tianmo valley (Ge et al. 2014). The width of the river channel was reduced from 180 m 100 m due to a partial-debris dam formed by debris flow deposits in the river (Deng et al. 2017). This dam rerouted the discharge in the river along one of the riverbanks, which supported a highway (G318). The rerouted discharge eroded the riverbank and the highway eventually collapsed. The Sichuan-Tibet highway was closed for round-the-clock emergency repair for 16 days and resulted direct economic loss of larger than 19.7 million RMB (Wei et al. 2018).

A field investigation by using UAV surveys is carried out in September 2017. The source area of the debris flow is identified from the glaciation region, and the transportation channel filled with glacial tills and colluviums is measured as 3.6 km from UAV survey (Fig. 2a). The three-dimensional (3D) model of the location where the debris flow entered the river was then reconstructed as shown in Fig. 2b. It reveals that the damaged highway about 900 m length which has eroded by the Parlung Tsangpo River was eventually diverted 170 m north of the existing alignment (Fig. 2b).

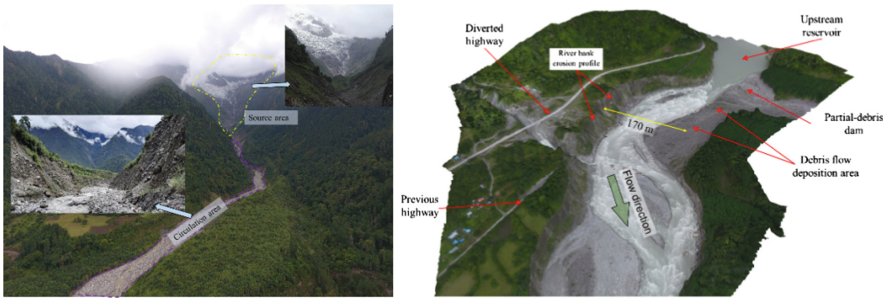

(a) (b)

Fig. 2. (a) Debris source and transportation area (Photo taken on 12 September 2017); (b) 3D reconstruction of site (UAV photo taken on 12 September 2017)

4 Causal Factors

4.1 Source Material

Tianmo gully has a north-east to south-east orientation, the elevation of the mountain ridge at the top of gully is about 5551 m, and the elevation near the downstream waterbody (Parlung Zangbo River) of gully is 2460 m. The modern maritime glaciers with an area of 1.42 km^2, hanging in the upper concave area of Tanami ravine, are distributed in an elevation from 4246 to 5551 m (Fig. 3). The remnants of lateral moraine with approximately 60 m high and 400 m width still deposited on both sides of the gully and moraine with 2 km length and about 5–8 m thickness deposited in the debris flow channel. These glacier till consist loosely consolidated sediment and can be easily entrained by debris flows.

The initiation of failure process of debris flow source area is affected by moraine distribution modes. In current study, two main distribution modes of the moraine as the source material of debris flow is identified from field investigation: moraine located on both sides slope of gully (Fig. 3A), and moraine located in the gully (Fig. 3B).

Three types of initiation mechanism of debris flow is purposed in current study based on the distribution of moraine: (1) The moraine distributed on both sides of the channel is likely contribute as the source material of debris flow under the effect of rainfall or earthquake. The failure initiation process of such moraine is closely related to the changes of soil micro structure, build up pore pressure, and strength reduction (Sassa 1984); (2) The moraine distributed on both sides of the gully is firstly deposited in channel by the effect gravity driven geomorphological process, such as slope wash. Then it is likely contribute as the source of debris flow under the effect of rainfall; (3) The moraine originally located in the channel is likely contribute as the source material of debris flow under the effect of rainfall, such as surface erosion fine grain migration during infiltration process. This kind of failure initiation process is related to particle size distribution, fine grain content, and the velocity of surface runoff (He et al. 2003). Field investigation indicated that the two debris flows in 2010 both initiated from the collapse of moraine located on side-slope of gully.

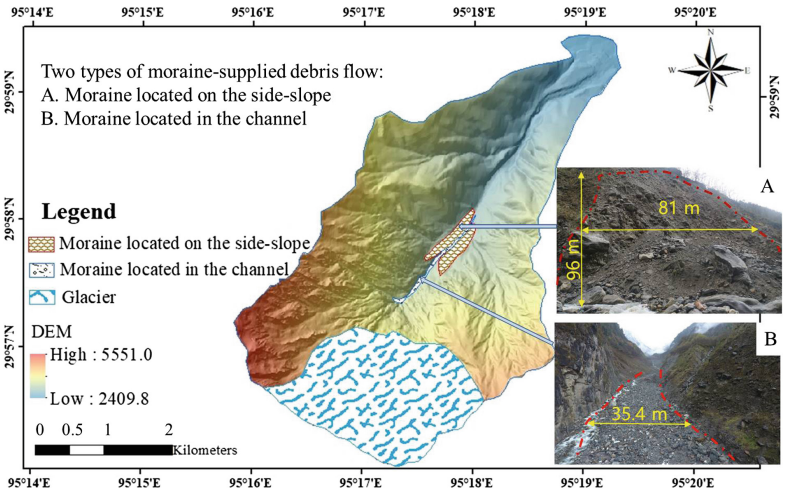

Fig. 3. The distribution of moraine in the source area of Tianmo gully

4.2 Terrain Condition

The imitation and movement of debris flow are controlled by basin topography condition. The geomorphic information entropy (GIE) value H is the quantitative indicators of landscape development (Ai 1987). This value is commonly used to indicate the degree of erosion of geomorphic surface of watershed, and also reflects the intensity of the crustal uplift in the Quaternary. The lower the value H, the stronger the tectonic activity (Liu et al. 1994). The mathematical formulation was based on analogy information entropy principle on the basis of Strahler area:

$$H = S - \ln s - 1 = \int_0^1 f(x)dx - \left[\int_0^1 f(x)dx\right] - 1 \quad (1)$$

where S is the value of Strahler hypsometric integral; $f(x)$ is the function of Strahler hypsometric curve. When calculating the H value, contour i is chosen as a reference, the whole watershed area is assumed to be A, and the area above the contour of the basin is a_i. The elevation difference between the contour and the lowest point of the basin is h_i, and the elevation difference between the highest and lowest points is H. The variables are set as: $x_i = a_i$ /A; $y_i = h_i$ /H. where x_i is the area percentage based on contour i, and y_i is the percentage of relative height difference. The points (x_i, y_i) in the rectangular coordinate system are linear fitting to form a curve: y = f(x), which is the Strahler hypsometric curve.

Based on the modification from Ai's (1987) classification system Liu et al. (2015) purposed a revised classification system on the evolution stages of debris flow basin (Table 1). In areas with strong tectonic movement, the effective energy is large, and the erosion of drainage basin is more serious. Debris flow basin is in an unstable juvenile period with violent changes, so the debris flow is prone to occur. Where in the

Table 1. Susceptibility classification of debris flow base on the GIE value H

The geomorphological information entropy value (H)	Evolution stage	Susceptibility of debris flow
$H \geq 0.4$	Old-age	Very low
$0.3 \leq H < 0.4$	Older-mature age	Low
$0.2 \leq H < 0.3$	Mature age	High
$0.111 \leq H < 0.2$	Younger-mature age	Very high
$H < 0.111$	Infancy age	Extremely high

region with stable tectonic movement, the effective energy is very small, the basin erosion tends to be stable. Debris flow basin is in an old-age period with stable fluctuation, so the activity of debris flow is low.

Using DEM data of the watershed and the H calculation method, the GIE value H of Tianmo gully was calculated as 0.19. In the current study, the watershed basin belongs to the Younger-mature age stage, and the susceptibility of debris flow is very high. Therefore, Tianmo gully watershed has a high susceptible geomorphic environment for debris flows.

4.3 Meteorological Conditions

The Tibetan Plateau, as the third pole, is more vulnerable under the global climate warming (Zhong et al. 2011). According to the recording from the Bomi meteorological station, 45 km southeast to Tianmo gully, the mean temperature over the past 20 years (from 1991 to 2010) has increased by approximately 1 °C with a rising rate of 0.05 °C a^{-1} (Fig. 4a). The glacier area in the source area of Tianmo ravine has decreased 13.6% based on interpretation of Thematic Mapper images from 2000 to 2006 (Deng et al. 2017). Meanwhile, the rainfall brought by the Indian monsoon, concentrated in summer time (from July to September), contributed about 50% of the whole annual rainfall.

In current study, the temperature nearby the source area of Tianmo ravine is adjusted 9.8 °C lower than that from the Bomi meteorological station due to the air temperature decreases with altitude (Li and Xie 2006) using a decline rate of 0.54 °C/100 m. The accumulation of positive temperature is often used to analyses the effect of air temperature on glacier melting (Rango and Martinec 1995). The positive temperature accumulation (°C) and duration of each debris flow event can be calculated when the lowest temperature exceeded 0 °C several days before the initiation of debris flow (Deng et al 2017). In current analysis, for the DF1, the calculated results of the positive temperature accumulation (°C) and duration were 47 days and 332.1 °C, while those data were 42 days and 320.4 °C for the DF2.

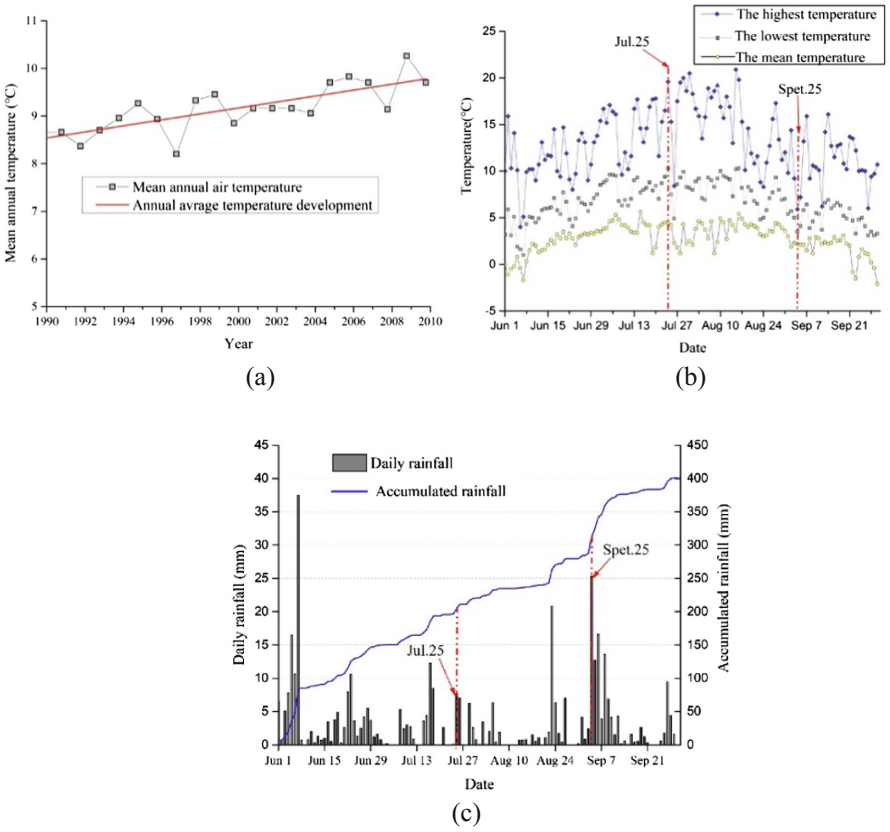

Fig. 4. Meteorological conditions of (a) Mean annual temperature in past 20 years; (b) Daily temperature from June to September 2010; (c) Daily rainfall from June to September 2010

When the DF1 occurred on 25th July, the air temperature nearby the source area of Tianmo valley reached a peak in 2010. However, the rainfall at the same time was only 72.9 mm, which is about 78% of the historical average (Fig. 4b). The "thaw" period in Tianmo gully began in the middle of Jun and the air temperature reached a maximum value on 25 July for that year, the positive air temperature accumulation reached 332.1 °C. But No rainfall recorded in this area for 5 days before DF1 (Fig. 4c) Therefore, the trigger factor of DF1 was probably the continuous percolation of meltwater due to the long-term increase in temperature. Before DF2, the temperature increased to another high value though the temperature firstly decreased in late August, and the positive air temperature accumulation reached 320.4 C. Meanwhile, rainfall began 3 days from September 2–4 prior to DF2 (Fig. 4c), and there was a concentrated rainfall of 50 mm and the rapid increase in rainfall intensity started 4 h before the initiation of DF2 and reached 3.8 mm/h (Deng et al. 2017). In conclusion, the heavy rain for a short time was responsible for the initiation of DF2.

4.4 Compound Geo-Hazards Pattern

Small-scale geo-hazards, such as shallow landslides, glacier lake outburst floods, debris flows, are able to be attributed to and converged into a large-scale compound geo-hazard event (Chen et al. 2011b). The disaster that occurred in Tianmo Gully could be concluded as a consequence of compounded mountain hazards, including debris flows and debris dam induced river bank erosion. Different hazards in different places are connected to each other through the mountain hazard chain that could amplify the disaster's effects (Cui and Jia 2015). The model of compound Mountain hazards occurring in Parlung Tsangbo is shown in Fig. 5. As the temperature continually increases under the global warming trend, the melting of internal ice particles in moraine induces a series of changes in the glacial till, which will reduce the shear strength of moraine and become the source material of initiation of debris flow. Meanwhile, the Indian monsoon will provide abundant precipitation that can last up to five months (from June to September), which is the most important trigger factor for debris flow initiation in this region. In addition, due to the extremely high erosion rates of larger than 5 mm/year in the Parlung Tsangbo (Zeitler et al. 2014), the prime-maturity geomorphological evolution stage of gully provide favorable slope gradient for the initiation and transportation of debris flow (Wei et al. 2018). In conclusion, the abundant glacier till source, favorable topographic conditions, meteorological conditions provided suitable prophase and inducing factors for the occurrence of compound geo-hazards.

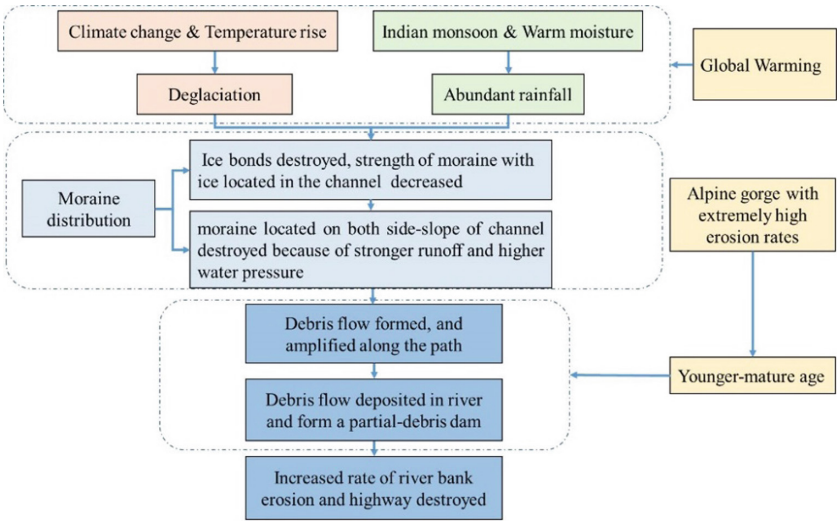

Fig. 5. The model of compound Mountain hazards occurring in Parlung Tsangbo

5 Conclusion

With the combination of remote sensing and field investigation. The source material, terrain condition, and climate condition were analyzed to have a comprehensive understanding of environmental background for hazard initiation in this study. Although heavy rainfalls are the trigger factor of this disaster, it should be realized that previous climate change induced temperature rise also play an important role in this disaster event. It is concluded that the occurring of this disaster event is the comprehensive result of multiple factors led by the climate change. Abundant antecedent precipitation, melting of the glacier, and the instability of rock and soil caused by wetting-drying cycles, led to the occurrence of the Tianmo Ravine disaster.

Based on taking various factors into account synthetically, the comprehensive effect is named using "Mountain hazards pattern in glacial alpine region under climate change (MH-GA-CC)". The climate is the special factor feature that should be taken into account emphatically. The study here provides a scientific base pattern for the future risk assessment of glacial alpine areas under regional climate change background.

Acknowledgments. The authors are grateful for financial sponsorship from the National Natural Science Foundation of China (Grant No. 41520104002), Key Research Program of Frontier Sciences, CAS (Grant No. QYZDY-SSW-DQC006) and the Opening Fund of State Key Laboratory of Hydraulics and Mountain River Engineering (SKHL1609). The authors would like to thank the support from the theme-based research grant T22-603/15 N and general research fund 16209717 of the Hong Kong Research Grants Council. Also, the authors are grateful for the financial sponsorship from the National Natural Science Foundation of China (5170091039) and the Hong Kong Jockey Club Charities Trust. Finally, the authors are grateful for the support of the HKUST Jockey Club Institute for Advanced Study and the financial support by the Hong Kong Jockey Club Disaster Preparedness and Response Institute (HKJCDPRI18EG01).

References

Ai N (1987) Comentropy in erosional drainage-system. J Soil Water Conserv 1(2):1–7

Choi CE, Cui Y, Au KYK et al (2018) Case study: effects of a partial-debris dam on riverbank erosion in the parlung tsangpo river. China Water 10(3):250

Costa JE, Schuster RL (1988) The formation and failure of natural dam. Geol Soc Am Bull 100:1054–1068

Cui P (2014) Progress and prospects in research on mountain hazards in China. Progress in Geography 33(2):145–152

Cui P, Jia Y (2015) Mountain hazards in the Tibetan Plateau: research status and prospects. Nat Sci Rev 2(4):397–399

Cui Y, Zhou X, Guo C (2017) Experimental study on the moving characteristics of fine grains in wide grading unconsolidated soil under heavy rainfall. J Mt Sci 14:417–431

Deng MF, Chen NS, Liu M (2017) Meteorological factors driving glacial till variation and the associated periglacial debris flows in Tianmo valley, south-eastern Tibetan Plateau. Nat Hazards Earth Syst Sci 17:345–356

Evans SG, Delaney KB (2015) Catastrophic mass flows in the mountain glacial environment, in snow and ice-related hazards, risks, and disasters. In: Haeberli W, Whiteman C, (ed), pp 568–606. Elsevier

Fan X, Tang CX, Western CJV, Alkema D (2012) Simulating dam-breach flood scenarios of the Tangjiashan landslide dam induced by the Wenchuan Earthquake. Nat Hazards Earth Syst Sci 12:3031–3044

Fu C, Fletcher JO (1985) The relationship between Tibet-tropical ocean thermal contrast and internannual variability of Indian monsoon rainfall. J Applied Meteorol Climatol 24:841–847

Ge Y, Cui P, Su F et al (2014) Case history of the disastrous debris flows of Tianmo Watershed in Bomi County, Tibet, China: Some mitigation suggestions. J Mt Sci 11:1253–1265

He W, Cao S, Liu X, Yuan J (2003) Incipient condition of uniform sediment on different bed slopes. Hydro-Sci Eng 9(3):23–26

Iverson RM (1997) The physics of debris flows. Rev Geophys 35:245–296

Liu L, Xu C, Chen J (2013) Debris-flow hazard evaluation based on geomorphic information entropy and landslide materials in the Lushan earthquake affected area. Seismol Geol 37(3):880–891

Liu X, Liu B, Guo D (1994) Morphological information entropy and seismic structure in Northeast China. Seismol Res Northeast China 10(2):29–36

Sassa K (1984) The mechanism starting liquefied landslides and debris flows. In: Proceedings of 4th international symposium on Landslides, Toronto, Canada

Wei R, Zeng Q, Davies T et al (2018) Geohazard cascade and mechanism of large debris flow in Tianmo gully, SE Tebetan Plateau and implication to hazard monitoring. Eng Geol 233:172–182

Yilmaz AG (2017) Climate change effects and extreme rainfall non-stationarity. In: Proceedings institution of civil engineers - water management, Thomas Telford Ltd, United Kingdom, vol 170, pp 57–65

Zeitler PK, Meltzer AS, Brown L (2014) Tectonics and topographic evolution of Namche Barwa and the easternmost Lhasa block. Tibet GSA Bull 507:23–58

Response Differentiation of Rock Characteristics Under Impact Loading

Naigen Tan(✉)

School of Civil and Environmental Engineering,
University of New South Wales, Sydney, NSW 2052, Australia
thamgai001@163.com

Abstract. An innovative dynamic test simulation system was used for impact drilling, a series of experiments were carried out on intact sandstone, limestone, gabbro and marble rocks. The reflected stress wave in the experimental bar was measured and the corresponding strain energy was calculated. The results have shown that the response degree of reflected stress wave depends on impact energy and lower threshold value of response. It is hard to detect under current technical conditions if the impact energy is below the threshold value. The peak reflected stress wave and the specific strain energy relate to rock type, strength and wave impedance. For the same type of rock, it grows with increasing impact energy, the ratio is related to the wave impedance instead of impact energy when it is over or equal to the threshold value. It shows significant differences in experimented rocks.

Keywords: Rock · Impact energy · Peak stress wave · Specific strain energy
Response differentiation

1 Introduction

Drilling is an indispensable means for the exploration of geology, mining, civil engineering, transportation, construction, hydropower and relevant productions. Based on the response characteristics to drilling load for determination of the geological strata structure, it is one of the key frontiers of intelligent drilling. The research in this field shows important application prospects in TBM excavation, geotechnical investigation and geological drilling. The test techniques such as conventional material test system, Charpy pendulum impact test, Schmidt hammer and split Hopkinson pressure bar have been widely used in the shock response test simulation.

For assessing the abrasion resistance of aggregates, the Los Angeles abrasion and impact test (LAAI) is usually performed. Some typical rocks have been tested to evaluate the correlations between the LAAI values and the physical properties (such as bulk density, Schmidt hardness, Shore hardness, P-wave velocity) and mechanical properties (such as uniaxial compressive strength, point load index, and indirect tensile strength of rocks [1]).

The Schmidt hammer and the sound velocity tests show significant non-linear correlations with the compressive strength of rock. There is no clear relation between the impact strength values and the compressive strength values for the coal measure

© Springer Nature Singapore Pte Ltd. 2019
L. Zhan et al. (Eds.): ICEG 2018, ESE, pp. 471–480, 2019.
https://doi.org/10.1007/978-981-13-2227-3_58

rocks. A weak nonlinear correlation is found between the impact strength values and the compressive strength values for the other rocks [2]. Differentiation of rocks types, rock microstructures and test conditions result in irregularities of observations. The dynamic strength of the sandstone is loading rate dependent [3–5].

The failure process of hard rock under impact loading indicates that the stress state transforms from elastic state to intrinsic friction state, then finally liquid hydrodynamics state. The deformation near impact loading in rock is similar to one-dimension at deformation near strong impact loading zone. The stress wave from the loading can be regarded as short wave similar to shock wave. The short wave has sharp varieties in a cabined zone near wave front [6]. Impact strength shows a fairly good correlation with penetration rate.

The effect of rock properties on percussive drilling shows that unaxial compressive strength, the Brazilian tensile strength, the point load strength and the Schmidt hammer value demonstrate strong correlations with the penetration rate. Weak correlations between penetration rate with both elastic modulus and natural density are found, but no significant correlation between penetration rate and P-wave velocity is found [7].

Evidently, the uniaxial compressive strength, the Brazilian tensile strength, the point load strength and the Schmidt hammer value are the dominant rock properties affecting the penetration rate of percussive drills. The dynamic failure characteristics of sandstone under one-dimensional coupled static and dynamic loads indicate that the dynamic response of rock is influenced remarkably by axial pre-compressive stress ratio.

When the strain rate remains constant, the impact compressive strength increases with an exponential function as the strain rate increases and reaches the maximum value when the axial pre-compressive stress ratio is 0.6–0.7. Within a certain range of axial pre-compressive stress ratios, the incident energy will influence the dynamic impact energy response of rock specimen [8].

The microstructure has a great influence on dynamic response of material under impact load. The investigation of dynamic compressive properties of pre-damaged concrete subjected to impact loading indicates that the degree of pre-damage has important influence on the dynamic compressive strength. A threshold exists: when the pre-damage is below the threshold, little effect of pre-damages exerts on the dynamic compressive strength; while beyond the threshold, the effect becomes tremendous.

The dynamic compressive strength of concrete increases with increasing strain rate. The increase of water content in concrete will cause a lower dynamic compressive strength [9]. The shock-induced damage in granite targets impacted by projectiles at different velocities is numerically simulated. Johnson-Holmquist shock damage constitutive model for brittle materials is applied to describe the damage and shear strain achieved in a confined volume of granite. A tensile crack softening model is coupled with the JH model to simulate the propagation of radial tensile cracks generated by the principal tensile stress perpendicular to the shock front [10]. To improve the reliability of drilling in complex strata, the effects of axial force, torque, radial force, the hardness, density, strength and brittleness of strata on vibration are considered.

It shows that the length of drill pipe is the dominant parameter causing the vibration of torsion and bending. The vibration magnitude is related to the drive torque, axial force and rotational speed. The impact vibration increases intensively when drilling in

hard and brittle rocks. A greater dynamic load will be generated when the loading frequency approximates the intrinsic frequency of drill. A large improvement in penetrating efficiency can be made by selecting suitable power parameters [11]. Impact simulation of different concrete (UHPFRC, NSC, FRC and HPC) under vehicle crash or falling rock was implemented by drop weight method. The results show that all concretes demonstrate strain hardening under quasi-static conditions and impact loading [12].

It is evident that when the structural shape, material, mass and impact speed of the projectile determined, the response of materials subjected to impact load is closely related to the loaded material composition, microstructure, strength and its characteristics, while the UCS of material has a good correlation with the point load strength. Bore bits with ball or button crowns are attributed a point load when drilling in rock; the drilling load is characterized with high impact frequency and high impact speed.

SHPB is the prime method to study the impact response of materials and structures under high strain rate conditions [13]. In this study, an impact rotary drilling response test simulation system is developed based on the improved SHPB. The propagation characteristics of the incident reflected stress wave in the bar are measured and the response nature of rock under impact load is revealed, which suggests a new method for borehole logging of formation while drilling.

2 Impulse Response of Test Simulation System

2.1 Basic Components of the System

The system is composed of impact loading, data acquisition and data analysis units (see Fig. 1). The impact loading unit consists of a testing platform, pulse generating unit and sample bin. The testing platform is an horizontal non-yielding prop directly erected on the ground, which provides a firm support for pulse emission tube, momentum trap and experimental bar (incident bar). The pulse generating unit includes pressure air source, pressure regulator, pulse generator, pulse shaper, momentum trap and experimental bar. The pulse generator consists of a triggering switch, a transmitting tube and an impact rod. The sample bin is an experimental compartment used to accommodate specimen; the chamber of bin is designed as cylindrical or prismatic to satisfy the shape and size of sample. The data acquisition unit is assembly of pressure sensors, strain transducers, laser velocimetry sensors, data switching box, dynamic strain gauge as well as data integrated box. The data analysis unit is formed by a computer, an oscilloscope or other terminals.

2.2 Testing Principle and Method

The impact process is simulated by the impact bar system, the incidence reflection and strain measurement follow the basic principle of SHPB [13]. In order to achieve the dynamic stress equilibrium and ensure single pulse loading, the pulse-shaper and the momentum trap techniques are adopted in our testing system [13, 14–16]. When it is loaded by the striker bar, the experimental bar obtains a certain speed and displacement

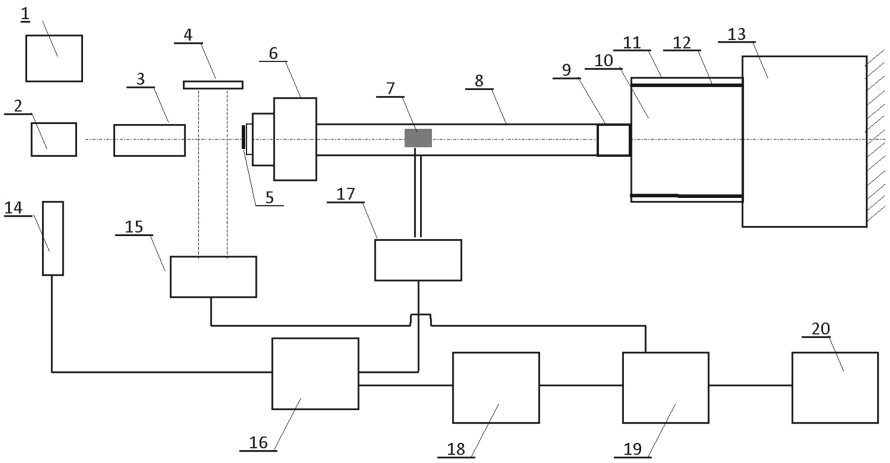

1-pressure source; 2-pressure regulator; 3-pulse generator; 4, 15-line laser velocimetry sensor; 5-pulse shaper; 6-momentum trap; 7-strain transducer; 8-experimental rod; 9-hemispherical tooth bit; 10-rock specimen; 11-sample compartment; 12-elasticcushion; 13-rigid fixed end; 14-pressure transducers; 16-switching box; 17-interface; 18-digital dynamic strain gauge;19-data integration box; 20-computer.

Fig. 1. Schematics of impact response testing simulation system

and stress wave in it. As the stress wave reaches the front face of the experimental bar, it impacts the specimen by the bit and exerts reflected stress wave at the face of the bit. The tensile, compressive and shear strains are collected from the bar through the data acquisition system. The signal is directly output to the data acquisition system in form of voltage or an electronic pulse in a preset sampling frequency, then input to the computer system where data storage, display, analysis, print and network upload are implemented. The parameters such as strain energy, torque and dynamic compressive strength can be calculated according to the principle of incident reflected stress wave in elastic rod. The launch pressure and loading velocity of the bar are obtained by speed transmitter and pressure transducer so that the structural and mechanical response properties of the material under impact conditions can be analyzed.

3 Schematic Design of the Test

This research adopts large scale intact rocks and $\varphi_b 36$ mm alloy steel bit. The experimental bar is inner cone coupled with the hemispherical tooth bit. The rock specimen resides in the cylindrical cavity of the bin and is closely coupled with the chamber; the opened end face of the specimen keeps contact with the bit front face without static pressure. The bin is a type of opened barrelally steel container (5.0 mm in wall thickness), which is assumed to be rigid so that it can satisfy the deformation restrain from the rock strata at the borehole bottom. Its inner diameter is consistent with the diameter of sample, the inner diameter of the barrel and the concentric precision are identical with the required sample. In order to improve the contact effect between

sample and cylindrical inner wall, a cylindrical embedding layer of asphalt paper (0.25 mm in thickness) is filled in the space between the sample and the inner wall of bin.

In this work, sandstone, marble, gabbro and limestone samples are used for the test simulation. The diameter of specimen is designed to be $\varphi_s \geq 5\,\varphi_b$, here $\varphi_s = 300.0 \pm 1.0$ mm, with height of $h = 150.0 \pm 1.0$ mm. The other requirements follow the methods suggested by ISRM. The primary parameters of specimens under quasi static load are measured and shown in Table 1.

Table 1. UCS and wave impedance of rock

Parameters\Type of rock	Sandstone	Limestone	Gabbro	Marble
UCS/MPa	107.8	137.0	235.5	171.5
Wave impedance/g • cm^{-3} m • s^{-1}	3170	6390	8790	18639

The dynamic test is conducted using a 25 mm in diameter bar system, composed of a striker bar (250 mm in length), an experimental bar (2,300 mm in length), all made of high strength maraging steel with high yield strength of 2.50GPa, density of 8.10×10^3 kg/m^3 and P-wave velocity of 4.79×10^3 m/s. In order to determine the response value of specimens, the samples are loaded in a progressive way in the test. The initial pressure is set to $P_0 = 1.0$ psi with the increment of $\Delta P = 1.0$ psi before P = 10.0 psi, and after the transmitting pressure is more than 10.0 psi, the increment of ΔP is adjusted up to 2.0 psi. The maximum impact pressure is set to 18.0 psi in this test. Here 18.0 psi is the upper limit pressure of marble specimen to break under the experimental conditions.

The velocity of the striker bar is measured by the laser velocimeter. The relation between impact velocity(v) and pressure of compressed air(p)is described by statistical regression in the formula (1).

$$v = -0.0349p^2 + 1.8265p - 0.2117, R^2 = 0.9981 \tag{1}$$

The impact energy (E_i) of the striker bar can be calculated and determined by the formula (2).

$$E_i = 0.1373p^2 + 11.26p - 20.832, R^2 = 0.9944 \tag{2}$$

Where p is the pressure value of compressed air, psi; v is the velocity of the striker bar, m/s.

4 Results and Discussions

4.1 Change of Peak Reflected Stress

The test reveals that the response of reflected stress wave in the experimental bar has a threshold for impact energy. In this research, the responsible threshold value of impact pressure of compressed air is 3.0 psi and the corresponding impact velocity 0.87 m/s and impact energy 0.38 J. When the triggered pressure is lower than the threshold value, the stress response in the experimental bar is very low. Under this condition, it is hard to detect the reflected stress wave with conventional techniques when the triggered pressure value is less than 3.0 psi. However, in the practical industry drilling, the impact energy of drilling rig is much greater than the threshold. For percussive drilling, the impact energy for a single strike is generally 30 J to 560 J. It is more than 40 J for pneumatic percussive drill, 130 J for hydraulic percussive drill and 80 J for down-hole drill for a single hit. Therefore, the responsible threshold value of impact energy is far lower than that of drilling machinery.

The change of peak reflected stress (R_{max}) with impact energy is illustrated (see Fig. 2). The R_{max} grows in an approximate linear way with impact energy. But due to the differences among lithology, material, microstructure, density, strength and impedance in the sample rocks, it performs differentiations in peak reflected stress. By linear regression, the gradient range of R_{max} curve of the rocks is determined as [25.138, 27.297], however, the curves are almost parallel. Among them, the gradient values are 25.138 and 25.140 for limestone and gabbro respectively, and R_{max} is 50.318 and 30.844 MPa under the threshold impact pressure. It is 26.605 and 27.297 for marble and sandstone and R_{max} is 30.400 and 36.564 MPa. Although R_{max} values are relatively close between marble and gabbro under the critical responsible pressure, the spacing between the curves is consistent, indicating that the response of between-classis good in impact energy.

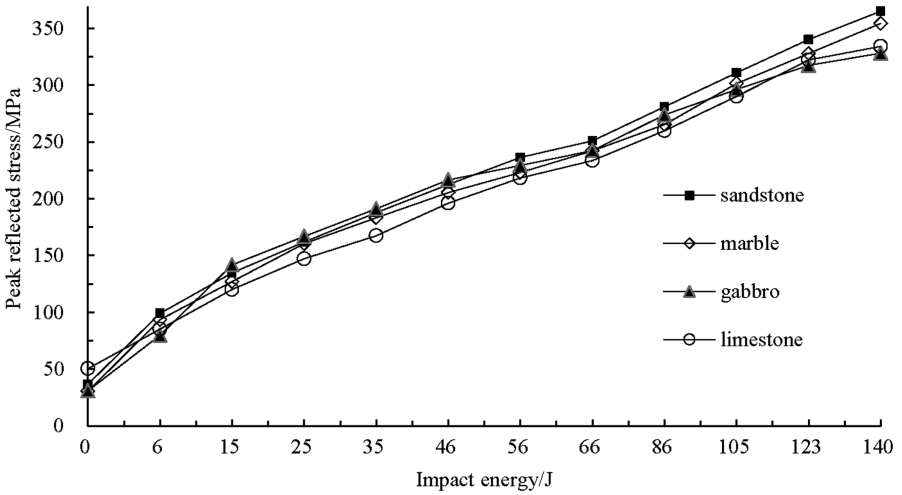

Fig. 2. Change of the peak reflected stress (R_{max})with impact energy

The ratio $(R/I)_{max}$ between peak reflected stress wave(R) and peak incident stress wave (I) in the above rock samples is exhibited in Fig. 3. From the figure, for the same kind of rock, after the impact energy reaches 35.07 J (7.0 psi), the peak reflected stress will increase with energy the increase of peak incident stress and the $(R/I)_{max}$ keeps almost constant. However, there are significant differences in $(R/I)_{max}$ in various rocks. The $(R/I)_{max}$ is the highest in sandstone, followed in sequence by limestone, gabbro and marble, their average peak ratios are 0.973, 0.910, 0.834 and 0.751 respectively, with a definite response of APR in grade. From Table 1, the $(R/I)_{max}$ decreases with the increase of both rock strength and wave impedance in general. The UCS of gabbro is higher than the one of marble rock in the experiment. However, the $(R/I)_{max}$ in marble is higher than in gabbro, indicating that the peak reflected stress from the interface between the drilling bit and rock is closely related to the strength of rock, but is not completely determined by the compressive strength of rock. The $(R/I)_{max}$ is inversely proportional to the wave impedance of rock. The R_{max} decreases with the increase of rock wave impedance.

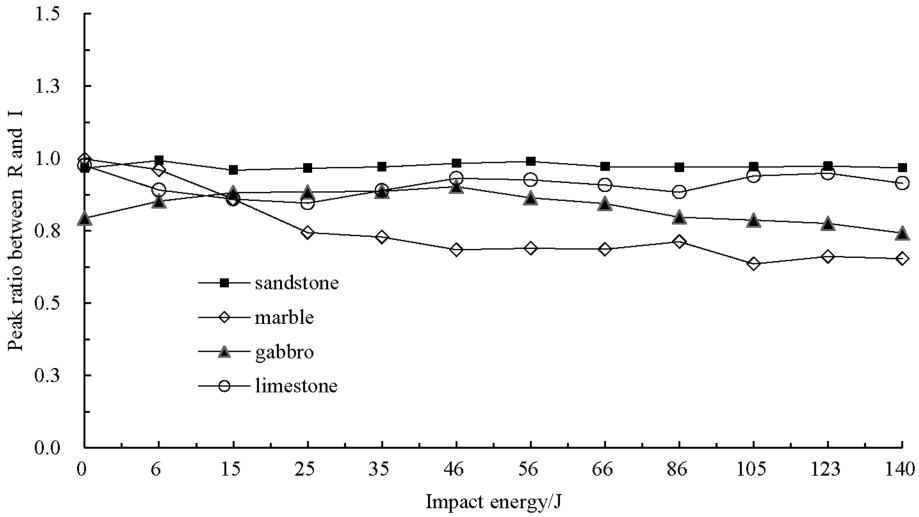

Fig. 3. Change of peak ratio $(R/I)_{max}$ between reflected stress and incident stress with impact

4.2 Change of Specific Reflected Strain Energy

Specific reflected strain energy is defined as reflected energy per unit volume of the bar. From Fig. 4, for the same rock, when the impact energy reaches the threshold value 6.0 J(4.0 psi), the ratio between specific reflected strain energy (R_{se}) and specific incident strain energy (I_{se}) keeps approximately constant and is free of the magnitude of impact energy. For the experimented rock samples, the R_{se}/I_{se} values are 0.89, 0.71, 0.60 and 0.17 respectively in sandstone, limestone, gabbro and marble. The minimum distance between classes is 0.11 and the maximum 0.63, suggests the distance of R_{se}/I_{se} between the rock samples is clear and the response is significant. With the increase of

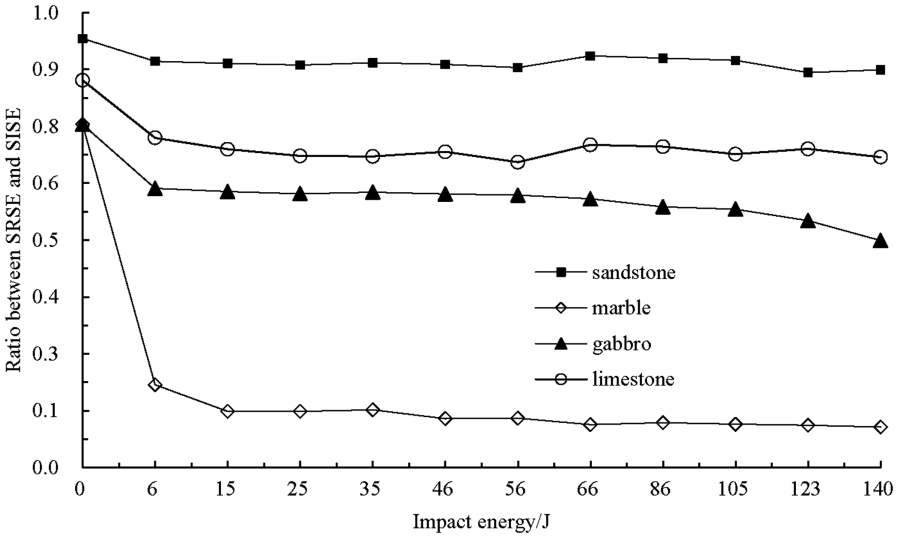

Fig. 4. Change of the ratio between SRSE and SISE with impact energy (SRSE = specific reflected strain energy, SISE = specific incident strain energy)

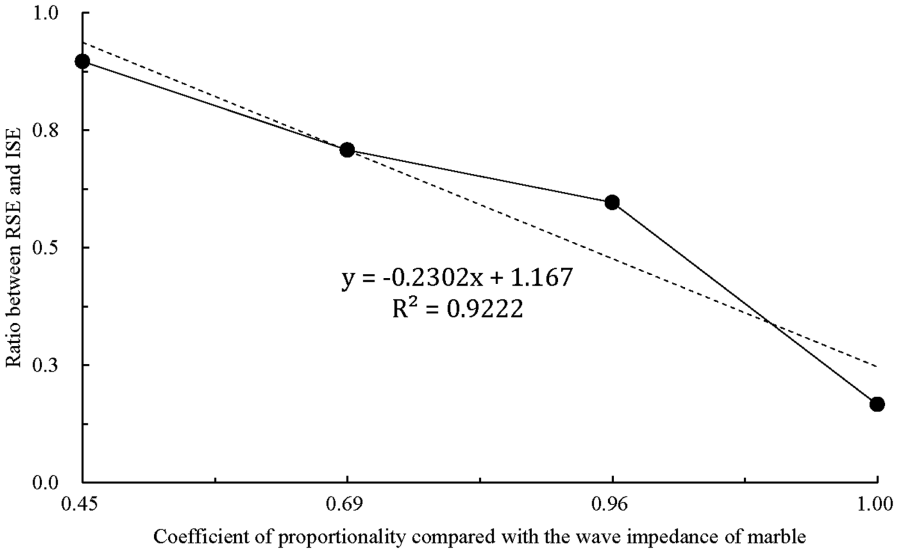

Fig. 5. Change of the ratio between RSE and ISE with wave impedance (RSE = reflected strain energy, ISE = incident strain energy)

rock wave impedance, the R_{se}/I_{se} goes down in a nearly linear way. It is shown in Fig. 5.

Besides, the results also indicate a coupling relation existing between the impact load and rock. For the identical type of rock, when the impact energy reaches the threshold, the peak reflected stress ratio and the specific strain energy ratio tends to be stable. The reason is that, in this case, a good contact can be made between the impact end and the rock interface with reduction in non-coupling effect of stress wave transmission between the interfaces and also in randomness and uncertainty of the test.

5 Conclusions

The response of reflected stress wave cannot occur until the impact energy reaches a threshold value under the experimental conditions. When it exceeds the critical value, the peak value of reflected stress wave increases with the increasing single impact energy, and is approximately linearly related with the impact energy. The ratio between peak reflected stress and peak incident stress is not related to the magnitude of impact energy but to the wave impedance of rock. It decreases with increasing wave impedance and increases with decreasing wave impedance. The within class distance is significant among rocks with different wave impedance.

It is worth noting that the compressive strength of rock plays an influence on the ratio between specific reflected strain energy and specific incident strain energy, as well as the ratio between peak reflected stress and peak incident stress. But the relation is not clear. Besides, although the ratio of peak stress and the ratio of specific strain energy are partitioned with significant inter-class, the reliability of zoning is to be further studied with regards to the rocks of similar wave impedance.

References

1. Ugur I, Demirdag S, Yavuz H (2010) Effect of rock properties on the Los Angeles abrasion and impact test characteristics of the aggregates. Mater Charact 61(1):90–96
2. Kahraman S (2001) Evaluation of simple methods for assessing the uniaxial compressive strength of rock. Int J Rock Mech Min Sci 38(7):981–994
3. Al-Harthi AA (2001) A field index to determine the strength characteristics of crushed aggregate. Bull Eng Geol Env 60(3):193–200
4. Fener M, Kahraman S, Bilgil A, Gunaydin O (2005) A comparative evaluation of indirect methods to estimate the compressive strength of rocks. Rock Mech Rock Eng 38(4):329–343
5. Gong FQ, Li XB, Dong LJ (2011) Experimental determination of dynamic tensile strength of sandstone at different loading rate. In: Rock mechanics: achievements and ambitions-proceedings, 2nd ISRM international young scholars' symposium on rock mechanics. CRC Press, Taylor & Francis Group, London, pp 789–792
6. Ge T, Wang MY (2007) Characters near strong impact loading zone in hard rock. Explosion Shock Waves 27(4):306–311
7. Kahraman S, Bilgin N, Feridunoglu C (2003) Dominant rock properties affecting the penetration rate of percussive drills. Int J Rock Mech Min Sci 40(5):711–723
8. Gong FQ, Li XB, Liu XL et al (2010) Experimental study of dynamic characteristics of sandstone under one-dimensional coupled static and dynamic loads. Chin J Rock Mech Eng 29(10):2076–2085

9. Yan DM, Liu KH, Li HD, Xu SL (2015) A study on the dynamic compressive behavior of pre-damaged concrete. J Hydraul Eng 46(9):1110–1118
10. Ai HA, Ahrens TJ (2006) Simulation of dynamic response of granite: a numerical approach of shock-induced damage beneath impact craters. Int J Impact Eng 33(1–12):1–10
11. Dong ZF, Yin S, Wang HW, et al (2010) The dynamic characteristics analysis of moon soil drilling device. In: 61st international astronautical congress 2010. International Astronautical Federation, IAF, Paris, pp 8239–8246
12. Maca P, Konvalinka P, Curbach M (2014) Behavior of different types of concrete under impact and quasi-static loading. Appl Mech Mater 486:295–300
13. Xia K, Yao W (2015) Dynamic rock tests using split Hopkinson (Kolsky) bar system. a review. J. Rock Mech Geotech Eng 7(1):27–59
14. Song B, Chen W (2004) Loading and unloading split Hopkinson pressure bar pulse-shaping techniques for dynamic hysteretic loops. Exp Mech 44:622–627
15. Xia K, Nasseri MHB, Mohantya F et al (2008) Effects of microstructures on dynamic compression of Barre granite. Int J Rock Mech Min Sci 45:879–887
16. Dai F, Xia K (2010) Loading rate dependence of tensile strength anisotropy of barre granite. Pure appl Geophys 167:1419–1432

Capacity Enhancement of Landfills on Sloping Ground Using Engineered Berms at the Toe

Abinash Mahanta(✉), Manoj Datta, and Gunturi Venkata Ramana

Indian Institute of Technology Delhi, Hauz Khas, New Delhi, India
abinashmahanta.am@gmail.com

Abstract. In the present study, a hazardous waste (HW) landfill on a sloping ground is considered. The base profile of the landfill exhibited significant elevation difference from one end to the other. Due to the inclined base and fixed waste footprint area, the waste retaining capacity of the landfill decreases significantly in comparison to a same plain base area. As a consequence, an engineered berm is provided at the lower end to act as a stabilizing berm and also to increase the waste filling space.

This paper describes the study done to check the stability of the HW landfill on the sloping ground for (a) without berm; (b) with earthen toe berm; and (c) engineered berm or mechanically stabilised earth (MSE) wall for the following critical influencing parameters: (a) leachate head due to temporary clogging; (b) pore water pressures in wet waste; (c) seismic forces. Limit equilibrium methods of analysis is adopted to check the stability for all the cases. Along with the stability, waste filling capacity for each configurations are evaluated. Eventually it is observed that on a sloping ground, the waste filling capacity is highest in case of landfill with MSE walls with optimal solution for stability with significant difference in waste filling capacity from the landfill without berm and earthen berm.

Keywords: Hazardous landfills · Capacity enhancement · Sloping ground
Engineered berm · Mechanically stabilized earth wall

1 Introduction

Unlike in plain terrain, landfills on sloping ground experience instability along weak interfaces in the basal lining systems [4, 6]. Contributory factors which triggers instability in a landfill are reported as temporary clogging of leachates, high pore pressures due to rainfall, earthquakes etc. [6]. Hence stabilizing measures such as berms at the toe of landfills are often adopted [4, 5, 7]. In some situations where waste footprint area is fixed, use of toe berm is a sustainable alternative to consider also for enhancement of capacity to existing as well as new landfills without increasing waste filling boundaries. This option will often entail the design of an engineered berm [1, 7], which in actuality is conventional mechanically stabilized and geosynthetic reinforced earth retaining wall around the waste boundary to increase the landfill waste filling space.

© Springer Nature Singapore Pte Ltd. 2019
L. Zhan et al. (Eds.): ICEG 2018, ESE, pp. 481–488, 2019.
https://doi.org/10.1007/978-981-13-2227-3_59

On a sloping ground, an engineered Hazardous Waste (HW) landfill is designed to accommodate 85 metric ton of waste per day for a design active life period of 15 years. Due to a significant elevation difference of the base, the waste retaining capacity of the landfill decreases significantly. A two dimensional geometrical prototype as shown in Fig. 1 is modeled closely in accordance to the available footprint of the waste boundary. The steepest cover slope is considered to be 3.5H: 1V with the bed profile inclination. The waste filling capacity of the particular landfill configuration is assessed and the stability is investigated for various influencing factors on three different modes of failures a, b and c as shown in Fig. 2.

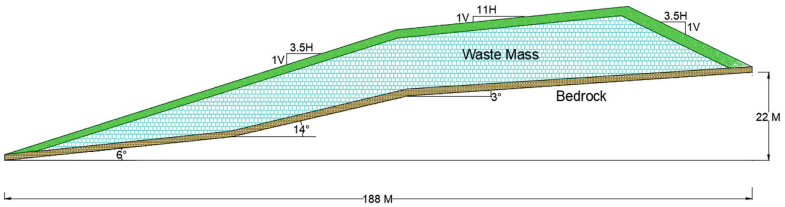

Fig. 1. Typical geometrical prototype of an engineered HW landfill on the sloping ground.

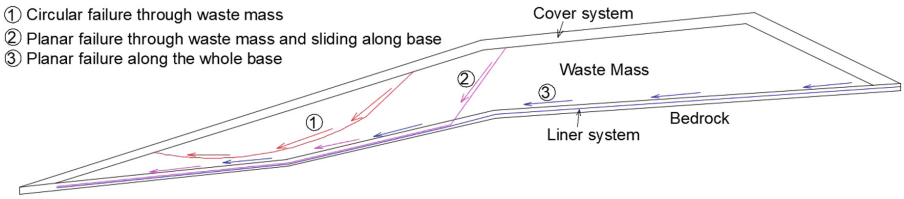

Fig. 2. Modes of failure for an engineered HW landfill on the sloping ground

The stability above landfill is enhanced by using earthen berm at the toe and a two dimensional geometrical prototype is shown in Fig. 3. The stability of the landfill is investigated for different geometric dimensions of the berm such as height, base width, back slope of the berm and the results highlighted in this paper for the optimal stability solution. For the optimal solution, waste filling capacity is assessed. The stability of the HW landfill with earthen toe berm is investigated for different modes of failure a, b and c as shown in Fig. 4 for all the critical influencing parameters.

Eventually the waste filling capacity of the HW landfill is increased by designing an optimally stable MSE wall and providing it at the toe periphery within the designated waste footprint boundary as shown in Fig. 5. The global stability of the landfill system is checked for the failure surfaces as shown in Fig. 6.

The objective of the present study is to investigate the stability of the HW landfill on the sloping ground for (a) without berm; (b) with earthen toe berm; and (c) engineered berm or mechanically stabilized earth (MSE) wall for the critical influencing parameters: (a) leachate head due to temporary clogging; (b) pore water pressures in

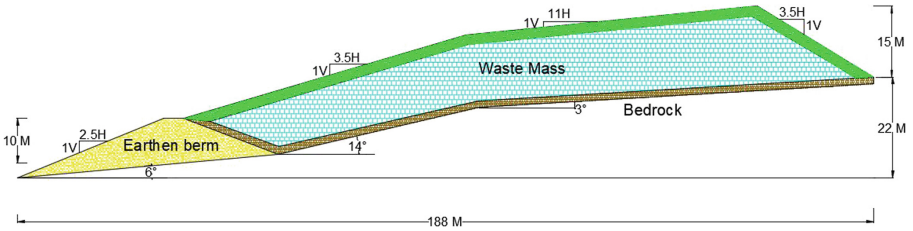

Fig. 3. Typical geometrical prototype of an engineered HW landfill on a sloping ground with earthen berm at the toe.

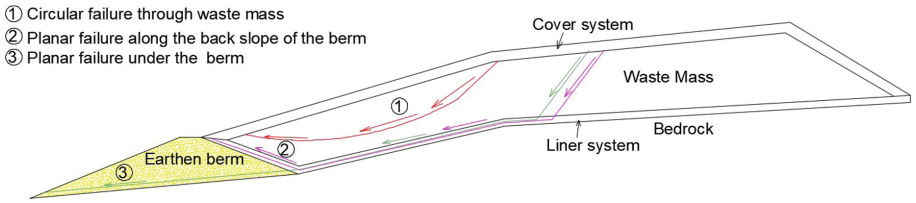

Fig. 4. Modes of failure for an engineered HW landfill on the sloping ground with earthen berm at the toe.

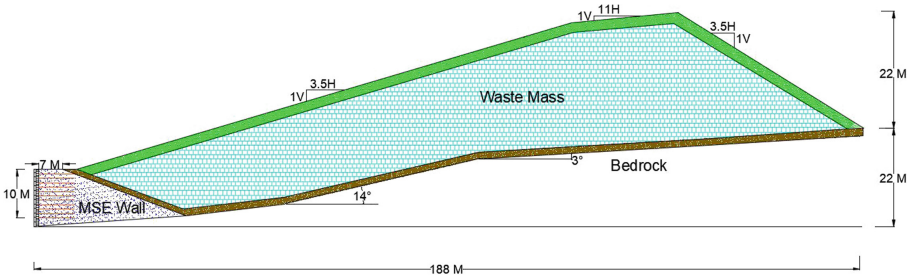

Fig. 5. Typical geometrical prototype of an engineered HW landfill on a sloping ground with MSE wall at the toe.

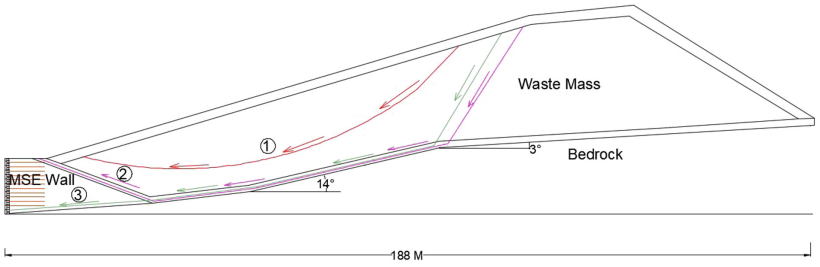

Fig. 6. Modes of failure for an engineered HW landfill on the sloping ground MSE wall at the toe.

wet waste; (c) seismic forces. Waste filling capacity for each configurations are evaluated with optimal stability solutions.

2 HW Landfills on Sloping Ground

2.1 Methods of Stability Analysis

The stability of the engineered HW landfill on the sloping ground is investigated against different modes of failures for different configurations. For the landfill without berm, three modes of failure are investigated: (a) circular failure through the waste mass, (b) planar failure through waste mass and sliding along weakest interface of geomembrane (GM) and compacted clay liner (CCL), and (c) sliding along complete lining system along the interface of GM and CCL are analysed. Landfill with earthen berms and MSE wall are also investigated for three modes of failure: (a) circular failure through the waste mass, (b) planar failure through waste mass and sliding along weakest interface of GM and compacted clay liner (CCL) extending along the back slope of the berms, and (c) planar failure through waste mass and sliding along weakest interface of GM and compacted clay liner (CCL) passing under the berms. All configurations are analysed for various influencing factors such as leachate head developed due to temporary clogging, pore water pressure in wet waste mass and due to earthquakes forces. The stability of the landfill system is investigated by Morgenstern and Price's (M-P) method which is found to be more suitable [6] as it satisfies both force and moment equilibrium equations to determine critical failure surface in calculating minimum value of Factor of Safety (FoS). For the present study, commercially available slope stability software Slope/W is used. The seismic condition is analysed by pseudo-static method for maximum earthquake forces.

2.2 Conditions of Analysis

For all the configurations, same critical influence parameters are considered. Initially all the cases are analysed for dry and wet waste for static conditions. The influence of leachate head (LH) on the stability is investigated with varying the input values of LH from 1 m to 2 m above the base. The influence of pore water pressures in waste mass was investigated with varying the input values of pore-water pressure ratio (r_u) from 0 to 0.2. The effect of earthquake forces on stability of the landfill are assessed by varying the horizontal earthquake force, α_h from 0.05 to 0.15 and vertical earthquake force, from α_v 0.03 to 0.1. For the present study, the interface between GM and underlying CCL in basal lining system is simulated with interface shearing resistance (δ) 18° (textured geomembrane).

2.3 Earthen Toe Berm

The dimensional variability of the berm has great influence in stability of the landfill and it's waste filling capacity. It is investigated that the higher base width and height with less steep back slope of the berm enhance the stability of the landfill however on

the other end it reduces the capacity of waste fill. In the present study an adequate size of earthen berm is adopted with optimal solution for stability for overall stabilization of the landfill where height of berm is 10 m, berm base width 32 m and back slope angle is 28^0. The material properties of the berm are put in Table 1.

Table 1. Geotechnical properties used in the stability analyses for various materials

Material	Unit weight (kN/m^3)	Cohesion intercept (kPa)	Angle of shearing resistance (°)
Hazardous waste	16	3	25
Subgrade soil	–Bedrock—		
Toe berm	20	5	30
		Adhesion intercept (kPa)	Interface shearing angle (δ in °)
Textured GM-clay interface	-	0	18

2.4 Mechanically Stabilised Earth Walls

The design of MSE wall and its optimal dimensions are fixed as per Federal Highway Administration guidelines [3, 5]. The geotechnical properties of the MSE wall fill materials are considered based on the available materials at the site such as angle of shearing resistance is 32° and unit weight of fill is 19kN/m3. The backfill material practically cohesion less but the backfill is considered having pseudo- cohesion [7]. The tension in each soil reinforcement layer is converted into equivalent cohesion using the pseudo-cohesion concept. The equivalent cohesion is found to be 13 kPa. For the present study, for a 10 m high MSE wall, cohesion is considered as 20 kPa as the berm needs more soil reinforcement than the design. Both internal and external stability for the MSE wall is carried out and the dimension for optimal stability solution is adopted in the present study. The Global stability of the landfill system is investigated for different failure modes under the influence of critical influencing parameters.

2.5 Materials and Geotechnical Properties

Various geotechnical properties [2] considered in modelling the HW landfill components are tabulated in Table 1.

3 Results

3.1 HW Landfill on Sloping Ground Without Berms

The stability analyses of the HW landfill on the sloping ground is carried out and the FoS values for different modes of failure for all critical influencing parameters are tabulated in Table 3. It is observed FoS values are below the minimum acceptable values for failure through the waste mass and sliding along the base even in static

condition when leachate head is 2 m and pore water pressure value is 0.2. For this particular mode of failure, effect of earthquake forces further reduces the FoS values. The waste filling capacity of the landfill with the analysed section is 1700 m^2 which is 67% of the total required waste fill capacity. It thus necessitates the stability enhancement of the landfill by using toe berm Table 2.

Table 2. Minimum acceptable values of FoS for different conditions of analysis

Conditions of analysis	Dry waste (ru = 0)	Temporary clogging (leachate head)	Wet waste/rain/seepage (ru > 0)	Earthquake (pseudo-static)	Leachate head and earthquake effect
Acceptable FoS	1.5	1.3	1.3	1.1	1.05

3.2 Landfill on Sloping Ground with Earthen Toe Berm

For the landfill with earthen toe berm, stability is investigated and FoS values are tabulated in Table 4. It is observed that the landfill is optimally stable due to application of the earthen toe berm. However the waste filling capacity of the landfill is 60% of the total desired waste filling capacity. The cross sectional area for the landfill with the earthen toe berm is 1570 m^2. Thus the application of toe berm reduces the waste fill capacity of the landfill on a sloping ground.

3.3 Landfill on Sloping Ground with MSE Walls

The MSE wall is so designed that its internal and external stability meets the required minimum acceptable limit [7]. Global stability of the HW landfill with the designed MSE wall is investigated and found to be stable for all the modes of failure under the

Table 3. FoS for HW landfill on sloping ground without berm

Description	FoS		
	Circular failure through waste mass	Planar failure through waste mass and sliding along base	Sliding failure along complete liner system
Static condition			
LH = 0 M, r_u = 0, δ = 18	1.68 (>1.5)	1.50 (~1.5)	2.64 (>1.5)
LH = 2 M, r_u = 0, δ = 18	1.65 (>1.3)	**1.26 (<1.3)**	1.68 (>1.3)
LH = 0 M, r_u = 0.2, δ = 18	1.50 (>1.3)	**1.20 (<1.3)**	1.57 (>1.3)
Seismic condition (pseudo-static method)			
LH = 0 M, α_h = 0.15, α_v = 0.1, δ = 18	**1.10 (~1.1)**	**0.96 (<1.1)**	1.22 (>1.1)

Table 4. FoS for HW landfill on sloping ground with earthen toe berm

Description	FoS'		
	Circular failure through waste mass	Planar failure FoS_{over}	Planar failure FoS_{under}
Berm height = 10 m, *Static condition*			
LH = 0 M, r_u = 0, δ = 18	1.78 (>1.5)	1.72 (~1.5)	3.68 (>1.5)
LH = 2 M, r_u = 0, δ = 18	1.75 (>1.3)	**1.45 (>1.3)**	3.58 (>1.3)
LH = 0 M, r_u = 0.2, δ = 18	1.62 (>1.3)	**1.36 (>1.3)**	3.42 (>1.3)
Berm height = 10 m, *Seismic condition*			
LH = 0 M, α_h = 0.15, α_v = 0.1, δ = 18	**1.29 (~1.1)**	**1.16 (<1.1)**	2.45 (>1.1)

influence of all the critical parameters. However the waste filling capacity of the landfill is 105% of the total desired waste filling capacity. The cross sectional area for the landfill with the MSE wall or engineered berm is 2940 m^2.

It is observed from Tables 3 and 4 that the planar failure along the weak interface of geomembrane and clay liner which extends through the waste mass is most critical. In both the cases of 'without berm' and 'with earthen toe berm', effect r_u shows the lowest FoS which is marginally safe in 'with earthen. In Fig. 7, change in FoS with effect of r_u for the most critical condition of analysis are shown for all the three cases.

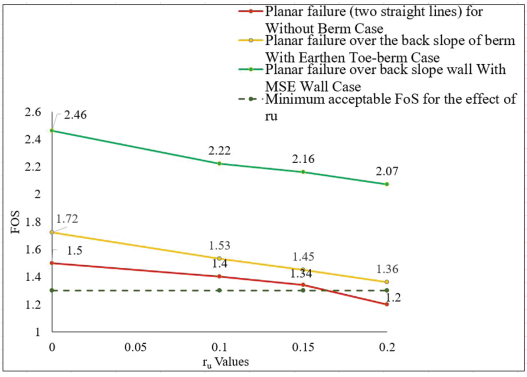

Fig. 7. Effect of r_u for without berm, with earthen toe-berm and with MSE wall

4 Concluding Remarks

This paper presents study of both stability and waste fill capacity of a HW landfill for three different configurations such as landfill with no berm, with earthen toe berm and with MSE wall the toe on a sloping ground. The results highlight the fact that for the sloping ground, landfill with no berm is unstable. However the landfill with earthen toe berm with optimal stability solution has a waste fill capacity of 60% percent that of

required capacity. In the present study, to enhance the stability as well as waste fill capacity, designed stable MSE wall is used. It is concluded that for landfills on sloping ground, adequate size of MSE walls help in enhancing stability as well as waste fill capacity upto significant extent.

References

1. Basha BM, Babu GLS (2010) Optimum design for external seismic stability of geosynthetic reinforced soil walls: a reliability based approach. J Geotech Geoenviron Eng 136(6):797–812
2. Bergado DT, Ramana GV, Sia HI, Varun (2006) Evaluation of interface shear strength of composite liner system and stability analysis for a landfill lining system in Thailand. Geotext Geomembr 24(6):371–393
3. BS:8006 (2010) Code of practice for strengthened/Reinforced soils and other fills. British Standards Institute, London
4. Feng SJ, Chen YM, Gao LY (2010) Translational failure analysis of landfill with retaining wall along the underlying liner system. Environ Earth Sci 60(1):21–34
5. FHWA (2001) Mechanically stabilized earth walls and reinforced soil slopes: design and construction guidelines. Publication FHWA NHI-00-43. Federal Highway Administration and National Highway Institute, Washington, DC, USA
6. Koerner RM, Soong T-Y (2000) Leachates in landfills - the stability issues. Geotext Geomembr 18(8):293–309
7. Leshchinsky D, Tatsuoka F (2003) Reinforced soil engineering. Marcel Dekker, Basel. Qian X, Koerner RM (2009) Stability analysis when using an engineered berm to increase landfill space. J Geotech Geoenviron Eng 135:1082–1091

Mapping of Risk Areas in Communities of João Pessoa, Paraíba, Brazil

Camila de Andrade Oliveira(✉), Hanna Barreto de Araújo Falcão, and Fabio Lopes Soares

Paraíba's Federal University, João Pessoa, Paraíba, Brazil
camisandrade95@hotmail.com

Abstract. The unplanned process of urbanization during the years has resulted in the emergence of risk areas occupied by the population in social and economic vulnerability. These areas, in it definition, are suject to risks of natural or induced disasters, such slides of earth and flood. In some cities in Brazil, the level of occupation is practically irreversible. The risks originating by this situation are since material losses to damages for the physical integrity, being this sometimes unrecoverable. The mapping of risk areas turn up indispensable to the mitigation plans of the risks found. The methodology adopted by the Brazil's Ministry of Cities was used as base for the mapping. The community Filipeia located in the neighbor of Tambiá at João Pessoa, Paraíba, Brazil, is a potential area of risk. Based on the collected data, the map of risk of Filipeia was developed. The mapping produced revealed that natural and anthropic factors are directly related with the risks for the human life and material assets, such the slope gradient, the kind of vegetation present there, the launch of wastewater on the face of the slope and the self-construction in improper areas.

Keywords: Slides · Occupation · Mapping · Community · Risk

1 Introduction

Disasters related to landslides are becoming more frequent in the city of João Pessoa, in the state of Paraíba, Brazil. These landslides, known as mass wasting, generally occur as a result of the association of natural factors and human intervention. Geological, geomorphological and, mainly, climatic conditions of the area contribute to natural disasters. Besides, the occupation of unsuitable areas aggravates the risk situation caused by natural factors, resulting in human-induced disasters. According to the Ministry of the Cities of Brazil, areas susceptible to the occurrence of these disasters are denominated risk areas.

In the mid-1930s, urban centers grew disorderly due to the federal government investment in the industrialization of Brazil. In the state of Paraíba, as well as in other states of the country, people migrated from surrounding towns and the countryside in an attempt to achieve better living conditions and employment opportunities offered in the capital cities. However, there wasn't enough infra-structure to settle properly the amount of population that, due to lack of information, ended up occupying susceptible areas next to slopes and hillslopes.

© Springer Nature Singapore Pte Ltd. 2019
L. Zhan et al. (Eds.): ICEG 2018, ESE, pp. 489–496, 2019.
https://doi.org/10.1007/978-981-13-2227-3_60

With the purpose of eradicating risks resulting from disorderly occupation, generally held by the socioeconomic vulnerable population, public bodies were created to manage urban planning in these areas. The public agency responsible for this issue in the city of João Pessoa is the municipal Civil Defense.

In 2012 and 2013, the municipal Civil Defense of João Pessoa carried out a study which identified 27 risk areas in the city. This paper aims to map risks in Filipeia community, one of the risk areas of João Pessoa, based on the methodology developed by the Ministry of the Cities of Brazil.

2 Methodology

2.1 The Community Filipeia

The Filipeia community is localized in Tambiá neighborhood, in the city of João Pessoa, Paraíba, Brazil. It consists of an area of approximately 0,756 hectares, close to downtown, which, over the last few years, has developed itself through a process of continuous expansion. The Hospital Santa Isabel is placed nearby the community, whose development occurs on the crest of a steep hillslope that borders an environmental preservation area, called Parque Natural Lauro Pires Xavier. Therefore, the Filipeia community is recognized by the municipal Civil Defense of João Pessoa as a risk area.

The disorderly occupation of the area began 24 years ago, and the community has been stablished since then, according to data from The Municipal Government of João Pessoa (PMJP/SEPLAN/COMDEC, 2008). Currently, this occupation is already consolidated and is predominantly composed by masonry houses and some small buildings. Water is provided by the water supply system of the city; there is public illumination on the streets and most of the streets are paved; most of the houses have electricity and urban garbage collection is carried out regularly. The sewerage system is unsatisfactory. Most houses are supplied with this public utility, but part of the community has no supply. In this last case, dis-charge of sanitary effluents is done in a communitary pit and wastewater is dumped directly on the slope down to Rio das Bombas, a river whose source is in the natural park. This situation occurs specially in relation to the houses that irregularly occupy the edge of the slope, which is the most risky area.

2.2 Methodology of the Ministry of the Cities

Bearing in mind that flooding and landslide processes are recurrent issues in the major Brazilian cities, mainly during the rainy seasons, the Ministry of the Cities of Brazil developed “the Training Course for Technicians and Municipal Managers on Mapping and Risk Management of Landslides and Floods, in partnership with the University Centre for Disaster Studies and Research, at the Federal University of Santa Catarina (CEPED/UFSC), and the Institute for Technological Research (IPT)” (Ministry of the Cities).

Identifying risk areas is important, primarily, due to the possible consequences resulting from the advances of landslide processes and the occurrence of flooding that, yearly, generate victims, including casualties in many cases, besides the loss of material assets.

The aim of the training promoted by the Ministry of the Cities of Brazil was to qualify the working group of municipal management departments to identify and handle risks of landslides and flooding in the cities, knowing that an efficient administration is possible through risk mapping techniques.

According to the methodology of the Ministry of the Cities, risk areas are divided in sectors and classified according to the risk degree: low, medium, high or very high.

The risk degree of the sector is defined through the observation of some factors which, in this paper, are grouped in the following categories: "Locality General Characterization" and "Geological and Geotechnical Characteristics", which are related to the locality where the community is established, and "Susceptibility Factors" and "Vulnerability Factors", which are related to each sector. In each of these categories, the aspects in Table 1 were observed.

Table 1. Categories of evaluation of the risk.

Category	Aspects
Locality general characterization	• Stage and mode of occupation; • Standard of the buildings; • Landform; • Hydrography; • Vegetation on slopes
Geological and geotechnical characteristics	• Structure, textures, and type of the soils; • Stability of the massifs
Susceptibility factors	• Characterization and types of the active processes; • Causes and aggravating factors of instability
Vulnerability factors	• Number of buildings in the sector; • Number of threatened buildings; • Existence of threatened public equipment

3 Results

It was verified, by means of visits to the community, that its occupation is consolidated with masonry buildings which were settled on the reserve boundary in a spontaneous and informal way. The presence of understory vegetation on the cliff face of the slope was noticed, as well as large trees and some fruit trees that are not appropriate for this area, as banana plants, for example. The impact of the population on the environment in which it is inserted enhances the risk the houses are subject to. Due to a precarious sewage treatment system, the community's residents throw their wastewater on the cliff face of the slope, which causes superficial erosion, soil contamination and slope instability. As an aggravating factor, the stream bed of Rio das Bombas, one of the

tributaries of an important river of the state, called Rio Paraíba, passes by the foothill, so the river's water can be contaminated by the effluents released into the ground.

On geological and geotechnical characteristics: slopes are constituted of Barreiras formation, current in cities of the Brazilian coast, composed of 18% of silt and clay, 52% of fine sand, 28% of coarse sand and 3% of pebble, according to the classification of the National Department of Transport Infrastructure (DNIT). In general, the hillslopes appeared stable on unsaturated soil.

The mapping of risk areas was carried out using geographical coordinates from a GPS device (Garmin) to obtain the location of the houses and also points of reference to facilitate the process.

Therefore, this process resulted in the development of the Risk Map of the community (Fig. 1), whose sectors were defined according to the degree of risk and are shown on the map by the following colors: green indicates low risk, yellow medium risk, red indicates high risk and purple indicates very high risk.

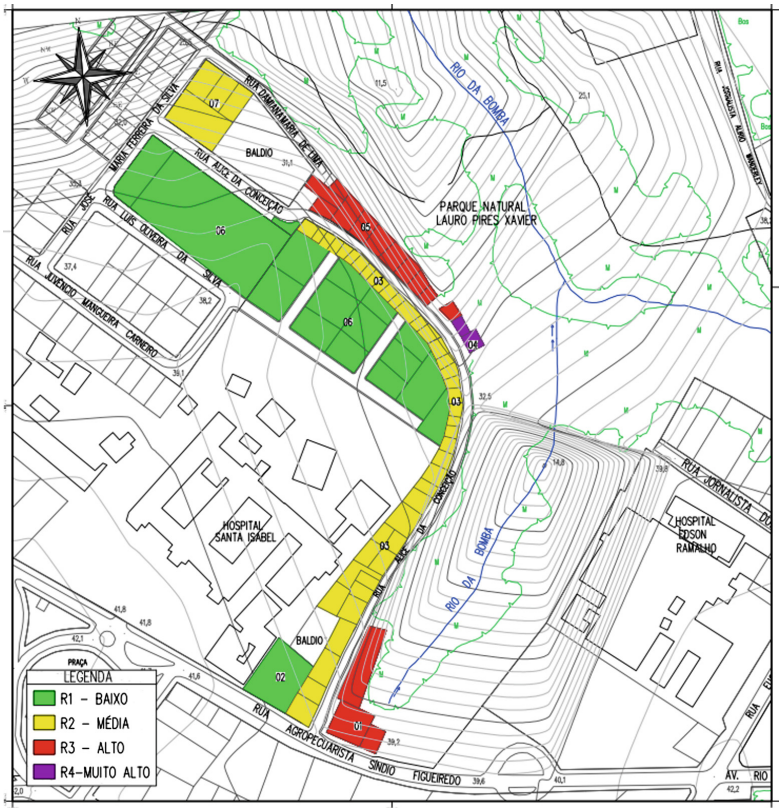

Fig. 1. Risk map of the community Filipeia

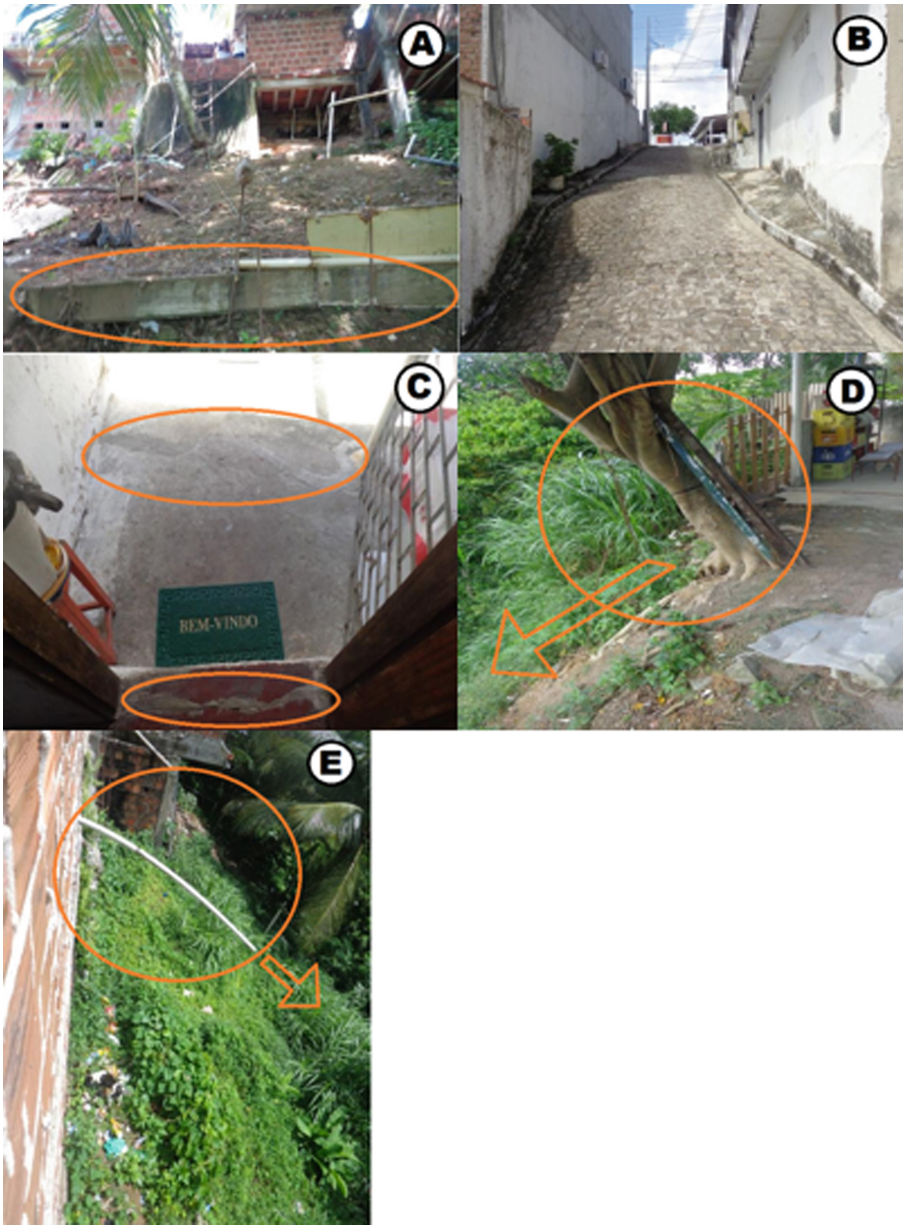

Fig. 2. Adversities presented in the community: (A) Elements placed in an attempt to contain landslides; (B) Steepness of the street in the direction of the slope; (C) Cracks on the floor of the house; (D) Large size vegetation that presents steepness on the crest of the slope; (E) Wastewater pipes releasing effluents directly into the slope.

The green area indicates low risk due to the fact that the buildings are nearby the areas of higher risk, although they do not suffer direct influence of the steep-ness of the hillslopes. There are, approximately, 17 buildings in this situation.

In the yellow area, classified as medium risk, there are approximately 46 buildings on the access lane to the community, which bounders the slope separating these residences from the crest by a distance of around 5 m. Due to that proximity, these buildings are susceptible to landslides that could compromise the access lane to the community.

Fig. 3. Conditions of the houses in very high risk: (A) Distance of the house from the slope on the crest; (B) and (C) Cracks found in both houses; (D) House with more than 3.50 m built below the crest of the slope; (E) Dumping waste on the face of the slope.

In the high risk area, indicated by the red color on the map, there was previous collapse of garbage, rubbish, and part of the soil on intense rainy days; there is no rainwater drainage system, there are large trees on the cliff face and groundwater spots in the slope. In all, there are 16 houses in this situation with signs of soil movement as well as cracks on the walls, floor and ceiling.

In the sector of very high risk there are two houses which are particularly in danger because they are at an intermediate level of the hillslopes (between the crest and the foothills), being more vulnerable to landslides. One of the houses is located 90 cm away from the slope formed upon the crest preceding the house. This part of the slope has been constantly excavated by the own residents or neighbors, increasing the possibility of landslides. The most expressive sign of mass wasting is the existence of cracks of 1.5 to 2.0 cm in process of expansion on the walls of both houses, indicating that the movement occurs in the direction of the foothills of the slope. There are also cracks on the floor and infiltration problems in the house. In addition, the dumping of waste and garbage on the slope is a common practice of the residents. This dump is, consequently, carried by the water on intense rainy seasons. The residents' lives are in imminent risk. Five people live in one of the houses, and 6 people in the other, totaling 11 potential victims, among which children, adolescents and elderly people. The Fig. 3 shows the conditions found in these two houses.

4 Conclusions

The emergence of risk areas is a result of several factors: natural factors, related to the geological history of the area, soil composition, steepness of the hillslopes, among others, and human-induced factors, resulting from the action of the residents on nature, as releasing of wastewater directly on the cliff face of the slope, self-building in unsuitable areas, deforestation, cut slope due to excavation, creating a situation of destabilization by the soil released in front of the hillslopes.

Such factors have direct effect on the continuity and development of risk areas. The prevention of the development of risk areas involves the application of structural measures, such as containment constructions and slope restoration of the area, as well as non-structural measures, focusing on the population.

Environmental education of the communities in risk areas is fundamental because it promotes the engagement of the community by means of information. However, for an effective result in the long term, the continuous monitoring of risk areas and the commitment of the population is fundamental.

Self-building is a problem that afflicts all the country, being mainly found in communities composed mostly by the socioeconomic vulnerable population. This is a public management issue due to the lack of a technical advising to the population, which resorts to self-building, resulting in the emergence of risk areas. The applicability of structural solutions requires an accurate assessment of the current situation of the area, being the proposition of this paper only to point these solutions.

Containment constructions can be carried out by retaining walls or slope restoration; the control of erosion can be associated with the use of geosynthetics as an appropriate mulching; implementation of palisades to contain eroded soil and to

naturally create a new geometry for the slope; drainage system and sewage collection should be carried out to decrease the damage caused by the presence of water in the soil.

References

Civil Defense of João Pessoa (2012–2013) Diagnóstico das Comunidades em Áreas de Risco. João Pessoa, Paraíba, Brazil

Ministry of Cities: Capacitação em Mapeamento e Gerenciamento de Risco. http://www.defesacivil.mg.gov.br/images/documentos/Defesa%20Civil/manuais/mapeamento/mapeamento-grafica.pdf. Accessed Feb 2018

National Department of Transport Infrastructure (2006) Manual de Pavimentação. IPR-179, Rio de Janeiro, Brazil

The Slope Stability Analysis Under the Coupling Effect of Earthquake and Rainfall

Yongfen Ruan[1(✉)], Bingjun Shi[2], Jun Yang[3], and Shuanshuan Peng[3]

[1] Faculty of Civil Engineering and Mechanics,
Kunming University of Science and Technology, Kunming 650500, China
ryy64@aliyun.com
[2] Southwest Non-Ferrous Exploration Design Co., LTD.,
Kunming 650051, China
[3] China Railway Eleventh Bureau Group City Rail Engineering Co., Ltd.,
Beijing 650228, China

Abstract. The rainfall and earthquake are two main causes of instability and failure of slope. To analyze the excess pore water pressure, the safety coefficient of slope and slope feature point displacement change with the time under the different earthquake intensity. The numerical modeling results of slope under the action of earthquake is inputted to the finite element analysis software, to the analysis dynamic change rule of volume moisture content and the formation of pore water pressure of slope soil mass under the condition of rainfall. Using the limit equilibrium method calculates and comparative analysis the slope stability after Coupling of earthquake and rainfall infiltration,and under the action of alone that earthquake or rainfall alone. The result shows that the earthquake makes slope geotechnical body to produce permanent deformation and increase the permeability coefficient of slope. Moreover, the rainfall infiltration will further decrease shear strength of slope, lead to the emergence of landslide. The earthquake combines with rainfall is more easily to induce landslide than single factor.

Keywords: Saturated-unsaturated seepage field
Coupling of earthquake and rainfall · Pour water pressure

1 Introduction

The rainfall and earthquake are main factors that induce landslides. When the earthquake magnitude is greater than 4.0, it will trigger the landslide disaster [1]. Earthquake caused a lot of loose mountain, development of a large number of collapse and unstable slope body in the front of mountain, that means the collapse and unstable slope body disasters increased significantly before the earthquake [2]. There is a saying, “Slide ten nine water”, and although it is not so comprehensive, it shows the important influence of the water from the angle of landslide stability. On August 11, 2006 in Kunming, the torrential rain lasted 1.67 h and induced 41 times landslides; On July 2, 2008 in Kunming, the heavy rain lasted 4 h. Induced 50 times landslides 50 [3].

© Springer Nature Singapore Pte Ltd. 2019
L. Zhan et al. (Eds.): ICEG 2018, ESE, pp. 497–506, 2019.
https://doi.org/10.1007/978-981-13-2227-3_61

There are lots of research on the earthquake [1–3], raining fall [4–6] and induced landslide recent years, but the destructive influence of rain after the earthquake also considers as an no ignore factors, for examples, the Chi-Chi earthquake of Taiwan took place in 1991, the landslide induced by rainfall after earthquake resulted in 3 time landslide area than earthquake [7]; 1999 landslides were induced by Wenchuan Earthquake on 12th May, heavy rainfall on Sept 24 induced 828 landslides and the original 150 earthquake landslide area was expanded due to the heavy rain on 24th Sep., Area of induced landslide resulted by rainfall accounted for 1/4 of total landslide area caused by earthquake. The frequency of landslide caused by heavy rainfall increased by 41.4%; not only the new landslides induces by heavy rainfall, but also it revitalizes the original landslide of earthquake, and gradually expands. The heavy rainfall resulted in the landslide area of earthquake expanded 68.7% of the original area [8].

Through the above analysis we can see, to study the slope stability under the coupling of seismic and rainfall is necessary and importance. In recent years, the coupling of seismic rainfall has been studied [9, 10], but it is in the initial stage. The continuous influential effect of rain fall after earthquake may bring coupling weaken impact on the stability of the slope, the correlation between rainfall landslides and potential disasters after the earthquake is worth of aware. For this reason, the numerical analysis method is used to carry out study and analysis for the change of seepage field and stability of the slope after the coupling of rainfall and earthquake.

2 The Selection of Calculation Parameter

The El centro platform classical records in the IMPERIAL valley (M7.1) as shown in Fig. 1. You can see from Fig. 1, the maximum earthquake acceleration (peak) in 2.14 s is 3.417 m/s^2. In order to ensure the calculation precision, a total of 500 groups of acceleration time history data was used the input that the representative band in the first 10 s is selected among the EL CENTRO seismic acceleration is the larger band.

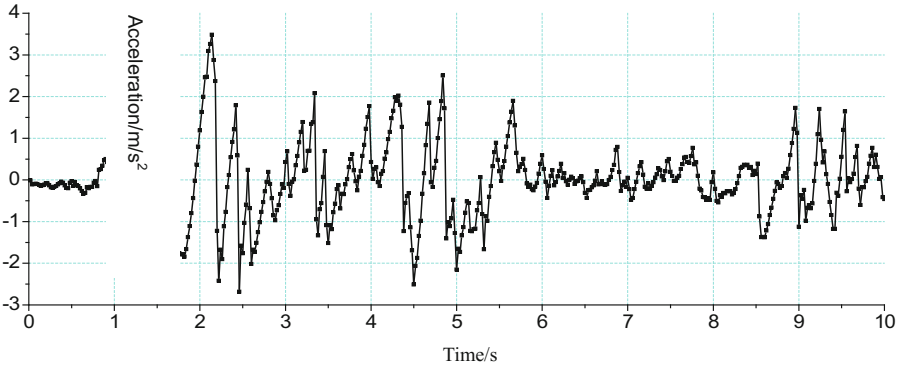

Fig. 1. **El** Centro wave of the X direction waveform in the first 10 s

Slope Silts Soils parameters as follows: $\gamma = 18\text{kN/m}^3$, c = 15kpa, $\varphi = 26.5°$[11]. $E_S = 5\text{MPa}$, $\mu = 0.35$, $\eta = 0.05$, permeability coefficient K is 1.1e-3 mm/s, saturated moisture content of 30%. Using the rainfall data of China's meteorological department statistics as the standard take 75 mm/d(8.68e-4 mm/s). Analysis the change law of slope seepage field and stability that the seismic intensity is 7, 8, 9° (peak acceleration a_{max} were 0.1 g, 0.2 g, 0.4 g). The slope high is 20 m, slope ratio is 1:1.5, the calculation model of the slope is shown in Fig. 2.

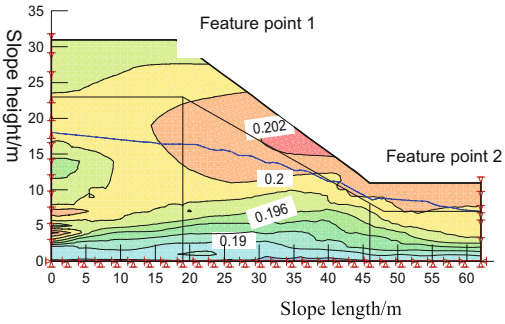

Fig. 2. Displacement contour map of the earthquake 10 s (9°)

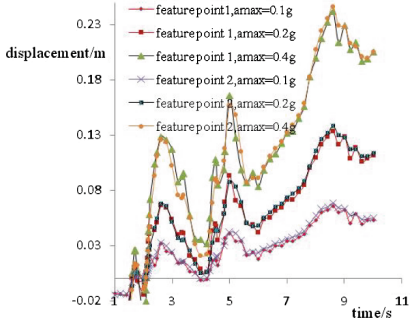

Fig. 3. Feature point displacement variation diagram

3 The Numerical Analysis of Slope Under the Earthquake Action

Main analyzed the earthquake force and excess pore water pressure cause a permanent deformation of soil mass slope. The seismic displacement contour map of the slope as shown in Fig. 2; the displacement change of feature point of slope how they change over time as shown in Fig. 3; as you can see from Figs. 2 and 3, the maximal displacement mainly appears in the upper regions and free face of slope, the displacement of the slope increases with seismic intensity, the slope maximal displacement is 54.4 mm, 114 mm and 202 mm respectively when the seismic load is 7, 8, 9°. Slope feature point displacement variation-time history is basically the same with the displacement up and down, but the overall trend is gradually increasing with time, this is a permanent displacement caused by seismic shaking force. Seismic load acceleration peak value appeared in 2.14 s, the slope displacement of three different earthquake intensity haven't reached the maximum, the moment of slope instability and failure is not necessarily the earthquake acceleration peak moment.

The slope deformation and destruction, and the excess pore water pressure increase and accumulation caused by seismic loads and earthquake force; the slope instability is the result of shaking force combined with excess pore water pressure. Taken a_{max} = 0.4 g (9°) as an example, the slope contour map of the excess pore water pressure at the end of the earthquake is shown in Fig. 4. It can be seen from the Fig. 4, the excess pore water pressure appear in saturated silt area below the underground water level.

The excess pore water pressure along with the slope from top to bottom respectively select several feature points such as 1, 3,…, 7, 8, 2 change of time as shown in Fig. 5. As can be seen from the Fig. 5, the excess pore water pressure appears and accumulates in a short period of time, also increases with depth. Excess pore water pressure will cause the loss of soil strength and result in cause the slope rock deformation and failure. The slope soil mass in the equilibrium state may experience a sudden loss of strength, stress redistribution and adjustment, the additional load not affected by the strength and strength loss to share in the region and stress redistribution process will be continued until the soil mass balance again. Permanent deformation is the result of stress redistribution when soil mass reach equilibrium once again, if the slope soil mass strength loss is too big, can lead to soil mass structure can't balance again, and slope will appear instability and failure.

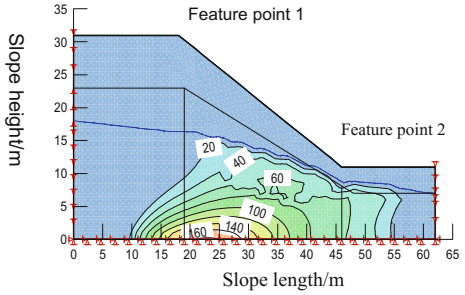

Fig. 4. Excess pore water pressure contour map the earthquake 10 s (9°)

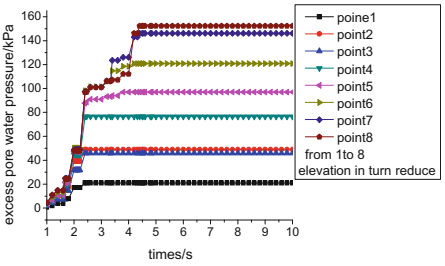

Fig. 5. Excess pore water pressure variation diagram (9°, a_{max} = 0.4 g)

The slope stability safety coefficient change process under seismic load is shown in Fig. 6. As you can see from Fig. 6, slope safety factor is fluctuant over time, the overall trend gradually decrease. In seismic peak acceleration time (2.14 s) the safety coefficient is k_{min}. The safety coefficient of time history curves of the minimum point on slope stability more than the critical value of 1.0 when the earthquake intensity is of 7°; Safety factor when the earthquake intensity is reaching 8° in graph all minimum points is getting close to 1.0 more than 7°, even have reached the critical value of 1.0; Earthquake intensity of 9° each time part of safety coefficient is less than the critical value of 1.0, But the instantaneous instability slope is not necessarily completely destroyed at the moment. So the criteria instability and failure of slope under seismic load should overall consider as a minimum safety factor and permanent displacement caused by seismic load. Three kinds of permanent deformation of slope under seismic load and the minimum safety factor k_{min} as shown in Table 1.

It can be seen from Table 1, the permanent deformation of slope under 7° earthquake load is 54.4 mm, k_{min} is 1.147, the stability of slope is higher; the permanent deformation under 8° seismic load is 114 mm, k_{min} is 0.989, the safety factor of less than the critical value of 1.0 occurrences only once, so the instability and failure of slope is possible; 9° slope under seismic load is permanent deformation up to 202 mm, the minimum safety factor of 0.907, less than the critical value the safety factor of 1.0

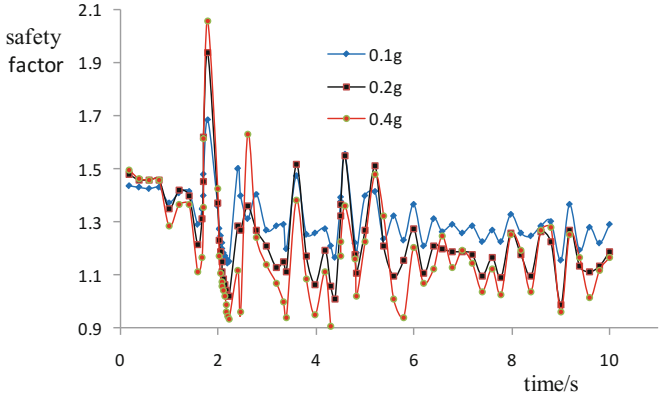

Fig. 6. The time-histories chart of the slope safety factor (7°, a_{max} = 0.1 g)

Table 1. Safety coefficient and permanent deformation under earthquake load

Earthquake intensity	a_{max}	Permanent deformation/mm	k_{min}	k<1.0 occurrence number	Rainfall infiltration depth/m
7°	0.1 g	54.4	1.147	0	6.95
8°	0.2 g	114	0.989	1	7.95
9°	0.4 g	202	0.907	11	8.97

for the number of occurrences of 11 times, under 9° seismic load is not stable. Relative to the horizontal seismic wave has little effect on vertical seismic wave on the slope, considering the influence of the level seismic wave only.

4 The Numerical Analysis of Slope Under the Coupling Action of Earthquake and Rainfall

The numerical simulation analysis result under earthquake loading is input to Seep module of software in order to analyze the change of pore water pressure and seepage field in the process of rainfall after the earthquake, the slope stability analysis model correspondent with seepage field is set up, and then import the GeoStudio software limit equilibrium calculation module for stability analysis.

Having the following hypothesis: if k_{min} equal to 1.0 then the software will continue the calculation; without considering moisture transpiration when rainfall infiltrate, the long computing time is used to weaken the effect for the calculation model antecedent precipitation. When we calculate with K equal to 1.0 used as limit analysis, and the slope threshold k in design of actual engineering can prevail according to code.

4.1 The Seepage Field Calculation and Analysis Under Coupling Action

Solution of rainfall infiltration: Rainfall intensity for 8.68e-007 m/s, duration of 3 days, computing time for 10 days after the rain stopped, the total computation time 13 days, 7° (a_{max} = 0.1 g), for example. Rainfall duration 3 days after the earthquake in the process of rainfall infiltration, pour water pressure distribution of the slope contour map shown in Fig. 7, the pore water pressure of A cross section of along with the elevation changes as shown in Fig. 8, the pore water pressure can create in the rain rises to the stable value after 25 h, and then remain stable value until the rain stops. Rainfall infiltration volume moisture content contour map as shown in Fig. 9, slope rainfall infiltration volume moisture content variation with time is shown in Fig. 10.

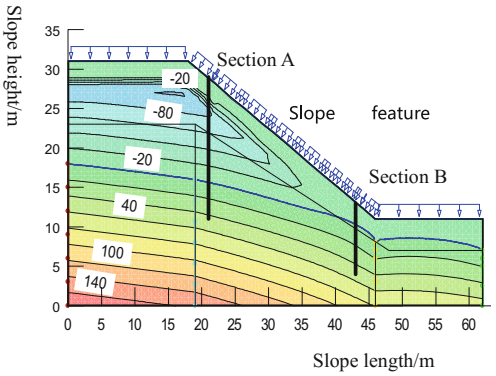

Fig. 7. Pore water pressure contour map

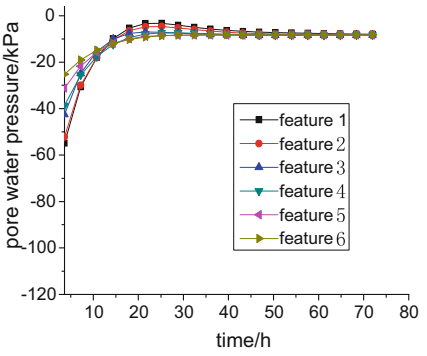

Fig. 8. Pore water pressure variation with time

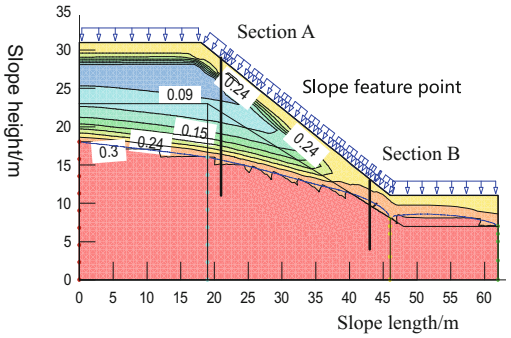

Fig. 9. Volume moisture content contour map

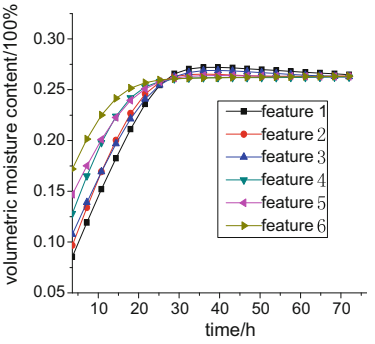

Fig. 10. Volume moisture content variation with time

Volumetric moisture content after rainfall 30 h. Every point up to stable value 0.275 and stay the same until the end of the rain, and then it will start decline along time, soil slope surface do not appear transient saturated zone during the process of

Table 2. Slope rainfall infiltration depth under different working condition

Working condition	7°	8°	9°	A single rainfall effect maximum infiltration depth
Rainfall infiltration depth/m	6.95	7.95	8.97	5

rainfall, namely the volumetric moisture content in the process of rainfall has been less than 0.3.

Rainfall infiltration depth under different earthquake intensity as shown in Table 2, it can be seen from Table 2, after the earthquake rainfall infiltration depth is much larger than single rainfall effect,and increases with the increase of the intensity of seismic load. The rain infiltration depth is even reaching 8.97 m under 9°.

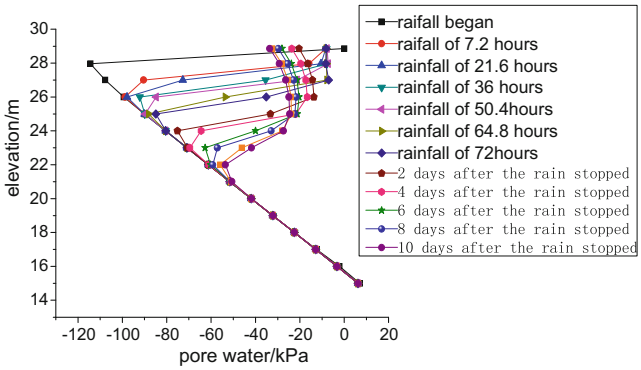

Fig. 11. Pore water pressure variation of rainfall infiltration with altitude in section A

The corresponding time about 13 days pore water pressure and moisture content change rule along with the elevation of A cross section, respectively as shown in Figs. 11 and 12. From Fig. 11 shows that a cross section in the slope area is far from ground water, so the negative pore water pressure of soil is bigger, the surface layer of soil mass affected by rainfall, along with the increase of slope deep influence degree is reduced, until we don't change. The influencing depth of the pore water pressure of slope by rainfall scope is 7 m. From Fig. 12, the surface layer of soil affected by rainfall moisture content change is bigger, along with the increase of slope deep influence degree is reduced until it don't change. Affected depth by rainfall range is 7 m.

From the above analysis shows that after the earthquake, the process of rainfall infiltration of slope is not in the transient saturated zone, rainwater infiltration depth is greater than the single rainfall, the main reason is that the rain infiltration is affected by the previous seismic action, slope soil mass disturbance under seismic loads, slope surface development, there is a lot of cracks caused by the seismic vibration load, earthquake shaking force and excess pore water pressure cause a permanent deformation of the slope soil mass, as a result, the slope soil mass permeability increase

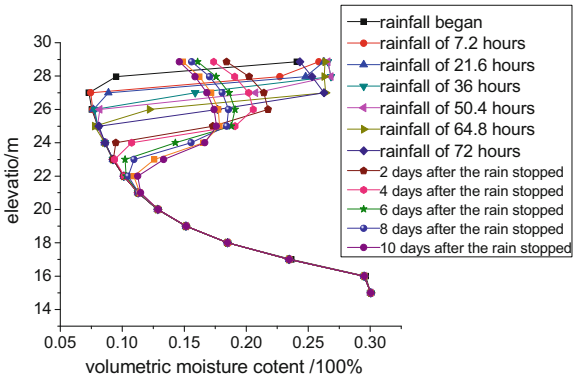

Fig. 12. Moisture content variation graph with elevation in section A

greatly, late in the process of slope rainfall infiltration velocity increases, the rain infiltration of rainwater will not gather on the surface of slope to form the transient saturated zone, but along the fissure water infiltration into the slope soil mass. Thus result in rainfall slope does not appear in the process of transient saturated zone, rainwater infiltration depth was widespread phenomenon.

4.2 The Slope Stability Analysis Under the Coupling Action of Earthquake and Rainfall

To analyze the changing process of the slope stability under three vibration load and the coupling action of seismic and rainfall by the limit equilibrium method, slope safety factor k graph is shown in Fig. 13. Safety factor decrease continuously along with long- lasting rainfall, at the end of the rain, it will decrease slowly in a certain period of time, then increase again with the dissipation of pore water. The four kinds of method such as M-P, Bishop, Ordinary and Yanbu method are used to calculate the stability of the slope, except M-P and Bishop method to calculate the safety factor is greater than 1

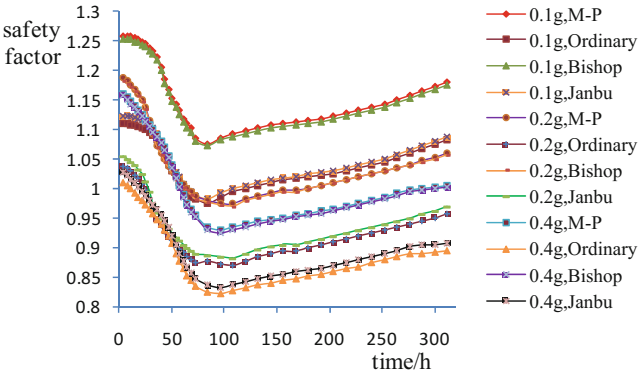

Fig. 13. Stability safety coefficient variation of slope

Table 3. The stability safety coefficient under coupling action of different earthquake intensity and rainfall (Morgenstern - Price method)

Seismic intensity	Natural state k	After the earthquake k_{min}	The coupling earthquake and rainfall k_{min}	k_{min} lower amplitude
$7^o(a_{max}$ = 0.1 g)	1.454	1.259	1.061	39.3%
$8^o(a_{max}$ = 0.2 g)	1.447	1.187	0.976	47.1%
$9^o(a_{max}$ = 0.4 g)	1.435	1.161	0.929	50.6%

when the earthquake intensity is 7°, the rest of the three kinds of seismic load and coupling action of rainfall and earthquake safety factor of slope is less than the critical stability safety factor 1.0, the model slope is in unstable state. The safety factors under three earthquake load change as shown in Table 3.

As can be seen from Table 3, under the coupling action of earthquake and rainfall, safety coefficient k_{min} is 1.061 when the seismic intensity is 7°, close to the critical value 1, there may be lost stability; instability and failure of slope will appear when these two seismic loads appeared again after the rain, because the k_{min} are 0.976, 0.929 under seismic intensity 8, 9°. When earthquake and rainfall are the combined action, the slope safety factor will show significant decline, the safety factor k_{min} lower amplitude is up to 50.6% under seismic intensity 9°.

5 Conclusions

The slope permanent deformation is caused under the action of earthquake force, there is a lot of cracks appears in slope mass, namely microstructure has damage, integrity is reduced, the slope is destroyed in certain extent, soil mass quality and mechanical properties are getting weak, while c and φ is reduced, the slope structure damage after earthquake is also getting bigger and the strength of slope decrease sharply. The appearance of fracture on slope increase its permeability, along with infiltration of rainfall in the late stage, the shear strength of rock and soil mass can reduce more, the safety factor of slope will greatly reduce, this will result in the final slope failure. That means that the coupled action of earthquake and rainfall are more likely to trigger the occurrence of landslides than the single rainfall or seismic action, hence the earthquake disaster prevention and control of earthquake after the rain should focus on prevention and attention. The prediction and prevention of landslide disaster has very important significance.

References

1. Keefer D (1984) Landslides caused by earthquakes. Geol Soc Am Bull 95:406–421
2. Keefer D (2000) Statistical analysis of all earthquake-induced landslide distribution: the 1989 Lama Prieta, California event. Eng Geol 58:231–249

3. Huang R, Li W (2008) Research on development and distribution rules of geohazards induced by Wenchuan earthquake on 12th May. Chin J Rock Mech Eng 27(12):2585–2592
4. Hu M, Wang R, Zhang P (2001) Primary research on the effect of rainfall on landslide-take the slope piled by old landslide in Jiangjiagou valley as example. Chin J Geotech Eng 23 (4):454–457
5. Oh WT, Vanapalli SK (2010) Influence of rain infiltration on the stability of compacted soil slopes. Comput Geotech 37(5):649–657
6. Zhang J, Meng F, Yang H et al (2012) Analysis on the saturated-unsaturated seepage and stability of an accumulation slope under rainfall infiltration. Saf Environ Eng 19(2):4–8
7. Lin CW, Liu SH, Lee SY et al (2006) Impacts on the Chi-Chi earthquake on subsequent rain-induced land-slides in central Taiwan. Eng Geol 86(2):87–101
8. Qi X, Tang C, Chen Z et al (2012) Coupling analysis of control factors between earthquake induced landslides and subsequent rainfall-induced landslides in epicenter area of Wenchuan earthquake. J Eng Geol 20(4):522–531
9. Gong WJ, Li MY, Wu Z (2012) Stability analysis of landslide under coupling action of earthquake and rainfall—taking the No. III landslide of Xihe County, Gansu Province as an example. Northwest Seismol J 34(2):161–166
10. Sun J, Wang L, Long P, et al (2011) An assessment method for regional susceptibility of landslides under coupling condition of earthquake and rainfall. Chin J Rock Mech Eng 30 (4):752–760

Use of Forecast Models for the Interpretation of the Stability of Earthworks

Moustafa Hamze-Guilart[1(✉)], Maria Eugenia Gimenez Boscov[1], Lineu Azuaga Ayres da Silva[2], and Guillermo Ruperto Martin-Cortés[2]

[1] Structures and Geotechnical Engineering Department, Polytechnic School, University of Sao Paulo, São Paulo, Brazil
moustafa@alumni.usp.br
[2] Mining Petroleum Engineering Department, Polytechnic School, University of São Paulo, São Paulo, Brazil

Abstract. Stability forecast models for earthworks are based on the transfer function modeling of two-time series (Xt and Yt) of field variables obtained by monitoring. The time series obtained in the geotechnical instrumentation monitoring of civil works can be considered as an atypical time series, since it usually contains missing and lagged observations, requiring regularization as continuous series for modelling. This paper presents concepts related to inferential prediction models and the results of predictive models of geotechnical behaviour obtained for a tunnel of the São Paulo Rodoanel Highway from data of surface settlement, depth settlement and water levels. Based on these results, considerations are raised for the utilization of forecast models in geotechnical instrumentation monitoring of mining tailings dams.

Keywords: Tunnel · Geotechnical instrumentation · Monitoring
Time series · Stability forecast models

1 Introduction

Times series are used for the development of forecast models. A time series is a collection of observations made sequentially over time, so that the order of the data is fundamental. In the case of monitoring data, the neighbouring observations are dependent, and analysing and modelling these dependencies are important steps of the process. Analysis of time series involve two stages: the first is to know the structure that generated the series, based on the self-correlation function model. The second, to predict future values of time series, is based on the mathematical model of transfer function. This article presents the theoretical basis of prediction models and shows an application for the interpretation of time series of monitoring data of three tunnel, from the self-correlation previous studies and to the expression that characterizes the forecast models.

© Springer Nature Singapore Pte Ltd. 2019
L. Zhan et al. (Eds.): ICEG 2018, ESE, pp. 507–514, 2019.
https://doi.org/10.1007/978-981-13-2227-3_62

2 Conceptualization

The forecast model is characterized by the expression:

$$Y_t = C + B_0X_t + B_1X_{(t-1)} + B_2X_{(t-2)} + \ldots + B_nX_{(t-n)} + \varepsilon \quad (1)$$

Y, X	modelled variables
t	time
B_0, X_t	terms related to instantaneous variables correlation
B_n X_{t-n}	terms related to lagged correlation
n	lack of cross-correlation
ε	fitted error of the model

Variables X and Y are composed of time series, that is, by many observations made over time in an observation frame. Forecast models are obtained by applying the transfer function to the two-time series.

A dynamic system is characterized by a series of input X_t, a series of output Y_t and a transfer function v_t [5]. Figure 1 illustrates a dynamic system.

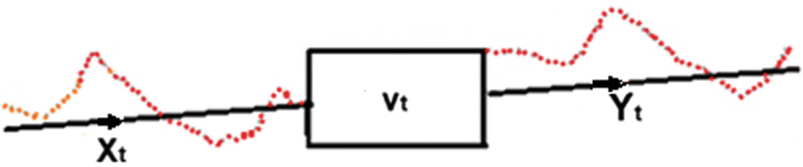

Fig. 1. Dynamic system [1]

To control a series of output Y_t is to approximate it to a desired value, this is achieved by conveniently fitting the input series X_t, what is necessary due to the disturbances that affect a dynamic system [5].

The linear filter model concept assumes being generated by a linear system, which input is white noise, where the input series is denoted as a_t, the output as z_t and the transfer function as Ψ(B) [5].

The modelling of the transfer function is shown, schematically, in Fig. 2.

First, series X_t and Y_t, which will be called x_t and y_t, respectively, are to be made stationary. Then, the x_t series must be pre-bleached until its residues become white noises. A series is considered pre-bleached when all lags fall within the confidence interval.

This white noise is denoted as a_{xi}, as shown in Fig. 2. Likewise, one must pre-bleach and filter y_t. To be filteres, y_t series is used as the a_{xt} (pre-bleached) input series. The output series is denoted by the residues a and t obtained by filtration.

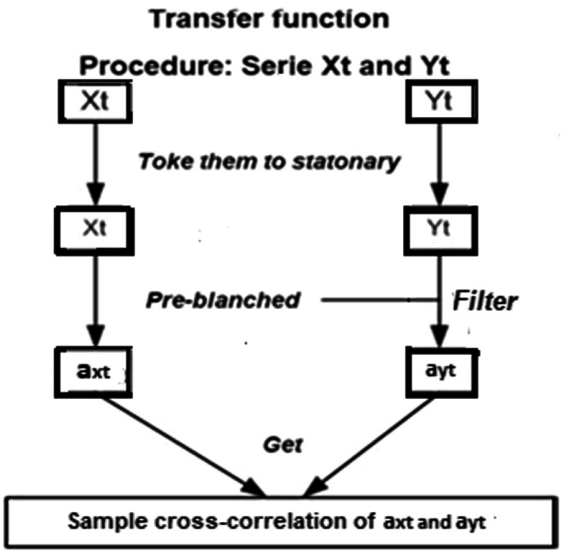

Fig. 2. Transfer function modeling [3]

3 Case Study

The construction of the tunnels for Sao Paulo Rodoanel Highway is shown in Fig. 3: on the left side the outer track and on the right the inner track, both under construction. The construction scheme and progress in different stages of both tunnels are illustrated in Fig. 4: initially the side tunnels are built, with their advances out of phase in time. With the progress of the excavation of the side tunnels, the third construction stage corresponding to the central tunnel begins. Tunnel 2 of the external track the focus of the case study.

Fig. 3. External and internal tracks of "São Paulo Rodoanel Highway" [2]

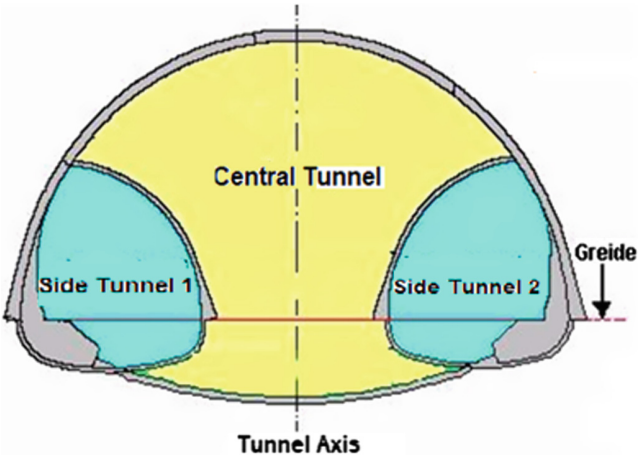

Fig. 4. Staged construction of tunnels of the "São Paulo Rodoanel Highway" [2]

3.1 Application of the Transfer Function for the Modelling of Tunnel 2 of the External Track of Sao Paulo Rodoanel Highway

"A time series is a set of numerical data obtained during regular periods over time" [4]. The time series obtained in monitoring by geotechnical instrumentation can be considered as atypical time series, since it contain lost observations, irregular intervals and outdated series, it is necessary to estimate these values to analyse time series [6].

Therefore, monitoring data by geotechnical instrumentation do not meet the requirements of continuous time series [5], so it was necessary to regulate the series, in this case, linear interpolation was used to generate daily observations and from there, weekly averages were taken from Saturdays.

Figure 5 shows the original series and the regularized series of the variable water under pressure of reference piezometer PZN11B2 in Sect. 1 in side tunnel 2: the original series given in meters per day and regularized in meters per week.

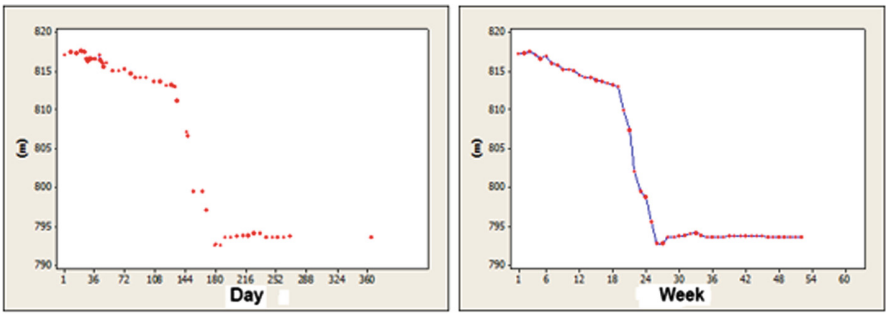

Fig. 5. Original time series and regularized series [3]

The next step is to make the series stationary, what was achieved by software E-Views. It should be noted that all these time series tended to become stationary with a simple difference.

In Fig. 6, which shows the autocorrelation of the PZN11B2 series difference, the limited space in red color is called the confidence interval, established in the statistical program, E-Views. As can be seen in Fig. 6(a), lag 1 is outside the confidence interval and the pre-lagging of x_t will consist of making lag 1 within the confidence interval. Figure 6(b) shows that x_t is white noise and all lags are within the confidence interval, so the series is pre-bleached.

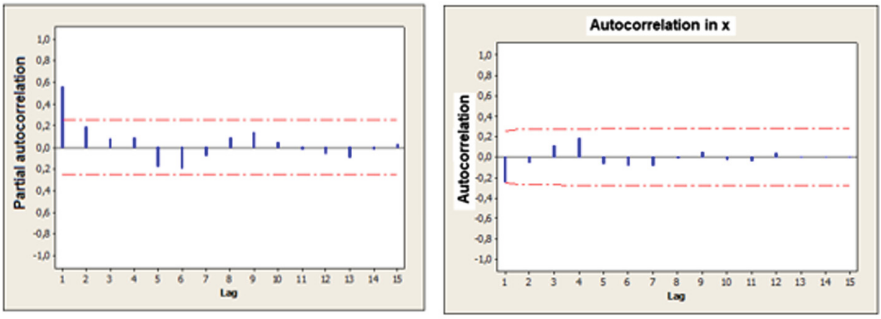

(a) (b)

Fig. 6. Pre-bleaching of the X_t series [3]

Then, the pre-bleaching of x_t will be: (2)

$$X_t = 0.1372 + 0.6392\, X_{(t-1)} + \varepsilon \tag{2}$$

It should be noted that the resulting model of pre-bleached x_t is expressed with the term of lag 1, what does not always happen. Consider the following case: when bleaching the first lag, the model could not achieve pre-bleaching because, for instance, the third lag could be out of the standard, i.e. above the confidence interval. In this case, after the pre-bleaching, the resulting model of x_t would be in function of lags one and three, as shown in expression (3).

$$X_t = C + B_1 X_{(t-1)} + B_3 X_{(t-3)} + \epsilon \tag{3}$$

After pre-bleaching both series, the prediction model is searched. Expression 4 exemplifies the model of the series MS11B2 (surface settlement) and PZN11B2 (water under pressure). Therefore, the series MS11B2 can be predicted using the observation of surface settlement from the previous week and the series PZN11B2 observations lagged at 1, 3, and 4 weeks.

$$Y_t = Y_{(t-1)} - 0.000132 + 0.00026\,X_{(t-1)} - 0.000085X_{(t-3)} - 0.000111\,AX_{(t-4)} \quad (4)$$

Expression 5 relates the model of the series TS4B (deep settlement) and MS4A1 (surface settlement). Therefore, the series TS4B can be predicted using its own observation from the previous week and the present observation of the series MS4A1 lagged at 1, 2 and 5 weeks.

$$Y_t = Y_{(t-1)} + 0.9639X_t - 0.3960\,X_{(t-1)} + 0.79368\,X_{(t-2)} - 0.2936X_{(t-5)} \quad (5)$$

As a trend the models obtained in the external tunnel, the terms related to the outdated correlations B_nX_{tn} prevail. The outdated correlations oscillate in a range of expressions 1 to 5. The results indicate that the structure of these models is a consequence of the constructive method, constituted by the phased opening of the side tunnels and the central tunnel, where the stresses have been relaxed with time, so the terms B_nX_{tn} behave as shock absorbers of movement.

3.2 Comparison with Results from Other Tunnels in Sao Paulo Metropolitan Area

These models obtained for Tunnel 2 of the external track of Sao Paulo Rodoanel Highway are compared to those obtained for two other tunnels built in Sao Paulo City.

The models of the Rebouças tunnel, in the terms $B_nX_{t\text{-}n}$, resulted in extreme correlations (5, 6, 7), for example; the expression 6 shows times series 6CC (surface settlement) X 6CB (surface settlement).

$$Y_t = Y_{(t-1)} + 0.3912X_{(t-2)} - 0.5965X_{(t-4)} + 0.3091X_{(t-5)} - 0.2574X_{(t-7)} \quad (6)$$

These models are characterized by changes in the geo-mechanical characteristics of the massif, by the application of cement injections to obtain a solidification of the massif. Because of that, the terms B_nX_{tn} behave as movement retarders.

The resulting models of the union tunnel of the Higienópolis Station are characterized by the terms of the instantaneous correlation B_0X_t for example; the expression 7 shows of times series 2TS1H (deep settlement) X 2MS3H (surface settlement).

$$Y_t = Y_{(t-1)} + 1.18697X_t \quad (7)$$

This happens because that tunnel, with a large section, was built in full section, where large displacements were developed consecutively over time. Therefore, the isolated term B_0X_t constitutes a movement accelerator.

4 Comments on the Utilization of Forecast Models for Tailings Dams

Time series forecasting modelling is promising to the interp retation and prediction of stability of mining tailings dams by means of geotechnical monitoring data, through variables such as displacements, normal water levels and water under pressure.

Considering the constructive characteristics and the nonhomogeneous consolidation of the tailings, interpretations of the physical behaviour of the mining tailings dams can be made with these models. From these interpretations, it would be possible to establish risk plans by sectors of the dam, and to take emergency or corrective measures to avoid accidents.

In the tailings densification stage, the structure of the models is supposed to be at a level between the access tunnel models of the Higienópolis Station and the Rodoanel Hihgway tunnel, that is, from an acceleration behaviour of the movement, in the initial stage of the consolidation, to a shock absorbers behaviour of the movement. In the case of deactivated dams, the behaviour of the models could be stable, as in the Rodoanel and Rebouças tunnels, or intermediate, as in the Rodoanel tunnel, between the tailings densification stage and the deactivation.

Considering the nonhomogeneous nature of the tailings, correlations between the geotechnical behaviour of the monitored variables and the physical properties of the tailings are necessary, such as grading curve, consistency limits, moisture content and permeability. Tailings samples should be collected in different parts of the dams, in different stages of densification, and their physical properties should be related to the results of the monitored variables and the resulting models.

5 Conclusions

The forecast models used to study the stability of the rocky and earthy masses subjected to underground excavations and tailings dams can also be used for the study of stability in other engineering fields where measurements of geotechnical instrumentation are carried out over time.

References

Box GEP, Jenkins GM, Reinsel G (1994) Time series analysis forecasting and control, 3rd edn. Prentice-Hall do Brasil, Ltda., Rio de Janeiro, p 598p

Hamze-Guilart M (2002) Avaliação de técnicas de instrumentação para o monitoramento de deformações nas escavações subterrâneas. Dissertação (Mestrado) – Escola Politécnica, Universidade de São Paulo, São Paulo, 155p

Hamze-Guilart M (2007) Metodologia para a interpretação do monitoramento de escavações subterrâneas. (Tese de Doutorado) – Escola Politécnica, Universidade de São Paulo, São Paulo, 158p. http://www.teses.usp.br/teses/disponiveis/3/3134/tde-14012008-164045/

Levine DM, Berenson ML, Stephan D (2000) Previsão com séries temporais para dados anuais. Estatística teoria e aplicações. Livros Técnicos e Científicos S.A. Rio de Janeiro, pp 629–678
Morettin PA, Toloi CMC (2004) Análise de séries temporais. Edgard Blucher Lyda, São Paulo, 535p
Pereira BB (1984) Séries temporais multivariadas. In: VI Simpósio Nacional de Probabilidade e Estatística, Rio de Janeiro, 218p

Enhanced Sustainable Soils: A Review

G. Di Emidio[1(✉)], J. Meeusen[1], D. Snoeck[2], and R. D. Verastegui Flores[3]

[1] Laboratory of Geotechnics, Ghent University, Technologiep. 905, 9052 Zwijnaarde, Belgium
gemmina.diemidio@gmail.com
[2] SLW Foundations, Waalstraat 230, 9870 Zulte, Belgium
[3] MOW Geotechniek, Technologiepark 905, 9052 Zwijnaarde, Belgium

Abstract. Issues associated with the production of waste and their disposal continue to be a major preoccupation for governments, public and private organizations and the general community around the world. This paper includes the current trends on the possible reuse of various waste streams for geotechnical and geo-environmental applications. After a general overview, specific examples will be described and new results on amended recycled sediments and amended soils will be presented. Examples of this sustainable concept to be further promisingly developed include: (1) the possible use of waste heat for the production of new amended raw materials, (2) the reuse of dredged sediments for various geotechnical and geo-environmental applications, (3) the use of various recycled soil amendments for mechanical and hydraulic enhancement techniques.

Keywords: Waste streams · Sustainable design · Reuse of waste
Ground improvement · Enhanced clays

1 Introduction

In soil engineering applications, many soil layers have unsatisfying hydraulic and mechanical properties. Nowadays, traditional materials are still used to improve these properties, which are energy consuming and in general relatively expensive. On top of that, the amount of deposited waste materials is accumulating yearly. This contradiction emphasizes the need for a more sustainable environment, which also implies to reuse waste in soil engineering applications.

Ideally, the aim for example would be of having bentonite slurries with performant hydraulic properties in cut-off walls which controls contaminant migration and groundwater flow. However, clayey soils lose their hydraulic performance in contact with electrolytes, which occurs in contact with the contaminants that they should confine. To avoid deterioration of the bentonite properties, the HYPER clay technology [1], may be applied to improve the efficiency of clay liners as encapsulation techniques for landfill disposals. This technology involves the modification of bentonite clay with an anionic carboxymethyl cellulose (CMC) polymer, and results into advanced hydraulic properties of the clay. However, in terms of sustainable development, the

© Springer Nature Singapore Pte Ltd. 2019
L. Zhan et al. (Eds.): ICEG 2018, ESE, pp. 515–522, 2019.
https://doi.org/10.1007/978-981-13-2227-3_63

production of polymers and bentonite has an environmental impact, which suggests the use of alternative suitable materials.

With respect to mechanical soil properties, in geotechnics the bearing capacity and erosion control of soils is of utter importance with respect to foundation design and thus the stability of civil engineering structures. Soil having poor mechanical properties can result into excessive settlements such that the serviceability limit state of structures can be exceeded, which eventually can lead to failure. However, soft soil layers are often encountered in construction projects such that ground improvement needs to be fulfilled. For this reason the native soil is often mixed with binders, to improve the strength characteristics. However, also the fabrication of binders is quite expensive, requires energy for manufacturing and causes significant carbon dioxide emissions.

Regarding soft soil, enormous amounts of sediments emerge from dredging works which are necessary to create, maintain and improve waterways. In the Port of Antwerp yearly about 450,000 tonnes (dry matter) of soil is dredged and for the whole of Europe about 300 million tonnes of sediments are dredged each year [2]. To overcome environmental and economic issues regarding soil disposal, a persevering waste management strategy is necessary in order to reuse dredged sediments in various soil engineering applications.

Besides dredged sediments, considering waste materials in a broader perspective, all kinds of waste materials appear either from material-related streams (including metal, glass, paper and cardboard, wood, rubber, textiles, bio-waste) either from product-related streams (including packaging, electronic waste, batteries and accumulators, end-of-life vehicles, mining, construction and demolition waste) [3].

Because of the current in-depth understanding of many soil engineering applications – such as for hydraulic barriers and ground improvement techniques - there are opportunities to reuse various waste materials as an alternative for traditional materials. In order to tackle problems of accumulating deposited waste materials, many studies have already attempted to reuse waste materials in various soil engineering applications. Furthermore, utilisation of waste materials is also becoming increasingly popular by saving of natural sources and energy as well as reducing air water pollutants and greenhouse gases. This paper describes the potential reuse of some promising waste materials in order to improve soil engineering properties for geotechnical and geoenvironmental purposes.

2 Dredged Sediments

To keep waterways navigable or even to create new waterways, dredging works are executed which lead to enormous amounts of dredged sediments. In order to avoid excessive disposal areas, persevering waste management is of utter importance. As a result, many different studies have been conducted to reuse dredged sediments in various soil applications.

In this regard, the Maryland Department of the Environment established a guidance document which describes innovative solutions to reuse dredged sediments. First the use of dredged sediments as a daily, intermediate or final cover as an alternative to

traditional earthen material in landfills is suggested. Second the reuse of dredged sediments in terms of soil and fill material is proposed [4].

Regarding the first application about landfills, Di Emidio et al. [5] evaluated the possible reuse of dredged sediments for hydraulic barriers in the field of geo-environmental engineering.

With respect to the second application about fill materials, Crawford [6] examined the beneficial reuse of dredged sediments for vertical cut-off wall backfill materials. For this purpose an appropriate mix of sediment and bentonite was searched. The results indicated that a suitable moisture content and viscosity of the dredged sediments can be found such that these materials can be usable in the mix design. Furthermore, it was concluded that an increased bentonite content leads to a decreased hydraulic conductivity. Finally, it was suggested that with an appropriate mix design, dredged sediments can serve as an effective inhibitor to the flow of groundwater [6].

Coming back to the first application, the presence of heavy metals in soil is a serious problem since human health can be endangered in case of direct exposure or via food chains. Among others, covers and cut-off walls can be used to isolate waste disposals and contaminated soils. These barriers have to resist advection and diffusion of the possible leaching heavy metals.

Di Emidio et al. [5, 21] reported about adsorption of lead (Pb^{2+}) and copper (Cu^{2+}) on kaolinite and dredged sediments treated with the HYPER clay technique as described in [1]. In that study kaolinite (K) and dredged sediments (DS) were treated with 2% anionic sodium CMC polymer. Batch sorption tests indicated that the treated material (K2 and DS2) adsorbed generally more heavy metals compared to the untreated material, for both kaolinite and dredged sediments. Comparing treated and untreated dredged sediments, it was observed that the adsorption of both lead and copper was higher for the dredged sediments than for kaolinite, likely due to the presence of montmorillonite in the dredged sediments.

The authors [5, 21] reported this difference in behaviour as a result of the larger negative surface and larger specific area for the dredged sediments compared to the kaolin clay. Specifically this was indicated by a larger CEC, more exchangeable cations and a higher content of 2:1 phyllosilicates. It was shown that the adsorption of lead was higher than the adsorption of copper for both treated and untreated materials. The slight decrease in adsorption at higher concentrations was reported to be a result of a decrease in pH. In case of lower pH values, more protons (H^+) are present which results into a competitive sorption between these protons and the metal cations [5, 21].

3 Soil Stabilisation Using Shredded Tyres

The amount of scrap tires is being accumulated yearly in large volumes causing an increasing threat for the environment. Specifically, yearly an estimated amount of 13.5 million tonnes of scrap tires are disposed worldwide. In terms of sustainable development and in order to avoid negative effects of deposition, there is a great interest in reusing these solid wastes. Up to now scrap tires have already proven their employment among others in artificial reefs, breakwaters and soil erosion control mats. Several studies also focussed on the use of scrap tires in geotechnical applications, especially as

embankment material. Tires can be used as lightweight material either in the form of powder, chips, shredded and as a whole [7–9].

As a summary, mainly the following opportunities regarding waste tires are discussed in literature:

- Shredded tire is a low-cost abundant material and is effective as a fill material in soil stabilisation because of their light-weight properties. Therefore, tire waste can be used to construct embankments on weak and compressible subsoils.
- Shredded tires will improve drainage below pavements and roads or prevent the underlying soil from freezing and will as such extend the lifetime of the construction;
- Shredded tires may be used for improving the load bearing capacity of soil by using it as a reinforcement material. To this regard, Singh J. reported an increase of 8% in unconfined compressive strength (UCS) for a pavement subgrade soil using shredded rubber tires (size of 10 × 20 mm);
- The use of waste tires as a fill material results in a more economical solution, compared to other alternatives. [7–9].

4 Soil Reinforcement Using Carpet Waste Fibres

The textile industry, which among other includes the carpet industry, generates 4 to 6 million tonnes of carpet waste per year worldwide, that results either from post-consumer use either from the industrial sector. In order to reduce the amount of deposited carpet waste material, many studies have been conducted in order to reuse carpet fibres as soil reinforcement. The principle of soil reinforcement in terms of geotextile fabrics is a well-established technique for soils having low tensile and shear strength, and as such provides opportunities to the possible reuse of carpet fibres [7].

Soil reinforcement with randomly distributed fibres aims to increase among others the internal cohesion of the soil. Studies have also proven that fibre reinforcement can improve the shear strength, compressive strength, bearing strength and the elastic modulus of soil. Therefore, a dosage rate of 0.2 to 2% by mass fibres were added to silt, clay, sand, or lime and cement stabilised soil in a research of Wang. These improvements appear because the fibres act as tensile reinforcing membranes in the soil. In fact the fibres do have a larger strength and stiffness compared to the soil, and can resist deformations because of the presence of shear stresses resulting from tensile strains through fibre/soil frictional interactions. Because of the addition of the fibres, the overall failure surface is larger and non-planar as well as the failure load and corresponding energy. In case the fibres are stretched because of a loading condition, they still provide resistance such that the post-peak strength retention is also increased, which indicates a more ductile behaviour [10].

Murray et al. evaluated the possible reuse of carpet waste fibres in a soil that was classified as a sandy silt. In this laboratory study various dosage rates (1, 2 and 3%) of carpet fibres were added to the soil. Tri-axial tests pointed out that for 3% by mass of carpet fibres, the peak stress increased by 157% at 34.5 kPa confining stress and by 204% at 69.0 kPa confinement. It was concluded that the peak stress increases by

increasing amount of carpet fibres. Within this study it was also reported that in case of soil applications, almost all types of carpet are suitable and therefore sorting is not necessary. This is clearly not valid in case of concrete, for which durability properties have to be considered [11].

Anyiko et al. studied the use of carpet fibres in a sandy soil, having lengths of 7.5, 15 and 30 mm in dosages of 0.1 to 0.5%, by means of direct shear tests. It was concluded that the soil cohesion increases but no significant effects regarding the friction angle were noticed. The soil cohesion increased by increasing length and fibre concentration, up to 27% for fibres with 30 mm length at a dosage of 0.5%. As a result, the soil strength and bearing capacity could be positively influenced by the presence of carpet fibres [12].

Ghiassian et al. reported about the reuse of carpet fibres in fine sand. In this study carpet strips having an approximately 5 × 5 mm square cross-section and various length of 5, 15, 25, 35, 45 mm were used, and fractions of 0.4 to 1% by mass were added. Based on drained tri-axial tests, it was demonstrated that the presence of carpet fibres led to an increased peak strength, compressive strength and ductility of the sand. Again results improved by increasing length and dosage of fibres [13].

5 The Use of Plastics in Geotechnical Engineering

5.1 Plastic Bottle Waste Material

Another worldwide concern is the recycling of plastic water bottles, which challenged the reuse of these materials into soil applications. Sivakumar et al. mixed plastic chips (12 mm long and 4 mm wide) into a sand at dosages of 0.5, 0.75 and 1.0% by dry mass of soil. Based on the results of one-dimensional consolidation and tri-axial tests, a reduced compressibility and an increased strength was observed. The latter is declared by an increase in friction and interlocking because of the soil and waste plastic interaction [14].

Luwalaga studied the addition of uniformly graded polyethylene terephthalate (PET) plastic waste flakes (ranged between 10 and 1.18 mm) to a uniformly graded sand of medium density (ranged between 1.18 and 0.075 mm), in dosages of 12.5%, 22.5% and 32.5% by mass. The sand-PET plastic composite mixture led to a lower density compared to the original unreinforced sand. This lightweight characteristic can be interpreted positively in case of fill materials. Tests pointed out that the optimum PET plastic dosage is 22.5%, which indicates that there is a limit for the amount of added waste material. Using the specified dosage, the shear strength increased with 15.3% which suggests an improved bearing capacity of the soil [15].

Similar conclusions were made in a study of Patil et al., in which plastic strips of size 1 × 1 cm were added to a very soft silty sand. For this reinforced material, tri-axial tests and direct shear tests indicated an increase in cohesion of 67% and 24%, respectively [16].

Also the possible reuse of PET plastic bottles was considered as geotechnical fill material in a study of Graettinger et al. The aim of this research was to develop a new lightweight geo-material made from PET plastic bottles, glued together in their original

post-consumer form. It was concluded that the engineered material can be used as a lightweight geotechnical fill over soft soil and behind retaining walls. Results showed that the composite material has similar properties as soft soil, which is promising regarding a future better understanding of the physical and mechanical properties of this engineering glued PET geotechnical fill material [17].

5.2 Plastic Bag Waste Material

Other materials which contribute to a high extent to the increasing amount of municipal waste are plastic shopping bags. Since the process of transforming plastic waste into raw material involves high energy consumption, various research programmes aimed to reuse this waste into geotechnical engineering applications.

In order to reduce the abundant amount of plastic bag waste, Chebet et al. studied the interaction between high-density polyethylene (HDPE) and two medium dense quartz sands with either round either angular shaped particles. The HDPE waste was added to the soil in the form of strips of distinct rectangular dimensions. Based on direct shear tests, it was found that the internal fiction angle increased by about 20%, which implies an increase in shear strength because of the addition of the plastic strips. However it was observed that, at certain thresholds, longer and wider strips led to a strength reduction. This study also proved that perforating the HDPE strips effected in an even further increased friction angle because of an increased interlocking. Finally, it was concluded that plastic strips with a length of 15 mm, strip width of 6 mm, concentration of 0.1% and perforation diameter of 2 mm resulted in the greatest improvements. Higher lengths, widths and concentrations indicated no significant improvements. Note that the friction angle on the average increased with 2° for every 1 mm increase in perforation diameter [18].

A study of Ilies tried to reuse polyethylene waste in a silty clay and compared this material to the traditional use of cement. The main conclusion resulting from this research was that an addition of 4% PET by mass resulted into notable improvements of the original soil. Compared to mixtures having the same amount of cement, the cohesion and internal friction angle of the PET added sample were 52% and 63% lower respectively [19].

Compared to the above research programmes about shredded plastics, Trudeep et al. studied the use of plastic bottle waste as an alternative for conventional geogrids. The main aim of the latter is to improve the load-settlement behaviour of soil. To this regard, soil beds consisting out of river sand at 70% relative density were prepared for which the cases of no reinforcement, reinforcement using conventional geogrid reinforcement and reinforcement using waste plastic reinforcement were examined. Compared to the unreinforced soil, the former resulted into a 22% ultimate bearing capacity increase whereas the latter led to a 15% increase. Based on this outcome, the use of waste plastic as a base material for geogrids was considered to provide opportunities. Furthermore, this study indicated a cost saving of 60% in case waste plastic is used compared to conventional materials for geogrids [20].

6 Conclusions

This paper included the current trends on the possible reuse of various waste streams for geotechnical and geo-environmental applications. After a general overview, specific examples were described and new results on recycled materials and soils were presented.

These results are promising in view of the suistainable reuse of waste products for geotechnical and geoenvironmental applications. More insights are needed to further develop and spread these concepts. Ongoing research is foreseen to investigate the possible reuse of waste recycled amendments, waste polymers and waste heat for geotechnical and geoenvironmental applications. Examples of this sustainable concept include: (1) the possible use of waste heat for the production of new amended raw materials, (2) the reuse of dredged sediments for various geotechnical and geo-environmental applications, (3) the use of various recycled soil amendments for mechanical and hydraulic enhancement techniques.

References

1. Di Emidio G (2010) Hydraulic and chemico-osmotic performance of polymer treated clays. Ghent University, Ghent
2. Snellings R et al (2016) Properties and pozzolanic reactivity of flash calcined dredged sediments. Sustainable Materials Management, VITO, Mol, Belgium
3. Bourguignon D (2015) Understanding waste streams - Treatment of specific waste. European Parliamentary Research Service
4. Maryland Department of the Environment (2017) Innovative reuse and beneficial use of dredged material - guidance document. Maryland Department of the Environment, Baltimore
5. Di Emidio G, Verastegui-Flores RD, Bezuijen A (2014) Reuse of dredged sediments for hydraulic barriers: heavy metal adsorption and hydraulic conductivity improvement through polymers. In: Proceedings of the seventh international congress on environmental engineering, 7th ICEG, ISSMGE, 10th – 14th November 2014. Australian Geotechnical Society, Melbourne
6. Crawford A (2004) Beneficial reuse of dredged sediments for vertical cut-off wall backfill material. University of Maryland, Department of Civil and Environmental Engineering, Maryland
7. Bolden J et al (2015) Utilization of recycled and waste materials in various construction applications. North Carolina A and T State University, Greensboro, North Carolina, United States
8. Umur J et al (2015) Soil stabilisation using shredded rubber type: a review. Int J Civil Struct Eng Res
9. Singh J (2017) Soil stabilisation of clayey soil using shredded rubber type. Int J Eng Res Technol (IJERT) V6(9)
10. Wang Y (2006) Utilization of recycled carpet waste fibres for reinformcent of concrete and soil. School of Polymer, Textile and Fiber Engineering, Georgia Institute of Technology, Atlanta, USA
11. Murray J et al (2000) The behavior of sandy soil reinforced with discontinuous fiber inclusions. Transp Res Rec 1714:9–17

12. Anyiko F et al (2011) Investigation of the suitability of recycled carpet fibres as a soil reinforcement material. Sampar Limited Consulting Engineers, Kampala, Uganda
13. Ghissian H et al (2004) Soil reinforcement with recycled carpet wastes. Waste Manage Res 22:108–114 ISWA
14. Sivakumar B et al (2010) Strength and compressibility response of plastic waste mixed soil. IGS Mumbai Chapter and IIT Bombay, Bangalore, India
15. Luwalaga J-G (2015) Analysing the behaviour of soil reinforced polyethylene terephthalate (PET) plastic waste. Stellenbosch University, South-Africa
16. Patil A et al (2016) Experimental review for utilisation of waste plastic bottles in soil improvement techniques. Int J Eng Res, **5**
17. Graettinger JA (2006) Recycling of plastic bottles for use as a lightweight geotechnical material. Civil and Environmental Engineering Department, University of Alabama, Tuscaloose, Alabama, USA
18. Chebet FC et al (2014) Laboratory investigation on re-using polyethylene (plastic) bag waste material for soil reinforcement in geotechnical engineering. Civil Eng Urban Plann: Int J (CiVEJ) 1(1):67
19. Ilies N-M et al (2016) Comparative study on soil stabilization with polyethylene waste materials and binders. Technical University of Cluj-Napoca, Cluj-Napoca, Romania
20. Trudeep ND et al (2017) Reuse of plastic waste in foundation soil reinforcement application. Institute of Infrastructure Technology Research and Management (IITRAM), India
21. Di Emidio G, Verastegui Flores RD, Mazzieri F, Dominijanni A (2017) Modified clays for barriers: a review. Innov Infrastr Solut 2(47)

Changes in Swelling Pressure and Permeability of Bentonite Caused by Ion Exchange of Montmorillonite

Yasutaka Watanabe(✉) and Shingo Yokoyama

Central Research Institute of Electric Power Industry,
1646 Abiko, Abiko-Shi, Chiba 270-1194, Japan
yasutaka@criepi.denken.or.jp

Abstract. Permeability tests of the compacted bentonite-sand mixture using salt solutions were carried out. Exposure of the Ca type-bentonite to NaCl or KCl solutions after fully saturation with deionized water caused ion exchange of the montmorillonite. After Ca ion exchanged to Na ion, the swelling pressure of the sample increased and the permeability decreased when the low ionic strength condition, comparing with the initial value before Na ion exchange. While, after Ca ion exchanged to K ion, increase in the swelling pressure and reduction of the permeability were insignificant. K and Na ions showed the different effect of ion exchange on the engineering properties of the bentonite.

Keywords: Bentonite · Montmorillonite · Exchangeable cation
Swelling · Permeability

1 Background

Compacted bentonite will be used as the engineered barrier in the radioactive waste disposal. It is expected that the bentonite is exposed to groundwater containing cation derived from sea water, leachate of cementatious materials and so on. Due to the chemical composition of pore fluid in the bentonite, the ion exchange of the montmorillonite will occur. The expansion property of the montmorillonite saturated by various cations has been investigated by X-ray powder diffraction (Sato et al. 1992). The compressibility of the montmorillonite has been influenced by the composition of exchangeable cation (Robinson and Allam 1998). The exchangeable cation of the montmorillonite is important in consolidation process, because osmotic effect became large when the bentonite was exposed to a salt solution (Maio 1996). Previous studies indicated that the ion exchange of the montmorillonite controls mass transport in the bentonite. Understanding of the change in permeability incident to the ion exchange of the montmorillonite is important for the evaluation of a long-term performance of the engineered barrier. Therefore, the purpose of this study is to investigate the effect of the ion exchange on the swelling pressure and the permeability of the compacted bentonite-sand mixture.

© Springer Nature Singapore Pte Ltd. 2019
L. Zhan et al. (Eds.): ICEG 2018, ESE, pp. 523–528, 2019.
https://doi.org/10.1007/978-981-13-2227-3_64

2 Sample

A bentonite (Kunibond/Kunimine Industries Co., Ltd.) with dominant exchangeable cation of Ca ion was used for the study. The amount of methylene blue adsorbed on the bentonite was 124 mmol/100 g. The montmorillonite content was 82% if the methylene blue adsorbed on the pure montmorillonite was 151 mmol/100 g (Watanabe and Yokoyama 2017). The bentonite was mixed with sand in the ratio of 3 to 7 in dry weight. The maximum and 50% diameter on grain size diagram of the sand were 2.0 mm and 0.59 mm, respectively. Water content of the material was adjusted to 13% and 17%, which were optimum water content plus/minus 2%.

3 Experimental Procedure

Permeability tests were performed on 60 mm diameter and 20 mm high soil specimens in the rigid wall permeameter. The specimen was produced using the bentonite-sand mixture by static axial loading. The dry density of the specimen was 1.81 Mg/m^3. The initial condition of the specimen is listed in Table 1. The apparatus as shown in Fig. 1 has a load cell inside to measure the swelling pressure of the material. The swelling pressure can be measured through slight deformability of the pedestal between the specimen and the load cell.

This study focused on the ion exchange of Ca-montmorillonite with K and Na ions. Considering the chemical composition of the leachate of cementatious materials, excluding the effect of alkali, 1.0 mol/L of NaCl and KCl solutions were used in the experiment, respectively.

Table 1. Initial condition of the specimen used in the permeability test and the experimental condition.

Case	CaBent-Na-dry	CaBent-Na-wet	CaBent-K-dry	CaBent-K-wet
Sample	Ca type-bentonite and sand mixture (3:7)			
Salt solution used in the permeability test	NaCl	NaCl	KCl	KCl
Water content [%]	Dry side to optimum water content	Wet side to optimum water content	Dry side to optimum water content	Wet side to optimum water content
	13.1	17.0	13.2	17.1
Degree of saturation [%]	72.8	94.2	75.8	98.0
Void ratio	0.461	0.462	0.461	0.461
Dry density [Mg/m^3]	1.810	1.807	1.810	1.809
Effective clay density [Mg/m^3]	1.029	1.025	1.029	1.027
Effective montmorillonite density [Mg/m^3]	0.903	0.900	0.903	0.902

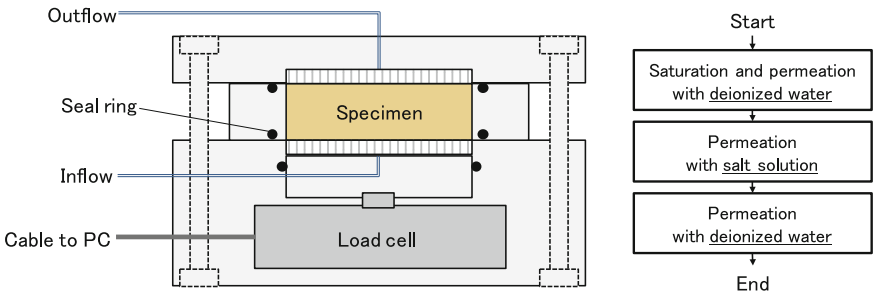

Fig. 1. Schematic image of the apparatus for the permeability test measuring swelling pressure of the compacted bentonite-sand mixture and the experimental procedure.

The specimen was initially saturated with deionized water. Fully saturation of the specimen was evaluated by the amount of adsorbed water when backpressure increased, as described by Boyle-Charles' law (Watanabe and Tanaka 2016). For the saturated specimen, the permeability and the swelling pressure were measured in steady state. Subsequently, the salt solution was passed through the specimen, and the ion concentrations of effluent solution were measured by ICP-AES. After confirming that the ion concentrations between the effluent and influent solutions were equal, the permeability and the swelling pressure had equilibrated, the deionized water was passed though again. The experiment was terminated after chemical breakthrough had been achieved.

The specimen used in the experiment was divided into three parts in the height direction, and washed by 80% alcohol. The exchangeable cation of the washed samples was determined by leaching with 1.0 mol/L-NH_4Cl solution.

4 Results and Discussion

The permeability and swelling pressure during permeation using deionized water and 1.0 mol/L NaCl and KCl solutions were shown in Figs. 2 and 3. The specimen saturated by deionized water showed the equilibrium swelling pressure, 690 to 930 kPa for 13% of initial water content and 310 to 540 kPa for 17% of initial water content. The coefficient of permeability, 1×10^{-11} to 4×10^{-11} m/s for 13% of initial water content and 2×10^{-12} to 8×10^{-12} m/s for 17% of initial water content, was obtained as initial values. Higher water content at producing specimen showed lower swelling pressure and lower permeability.

After the influent solution was exchanged to NaCl or KCl solution, the swelling pressure of the compacted bentonite decreased. However, no increase in the permeability was observed in the case of NaCl solution. In the case of KCl solution, the permeability slightly increased to twice value.

The ion concentrations of effluent solution during permeation using deionized water and 1.0 mol/L NaCl and KCl solutions were shown in Fig. 4. After permeation of 290 to 500 days, the concentrations of Na and K ion of effluent solution almost reached the

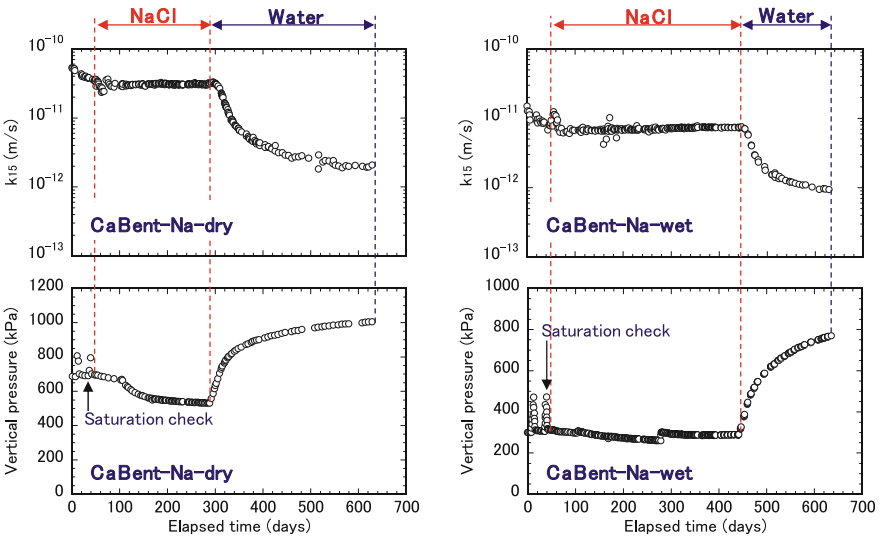

Fig. 2. Permeability and vertical pressure during permeation using deionized water and 1.0 mol/L-NaCl solution.

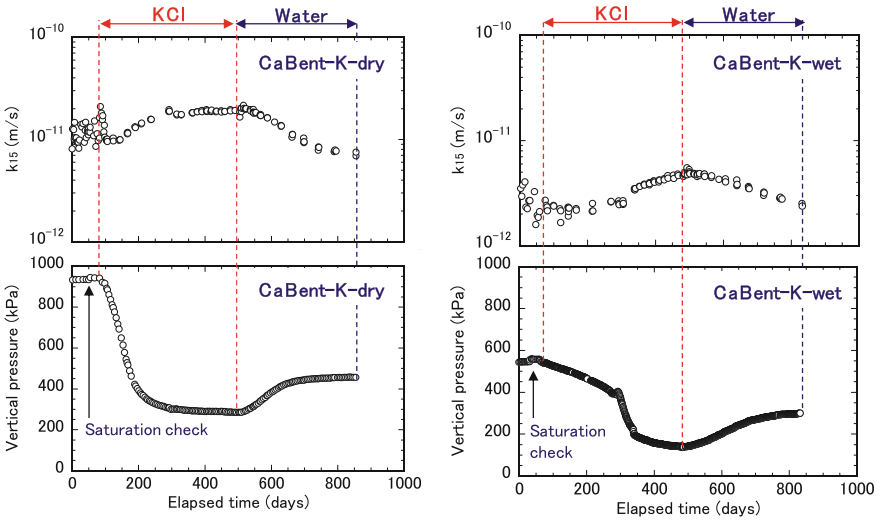

Fig. 3. Permeability and swelling pressure during permeation using deionized water and 1.0 mol/L-KCl solution.

concentration of influent solution. At that moment, the swelling pressure and the permeability became steady state. Each breakthrough curve described by the pore volume ratio showed similar curve regardless of initial water content of the specimen.

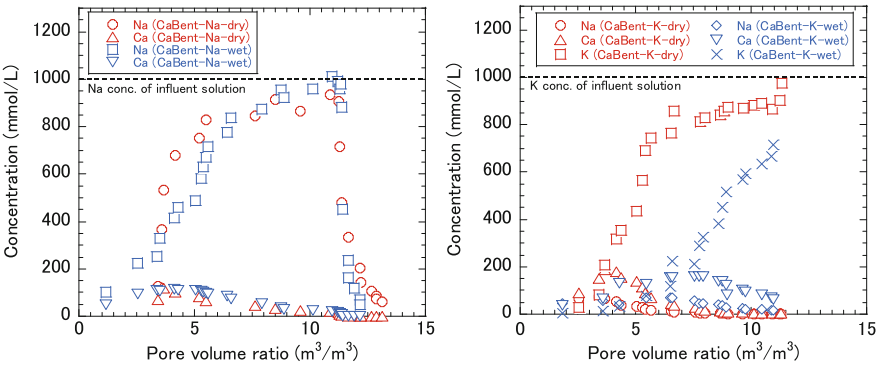

Fig. 4. Ion concentrations of effluent solution during permeation using deionized water and 1.0 mol/L of NaCl solution (left) or KCl solution (right).

Finally, the permeate solution returned to deionized water. In the case of NaCl solution, the swelling pressure gradually increased and the coefficient of permeability decreased. Note that the swelling pressure became 1.5 to 2.5 times of the initial value of the specimens, and the coefficient of permeability reduced to approximately 1×10^{-12} m/s. Although the initial value of permeability was different due to initial water content, almost same permeability was obtained after permeation of NaCl solution.

In the case of KCl solution, increase in the swelling pressure and reduction of the permeability were obvious after re-permeability of deionized water, but the change was less than that in NaCl solution. The permeability of the specimen was almost the same as the initial value just after saturation with deionized water. The swelling pressure returned to 300 kPa to 460 kPa that were 49% to 57% of the initial value, respectively.

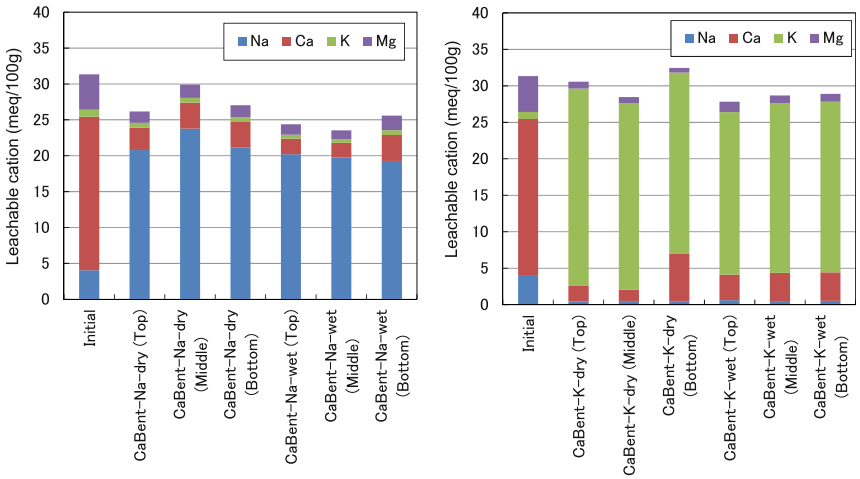

Fig. 5. Leachable cation of the specimens permeated with 1.0 mol/L of NaCl solution (left) or KCl solution (right) using 1.0 mol/L-NH_4Cl solution.

The leachable cation of the divided specimens were shown in Fig. 5. Initially, the dominant leachable cation was Ca ion. After the experiment, the leachable cation of the samples was changed by the main composition of the influent solution. Ion exchange occurred in each part of the specimens homogeneously.

It is indicated that the ion exchange reaction from Ca-montmorillonite to Na-montmorillonite due to highly Na ion concentration improved the performance of the compacted bentonite-sand mixture after the condition of pore fluid changed to low ionic strength. Meanwhile, it is suggested that the swelling property of the compacted bentonite-sand mixture would be lost by the ion exchange reaction from Ca-montmorillonite to K-montmorillonite. Although K and Na ions were monovalent, the change in the engineering properties of the compacted bentonite-sand mixture caused by the ion exchange reaction was quite different.

5 Concluding Remarks

This study investigated the effect of the ion exchange on the swelling pressure and the permeability of the compacted bentonite-sand mixture. Exposure of the Ca type-bentonite-sand mixture to NaCl or KCl solutions after fully saturation with deionized water caused ion exchange of the montmorillonite. Although K and Na ions were monovalent, the changes in the engineering properties of the compacted bentonite-sand mixture caused by the ion exchange were different. After ion exchange from Ca ion to Na ion, the increase in the swelling pressure and reduction of the permeability were observed when the deionized water permeated. While, after ion exchange from Ca ion to K ion, there was no significant recovery of the swelling pressure from the state of high ionic strength when the deionized water permeated.

References

Maio CD (1996) Exposure of bentonite to salt solution: osmotic and mechanical effects. Géotechnique 46(4):695–707

Robinson RG, Allam MM (1998) Effect of clay mineralogy on coefficient of consolidation. Clays Clay Miner 46(5):596–600

Sato T, Watanabe T, Otsuka R (1992) Effects of layer charge, charge location, and energy charge on expansion properties of dioctahedral smectites. Clays Clay Miner 40(1):103–113

Watanabe Y, Tanaka Y (2016) Permeability test for Ca-type bentonite using a rigid wall permeameter. In: Proceedings of the 60th JGS symposium on geotechnical engineering, Japan, pp 1–4

Watanabe Y, Yokoyama S (2017) Measurement of montmorillonite content of bentonite by methylene blue adsorbed. In: Proceedings of the Goldschmidt 2017, Paris

Risk Assessment for Planning the Nulear Power Plants Construction in the Areas of Karst Development

E. Stanis[1(✉)], K. Shunenkova[1], and A. Anikeev[2]

[1] Department of Geoenvironment, Peoples Frendship University of Russia, (RUDN University), Moscow, Russia
estanis@mail.ru
[2] Institute of Environmental Geoscience, RAS, Moscow, Russia

Abstract. When choosing a site for the construction of high-risk objects, it is necessary to take into account all the processes that may adversely affect the safety of the station. In connection with planning the construction of nuclear power plant in the region, where karst is the most dangerous process, several methods of assessing karst risk have been developed. Formulas, that allow to find physical damage from the destruction of territories and engineering objects by geological processes, are written in the article. It is shown that physical risk values are used as the basis for constructing a scale that allows to objectively evaluate the degree of failure hazard by two generally accepted indicators - the average diameter of karst-suffosion sinkholes and the intensity of their formation. The physical risk of land loss is the simple integral characteristic of the both probability and strength of karst impact on the technosphere objects. The evaluation of karst danger of territory of construction of object of the raised danger is given.

Keywords: Karst · Karst-suffusion sinkholes · Danger · Risk
Nuclear power plants

1 Introduction

All over the world (Regulatory Guide 2010; the Canadian Foundation Engineering Manual 2006; Eurocode 7 2006) and in the Russian Federation (Resolution No. 45 on the procedure for conducting state expertise of project documentation, and the results of engineering surveys 2009) NPPs are included in the list of especially dangerous and technically complex facilities, which might have catastrophic consequences going beyond the area of their deployment.

When choosing a site for the construction of nuclear power plants, all the conditions that can play any role in its safety should be taken into account. It is not recommended to place nuclear power plants on the territories of development of salt karst, as well as on areas with a high intensity of other kinds of karst (in the presence of surface manifestations with sinkholes larger than 20 m in diameter and/or in the presence of one sinkhole or more on an area less than or equal to 10 km^2 (Engineering site investigations for nuclear power plants construction 2012).

© Springer Nature Singapore Pte Ltd. 2019
L. Zhan et al. (Eds.): ICEG 2018, ESE, pp. 529–536, 2019.
https://doi.org/10.1007/978-981-13-2227-3_65

These studies were carried out in connection with the construction of a nuclear power plant in the Nizhny Novgorod region, at a selected site of 16 km^2 in 2009 near the Monacovo village in 2009.

The aim of the presented work is a retrospective analysis of the karst hazard of the selected site using the method of "remoteness from the nearest manifestation of karst (Savarensky and Mironov 1995) and the karst hazard scale (Anikeev 2016) to assess the possibility of their application at the preproject stage and to increase their economic efficiency.territory.

2 General Geological and Geographic Conditions of the Area and Nuclear Power Plants

The research area is located within the Volga Upland. The southern part of the research area is mainly composed of alluvial deposits of floodplain terraces and floodplains. The construction site is located on the water-glacial plain with absolute elevations of 90-130 m. The northern watershed part of the study area, which covers the interfluve of Tesi and Oka, in the geological structure is predominantly deposited by the Permian system (P): in the upper part there are mainly terrigenous rocks of the Urzhumian stage (P_2ur) and sulfate-carbonate rocks of the Kazanian stage of the Permian system (P_2kz) which are underlain by sulfate rocks (gypsum, anhydrite) of the Sakmara (P_1s) and Asselian stage (P_1a). Sakmara (P_1s) and Asselian stages (P_1a) are the regional water reservoir. Urzhum strata are covered with a thin cover of fluvioglacial and glacial deposits of the Don glacier (gIkš2) (Anikeev 2017) (Fig. 1).

The hydrographic network of the studied area refers to the basin of the lower flow of the river Oka. The climate of the region is moderately continental. However, the greatest danger on the construction site and adjacent territory is the karst. This process is developed due to the presence of a thick strata (up to 40 m) of carbonate and sulfate rocks lying in the valleys of the river. Oka and Tesha are close to the surface of the day surface, and the presence of low-mineralized aggressive waters in the alluvial stratum. Karst is considered to be a complex process that leads to failures and subsidence of the earth's surface.

As a result of the analysis of research materials conducted by the Institute of Geoecology of RAS in 2010, it was revealed that 335 surface karst forms were recorded on the territory of 16 km^2.

3 Evaluation of the Karst-Suffosion Risk of the Territory

We can assume that the risk is a probable damage that can be caused to a certain object (the recipient of danger and risk) for a certain time. From the standpoint of engineering geology, recipients of geological processes are: (1) territories, (2) buildings and structures, (3) population, (4) the environment. In this case, two independent risk groups are obtained: physical (I) and economic (II), within which we can rightly consider: (1) territorial, or land; (2) engineering, or technical; (3) social; and

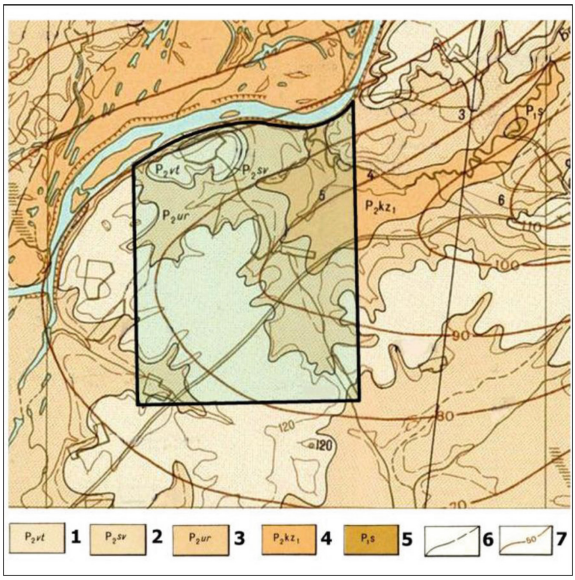

Fig. 1. Geological map of the territory with the examined site (highlighted). The deposits of Permian system: 1- Tatarian Stage, upper substage; sandstones, clays, siltstones. 2- Tatarian Stage, upper substage; clays, marls, limestones, siltstones, sandstones, dolomites. 3- Tatarian Stage, the lower substage; siltstones, clays, dolomites, marls, sandstones. 4 - Sakmarian stage; anhydrite, gypsum, dolomite, limestone. 5- Assel Stage; dolomites, limestones, gypsum. 6- The boundary of stratigraphic contact (reliable and prospective). 7- Structure countourson the base of the Tatarian stage, carried out after 10 m

(4) environmental risks, depending on from the units in which they are expressed (Anikeev 2016).

Discussing the stability of karst areas, especially to ensure the safety of such critical facilities as nuclear power plants, two issues must be considered. The first one is an assessment of the speed and intensity of the development of the karst process itself. The second is the forecast of the karst-suffosion process, the formation of sinkholes in the integumentary thickness of the karst mass.

At present, in the practice of developing karst areas methods, that indirectly assess the degree of karst danger by qualitative characterization of the conditions for the development of karst and the quantification of certain parameters of the karst process, are used. Here are some of them.

The indicator of the intensity of karst sinkholes was proposed by Makeev in 1947. It refers to the average annual number of karst sinkholes per unit area of the karst territory (Makeev 1947).

Kammerer (Kammerrer 1962) believes that the basis for the engineering evaluation of the karst areas is the accounting of the intensity of occurrence of karst sinkholes. However, he suggests finding the critical diameter of the failure, in which there is an immediate danger of destruction of structures.

To characterize the area affected by karst sinkholes, Golubeva proposed an area coefficient of karst formation (Golubeva 1953).

V.P. Kostarev raises the question of the need to search for correlations between the various karst parameters and the indicator of the intensity of karst sinkholes and their size (Kostarev 1979). In engineering geological practice, there are examples of determining such connections. (Martin 1979).

The main disadvantage of these methods is the underestimation of the possible diameters of karst sinkholes, which have a dual effect on the degree of karst danger. The diameter of the karst sinkholes is considered to be the main parameter in the design of the anti-karst strengthening of buildings and structures. Due to the fact that this parameter is not considered in the existing methods of assessing karst danger, recently there have been attempts to assess the degree of karst hazard, depending on the value of the diameter of the sinkholes.

The main indicator of the impact force of funnels in karst regions on the objects of the technosphere is their diameter (Anikeev 2016): the average (D_{av}) or the maximum (D_{max}). The main probabilistic indicator is the intensity of failure λ:

$$\lambda = \lambda^*/T = N/TS, \tag{1}$$

where N, T, S — quantity, time of formation and area of distribution of sinkholes; $\lambda*$— frequency, or the average probability of their occurrence:

$$\lambda* = N/T \tag{2}$$

A scale of karst-sufosion danger and risk was developed by the author of this work A.Anikeev, taking into account the diameter of the karst sinkholes and the intensity of failure (Fig. 2) (Anikeev 2016).

In accordance with the guidelines (Savarensky, Mironov 1995) for the construction site, we performed a statistical analysis of the data on the development of karst with plotting the graphs of the frequency of occurrence of karst sinkholes in accardance with their diameter Dav. As follows from the graph (Fig. 2), the distribution of diameters corresponds to an exponential law, more than 50% of karst-suffosion sinkholes have diameters less than 10 m, about 30% of sinkholes have the size from 10 to 20 m and only 0.6% have the diameter more than 70 m. The quantitative distribution of funnels in the territory by number and diameter is shown in the diagram (Fig. 4).

The size of the karst funnels and their diameter, have a dual effect on the degree of hazards: 1 - when a dip occurs in the base of the structure: the larger the diameter of the dip, the greater (other things being equal) the damage and the danger; 2 - the probability of a dip under the foundation of the structure depends on the diameter of the dip and its occurrence. Since the frequency of occurrence of karst-suffusion dips with a diameter less than 10 m in the investigated territory is the largest (Fig. 4), then funnels of small diameters are more likely to form under the structures than large karst dips.

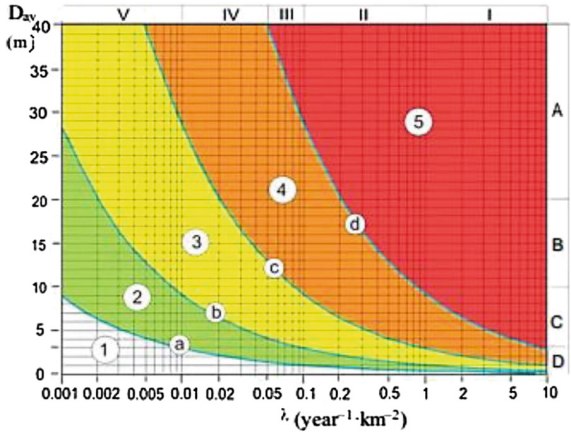

Fig. 2. The scale of karst danger and risk of formation of karst-suffusion sinkholes: D_{av}, λ - average diameter and intensity of appearance of surface karst forms; I-V, A-D - categories of stability. Zones: 1 - failures without consequences for economic objects; 2 - the permissible risk; 3 - increased attention; 4 - serious threat; 5 - the inevitable destruction (Anikeev 2016)

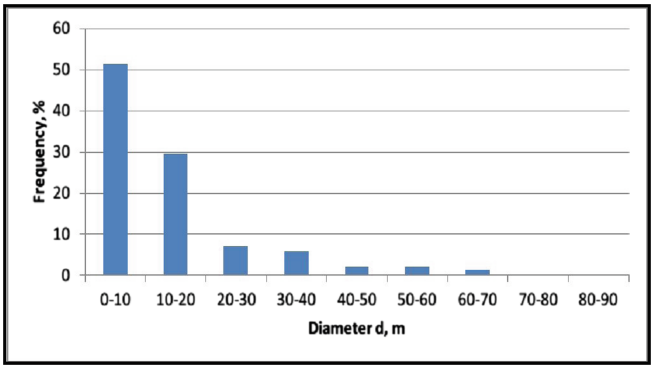

Fig. 3. Graph of the distribution of karst funnels of the construction site according to the diameter d

4 Risk Assessment Using the Remoteness Method and the Karst Hazard and Risk Scale

To estimate the values of the intensity index of the formation of 1, we used the "distance from the nearest manifestation of karst" method (Savarenskii and Mironov 1995). The essence of this method is to construct a map of "distance isolines", each point of which is removed from the center of the nearest karst funnel by a given distance Ri. The values of R are taken as multiple modular distances, in accordance with the scale of the investigation, in this case 250 m.

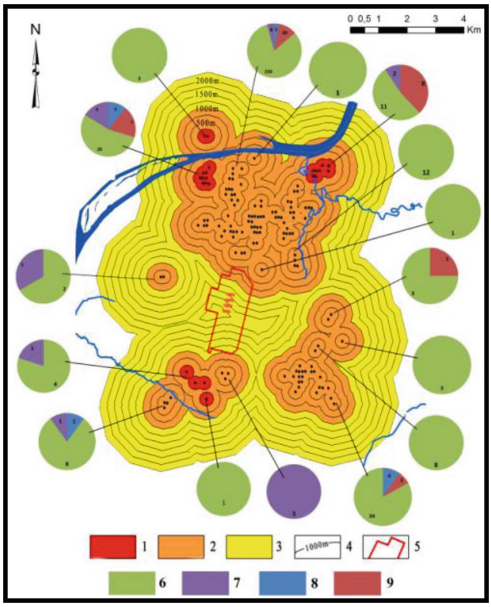

Fig. 4. The scheme of the risk of loss of land on the territory of the proposed construction of, the Nizhny Novgorod NPP. The points on the map are with the designation number of each sinkhole. 1- zone of the inevitable destruction, 2- zone of serious threat, 3 - zone of increased attention, 4 - the radius of distance, 5 - the border of the NPP. The number of: 6 - karst funnels, d < 20 m; 7 - depressions of unknown origin; 8 - karst failures; 9 - karst funnels, d > 20 m.

Around each funnel, circles were made with calculated radii of remoteness. The maximum R9 is 2250 m. Where the distance between the funnels is less than 2R the territory forms a single contour, and where the distance is more than 2R, isolated circles are formed. The boundaries of the resulting contours are isolines of remoteness, where each point is removed from the nearest funnel by a distance Ri. Scheme of isolines of remoteness with R = 250 m, R = 500 m, R = 750, m R = 1000 m, R = 1250 m, R = 1500 m, R = 1750 m, R = 2000 m, R = 2250 m is represented in Fig. 4.

Then, for each site, contoured by isolines with different values, the intensity of karst formation was calculated from formulas (1, 2). The age of the funnels where the lakes were formed was T = 100 with a large margin, all others - T = 50.

For each of the 9 isolated sites on the scheme, the parameters of the surface karst formation were calculated: the intensity of the formation and the average diameter of the sinkholes. The calculated indexes are presented in Table 1.

Since the possibility of forming funnels with a diameter of 20 m or less may be much larger than that of forminf large dips, the specific risk of losing land Rud (Anikeev 2016) calculated as:

$$R_{sp} = \lambda * (S)_{av}/S = (S)_{av} * \lambda = \lambda\pi(D_{av})2/4, \quad (3)$$

Table 1. Average values of karst indexes for sites with different radii of remoteness

Index	Radius R1…R_9 (m)								
	250	500	750	1000	1250	1500	1750	2000	2250
D_{cp}	17	16,1	15,93	15,92	14,7	14,7	14,7	14,7	14,7
λ	0,37	0,094	0,066	0,048	0,042	0,04	0,037	0,033	0,030

where $(S)_{av} = \sum (S)_i/N$—average area of the sikhole. Its dimension is $[T^{-1}]$, Its dimension is m^2/km^2year, or %/year and is also called the area intensity of the process.

The estimation of karst risk of loss of lands was carried out according to the karst hazard and risk scale (Anikeev 2016) (Fig. 1).

Based on the obtained indices and taking into account already constructed isolines of remoteness, the following scheme was obtained by the authors (Fig. 3).

Thus, studies have shown that most of the territory of the projected nuclear power plant is located in zone 3 (zone of increased attention), where minimally necessary and preventive measures of protection from karst danger are required. A small part of the territory in the north is referred to the 4th zone (a zone of serious threat), where the implementation of geotechnical or constructive protection measures against karst danger is mandatory. The nuclear reactor is supposed to be located in the zone of increased attention.

5 Conclusion

Assessment of the risk of occurrence of karst dips in the territory of the projected Nizhny Novgorod NPP allowed zoning of the territory taking into account the diameter of karst funnels.

In the presented work, it is shown that the territory chosen for the construction of the AS is optimal for this region. At the same time, the results obtained coincide with the results obtained with detailed engineering and geological surveys. It can be concluded that the proposed methodology for assessing karst danger can be used in the preliminary stage of site selection for the construction of nuclear power plants and other hazardous industrial facilities. This will reduce the amount of subsequent engineering and geological survey for construction and reduce the cost of their implementation.

The publication was prepared with the support of the “RUDN University Program 5–100”.

References

Anikeev AV (2016) Sinkhole hazard and risk of its farmation in karst areas: main indices, approaches and methods of evaluation. Eng Geol 5:10–18

Anikeev AV (2017) Dips and funnel subsidence in karst areas: formation mechanisms, prognosis and risk assessment. RUDN University, Moscow

Canadian Geotechnical Society (2006) Canadian foundation engineering manual. 4th edn, Canada

European comission (2013) Eurocode 7: geotechnical design. Publications Office of the European Union, Luxembourg

Federal Agency for Construction and Housing and Communal Services (2012) Engineering site investigations for nuclear power plants construction. Federal Agency for Construction and Housing and Communal Services, Moscow, Russia

Golubeva LV (1953) On the density of karst funnels in various geomorphological conditions. The report of the USSRAS, vol 90, no 1, pp 186–191

Government of the Russian Federation (2009) Resolution No. 45 on the procedure for conducting state expertise of project documentation and the results of engineering surveys. Government of the Russian Federation, Moscow, Russia

Kammerer F (1962) Engineering geological methods in lands and subsidenc. Freib. Forsch.-H., Berlin, Germany

Kostarev VP (1979) On the quantitative indicators of karst and their use in the engineering-geological assessment of karst areas. Engineering and construction surveys, no 1

Makeev ZA (1947) Karst and issues of underground flow. In: Abstracts of the Molotov Karst Conference, pp 10–12

Martin VI (1979) Methods of zoning of karstic territories according to the degree of stability for construction. Engineering and construction surveys, no 3

Office of nuclear regulatory research (2010) 1.28. Regulatory Guide. US Nuclear Regulatory Comission, United States

Savarenskiy IA, Mironov NA (1995) Rukovodstvo po inzhenerno- geologicheskim izyskaniyam v rajonah razvitiya karsta [Guide to engineering and geological surveys in the areas of karst development]. Industrial and Research Institute for Engineering Surveys in the Construction, Moscow, Russia

Sustainability in Life Cycle Analysis of Nanomaterials Applied in Soil Remediation

Visentin Caroline(✉) and Thomé Antônio

Posgraduate Civil and Environmental Engineering,
University of Passo Fundo, Passo Fundo, Brazil
caroline.visentin.rs@gmail.com, thome@upf.br

Abstract. The use of nanoparticles in soil remediation is an emerging and innovative technology. With the advancement of sustainable remediation, concern about the remediation technologies sustainability should be considered as criteria in decision-making. Countless tools can be employed in order to assess sustainability in soil remediation, e.g. life cycle analysis (LCA) for environmental impacts assessment. However, to be considered sustainable the LCA must also understand the economic and social aspects. This study aims to carry out a systematic and bibli- ometric analysis of scientific production in the field of LCA, sustainability and nanoparticles applied in the remediation of contaminated sites. Represented by the scientific articles indexed in the database Scopus and Web of Science. It is concluded that the evaluation of sustainability by means of the Sustainable-LCA in soil remediation is an innovative tool. The application of sustainability in its principles, environmental, economic and social, has not yet been carried out in nanoremediation.

Keywords: LCA · Sustainability · Remediation · Nanomaterial
Bibliometric analysis

1 Introduction

Use of nanoparticles in soil remediation was bom in 1990's in USA, with application for countless pollutants (Thome et al. 2015; Cecchin et al. 2016). The in creasing application of nanoremediation occurs due to high efficiency of this technique, shorter treatment times, in addition to better costs and benefits (Thome et al. 2015). Among the nanomaterials employed in remediation, the nanoscale zerovalent iron (NZVI) stands out as one of the most used nanomaterials for toxic contaminated sites (Cecchin et al. 2016).

Over the years, numerous changes in the management of contaminated sites have been seen. In the years 2000, the concern with environmental, social and economic impacts became employed in the decision-making process, through the application of sustainable remediation concepts (Rizzo et al. 2016).

For a technique to be considered sustainable, it life cycle much be analysed encompass all the environmental, social and economic aspects of the process throughout its life cycle (Rizzo et al. 2016). In this sense the life cycle analysis (LCA) is used as a means of sustainability evaluating of remediation technologies, as

© Springer Nature Singapore Pte Ltd. 2019
L. Zhan et al. (Eds.): ICEG 2018, ESE, pp. 537–543, 2019.
https://doi.org/10.1007/978-981-13-2227-3_66

well as being an important environmental tool to decision support (Singh et al. 2008; Hotze and Lowry 2011). However, the life cycle analysis in its essence does not consider the product social and economic aspects, so a broader approach is necessary. In this context application of life cycle sustainability analysis comes in order to supply the needs of LCA. In this sense, this study aims to carry out a systematic and bibliometric analysis of the scientific production in the field of LCA, sustainability and nano particles applied in the remediation of contaminated sites, represented by the scientific articles indexed in the Scopus and Web of Science database.

2 Methodology

The present study was developed from a systematic research and temporal bibliometric of quantitative nature. Aiming to broaden the knowledge regarding publications related to life cycle analysis, sustainability and nanoparticles, applied in the remediation of contaminated sites. Represented by the scientific articles indexed in the database Scopus (scopus.com) and Web of Science (wokinfo.com).

The research was carried out in two parts. Firstly was analysed the temporal distribution of sustainability in the LCA and soil remediation, through the topics "LCA/Life Cycle Analyses/Life Cycle Assessment AND Sustainability AND Remediation". The second evaluated the implementation of sustainability in LCA in soils remediation with nanomaterials, employing the following topics "LCA/Life Cycle Analyses/Life Cycle Assessment AND Sustainability AND remediation, nanomaterial (s)/nanoparticle (s)/Nanotechnology, Nano iron/Nano scale zero valent iron." In each of the phases were evaluated the theoretical evolution of the theme and the countries and authors with the highest number of publications on the subject.

3 Results and Discussion

3.1 Sustainability in the LCA and Soil Remediation

In the research first phase were found 60 publications. The distribution of these articles refers to the temporal clipping between the years 2007 to 2018, as shown in Fig. 1.

The concern with remediation techniques sustainability was verified from the years 2000. According to Rizzo et al. (2016) because of the growing inclusion of sustainability in soil remediation. However, the application of principles sustainable remediation and LCA in remediation was observed only in 2007. In 2008 there is an increase in studies, with decline in 2010 and 2012. However, from 2013, there is a growth in publications, correspond to 67% of the total. This growth is explained due to the dissemination of the application of sustainability in both soil remediation and LCA (Valdivia et al. 2012; Rizzo et al. 2016; Trentin et al. 2017).

According to Martins et al. (2017) in soil remediation the LCA is generally used to evaluate the performance of different technologies, compared to environmental impacts associated with each remediation technology. In this sense, most studies indicate that in situ processes result in lower environmental impacts than the processes carried out

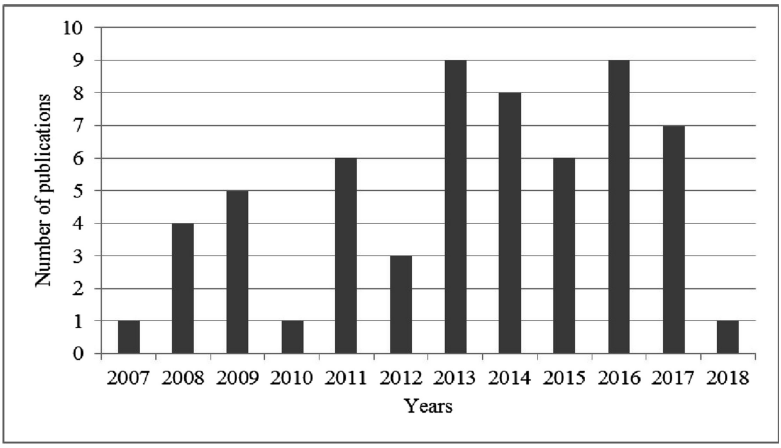

Fig. 1. Temporal evolution of scientific production on life cycle analysis, sustainability and remediation.

ex situ. The excavation of contaminated soil for treatment results in increased exposure of workers to pollutants, in addition to high energy consumption and high emissions (e.g. Harbottle et al. 2007; Harbottle et al. 2008; Cappuyns 2010; Hou et al. 2014a; Vigil et al. 2015; Hou et al. 2016; Song et al. 2018). However, in situ remediation methods are often more time consuming, and there is much more uncertainty about its efficiency (Cappuyns 2010).

One of major shortcomings of studies already undertaken is the application of sustainability concept erroneously, since, in order to be sustainable, environmental, economic and social aspects should be considered in a joint manner. Most studies carry out a "sustainability" analysis with only the environmental pillar (Cappuyns 2013; Gallagher et al. 2013; Hou et al. 2014b; Brecheisen and Theis 2015; Vigil et al. 2015; Hou et al., 2016; Vocciante et al. 2016), or environmental and economic (Harbottle et al. 2007; Martins et al. 2017).

For quantitative analysis of environmental impacts of remediation techniques with the LCA numerous tools can be employed. There is a greater emphasis on the use of SimaPro, GaBi, OpenLCA, Umberto, among others.

Considering the tendency to include sustainability in LCA by means of a broader approach through the sustainable life cycle analysis. The perspective for publications is an analysis covering beyond the environmental impacts of remediation technologies, social and economic impacts. The sustainability assessment considering the three pillars is carried out through LCA, socio-economic analysis and multi-criteria analysis, according to the studies of Hou et al. 2014a; Goldenberg and Reddy 2014; Sondergaard et al. 2017; Hou et al. 2017; Song et al. 2018.

The authors who published more about the LCA, sustainability and remediation in the analysed period are Hou, D. (six publications), Al-Tabbaa, A. (five publications) and Cappuyns, V. (four publications). Following the authors with Harbottle, M. J., Gallagher, P. M., Favara, P. and Brecheisen, T. with three publications each. In this analysis were considered all the authors (both as principal authors, as contributors authors).

The author Hou, D. (Deyi Hou) is the main author of the publications pertaining to LCA, sustainability and remediation, with only one collaboration, and the others as the main author. Its publications can be divided into studies comparing the environmental impacts between different remediation technologies (Hou et al. 2014a; Hou et al. 2014b; Hou et al. 2016; Hou et al. 2017; Song et al. 2018), and also in a detailed analysis of the growth of sustainable remediation, as well as the proposal for a framework for the evaluation of sustainability and decisionmaking (Hou and Al-Tabbaa 2014). In addition, it also highlights the development and applications of different methodologies for the life cycle analysis, as a hybrid model of LCA (Hou et al. 2014b), a methodology for the evaluation of sustainability in agricultural soils of China, proposing environmental, economic and social indicators for evaluation (Hou et al. 2017), and also through selection of environmental, social and economic indicators for a sustainability life cycle analysis (Song et al. 2018).

The publications of Al-Tabbaa, A. (Abir al-Tabbaa) refer to collaborations with the authors Hou, D. (Hou and Al-Tabbaa 2014; Hou et al. 2014b) and Harbottle, M. J. (Harbottle et al. 2007; Harbottle et al. 2008). The publications of Cappuyns, V. (Valerie Cappuyns) bring an overview of LCA implementation (and its methodologies), as well as the limitations of many students who do not consider the monetary aspects of these techniques, much less the impacts on health and eco toxicity (Cappuyns 2011). The implementation of LCA to evaluate the environmental impacts of different remediation technologies (for three case studies) was also carried out by Cappuyns. Through an analysis employing simultaneously the tools of "best available technique not Including excessive costs", LCA and a CO_2 calculator (Cappuyns 2013). In addition to an analysis of the sustainable assessment in remediation, casting criteria covering the environmental, economic and social aspects in a framework of support decision-making (Huysegoms and Cappuyns 2017).

Other authors, Gallagher, P. M., Favara, P., and Brecheisen, T., assessed environmental impacts of different remediation processes (Gallagher et al. 2013; Brecheisen and Theis 2013; Brecheisen and Theis 2015; Favara et al. 2016; Favara and Gamlin 2017).

The largest number of publications are identified in major global economies, United States (19 publications) and the United Kingdom (eight publications). These countries present high rates of awareness and adoption of sustainable remediation compared with developing countries, which have less awareness of the sustainability of contaminated sites (Trentin et al. 2017). The biggest concern of the developed countries with the sustainable remediation is due to the existence of organizations and institutions focused solely on the introduction and dissemination of sustainability concepts in remediation activities (Trentin et al. 2017).

Other countries with major publications are China with five, Germany, Belgium and Italy with four publications. Denmark, Spain, Finland and Norway have two publications each.

3.2 Application of Sustainability in the LCA and Soil Remediation with Nanomaterials

The second part of this study evaluated in particular the nano iron, due to its extensive application in nanoremediation processes (Cecchin et al. 2016). In this stage only three publications were found, these being in 2008 (Singh et al. 2008), 2011 (Hotze and Lowry 2011) and 2017 (Martins et al. 2017).

The main authors of the publications of this second part of the research (Singh et al. 2008; Hotze and Lowry 2011; Martins et al. 2017) were not observed in any of the first phase studies. In relation to the countries, two of the publications are from the United States (Singh et al. 2008; Hotze and Lowry 2011), and one from Portugal (Martins et al. 2017).

The study of Martins et al. (2017), comprised an analysis comparing the environmental impacts and costs of the nano iron production in a laboratory scale, by two methods of synthesis: traditional (using the reduction through boron sodium hydride) and green (using extracts of natural products), through an LCA. According to Martins et al. (2017) in the traditional one were observed the greatest environmental impacts and costs.

The other studies consist of impact analyses of carbon nanotubes production (Singh et al. 2008). And the potential of nanomaterials to improve the sustainability of the treatment and remediation of surface and groundwater waters, through the use of these nano products in order to improve existing technologies (Hotze and Lowry 2010).

Unlike that observed in the LCA implementation analysis and sustainability in remediation of contaminated sites, with have numerous case studies concerning different analyses. Studies with nanomaterials are still in the early stages of knowledge regarding the environmental impacts associated with production. Due comparing to the fact that the application of nanomaterials in soil remediation is a relatively new process. Studies focus on the environmental impacts analysis resulting of the manufacture of nanomaterials, whereas, in comparison with the techniques of remediation, which are constantly applied, and are consolidated in the international remediation market.

4 Conclusion

The bibliometric analysis provides an overview of the published studies on life cycle analysis and sustainability in remediation of contaminated sites and also in relation to use of nanomaterials in due process. In addition, this information brings scientific knowledge about the subject evolution, its temporal distribution, as well the main authors and countries of these publications.

The research demonstrated that sustainability in the LCA and remediation is an new subject, but on the rise, verified by the highest number of publications in the last five years. However, most of these publications focus only the environmental pillar. A greater interest is observed in the approach to sustainability as a whole, considering the environmental, social and of remediation technologies, especially in the year 2017. In this sense, the perspective is that the LCA studies in the remediation of soils walk towards an analysis of complete sustainability of remediation technologies.

According to the data analysed in the first part of the research, the author who obtained the most publications was Deyi Hou with six, live of these as the main author. Secondly the author Al-Tabbaa, A. with five publications and Cappuyns, V. with four. At this stage, the United States is the maim publishing country in the area of LCA, sustainability and remediation, followed by the UK and China.

In the second part of this research were analysed the publications concerning the application of sustainability in the LCA in the remediation with nanomaterials, resulting in only three publications. Two evaluated the environmental impacts of the nanomaterials manufacturing in a theoretical and quantitative way. One compared the environmental impacts and costs of two productive processes of the nano iron. Of these publications, two are from the United States and one from Portugal.

Based on the analyses carried out in this study, it is understood that LCA in a sustainable approach can be applied as a tool for evaluating the impacts of remediation technologies (traditional and those with nanomaterials). Assisting in decisionmaking by considering the principles of sustainable remediation.

References

Brecheisen T, Theis T (2013) The Chicago Center for Green Technology: life-cycle assessment of a brownfield redevelopment project. Environ Res Lett 8(1):1–13

Brecheisen T, Theis T (2015) Life cycle assessment as a comparative analysis tool for sustainable brownfield redevelopment projects. In: Assessing and measuring environmental impact and sustainability, pp 323–365

Cappuyns V (2011) Possibilities and limitations of LCA for the evaluation of soil remediation and cleanup. Sustainable, Chemistry, pp 213–223

Cappuyns V (2013) Environmental impacts of soil remediation activities: quantitative and qualitative tools applied on three case studies. J Clean Prod 52:145–154

Favara P, Tunks J, Hatton J, DiGuiseppi W (2016) Sustainable remediation considerations for treatment of 1,4-dioxane in groundwater. Rem J 27(1):133–158

Favara P, Gamlin J (2017) Utilization of waste materials, non-refined materials, and renewable energy in in situ remediation and their sustainability benefits. J Environ Manage 204:730–737

Gallagher PM, Spatari S, Cucura J (2013) Hybrid life cycle assessment comparison of colloidal silica and cement grouted soil barrier remediation technologies. J Hazard Mater 250–251:421–430

Goldenberg M, Reddy KR (2014) Sustainability assessment of excavation and disposal versus in situ stabilization of heavy metal-contaminated soil at a superfund site in illinois. In: Geo-congress 2014: geo-characterization and modelling for sustainability, pp 2245–2254

Harbottle MJ, Al-Tabbaa A, Evans CW (2007) A comparison of the technical sustainability of in situ stabilisation/solidification with disposal to landfill. J Hazard Mater 141(2):430–440

Harbottle MJ, Al-Tabbaa A, Evans CW (2008) Sustainability of land remediation. Part 1: overall analysis. In: Proceedings of the ICE-geotechnical engineering, vol 161, no 2, pp 75–92

Hotze M, Lowry G (2011) Nanotechnology for sustainable water treatment. Issues in Environmental Science and Technology, pp 138–164

Hou D, Al-Tabbaa A (2014) Sustainability: a new imperative in contaminated land remediation. Environ Sci Policy 39:25–34

Hou D, Al-Tabbaa A, Guthrie P, Hellings J, Gu Q (2014a) Using a hybrid LCA method to evaluate the sustainability of sediment remediation at the London Olympic Park. J Clean Prod 83:87–95

Hou D, Al-Tabbaa A, Luo J (2014b) Assessing effects of site characteristics on remediation secondary life cycle impact with a generalised framework. J Environ Plan Manage 57 (7):1083–1100

Hou D, Gu Q, Ma F, O'Connell S (2016) Life cycle assessment comparison of thermal desorption and stabilization/solidification of mercury contaminated soil on agricultural land. J Clean Prod 139:949–956

Hou D, Ding Z, Li G, Wu L, Hu P, Guo G, Wang X, Ma Y, O'Connor D, Wang X (2017) A sustainability assessment framework for agricultural land remediation in China. Land Degrad Dev 29:1–14

Huysegoms L, Cappuyns V (2017) Critical review of decision support tools for sustainability assessment of site remediation options. J Environ Manage 196:278296

Martins F, Machado S, Albergaria T, Delerue-Matos C (2017) LCA applied to nano scale zero valent iron synthesis. Int J Life Cycle Assess 22(5):707–714

Rizzo E, Bardos P, Pizzol L, Critto A, Giubilato E, Marcomini A, Albano D, Darmendrail D, Doberl G, Harclerode M, Harries N, Nathanail P, Pachon C, Rodriguez A, Slenderso H, Smith G (2016) Comparison of international approaches to sustainable remediation. J Environ Manage 184:4–17

Singh AK, Lou HH, Pike RW, Agboola A, Li X, Hopper JR, Yaws CL (2008) Environmental impact assessment for potential continuous process for the production of carbon nanotubes. Am J Environ Sci 4(5):522–534

Sondergaard GL, Binning PJ, Bondgaard M, Bjerg PL (2017) Multi-criteria assessment tool for sustainability appraisal of remediation alternatives for a contaminated site. J Soils Sed 2017 (2):1–15

Song Y, Hou D, Zhang J, O'Connor D, Li G, Gu Q, Li S, Liu P (2018) Environmental and socioeconomic sustainability appraisal of contaminated land remediation strategies: a case study at a mega-site in China. Sci Total Environ 610–611:391–401

Thome A, Reddy KR, Reginatto C, Cecchin I (2015) Review of nanotechnology for soil and groundwater remediation: Brazilian perspectives. Water Air Soil Pollut 226(4):1–20

Trentin AWS, Braun AB, Thome A (2017) Characteristics of Publications on Sustainable Remediation Between 1980–2016. In: IX Seminario de Engenharia Geotecnica do Rio Grande do Sul, 2017, Brazil (in Portuguese)

Valdivia S, Ugaya CML, Hildenbrand J, Traverso M, Mazijn B, Sonnemann G (2012) A UNEP/SETAC approach towards a life cycle sustainability assessment—our contribution to Rio+ 20. Int J Life Cycle Assess 18(9):1673–1685

Vigil M, Marey-Perez MF, Huerta MG, Cabal AV (2015) Is phytoremediation without biomass valorization sustainable?—Comparative LCA of landfilling vs. anaerobic co-digestion. Sci Total Environ 505:844–850

Vocciante M, Caretta A, Bua L, Bagatin R, Ferro S (2016) Enhancements in electro kinetic remediation technology: environmental assessment in comparison with other configurations and consolidated solutions. Chem Eng J 289:123–134

Reliability Evaluation of Two Compacted Tropical Soils for Use in Municipal Solid Waste Containment Application

A. M. Kundiri[1(✉)] and K. J. Osinubi[2]

[1] Department of Civil and Water Resources Engineering, University of Maiduguri, Maiduguri, Nigeria
alikundiri@yahoo.com
[2] Department of Civil Engineering, Ahmadu Bello University Zaria, Zaria, Nigeria

Abstract. The paper presents the results of reliability assessment of the suitability of two tropical soils (laterite and clay sand) for use as liner materials in waste containment application. The evaluation was based on the use of compositional variables (moulding water content relative to optimum, hydraulic conductivity, initial saturation, plasticity index, clay content and compactive effort) using the First Order Reliability Method (FORM) version 5. The results of the study revealed the variation of reliability indices as the coefficient of variation (COV) for the independent variables increases using the normal and lognormal distributions. Three compactive efforts of standard Proctor (SP), West African standard (WAS) and modified Proctor (MP) were considered. The predictive model was developed with a view to assessing the safety of the hydraulic barrier for waste containment facilities.

Keywords: Reliability · Waste containment · Compositional variables

1 Introduction

In municipal waste containment application, compacted liners form the integral component of the lining system [1]. The compacted clay liners are required to be within the range of ≥ 20 to 25%, and has the ability to impede the flow of water and other contaminants with a view to achieving a minimum of hydraulic conductivity of less than or equal to 1×10^{-7} cm/s [2–4]. Hydraulic conductivity is taken as one of the basic parameters for design and characterization of liners performance and reliability [5, 6]. Nevertheless, soil liner reliability could be based on other performance parameters, such as the travel time of contaminant through the liner [7–9]. The most significant factors affecting hydraulic conductivity in decreasing order of importance are: initial saturation; compactive effort; plasticity index and clay content. For most soils, hydraulic conductivity decreases with increases in initial saturation, plasticity index and compactive effort but increases with increasing clay content [1].

By and large, deterministic hydraulic analyses of the spatially variable soil will not properly account for these uncertainties. In effect, the knowledge of hydraulic and associated uncertain properties of soil can be mathematically incorporated into

© Springer Nature Singapore Pte Ltd. 2019
L. Zhan et al. (Eds.): ICEG 2018, ESE, pp. 544–554, 2019.
https://doi.org/10.1007/978-981-13-2227-3_67

probabilistic modeling [10]. The soils generally are said to be heterogeneous and anisotropic due to the spatial variability in their natural properties from place to place. These soils are not only spatially variable, but can fluctuate considerably within short distances as a result of the inherent differences in consistency and composition during the process of their formation [11–13]. The variation in soil properties could be responsible for the envisaged uncertainties. Engineering judgement is indispensable in many aspects of geotechnical engineering reliability analysis and merely removes the need for guess work on how uncertainties affect the performance criterion [14].

Inconsequence, reliability assessment provides a means of evaluating the combined effects of uncertainties, and distinction between conditions where uncertainties are particularly high or low. In design evaluation involving selection of values for a soil parameter to be used for geotechnical analysis, application of reliability analysis for probabilistic concepts takes care of the uncertainties [15–18]. Probability theory has been widely used in engineering, and its application to engineering analysis requires the knowledge of some statistical attributes of relevant random variables such as values of the mean (the central tendency), variance (the dispersion about the mean) and standard deviations [19]. One of such probabilistic methods used in geoenvironmental engineering is the reliability analysis [20, 21]. However, there is scanty literature on the reliability assessment of lateritic and clayey sand tropical soils, thus the need for the research.

1.1 Background

The major problem facing the analysis of contaminant migration through soil liners is the heterogeneity of hydraulic properties of compacted soils. [22], relate the probability of survival throughout the useful life, or at least some specified design period of the liner in the face of uncertainties as human error inputs, various environmental conditions, variation in material and engineering properties as well as prediction of future events. This concept is referred to as reliability. The probability of survival, $\mathbf{P_X}$ could be expressed in terms of probability of failure $\mathbf{P_f}$ as:

$$P_X = 1 - P_f \tag{1}$$

The probability of failure is a vital tool for assessing the uncertainty or risk associated with the system reliability, which is the probability of survival of the whole structure. Similarly, [23], represent probabilistic measure of assurance of the post – construction performance of compacted soil liner reliability in terms of

$$R = P(K_e < K_s) \tag{2}$$

Where K_e = Expected hydraulic conductivity and K_s = the specified hydraulic conductivity limit which conformed to the regulatory maximum hydraulic conductivity of 1×10^{-7} cm/s or 1×10^{-9} m/s.

The soil hydraulic conductivity has been described as a log-normal variate, and can properly represent a wide range of measured hydraulic conductivities typically observed in a liner [24]. First order reliability method (FORM) has been designed for

the approximate computation of general probability integrals over given domains with locally smooth boundaries [25].

$$P_f = P(\underline{X} \subseteq f) = P(g(\underline{x}) \leq 0) = \int_{g(\underline{x})\langle 0} dF_{\underline{x}}(\underline{X}) \tag{3}$$

During the design life or service period of compacted soil liners, the reliability of failure would occur when the liner hydraulic conductivity is equal or greater than the regulatory maximum (1×10^{-7} cm/s or 1×10^{-9} m/s). The probability of failure (P_f) can then be formulated as:

$$P_f = P\{K_e - K_s(Si, PI, C, E) \leq 0\} \tag{4}$$

Where, K_e = Expected hydraulic conductivity, K_s = Specified regulatory maximum hydraulic conductivity, Si = Initial degree of saturation, PI = Plasticity Index, C = Clay content and E = Compaction energy or compactive effort.

These are the parameters affecting the hydraulic conductivity, and are used in the prediction of laboratory hydraulic conductivity values.

The appropriate limit state function hydraulic conductivity is of the form:

$$g(x) = \ln K_e - \ln K_s \tag{5}$$

Failure is said to occur when K_e (expected hydraulic conductivity) exceeds K_r, the regulatory maximum hydraulic conductivity. [25], represented the expected hydraulic conductivity K_s in the form:

$$\ln K_s = Y = X\beta' + \varepsilon \tag{6}$$

Where **Y** = random variable describing the distribution of $\mathbf{lnK_e}$,
X = a number containing **n** random variables that describe the spatial distribution of **n** related to hydraulic conductivity such as the index properties and compaction variables,
β = a vector coefficient and
ε = an independent

2 Evaluation of Compositional Variables Using FORM

The first-order reliability method (FORM) version 5 was employed to assess the potential of the two compacted tropical soils (i.e. lateritic soil from Shika and clayey sand soil from Yanranda all in the area of Samaru in Zaria and its environs) by means of evaluating the effect of some of the compositional variables such as moulding water content relative to optimum, initial saturation, clay content and compactive effort

during the construction stage. The statistical characteristics such as mean, standard deviation and coefficient of variation of the soil as well as the compaction variables for the lateritic and clayey sand soils were evaluated using the different statistical distributions in Table 1.

Table 1. Initial input data for reliability analysis of lateritic and clayey sand soils based on Laboratory hydraulic conductivity using FORM 5

S/No.	Variables	Distribution type	Mean E(X)	Standard deviation S(X)	Coefficient of variation COV (%)
1.	Hydraulic Conductivity, ***K***	Log normal (=3)	$1x10^{-9}$m/s	$2.7x10^{-10}$m/s	19
2.	Initial Saturation, ***Si***	Log normal (=3)	79.489	19.794	24.902
3.	Plasticity Index, ***PI***	Log normal (=3)	16.250	4.573	28.142
4.	Clay Content, ***C***	Normal (=2)	16.233	10.63	65.5
5.	Compactive effort Index, ***E***	Deterministic Parameter	(−1, 0, 1)	–	–

The probability distribution for the independent variables in the regression Eq. (7), were established using the initial input parameter for reliability analysis incorporated into FORTRAN – based programme FORM 5, with which the reliability index (β) values were evaluated using the different statistical distributions with numbers coded in brackets in column 3 [25]. The initial input parameter considered the initial saturation and plasticity index as lognormally distributed, clay content is normally distributed, while the compactive effort is a deterministic parameter. The resulting regression equation obtained by [1] is:

$$\ln K = -15.0 - 0.087Si - 0.054PI + 0.022C + 0.91E + \varepsilon \tag{7}$$

Where, ***k*** is hydraulic conductivity (m/s), ***Si*** is initial saturation (%), ***PI*** is plasticity index (%), ***C*** is clay content (% < 2 μm), ***ε*** is a Gaussian random error term, and ***E*** is an integer describing the compactive effort index, assigned as −1, 0, and 1 for SP, WAS, and MP compactive efforts.

The regulatory maximum hydraulic conductivity for compacted soil liners was set as 1×10^{-7} cm/s or 1×10^{-9} m/s as the upper limit with corresponding values of standard deviation and coefficient of variation of 2.7×10^{-10} m/s and 19. The sensitivity analysis for each variable was made assuming the values of coefficient of variation ranging from 20–100 (or 0.1–1.0). The hydraulic conductivity value was initially varied, while other input parameters were kept constant for the lognormal distribution of the hydraulic conductivity function. Reliability indices were obtained for the three compactive efforts of standard Proctor (SP), West African standard (WAS) and modified Proctor (MP). Traditionally, hydraulic conductivity is assumed to be lognormal

distribution [2, 5, 10, 11, 24, 27]. However, a Kolmogorov-Smirnov (K-S) test for goodness of fit performed by [27] using 30 data points ranked hydraulic conductivity data as beta, gamma, normal and lognormal in order of preference as to its distribution.

3 Discussion of Results

3.1 Effect of Hydraulic Conductivity on Reliability Index

The effect of hydraulic conductivity on reliability index for normally and log normal distributions for the hydraulic conductivities are shown in Figs. 1 and 2 respectively. The normal distribution function has not revealed any distinct relationship since it is characterised with no change in reliability indices as the COV increases from 20 to 100% for the three compactive efforts. The lognormal distribution for the hydraulic conductivity showed a non-linear decreasing trend from 1.61 to 1.35 for SP, 0.96 to 0.72 for MP and 0.37 to 0.16 for WAS, as the values of the COV increased. It was observed generally, that soil samples prepared at higher compactive effort gave relatively higher values of reliability indices and hence reduced values of hydraulic conductivity.

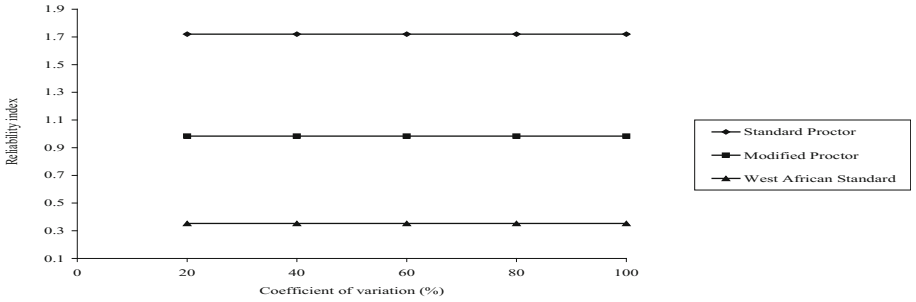

Fig. 1. Variation of Reliability index with COV for normal distribution for hydraulic conductivity

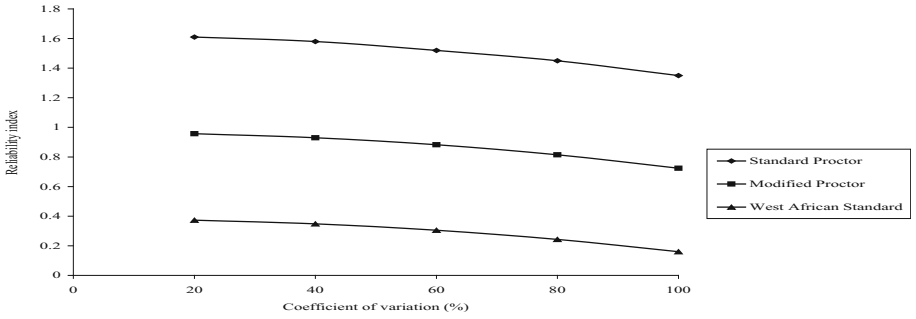

Fig. 2. Variation of Reliability index with COV for lognormal distribution for hydraulic conductivity

Effect of Initial Saturation on Reliability Index

The variations in reliability indices as the COV increased from 20 to 100% for the normal and lognormal distributions for initial saturation are presented in Figs. 3 and 4. The normal distribution function decreased from 1.8 to 0.37 at SP effort, reliability index reduced from 1.16 to 0.24 at MP effort and for WAS effort the reliability index reduced from 0.52 to 0.11. In the same vein, the normal distribution function decreased from 2.10 to 0.14 for SP, from 1.22 to −0.09 for MP and from 0.46 to −0.28 for WAS as the values of the COV increased. It could be deduced therefore, that the rapid change in reliability indices as the COV of the initial saturation (***Si***) increased from 20 to 100% clearly demonstrates that ***Si*** is affected by the hydraulic conductivity. In practice, either increasing the compaction water content or compactive effort or both can increase the ***Si*** [1].

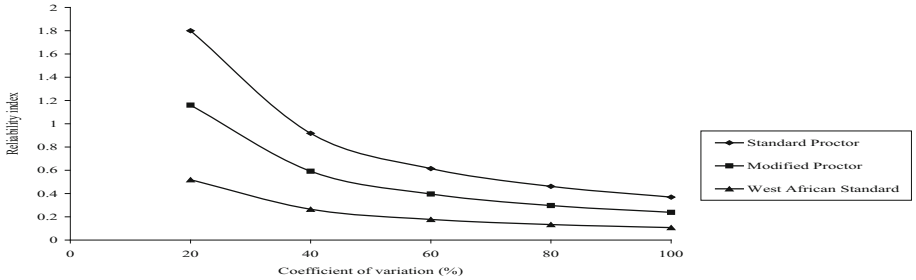

Fig. 3. Variation of Reliability index with COV for normal distribution function for ***Si***

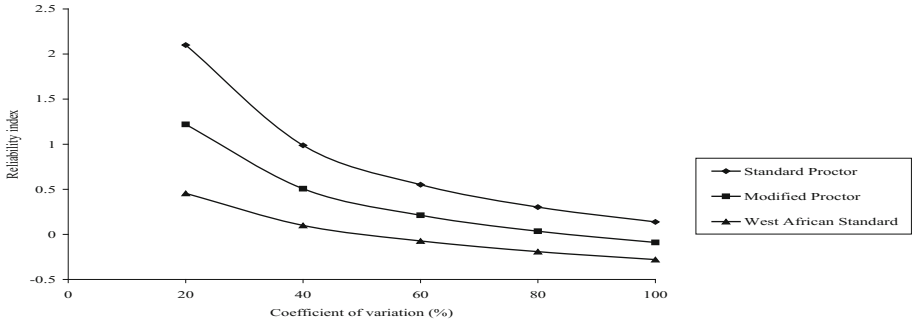

Fig. 4. Variation of Reliability index versus COV for lognormal distribution function for ***Si***

Effect of Plasticity Index on Reliability Index

The reliability indices decreased as the COV of the plasticity index increased from 20 to 100% for both normal and log normal distribution functions as shown in Figs. 5 and 6. There is similarity in trend for both the normal and lognormal distribution function for the plasticity index. The reliability index linearly decreased from 1.73 to 1.41 at SP effort, from 0.99 to 0.84 at MP effort and from 0.35 to 0.31 at WAS effort for the

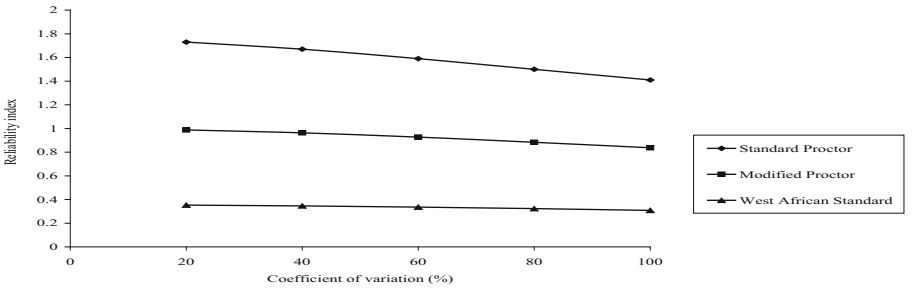

Fig. 5. Variation of Reliability index with COV for normal distribution function for plasticity index

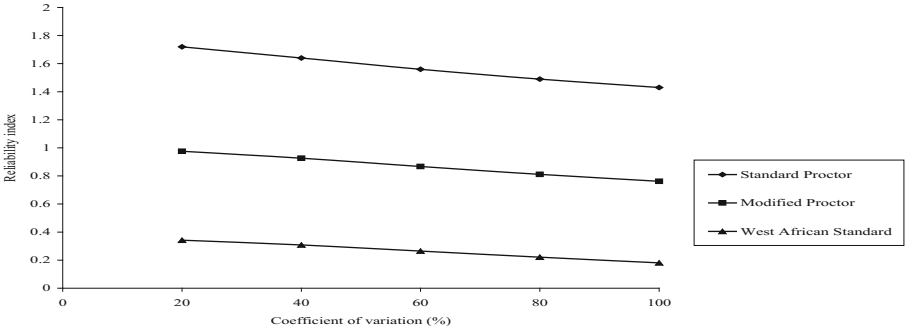

Fig. 6. Variation of Reliability index with COV for lognormal distribution function for plasticity index

normal distribution function. For log normal distribution function, the reliability index reduced from 1.72 to 1.43 for SP, 0.98 to 0.76 for MP and 0.34 to 0.18 for WAS, as COV increased. These reliability indices showed that the values of plasticity indices fall below the range (i.e., <7–10%) prescribed for construction of compacted clay liners by most regulatory agencies.

Assessment of the Model Suitability

In structural reliability and/or the ultimate limit state, the reliability index (β) ranged between 2.5 and 4.0, with a corresponding probability of failure less than 6.25 x 10^{-3} being reasonably safe. A minimum reliability index (β) value of 2.5 has been adopted as the bases for assessing the hydraulic conductivity of the model generated for this study. Reliability indices obtained at the SP effort, were close to the value of 2.5 and ranged between 0.37 and 2.48. For the MP and WAS efforts, the reliability indices obtained were between 0.24 and 2.48 as well as −0.226 and 0.49 respectively.

Nevertheless, all the β values for the reliability indices for the COV ranging between 20 – 100% were deemed acceptable, and are within the range of 2.5 and 4.0. From these results, it could be concluded that WAS and MP compactive efforts should be used in order to achieve the required minimum hydraulic conductivity in the field.

Thus, the probability distribution type for compactor weight is important in making reliability estimates.

Statistical Analysis

Two-way analysis of variance without replication were performed at *5%* level of significance ($\alpha = 0.05$) for the reliability indices of the compositional variables was carried out using the Numerical tool analysis of Quattro Pro 9 in Microsoft Word Perfect Office 2000 software. All the calculated F-values are greater than the F-critical, which inferred that the effect of these variables is statistically significant. The highest F-values of the treatment (COV) for the various variables for hydraulic conductivity (F = 268.69), followed by plasticity index (F = 35.89). The effects of variations in ***Si*** and clay content on reliability indices though statistically significant, showed lower F-values of 13.83 for ***Si*** and 4.55 for the clay content. However, the overwhelming influence on F-values for the reliability indices of compactive effort for hydraulic conductivity, plasticity index, clay content and initial saturation are 18196.98, 3169.80, 621.41 and 13.42 respectively. The results of this analysis are presented in Table 2.

Table 2. Analysis of variance of reliability index values and test of significance

S/No.	Variables	Source of variation	Df	F-cal	F-crit.	P-value	Statistical significance
1	Hydraulic Conductivity (***k***)	COV	4	268.69	3.84	1.5E − 08	Significant
		Compactive Effort	2	1819698	4.46	2.3E − 15	Significant
		Error	8				
		Total	14				
2	Initial Saturation (***Si***)	COV	4	13.83	3.84	0.0011	Significant
		Compactive Effort	2	13.42	4.46	0.0028	Significant
		Error	8				
		Total	14				
3	Plasticity Index (***PI***)	COV	4	35.89	3.84	3.7E − 05	Significant
		Compactive Effort	2	3169.0	4.46	2.5E − 12	Significant
		Error	8				
		Total	14				
4	Clay Content (***C***)	COV	4	4.55	3.84	0.033	Significant
		Compactive Effort	2	621.41	4.46	1.7E − 09	Significant
		Error	8				
		Total	14				

Implications for Practical Application

The compactive effort used in the laboratory simulates the actual compactor weight under field conditions. The higher the compactive effort, the higher the reliability indices obtained at any given coefficient of variation. The compactor weights are those of sheep foot rollers reported in the database as developed by [26]. These weights are

globally the same and are not restricted to certain parts of the world. Mostly, the major difference between laboratory-scale and field-scale hydraulic conductivities is that the results obtained from laboratory experiments cannot be completely relied upon. However, laboratory results are often used for this purpose, even though laboratory-scale compaction does not perfectly duplicate the repeated passages of compaction equipment over each lilt of soil in the field. The normal distribution depicted some levels of non significance for COV and compactive effort. The results of the statistical analysis for the different distributions are shown in Table 3.

Table 3. Analysis of variance for reliability distribution function

Type of distribution	Source of variation	Df	F-cal	F-crit.	P-value	Statistical significance
Normal	COV	4	−1.40	3.84	0	Non
	Compactive					Significant
	Effort	2	−4E15	4.46	0	
	Error	8				Non Significant
	Total	14				
Lognormal	COV	4	268.69	3.84	1.5E − 08	Significant
	Compactive					
	Effort	2	18196.98	4.46	2.3E − 15	Significant
	Error	8				
	Total	14				

4 Conclusion

The predictive model was developed using the initial input compositional variables for reliability analysis based on FORM 5 was evaluated, and the results of the two-way ANOVA without replication were performed at *5%* level of significance with the aid of the numerical tool (Quattro Pro 9 in Microsoft Word Perfect Office 2000 software). The reliability indices obtained at the SP and MP efforts were close to the value of 2.5 and ranged between 0.37 to 2.48 and 0.24 to 2.48 respectively. All the calculated F-values are greater than the F-critical, which shows that the effect of these variables is statistically significant, and there is an overwhelming influence on F-values for the reliability indices of compactive effort for hydraulic conductivity, plasticity index, clay content and initial saturation. This model therefore, inferred that WAS and MP compactive efforts can be used to achieve the minimum hydraulic conductivity of 1×10^{-7}cm/s in the field suitable for landfill in waste containment application.

References

1. Benson CH, Trast J (1995) Hydraulic conductivity of thirteen compacted clays. Clays Clay Miner 43(6):669–681
2. Benson CH, Daniel DE (1994a) Minimum thickness of compacted soil liners: I. stochastic models. J Geotech Eng, 120(1):129–152. ASCE
3. Rowe RK, Quigley RM, Booker JR (1995) Clayey barrier systems for waste disposal facilities. E & FN Spon. http://www.getcited.org/pub/103216515
4. Eberemu AO, Afolayan JO, Abubakar I, Osinubi KJ (2014) Reliability evaluation of compacted lateritic soil treated with Bagasse Ash as material for waste landfill Barrier, Geo-congress, Technical papers
5. Bogardi I, Kelly WE, Bardossy A (1989) Reliability model for soil liners: Initial design. J. Geotech. Eng. 115(5):658–669 ASCE
6. Osinubi KJ, Kundiri AM (2008) Hydraulic conductivity of compacted clayey sand. In: Proceedings of bi – monthly meetings/workshops, materials society of Nigeria, January–December, pp 21–29. Zaria chapter
7. Shackelford CD (1996) Modelling and analysis in environmental geotechnics: an over view of practical applications. In: Proceedings of the 2nd international congress on environmental geotechnics,5–8 November, Osaka, pp 1375–1404
8. Nwaiwu CMO, Osinubi KJ, Afolayan JO (2005) Statistical evaluation of the hydraulic conductivity of compacted lateritic soils. Geotech Test J 28(6):1–10
9. Kundiri AM (2009) Chemical transport and water flow through two compacted tropical soils. Ph.D Dissertation, Ahmadu Bello University, Zaria
10. Benson CH, Daniel DE (1994b) Minimum thickness of compacted soil liners: II. analysis and case histories. J. Geotech. Eng. 120(1):153–172. ASCE
11. Gui S, Zhang R, Turner JP, Xue X (2000) Probabilistic slope stability analysis with stochastic soil hydraulic conductivity. J Geotech Geoenviron Eng 126(1):1–9 ASCE
12. Chaudhuri A, Sekhar M (2005) Probabilistic Analysis of pollutant migration from a landfill using stochastic finite element method. J. Geotech. Environ. Eng. 131(8):1042–1049 ASCE
13. Bello AA (2012) Reliability assessment of reddish brown tropical soil as a liner material. Geotech. Geologic. Eng. 31(1). https://doi.org/10.1007/s10706-012-9558-6
14. Phoon KK, Kulhawy FW (2003) Evaluation of model uncertainties for reliability-based function design. In: International proceedings of 9th international conference on applications of statistics and probability in civil engineering, Sanfrancisco, (2):1351–1356
15. Duncan JM (2000) Factors of safety and reliability in geotechnical engineering. J Geotech Environ Eng 126(4):307–316 ASCE
16. Christian JT (2001) Baccher GB (2001) Discussion of factor of safety and reliability in geotechnical engineering. J Geotech Environ Eng 127(8):700–703 ASCE
17. Gu Q, Barbato M, Conte JP (2008) A new sensitivity and reliability analysis framework for structural and geotechnical system. In: The 14th world conference on earthquake engineering, 12–17 October, Beijing, China
18. Honjo Y (2011) Challenges in geotechnical reliability based design. In: Vogt N, Schuppener B, Straub D, Brau G (eds) ISGSR2011, pp 11–27
19. Kaymaz I, McMahon C, Xianyi M (1998) Reliability based structural optimisation using the response surface method and Monte Carlo simulation. In: 8th international machine design and production conference, Ankara
20. Belabed L, Benyaghla H (2011) Reliability analysis in geotechnical engineering. In: 6th international advanced technologies symposium (IATS 2011), 16–18 May, Elaz Turkey, pp 25–30

21. Oriola FOP, Moses G, Afolayan JO (2012) Reliability estimates of field hydraulic conductivity of compacted Bagasse Ash Treated Foundry Sand. J Environ Earth Sci 2(6):1–13
22. Whitman RV (2000) Organizing and evaluating uncertainty in geotechnical engineering. J Geotech Geoenviron Eng 126(7):583–593 ASCE
23. Borgadi I, Kelly WE, Bardossy A (1990) Reliability model for soil liners: post construction. J Geotech Eng 116(10):1502–1520 ASCE
24. Benson CH (1993) Probability Distributions for hydraulic conductivity of compacted soil liners. J Geotech Geoenviron Eng 119(3):471–486 ASCE
25. Gollwitzer S, Abdo T, Rackwitz R (1988) First order reliability method (FORM) user's manual, Munich, p 47
26. Benson CH, Zhai H, Wang X (1994) Estimating hydraulic conductivity of compacted clay liners. J Geotech Eng 120(2):366–387 ASCE
27. Harrop–Williams K (1985) Clay liner permeability: evaluation and variation. J Geotech Geoenviron Eng 117(2):241–271

Assessment of Physical Vulnerability to Landfill Failure-Taking Shenzhen as an Example

S. Zhang(✉), Y. Liu, and C. Li

MOE Key Laboratory of Soft Soils and Geo-Environmental Engineering, Zhejiang University, Yuhangtang Road 866#, Hangzhou 310058, China
{zhangshuaiqj,2l8l2l44}@zju.edu.cn

Abstract. Municipal solid waste (MSW) have increased in the accumulation rate in China and landfill is the most common method of MSW disposal management. A landfill failure occurs when the great majority of rocks, soil materials or debris flows move down from a slope due to gravity. The physical vulnerability of the catastrophic landfill failure occurred in Shenzhen 2015 is analyzed in this paper. It deduced that the vulnerability would increase with the impact pressure and maximum bending moment of each building. Typical deformation characteristics of affected buildings, such as bending moment and shear force are simulated using ETABS to determine whether the building will collapse after the impact of the landfill failure. A vulnerability curve indicates the relationship between impact pressure of the landfill failure, the building type, building use and the damage degree of the building.

Keywords: Landfill failure · Physical vulnerability · MSW · ETABS

1 Introduction

A catastrophic landfill failure event occurred on 20 December 2015, caused 69 total deaths, 8 missing and serious damage to properties. The mud had swept through many of the buildings, with the chances of survival seen as extremely small (Walker 2015). During this event, approximately 2.51 × 106 m^3 of construction waste slid out of the dump site affecting approximately 0.38 km^2 and the area of Guangming New District is 156 km^2 (Zhan et al. 2018). The range of the landfill failure involved over 24% which belongs to High Damage and most of the damaged buildings were Brick Concrete and Temporary Building.

The vulnerability assessment should be conducted for warning people and be a system to identify and qualify the landfill failure. Several studies have proposed different vulnerability assessment methodologies using a variety of vulnerability parameters (Singhal and Kiremidjian 1996). A physical vulnerability can be defined as the degree of the hazard within the area which is affected and physical vulnerability is conditional probability. Therefore, the assessment should require the interaction between the exposed landfill failure and the hazard event. This interaction can be presented by vulnerability curves. Building vulnerability was defined as the ratio of the

© Springer Nature Singapore Pte Ltd. 2019
L. Zhan et al. (Eds.): ICEG 2018, ESE, pp. 555–563, 2019.
https://doi.org/10.1007/978-981-13-2227-3_68

cost of repairing the damages and the value of the building (Blong et al. 2017). In the research of quantitative risk analysis, building vulnerability is determined by statistical analysis with historical disaster records or numerical model (Bell and Glade 2004). The vulnerability curves can be established to illustrate the damage functions of the rock fall of the buildings by the function of impact pressure and structure features.

2 Study Site

2.1 Geological Conditions

The landfill is located at 5 km from Guangming New District and 23 km away from Shenzhen, and the landfill is surrounded by Dayan Mountain which is three ridges with a moderate slope gradient. The peak elevation of Dayan Mountain is 306.8 m. The landfill failure is located on the hillside of the Mid-Levels, up to 12 stories, around 45 m (Fig. 1).

Fig. 1. Location of the landfill failure

There is some rainwater stored in some holes on the surface of the landfill, a large scale pond was formed because of groundwater and rainfall accumulation in 2013. Since the accumulation rate of the waste filling was considerably fast, the holes were covered around 2014 (Zou 2016). According to operation records in March 2014, approximately 1.62×10^5 m^3 construction soils were dumped into the landfill per month and the total amount was 1.79×10^6 m^3. Moreover, the height of the landfill has increased rapidly which from 115 of elevation in February 2014 enhanced to 160 of elevation in December 2015, resulting in 45 m increase in the elevation of the landfill.

2.2 Hydrological Conditions

From the Tangjia rain monitoring station, the cumulative precipitation in the month before the landfill failure is 95.7 mm. The average annual rainfall in 2015 was 1500 mm, while the annual average evaporation was 1100 mm. Drainage channels of

the dumpsite was abandoned surrounding peripheral of the landfill. Also, the surface water failed to divert into the peripheral drainage channel since the damaged drainage pipes were not repaired and the drainage pipes were insufficient in the landfill. Therefore the rainwater will be concentrated the pit at the bottom of the soil (Xu et al. 2016).

2.3 Characteristics of Damaged Buildings

On December 20, 2015, the landfill failure occurred in two successive surges with a duration of 13 min (Zhan et al. 2018). There are about 70 buildings totally damaged which were the closest with the landfill, around 60 buildings were high damaged by the landfill failure, belike 55 buildings were light damaged. The degree of damage to the building is inversely proportional to the distance from the slope, because the impact pressure of the landfill failure will directly attack the closest buildings. The subsequent plants will be caused by a lower degree of damage due to the impact pressure had been reduced by the resistance of the closest buildings. The distance from the landfill can also affected the value of the impact pressure. Some damaged building on site is presented in Fig. 2.

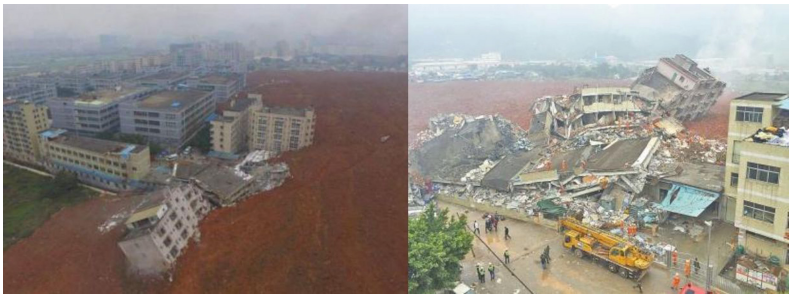

Fig. 2. Some damaged buildings on site

3 Methodology

3.1 Numerical Simulation

Most of the identification of geological hazard was using a common method which based on satellite images, aerial-photo interpretation, field surveys and collection of local data (Zhang et al. 2012). The damage level of the buildings can be calculated by the software ETABS. This software is used to simulate the situation when the buildings are facing landfill failure. After entering the data of the landfill failure including impact pressure and the structure and material of the buildings into ETABS, the bending moment, shear force and deformed shape of the building structure will be simulated. The damage degree of the buildings can be also simulated.

The data including the value of the impact pressure of the landfill failure will be simulated and the formula will according to Eq. 1.

$$P = \rho \times g \times h \times tan\,\theta \tag{1}$$

The impact pressure will use the density of soil, the height and the slope of the landfill failure and the gravity, the material of the landfill failure are sand and wet so the density of the material is 1905 kg/m^3. The gravity is 9.81 m/s^2 and the height and the slope of Dayan Mountain are 45 m and 2–3°. Besides, there are distributed to 3 zones in the study area and 2 to 3 buildings for each zone will be calculated the damage degree (Fig. 3). The impact pressure of each building have been calculated by the Eq. 1 and the result was showed at the Table 1. Also, the material of the buildings is a factor to estimate the damage degree of the buildings. Therefore, it created a vulnerability of economics loss after the landfill failure and the factor of the vulnerability was calculated by Chen (Table 2). The data can simulate the vulnerability curve of building by using the damage degree of the building, building type and building use.

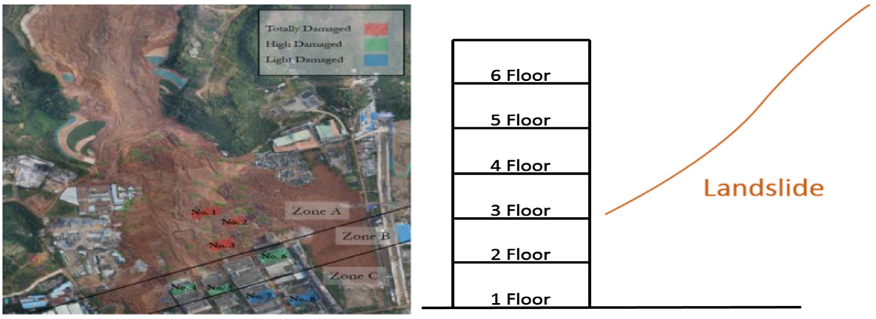

Fig. 3. Distribution of No. 1–8 buildings in zone 1–3 and the model of landfill failure

3.2 Analysis of Interaction Between Landfill Failure and Building

There were two main reasons for the landfill failure analyzed. The first reason was the groundwater flow stagnated in the garbage dump and it enhanced the weight of the landfill, resulting in the water table or water pressure inside the waste pile be too high. Also, the granite stratum was impermeable, so it resulted that the waste filling and high pore-water pressure were saturated. The landfill failure was occurred finally because of the pressure by the landfill failure deposit (Xu et al. 2016). Besides, the second reason was caused by the human. Since there are many wastes produced every day to form pile, the pile being too high for the overall slope angle and the pile being too steep for the final pile height could cause landfill failure.

The calculation of the impact pressure of the building will use the Eq. 1 and assumed that the area of the building is same since the main aim is to estimate the influence of the building type and the use. After calculating the impact pressure, it is suggested to create 21 cases for estimating the effect of the landfill failure which attacked in different depth of one storey building. Besides, the vulnerability of building has been calculated in different building damage degree of each storey.

Table 1. Impact pressure of each build

Building no.	Distance (m)	Angle	Pressure (kN/m^2)	Equation 1
A1	846	3.0448	44.73	$P = \rho \times g \times h \times \tan\theta$ $\rho = 1905\ kg/m^3$ $g = 9.81\ m/s^2$ Landfill failure height: $h = 45\ m$
A2	885	2.9108	42.76	
A3	923	2.7912	41.00	
B4	1115	2.3111	33.94	
B5	1120	2.3008	33.79	
B6	1077	2.3925	35.14	
C7	1185	2.1747	31.93	
C8	1246	2.0684	30.37	
21 assuming cases	1000	2.5766	37.84	

Table 2. Factor of building, Chen Cong Shan

Building damage degree	Building use	Building type
Totally damaged 1.0	Commercial 1.0	Reinforced-concrete 1.0
High damage 0.8	Industrial 0.7	Brick-concrete 0.8
Light damage 0.3	Residential 0.5	Temporary building 0.3

4 Analysis of Simulation Result

After entering the parameter and the dimension of each properties to the software (see Table 3), the model of each building will be showed (see Fig. 4). It is assumed that the impact pressure of the landfill failure will attacked to all building horizontally and uniformly. The deformed shape of buildings will be showed after simulation (see Fig. 5). On the other hand, all property data of the assuming cases will be set as the same and the maximum bending moment of these building showed in Figs. 6 and 7.

5 Development of Vulnerability Model

This landfill failure caused a large number of casualty and serious damage to properties. It affects the safety of the locals and the government needs to help for repairing damaged houses. The government subsidizes the redevelopment of housing and builds some basic facilities for the affected areas. Therefore, it is suggested to create a calculation to estimate the vulnerability of the building, and the factors of calculation includes the building damage degree, building use and building type. If the material of the building is weak such as aluminum for temporary building, the building structure will easily failed to resist the impact pressure of the landfill failure. The high building damage degree can cause serious property damage because there are many damage area require to repair and the maintenance cost of the area is higher than relatively less damage degree of the building. Also, the building type can affect the vulnerability of

Table 3. Information of all buildings

Building no.	Long (m)	Width (m)	Height (m)	Storey	X	Dimension (mm)	Y	Dimension (mm)
A1	75	36	4	6	1	7500	5	7200
A2	43	19	4	6	5	8600	3	6333
A3	65	40	4	6	1	6500	6	6667
B4	57	19	4	6	8	7125	3	6333
B5	47	22	4	6	6	7833	4	5500
B6	69	38	4	6	1	6900	6	6333
C7	57	19	4	6	8	7125	3	6333
C8	57	19	4	6	8	7125	3	6333
21 assuming cases	75	32	4	1/3/6	1	7500	5	6400

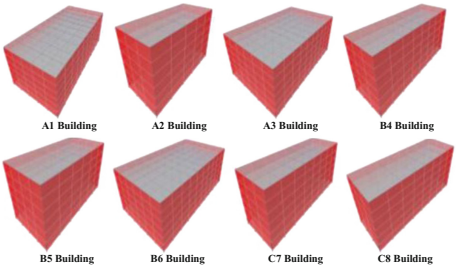

Fig. 4. Model of A1 to C8 Building in ETABS

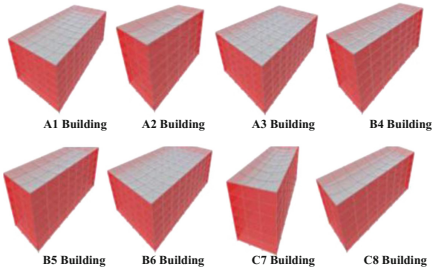

Fig. 5. Deformed shape of A1 to C8 Building

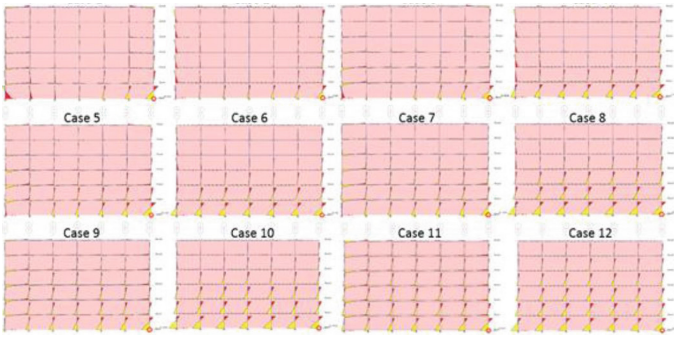

Fig. 6. Bending moment of the case 1–12 (Y-Direction)

the building, as the building use may affect the local economy such as commercial. After entering the vulnerability of building and the impact pressure of each building to the chart (see Table 4), the line chart of vulnerability of the building of this landfill failure will be created (see Fig. 8).

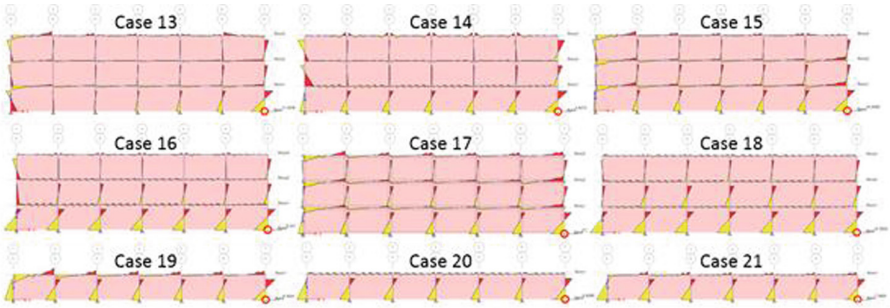

Fig. 7. Bending moment of the case 13–21 (Y-Direction)

Table 4. Calculation of vulnerability of building

Building no.	Building damage degree	Building use	Building type	Vulnerability of building	Pressure (kN/m^2)
A1	1	1	0.8	0.8	44.73
A2	1	0.7	0.8	0.56	42.76
A3	1	0.5	1	0.5	41.00
B4	0.8	1	1	0.8	33.94
B5	0.8	0.5	1	0.4	33.79
B6	0.8	0.7	0.3	0.168	35.14
C7	0.3	0.5	1	0.15	31.93
C8	0.3	0.7	0.3	0.063	30.37

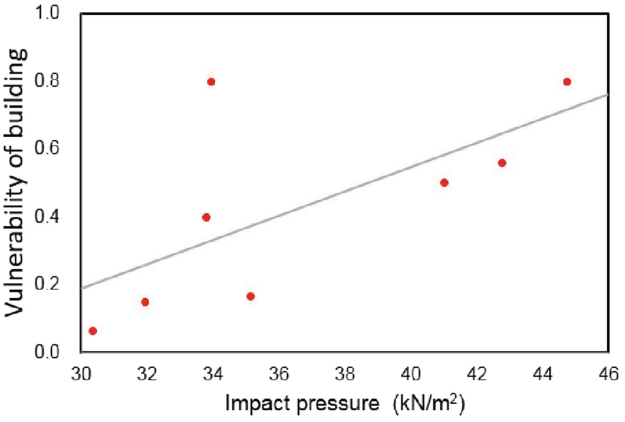

Fig. 8. Vulnerability curve of building of Shenzhen landfill failure

For the vulnerability of building with different damage, after calculating the impact pressure of each floor and the vulnerability of different type and use of the building, the relationship of that will be demonstrated. Whether it is a one storey building, three storey building or six storey building. The vulnerability is proportional to the maximum bending moment of the building. Since the greater bending moment will increase the damage degree of building and the casualties in the study area.

6 Conclusions and Suggestions

This landfill failure occurred in Shenzhen 2015, it led 69 total death and 8 missing. Since the accumulation rate of the solid waste and total volume of the waste filling were in excess of the design capacity, and there were a lot of excess pore water located on the slope to increase the pressure of the landfill. Furthermore, the waste pile in the landfill have increased, resulting in the pile being too high for the overall slope angle and the pile being too steep for the final pile height, which caused the landslide. From this paper, following conclusion can be drawn.

(i) In this paper, the damaged buildings are divided into three zones. The distance between the buildings in different zones and the landfill is different, and the impact pressure of the landfill failure is different. In the zone A, the distance of building A1 is 846 m, and the impact pressure is 44.73 kN/m^2, but in the zone C, the distance of C8 is 1246 m, correspondingly the impact pressure is 30.37kN/m^2. Therefore, the closer the distance, the greater the impact pressure received by the building.

(ii) It is concluded from the vulnerability curve of building of Shenzhen landfill failure that the vulnerability of building is 0.063 and building damage degree is 0.3 when the impact pressure is 30.37 kN/m^2. When the impact pressure increases to 44.73 kN/m^2, the vulnerability of building reaches 0.8 and the building damage degree reaches 1. Moreover, the vulnerability increases with the impact pressure. Accordingly, impact pressure and the vulnerability of building generally have a linear correlation. The closer the building is to the landfill, the greater the impact pressure and the more severe the damage.

It is suggested that engineers should create some new defensive measures and develop some policies to avoid serious casualties or property effects when the next landfill failure occurs. It is recommended that surface water drainage systems should be installed on site, particularly above and around the dump site. Since constructing a surface water drainage systems inside the waste pile can prevent water from flowing into the dump site and help drain the pile.

References

Bell R, Glade T (2004) Quantitative risk analysis for landslide–Examples from Bildudalur, NW-Iceland. Nat Hazards Earth Syst Sci 4(1):117–131

Walker P (2015) Shenzhen landslide: 85 still missing after construction waste hits buildings. https://www.theguardian.com/china-landslide-dozens-missing-shenzhen-construction-waste-collapses. Accessed 21 Dec 2015

Blong RJ, Grasso P, Jenkins SF, Magill CR, Wilson TM (2017) Estimating building vulnerability to volcanic ash fall for insurance and other purposes. J Appl Volcanol 6(1):1–13

Singhal A, Kiremidjian AS (1996) Method for probabilistic evaluation of seismic structural damage. J Struct Eng 122(12):1459–1467

Xu Q, Liu H, Ran J, Li W, Sun X (2016) Field monitoring of groundwater responses to heavy rainfalls and the early warning of the Kualiangzi landslide in Sichuan Basin, southwestern China. Landslides 13(6):1555–1570

Zhan LT, Zhang Z, Chen YM, Chen R, Zhang S, Liu J, Li AG (2018) The 2015 Shenzhen catastrophic landslide in a construction waste dump: reconstitution of dump structure and failure mechanisms via geotechnical investigations. Eng Geol 238:15–26

Zhang S, Zhang LM, Peng M, Zhang LL, Zhao HF, Chen XH (2012) Assessment of risks of loose landslide deposits formed by the 2008 Wenchuan earthquake. Nat Hazards Earth Syst Sci 12(5):1381–1392

Zou DH (2016) Exploring a waste dump site failure – possible causes and prevention measures. Int J Geo-Hazards Environ 2(1):25–33

Quantitative Assessment of Human Risk from Landfill Failure in Shenzhen, China

S. Zhang(✉), C. Li, and Y. Liu

MOE Key Laboratory of Soft Soils and Geoenvironmental Engineering, Zhejiang University, Yuhangtang Road 866#, Hangzhou 310058, China
zhangshuaiqj@zju.edu.cn

Abstract. Seventy-three people dead and 4 people missing in a landfill failure occurred at Shenzhen, China at 11:40 a.m. 20 December 2015. The Shenzhen landfill failure was caused by the accumulation of waste in a former quarry in the Shenzhen. To evaluate the loss of life caused by the Shenzhen landfill failure, a quantitative risk assessment was conducted. The risk could be defined as the product of the probability of occurrence, the consequence and the element at risk in a quantitative measurement. A slope model is used to analyze the slope stability and reliability. The runout behavior, temporal-spatial probability, and the element at risk are analyzed. The vulnerability factor is referred to established table based on different degree of damaged buildings. The potential annual loss of life from a single hazard is then obtained by combining the probability of occurrence and the consequence as a societal risk. The societal risk is visualized and evaluated by the presentation of F-N curves resulting in an unacceptable region which proved that the real case of landfill failure was under an unacceptable risk. This study provides a quantitative way for the risk assessment of Shenzhen landfill failure and develops a risk assessment model for landfill.

Keywords: Landfill · Failure · Slopes · Stability · Risk assessment

1 Introduction

The Shenzhen landfill failure caused total death toll of 69 and 8 missing and damaged 33 buildings. The damaged buildings were located in the Hengtaiyu Industrial Park, Guangming New District of Shenzhen, China (Fig. 1). The landslide volume was about 2.7×10^6 m^3 and its covering area was about 3.8×10^5 m^2. The length and maximum width of landslide were about 1100 m and 630 m respectively. The failure may be triggered by the high porewater pressure leading to a phenomenon 'liquefaction' (Xu et al. 2016). To evaluate the risk of Shenzhen landfill failure, a quantitative risk assessment should be established. This paper aims to quantify the human risk posed by the Shenzhen landfill failure. Required data is collected by Google earth and literatures to achieve the above research objectives.

© Springer Nature Singapore Pte Ltd. 2019
L. Zhan et al. (Eds.): ICEG 2018, ESE, pp. 564–572, 2019.
https://doi.org/10.1007/978-981-13-2227-3_69

Fig. 1. Location of landfill failure

2 Methodology

Risk could be presented as societal risk which concerns the risk to the population as a whole, independent of geographical location and individual risk which regards the risk to a single person at a specific location (Zhang et al. 2012). The societal risk could be expressed in terms of a F-N curve and annual potential loss of life. The F and N in F-N curve are the cumulatively frequency of N or more fatalities against the number of fatalities on a log-log scale (Zhang et al. 2012). The annual potential loss of life is the sum of the products of the conditional temporary and spatial probabilities and the consequence caused by the individual loose deposits.

A simply equation could express the risk assessment calculation (Morgan et al. 1992):

$$\mathrm{R} = (\mathrm{H} \times \mathrm{C} \times \mathrm{E}) \tag{1}$$

where H = probability of occurrence of a potentially damaging event within a given period of time, a given area and with a given magnitude, C = (potential) outcomes arising from the occurrence of an event, E = elements at risk (people in buildings),

The annual potential loss of life ($\mathrm{R}_{(\mathrm{LOL})}$) could be calculated as the following equation (Morgan et al. 1992):

$$R_{(\mathrm{LOL})} = \sum_{i=1}^{n} \left[P_{(L)i} \times P_{(T:L)i} \times P_{(S:T)i} \times V_{(D:T)i} \times E_i\right] \tag{2}$$

where $\mathrm{P}_{(\mathrm{L})}$ is the annual probability of occurrence of landfill failure, $\mathrm{P}_{(\mathrm{T:L})}$ is the probability of landfill failure reaching the highway, $\mathrm{P}_{(\mathrm{S:T})}$ is the temporal spatial probability of the element at risk, $\mathrm{V}_{(\mathrm{D:T})}$ is the vulnerability of the person to the landfill failure event (i.e. the chance of losing life when a person is impacted by the landfill failure), E is the number of persons at risk.

The individual risk of loss of life($P_{(DI)}$) could be calculated as the following equation (Australian Geomechanics Society Sub-Committee on Landslide Risk Management 2000):

$$R_{(\mathrm{LOL})} = \sum_{i=1}^{n} \left[P_{(L)i} \times P_{(T:L)i} \times P_{(S:T)i} \times V_{(D:T)i}\right] \tag{3}$$

2.1 Determination of Occurrence Probability

Stability Analysis

A numerical modelling was adopted in this paper to measure the failure probability by using Slope/W. The stability of the landfill could be analyzed by the factor of safety. The factors include slope profile, slope angle, slope height, slope length, soil strength, and water condition. The slope profile of slope height, slope angle, and slope length was based on the Google Earth. The landfill material strength can be defined as three parameters which are cohesion, friction angle and unit weight (c, Φ, γ). The value of the landfill strength was estimated by the empirical soil properties. The landfill layers were estimated by observation of the variation of the changes of the landfill topography.

Reliability Analysis

The reliability analysis could be used for the evaluation of above uncertainty. Four steps to obtain the reliability analysis proposed by Duncan (2000) are adopted. The equation below shows the calculation of lognormal reliability index.

$$\beta_{LN} = \frac{ln\left(\frac{F_{MLV}}{\sqrt{1+V^2}}\right)}{\sqrt{\ln(1+V^2)}} \tag{4}$$

where β_{LN} = lognormal reliability index; V = coefficient of variation of factor of safety; and F_{MLV} = most likely value of factor of safety. When β_{LN} has been computed, the value of P_L can be determined. The assumption is made that there is a lognormal distribution of factor of safety values.

Determination of Occurrence Probability

The failure probability P_f could be found by using the value of lognormal reliability index (β_{LN}). Duncan (2000) proposed to use the built-in function NORMSDIST in Excel.

2.2 Runout Distance Analysis

$P_{(T:L)}$ is measured by taking considered in the travel distance of the landslide, the location of the source landslide, and the element at risk for the situation of the buildings or persons located below the source area of the landslide and in the path of the resulting travel distance of the landslide. (Fell et al. 2005) The probability of a landfill failure reaching the elements at risk and the vulnerability factor can be obtained by the runout

distance of the landfill failure. In Fig. 2, where L is the run-out distance, L_0 is the projected distance from the landfill failure scar to the inside edge of the buildings, and ΔL is the travel difference between L and L_0, which denotes the distance that the landfill failure debris runs out beyond the inside edge of the buildings. $\Delta L > L_f$ indicates that the landfill failure debris buries the buildings, whereas a negative $\Delta L < L_f$ value reveals that the landfill failure debris does not reach the buildings and hence imposes no risk to people on the buildings.

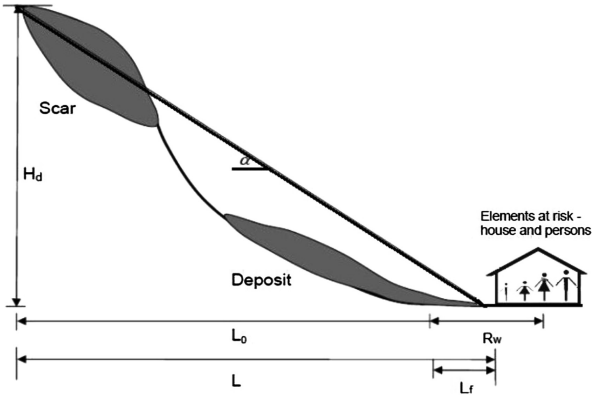

Fig. 2. Runout distance analysis scheme

Here, the relation proposed by Corominas (1996) is adopted:

$$\frac{H_d}{L} = AV^B \tag{5}$$

where H_d is the elevation difference; L is the runout distance; V is the landslide volume calculated by multiplying the depth of sliding surface by the slide area A and B are random variables.

2.3 Temporal Spatial Probability

As no survey is done to evaluate the occupancy of the houses, it shows that the person is mostly at risk when he is in one of the houses. So the temporal spatial probability can be calculated by how long people stay in the house.

2.4 Vulnerability Assessment

In this case, most buildings are collapsed by the Shenzhen landfill failure and the corresponding vulnerability factor is 1.0. Some buildings are inundated with debris and person is buried in this case and its corresponding vulnerability factor is 0.8. Debris strikes the building only and its corresponding vulnerability factor is 0.3. If no damaged is affected the buildings and person its corresponding vulnerability factor is 0.

2.5 Element at Risk

Element at risk is the number of people exposed at risk. The equation for measuring the element at risk is as follow:

$$E = \frac{Ia}{Id} + \frac{Ca}{Cd} + \frac{Ra}{Rd} \tag{6}$$

where I_a is the area of industrial building, I_d is the population density of industrial building, C_a is the area of commercial building, C_d is the population density of commercial building, R_a is the population density of residential building, R_d is the area of residential building.

3 Result of Quantitative Risk Assessment

By using the Slope/W model, the result presents the possible factor of the landfill in four stages. The stages were based on geomorphic photo from Google Earth (Fig. 3). The Slope/W simulates the slope model and failure model of the four stages. Figure 4 shows the final stage of slope model and failure model. The factor of safety decreased with adding terrains. The lowest factor of safety was in the final slope model which was 1.347. With $F_{MLV} = 1.347$ and $V = 44\%$, is $\beta_{LN} = 0.4977$. The standard cumulative normal distribution function (the reliability) corresponding to $\beta_{LN} = 0.4977$ is 0.6907 by excel. The probability of failure is one minus the reliability, $P_f = 1 - 0.6907 = 30.93\%$.

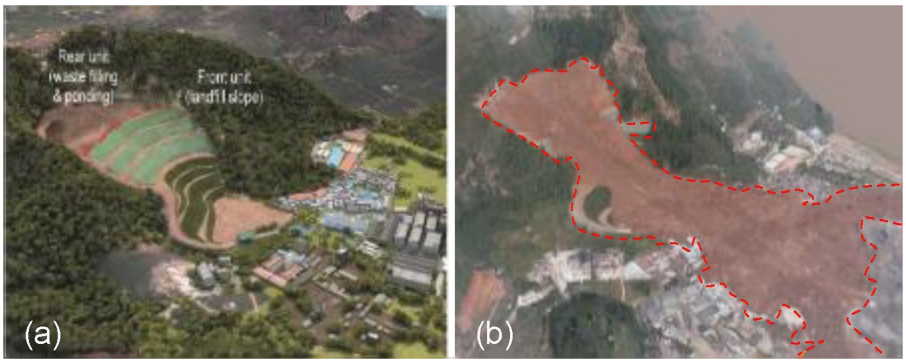

Fig. 3. Evolution of topography of the landfill failure: (a) before sliding; (b) after sliding. (after Xu et al. 2016)

An assumption is made that the random variables as coefficients A (0.719) and B (−0.08) follow normal distribution with a coefficient of variation of 0.2. The Monte Carlo simulation generates of 10,000 pairs of random variables for determining the probability of loose deposits reaching the buildings. The runout distance and elevation

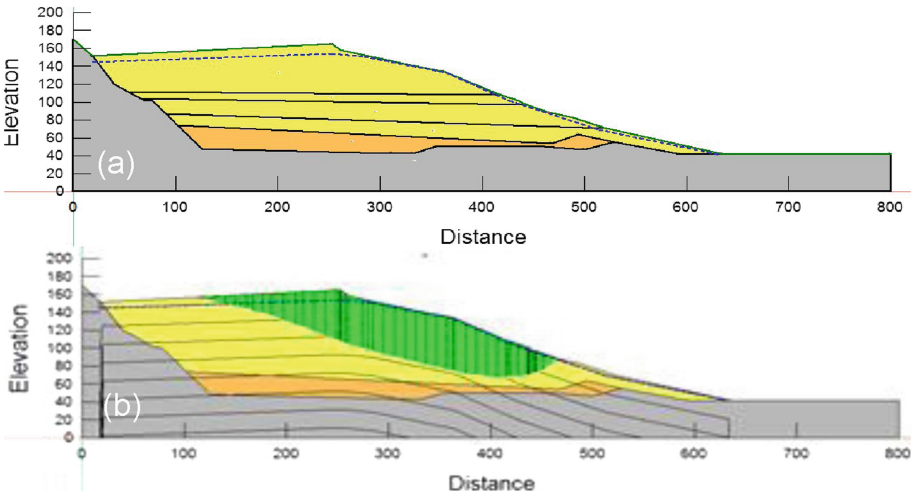

Fig. 4. Final stage of Slope/W simulation: (a) slope model; (b) failure model.

of the flow slide was 1204.67 m and 111.31 m respectively. (Xu et al. 2016) Therefore, the probability of loose deposits reaching the buildings which is equal to 0.54%.

A survey showed that most of the industrial workers began their work at 8:00 a.m. and got off at 7:00 p.m. in the Shenzhen Industrial Park (Didi research and CBN Data, 2016). The statutory holidays in China is 11 days. Therefore, $P_{(S:T)} = 11/24 \times 354/365 = 44.45\%$.

The GIS map has shown the location of the buildings and there are various photos taken in different degree of damaged of the buildings. To present the vulnerability factor quantitatively, each building vulnerability factor would be measured as an average value which is 0.42. By using GIS, the total number of building in the studied area can be measured (Fig. 5). The total number of people occupied in all 344 building is the element at risk which can be estimated by the area of each type of the building divided to the population density specified in Hong Kong Planning Standard and Guidelines. There are three types of building which are industrial, commercial and residential building. There are 195 industrial building, 34 commercial building, and 115 residential building. The area of the industrial building is 113150.8 m^2. The area of the commercial building is 18441.4 m^2. The area of the residential building is 57075.3 m^2. The overall area of the building is 188667.4 m^2. The population density of commercial and residential building is 25-m^2 per people. The population density of industrial building is 10000-m^2 per 300 people. So $E = \frac{113150.8}{\left(\frac{10000}{300}\right)} \times \frac{18441.4}{25} \times \frac{57075.3}{25} = 3040$.

With the given values of the probability of failure, the element at risk, and the vulnerability factor for the Shenzhen landfill failure, the societal risk could be presented as ($R_{(LOL)}$) and F-N curves. The $R_{(LOL)} = 30.93\% \times 0.54\% \times 44.45\% \times 0.42 \times 3040 = 0.9480$/annual. The individual risk is presented as the $R_{(LOL)} = 30.93\% \times 0.54\% \times 44.45\% \times 0.42 = 3.118 \times 10^{-4}$/annual.

Fig. 5. Distribution of element at risk before the event.

The F-N curve can be used to explain the risks and evaluated the acceptability. Since our study area had no the risk acceptability criteria, so the risk of Hong Kong acceptability criteria is used to assess the risk of potential harm our study area, as an indicator.

In an F-N curve, regions of acceptable, as low as practicable reasonable (ALAPR) and unacceptable are defined in the graph. The acceptable risk boundary consists of a line with slope of −1 and y-intercept of 10^{-5} accidents at 1 or more fatalities per year, and the maximum acceptable number of fatalities is 1000 regardless of occurrence probability. The ALARP boundary is a line with slope of −1 and y-intercept of 10^{-3} accidents at 1 or more fatalities per year, and similarly, the maximum acceptable number of fatalities is 1000 regardless of occurrence probability (GEO 1998).

By inspecting the F-N curve, the graph show that the case was located in the unacceptable regions. It indicated the case is hazardous (Fig. 6). Thus, mitigation measures should be implemented. The high risk may be due to the large number of the population.

4 Summary and Conclusions

Seventy-three people dead and 4 people missing in a landfill failure located at Shenzhen, China at 11:40 a.m. 20 December 2015. The Shenzhen landfill failure was caused by the accumulation of waste in a former quarry in the Shenzhen. A quantitative risk assessment was adopted to evaluate the risk of the Shenzhen landfill failure. The risk could be defined as the product of the probability of occurrence, the consequence and the element at risk in a quantitative measurement. The runout distance analysis, temporal spatial probability, and the element at risk are calculated. The vulnerability factor is referred to established table. The potential annual loss of life from a single hazard is

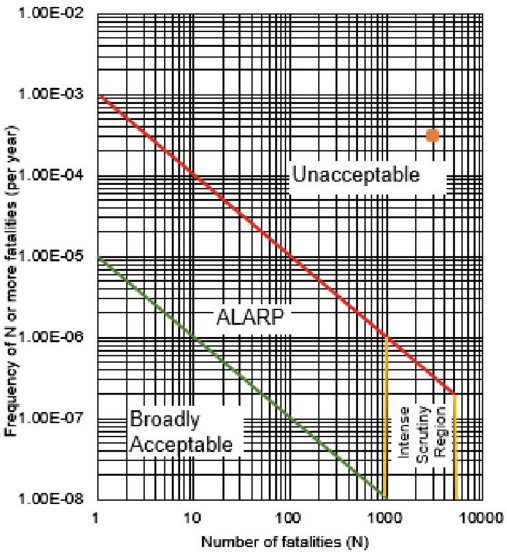

Fig. 6. F-N curve

then obtained by combining the probability of occurrence and the consequence. The societal risk is visualized and evaluated by the presentation of an F-N curve. Several conclusions can be drawn:

(1) A slope model is used to analyze the slop stability and reliability which were based on estimation of the soil strength and slope profile by Google Earth. The factor of safety of the landfill was continuously decrease from 2008 to 2015. The final stage of factor of safety is 1.347 which is an unstable value. The reliability analysis has considered the uncertainty of the soil strength. With the reliability, the failure probability could be measured and it equal to 30.93%.

(2) The runout distance was measured by an empirical relation which is using the volume of the landfill and the elevation of the slope to analyze whether the runout distance reached the affected area by the Monte Carlo simulation. The result indicated the probability of the runout distance reach affected area was low as the runout distance was long. The vulnerability factor is result by the situation of the landfill failure which is collapse.

(3) Risk defined as societal risk in two ways which are F-N curve and the potential annual loss of life. With the high failure probability and the high vulnerability factor, the potential annual loss of life is equal to 0.9480/annual. The individual risk is 3.118×10^{-4}/annual. The F-N curve also the case is in unacceptable regions which indicated the case was hazardous.

References

Australian Geomechanics Society Sub-Committee on Landslide Risk Management (2000) Landslide risk management concepts and guidelines. Aust Geomech 35:49–92

Corominas J (1996) The angle of reach as a mobility index for small and large landslides. Can Geotech J 33:260–271

Duncan JM (2000) Factors of safety and reliability in geotechnical engineering. J Geotech Geoenviron Eng 126:307–316

Fell R, Ho K, Lacasse S, Leroi E (2005) A framework for landslide risk assessment. In: Proceedings of the international conference on landslide risk management, Vancouver, Canada, pp 3–25

Geotechnical Engineering Office (GEO) (1998) Landslides and boulder falls from natural terrain: interim risk guidelines. GEO Report No. 75. Geotechnical Engineering Office, Hong Kong, p 183

Morgan GC, Rawlings GE, Sobkowicz JC (1992) Evaluating total risk to communities form large debris flows. In: Proceedings of the 1st Canadian symposium on geotechnique and natural hazards, Vancouver, Canada, pp 225–236

Xu Q, Peng DL, Dong XJ, Hu W, Tang MG, Liu FZ (2016) "The catastrophic landfill flowslide At Hongao Dumpsite" on December 20, 2015 in Shenzhen, China. Nat Hazards Earth Syst Sci 17:1–19

Zhang S, Zhang LM, Peng M, Zhang LL, Zhao HF, Chan HX (2012) Assessment of risks of loose landslide deposits formed by the 2008 Wenchuan earthquake, pp 11–41

Correction to: Proceedings of the 8th International Congress on Environmental Geotechnics Volume 3

Liangtong Zhan, Yunmin Chen, and Abdelmalek Bouazza

Correction to:
L. Zhan et al. (Eds.):
***Proceedings of the 8th International Congress on Environmental Geotechnics Volume 3*, ESE,**
https://doi.org/10.1007/978-981-13-2227-3

The original version of the book was inadvertently published without incorporating the author corrections. The book has been updated with the changes.

The updated version of the book can be found at
https://doi.org/10.1007/978-981-13-2227-3

© Springer Nature Singapore Pte Ltd. 2019
L. Zhan et al. (Eds.): ICEG 2018, ESE, p. C1, 2019.
https://doi.org/10.1007/978-981-13-2227-3_70

Author Index

© Springer Nature Singapore Pte Ltd. 2019
L. Zhan et al. (Eds.): ICEG 2018, ESE, pp. 573–575, 2019.
https://doi.org/10.1007/978-981-13-2227-3